HOW THE GALACTIC CENTRE ENVIRONMENT IMPACTS STAR FORMATION

Daniel Callanan

A thesis submitted in partial fulfilment of the requirements of
Liverpool John Moores University
for the degree of
Doctor of Philosophy

July 2021

Declaration

The work presented in this thesis was carried out at the Astrophysics Research Institute, Liverpool John Moores University. Unless otherwise stated, it is the original work of the author.

The data calibration for the CMZoom survey was completed by the entire survey team prior to my joining. My role in the project was to lead the imaging and analysis of all the spectral line data.

While registered as a candidate for the degree of Doctor of Philosophy, for which submission is now made, the author has not been registered as a candidate for any other award. This thesis has not been submitted in whole, or in part, for any other degree.

Daniel Callanan
Astrophysics Research Institute
Liverpool John Moores University
146 Brownlow Hill
Liverpool
L3 5RF
UK

July 2021

Abstract

In the centres of the Milky Way and M83, the global environmental properties thought to control star formation are indistinguishable within observational uncertainties. Despite this, present-day star formation rates in the centres of each galaxy differ by an order of magnitude. In this thesis, I explore the gas kinematics of both regions to understand the origin of this difference.

In Chapter 2, I present an overview and data release of the spectral line component of the SMA Large Program, *CMZoom*. The *CMZoom* survey targeted 10 dense gas and shock tracers in all gas within the Central Molecular Zone (CMZ; inner few hundred pc of the Galaxy) above a column density of $N(H_2) \geq 10^{23}\,cm^{-2}$, between an observing frequency of 216−232 GHz, including three CO isotopologues, multiple transitions of H_2CO, SiO, OCS and SO. I extracted spectra from all compact 230 GHz continuum sources (cores) in the previously published *CMZoom* catalogue and fit line profiles to the spectra. After detailed quality controls, I used the fit results from the H_2CO 3(0,3)-2(0,2) transition – which represents 88.8% of the total mass of *CMZoom* cores – to determine the core kinematic properties. I find that only four cores are self-gravitating, but that the remainder are consistent with being in hydrostatic equilibrium and confined by the high external pressure in the Galactic Centre. Using star formation tracer associations from an forthcoming publication, I estimate a present-day star formation rate of 0.009 $M_\odot\ yr^{-1}$ for all cores in the Galactic Centre with an H_2CO detection. I find that the line ratios of *CMZoom* cores in the Galactic Centre are indistinguishable from *CMZoom* cores which lie outside the Galactic Centre. This suggests that the chemical differences observed between the CMZ and disk clouds does not propagate down to core scales. I find only two convincing proto-stellar outflows throughout the survey, ruling out the possibility of a previously undetected population of forming high-mass stars. Despite having sufficient sensitivity and resolution, in the large *CMZoom* survey area I find

no high-velocity compact clouds (HVCCs) which have been claimed as evidence for intermediate mass black holes interacting with molecular gas clouds.

In Chapter 3, I use ALMA observations of HCN $(1-0)$ and HCO^+ $(1-0)$ to trace the dense gas at the size scale of individual molecular clouds ($0.54''$, 12pc) in the inner $\sim$500 pc of M83, and compare this to gas clouds at similar resolution and galactocentric radius in the Milky Way. I find that both the overall gas distribution and the properties of individual clouds are very similar in the two galaxies, and that a common mechanism may be responsible for instigating star formation in both circumnuclear rings. Given the remarkable similarity in gas properties, the most likely explanation for the order of magnitude difference in SFR is time variability, with the Central Molecular Zone (CMZ) currently being at a more quiescent phase of its star formation cycle. I show M83's SFR must have been an order of magnitude higher $5-7$ Myr ago. M83's 'starburst' phase was highly localised, both spatially and temporally, greatly increasing the feedback efficiency and ability to drive galactic-scale outflows. This highly dynamic nature of star formation and feedback cycles in galaxy centres means (i) modeling and interpreting observations must avoid averaging over large spatial areas or timescales, and (ii) understanding the multi-scale processes controlling these cycles requires comparing snapshots of a statistical sample of galaxies in different evolutionary stages.

Publications

Within this thesis, the work within Chapters 2 and 3 have been submitted in the following publications:

1. *CMZoom III: Spectral Line Data Release*
D. Callanan, S. N. Longmore, H. P. Hatchfield, J. D. Henshaw, D. Walker, C. Battersby, E. Keto, A. Barnes, A. Ginsburg, J. Kauffmann, J. M. D. Kruijssen, X. Lu, E. A. C. Mills, T. Pillai, Q. Zhang, J. Bally, N. Butterfield, Y. A. Contreras, L. C. Ho, K. Immer, K. G. Johnston, J. Ott, N. Patel and V. Tolls, MNRAS, in prep.

2. *Twins at Heart: The Centres of M83 and the Milky Way as Opposite Extremes of a Common Star Formation Cycle*
D. Callanan, S. N. Longmore, J. M. D. Kruijssen, A. Schruba, A. Ginsburg, M. R. Krumholz, N. Bastian, J. Alves, J. D. Henshaw, J. H. Knapen and M. Chevance, MNRAS, Submitted

Whilst writing this thesis, D. Callanan has also contributed to the following publications, which are focused on topics related to the thesis work:

3. *CMZoom: Survey Overview and First Data Release*
C. Battersby, E. Keto, D. Walker, A. Barnes, **D. Callanan**, A. Ginsburg, H. P. Hatchfield, J. Henshaw, J. Kauffmann, J. M. D. Kruijssen, S. N. Longmore, X. Lu, E. A. C. Mills, T. Pillai, Q. Zhang, J. Bally, N. Butterfield, Y. A. Contreras, L. C. Ho, K. Immer, K. G. Johnston, J. Ott, N. Patel and V. Tolls, MNRAS, 2020

4. *CMZoom. II. Catalog of Compact Submillimeter Dust Continuum Sources in the Milky Way's Central Molecular Zone*
H. Perry Hatchfield, C. Battersby, E Keto, D Walker, A. Barnes, **D. Callanan,** A.

Ginsburg, J. D. Henshaw, J. Kauffmann, J. M. D. Kruijssen, S. N. Longmore, X. Lu, E. A. C. Mills, T. Pillai, Q. Zhang, J. Bally, N. Butterfield, Y. A Contreras, L. C. Ho, J. Ott, N. Patel and V. Tolls, APJS, 2020

Acknowledgements

I'd like to begin by thanking my supervisor, Steven Longmore, whose support and experience has helped me to confidently pursue this PhD. His encouragement led me to step out of my comfort zone and give talks at international conferences and even moving to the US. Secondly, I'd like to thank Qizhou Zhang as my supervisor at Harvard University. He welcomed me into his group at the Centre for Astrophysics and provided his wealth of experience in interferometric data to help me with the otherwise daunting task of imaging the CMZoom survey.

I also owe a special thanks to Cara Battersby, who welcomed me into the CMZoom project and supported me greatly in my role leading the spectral line side of imaging. I am also grateful to Diederik Kruijssen, Andreas Schruba, Adam Ginsburg, Mark Krumholz, Nate Bastian, Joao Alves, Jonathan Henshaw, Johan H. Knapen, Mélanie Chevance, Dan Walker, Ashley Barnes and the rest of the CMZoom team for their feedback on papers, figures and code since the very beginning.

I almost certainly wouldn't have made it to this point without the far too regular coffee breaks I took with my office (and occasional flat)-mates, so thanks to Kirsty, Jon, Egidijus, Hannah, Seb and Maisie for the distractions. Special thanks to Kirsty, who suffered through numerous sunday work sessions with me to get our theses to this stage.

Lastly I would like to thank my friends, family and girlfriend. My parents for supporting me in pursuing my interests and passions from the very start, my friends for the nights of distractions and in the case of Melissa Hale and Rhys Hawker for helping me find a new obsession in bouldering, and lastly my girlfriend Jessica Going for the ongoing support through thick and thin of the process.

Daniel Callanan July 2021

"Here we stand, feet planted in the earth, but might the cosmos be very near us, only just above our heads?"

Cosmic Eye Watcher Badge, Bloodborne

Contents

List of Figures

List of Tables

Chapter 1

Introduction

A key finding of modern astrophysics research is that the mass flows and energy cycles that take place in the centres of galaxies play a vital role in shaping galaxy populations and the Universe at large. The aim of this thesis is to tackle some of the open questions in understanding these mass flows and energy cycles through detailed observational studies of nearby galaxies, including our own. However, it is only surprisingly recently that the structure of the Milky Way was uncovered, and the 'Galactic centre' became a region of great interest. In order to place my thesis results in the wider context of intellectual discovery, I therefore begin by providing some historical background of how we came to know our place in the Universe, and the breakthroughs required to reach our current understanding of Galactic structure.

1.1 Our Place in the Universe: A Historical Context

For as long as humanity has looked up at the night sky, we have pondered the fundamental question: "What is our place in the Universe?" Early attempts to explain the motions of the stars and planets, dating back to several hundred years BC, assumed that the Earth sat at the very centre of the Universe with all other celestial bodies orbiting around it. These ideas weren't refined into a predictive model until the 2^{nd} century AD by the Greek polymath Claudius Ptolemaeus (Ptolemy). In his work *The Amalgest*, Ptolemy argued that all stars in the night sky sat at the same distance from the Earth and as the number of stars above and below the horizon were roughly equal, the Earth

must be at the centre of the Universe, as any displacement in the Earth's position would change the distribution of stars.

Arguments against geocentric models of the Universe were made well before and well after this formalism, but in general Ptolemy's model held for many centuries. The first real contender was Copernicus' *On the Revolutions of the Heavenly Spheres* in 1543, in which Copernicus posited that the Earth and all other planets orbited the Sun. This model struggled to take hold, however, as it proved no more accurate at predicting the motion of celestial bodies than the model of Ptolemy. The invention of the telescope, and the subsequent discovery of Jupiter's moons, weakened Ptolemy's model further, as these moons were orbiting Jupiter and not Earth, calling into question the fundamental basis of Ptolemy's model that everything orbitted Earth. Further problems with Ptolemy's model came in the form of observations of Venus showing similar phases as the moon, as this model expected only crescent and dark or gibbous and full but not all phases. Further work into the elliptical orbits of planets (by Kepler) and the measurement of distances to stars using parallax (by Bessel) continued to weaken the geocentric model of the Universe until eventually the heliocentric model became the de facto description of the Universe. These parallax measurements were important for two reasons: firstly, Ptolemy asserted that the parallax motion of stars does not exist so a measurement of such was a significant flaw in this model, and secondly, this measurement showed for the first time just how distant these stars were.

The invention of the telescope also lead to the discovery that the Milky Way - the bright disk that gives our Galaxy its name - was made up of a vast population of stars too faint for the human eye to see. Based on these observations and work by Thomas Wright, who suggested the appearance of the Milky Way was an optical effect caused by our solar system being immersed in a flat layer of stars, Immanuel Kant suggested that the Milky Way was an 'island universe' - a large collection of stars held together by gravity in much the same way our Solar System is. Kant also suggested that some nebula that had been observed were in fact external 'island universe's and not a part of the Milky Way. This was the first time the notion of a 'galaxy' entered the conversation.

The question of the nature of these nebulae culminated in *The Great Debate*, involving two prominent astronomers - Harlow Shapley and Heber Curtis. Harlow Shapley was of the opinion that that Milky Way was the entire universe, and nebulae like the Andromeda

nebula had to be at an (at the time) incomprehensible distance to be outside the Milky Way given their relative sizes. On the other side of the debate, Curtis observed a number of novae within the Andromeda nebula, a larger population than observed elsewhere in the Milky Way. This lead Curtis to support the 'island universe' notion, as this population of novae implied that Andromeda had a different nova rate and age than the Milky Way. One point that Curtis conceded was the claim by Van Maanen that he had observed the Pinwheel Galaxy rotating. Given the rotation speed that Van Maanen measured, if it were an external galaxy it would be rotating at an orbital velocity in excess of the speed of light. This, however, was resolved quite simply as this claimed rotation was incorrect and the Pinwheel Galaxy can not be seen to rotate over such a short period of time. The debate itself was resolved not long afterwards due to the revolutionary work of Edwin Hubble, who used a new telescope to resolve the outer parts of these controversial nebulae, finding them to be collections of stars. He also devised a new technique for distance estimates using Cepheid variables, finding Andromeda to be well outside of the current size estimate of the Milky Way.

1.2 Finding the Centre of Our Galaxy

Once the nature of the Milky Way was settled, people were naturally curious about what sat at the very centre of the Galaxy. As a result of the vast amounts of interstellar dust that sits between us and the centre of our Galaxy, observations of the region with the naked eye are impossible. Despite this, Kant (1755) posited that a large star (potentially Sirius) claimed the title. The Sagittarius constellation entered the conversation with Shapley (1918) using parallax distances to Milky Way's halo of globular clusters to estimate the location of the centre, placing it roughly within the constellation.

Baade (1946) tied the probability of observing the nucleus of our Galaxy to the type of Galaxy we lived in, because of the varying size of the nucleus within differing galaxy types. In the instance of a late type (Sc) galaxy, the nucleus would be too small to be observable given the limitations of technology at the time, whereas the nuclei of early type (Sb) galaxies is large enough to potentially observe the outer regions of the nucleus. In attempting to test this, Baade (1946) discovered a small gap (now referred to as Baade's window) in this thick dust that allowed for a relatively clear view of the population of stars surrounding the nucleus. With the advancement in

radio astronomy came equally rapid advancements in our knowledge of the Galactic centre, because while visible light is significantly attenuated by the intermediate dust, radio waves are unobstructed and can reach us unimpeded. Pawsey (1955) used an early form of interferometry, 'sea-interferometry' to detect a plethora of bright radio sources, including the extremely bright radio belt in Sagittarius. The brightest point source within this radio belt, known now as Sagittarius A, was redefined as the de facto centre of our Galaxy. We now know that Sagittarius A consists of three major components: a supernova remnant called Sagittarius A East, a three-armed 'minispiral' called Sagittarius A West, and lastly, at the bottom of the gravitational potential of our Galaxy, sits Sagittarius A*, a supermassive black hole (SMBH) within the Saggitarius A radio source.

1.3 Thesis Structure Outline

However, the answer to the fundamental question posed at the beginning of this chapter incorporates much more than just where our Solar System sits in just one of billions of galaxies across the Universe. It is also a question of how structures of these various size scales come to be, from solar systems to galaxies. One important process that the evolution of each of these systems share is the formation and evolution of stars. This process is fundamental to understanding how planets form surrounding a star and the ongoing energy output across a star's lifetime from birth to death dictates much of how a galaxy will evolve. However, star formation has not occurred at the same rate since the first generation of stars were formed, meaning the evolution of solar systems and galaxies in turn has not been consistent. To understand this we must probe the process of star formation in all environments and in particular the environment of redshift $z \sim 2$ galaxies where the star formation rate peaked and when the majority of stars in the centres of galaxies were likely forming. While the galaxies themselves are distant and hard to resolve with current telescopes, the conditions of the centre of our Galaxy are similarly extreme and it is therefore the best place to study the environmental dependence of these processes on the smaller scales.

This thesis is structured in the following way: this chapter presents our current understanding on a number of fundamental aspects of this research, with particular focus on the processes and environmental dependence of star formation, as well as the technical

details of interferometric techniques that underpin much of the following works. Chapter 2 presents the spectral line data from the CMZoom survey, a large-scale Submillimetre Array (SMA) survey of the dense gas within the Central Molecular Zone (CMZ). Chapter 3 presents high-resolution ALMA data of the central region of the nearby galaxy M83, a Milky Way analogue that produces stars at a far more rapid rate than our own Galactic centre. These observations are used to infer the extent to which star formation processes depend on the environment and are presented in Callanan et al. (2020).

1.4 Star Formation

As I describe in detail below, the 'how' and 'where' of star formation underpins many important processes across cosmic time. Star formation plays a vital role in the formation and evolution of galaxies and their internal structure. Stars act as factories in which elements more complex than hydrogen and helium are formed, and in death stars both drive the energy and momentum feedback cycles that shape the evolution of galaxies and seed molecular clouds with the elements necessary for the formation of planets and even life.

The 'how' of star formation details the processes by which a cloud composed mainly of hydrogen forms into one, or several stars and how the intermediate phenomenon such as accretion, jets and outflows produced during this process impact the ongoing evolution. The 'where' informs how the environment and conditions in which the molecular cloud sits can impact these processes and the timescales over which they occur.

In this section, I will summarise the current understanding in the field of star formation, and overview the ongoing research into these questions.

1.4.1 Molecular Clouds and Stellar Nurseries

Star formation takes place exclusively within clouds of molecular gas. Observations of external Milky Way-like galaxies (e.g. Schinnerer et al., 2013) suggest that most of these molecular clouds are found in spiral arm structures. Regardless of their location within the galaxy, these molecular clouds do not have consistent masses or sizes. By compiling a number of contemporaneous surveys, Williams & McKee (1997) found the distribution

of molecular cloud mass (M) throughout the plane of the inner Galaxy is well fit to a power law of the form

$$\frac{\mathrm{d}\ N}{\mathrm{d}\ \ln\ M} = N_{\mathrm{cu}} \left(\frac{M_{\mathrm{u}}}{M}\right)^{-(\alpha_M - 1)}, \tag{1.1}$$

where N is the number of molecular clouds per mass bin, M_u is the upper mass limit for which this power law holds which Williams & McKee (1997) found to be 6×10^6 $\mathrm{M}_\odot$, and N_{cu} is the number of clouds near this upper mass limit. Williams & McKee (1997) found this held over a mass range of $10^4 < M < 10^7$. $\alpha_M - 1$ was found to be 1.6 by Williams & McKee (1997) though it has since been refined as this was found not to fit molecular clouds in the outer Galaxy, with Rosolowsky (2005) using a larger number of Galactic plane surveys to estimate an exponent of $\alpha_M - 1 \approx 1.5 - 2.1$ for inner disk molecular clouds and outer disk molecular clouds respectively.

Likewise, the distribution of the physical sizes of the clouds is expressed as

$$\frac{\mathrm{d}N}{\mathrm{d}L} \approx L^{-\alpha_L} \tag{1.2}$$

where L is the beam-corrected diameter, with Elmegreen & Falgarone (1996) estimating $\alpha_L \approx 3.4$. These values imply an interesting population of molecular clouds. While the majority of molecular clouds are small and low mass, a majority of the total mass of molecular clouds are constrained to more massive clouds.

The origin of molecular clouds, in particular the most massive clouds that make up the bulk of the total molecular gas mass, is not well understood. Specifically, there are two main concepts, invoking either a 'bottom-up' or a 'top-down' scenario. The 'bottom-up' scenario describes the process by which smaller and more populous clouds of masses ~ 100 $\mathrm{M}_\odot$ collide in the presence of an external shock wave to form a single larger cloud. While cloud velocities in inter-arm regions of galaxies are low enough that the timescale for this process would be > 100 Myr, clouds within spiral arms have far more frequent collisions and therefore a much shorter build-up timescale. Via simulations of molecular clouds with no stellar feedback Tasker & Tan (2009) found that this mechanism is an efficient way to add turbulence to these small clouds faster than the turbulence can

dissipate. This keeps the molecular clouds somewhat gravitationally bound, as is seen in a large number of molecular clouds observed in the disk.

Blitz & Shu (1980) showed that the timescales involved in the 'bottom-up' scenario are too long to explain the observed populations of molecular clouds, and as a result the 'top-down' scenario was proposed. The 'top-down' scenario (Elmegreen, 1982; Kim & Hong, 1998) invokes large-scale gravitational instabilities to construct molecular clouds and can be broken into two models: the Parker instability (Parker, 1966) and the large scale gravitational instabilities (Toomre, 1964; Goldreich & Lynden-Bell, 1965). The Parker instability is the result of the normally horizontal (with respect to the plane of the disk) magnetic field twisting or buckling, trapping gas within the mid-plane of the disk. While this instability does produce over-densities within the ISM, the extent to which it is capable of producing the more massive molecular clouds is as of yet unknown, with Kim & Ostriker (2006) finding no evidence of the Parker instability controlling the spiral arm substructures that emerge in numerical magneto-hydrodynamic (MHD) simulations. While dependent on magnetic fields, Jiang & Jiang (2019) found that sufficiently large magnetic fields can limit, or even prevent the Parker instability from occurring.

On large scales, gravitational instabilities drive galactic dynamics and have been found to be responsible for the formation of spiral arms (Wada et al., 2011). Galaxy mergers and converging flows can lead to these instabilities forming giant clouds (Li et al., 2005) which are then themselves vulnerable to differential rotation, which can lead to the cloud being sheared and eventually dissipating. The impact of differential rotation on the collapse of a molecular cloud is best described by exploring the counterbalance between rotational shear and the gravitational potential, which is given by the Toomre parameter (Toomre, 1964),

$$Q = \frac{\kappa c_s}{\pi G \Sigma}, \tag{1.3}$$

where κ is the epicyclic frequency, c_s is the sound speed, G is the gravitational constant and Σ is the surface density of the gas. In the instance of an axisymmetric perturbation within a thin disk, these instabilities can occur when $Q < 1$, however for non-axisymmetric perturbations, this Q threshold is significantly higher as we find that rotation shears the gas before these instabilities can grow. Numerical simulations have

determined a range of $Q = 1.2 - 1.4$ for this threshold when considering a thin disk (Kim & Ostriker, 2001), but when adding stellar gravity and magnetic fields, Kim et al. (2003) found that this threshold increases to $Q = 1.5$. For molecular clouds that are stable against rotational shear, the cloud is able to collapse on smaller scales via the Jeans instability.

The Jeans instability describes the ability of thermal pressure, or gas kinetic energy, to support a cloud against its own self-gravity, though this scenario only holds for stationary gas with no rotation, shear, magnetic fields of non-thermal motions. We consider a stationary parcel of gas with a uniform temperature, T, and density, ρ_0. We then consider some outside source perturbating this system, where the perturbation in density propagates in the form of a wave, i.e. $\rho_1 = Ae^{i(kx-\omega t)}$, where A is the amplitude, k is the wave number given by $k = 2\pi/\lambda$ and ω is the angular frequency. Under the condition that this perturbation must conserve both mass and momentum, we find that this perturbation acts like a wave described by

$$\frac{\partial^2 \rho_1}{\partial t^2} - c_s^2 \nabla^2 \rho_1 - 4\pi G \rho_0 \rho_1 = 0, \tag{1.4}$$

gives us

$$\omega^2 = c_s^2 k^2 - 4\pi G \rho_0, \tag{1.5}$$

where c_s is the sound speed and G is the gravitational constant. We now define a critical wave number, henceforth called the Jeans wave number as $k_J = \sqrt{(4\pi G \rho_0)/c_s^2}$, which is derived by setting $\omega = 0$. From this, we can rewrite Equation 1.5 as

$$\omega^2 = c_s^2 (k^2 - k_J^2). \tag{1.6}$$

If $\omega^2 > 0$, then our density perturbation is stable and continues as $\rho_1 = Ae^{i(kx-\omega t)}$ through the medium unchanged, whereas if $\omega^2 < 0$, the exponent of $\rho_1 = Ae^{i(kx-\omega t)}$ becomes positive and real, leading to exponential growth of the perturbation. The transition between these two scenarios is represented by the Jeans wave number defined

previously, and from this we can define a corresponding critical, or Jeans, length scale using $\lambda = 2\pi/k$, which gives

$$\lambda_J^2 = \frac{\pi c_s^2}{G\rho_0}. \tag{1.7}$$

Under the assumption of spherical symmetry, the mass corresponding to this length scale is simply

$$M_J = \frac{4\pi}{3}\rho_0 R_J^3, \tag{1.8}$$

where R_J is the half the Jeans length. More formally, this can be written as

$$M_J = \frac{45}{16}\sqrt{\frac{5}{\rho}}\left(\frac{kT}{Gm_H\mu}\right)^{3/2}, \tag{1.9}$$

where μ is the mean molecular weight of the gas and m_H is the mass of hydrogen. Equations 1.7 and 1.8 are the key results of Jeans analysis and tell us that clouds more massive than the Jeans mass, or larger than the Jeans length, will collapse. From Equation 1.9 we see that the Jeans mass is inversely dependent on the square root of the density of the cloud. This means that as the cloud collapses and the density increases, the Jeans mass decreases, and smaller regions in excess of this mass will begin to contract. This process, known as thermal fragmentation, continues until the density gets high enough that the gas itself becomes optically thick. This prevents energy from escaping and increases the temperature of the system, and with the increase in temperature comes an increase in pressure such that the fragmentation process halts. This halted process of fragmentation is why stars often form in clusters or groups, and not in isolation. The time it takes for this collapse to occur is given by the free fall time of the cloud,

$$t_{\rm ff} = \sqrt{\frac{3\pi}{32G\bar{\rho}}} \approx (1.06\times10^6\ {\rm yr})\left(\frac{n}{10^3\ {\rm cm}^{-3}}\right)^{-1/2}, \tag{1.10}$$

where $\bar{\rho}$ is the mean mass density of the cloud and $n = \bar{\rho}/\mu$ is the number density, with $\mu = 2.36m_H$.

While powerful, Jeans analysis is simple and neglects a number of factors that complicate the situation. Jeans analysis assumes a uniformly distributed cloud with no bulk rotational, turbulent or magnetic energy surrounded by a static infinite medium. The complex internal geometry of the cloud likely leads to over- and under-densities which will encourage or limit the contraction respectively. Turbulence also plays a vital role in determining the rate at which collapse can occur, as isotropic sources of turbulence will provide support against gravitational collapse while non-isotropic turbulence from shocks can increase densities as the post-shock density is proportional to the Mach number of the shock squared, which has the effect of encouraging collapse (Mac Low, 1999). Finally, astrophysical phenomena such as magnetic fields (Heitsch et al., 2001) and shear (Toomre, 1964) can also slow gravitational collapse down.

Regardless of the formation mechanism, molecular clouds are cold and dense enough (with typical temperatures and densities of ~ 20 K and $n_H \sim 10^{2-5}$ cm^{-3}, Larson, 2003) to be the ideal locations for star formation. The gas within these molecular clouds is not smoothly distributed but is in fact fractal and hierarchical (Rosolowsky et al., 2008; Elmegreen, 2008), and while the nomenclature of the various structural components is somewhat fluid, it can be broadly broken down into *clouds*, *clumps* and *cores* (Williams et al., 2000). A *cloud* is the overall structure which can account for structures large enough to cover significant fractions of a spiral arm (Ragan et al., 2014; Zucker et al., 2018). A *clump* in this context refers to over-dense regions which will likely go on to form stellar clusters, whereas a *core* is a gravitationally bound region that will go on to form individual stellar systems (individual stars or binaries and beyond).

The separation between these structures typically depend on the mass/size/density of the structures in question. Where *clouds* can be up to hundreds of pc in size with masses of 10^{2-6} M$_\odot$ and densities of 10^{1-3} cm^{-3}, *clumps* are smaller (on parsec scales), less massive (10^{1-2} M$_\odot$) and more dense (10^{3-4} cm^{-3}). Within these clumps are *cores* which are of order 0.1 pc or smaller, with masses ≤ 1 M$_\odot$ and densities of $\sim 10^{4-6}$ cm^{-3}. In-depth studies of molecular clouds have found that this simple categorisation doesn't tell the full picture. Infrared observations of molecular clouds throughout the Galactic plane have shown that their internal structures are in fact dominated by vast filamentary structures and not single isolated clumps, with a majority of the cores within a cloud are associated with these filaments (Molinari et al., 2010; André et al., 2010, 2014, 2016).

The highly substructured nature of molecular clouds is likely a consequence of the turbulence of the gas within the cloud. A convenient tool used often within the literature to estimate how stable a gas cloud is to the affects of turbulence is the virial parameter (e.g. Contreras et al., 2013; Hopkins et al., 2013; Kauffmann et al., 2013), which is defined as the ratio of the kinetic energy of the gas within the cloud to the gravitational energy of the cloud, i.e.

$$\alpha_{\rm vir} = \frac{5\sigma^2 R}{GM} \propto \frac{E_{\rm kin}}{|E_{\rm pot}|}, \tag{1.11}$$

where σ is the velocity dispersion, M is the mass, T is the kinetic energy and W is the gravitational energy of the cloud. The definition of the virial parameter sets an equilibrium criterion of $\alpha_{\rm vir} = 1$, where the turbulent energy and the gravitational energy are equal. If $\alpha_{\rm vir} < 1$, then the gravitational energy exceeds the turbulent energy of the cloud and the cloud is gravitationally bound, though not necessarily collapsing as magnetic fields may prevent collapse from occurring. On the other hand, if $\alpha_{\rm vir} > 1$ then the turbulent energy is dominating the gravitational energy and the cloud will disperse unless some external pressure prevents this from occurring. Using the Galactic Ring Survey (see Jackson et al., 2006), Heyer et al. (2009) found that most molecular clouds within the Galactic plane are roughly in a state of equilibrium, where $\alpha_{\rm vir} \approx 2$. It should be noted that there is the potential for an observational bias here, given the timescales over which clouds with virial parameters larger or smaller than this will disperse or collapse.

Larson (1981) found that the structure and the observed velocity dispersion of a molecular cloud were well correlated via a series of relations now referred to as 'Larson's relations'. These relations relate the velocity disperion σ to the size of the cloud, R,

$$\sigma\left(\mathrm{km\ s^{-1}}\right) = 1.10\, R\,(\mathrm{pc})^{0.38}\,, \tag{1.12}$$

the mean number density of H_2 to the size of the cloud,

$$\langle n(H_2)\rangle\left(cm^{-3}\right) = 3400\, R\,(\mathrm{pc})^{-1.10}\,, \tag{1.13}$$

both of which Larson (1981) found held over sizes of $0.1 \leq R \leq 100$ pc, and finally the velocity dispersion to the mass of the cloud, M,

$$\sigma \left(\text{km s}^{-1}\right) = 0.42\, M\, (M_{\odot})^{0.20}\,, \tag{1.14}$$

which holds for $1 \leq M \leq 10^6\ M_{\odot}$. The implication of this relation is that smaller regions have less turbulence than larger regions. This relation has a similar form ($\sigma \propto l^{1/3}$) to the spectrum of turbulence proposed by Kolmogorov (1941). As one would expect, the areas of the largest turbulence show the largest 'eddies' of motion within a molecular cloud and this is where the bulk of the kinetic energy is found. This energy then cascades down from the largest scales through to intermediate scales and finally to the smaller scales, where the kinetic energy can dissipate.

Solomon et al. (1987) later confirmed the general form of Larson's relations, though they revised the exponents to $\sigma \propto R^{0.5}$ and $n \propto R^{-1}$. The implications of these relations, regardless of their precise formulation, is that molecular clouds are generally considered to be close to equilibrium, and that the column density of molecular clouds is approximately constant and does not depend on size.

1.4.2 The Initial Mass Function

Since the gas structure in molecular clouds is fractal and the resulting overdensities vary in mass it seems reasonable to expect that the stars produced via this fragmentation also vary from neighbour to neighbour. This distribution of stellar masses at the point of formation is described by the stellar Initial Mass Function (IMF) (Bastian et al., 2010). Given that these early stellar populations are typically shrouded in gas and dust, determining an IMF exactly is very difficult. Current estimates of the IMF are provided by taking observed stellar counts with (preferably) well known ages, distances and extinctions, determining a Present Day Luminosity Function (PDLF) and from this a Present Day Mass Function (PDMF) and then assuming some evolutionary sequence and star formation history to arrive at an IMF. This process, however, is fraught with assumptions and complexities.

Beyond the difficulty of accurately determining the ages, distances and extinctions of a stellar population, converting a PDLF to a PDMF relies on a reliable understanding of the mass-luminosity relation and is also known to be dependent on the metallicity of the population and aspects of the observational setup such as bandpass. The conversion of this PDMF to an IMF is also dependent on the metallicity of the population while the assumed evolutionary sequence and star formation history can also introduce significant uncertainties.

As a result of these difficulties and the requirement of resolving individual stars, the IMF has only been measured in the local Universe. The remarkable result with these measurements is that up until now, they have been consistent with an invariant IMF (Bastian et al., 2010). These measurements do carry significant uncertainties given the low number of more massive stars, as well as the difficulty in resolving individual stars from binaries, but the implications of this invariance are immediately striking as it tells us that molecular clouds should produce the same ratio of more massive stars irrespective of environment. Given that the lower metallicity clouds observed in the early universe are less efficient at cooling we would naively expect that the Jeans mass would be larger and the stars are more massive. The observed invariance in the IMF has serious implications for our understanding of star formation across cosmic time and there is a large amount of observational effort to identify regions where the IMF may vary (van Dokkum, 2008; Cappellari et al., 2012; Conroy et al., 2013).

The earliest formulation of the IMF was devised by Salpeter (1955) who used the observed total luminosity function and calculated the rate of star formation as a function of stellar mass. In doing so, Salpeter (1955) found the IMF takes the form

$$\xi(m)\Delta m = \xi_0 \left(\frac{m}{M_\odot}\right)^{-2.35} \left(\frac{\Delta m}{M_\odot}\right), \tag{1.15}$$

where $\xi(m)\Delta m$ (sometimes written as N(m)dm) is the number of stars within the mass range $\Delta m = m + dm$ and ξ_0 is a constant related to the local stellar density, which is now referred to as the Salpeter IMF. This tells us that the population of stars decreases rapidly as m is increased. However, as observational data improved, this formulation was found to fail at the lower end of the mass spectrum, particularly when considering stellar masses $< 1 M_\odot$. It was modified into the Miller-Scalo form (Miller & Scalo, 1979) which

assumed an exponent of 1 at these lower masses. Further refinement later occurred when Kroupa (2001) used improved observational stellar counts to increase the accuracy of this exponent, introducing a three component power law $\xi \propto M^{-\alpha}$ with $\alpha = 2.3, 1.3$ or 0.3 for the mass ranges $m > 0.5, 0.5 > m > 0.08, 0.08 > m$, respectively. Figure 1.1 shows several of the most commonly used forms of the IMF. Reviewing observational constraints, Chabrier (2003) refined the log normal formulation of the IMF, arriving at seperate formulations for individual stars

$$\begin{aligned} \xi(m) &= 0.158 \exp\left[-\frac{(\log m - \log 0.08)^2}{2(0.069)^2}\right] \text{ for } m < 1\mathrm{M}_\odot, \\ &= km^{-2.3\pm0.3} \text{ for } m > 1M_\odot \end{aligned} \tag{1.16}$$

and multiple stellar systems

$$\begin{aligned} \xi(m) &= 0.086 \exp\left[-\frac{(\log m - \log 0.22)^2}{2(0.057)^2}\right] \text{ for } m < 1\mathrm{M}_\odot, \\ &= km^{-2.3\pm0.3} \text{ for } m > 1\mathrm{M}_\odot \end{aligned} \tag{1.17}$$

though Dabringhausen et al. (2008) showed that distinguishing between this form and the Kroupa (2001) IMF is very difficult. Parravano et al. (2011) argue that over large enough temporal and spatial scales, the IMF should universally take the shape of a smoothed two-power law of the form,

$$\psi(m) = Cm^{-\Gamma}\{1 - \exp[(m/m_{ch})^{\gamma+\Gamma}]\}(m_l < m < m_u), \tag{1.18}$$

where m_l is the lower mass limit, m_u is the upper mass limit (which Parravano et al. (2011) set to 0.004 $M_\odot$ and 120 $M_\odot$), Γ is the high-mass slope parameter, set to the Salpeter value of 1.35. γ and m_{ch} are the low-mass slope parameter and the characteristic mass, which is comparable to the mass where the IMF peaks, were determined to be $\gamma = 0.51$ and $m_{ch} = 0.35$. This form of the IMF agrees well with the Chabrier (2005) form but predicts more very low mass stars (< 0.03 $\mathrm{M}_\odot$.

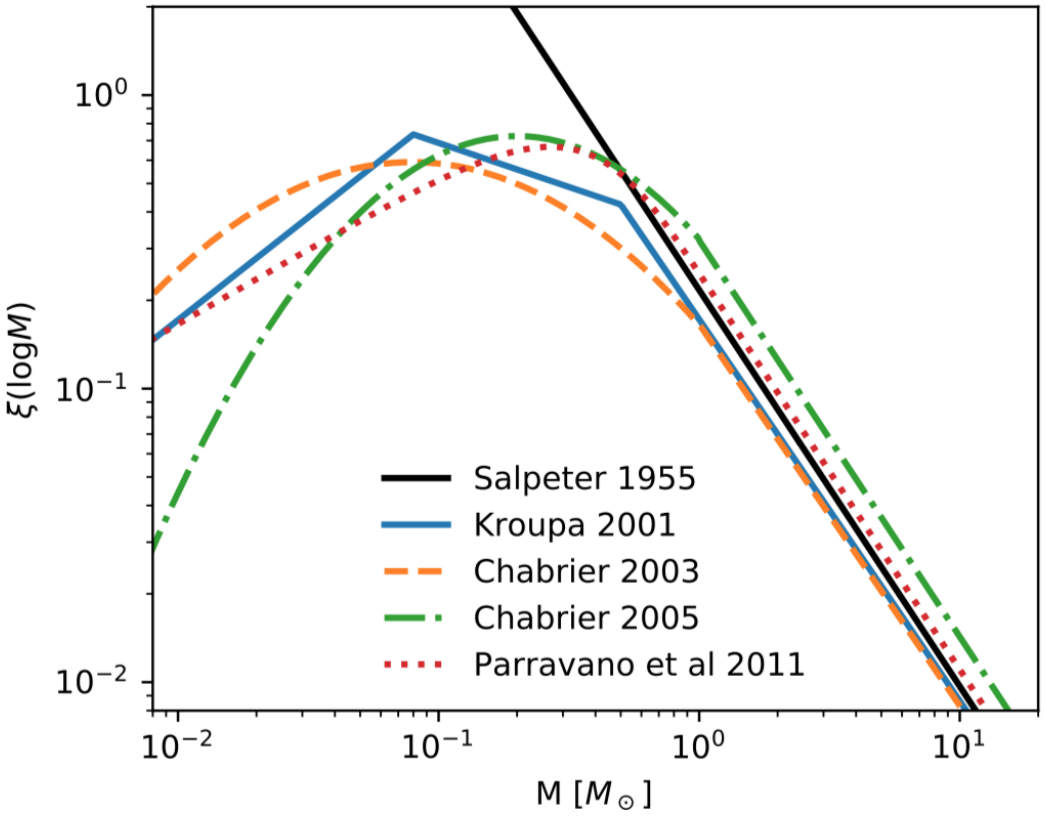

FIGURE 1.1: A plot of the most commonly used forms of the IMF taken from Colman & Teyssier (2020). All but the Salpeter (1955) form have been normalized such that the integral under each curve is 1.

1.4.3 The Star Formation Process

Star formation is typically split into two separate categories based on the time within which prestellar clumps turn into a protostar. This division occurs at the Kelvin-Helmholtz time, equivalent to

$$t_{KH} = \frac{Gm_*^2}{R_* L_*}, \tag{1.19}$$

where m_*, R_* and L_* are the mass, radius and luminosity of the star respectively. The Kelvin-Helmholtz time is the amount of time it will take any given star to radiate away its kinetic energy at its current luminosity. For low mass stars, this time scale is larger than the free fall time ($t_{KH} > t_{ff}$) and they will reach the main sequence after accretion of the surrounding material has stopped, whereas for high mass stars the free fall time exceeds t_{KH} (Kahn, 1974) and the star will reach the main sequence while accretion is

still taking place. This division can also be made at a stellar mass, with 'high mass' stars being those being massive enough to produce a type II supernova, i.e. ≥ 8 $M_\odot$ (Smartt, 2009). Below this mass the luminosity of the protostar is dominated by accretion of the surrounding medium onto the surface, whereas above this mass it is nuclear burning that dominates the emission.

The formation of a low mass star begins with a roughly Jeans length sized gravitationally bound ($\alpha_{\rm vir} < 1$) core. These cores will typically become centrally concentrated with a density profile of the form $\rho \propto r^{-2}$ (Larson, 1969). As the outer edge of the cloud collapses, the instability propagates inwards, encouraging collapse on smaller and smaller scales until the density reaches $\rho \approx c_s^2/(Gr^2)$ and a protostar is formed. The infall rate of this collapse is given by $\dot{m} = \phi c_s^3/G \propto M_{core}\rho^{1/2}$. ϕ is a numerical factor that varies over the infall time and it depends greatly on the starting assumptions made. While Stahler et al. (1980) proposed that $c_s^2 \rightarrow c_{\rm eff}^2 = c_s^2 + v_{\rm A}^2 + v_{\rm turb}^2$ for a cloud supported by magnetic fields (represented here by Alfven speed, $v_{\rm A}$), turbulence ($v_{\rm turb}$) and thermal pressure (c_s), Shu et al. (1987) notes that this form doesn't account for the anisotropies of the magnetic and turbulent support and instead suggest an upper limit of $c_{\rm eff} \lessapprox 2c_s^2$.

Shu (1977) assumed that the evolution of the density profile of these protostellar cores is quasi-static such that velocity of infall is negligible at the time of formation of the protostar. This initial state is the singular isothermal sphere, the collapse of which starts at the centre and the edge of this infalling area propagates outward at the sound speed, and as such this process is referred to as "inside-out" collapse. At any given time, t, during this collapse, the edge of the infalling area, i.e. the "expansion wave", will be at $R_{\rm ew} = c_s t$. The gas outside of this radius is unaware of the collapse and the density remains as that of the SIS, $\rho = c_s^2/\left(2\pi G r^2\right)$, while gas within this radius accelerates towards the centre until it reaches free fall velocity, $v = -\left(2Gm_*/r\right)^{1/2}$. The infall of this "inside-out" collapse is

$$\dot{m}_{\rm in} = 0.975\, c_s^3/G = 1.54 \times 10^{-6}\, (T/10\, K)^{3/2}\, M_\odot\, yr^{-1} \tag{1.20}$$

and is constant in time. Contrary to this, Larson (1969), Penston (1969) and Hunter (1977) considered a static cloud with a constant density, and instead allow this $\rho \propto r^{-2}$ profile to develop. At the time when the protostar forms, the rate at which gas infalling

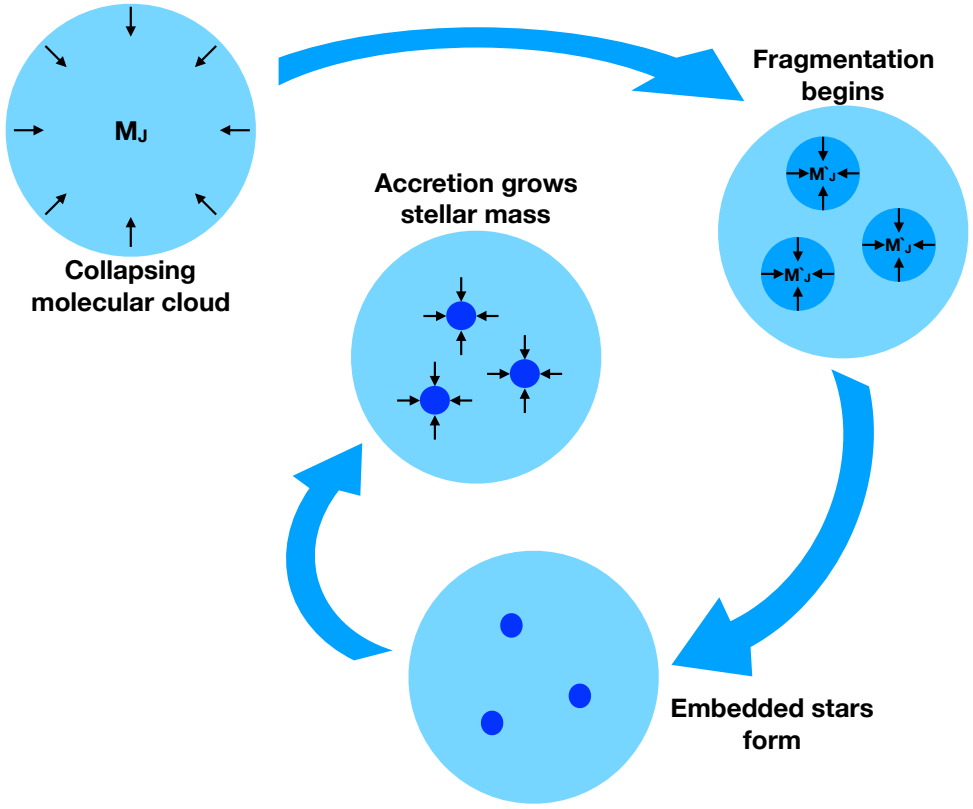

FIGURE 1.2: The main stages of the star formation process from the initial collapse of a molecular cloud of mass M_J, through to the internal fragmentation of smaller regions as the density and the Jeans mass decreases. This leads to multiple stars formed within the cloud, which continue to grow through accretion.

onto the star begins to increase sharply from $\dot{m} = 29\, c_s^3/G$ to $\dot{m} = 47\, c_s^3/G$, and will begin to decrease again after the formation of the star. While these two scenarios are contrasting, Larson (2003) suggests that these are extremes and that star formation proceeds somewhere in between these two idealised models.

Above the mass of 8 $M_\odot$, we enter the regime of high mass star formation. Given the initial mass function, one might assume that high mass stars (and thus their formation) is less important due to the relatively small number of stars that are within this mass regime. However, assuming a mass-luminosity relation of $L_* \propto M_*^{3.5}$ (Harwit, 1988), the energy output of these massive stars dominates the total energy budget of all stars. This energy also makes them the only young stars we can observe in external galaxies. The output of energy occurs at all stages of a high mass stars lifespan, from the jets that exist as they form, to the intense amounts of radiation they output and to their inevitable destruction by supernova explosion. High mass stars are therefore vital in the evolution of both the ISM and the host galaxy at large.

Understanding high mass star formation has been a challenge because they are both rare in number (the nearest high mass star forming region to us is in the Orion Nebula at a distance of 389^{+24}_{-21} pc Sandstrom et al., 2007) and fast to form, as their freefall time is larger than the Kelvin-Helmholtz time scale and hydrogen burning can begin before accretion has finished (Kudritzki, 2002). Several scenarios have been proposed to explain how these more massive stars formed based on the limited observations made thus far. The two most widely cited are an accretion model that resembles a scaled up version of low mass star formation models, and secondly a competitive accretion model that utilises the high likelihood of high mass stars forming in cluster environments.

In the first scenario, that of a scaled up low-mass accretion model, the accretion rate is controlled by the supersonic, non-thermal turbulence as opposed to the thermal turbulence dominating in the low mass variation. This turbulence acts to support the core against gravitational collapse up to much higher masses, meaning that when accretion does occur it is at a much higher rate than that of the low mass star accretion (McKee & Tan, 2002, 2003).

As discussed in Section 1.4.1, turbulence is the predominant cause of substructure within molecular clouds, and with substructure comes fragmentation. This is problematic for the scaled up low-mass accretion model as a highly substructured molecular cloud will likely produce a population of low mass stars instead of the single high mass star that this model was proposed to explain. Several scenarios have been proposed to explain how a molecular cloud overcomes this issue and goes on to form a high mass star, with the more popular suggestions invoking radiation feedback (Krumholz et al., 2007), column density thresholds (Krumholz & McKee, 2008) or magnetic fields (Tan et al., 2013).

Using radiation-hydrodynamic simulations, Krumholz et al. (2007) proposed that an initial generation of low mass protostars can provide sufficient radiative feedback to inhibit further fragmentation of the gas, meaning that the bulk of the remaining gas mass can collapse in one or a couple of more massive objects. However, a study of the massive protocluster G8.68-0.37 by Longmore et al. (2011) find that the number of protostars required to generate the radiative support necessary to prevent fragmentation is unfeasible. Similarly, Zhang et al. (2009) observed another protocluster, G28.34+0.06, and found that protostars do not provide significant thermal feedback on small scales.

Krumholz & McKee (2008) suggests that clouds must have a column density ≥ 1 g cm^{-2} to avoid the fragmentation process, a proposition that also explains the current state of high mass star observations. This column density is rare in molecular clouds, even those with currently observed star formation. However all known nearby regions with high mass stars present sit at or above this column density threshold (Plume et al., 1997; Mueller et al., 2002; Shirley et al., 2003; McKee & Tan, 2003; Kauffmann & Pillai, 2010; Kauffmann et al., 2010a,b).

As an alternative, Tan et al. (2013) instead proposed that strong magnetic fields, i.e. those with strengths of ~ 1 mG, are capable of supporting the gas against fragmentation. In particular they propose that this is the dominant way in which infrared dark clouds (IRDCs) prevent fragmentation, as they are otherwise too cold for radiative heating to be occurring. These stronger magnetic fields would also not require column densities as high as those proposed by Krumholz & McKee (2008). Regardless of the physics responsible for the prevention of fragmentation within molecular clouds, this model of core accretion predicts an initial condition of a very massive, starless core. It is currently unknown, however, if any such massive starless cores have in fact been detected (Cyganowski et al., 2014; Kong et al., 2017; Nony et al., 2018)

While some high mass stars have been observed in isolation (Tremblay et al., 2015; Harada et al., 2019), it is far more common for high mass stars to form in cluster environments (Lada & Lada, 2003; Bressert et al., 2012). To explain this, the notion of formation via competitive accretion scenario was proposed (Bonnell et al., 1997; Zinnecker & Yorke, 2007). This model begins with a highly fragmented molecular cloud which forms a number of cores distributed throughout the cloud with masses close to the thermal Jeans mass (Equation 1.11 with $\alpha = 2$ and $\sigma = c_s$). Cores close to the centre will accrete material at a faster rate than those at larger radii as gas will be funneled from these radii toward the centre. As the central stars grow in mass, the accretion rate increases and the star continues to dominate the gas reservoir.

This model has the benefit of roughly producing a population of stars consistent with the IMF, as the process typically results in the formation of one (or a couple of) massive star(s) in the central regions of the molecular cloud with low mass stars further out, which is consistent with the mass segregation observed in young and old stellar clusters alike, as seen in Figure 1.3 (Hillenbrand & Hartmann, 1998; Fregeau et al., 2002). Those

massive stars that have been observed in isolation pose somewhat of a challenge to this model, as no competitive accretion scenario will lead to a single massive star. However, it is possible that these isolated stars did not form in isolation but were merely ejected from their cluster environments after their formation. The frequency of runaway stars with respect to total stellar counts appears dependent on stellar type itself with $f \approx 20\%$ among early O type stars to $f \leq 2.5\%$ for B type stars (Blaauw, 1961). This model also would not produce massive starless cores, and if the observed candidate massive starless cores are confirmed, this will be a significant challenge to the mode.

Once the protostar is formed it continues growing via the accretion of material, with Hoyle & Lyttleton (1939) and Bondi & Hoyle (1944) proposing that the rate at which this accretion takes place is determined by the relative motion of the star with the surrounding medium. The rate at which a star in either regime accretes mass from its surrounding material of density ρ with a sound speed of c_s^2 is given by

$$\dot{M}_{\rm BH} = 4\pi\tilde{q}\frac{G^2M^2\rho_\infty}{\left(c_{s,\infty}^2 + V^2\right)^{3/2}} \tag{1.21}$$

where $\tilde{q}$ is a factor of order unity, G is the gravitational constant, M is the mass of the star, ρ_∞ is the density of the surrounding medium far from the star, $c_{s,\infty}^2$ is the sound speed far from the star and V is the velocity of the star. This rate is clearly an idealised rate however, as it does not take into account magnetic fields, turbulent motion or self-gravity of the surrounding medium (though the latter will be negligible when compared to the gravity of the protostar itself).

Both models have pros and cons as to their applicability to the observed population of massive stars and clusters, and it is likely that in reality a combination of the two processes occur in the formation of high mass stars. Further observations with higher spatial and spectral resolutions will inform these models as technology improves but the limited number of these stars in our Galaxy will remain a challenge (Beuther et al., 2018, ALMA-IMF large program).

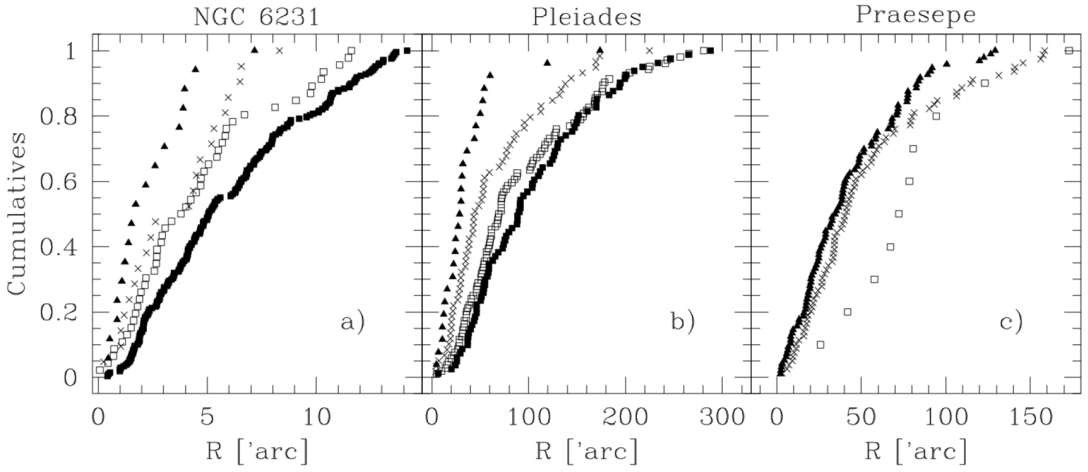

FIGURE 1.3: Cumulative distribution of stellar masses in a 4 Myr, 100 Myr and 800 Myr old open cluster. The masses are split into three mass bins of $M \geq 0.36$ M_{max} (triangles), 0.23 $M_{max} \leq M < 0.36$ M_{max} (crosses), 0.14 $M_{max} \leq M < 0.23$ M_{max} (open squares) and $M < 0.14$ M_{max} (filled squares), where M_{max} is the maximum stellar mass of the given cluster. Each distribution shows the more massive stars peaking at lower radii, with less massive stars peaking toward the edges of the cluster. Plot taken from Raboud & Mermilliod (1998).

1.4.4 Environmental Dependence on Star Formation

Many of the models devised to explain the rate at which we expect stars to form in a given cloud are based on observations of clouds within the disk of our own Galaxy, or in the nearest galaxies in the local group. These models, however, have had varying degrees of success when it comes to predicting the observed star formations rates in different environments. While they typically hold up well when compared to molecular clouds in disk environments, they typically fail in the more extreme environments such as the centre of our own Galaxy, the Central Molecular Zone. In this subsection, we look at these models in more detail, before discussing environments that pose challenges to these models.

The most commonly used model is the Kennicutt-Schmidt relation, which relates the star formation rate surface density, $\Sigma_{\rm SFR}$, of a cloud to the overall (atomic and molecular) gas mass surface density, $\Sigma_{\rm gas}$ of the cloud, and is given as

$$\Sigma_{\rm SFR}\left(\mathrm{M_\odot yr^{-1} kpc^{-2}}\right) \propto \Sigma_{\rm gas}^{\rm N}\left(\mathrm{M_\odot pc^{-2}}\right), \tag{1.22}$$

(Kennicutt, 1998a; Bigiel et al., 2008a; Leroy et al., 2008a; Schruba et al., 2011a; Gutermuth et al., 2011a; Lada et al., 2012a; Krumholz & Dekel, 2012a). The exponent, N, was originally determined to be $N = 1.4 \pm 0.15$, but was later found to be dependent on the dominant process or characteristic that controls star formation the most. If we assume that only the mass of a molecular cloud controls the star formation process such that a given mass of molecular gas will produce a constant SFR then $N \approx 1$, however, if it is controlled by cloud-cloud collisions then $N \approx 2$ (Pan et al., 2014, and references therein). Typically the value of N is determined by observations of ^{12}CO and depend on the CO to H_2 conversion factor. While this is typically set to $X_{\rm CO} = 2.3 \times 10^{20}$K km s^{-1}, this value has been found to depend on metallicity, CO intensity as well as oxygen abundance (Bolatto et al., 2013).

Work by Lada et al. (2012a) suggests a surface density threshold of 130 M$_\odot$ pc^{-2} above which star formation triggers. This surface density roughly corresponds to a volume density of $\sim 10^4$ cm^{-3} (Lada et al., 2010). While based on observations of molecular clouds in the disk of our own Galaxy, this relation has been expanded to extragalactic sources and found to hold over a range of 8 orders of magnitude of masses, as shown in Figure 1.4. This relation falters when it comes to predicting star formation in galactic centre environments. Longmore et al. (2013b) found that while the centre of our Galaxy contains a significant fraction of gas above this density threshold, the current star formation rate within the region $1^\circ < l < 3.5^\circ$, $|b| < 0.5^\circ$ is only 0.06 M yr^{-1}. Barnes et al. (2017) expanded on this by comparing the star formation rate measurements using different methods over the region $|l| < 1$, $|b| < 0.5^\circ$ and measured a global value of 0.09 ± 0.02 M$_\odot$ yr^{-1}. This suggests that something is required in addition to a surface density to predict star formation rates.

The normalisations for these relations comparing the surface density of gas to the SFR surface density rely heavily on assumptions of the star formation efficiency (SFE) of the gas, so we can instead look at the efficiency with which star formation is taking place on various scales. The SFE is the fraction of gas mass that is converted into stellar mass i.e.

$$\epsilon = \frac{M_{*,\rm tot}}{M_{*,\rm tot} + M_{\rm gas}}, \tag{1.23}$$

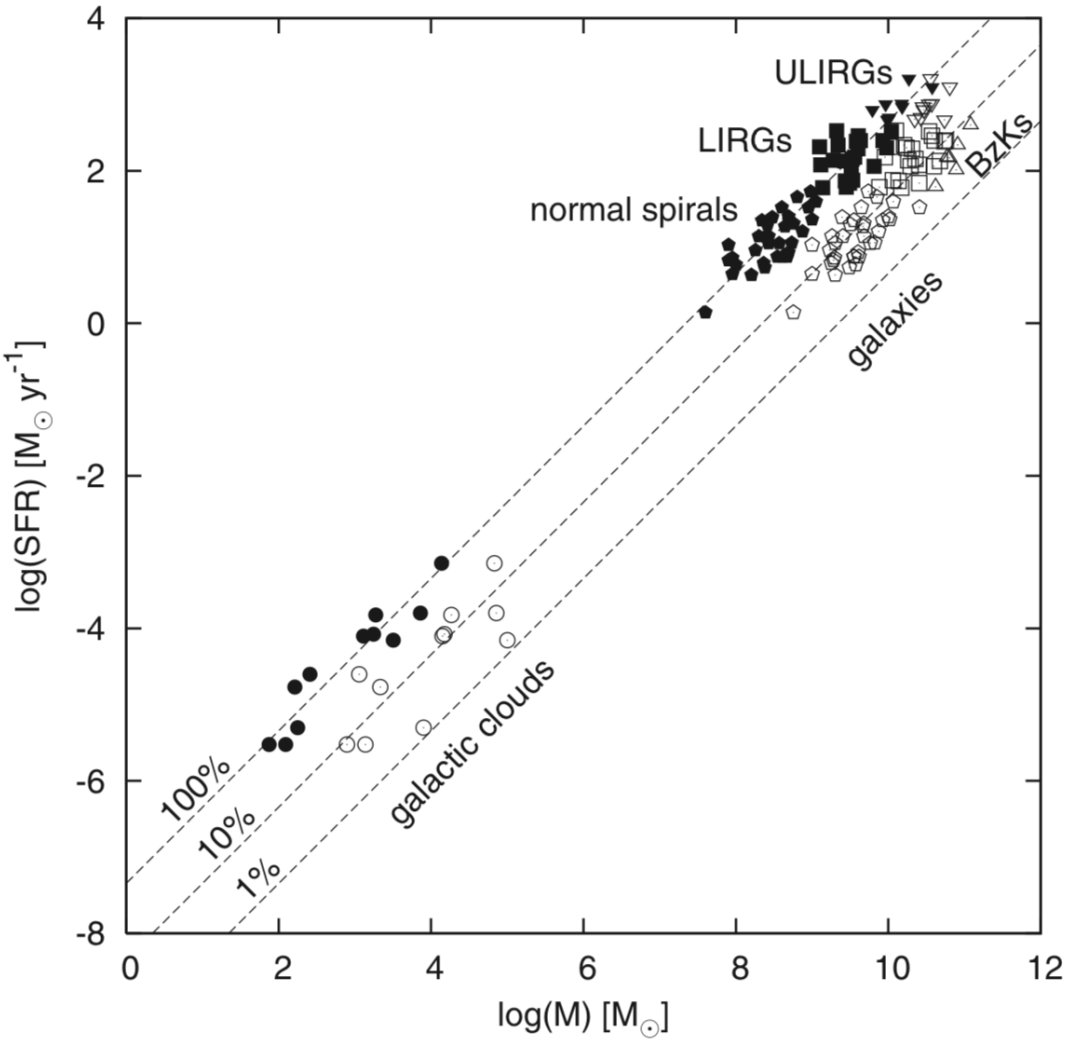

FIGURE 1.4: SFR against molecular mass for molecular clouds within the Milky Way Disk and whole galaxies from Gao & Solomon (2004a) as taken from Lada et al. (2012a). Filled circles show masses calculated from HCN observations for galaxies or dense gas masses from extinction observations for galactic clouds, whereas open circles show masses calculated from CO observations for galaxies or total cloud masses from extinction observations for galactic clouds.

where $M_{*,\mathrm{tot}}$ is the total stellar mass and M_{gas} is the gas mass. This can be calculated for gas on all scales from clumps within clouds to whole clouds to entire galaxies. While Matzner & McKee (2000) estimated that individual star formation events have star formation efficiencies of $25\% - 70\%$ and a star forming clump typically has efficiencies less than 50%, Myers et al. (1986) found that a large fraction of the molecular cloud complexes throughout the Milky Way have SFEs $\sim 2\%$. Measurements of the SFE of clouds throughout the disk of the Galaxy show significant scatter, though Kruijssen & Longmore (2014a) and Kruijssen et al. (2018) found that this scatter was dependent on the spatial scale and timescale in question and developed the 'uncertainty principle' to

interpret the failings of these measurements on smaller scales. From observations of a nearby flocullent galaxy NGC 300, Kruijssen et al. (2019c) found that star formation appears to be controlled by short periods of efficient stellar feedback. The cloud is then dispersed on timescales of ~ 1.5 million years (or $1-5$ million years once massive stars emerge; Chevance et al., 2020a). Likewise, Grudić et al. (2019) suggest that the scatter observed in these relations are indicative of various stages of the star formation process, with low SFEs ($< 1\%$) correspond to the earlier stages of star formation and large SFEs ($> 10\%$) are the result of the disruptive processes post star formation.

Figure 1.5 shows the parameter space of interest in Equation 1.23 and we see that while most of the star forming but non-starburst galaxies sit between the 1% and 10% SFE lines, starburst galaxies appear to be producing stars much more efficiently, up to $\sim 100\%$. Measurements of star formation efficiencies $\geq 100\%$ are of course unphysical, and are the result of overestimates of the SFR surface density, underestimate of the gas surface density or using spectral lines that trace older generations of star formation that took place inside of a larger gas reservoir than is observed today. By studying a selection of central starburst galaxies, Ellison et al. (2020) suggest that while this $\Sigma_{\rm SFR}$ is predominately controlled by the amount of molecular gas, it is the SFE that determines vertical scatter from this relation.

Another way to measure the prevalance of star formation is to look for 70 μm counterparts. By checking the fraction of sources throughout the Galaxy with this counterpart, Ragan et al. (2016) measured the 'star-forming fraction' (SFF) as a function of galactocentric radius and found that despite a constant dense gas mass fraction within the inner Galaxy, the measured SFF declines with a rate of -0.026 ± 0.002 kpc^{-1}. Ragan et al. (2016) proposed that the SFF may therefore depend on some other, larger scale properties, with the dense substructures inheriting some properties depending on their environment.

1.5 Galactic Centres

As the nearest galactic centre, the Milky Way's nucleus represents a powerful laboratory for testing key predictions in cosmology, high energy physics, time domain physics (tidal disruption events), and star formation (Morris & Serabyn, 1996a; Ghez et al., 2008;

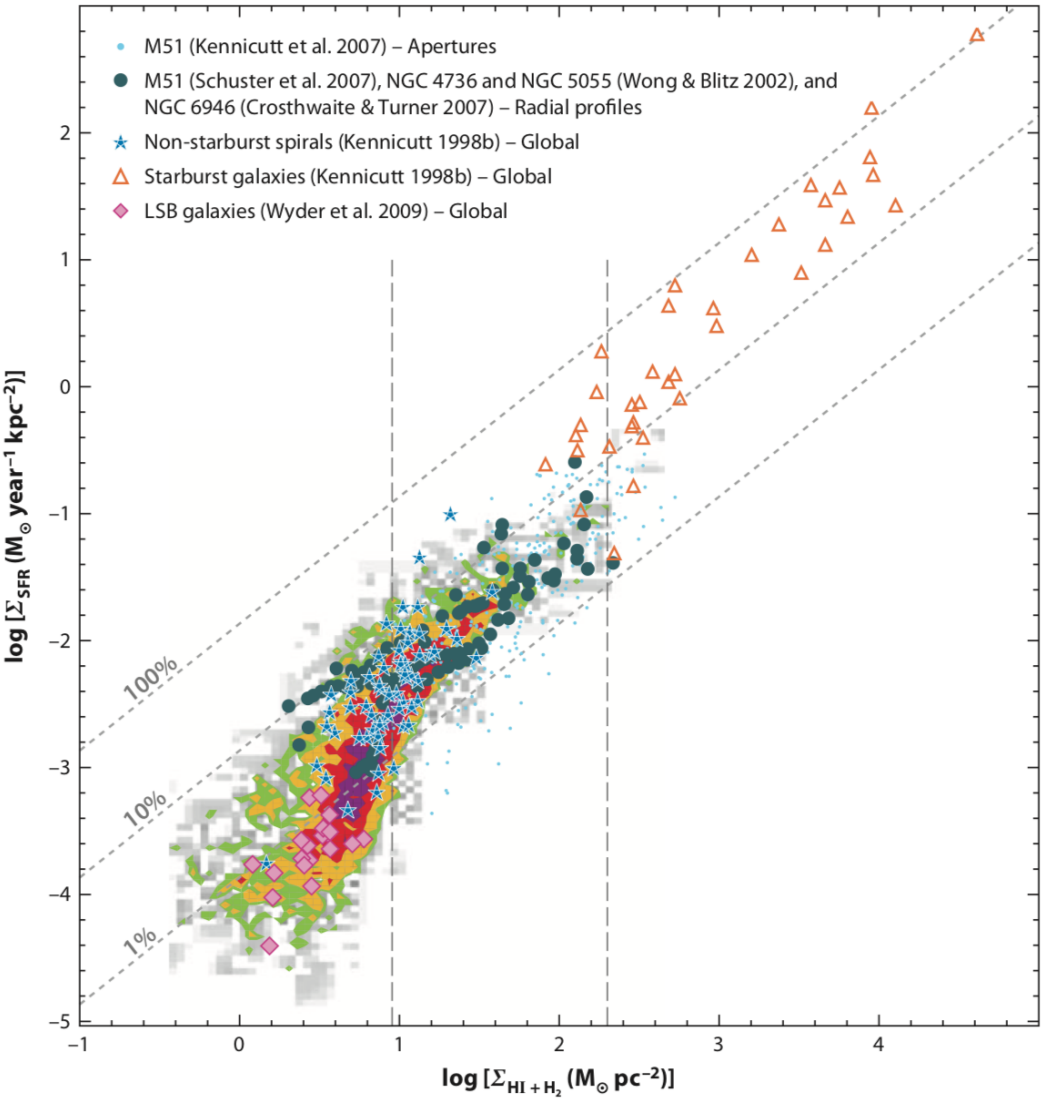

FIGURE 1.5: The relationship between the surface densities of gas and star formation rate, taken from Kennicutt & Evans (2012). The gray, yellow, green and red coloured data points show the distribution of measurements taken from the SINGS survey. The other coloured points are taken from different techniques and sources. The dashed diagonal lines indicate constant global star formation efficiencies of 1%, 10% and 100%. The vertical dashed lines represent three distinct regimes for this SF relation (see Bigiel et al. (2008a) for details). While the centre of M83 shares the parameter space with the rest of the starburst galaxies by Kennicutt (1998a), the CMZ is an order of magnitude lower than this population in terms of $\log(\Sigma_{SFR})$.

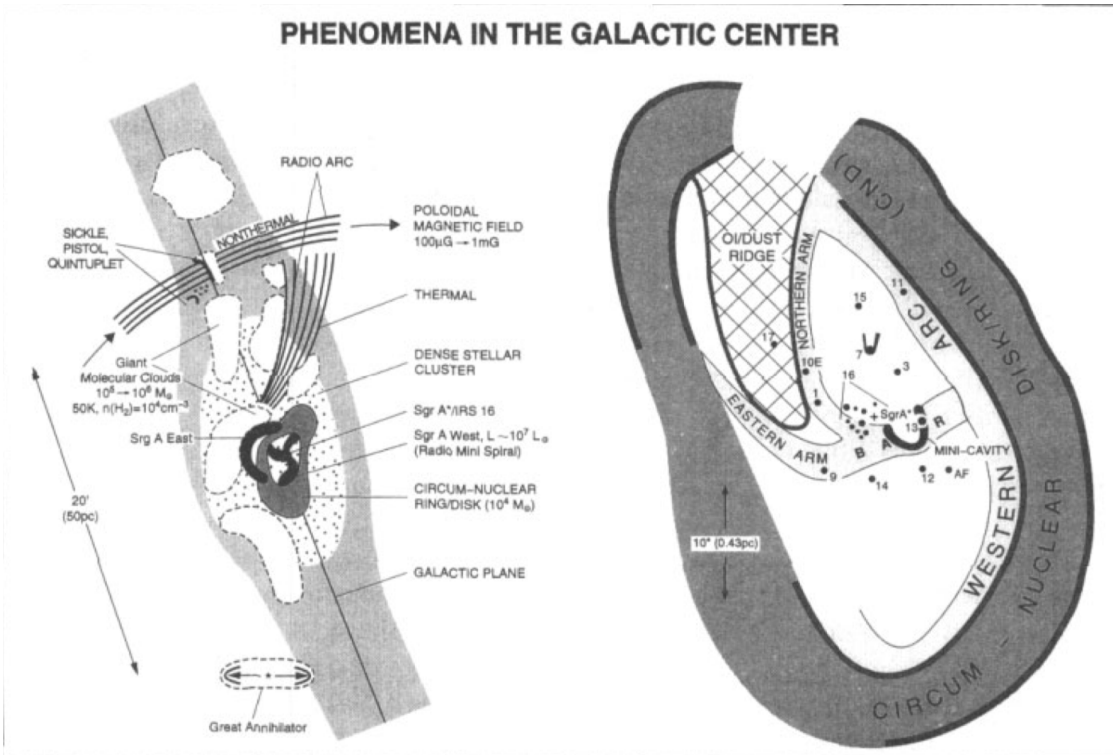

FIGURE 1.6: Schematic of the structure and phenomena found in the centre of our Galaxy, taken from Genzel et al. (1994) which details these structures and numerical labels in more detail.

Genzel et al., 2010b; Gravity Collaboration et al., 2018; Heywood et al., 2019). In this section, I will provide a brief review of the structure of our Galactic Centre, before focusing on the key structural component for this thesis; the Central Molecular Zone (CMZ). I will then briefly discuss the benefits of studying the centres of external galaxies.

At the very centre of the Galaxy sits the supermassive black hole (SMBH), Sagittarius A*, which is visible as an intense radio source within the Sagittarius constellation. Using parallax measurement of stars orbiting the SMBH over nearly 2 decades, Gillessen et al. (2009) found that the SMBH at this position must contain a mass of 4.31×10^6 $M_\odot$. In the cubic parsec surrounding the SMBH sits the stellar nuclear cluster, a halo of millions of primarily old red giant stars, as well as a significant population of massive stars. At 2 parsecs around Sagittarius A* sits a circumnuclear disk of molecular gas being fed by ambient molecular clouds further out via dense molecular streamers (Hsieh et al., 2017), as seen in Figure1.6.

Further out from these ambient molecular clouds is a vast reservoir of molecule gas known as the Central Molecular Zone (CMZ). As this is the region I focused on, I will now provide an in-depth overview of the work in this region before explaining how

comparitive studies of our CMZ with CMZs in other galaxies can help understand some of the main open questions in the field.

1.5.1 Central Molecular Zone (CMZ)

The CMZ is a region of dense molecular gas extending several hundred parsecs radially outwards from Sgr A*, containing approximately 5% of our Galaxy's total molecular gas budget (Dahmen et al., 1998a). This large proportion of gas in so small a region of the Galaxy means the average surface density of gas clouds in the CMZ is two orders of magnitude greater than those observed in molecular clouds within the disk of the Galaxy. The gas is also hotter than gas in the disk, with temperatures reaching several hundreds of Kelvin (Mills & Morris, 2013a; Ginsburg et al., 2016; Krieger et al., 2017a; Ao et al., 2013) and observed to have densities much higher than disk cloud densities at $> 10^4$ cm^{-3} on 1 pc scales (Longmore et al., 2013d). The measured turbulence is also significantly elevated when compared to disk clouds (Shetty et al., 2012; Kauffmann et al., 2017a; Henshaw et al., 2019a), with a much richer chemistry (Requena-Torres et al., 2006, 2008; Armijos-Abendaño et al., 2015; Zeng et al., 2018; Jimenez-Serra et al., 2020).

The CMZ conditions are far more extreme than those in the disk. The clouds in this region experience significant UV ($G_0 \sim 10^3 - 10^4$; Lis et al., 2001; Goicoechea et al., 2004; Clark et al., 2013), cosmic ray (Oka et al., 2005; Goto et al., 2013; Harada et al., 2015), and X ray irradiation (Terrier et al., 2010, 2018). Due to the strong gravitational potential of the central nucleus, the gas orbitting at these radii are affected by significant dynamical stresses, such as shearing and compression (Güsten & Downes, 1980; Longmore et al., 2013d; Krumholz et al., 2017; Kruijssen et al., 2019b; Dale et al., 2019b; Armillotta et al., 2019a). Given the proximity to both a SMBH and the surrounding nuclear stellar cluster, the gas has likely been exposed to considerable active galactic nucleus (AGN) and star formation feedback, which is less energetic and occurs on smaller scales than AGN feedback, in the past (Sofue & Handa, 1984; Su et al., 2010; Heywood et al., 2019; Ponti et al., 2019), though currently both of these factors are likely to be at a minimum. Compared with molecular clouds in the disk of the Galaxy, the gas conditions in the CMZ are much more similar to the conditions observed in the high redshift Universe, at $1 < z < 2$ (Kruijssen & Longmore, 2013a), where star formation

throughout the Universe was at its peak. This makes the region uniquely suitable for testing star formation models and theories on a range of spatial scales, and the currently observed dearth of star formation in the CMZ compared to that expected from such a large reservoir of dense gas makes makes this even more interesting to study.

Due to the rich complexity and chemistry of the gas in the CMZ, it is unsurprisingly targeted by a significant number of observations across the whole electromagnetic spectrum (Aguirre et al., 2011a; Walsh et al., 2011a; H. E. S. S. Collaboration et al., 2018; Krieger et al., 2017a) including the CMZoom survey (Battersby et al., 2017a) which targeted dust continuum and a frequency range covering a number of key spectral lines (see Figure 1.7 for the spatial coverage of the CMZoom survey). A number of more targeted observations have also been made to reinforce these large scale surveys with a particular focus on specific clouds (Longmore et al., 2012; Henshaw et al., 2016c; Walker et al., 2018a; Ginsburg & Kruijssen, 2018; Henshaw et al., 2019a).

One of the defining structural components is this orbital stream - a circumnuclear ring of gas at $\sim$ 100 pc from Sagittarius A*. For a majority of the disk of our Galaxy the rotation curve is flat, but close to the nucleus it transitions into a solid body-like rotation curve. This transition occurs at $\sim$ 100 pc and was predicted to cause gas to pile up at this radius leading to the formation of a circumnuclear ring, which was reported by Molinari et al. (2011b) who found this ring of gas at the same galactocentric radius using Herschel. While Molinari et al. (2011b) suggested that this stream of gas took the form a closed twisted elliptical orbit – an update on earlier attempts to model the kinematics of the central region by Sawada et al. (2004) who assumed these structures were inner spiral arms. Kruijssen et al. (2015) fit the structures in $\{l, b, v_{\rm los}\}$ space using the gravitational potential model proposed by Launhardt et al. (2002) and instead found an eccentric open stream. While the 3D geometry of these ring is difficult to constrain, both the large scale CMZ surveys and the more targeted observations of individual clouds throughout the region have painted a picture of strong tidal forces triggering the collapse of clouds as they travel through these orbital streams, which suggests that the star formation activity in the CMZ evolves as the gas ring orbits.

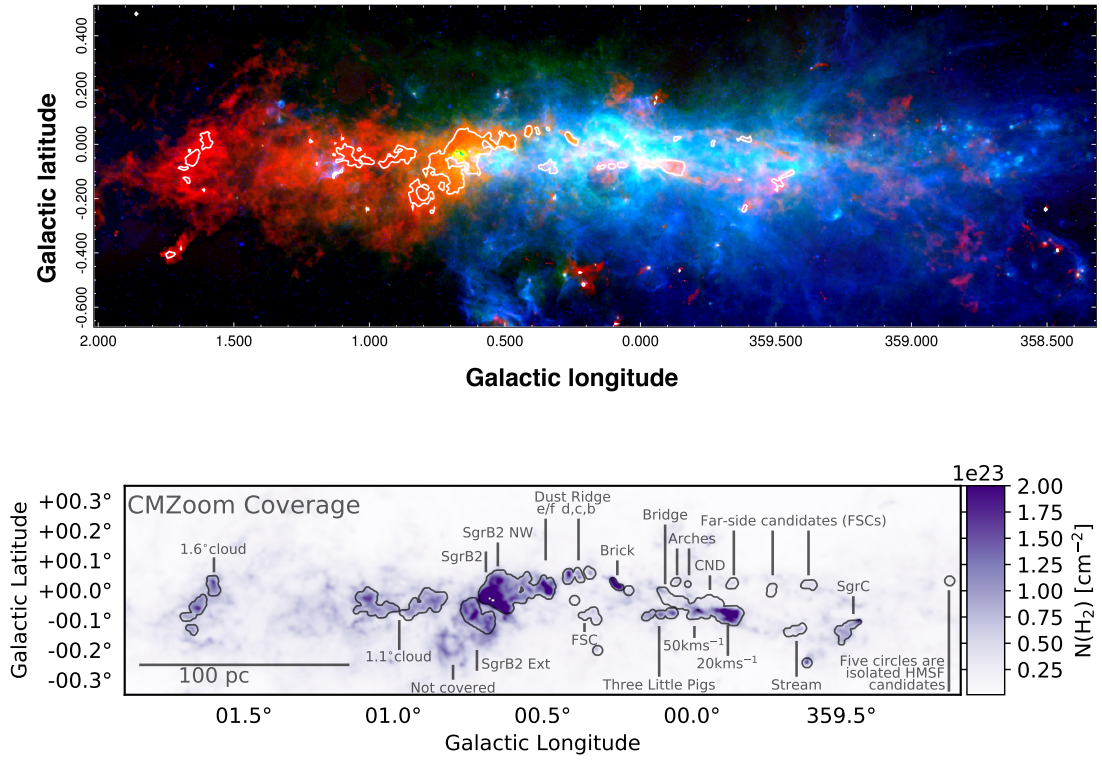

FIGURE 1.7: Three colour image of the Central Molecular Zone composed molecular hydrogen column density (in red), Hi-GAL 70μm (in green) and GLIMPSE 8μm (in blue). The white contours show the approximate coverage of the CMZoom survey - see Chapter 2. Bottom: The Central Molecular Zone as seen in N(H_2) derived from the Herschel cold dust continuum (Molinari et al., 2010, Battersby et al., in prep.) in units of cm^{-2} in the colorscale with the *CMZoom* coverage is shown as gray contours. The *bottom* figure shows colloquial names or notes on each observed region, as they are referenced to throughout the text. Within the inner 5° longitude × 1° latitude of the Galaxy, *CMZoom* is complete above a column density threshold of 10^{23} cm^{-2}, with the exception of the cloud to the SE of Sgr B2 and isolated bright pixels, and with the addition of a few clouds. *CMZoom* covered 974 individual mosaic pointings over about 550 hours on the SMA.

1.5.2 External Galactic Nuclei

While evidently a powerful laboratory for testing star formation, among a wide array of other astrophysical phenomena, the centre of our Galaxy provides some unique problems when it comes to observations. Sitting 8.4 kpc from us in the plane of the Galaxy, the kinematics and 3D geometry is not easy to unravel (Kruijssen et al., 2015; Henshaw et al., 2016b; Longmore & Kruijssen, 2018). While the general velocity gradients of the overarching structures are well known, fitting an orbital model to these observations has proved non-trivial. In addition to this, the measured inflow rate of gas into the region (Sormani & Barnes, 2019a) and simulations of gas flows in the CMZ and CMZ-like environments (Sormani et al., 2015a,b,c, 2018) have been seen to be highly clumpy,

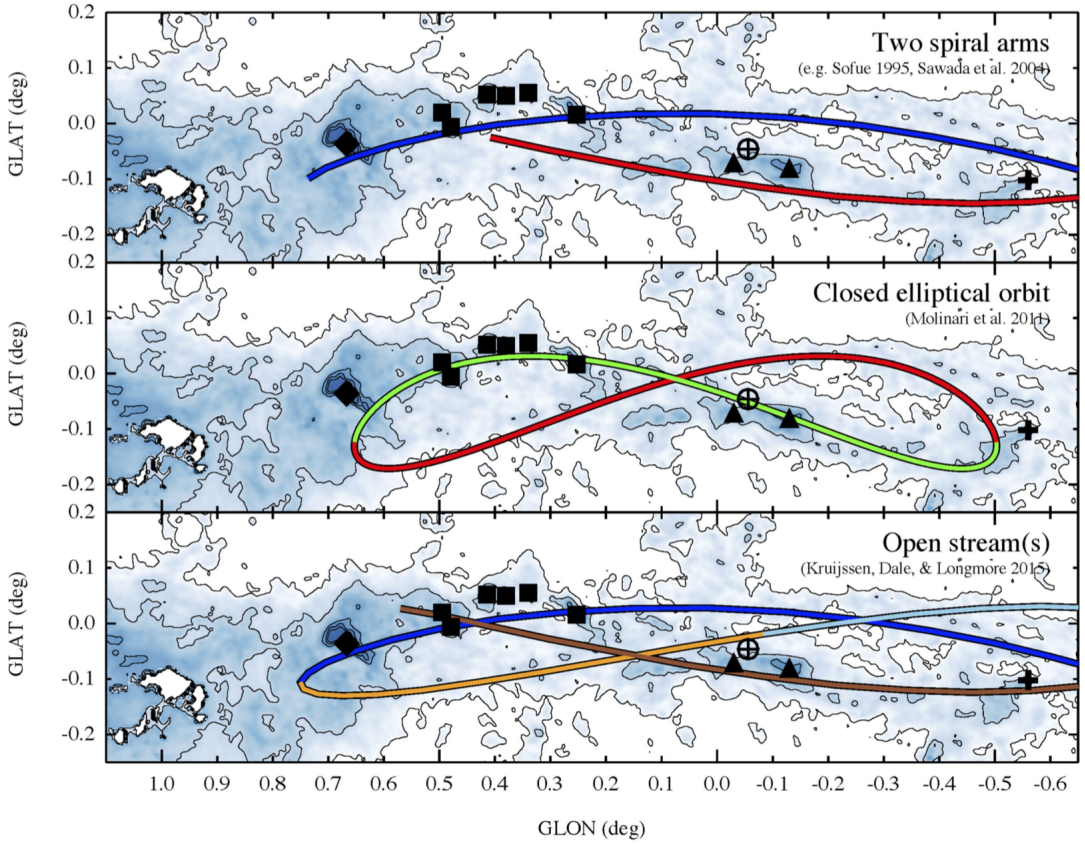

FIGURE 1.8: Herschel derived column density of molecular hydrogen overlaid with three recent models of the 3D structure of 100 pc gas stream, made by Henshaw et al. (2016b).

with significant time variability. This means that the CMZ represents one snapshot of a number of processes that can vary drastically as a result of this clumpy gas inflow, in particular star formation and the proceeding feedback as well as the AGN feeding and feedback cycle.

To remedy these potential issues with observations of our own Galactic Centre, we can instead turn to the centres of other galaxies. While considerably further away than our own galactic nucleus, the ongoing advances in interferometric technology, in particular ALMA and EVLA, makes it possible to determine the properties of gas at cloud (pc) scales. This has the benefit of minimising both issues in observing our own CMZ. Firstly, by directing our attention to the centres of close to face-on galaxies, determining the 3D geometry of the gas becomes less complicated and can provide insight to the models designed to estimate the 3D geometry of our own CMZ. Additionally, observing the centres of other Milky Way-like Galaxies at different stages of these seemingly highly

time-variable processes informs how the galactic centre might look at various stages of this clumpy infeeding process, potentially making it possible to build a rigid timeline of star formation in this extreme environment.

1.6 Astrochemistry

One hurdle that has to be overcome when studying molecular clouds and stellar populations in their infancy is the composition of the molecular cloud itself. The bulk of the material within a molecular cloud is cold (i.e. 10 - 40 K, though molecular clouds in the extreme regions of galactic nuclei have much hotter temperatures, e.g. Krieger et al., 2017a) molecular hydrogen. In its atomic form, hydrogen is easily observable even at low temperatures as a result of its hyperfine spin-flip transition at 1.4 GHz (21 cm). However, in its molecular form, hydrogen has no permanent electric dipole moment and has a lower excited rotational state at 100-200 K. Since molecular clouds are far below even the lowest temperatures capable of exciting this transition of molecular hydrogen, we are forced to utilise proxies to study these regions. Astrochemistry is the study of the processes that form, excite and destroy particles and can be used to infer a great deal about the environment and related processes shaping a region, and this study is vital in understanding the evolution of molecular clouds.

One of the main proxies, due to its abundance within molecular clouds, is dust. Dust grains are much larger than hydrogen molecules and as a result they are capable of absorbing high energy radiation and re-radiating at longer wavelengths from 10's of μm to sub-millimetre wavelengths. At shorter wavelengths, the dust increases the opacity of the gas cloud, making it more difficult for observations to penetrate deeper into these clouds, as shown in Figure 1.10. Even this can be observationally beneficial, as the increased opacity at shorter wavelengths leads to absorption features in spectra from background sources that can be used to infer the molecular make up of the cloud.

1.6.1 Radiative Transfer

The radiation that we observe from a molecular cloud can be a complex mixture of emission and re-emission, absorption and self-absorption. While the clouds emit radiation across a wide range of wavelengths, as this radiation moves outwards through the cloud

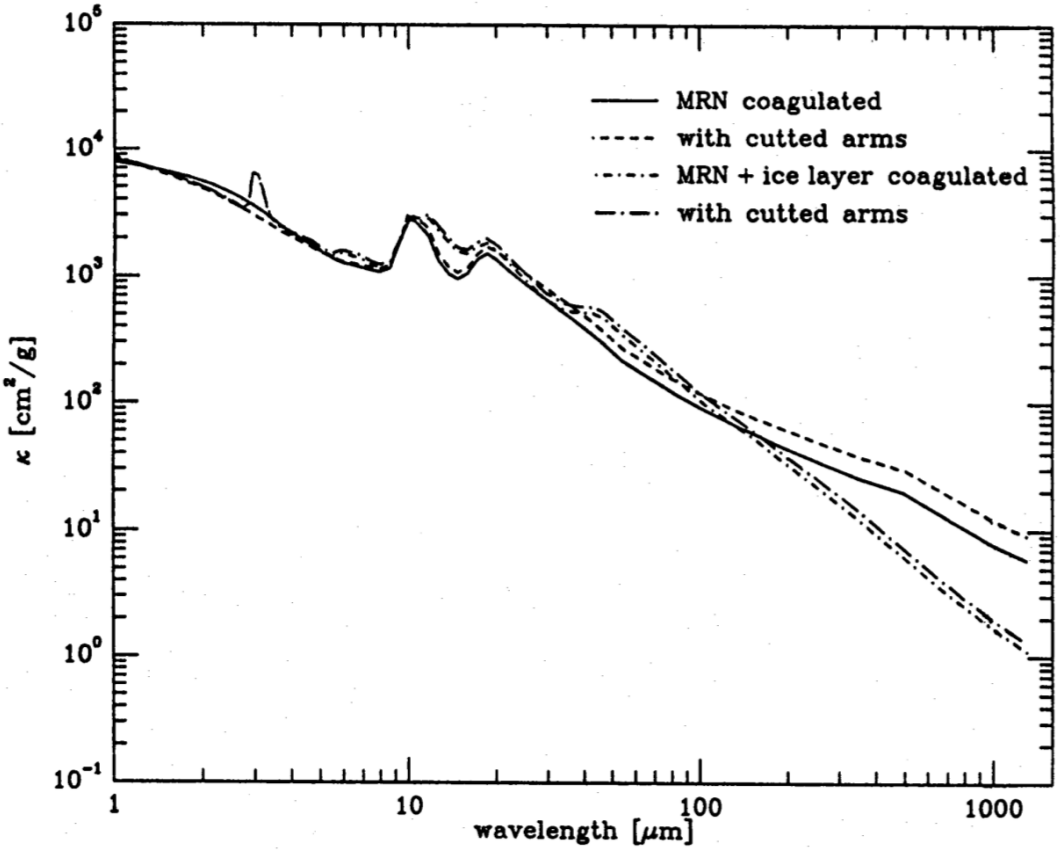

FIGURE 1.9: Total opacity of dust as a function of wavelength by Ossenkopf & Henning (1994) using the standard MRN distribution of grain sizes (Mathis et al., 1977).

it experiences a train of absorption and re-emission. Radiation from background sources along the line of sight will also be absorped by the foreground molecular cloud and be re-emitted at different wavelengths depending on the chemical composition of the cloud.

The radiation passing through such a molecular cloud will be affected differently depending on its frequency according to the equation of radiative transfer,

$$\frac{dI_\nu}{ds} = j_\nu - \kappa_\nu I_\nu, \tag{1.24}$$

where I_ν is the intensity of the radiation integrated along the line of sight, s is the thickness of the cloud, j_ν is the emissivity and κ_ν is the opacity of the gas. The ratio of these two parameters, i.e. the ratio of emission to absorption of a gas, is called the 'source function' and is given by

$$S_\nu \equiv \frac{j_\nu}{\kappa_\nu}. \tag{1.25}$$

If we assume the gas is in local thermal equilibrium then the emissivity, j_ν, is given by

$$j_\nu = \kappa_\nu \rho B_\nu(T), \tag{1.26}$$

where ρ is the mass density of the cloud and $B_\nu(T)$ is the Planck function,

$$B_\nu(T) = \frac{h\nu^3}{c^2} \frac{1}{e^{h\nu/kT} - 1}. \tag{1.27}$$

As a differential equation, Equation 1.24 can be written in the form of an integral, such that

$$I_\nu = I_\nu(0) e^{-\tau_\nu} + \int_0^{\tau_\nu} S_\nu(\tau_\nu^{'}) e^{-(\tau_\nu - \tau_\nu^{'})} d\tau_\nu^{'}, \tag{1.28}$$

where $I_\nu(0)$ is the background intensity, $d\tau_\nu = \kappa_\nu ds$ is the optical depth of a cloud of thickness s and $\tau_\nu^{'}$ is a dummy integration variable. The optical depth can also be expressed as a product of the mass surface density and the linear absorption coefficient ($\tau = \Sigma\kappa_\nu$). The first term in the right-hand expression of Equation 1.28 describes how a gas cloud between a background source and an observer impacts the observed intensity of the background source, while the second term on the right-hand side describes the emission released along the line of sight throughout the cloud. The sum of these leads to the overall observed intensity, I_ν. The subscript ν on the source function is just to make it explicit that the value is frequency dependent.

A typical value for the opacity of a gas at sub-millimetre wavelengths is 0.01 g cm^{-3}. which means we can effectively set the second term in Equation 1.24 to zero and thus perform a simple integration

$$I_\nu = \int j_\nu ds = \Sigma\kappa_\nu B_\nu(T) = \tau_\nu B_\nu(T) \tag{1.29}$$

where $\Sigma = \int \rho ds$ is the surface density of the gas and $\tau_\nu = \Sigma\kappa_\nu$. As a result, if we know the temperature and opacity of a cloud, it becomes trivial to determine the column density and thus the cloud mass using sub-millimetre observations.

We now consider the source function for a given transition from an upper level u to a lower level l. The local emission of a transition with rest frequency ν_{ul} can be expressed as

$$j_\nu = \frac{h\nu_{ul}}{4\pi} n_u A_{ul} \phi_\nu, \tag{1.30}$$

where n_u is the number density of molecules at the upper level, A_{ul} is the rate at which molecules at the upper level spontaneously transition to the lower level, and ϕ_ν is the line profile of emission.

Similarly, the absorption coefficient can be expressed as

$$\alpha_\nu = \frac{h\nu_{ul}}{4\pi} \left(n_l B_{lu} \psi_\nu - n_u B_{ul} \chi_\nu \right) \tag{1.31}$$

where n_l is the number density of molecules at the lower energy level, B_{lu} and B_{ul} are the Einstein coefficients for photon absorption and induced emission emission, ψ_ν is the absorption line profile and χ_ν the line profile of stimulated absorption, which here is considered a negative extinction process.

If we make the assumption that collisional excitation is dominating then we can assume that the emitted photons will be redistributed both in direction and frequency such that these three line profiles are equivalent, which means the source function can be written as

$$S_{\nu_{ul}} = \frac{n_u A_{ul}}{n_l B_{lu} - n_u B_{ul}} \tag{1.32}$$

If we assume thermal equilibrium, then the source function resembles a Planck distribution, so

$$S_\nu = \frac{n_u A_{ul}}{n_l B_{lu} - n_u B_{ul}} = \frac{n_u}{n_l} \frac{A_{ul}}{B_{lu} - (n_u/n_l) B_{ul}} = \frac{2h\nu^3}{c^2} \left(e^{\frac{h\nu}{kT}} - 1 \right)^{-1}. \tag{1.33}$$

We now introduce the Boltzmann factor, which describes the ratio of probabilities of these two energy states u and l, given

$$\frac{n_u}{n_l} = \frac{g_u}{g_l} e^{-h\nu/kT}, \tag{1.34}$$

where g_u and g_l are the statistical weights of these upper and lower energy levels and $h\nu = \Delta E$ is the energy difference between these energy levels, so Equation 1.33 can be rewritten as

$$S_\nu = \frac{2h\nu^3}{c^2} \left(\frac{n_u g_l}{n_l g_u} - 1 \right)^{-1}. \tag{1.35}$$

Therefore, the source function (per transition), and hence the observed intensity per line of sight, is heavily dependent on the ratio of particles in the upper energy level that are capable of emitting a photon and particles in the lower energy level capable of absorping a photon.

The intensity of any given molecular line will depend not only on the abundance, temperature and density of the gas, but also on the 'critical density' of that given molecule. The implications of this are that if we know the molecule that is being detected and the critical density at which it gets excited, we can infer lower limits on the density of the gas cloud itself. The critical density is defined as the density at which radiative decay rate from state i to state j is equal to the rate at which collisions depopulate this state i and is given by

$$n_{\rm crit} = \frac{A_{ji}}{\langle \sigma_{\rm cross} v_{\rm therm} \rangle} \tag{1.36}$$

where A_{ji} is the Einstein coefficient of a particular transition, $\sigma_{\rm cross}$ is the collisional cross section and $v_{\rm therm}$ is the thermal velocity of the gas. For example, the critical density of CO (J = 1 - 0) is 3000 cm^{-3} whereas the critical density for HCN is $\sim 10^{4-5}$ cm^{-3}. To see how a gas behaves above or below this density, we introduce the level population of a given molecule species,

$$\frac{\mathcal{L}}{n_X} = E A_{ji} \frac{e^{-E/kT}}{Z + n_{crit}/n}, \tag{1.37}$$

where $Z = 1 + e^{-E/kT}$ is the partition function of the gas. In the instance of $n >> n_{\rm crit}$, the partition function dominates the fraction and we end up getting a luminosity independent of the density of the emitting line, just the number of emitting particles. In the other limited instance of $n << n_{\rm crit}$, we get the $n/n_{\rm crit}$ term dominating and we end up with a luminosity dependent on the density of the gas. Observations of different transitions with different critical densities can therefore provide a rough estimate on the likely density range of the gas.

It is, however, possible for transitions to be observable in gas with a density below this 'critical' density. As such, an 'effective' density, $n_{\rm eff}$, was introduced by Evans (1999) and is the density that produces the (arbitrarily selected, but useful given typical observational sensitivity limits) integrated intensity of 1 K km s^{-1}. Given the definition it is clear that the 'effective' density is an observational parameter as opposed to the 'critical' density which is defined in terms of the properties of the molecules. Another benefit that this less formal definition can account for radiative trapping, which is the process by which an optically thick cloud may absorb a significant amount of the radiation that the cloud itself is emitting, effectively 'trapping' the radiation inside the cloud. By comparing the effective and critical densities of 12 of the most commonly observed dense gas tracers Shirley (2015a) found that the effective density is typically $1-2$ orders of magnitude less than the critical density.

1.6.2 Ice

Another reason that a solid understanding of dust in molecular clouds is vital is that dust catalyses the formation of molecules that otherwise cannot form. Dust is vital as in its absence, the density of the ISM means the simple molecules that go on to make more complex molecules do not interact sufficiently long enough periods of time for three body reactions to occur. The dust grain surface is cool enough for atoms to stick to it, but is sufficiently warm for them to move around, either by quantum tunneling in the instance of hydrogen atoms (Manicò et al., 2001) or via thermal hopping for heavier elements such as carbon or oxygen (Tielens & Allamandola, 1987). As such, they stay near each other for long enough periods of time for chemical reactions to occur. While on the surface of dust grains, these complex molecules are in the solid phase as ice mantles

which can only form in the cold and dense conditions of a molecular cloud on the surface of a dust grain.

The compositions of the gas and dust in the molecular cloud and the ices that form on the dust are heavily dependent on the local density within which the dust sits (Caselli et al., 1999). Observations of dust have found a variety of composite materials that can make up dust grains. Most interstellar dust is made up of silicate material, and while cosmic abundances would suggest the most likely metal ions found in these silicates are either Magnesium (Mg) or Iron (Fe), Molster et al. (2002) found these silicate materials to be predominately Mg-rich but Fe-poor. Spitzer & Fitzpatrick (1993) proposed this apparent Fe-poor composition is simply due to silicate dust grains having an Fe-rich core obfuscated by the Mg-rich mantle. Other proposed grain compositions are carbonaceous - implied primarily by a spectral feature at 2175 Å which indicates sp^2 bonded carbon, SiC - though Whittet et al. (1990) found that this only accounts for a few percent of interstellar dust, and carbonates such as $CaCO_3$ and $CaMg(CO_3)_2$ which appear to contribute less than 1% of interstellar dust.

It is no surprise that given the vast quantities of hydrogen gas that makes up molecular clouds, many of the more prevalent ice species that form on dust grain surfaces at low densities are dominated by hydrogen. The most common ice to form on the surface of dust is water ice, followed by carbon monoxide (CO), carbon dioxide (CO_2) and methanol (CH_3OH), with smaller abundances of methane (CH_4), ammonia (NH_3), formaldehyde (H_2CO) and methanoic acid (HCOOCH) plus many more ionic species (van Dishoeck, 2014a).

As the density of the gas increases to $\sim 10^5$ cm^{-3}, the freeze-out time (i.e the time it takes for the abundance of a species to deplete by a factor of e) shortens drastically to less than the lifetime of the core and as a result we see CO freezing out onto these now icy surfaces of the dust. This is important as CO is another highly valuable tracer of dense gas due not only to its low rotational transitions but also its relatively low critical density compared to other gas tracers. These leads to two separate layers of ice; the initial 'water-rich' layer on the direct surface of the grain and a second 'water-poor' layer with a high CO-H_2O ratio above the first. This 'water-poor' layer remains in place long enough for the molecular complexity to increase, as further hydrogen and oxygen continues to freeze out onto the surface, forming molecules like formaldehyde

(H_2CO) and methanol (CH_3OH). Irradiation of these ices can go on to produce even more complex molecules such as $HCOOCH_3$.

The dust closer to the forming protostars within a molecular cloud experience hotter and hotter temperatures. As the temperature rises above 20K the CO on the dust grain surface sublimates into the gas and more complex carbon chains begin to form in the gas. At higher temperatures, other molecules sublimate from the surface in order of the binding energy of the molecule until we arrive at what is referred to as the 'hot core' regime in which the luminosity of an embedded protostar heats the gas up to several hundred Kelvin. In this regime, even the more embedded water and methanol ices sublimate into the gas, including the minor molecules contained within the ice. Within this region, the abundance of sublimated molecules and the high temperatures typically lead to second phase of organic molecule formation. Figure 1.10 shows the chemical composition of the various stages of chemical evolution on the surface of dust.

As many molecules within these processes form with hydrogen, so to do many molecules form with the heavier hydrogen isotope deuterium, such as HDCO and DCN. In fact these cold clouds typically show a far greater proportion of deuterium to hydrogen than average, leading to molecules containing more than one deuterated hydrogen atom. This high proportion of deuterated molecules has the effect of increasing the rate and number of exothermic reactions occurring within a cloud, as a result of the lower zero-point rotational energy of deuterated molecules. On top of this it also has the affect of increasing the deuteration fraction of the molecules formed on a grain surface, particularly during the freeze out phase of CO.

While many of the molecules discussed previously can be indicative of a collapsing cloud on the path to forming a protostar, further molecules can inform us about the following stages and process. Some molecules require significantly higher temperatures to be formed. The most common mechanism attributed to their formation are shocks, which are very common within the ISM. When a nearby supernova explodes, two clouds collide (Cosentino et al., 2018) or jets and winds from adjacent astrophysical processes interact with a cloud (Tabone et al., 2020), a pressure wave travels through the cloud and increases the density and temperature drastically, for a short period of time, with temperatures typically reaching thousands of Kelvin. Not only does this encourage the more endothermic reactions to take place within the gas, but shocks can be sufficiently

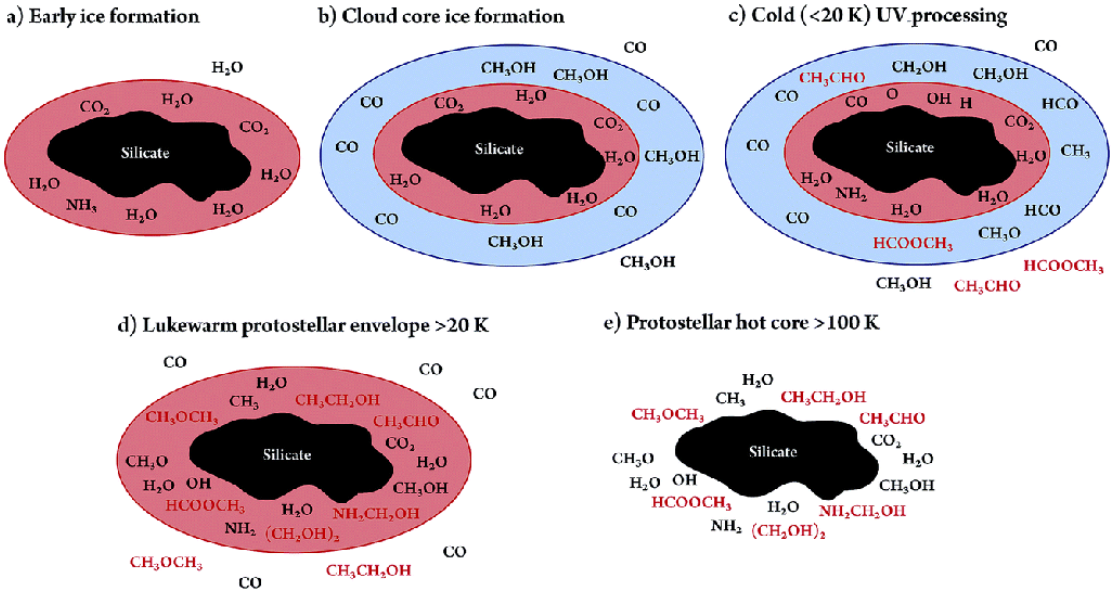

FIGURE 1.10: Diagram of the main stages of chemical evolution on the dust grain surface (in this instance, a silicate based dust grain), and the dependence on temperature, taken from van Dishoeck (2014b).

large to disrupt the accretion and formation of molecules on dust grain surfaces which can increase the abundance of H_2O in the gas, as well as being capable of destroying the dust grain itself.

The destruction of the dust grain leads to an increase in silicates (among other materials) within the gas and therefore the formation of molecules such as SiO, SO and SO_2. The sputtering of the ice mantle desorbs molecules into the gas phase, revealing these species in much colder and darker clouds than is typically required for the desorption of these molecules (Flower et al., 1996).

Therefore, while clouds are dominated by hydrogen, the presence (or lack thereof) of a plethora of different molecules can tell us a great deal about the properties and internal workings of a molecular cloud. The emission of many transitions of these molecules are readily observable with existing observational facilities and due to the temperature of the gas, and their spectral lines fall well within the sub-millimetre regime.

Again, under the assumption of an optically thin cloud, we can measure the motions of gas within a cloud using the Doppler shift of the line frequency caused by the motions of the gas. This is because any motion of the gas has the effect of shifting the frequency of the emitted radiation from each molecule away from the rest frequency of the transition. The emission frequency of a particle, ν is related to its velocity v via

$$\nu = \nu_0 \left(1 - \frac{v}{c}\right) \tag{1.38}$$

where ν_0 is the rest frequency of the transition and c is the speed of light. The velocity distribution $\psi(v)$ of these particles can therefore be derived from the line profile $\phi(\nu)$ using

$$\phi(\nu) = \psi\left(c\left[1 - \frac{\nu}{\nu_0}\right]\right) \tag{1.39}$$

If these random motions are the result of thermal energy, we can use this information to determine a temperature of the gas. In the instance of thermal motions, $\psi(v)$ will have the form of a Maxwellian distribution $\psi(v) \propto e^{-(\nu-\nu_{cent})^2/\sigma_\nu^2}$ where ν_{cent} is the central frequency, determined by the plugging the median velocity $\bar{v}$ into Equation 1.38. The width of this line profile is then given by

$$\sigma_\nu = \left(\frac{kT}{\mu}\right)^{1/2} \tag{1.40}$$

The bulk motion of the cloud, as well as random non-thermal motions of the particles, can impact this distribution significantly as well. The issue here is that as a result of these bulk, or non-thermal, motions, the resultant distribution can be Maxwellian. To distinguish between these two scenarios that produce very similar distributions, multiple transitions from the same molecule can be observed. If we return to the level population for a given molecule,

$$\frac{\mathcal{L}}{n_X} = E A_{ji} \frac{e^{-E/kT}}{Z + n/n_{crit}}, \tag{1.41}$$

we have three unknowns (T, n and n_x), so observing three transitions gives three equations to solve for these unknowns.

While the velocity and temperature of a molecular cloud can be inferred from optically thin gas, we typically infer the mass of a molecular cloud using a more optically thick line such as CO J = 1 → 0 or CO J = 2 → 1 (as well as transitions of ^{13}CO and HCN), as these tend to be brighter. This appears counter-intuitive at first, as optically

thick lines only show us the surfaces of clouds and therefore don't tell us much about the internal structure or density. These calculations make the assumption that the gas cloud is at virial equilibrium, take some characteristic volume density and then apply an observationally calibrated X-factor to convert the luminosity of a given optically thick line to a mass of the cloud.

1.7 Radio Astronomy

The radiation of many of the molecules discussed in section 1.6 is emitted within the submillimetre wavelength regime. This thesis focuses on the observation of submillimetre molecular line transitions, so this section describes the observational tools required to detect this radiation.

1.7.1 Receivers

Given the limitation of the human eye, the only way to observe light within the submillimeter wavelength regime of the electromagnetic spectrum is with the use of electronic receivers. The two main types of receivers used in radio astronomy today are bolometric and heterodyne receivers.

Bolometers measure the intensity of incoming radiation via the direct heating of the detector material. This material, typically an absorptive metal, is connected to a thermal reservoir that is cooled to a constant temperature such that each photon of incoming radiation is absorbed by the material and the energy is deposited in the form of heat. This change in temperature, given by $\Delta T = E/C$ (where E is the energy of the photon and C is the heat capacity of the detector material), is then measured either by a connected thermometer or by a change in the resistance of the material itself, measured by a voltage change. The sensitivity of a bolometer is typically given in terms of input signal that is required to produce an output of unity at the detector, referred to as the noise equivalent power (NEP). The NEP of a bolometer is inversely proportional to the square of the temperature of the bolometer material. As such, these receivers must be kept cool to achieve optimal sensitivity.

Bolometers are particularly useful for continuum observations as they have large bandwidths over which they keep a flat spectral response. However, by themselves, these receivers provide little to no spectral resolution, meaning they are quite poor tools for molecular line observations. They can be fitted with a filter, such as a Fourier transform spectrometer, to be used to observe some rotational transitions. Another drawback of bolometers, until the recent application of multi element arrays, is that a single bolometer acts as one pixel such that a single science target would require mosaicing of multiple observations.

Heterodyne receivers detect not only the intensity of the incoming radiation but also the phase. The frequency of the impinging radiation is then converted down to a lower 'intermediate frequency' (IF) driven by a local oscillator (LO). This process of frequency mixing gives the receiver its name. This technique has the benefit of allowing for hardware to be built which operates at a lower frequency, allowing for cheaper and more readily available electronics to be used.

This frequency mixing process produces two sidebands depending on how the frequencies are mixed, centred on $\nu_{IF} - \nu_{obs}$ and $\nu_{obs} - \nu_{IF}$ (where ν_{obs} is the observed frequency of the incoming radiation) for the lower and upper sidebands respectively. These sidebands can then be separated further by either polarisation if linear or circular polarisations are required or frequency if smaller bandwidths with higher spectral resolutions are required.

While bolometers are limited in use when it comes to molecular line observations, heterodyne receivers do not have this drawback, being equally capable of continuum and spectral line observations. Their ability to detect the phase of the impinging radiation on top of the intensity is also vital to interferometry, which I discuss in the next section. Both the Sub-Millimetre Array (SMA) and the Atacama Large Millimetre Array (ALMA) data used in this thesis make use of heterodyne receivers.

1.7.2 Interferometry

The angular resolution of a telescope is limited by two things: the wavelength of the light being observed, λ and the physical diameter of the telescopes dish, D, such that

$$\theta \propto \frac{\lambda}{D}. \tag{1.42}$$

As the wavelength of sub-millimetre light is several orders of magnitude larger than optical light, the physical diameter of the telescope must also be several orders of magnitude larger to achieve the same angular resolution. This increase in diameter size is impossible given the challenges in construction, as well as cost, that it would lead to.

As a solution to this problem, we use the technique of interferometry. This involves using systems of multiple telescopes in such a way that each individual pair of antenna seperated by some distance can be combined into a single telescope with an arbitrarily large dish size. This means instead of being limited to 10's of metres, we can achieve dish sizes of the order of hundreds of metres and up.

We will now consider the most simple possible iteration of an interferometer - that of two antenna seperated by a distance D (see Figure 1.11). Due to the geometry of this pair of antenna, as an incoming plane parallel light wave of the form $E\,e^{i\omega t}$, where E is the amplitude and ω is the angular frequency of the wave, hits one antenna there will be a short time delay, τ, before the same light wave hits the second antenna. This second signal will have the form $Ee^{i\omega(t-\tau)}$. Over the total observational time T, these two signals are then correlated into a single signal, R(τ),

$$R(\tau) \propto \frac{E^2}{T} \int_0^T e^{i\omega t} e^{-i\omega(t-\tau)} dt. \tag{1.43}$$

The total time of observation T will be much larger than the period of the incoming wave, $T >> 2\pi/\omega$. This means that the average signal over the entire observational time will be approximately the same as the average signal over a single period, which gives

$$\begin{aligned} R(\tau) &\propto \frac{\omega}{2\pi} E^2 \int_0^{2\pi/\omega} e^{i\omega\tau} dt \\ &\propto E^2 e^{i\omega\tau} \end{aligned} \tag{1.44}$$

This means that if our system remains static, i.e. if the relative geometry of the distance between our telescopes and the incoming wave remains constant, the incoming signal will remain the same as τ is unchanging, however if this orientation were to change, as

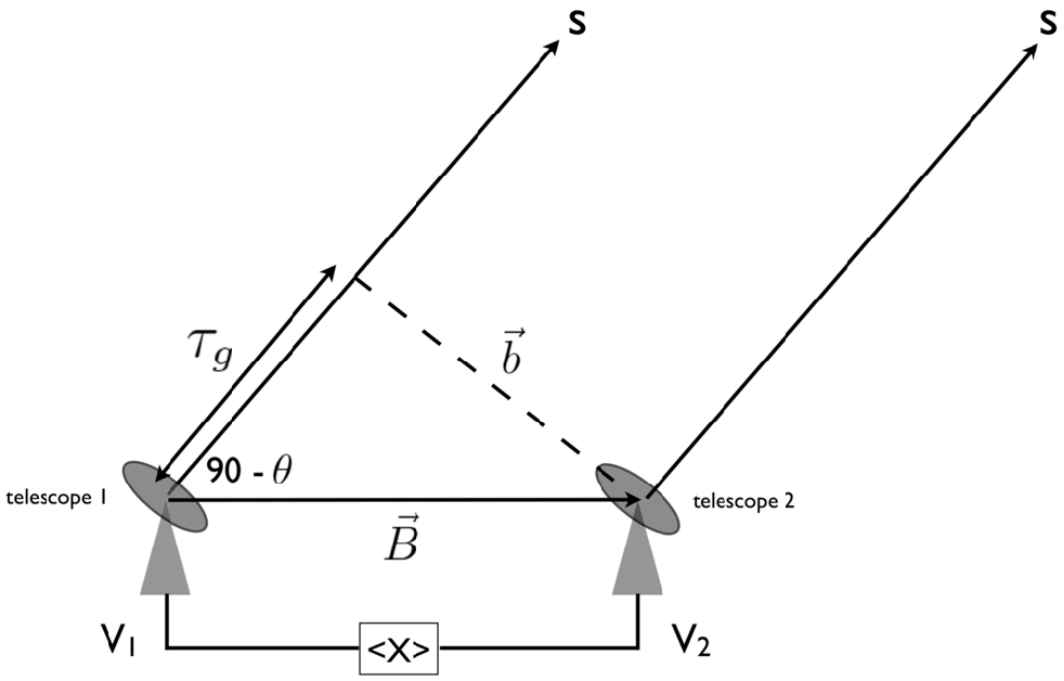

FIGURE 1.11: Most basic iteration of a radio interferometer. Two telescopes seperated by a 'baseline' $\vec{B}$ observing an astrophysical source, S. Telescope 1, which is further away from the source than telescope 2, observes incoming radiation slightly behind telescope 2 by an amount τ_g. The two signal, V_1 and V_2 are then correlated.

it does due the rotation of the Earth, this system will naturally measure interference fringes over time.

This form of the correlation function is highly simplified, with the overall form of the correlation function over a range of frequencies over an entire source is

$$R(\mathbf{B}) = \int_S \int A(\mathbf{s}) I_\nu(\mathbf{s}) \exp\left[i2\pi\nu\left(\frac{1}{c}\mathbf{B}\cdot\mathbf{s} - \tau_i\right)\right] d\mathbf{s}d\nu \tag{1.45}$$

where $\mathbf{B}$ is the vector distance between the telescope, $\mathbf{s}$ is the vector towards the source, $A(\mathbf{s})$ is the primary beam distribution, τ_i is the delay between signals caused by the instrument itself and d ν is a small frequency bin.

To solve this for $I_\nu(\mathbf{s})$ we introduce the vector $\mathbf{s} = \mathbf{s}_0 + \sigma$ where $\mathbf{s}_0$ is some point chosen at the centre of the source and σ is a phase correction to produce zero delay at this centre point. Plugging this in to Equation 1.45 gives

$$R(B) = \exp\left[i\omega\left(\frac{1}{c}B \cdot s_0 - \tau_i\right)\right] d\nu \int_S \int A(\sigma)I(\sigma)\exp\left(i\frac{\omega}{c}B \cdot \sigma\right) d\sigma \tag{1.46}$$

This integral is defined as the visibility function, while the initial exponential describes a plane wave with the phase of R(B). We then define u, v and w to be the coordinate system in units of the wavelength of light pointing in the east, north and in the direction of the source respectively. We define $\sigma = (x, y, z)$ such that x and y are cosines with respect to u and v. We rewrite the above as

$$\begin{aligned} V(u, v, w) = &\int_{-\infty}^{\infty}\int_{-\infty}^{\infty} A(x, y)I(x, y) \\ &\times \exp\left[i2\pi\left(ux + vy + w\sqrt{1 - x^2 - y^2}\right)\right] \frac{dxdy}{\sqrt{1 - x^2 - y^2}} \end{aligned} \tag{1.47}$$

These limits are set such that outside of the primary beam of the telescope, we observe an A(x,y) = 0, which has the benefit of making the above equation resemble a Fourier transform. We make the added assumption that for small region of the sky $\sqrt{1 - x^2 - y^2} \approx$ constant ≈ 1. With this assumption, this becomes

$$V(u, v, w)e^{-i2\pi\omega} = \int_{-\infty}^{\infty}\int_{-\infty}^{\infty} A(x, y)I(x, y)e^{i2\pi(ux+vy)}dxdy \tag{1.48}$$

Since $V(u, v, w)e^{-i2\pi\omega} \approx V(u, v, 0)$, if we subsititute this in and take the inverse Fourier transform, we get

$$I^{'}(x, y) = A(x, y)I(x, y) = \int_{-\infty}^{\infty}\int_{-\infty}^{\infty} V(u, v, 0)e^{-i2\pi(ux+vy)}dudv \tag{1.49}$$

.

To arrive at the observed intensity I(x,y) from this form, we simply take the inverse Fourier transformed $I^{'}(x, y)$ and divide through by A(x,y).

This is a highly simplified scenario. It doesn't take into account the Earth's rotation leading to a visibility function varying with time, and it only takes two telescopes into consideration. Figure 1.12 shows a real world example of the UV coverage of a multitelescope set up, varying with time. Each dotted line is paired with an identical dotted

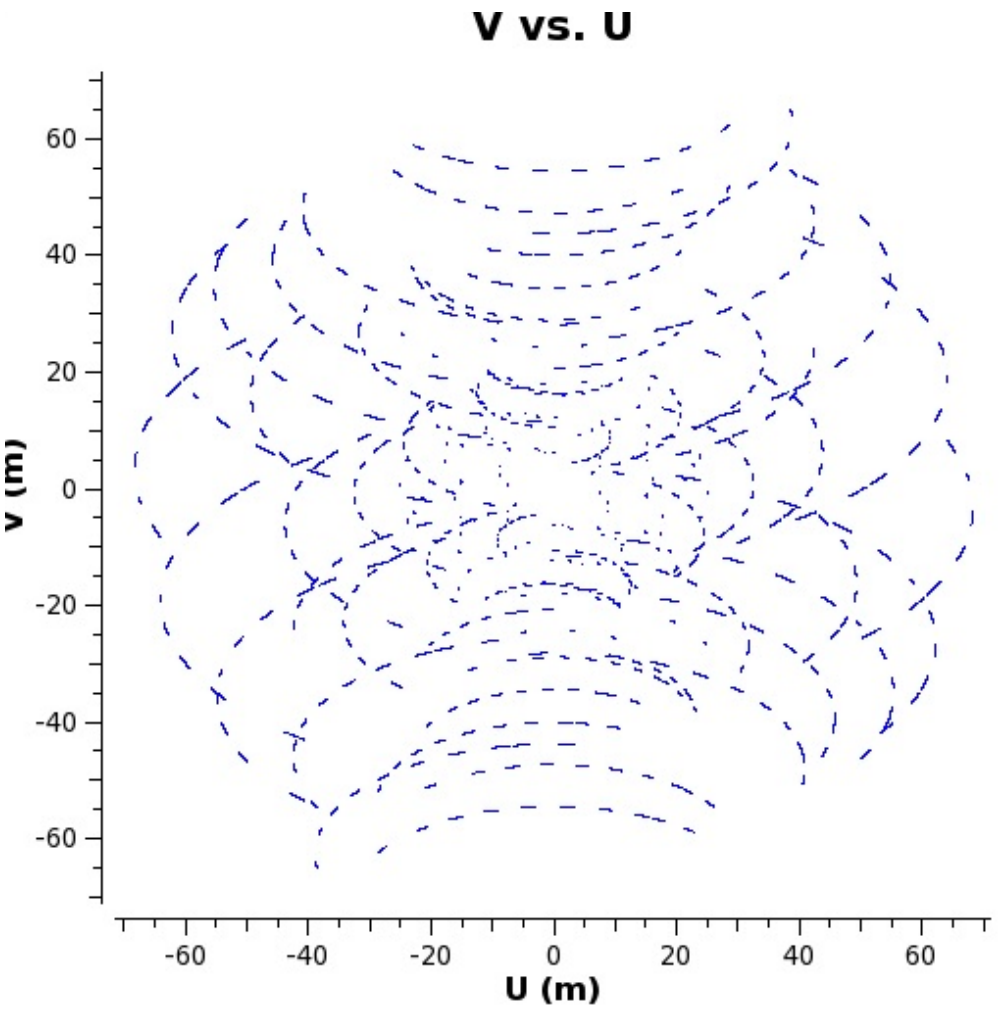

FIGURE 1.12: Example UV coverage of a real observational setup

line mirrored on each axis. These paired lines represent individual baselines and how the antenna, and therefore the baseline, moves over an observational period. The axes represent the physical distance between antenna in the **u** and **v** directions (in units of metres). The trajectories are shown using dotted lines as opposed to solid lines because during longer observations, the antenna often intermittently observe reference sources for error correction that is performed after the observational period.

While this is clearly far more complicated, the general process of converting the signals detected to an intensity in (x,y) space follows the same steps. However, these steps are idealised, and in reality a number of errors arise that will impact the signal. Not only do the electronics and the antenna present potential sources of error, Earth's atmosphere is inconsistent and can cause significant fluctuations in the incoming radiation. For these reasons, there is considerable amounts of calibration that must be done to observations

before they are science-ready.

One source of error is the primary beam distribution term, A(x, y). This distribution should not vary with time or from antenna to antenna, assuming all antenna within an array are designed to be identical - some arrays contain antenna of different sizes to sample different spatial scales of the target source. Optimally, the focal point of each primary beam must accurately track the centre of the source independently, with an accuracy of 10% of the full-width to half power of the primary beam. The difference in the centre of the primary beam and the centre of the source is called the antenna pointing error and can be estimated moderately well by observing a bright reference source. This reference source is selected because its position known accurately but a single reference source does not allow for the pointing error to be modeled to an 'acceptable' level. Repeating this cross reference over several bright stars, the estimation of the pointing error can be improved and informs the spatial alignment of the error. With enough reference sources, a model can be constructed to bring this error down to milli- or even micro-arcsecond level. This modelling can also be used to rectify errors caused in the gain when observing sources nearer the horizon, which can deform the surface of the antenna itself (Kundert et al., 2017).

Earth's atmosphere can also vary significantly over an entire observational period. As atmospheric conditions – such as pressure, temperature or humidity – fluctuate, the amplitude of the incoming signal, and the phase between a pair of antenna, can change drastically. This can have a serious impact on the conversion from measured to observed visibilities. Much like the pointing source error, this variation is calibrated by intermittently studying a reference source. This reference source is chosen to be a point source close to the observation target to ensure the air mass, and therefore the atmospheric conditions, are as similar as possible. As this point source is expected to have a consistent amplitude, as well as a consistent phase between each pair of antenna, a model of how conditions are affecting the phase and amplitude is made for each antenna pair. While these models are made using much shorter observations of a reference source, they are then extrapolated over the entire observational period and then used to correct any variations in the phase and amplitude of observations of the target source.

For observations over large bandwidths, it is possible for the phase and amplitude of the bandpass to vary significantly even if there were no atmospheric variations. This would

potentially mask weaker emission on a continuum source, replicating a changing line structure across frequency, or create positional offsets of lines with frequency, resembling a doppler shift.

To minimise this, the phase and amplitude of the bandpass is calibrated by measuring variations of a reference source which is known to have a flat spectrum, and no variability on the timescale of the observations. Once these observations are made, the bandpass is either calibrated on a channel-to-channel basis or a smooth function is fit to the entire bandpass before this model is then applied to the observation target. These general steps, while slightly varied, are performed at each interferometer across the world. In this thesis, both the Atacama Large Millimetre Array (ALMA) and the SubMillimetre Array (SMA) were used for observations. The more detailed calibration and imaging steps undertaken for the data used in the thesis are described in each of the relevant chapters.

1.8 Thesis Outline

This thesis explores the extreme conditions of Galactic centres and aims to bridge the gap between our current understanding of the evolution of gas in our CMZ and the nuclei of external galaxies.

In Chapter 2, I present the CMZoom survey and spectral data of the CMZoom survey, a high angular resolution SMA survey aimed to locate massive star precursors as well as current and future star formation sites and explain the dearth of star formation throughout the region. In Chapter 3 I present ALMA observations of dense gas tracers HCN and HCO^+ at the centre of M83, a nearby barred spiral galaxy comparable to the Milky Way in a number of ways, barring the recent starburst history at its very centre.

Chapter 2

CMZoom

Preface

Section 2.2 up to 2.2.5 of this chapter is taken from Battersby et al. (2020) to provide context for the CMZoom survey and the steps made to image the dust continuum data [1]. The work presented in the rest of this chapter is taken from Callanan et al. (2021). The co-PIs of the CMZoom survey are Cara Battersby and Eric Keto. Data calibration occurred during the entire period of observations by a number of members of the CMZoom survey, including Cara Battersby, Xing Lu, Qizhou Zhang, Nimesh Patel, Thushara Pillai, Dan Walker and Erik Keto. The continuum imaging pipeline was primarily developed by Dan Walker with some assistance from me at the later stages. I developed the spectral data imaging pipeline and conducted all the subsequent analysis.

2.1 Introduction

The central ∼500 pc of our Galaxy – the 'Central Molecular Zone' (CMZ) – provides a unique insight into the environmental dependence of the processes that govern star formation (Morris & Serabyn, 1996b; Longmore et al., 2013c; Kruijssen et al., 2014b). The conditions found within the CMZ are far more extreme than those found in the Galactic disk, more closely resembling high redshift galaxies (Kruijssen & Longmore,

[1] CMZoom: Survey Overview and First Data Release, C. Battersby et al., The Astrophysical Journal Supplement Series, Vol. 249, Issue 2., Aug 2020, © AAS. Reproduced with permission

2013b). The dense molecular gas in the CMZ, from which stars are expected to form, has been extensively studied both as part of large-scale Galactic plane surveys (e.g. Dame et al., 2001; Walsh et al., 2011b; Purcell et al., 2012; Longmore et al., 2017; Jackson et al., 2013), as well as more targeted observations (e.g. Rodríguez-Fernández et al., 2004; Oka et al., 2007; Bally et al., 2010; Molinari et al., 2011b; Jones et al., 2012; Mills & Morris, 2013b; Rathborne et al., 2015; Krieger et al., 2017b; Mills & Battersby, 2017b; Kauffmann et al., 2017b; Ginsburg et al., 2018a; Walker et al., 2018b; Pound & Yusef-Zadeh, 2018; Mills et al., 2018b; Lu et al., 2019).

The *CMZoom* survey (Battersby et al., 2017b, 2020) aimed to fill a key unexplored part of observational parameter space by providing the first sub-pc spatial resolution survey of the CMZ at sub-millimetre wavelengths, targeting all dense gas above a column density of $N(H_2) \geq 10^{23}\,cm^{-2}$. The survey goals were to provide (i) a complete census of the most massive and dense cloud cores; (ii) the location, strength and nature of strong shocks; (iii) the relationship of star formation to environmental conditions such as density, shocks, and large-scale flows.

A detailed overview of the *CMZoom* survey and the continuum data release was provided by Battersby et al. (2020, hereafter called 'Paper I'). Paper I found that while the CMZ has a larger average column density than the Galactic disk, the compact dense gas fraction (CDGF) is significantly lower. As star formation can only proceed within these compact substructures, Paper I concludes that identifying and understanding the processes that inhibit the formation of compact substructures is vital in explaining the current dearth of star formation within the CMZ (Longmore et al., 2013c; Kruijssen et al., 2014b; Barnes et al., 2017).

The complete catalog of compact ($< 10''$) sources was derived using dendrogram analysis and was presented in Hatchfield et al. (2020, hereafter called 'Paper II'). Two versions of this catalog were produced: a robust catalog that contains only sources detected with high confidence; and a second catalog focusing on completeness across the CMZ. The catalogs contain 285 and 816 sources, respectively. These sources have typical sizes of $0.04 - 0.4\,pc$ and are likely sites for future star formation. Using this catalog, Paper II estimates a maximum star forming potential in the CMZ of $0.08 - 2.2\,M_\odot\,yr^{-1}$, though this drops to $0.04 - 0.47\,M_\odot\,yr^{-1}$ when Sagittarius B2 – the dominant site of active star formation in the CMZ – is excluded.

In addition to the 230 GHz continuum data, the *CMZoom* survey also observed spectral line emission with an 8 GHz bandwidth using the ASIC correlator, and an additional 16 GHz using the SWARM correlator during latter stages of the survey. In this paper, we give an overview of the spectral line data of the *CMZoom* survey, and present the full spectral data cubes. We have focused on the data from the ASIC correlator to avoid variation in bandwidth resulting in the phasing in of the SWARM correlator. The spectral set-up (detailed in Paper I) targeted a number of dense gas tracers (CO isotopologues, multiple H_2CO transitions), as well as key shock tracers (SiO, SO, OCS) and compact hot core tracers (CH_3OH).

This paper is organised as follows. Section 2.2 details the CMZoom survey, and the imaging pipeline for the continuum data as described by Paper I and for the spectral line data. Section 2.3 outlines the generation and fitting of spectra and the production of moment maps. Section 2.4 describes the data across the whole survey region before describing the data on a per region basis. Section 2.5 explores the variation in line emission across the survey. Section 2.6 examines the line properties of the *CMZoom* continuum sources identified by Hatchfield et al. (2020). In Section 2.7, we use the results of the line fitting and conclusions in Section 2.6 to determine the likely virial state of the continuum cores, search for signs of proto-stellar outflows and intermediate-mass black holes in the CMZoom line data.

2.2 The *CMZoom* survey

The *CMZoom* survey was one of the first large-scale projects undertaken at the Sub-millimeter Array (SMA). The survey (Project ID: 2013B-S091) took about 550 hours on the SMA, in compact and subcompact configuration, at 230 GHz covering wideband (8+ GHz) dust continuum and a number of key spectral lines. The resulting images have an angular resolution of about 3″ (0.1 pc), and a spectral resolution of about 1 $\mathrm{km\,s^{-1}}$, over all of the highest column density gas in the inner 5° × 1° of the Galaxy (about 700 × 150 pc based on Galactic Center distance of 8.15 kpc from Reid et al., 2009). In total, the *CMZoom* mosaic covered about 5×10^6 $M_\odot$ of dense gas in the CMZ (measured from the Herschel column density map). With a total CMZ mass of about $(2-6) \times 10^7$ $M_\odot$ (Morris & Serabyn, 1996a), this corresponds to covering about 10−25% by mass of the CMZ, selected to be of the highest column density which we expect to

be the most relevant for understanding high-mass star formation, and such regions are well-suited to observation with the SMA.

Our column density cutoff is based on smoothed column density contours, in an effort to produce maps of mostly contiguous regions, therefore individual bright pixels above this threshold are not included. Similarly, some lower-level emission at the edges of clouds, or in between bright emission is included. With the inclusion of select regions of interest with lower column densities, the full column density distribution of the mapped regions is not a clean cutoff at 10^{23} cm^{-2}. These additional regions include 'far side cloud candidates', the circumnuclear disk (CND), pointings toward the 'Arches' ionized filaments, isolated high-mass star forming (HMSF) candidates and a bridge of emission, connecting the Dust Ridge and the 50 km s^{-1} cloud detected to have strong H_2CO features in the APEX-CMZ survey (Ginsburg et al., 2016). This leads to a total area of approximately 350 square arcminutes

Observations for the *CMZoom* survey were completed using the 230 GHz receiver at the Submillimeter Array (SMA) over the course of four years (May 2014 to July 2017), during which time the SMA was gradually upgraded from the ASIC correlator to the wideband SWARM correlator (Primiani et al., 2016) in phases. Therefore, the *CMZoom* survey mirrors this variable bandwidth coverage over time, with the first observations being limited to the 8 GHz ASIC correlator covered 216.9 GHz to 220.9 GHz in the lower sideband, and 228.9 GHz to 232.9 GHz in the upper sideband while the final observations contained the full 16 GHz SWARM coverage, the most extended of which is 211.5 - 219.5 GHz in the lower sideband and 227.5 - 235.5 GHz in the upper sideband. Most observations are bookmarked by these extremes (Figure 2.1). The spectral resolution is consistently about 0.812 MHz (1.1 km s^{-1}) over the entire bandwidth across the published datasets.[2]

In addition to the 230 GHz dust continuum, which is the focus of this paper, the following spectral lines were targeted and consistently included in all observations. In the lower sideband, *CMZoom* observed the triplet of para-H_2CO lines of $3_{0,3}$–$2_{0,2}$, $3_{2,2}$–$2_{2,1}$, and $3_{2,1}$–$2_{2,0}$ at 218.222192, 218.475632, and 218.760066 GHz (all frequencies are rest frequencies from CDMS Müller et al., 2005, as compiled on splatalogue[3]), respectively,

[2]We note that the newer raw SWARM data are of substantially higher spectral resolution (a factor of 8), but were spectrally smoothed to 1.1 km s^{-1} to maintain consistency with previous ASIC data and to maintain manageable file sizes for image processing and analysis.

[3]https://www.cv.nrao.edu/php/splat/index.php

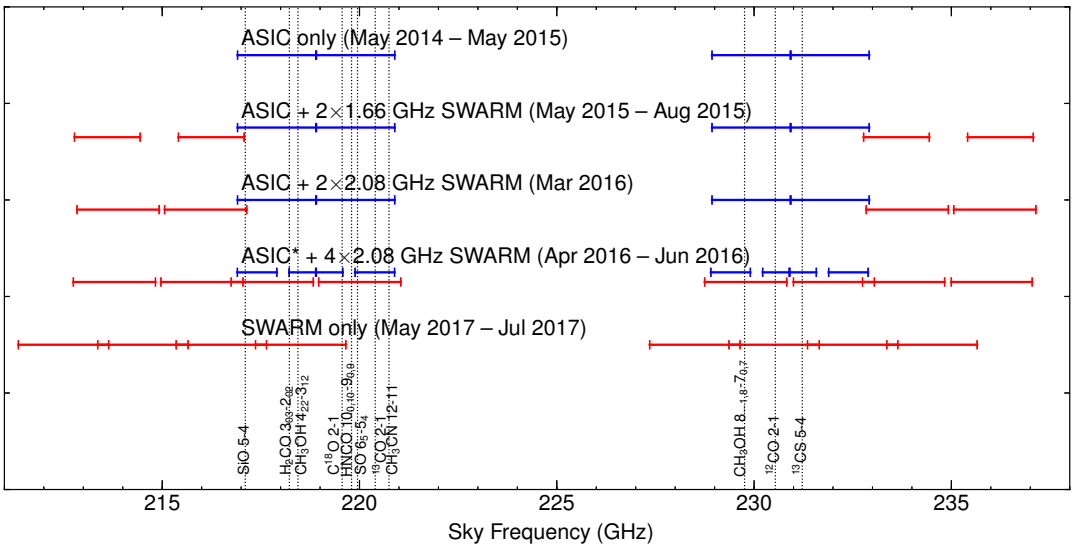

FIGURE 2.1: Spectral coverage of the *CMZoom* survey over time. Observations for the *CMZoom* survey took place over the period of May 2014 to July 2017. During this time, the SMA transitioned from the ASIC to the SWARM correlator, starting with ASIC only (spectral coverage shown in blue) and ending with SWARM (spectral coverage shown in red) only, with varying degrees of overlap in between. The ASIC* from April to June 2016 indicates a transitionary period where ASIC was operating differently than its standard mode. Our key target spectral lines are shown as dashed lines in the plot. Coverage of these lines was maintained over the lifetime of the survey, except for a few tertiary lines in the three tracks observed in 2017 and a few other oddities that will be discussed in the spectral line data release paper.

^{13}CO and C^{18}O J=2–1 at 220.39868420 and 219.56035410 GHz, respectively, SiO 5–4 at 217.104980 GHz, and a number of CH_3OH and CH_3CN lines. In the upper sideband, *CMZoom* observed the ^{12}CO J=2–1 line at 230.538000 GHz, the H30α recombination line at 231.90092784 GHz, as well as a number of CH_3OH transitions. We note that the extended bandwidth observations cover substantially more spectral lines than those listed here. Preliminary analysis suggest incredibly rich spectra toward Sgr B2 and other Galactic Center regions, which clearly illustrate the benefits of the extended spectral coverage.

2.2.1 SMA Data Calibration

All datasets, independent of their correlator setups (ASIC-only, ASIC+SWARM and SWARM-only), were calibrated using the MIR IDL software package following standard SMA calibration procedures. Some tracks required an updated baseline calibration, as noted in the SMA observer logs, which was the first step in the calibration process. For the most

part, poor weather visibility datasets with system temperatures higher than 400 K were discarded, however, this was not a strict rule. Generally, any data of sufficient quality to improve the overall region RMS was included.

Once the above tasks were completed, the first calibration step was to calibrate the system temperature over the course of the night. The next step was to perform a bandpass calibration using observations of either 3C454.3, 3C279, Saturn, or a combination of these sources when available. Bandpass data were inspected for noise spikes in every baseline, which were subsequently removed by averaging the adjacent channels. When multiple correlators (ASIC+SWARM) were used for the observations, they were bandpass calibrated independently. Gain calibration is the next step, both phase and amplitude, performed with standard SMA routines. Both phase and amplitude of our phase calibrators on each baseline were inspected to identify "bad" data and phase jumps. Phase jumps required some data to be flagged, split into separate time intervals and calibrated independently.

Flux calibration was performed based on comparison with the brightness of planets and their satellites, based on models of brightness temperature adopted from the Atacama Large Millimeter/submillimeter Array's (ALMA's) CASA software as outlined in Eric Keto's MIR IDL webpage. Flux calibrations were checked against the standard SMA calibrator list[4] with reasonable agreement. The uncertainty in the absolute flux calibration was estimated to be $\sim 10-20\%$. Next, Doppler corrections were performed on all science targets. The final step of the data calibration was a careful inspection of the data as a function of time and frequency. At the end of data reduction, we imaged our secondary gain calibrator (1744-312) for every track to verify the quality of phase transfer that was based on our primary calibrator (1733-130). The imaging and deconvolution were accomplished using the MIRIAD and CASA software packages, as explained in further detail in the following section.

2.2.2 Imaging Pipeline

The fully-calibrated SMA compact and subcompact data are merged, deconvolved (cleaned), and imaged in CASA. First, however, the calibrated MIR data files produced by MIR IDL must be processed and prepared for imaging. Due to the large number of data files

[4] http://sma1.sma.hawaii.edu/callist/callist.html

we opted to develop an imaging pipeline, such that the full survey data products could be generated in a fully-automated, uniform, and repeatable manner. In the following subsections, we describe this process in detail, and the complete scripts have been made publicly available on the CMZoom GitHub page[3].

The first step of the pipeline is to extract the relevant data for the given science target. The script takes the given name of the science target and the path(s) to the corresponding calibrated SMA data files. In general, each source will have at least two calibrated data files, corresponding to the compact and subcompact array, separated by a maximum baseline of 70m and 30m respectively. However, many sources were observed over multiple nights and therefore can have many associated data files. This is typically either because the source is large, and therefore required multiple tracks to complete the pointing mosaic, or because the track was of marginal quality and had to be repeated to achieve satisfactory quality when combined.

Each file is successively loaded into MIR, where the meta-data are inspected to determine whether the data were taken with the ASIC or SWARM correlator, or some combination of the two. It is necessary to make such a distinction, as the data from the two correlators must be exported and processed separately prior to imaging. This is due to the fact that the SWARM correlator provides many more channels per spectral window, and therefore requires a greater number of channels to be flagged on the edges of the windows. Having determined the correlator information, the script then uses the IDL2MIRIAD routine to export the source data in MIRIAD format. At the time of our analysis, there was a known bug when exporting entire sidebands and converting to CASA measurements sets, where the frequency information of data cubes is offset and gaps are introduced between each spectral window. To circumvent this, we export each spectral window individually, process it separately, and recombine all windows again before imaging.

All spectral window data associated with the given science target are loaded into MIRIAD to be processed prior to imaging. In general, there are 48 spectral windows for the ASIC data and 2–4 for the SWARM data. The noisy edge channels for each spectral window are flagged using the *uvflag* command. The number of edge channels flagged are 10 and 100 for the ASIC and SWARM windows, respectively, which corresponds to approximately 10% of the full bandwidth. Each spectral window is then exported as a *uvfits* file using the *fits* command, and then imported into CASA as a MeasurementSet. For a

given source, all corresponding tracks are concatenated per sideband using the *concat* command. This ultimately results in two or four measurement sets per source, depending on the correlator used, either ASIC or SWARM, which each have two sidebands.

2.2.3 Continuum imaging

Prior to imaging the dust continuum emission, the continuum component of the emission must be subtracted from the spectral line data by identifying the line free channels. To do this in an automated way, we utilized the *findContinuum* function of the hif_findcont task of the ALMA Cycle 7 pipeline version 5.6.1 (Humphreys et al., 2016).[5] This is done in the image plane and is used to inspect data cubes and determine the uncontaminated continuum-only channels. First we use the *tclean* command with zero iterations to generate dirty cubes for all measurement sets for a given source. The *findContinuum* routine then takes each dirty cube, creates an averaged spectrum, and searches for any emission that is greater than some user-defined threshold, which we choose to be 5-σ (anything fainter than this is not likely to contribute substantially to the continuum flux). The program then determines the range of channels that do not have emission above this limit (i.e. the line-free, continuum-only channels). This routine outputs the identified line-free channels in plain-text format such that they can be fed directly into the *tclean* command in CASA to generate a continuum image from the data cubes.

To generate images of the 1.3 mm dust continuum emission, all measurement sets for a given source are imaged together using *tclean* using the multi-frequency synthesis gridder. The *spw* parameter is used to specify the continuum-only channels for each measurement set that were determined in the previous step using *findContinuum*. A range of input parameters were explored for *tclean* to determine how they affected the resultant images. We decided to use the *multiscale* parameter with scales of [0, 3, 9, 27], to better recover both the large- and small-scale structures within the images. We use the *Briggs* weighting scheme with a *robust* parameter of 0.5, as this yields a fair compromise between the angular resolution and the noise properties of the resulting image. We also set the pixel scale to 0.5″, which equates to 6-8 pixels per beam major axis given typical synthesized beams of approximately 3-4″. To apply clean masks during the cleaning, we used the *auto-multithresh*[6] parameter in *tclean* (Kepley et al., 2020).

[5] https://almascience.nrao.edu/documents-and-tools/alma-science-pipeline-users-guide-casa-5-6.1
[6] https://casa.nrao.edu/casadocs/casa-5.3.0/synthesis-imaging/masks-for-deconvolution

This auto-masking algorithm is implemented to iteratively generate and grow masks in a way that is similar to how a user would manually create masks. This requires several user-defined input parameters. We use the recommended parameter values for ALMA 7 m (ACA) observations, as the array is reasonably similar to the SMA. These parameters are: *sidelobethreshold* = 1.25, *noisethreshold* = 5.0, *lownoisethreshold* = 2.0, *minbeamfrac* = 0.1, and *growiterations* = 75. To determine the appropriate cleaning threshold for each region in the survey, we first make rough continuum maps using a uniform cleaning threshold of 5 mJy beam^{-1}, which corresponds to $\sim$2 σ RMS of the survey. We then take the residual maps for each region, and measure the RMS using a number of rectangular regions of various sizes that are placed randomly within the confines of each mosaic. We then take the median of the RMS values, which is used as the final cleaning threshold per region, which we set to 2 σ. We set the clean iterations arbitrarily high such that the algorithm reached the threshold value and was not limited by the number of iterations. The images used in the remainder of the paper have been corrected for the primary beam using *pbcor*, but we also release the uncorrected version of the data.

The final images are then exported from CASA as FITS files. In addition to FITS files of the individual source dust continuum emission, we also produce a full CMZoom survey dust continuum emission mosaic FITS file. We do this via a combination of different Python packages. First, each individual survey image is transformed from units of Jy beam^{-1} to MJy Sr^{-1} using RADIO_BEAM[7] to extract the beam information, which is then used with ASTROPY[8] to account for the beam and transform the units. This conversion is performed as the different survey regions have differing beam properties, and it is therefore not appropriate to include the beam information in the units of the mosaic. The transformed images are then reprojected on to a large fits image using the REPROJECT[9] package to obtain a full survey mosaic with consistent units of MJy/sr. The REPROJECT package is also used to transform the native images from J2000 to Galactic coordinates, due to a known bug at the time in the CASA transformation that has since been fixed[10].

[7] https://github.com/radio-astro-tools/radio-beam
[8] http://www.astropy.org/
[9] https://reproject.readthedocs.io/en/stable/
[10] https://casa.nrao.edu/casadocs/casa-5.4.0/introduction/release-notes-540

2.2.4 Combination with Single-Dish Data

We release SMA-only data products, including the combined SMA compact and sub-compact configuration data for each region, as well as data products that have been combined with single-dish (zero- and small-spacing) data to achieve better recovery of structure at large spatial scales.

The Bolocam Galactic Plane Survey (BGPS) surveyed the Galactic center region at 1.1 mm (271.1 GHz) with a resolution of 33″ (Bally et al., 2010; Aguirre et al., 2011b; Ginsburg et al., 2013), and is currently the best data for combination, due to its proximity in frequency, and resolution being reasonably well-matched with the SMA primary beam (about 45″). For the dust continuum emission, we scale the BGPS data to the SMA-observed wavelength (about 1.3mm), assuming a spectral index of 1.75 (Battersby et al., 2011) and combine with the SMA and BGPS data using the CASA task FEATHER. The BGPS achieves a complete sensitivity to large spatial scales of 80″ or 3 pc and partial recovery of spatial scales up to 300″ or 12 pc (for more details see Ginsburg et al., 2013).

We have investigated other methods for single-dish combination, such as using the single-dish data as a model for the SMA cleaning, then combining. However, we find that the *feather* task performs equally well and choose this method for this work.

2.2.5 Spectral Imaging Pipeline

Given the size of the survey both spatially and spectrally, a pipeline was developed to take the data from post-calibration to final imaging steps. We used the software package CASA[11] to ensure a consistent approach to data reduction across the whole survey. In this section, we describe the stages of this pipeline.

The input for the pipeline is the source name (variable 'sourcename') and the file paths corresponding to the relevant calibrated datasets in MIR[12] format. Each of these datasets are called into MIR, which we use to determine the associated correlator (or combination of correlators for observations taken within the middle of the observing period). Once this is determined, we use IDL2MIRIAD to convert the data from MIR to

[11] https://casa.nrao.edu/
[12] https://www.cfa.harvard.edu/ cqi/mircook.html

MIRIAD format. We split the dataset into chunks, with the number of chunks depending on the correlator, before we flag the data. We enforced an 8 channel and 100 channel flag for each chunk of data from the ASIC and SWARM correlators, respectively, to remove noisy channels from both edges of the bandpass. We then convert these flagged data into *uvfits* format using MIRIAD's *fits* command with *line* set to *channel*.

These *uvfits* files are then loaded into CASA and converted into a readable format using the *importuvfits* task in frequency mode with an LSRK outframe. They are then concatenated into full upper and lower sidebands for each correlator using *concat*. These sidebands are then continuum subtracted individually, using *uvcontsub*. We do this by estimating the baseline for all channels, excluding those surrounding the brightest line within each sideband, which in this case we took to be the ^{12}CO and ^{13}CO transitions for the upper and lower sidebands, respectively.

To image these continuum-subtracted datasets, we first calculate the phase center with the *SkyCoord* function of astropy in a Galactic reference frame, using the sourcename for the longtitude, l, and latitude, b, coordinates. The output of this is then transformed to fK5 and output in the appropriate R.A. and Dec. format.

We then generate a 'dirty' image cube to determine the appropriate R.M.S. noise level for the cleaning process. To do this, we run CASA's *tclean* task with 0 iterations over a patch of size 100 x 100 pixels around the phase center. We also perform this over a 100 channel sub-chunk of the whole frequency space to minimise the time taken. This channel range has been predetermined to be line-free by eye in all cubes. We then use *imstat* to calculate the average R.M.S. noise level throughout this cube.

Given the large variety of mosaic sizes and limited computing power, we implemented two separate methods to produce cleaned images. These methods are separated by image size, with a cut at 1000 pixels per spatial axis. For images smaller than this, we simply pass the full cube into a *tclean* task. We set the pixel size to $0.5''$, corresponding to 6-8 pixels per roughly 3-4$''$ beam. We used a *multiscale* deconvolver with scales equal to $0''$, $3''$, $9''$ and $27''$to recover both large and small scale structures. A channel width of 0.8 MHz, or 1.1 km s^{-1} was enforced. The weighting for each image was set to *briggs*, with a *robust* parameter of 0.5. The *threshold* is set to 5σ where possible, with σ calculated from the dirty cube previously discussed, with an arbitrarily high number (10^8) of *iterations* to ensure we reach this threshold. For some clouds, this 5σ threshold

led to severe imaging artifacts so the threshold for these clouds were manually modified to remove the artifacting. We make use of the *chanchunks* parameter for these cleans, setting it to -1 to allow for the number of chunks that the datacube is split up into to be determined based on the available memory. We do not utilise the *auto-multithresh* parameter as used for the continuum images at this stage.

For images larger than the 1000 pixel cut described above, we instead clean separate cubes surrounding a number of key spectral lines that the CMZoom survey targeted (see Table 2.1 for details). For the upper sideband, this is ^{12}CO(2-1) and OCS, and for the lower sideband we include three transitions of H_2CO in the range of 218 - 219 GHz, ^{13}CO(2-1) , C^{18}O(2-1) , SiO, OCS and SO. Each of these cubes is 0.3 GHz wide, centred on the rest frequency of the corresponding transition, which is passed into the task within the *restfreq* parameter to allow for easy estimation of the velocity. All other parameters in these *tclean* tasks are the same as the smaller cubes.

Each output image is then primary beam corrected by dividing the image by the corresponding .pb file using CASA's *immath*.

2.2.6 Beam Correction

A quick by-eye inspection of these cubes showed that for a number of channels the beam size increased by factor of a few, typically at the start and end of the frequency coverage, as well as the centre of the datacube, where there is a natural gap in frequency coverage. Figure 2.2 shows the variation in beam area as a function of frequency for an example region, G0.001-0.058. While the cause of this variation is unknown, we believe this is the result of a natural gap in the SMA's spectral coverage which shifts in absolute frequency depending on when the observation is taken. As these data are the combination of compact and subcompact configurations, if the frequency shift causes a channel to only have compact or subcompact data the beam will be different. This variation in beam size typically resulted in a very different noise profile within these channels in the cube, causing spikes in the spectra that could be mistaken as line emission.

To resolve this issue, we used the python package *spectral cube* to identify these 'bad' beams. We found that defining 'bad' beams as those that vary from the median beam by 30% either in semimajor or semiminor axis, or beam area, identified all the problem

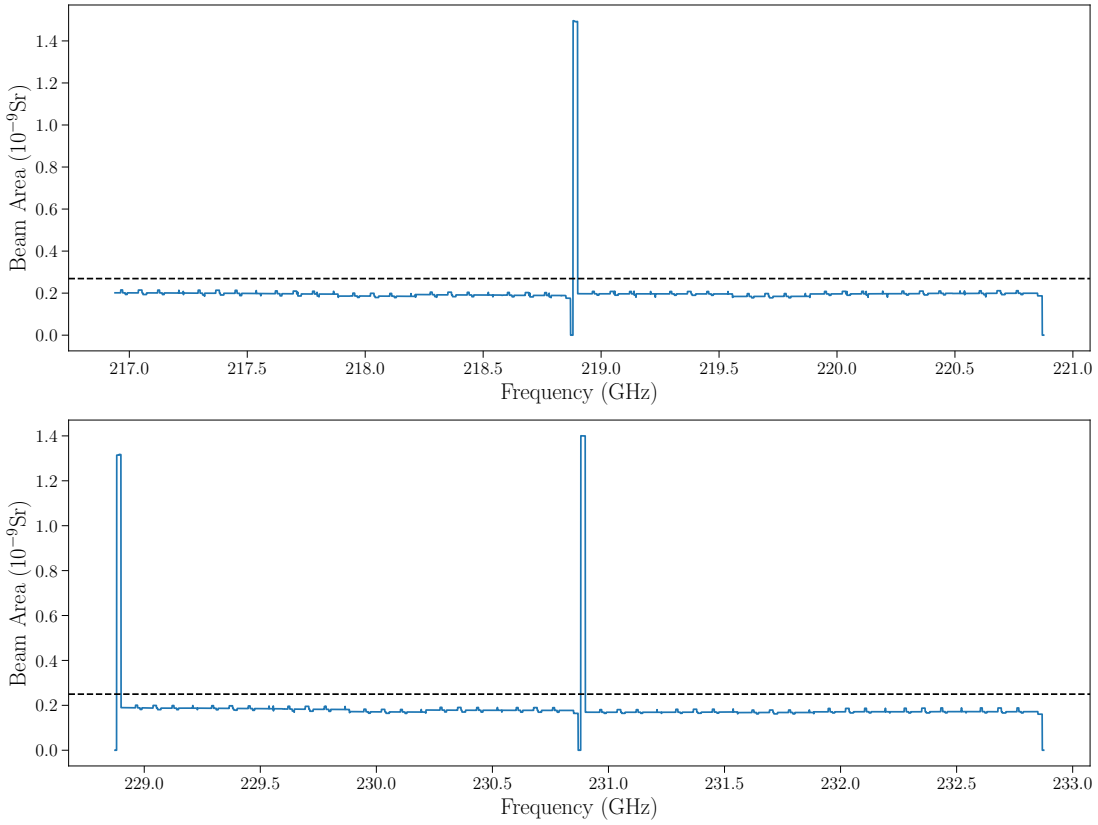

FIGURE 2.2: Beam area versus frequency for both ASIC sidebands for the source G0.001-0.058. The sharp peaks at the centre of both panels and the left of the bottom panel show the channels with a problematic beam. The horizontal dashed line indicates the area of the smoothed beam in the final cube.

channels. The channels with beams that are caught by this flag are masked and then the rest of the cube is convolved to a beam corresponding to the smallest beam size that exceeds all unmasked beams.

The cubes are then reprojected into Galactic coordinates using the python package *reproject*. We do this using python instead of CASA due to a known bug that introduces a slight offset when reprojecting within the *imregrid* task[13]. At this stage, the cubes are split into smaller subcubes targeting key dense gas tracers as well as star formation and shock tracers.

[13]This bug has been fixed as of CASA version 5.4.0 (see https://casa.nrao.edu/casadocs/casa-5.4.0/introduction/release-notes-540) for details

2.3 Spectral line fitting and moment map generation

In this section, we first describe the process used to identify and fit spectral line emission from the compact continuum sources identified in Paper II. We then describe the process used to create moment maps to show the spatial variation in line emission across the region.

Spectra for each compact continuum source identified in Paper II were produced by averaging all emission per channel over the mask produced for that leaf within the robust dendrogram catalog in Paper II. These spectra were then fit using *scousepy*,[14] a tool for systematically fitting large amounts of spectral line data (Henshaw et al., 2019b). We set a default signal-to-noise ratio (SNR) of 5 to determine the initial threshold at which fits are accepted. The default kernel was set to 5, which smooths the spectrum by averaging every 5 channels. By-eye inspection showed that this produced reliable results for the majority of spectra. Approximately $\sim 5\%$ of spectra required manual fitting as the interactive *scousepy* fitter was unable to find a combination of SNR threshold and smoothing kernel to fit these spectra.

Before analysing these fits, we enforced a series of cuts to the data that by-eye inspection showed reliably removed bad fits. We enforced a cut on the velocity dispersion, σ, and centroid velocity, $V_{\rm LSR}$, uncertainties to only keep fits with uncertainties smaller than 1.5 km s^{-1}, and only allowed for a maximum uncertainty on the amplitude of 0.5 Jy beam^{-1}. To mitigate any issues with fitting multiple peaks as one single peak, we also cut out any fits that had velocity dispersions larger than 20 km s^{-1}, and removed peaks narrower than 0.5 km s^{-1}. Due to a combination of imaging artefacts caused by spatial filtering, and inherently more complex spectra, the ^{12}CO and ^{13}CO spectral line fits were both deemed too unreliable throughout most of the survey and so were removed from this process.

The spectra show emission from a number of lines beyond the 10 key lines targeted by the survey (see Table 2.1). To identify these lines, a single $\rm V_{LSR}$ was determined for every core using the weighted average $\rm V_{LSR}$ of all detected lines. Any lines with a centroid velocity that differed by this $\rm V_{LSR}$ by more than $\pm$20 km s^{-1} were flagged as unidentified As this $\rm V_{LSR}$ difference was sufficiently large enough to avoid misidentifying spectra

[14] https://github.com/jdhenshaw/scousepy

with multiple components. These lines had their frequency calculated and then passed through Splatalogue[15] with a search range of ±0.04 GHz with an kinetic temperature maximum of 100 K to manually identify a first guess for the transition based on an assessment of the Einstein coefficient and upper energy level.

Once additional lines were assigned a most likely transition, we explored the quality of all the data by assessing the line of sight velocities, velocity dispersions, peak intensities and root-mean-square (RMS) of each core in the survey.

Figure 2.3 shows the histogram of all *scousepy* fit V_{LSR} measurements across the survey while Figures 2.4 and 2.5 show the average and standard deviation of these V_{LSR} measurements for each unique core. Figure 2.6 shows the maximum difference in fit V_{LSR} for each core. Figure 2.7 shows a breakdown of Figure 2.3 for 8 of the 10 key transitions targeted by this survey. We do not examine the values for ^{12}CO and ^{13}CO as these spectra were too complicated to reasonably fit with the current data. We see that the majority of the emission observed throughout the region lies between 0 km s^{-1} and 100 km s^{-1}, as this range in V_{LSR} contains most of the dense gas in the CMZ. While Figure 2.5 shows a typical standard deviation of ~ 30 km s^{-1} in the non quality controlled data set, this drops to ≤ 5 km s^{-1} in the quality controlled data set, with only a single outlier at ~ 30 km s^{-1}.

Figure 2.8 shows the histogram of all *scousepy* fit velocity dispersion measurements across the survey while Figures 2.9 and 2.10 show the average and standard deviation of these velocity dispersion measurements for each unique core. Figure 2.11 shows a breakdown of Figure 2.8 for 8 of the 10 key transitions targeted by this survey. Figure 2.8 shows that quality control does not have a drastic impact on the typical velocity dispersion of a fit spectral peak. However, it removes several broad components. The points at ~ 12 km s^{-1} in the right hand panel of Figure 2.9 belong to G0.001−0.058r and G0.489+0.010j. These are regions with complicated velocity structure, containing multiple peaks with small velocity dispersions superimposed on a broader component. The narrow peaks were removed by the quality control conditions, leaving behind single broad peaks.

Figure 2.12 shows the histogram of all *scousepy* fit peak intensity measurements across the survey while Figures 2.13 and 2.14 show the average and standard deviation of these

[15] https://splatalogue.online/

peak intensity measurements for each unique core. Figure 2.15 shows a breakdown of Figure 2.12 for 8 of the 10 key transitions targeted by this survey. Figure 2.12 shows a number of very bright peaks that are removed by the quality control conditions as they belong to ^{12}CO, a transition that suffer from severe imaging issues. The majority of spectral peaks in both data sets have low peak intensities and are not affected by quality control.

Figure 2.16 shows the histogram of the RMS of all spectra across the survey while Figure 2.17 shows a breakdown of Figure 2.16 for 8 of the 10 key transitions targeted by this survey. While a majority of spectra in the survey have low RMS values in the left hand panel of Figure 2.16, there are a number of very noisy spectra that were removed due to the quality control condition.

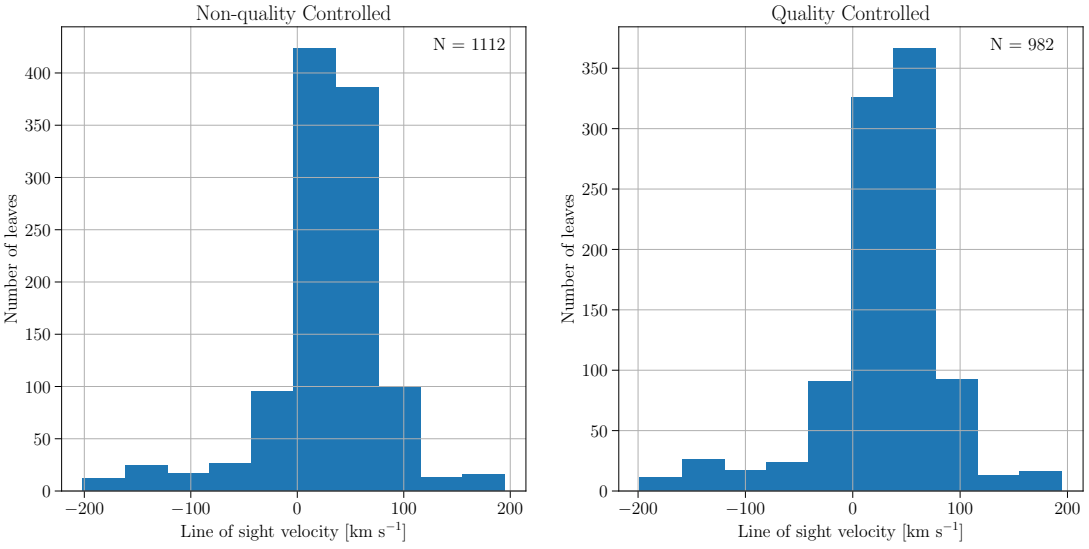

FIGURE 2.3: Histogram of all *scousepy* fit V_{LSR} measurements throughout the survey for the original data set [left] and the quality controlled data set [right]. A similar format is used for the figures up to Figure 2.17. The majority of the spectral line emission observed by CMZoom lies between 0 km s^{-1} < V_{LSR} < 100 km s^{-1}

With all lines identified, a single V_{LSR} was calculated for each core using the average V_{LSR} for all lines detected for that core, weighted by the uncertainty on each V_{LSR} measurement. Moment maps were then produced over a velocity range of ±20 km s^{-1} surrounding all dendrogram cores within a region. To generate these moment maps, an RMS map was first produced by measuring the RMS per pixel and then cutting anything over a threshold as determined by the number of channels in each pixel, so as to limit

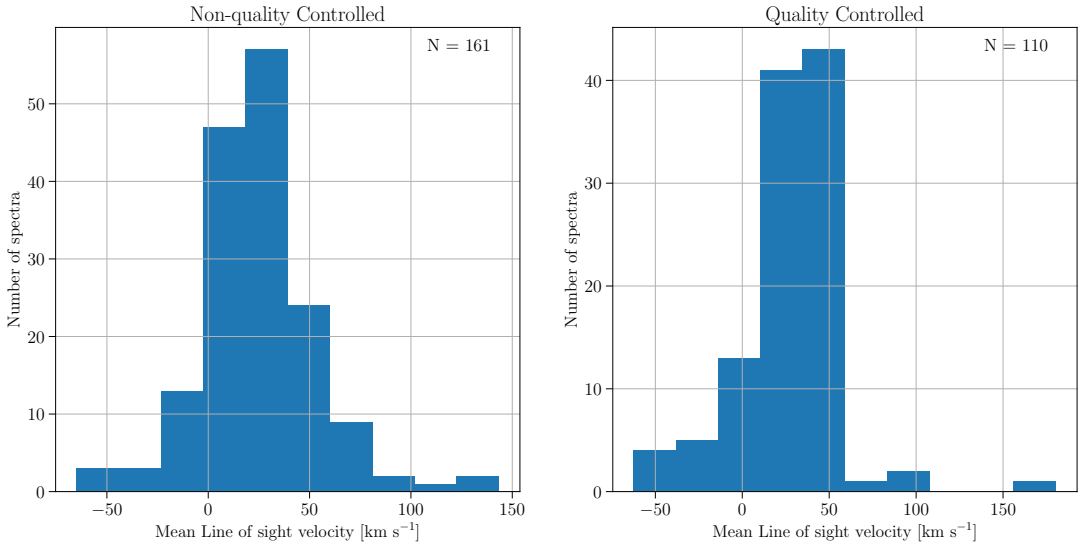

FIGURE 2.4: Histogram of average *scousepy* fit V_{LSR} measurements for each unique core.

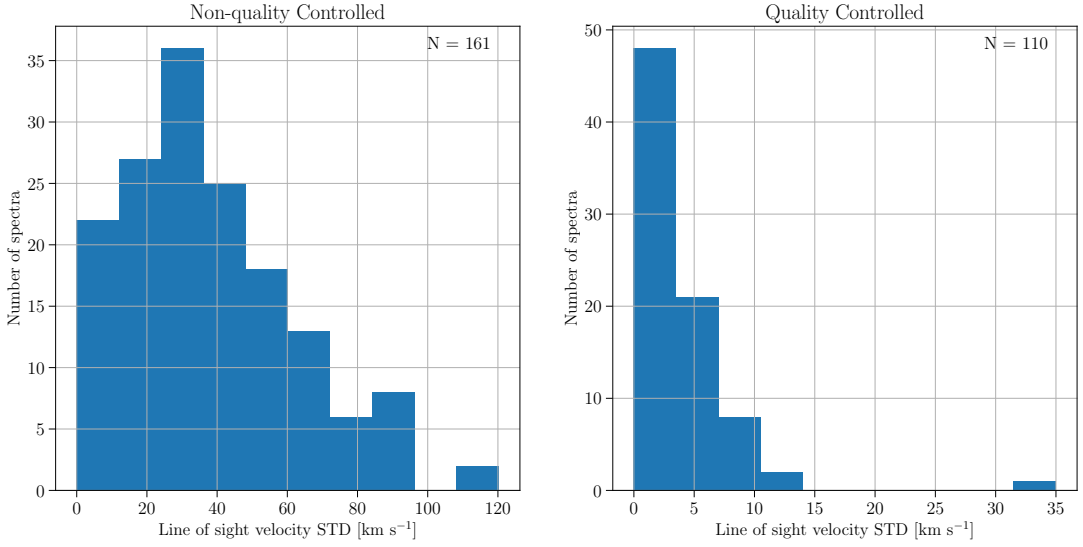

FIGURE 2.5: Histogram of the standard deviation in *scousepy* fit V_{LSR} measurements for each unique core.

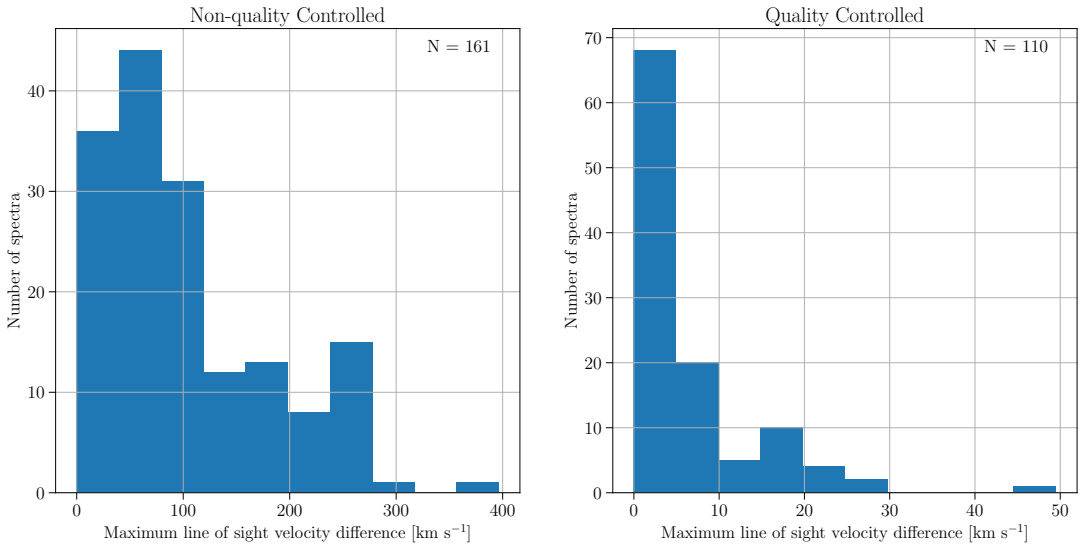

FIGURE 2.6: Histogram of the difference between the maximum and minimum *scousepy* fit V_{LSR} measurements for each unique core.

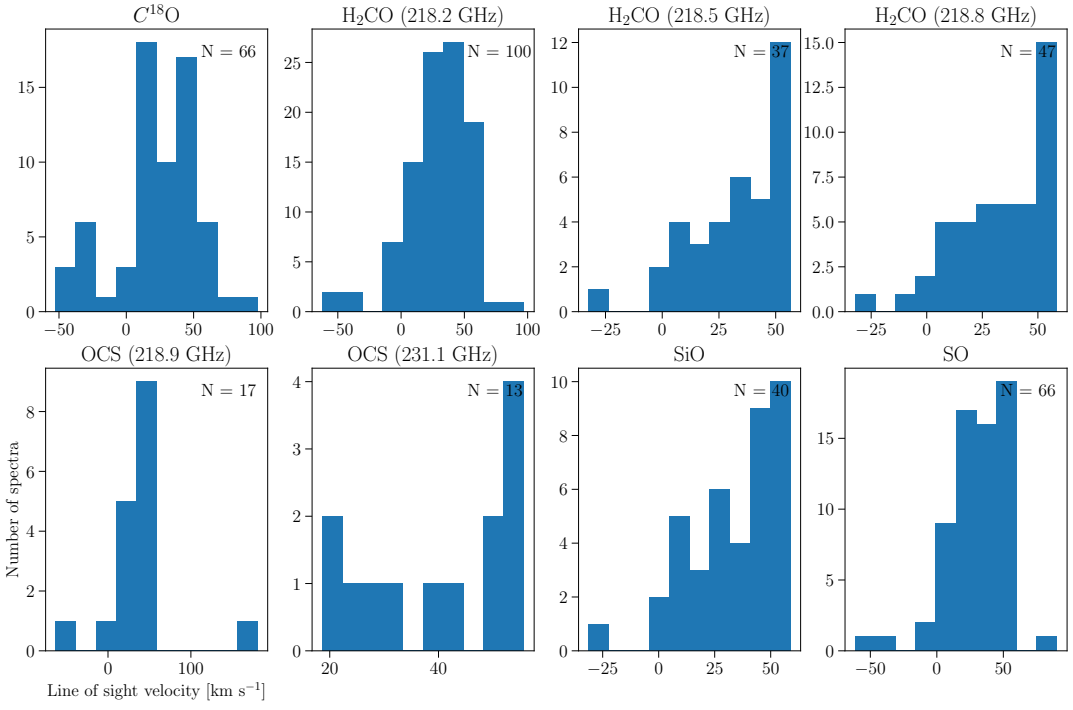

FIGURE 2.7: Histogram of *scousepy* fit V_{LSR} measurements broken down into 8 of the 10 key transitions. ^{12}CO and ^{13}CO are not included as their spectral line profiles are often unreliable.

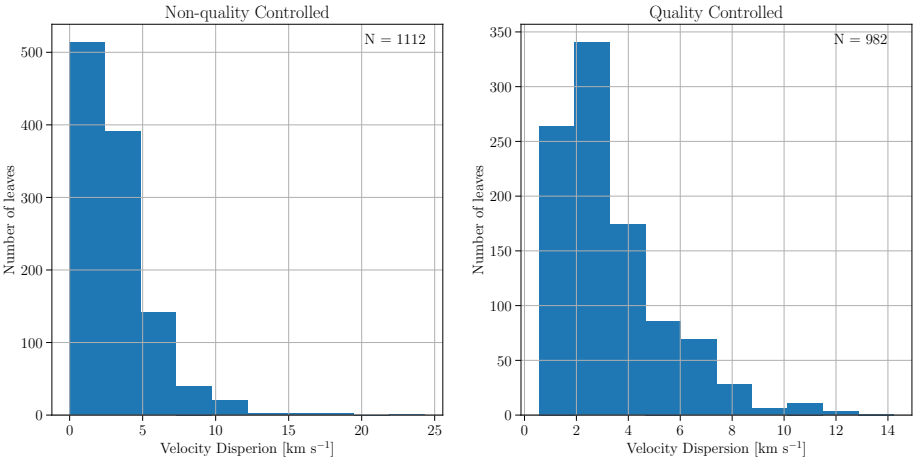

FIGURE 2.8: Histogram of *scousepy* fit velocity dispersion measurements for each unique core.

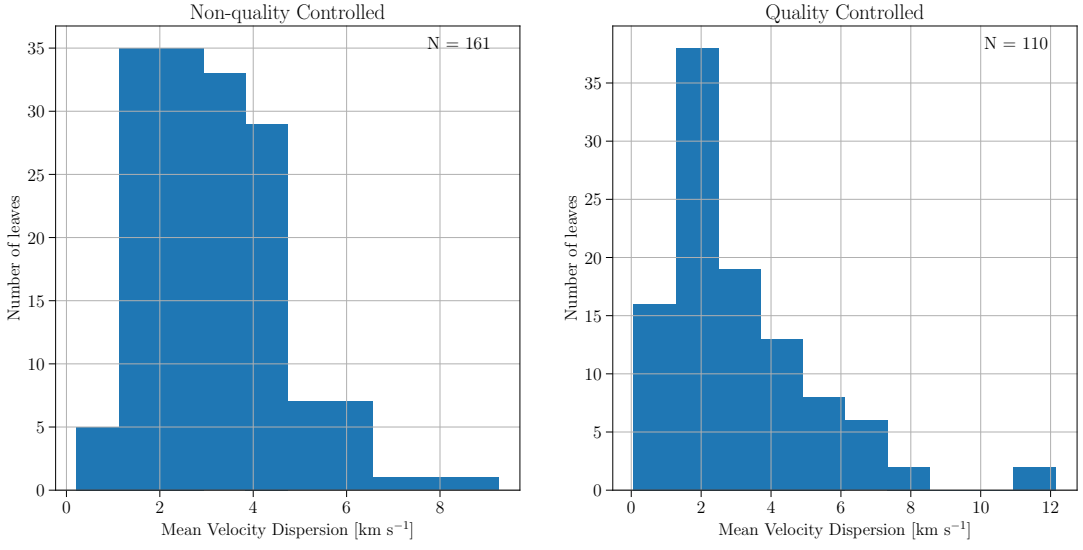

FIGURE 2.9: Histogram of the mean *scousepy* fit velocity dispersion measurements for each unique core.

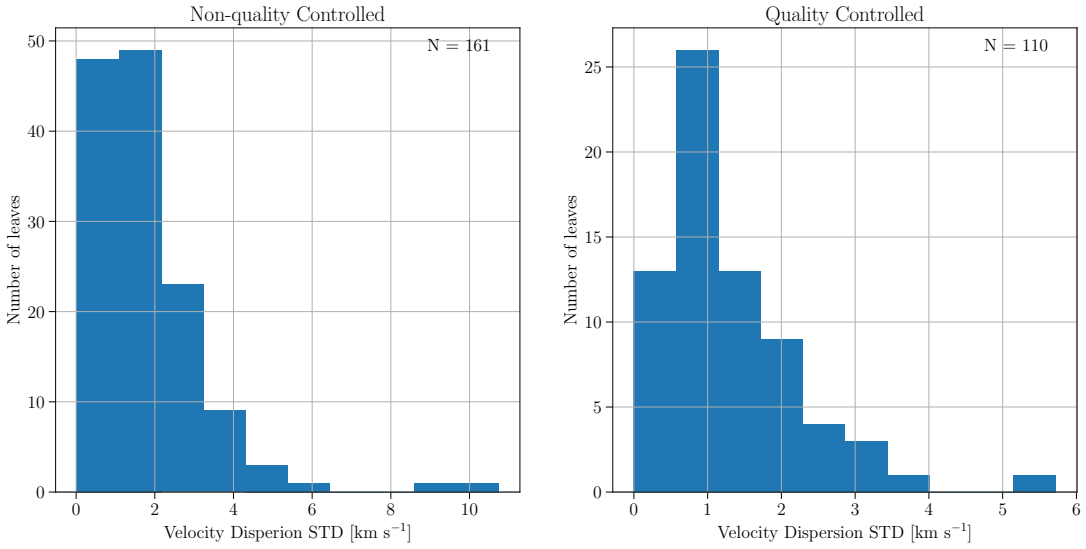

FIGURE 2.10: Histogram of the standard deviation in *scousepy* fit velocity dispersion measurements throughout the survey.

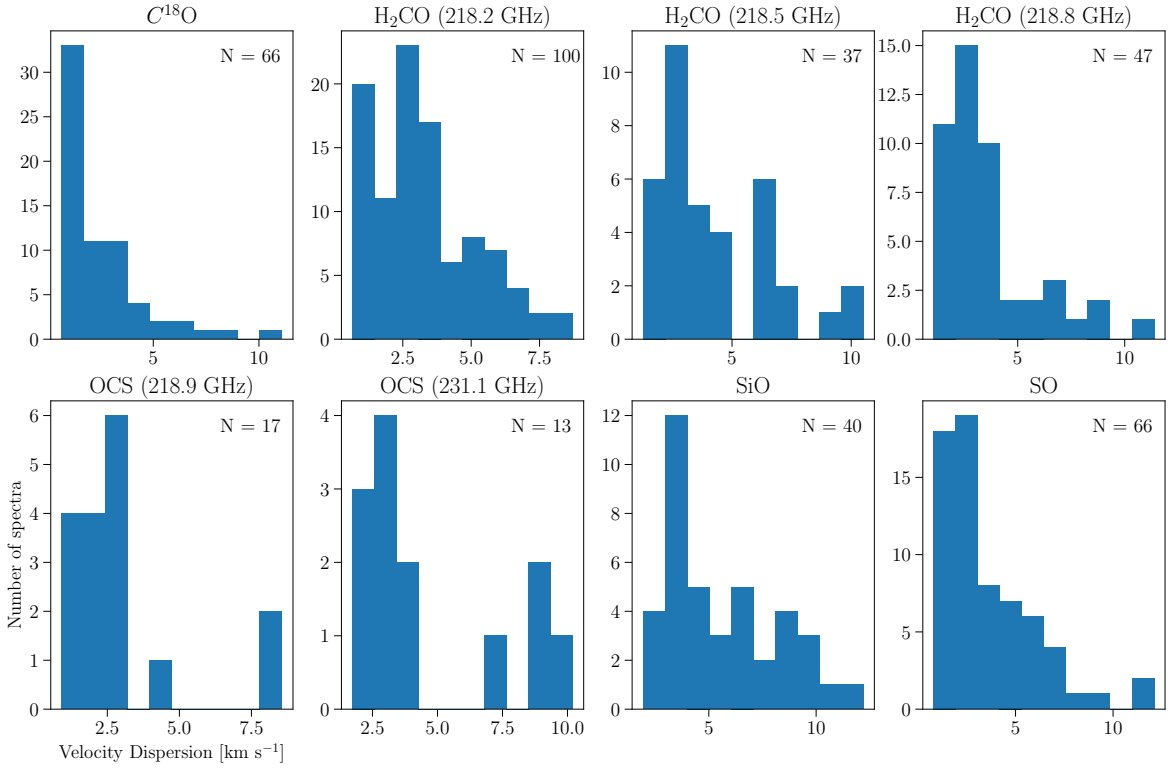

FIGURE 2.11: Histogram of *scousepy* fit velocity dispersions for each unique core broken down into 8 of the 10 key transitions. ^{12}CO and ^{13}CO are not included as their spectral line profiles are often unreliable.

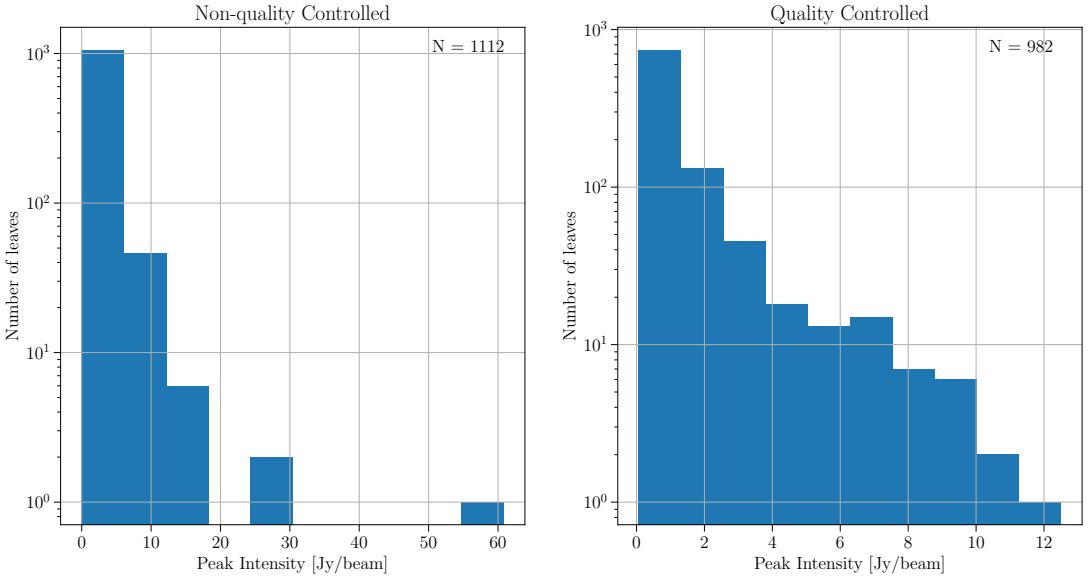

FIGURE 2.12: Histogram of all *scousepy* fit peak intensities throughout the survey.

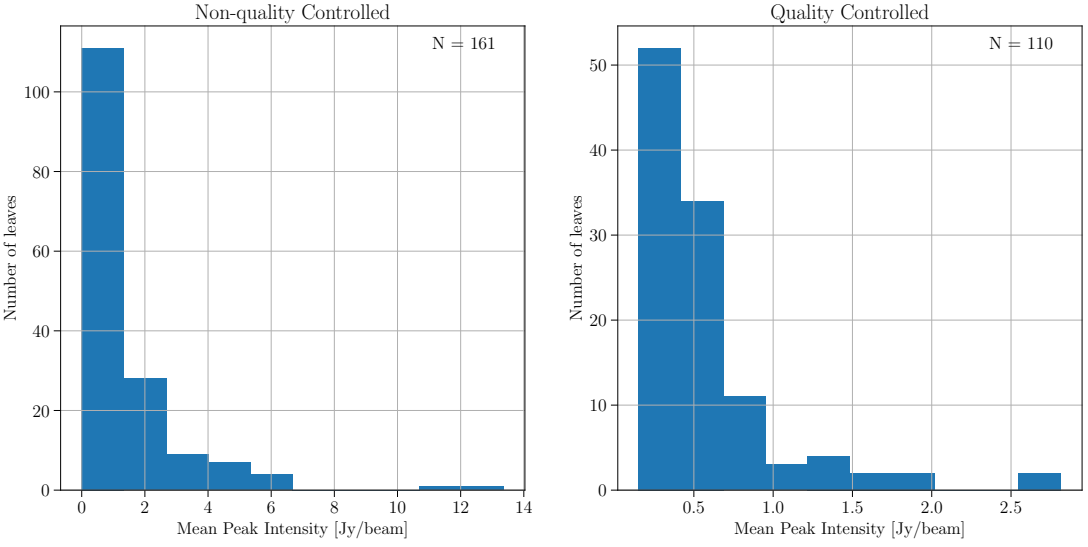

FIGURE 2.13: Histogram of the mean *scousepy* fit peak intensity measurements for each unique core.

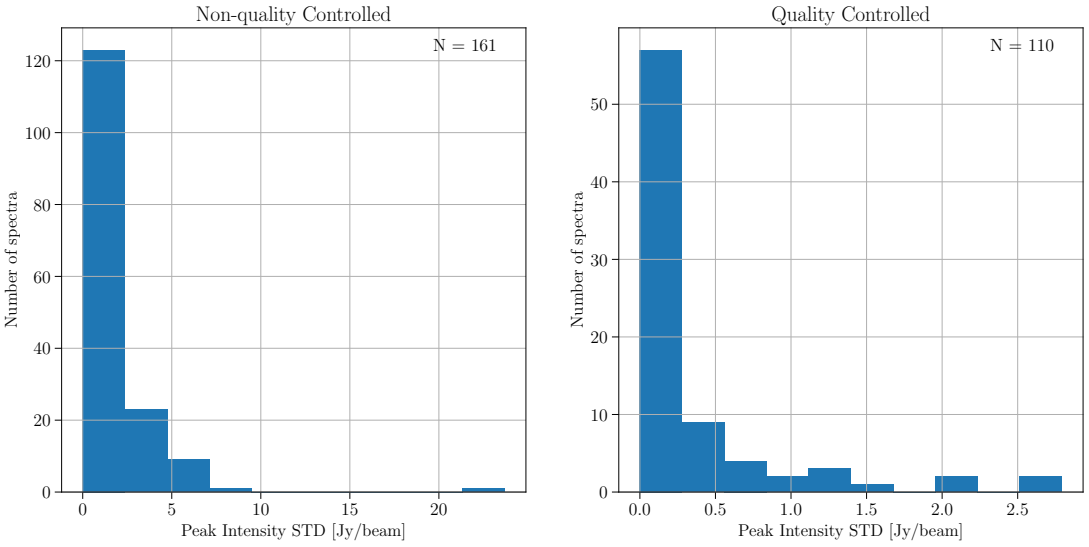

FIGURE 2.14: Histogram of the standard deviation in *scousepy* fit peak intensity measurements throughout the survey.

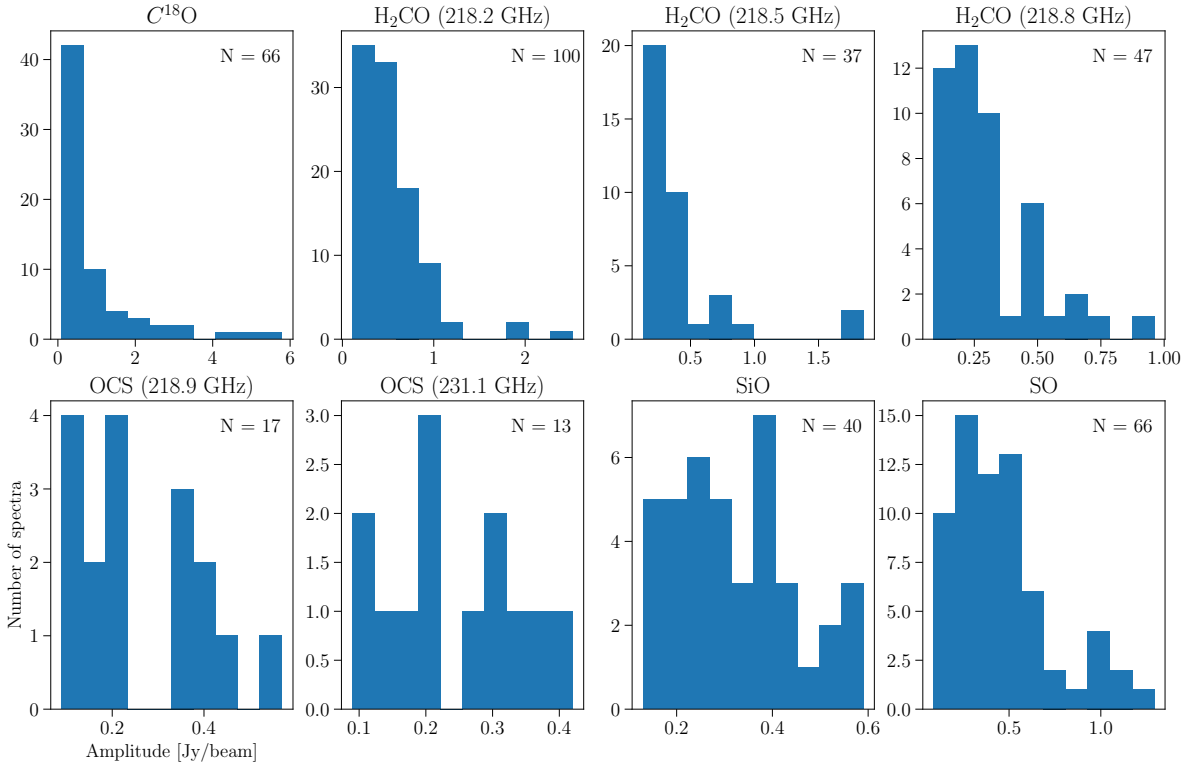

FIGURE 2.15: Histogram of *scousepy* fit peak intensities for each unique core broken down into 8 of the 10 key transitions. ^{12}CO and ^{13}CO are not included as their spectral line profiles are often unreliable.

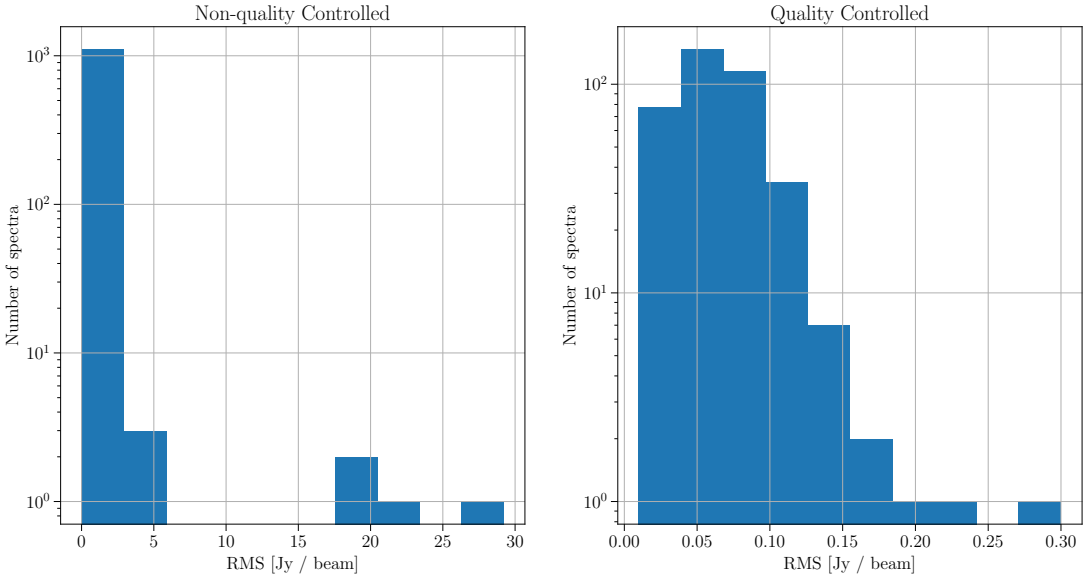

FIGURE 2.16: Histogram of the RMS for each unique core.

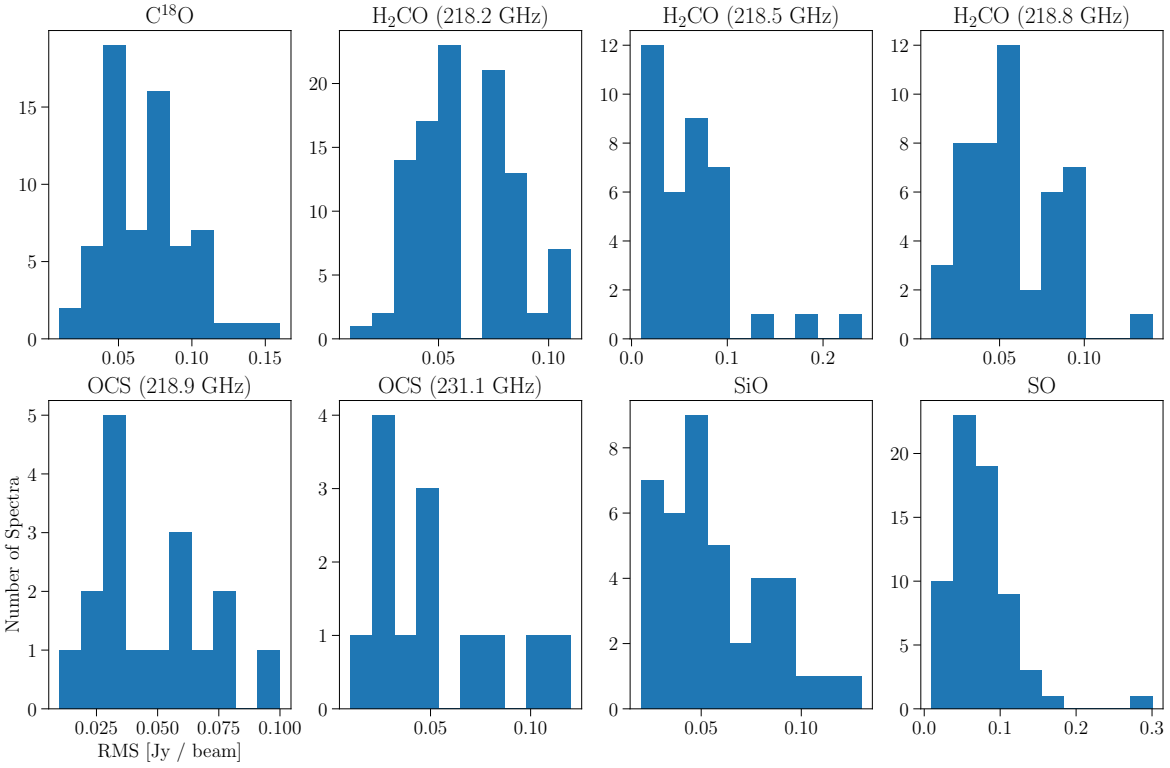

FIGURE 2.17: Histogram of the RMS for each unique core broken down by 8 of the 10 key transitions.

Molecule	Rest Frequency (GHz)	Quantum Number	Upper Energy Level (K)	Tracer
^{12}CO	230.53800000	J=2-1	16.59608	Dense Gas
^{13}CO	220.39868420	J=2-1	15.86618	Dense Gas
C^{18}O	219.56035410	J=2-1	15.8058	Dense Gas
H_2CO	218.22219200	3(0,3)-2(0,2)	20.9564	Dense Gas
H_2CO	218.47563200	3(2,2)-2(2,1)	68.0937	Dense Gas
H_2CO	218.76006600	3(2,1)-2(2,0)	68.11081	Dense Gas
SiO	217.10498000	5-4	31.25889	Protostellar outflows & shocks
OCS	218.90335550	18-17	99.81016	Shocks
OCS	231.06099340	19-18	110.89923	Shocks
SO	219.94944200	6-5	34.9847	Shocks

TABLE 2.1: Summary of 10 key transitions targeted by the CMZoom survey tracing dense gas, protostellar outflows and more energetic shocks.

the chance of noise producing a spike above this threshold to 25%. This robust RMS map was used to enforce a 10σ cut in order to identify the most significant emission within a region. This mask was then grown outwards using a lower SNR cut, down to 5σ in order to detect low level extended emission surrounding the most robust emission. Not all regions have emission at the 10σ level, so this process was repeated with an iteratively lower SNR threshold until some emission was detected. If no emission was detected down to 5σ, the region was flagged as having no emission.

2.4 Data presentation

Below we present the spectral line data cubes of the 10 main molecular line transitions covered in the CMZoom spectral setup. Table 2.1 lists these transitions and their relevant properties.

We start by providing a summary of the general emission and absorption characteristics for each transition across the full survey region, focusing on comparing the spatial extent and velocity range of the emission for the different transitions and also with the 230 GHz continuum emission reported in Papers I and II. Our goal here is to provide the reader with a qualitative idea of the quality and the breadth of the data across the whole survey and on a per region basis.

Table 2.2 provides a description of the survey line detections per region, as well as highlighting any issues which affect the robustness and reliability of the images for science. We find that the ^{12}CO and ^{13}CO emission is detected in 100% and 90% of the regions, respectively. In nearly all regions, the emission is spatially extended across a

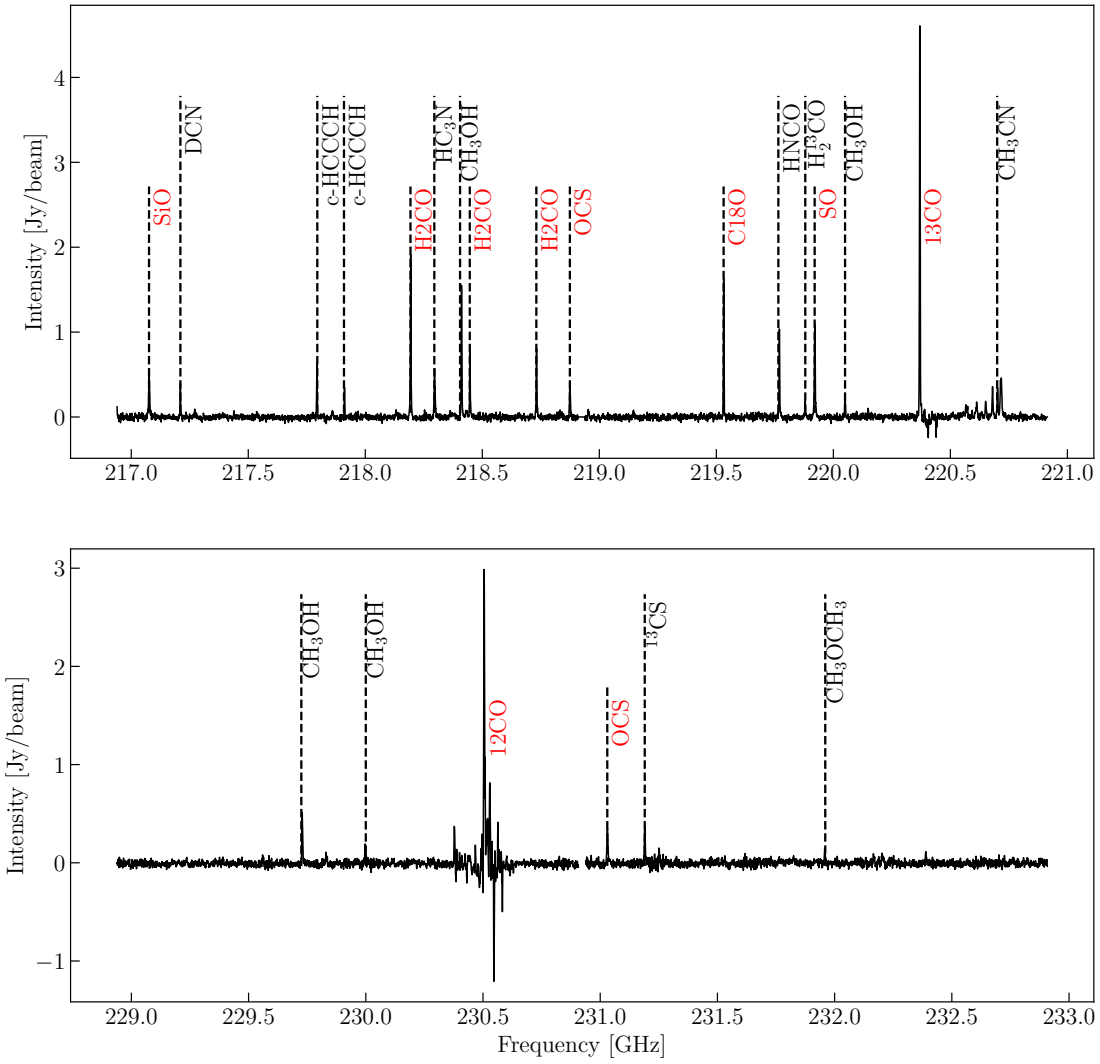

FIGURE 2.18: Complete spectra for the lower (top) and upper (bottom) sidebands for the region G0.380+0.050, colloquially referred to as 'cloud C'. Red labels indicates the 10 transitions targeted by the CMZoom survey, with over a dozen additional lines labeled in black.

large fraction of the survey area. There is little correspondence between the ^{12}CO and ^{13}CO integrated intensity emission and the 230 GHz continuum emission. However, the ^{12}CO and ^{13}CO emission often suffers from severe imaging artefacts due to missing flux problems and also absorption from foreground gas clouds along the line of sight. For that reason we urge caution in interpreting the integrated intensity and moment maps from these transitions, and more generally, in blindly using the ^{12}CO and ^{13}CO data without the addition of zero-spacing information. Similarly, we have opted to not use these data products during the analysis until these imaging artefacts are resolved in a future paper.

C^{18}O is detected towards 60% of the regions. The imaging artefacts are much less severe for C^{18}O than for the other CO transitions. The emission generally does appear spatially associated with the 230 GHz continuum emission.

SO and SiO are detected towards 7 and 5 regions, respectively, and are mostly well correlated – all regions with detection SiO emission are also detected in SO. This is perhaps unsurprising given they are both thought to trace shocks as they are predominantly locked within dust grains until the extreme temperature of a shock obliterates the grain material. We explore the correlation between different tracers more fully in § 2.6.

As expected, the three H_2CO transitions show a very good correspondence, both spatially and in velocity. At least one transition of H_2CO was observed towards 50% of regions. In the spectra containing the H_2CO 3(2,2)-3(2,1) transition, there is often an additional velocity component offset by 50 km s^{-1} from the main velocity component that we attribute to CH_3OH-e (4(2) - 3(1)) with a rest frequency of 218.44006300 GHz.

We now discuss each of the CMZoom regions in turn, focusing on notable characteristics of the emission and specific issues with the data. The emission characteristics and issues for all regions are summarised in Table 2.2. Figures A.1 to A.81 show the integrated moment maps, moment 1 maps and moment 2 maps for each region. Through visual inspection of the spectral line data cubes and integrated intensity maps, we found that except where specifically mentioned, there is significant emission in all ^{12}CO and ^{13}CO cubes, often with strong emission and absorption over a V_{LSR} range of $\pm$100 km s^{-1}. However, there are severe imaging artefacts, including strong negative bowls due to missing extended structure, making these cubes unreliable. We therefore do not discuss the ^{12}CO and ^{13}CO data below unless there are particular aspects of the data which are

relavent to highlight. The phrase 'continuum emission' below, refers exclusively to the 230 GHz CMZoom continuum emission.

2.4.1 G0.001−0.058

$C^{18}O$(2-1) emission is confined to two spectral components found at $-10\,\mathrm{km\,s^{-1}}$ and $30\,\mathrm{km\,s^{-1}}$. Two of the three transitions of H_2CO show significant emission between $30-40\,\mathrm{km\,s^{-1}}$, coinciding well spatially with the continuum emission. The middle transition of H_2CO also shows a second spectral feature at 80 $\mathrm{km\,s^{-1}}$, likely corresponding to CH_3OH-e at 218.44006300 GHz. Weak OCS emission is detected, though only in the higher frequency transition (231.1 GHz). The OCS spatial distribution corresponds well with the continuum structure and both SiO and SO emission.

2.4.2 G0.014+0.021

H_2CO 3(2,1)-3(2,0) and both transitions of OCS and the velocity range from 10 to $-200\,\mathrm{km\,s^{-1}}$ of the ^{12}CO transition was masked during the beam correction process (see § 2.2.6). In the unmasked channels of the ^{12}CO data cube, significant emission is detected, but there are severe image artefacts including strong negative bowls due to missing extended structure, making this cube entirely unreliable. Two spectral components were observed in the ^{13}CO cube, with a single narrow peak at $-15\,\mathrm{km\,s^{-1}}$ and a broader component from $0-30\,\mathrm{km\,s^{-1}}$. No emission was observed in any other line.

2.4.3 G0.068−0.075

$C^{18}O$ traces the continuum emission well, with two spectral components at 45 $\mathrm{km\,s^{-1}}$ and 70 $\mathrm{km\,s^{-1}}$. Two of the three H_2CO transitions show strong emission around the continuum structures, with multiple peaks at 45 $\mathrm{km\,s^{-1}}$ and 55 $\mathrm{km\,s^{-1}}$. CH_3OH-e is also detected at the same velocity. No emission was observed in any other lines.

2.4.4 G0.106−0.082

$C^{18}O$ emission is spatially compact, with two spectral components found at $55\,\mathrm{km\,s^{-1}}$and $70\,\mathrm{km\,s^{-1}}$. There is a potential spatial offset between these two components and an

overall offset in the $C^{18}O$ emission with respect to the continuum emission. Two of the three H_2CO transitions also also show several spectral components. The spectral feature at 100 $km\,s^{-1}$relative to the rest frequency of H_2CO 3(2,2)-3(2,1) is most likely to be CH_3OH-e at 218.44 GHz. SiO and SO both trace the same spatial structures, and the line profile of both transitions show the same double peaked distribution. No OCS emission was observed in the region.

2.4.5 G0.145−0.086

$C^{18}O$ emission peaks at the lower continuum peak at $-15\,km\,s^{-1}$. No emission is detected in any other line.

2.4.6 G0.212−0.001

$C^{18}O$ and H_2CO $3_{03}-2_{02}$ both peak at 45 $km\,s^{-1}$ coinciding very well with the continuum emission. No emission is seen in any other line.

2.4.7 G0.316−0.201

$C^{18}O$ emission peaks at 18 $km\,s^{-1}$ at the continuum peak. However, significant negative bowls are present within this data cube. Each of the three H_2CO transitions have emission at this same V_{LSR}, though the intensity of emission at 218.8 GHz is too low to appear in the moment map. Within the cube for H_2CO (218.5GHz) a second line appears at 66 $km\,s^{-1}$, likely corresponding to CH_3OH-e. SO emission is also seen at 18 $km\,s^{-1}$ at the location of the continuum peak, but no emission is seen in any other line.

2.4.8 G0.326−0.085

The current emission in the $C^{18}O$ moment map is the result of a single channel peak which is likely masking the real emission seen at 15 $km\,s^{-1}$ and causing anomalous moment 1 and 2 maps. No emission is seen in any other line.

2.4.9 G0.340−0.055

No emission was detected in any lines other than ^{12}CO and ^{13}CO.

2.4.10 G0.380+0.050

Including ^{13}CO, all lines other than both OCS transitions show strong emission at 40 $\mathrm{km\,s^{-1}}$. Other lines are present: in the C^{18}O datacube at 110 $\mathrm{km\,s^{-1}}$, in the 218.2 GHz H_2CO datacube at $-100\,\mathrm{km\,s^{-1}}$, in the H_2CO 218.5 GHz cube cube at $85\,\mathrm{km\,s^{-1}}$, and in the H_2CO 218.8 GHz cube at $-160\,\mathrm{km\,s^{-1}}$. Similarly, a second line is observed in the SiO cube at $-150\,\mathrm{km\,s^{-1}}$ and two additional lines associated with the SO cube at $95\,\mathrm{km\,s^{-1}}$ and $-140\,\mathrm{km\,s^{-1}}$.

2.4.11 G0.393−0.034

Two spectral components are observed at 75 $\mathrm{km\,s^{-1}}$and 92 $\mathrm{km\,s^{-1}}$in both C^{18}O and the lower energy transition of H_2CO . No emission was detected in any other line.

2.4.12 G0.412+0.052

C^{18}O shows a single peak at 37 $\mathrm{km\,s^{-1}}$, though this emission lies far from any continuum structures. Emission from the lowest energy transition of H_2CO appears associated with the central continuum peak at a V_{LSR} of 27 $\mathrm{km\,s^{-1}}$. No emission was detected in any other line.

2.4.13 G0.489+0.010

C^{18}O and the lower transition of H_2CO shows emission at a V_{LSR} of 32 $\mathrm{km\,s^{-1}}$, though this does not coincide well with the continuum emission. The lower continuum peak also shows SO emission at a V_{LSR} of 29 $\mathrm{km\,s^{-1}}$. No emission was seen in any other line.

2.4.14 G0.619+0.012 and G0.699−0.028

Due to these regions' proximity to Sgr B2, the pipeline was unable to suitably clean this data without the appropriate single dish data to include the zero-spacing information. For this reason, these regions have been removed from all proceeding work.

2.4.15 G0.891−0.048 and G1.038−0.074

These two regions, both associated with the 1.1° cloud, suffered from significant imaging problems and have not been included in this work.

2.4.16 G1.085−0.027

Significant emission is detected throughout the ^{13}CO cube, the bulk of which occurs at 28 km s^{-1}. Emission in C^{18}O, the upper transition of H_2CO , and the upper transition of OCS is detected in a single channel and is therefore unreliable. No emission is seen in any other line.

2.4.17 G1.602+0.018

No emission is seen in any lines other than ^{12}CO and ^{13}CO.

2.4.18 G1.651−0.050

Two spectral components are seen in ^{13}CO at −35 km s^{-1}and 55 km s^{-1}. These components are separated spatially from the continuum emission but coincide well with each other. No emission is seen in any other line.

2.4.19 G1.670−0.130 and G1.683−0.089

Half of the ^{12}CO, H_2CO 3(2,1)-3(2,0) and both transitions of OCS were entirely masked during the beam correction process described in Section 2.2.6. This prevents a reasonable production of the moment map, as the unmasked half contains mostly emission and not

enough emission free channels to accurately measure the rms. As such this moment map should not be considered reliable. No emission is seen in any other line.

2.4.20 G359.137+0.031

^{13}CO shows two structures separated both spatially and kinematically, with a peak at the continuum emission at a V_{LSR} of 0 $km\,s^{-1}$, and a secondary peak at $-40\,km\,s^{-1}$ which lies south of the continuum peak. $C^{18}O$ and the lower transition of H_2CO peak at 0 $km\,s^{-1}$, with a peak at this V_{LSR} in the middle transition of H_2CO that is too weak to be included in the moment map. The baseline within the upper transition of OCS is offset from 0, and as such the moment map should not be considered reliable. No emission was seen in any other line.

2.4.21 G359.484−0.132

Emission is detected in $C^{18}O$, the lower two transitions of H_2CO , both transitions of OCS, as well as SiO. There appears to be no consistent position or V_{LSR} for the emission between the transitions. No emission was seen in any other line.

2.4.22 G359.611+0.018

No emission is seen in any line other than ^{12}CO and ^{13}CO.

2.4.23 G359.615−0.243

$C^{18}O$ and all three H_2CO transitions show emission at a V_{LSR} of 20 $km\,s^{-1}$. A peak at 70 $km\,s^{-1}$ in the cube of the middle H_2CO transition is likely produced by CH_3OH-e. A peak at $-120\,km\,s^{-1}$ was also detected in both the 218.2 GHz and 218.8 GHz H_2CO transitions, with an additional peak in this latter cube at $-175\,km\,s^{-1}$. The emission seen in the moment map of OCS (218.9 GHz) is detected in a single channel, leading to anomalous moment 1 and 2 maps. Emission is also detected at a V_{LSR} of 20 $km\,s^{-1}$ in SO. All of these lines coincide well within the single continuum peak. No emission is seen in any other line.

TABLE 2.2: Summary of conditions of data cubes for all regions and across 9 key molecular lines as a check of robustness and reliability for science. Each cube has been checked for a number of flags depending on extracted spectra and a visual inspection of the cubes. The flags are given as acronyms: multiple velocity components (MVC), imaging artefacts (IA), missing channels (MC), (self-)absorption (SA, A), broad lines (GC) or narrow lines (N), line-wings (LW), non-detection (ND) and contamination of other spectral lines (C).

Sourcename	^{13}CO	C^{18}O	H2CO	H2CO (218.2 GHz)	H2CO (218.5 GHz)	OCS (218.8GHz)	OCS (218.9 GHz)	SiO (231.1 GHz)	SO
G0.001-0.058	IA	MVC	MVC	MVC		MC	ND	MVC	MVC
G0.014+0.021		ND	ND	MC	MC	MC	MC	ND	ND
G0.0.68-0.075	IA	MVC	GC, MVC	MVC, C	MVC, GC	MC	ND	ND	ND
G0.070-0.035									
G0.106-0.082	IA	MVC	MVC, C	MVC	MC	ND	GC, LW	LW	
G0.145-0.086	IA	MVC	MVC	ND	MC	MC	BB	ND	ND
G0.212-0.001	IA			MVC		MC	MC	MC	ND
G0.316-0.201			C	C		MC	MC		ND
G0.326-0.085	IA	ND	ND	ND	ND	MC	MC	ND	ND
G0.340+0.055	IA	ND		ND	ND	MC	MC, BB	ND	ND
G0.380+0.050	MVC	C	C	C	C	MC	MVC, MC	C	MVC, C
G0.393-0.034		MVC	MVC	ND	ND	MC	MC	ND	ND
G0.412+0.052	IA				ND	MC	MC, ND	ND	ND
G0.489+0.010									
G1.085-0.027			ND	ND	MC	MC, ND	BB	ND	ND
G1.602+0.018		ND	C	C	MC, ND	MC	BB		
G1.651-0.050	MVC			C	MC	MC	ND	ND	ND
G1.670-0.130	ND	ND	ND	MC	MC	MC	MC	ND	ND
G1.683-0.089	ND	ND	ND	MC	MC	MC	MC	MC	MC
G359.137+0.031	C		C	C	MC	MC	BB	N, GC	MVC, C
G359.484-0.132	IA					MC	MC, BB	BB	BB
G359.611+0.018		ND	ND	ND	ND	MC	MC, BB	ND	ND
G359.615-0.243	IA		C	C	C	C MC	MC	MC	MVC, C
G359.734+0.002	IA		C	C	C	MC, C	MC, C	MC	C
G359.865+0.022									
G359.889-0.093	IA		MC	ND	ND	ND	MC	ND	ND
G359.948-0.052					MC	MC	MC		

2.4.24 G359.865+0.022

^{13}CO shows multiple velocity components at -40, 10 and 60 km s^{-1}, with C^{18}O also peaking at a V_{LSR} of -4 km s^{-1}. No emission is seen in any other line.

2.4.25 G359.889−0.093

C^{18}O, three transitions of H_2CO , SiO and SO all show strong emission at a V_{LSR} or $\sim$ 15 km s^{-1} coinciding strongly with the continuum emission, with numerous other peaks throughout the region within the range of $\pm$50 km s^{-1}, likely the result of contamination from other transitions. The OCS transition in the lower sideband shows weak emission at $\sim$ 15 km s^{-1}, however channels from $-30 - 10$ km s^{-1} were masked during the beam correction process described in Section 2.2.6. The OCS transition in the upper sideband shows emission from $\pm$50 km s^{-1}, but with no coincidence with the continuum emission.

2.5 Spatial variation in line emission across the CMZ

With a uniform sensitivity across the CMZ and a homogeneous analysis of the emission, CMZoom is well suited to investigating changes in line brightness on sub-pc scales as a function of location. Detailed modelling of this line emission is required to fully understand the excitation conditions, opacity and chemistry to derive accurate physical properties of the gas. Such detailed modelling is beyond the scope of this paper. Instead, in this section we search for large differences in line strength ratios between clouds as a rough indicator of variations in conditions as a function of position throughout the CMZ .

For every region, if a transition was detected, all unmasked pixels in the moment map (see § 2.3) were summed and compared to the total integrated intensity of $C^{18}O$ and the 230 GHz continuum emission. Figures 2.19 and 2.20 show the distribution of these ratios as a function of Galactic longitude. Note that the Sgr B2 region (between $0.50° < l < 0.72°$) and the circumnuclear disk are not included on these figures due to the imaging difficulties described in § 2.4.

Comparing the longitude range of the different transitions, ^{12}CO and ^{13}CO are detected across the full survey extent. With the exception of G1.085−0.027, which has a strong OCS (231.1 GHz), detection the ratios for all other transitions are confined to $|l| < 0.5°$.

As expected for such an unsophisticated approach which does not solve for excitation, opacity, chemistry, etc., there is a large (order of magnitude) scatter in the line brightness ratios between clouds. Nevertheless, there are several interesting aspects of these figures.

Firstly, the line ratio values and number of regions with enough emission to appear on these plots for different transitions follows the expected trends, with ^{12}CO and ^{13}CO having the highest ratios and number of regions, followed by $C^{18}O$ and the lowest energy transition of H_2CO.

Secondly, the line ratios with respect to dust emission of SO, SiO, and the two upper energy levels of H_2CO all increase by several orders of magnitude towards the Galactic Centre (i.e., as $|l| \rightarrow 0°$). Detailed modelling is required to understand the origin of this, but it is interesting to note that the highest excitation lines and shock tracers all increase in the same way, as may be expected due to changing physical conditions (e.g.

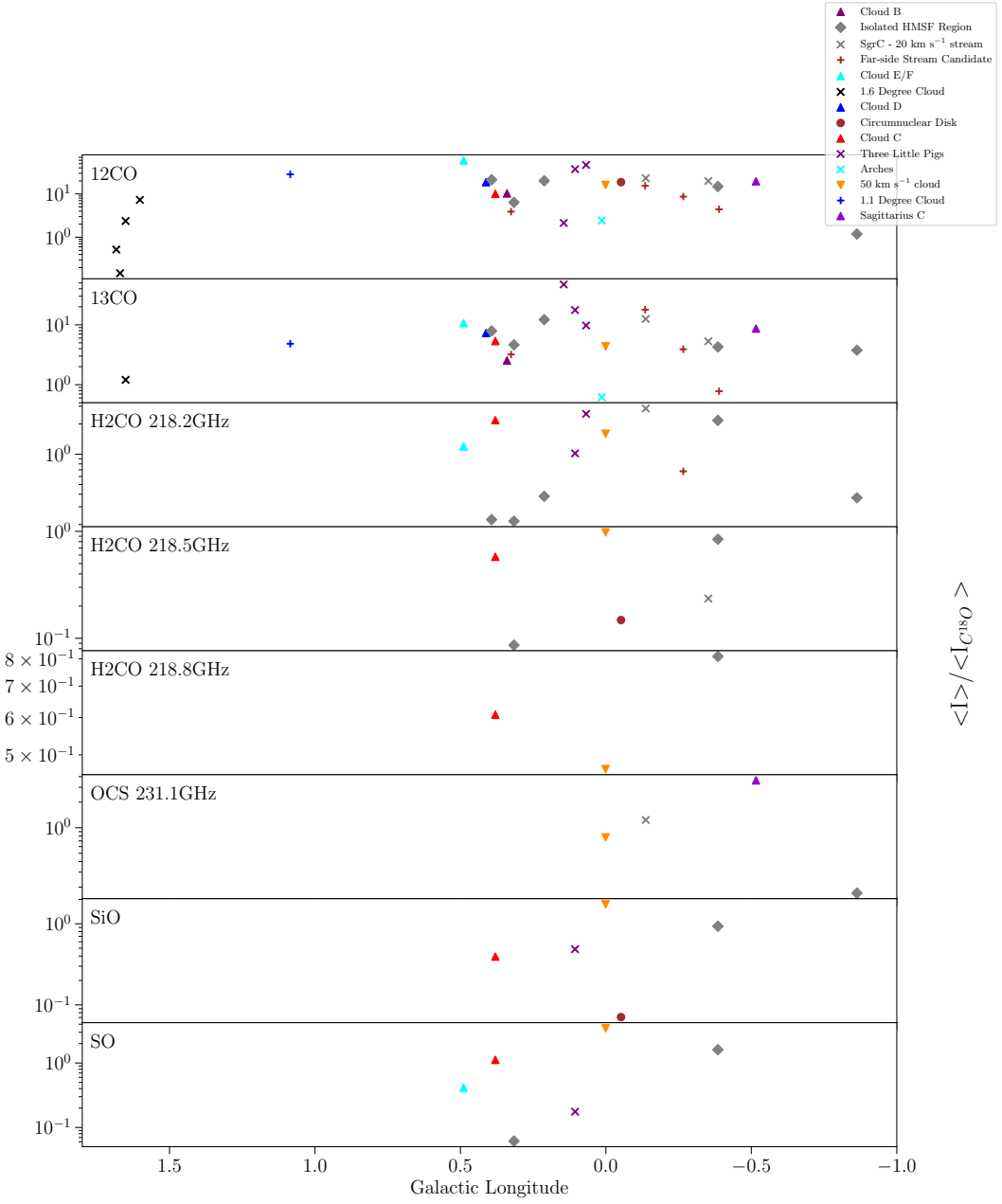

FIGURE 2.19: Normalized integrated intensity ratios for each observed transition in each region normalised by the integrated intensity of the $C^{18}O$ emission in that region.

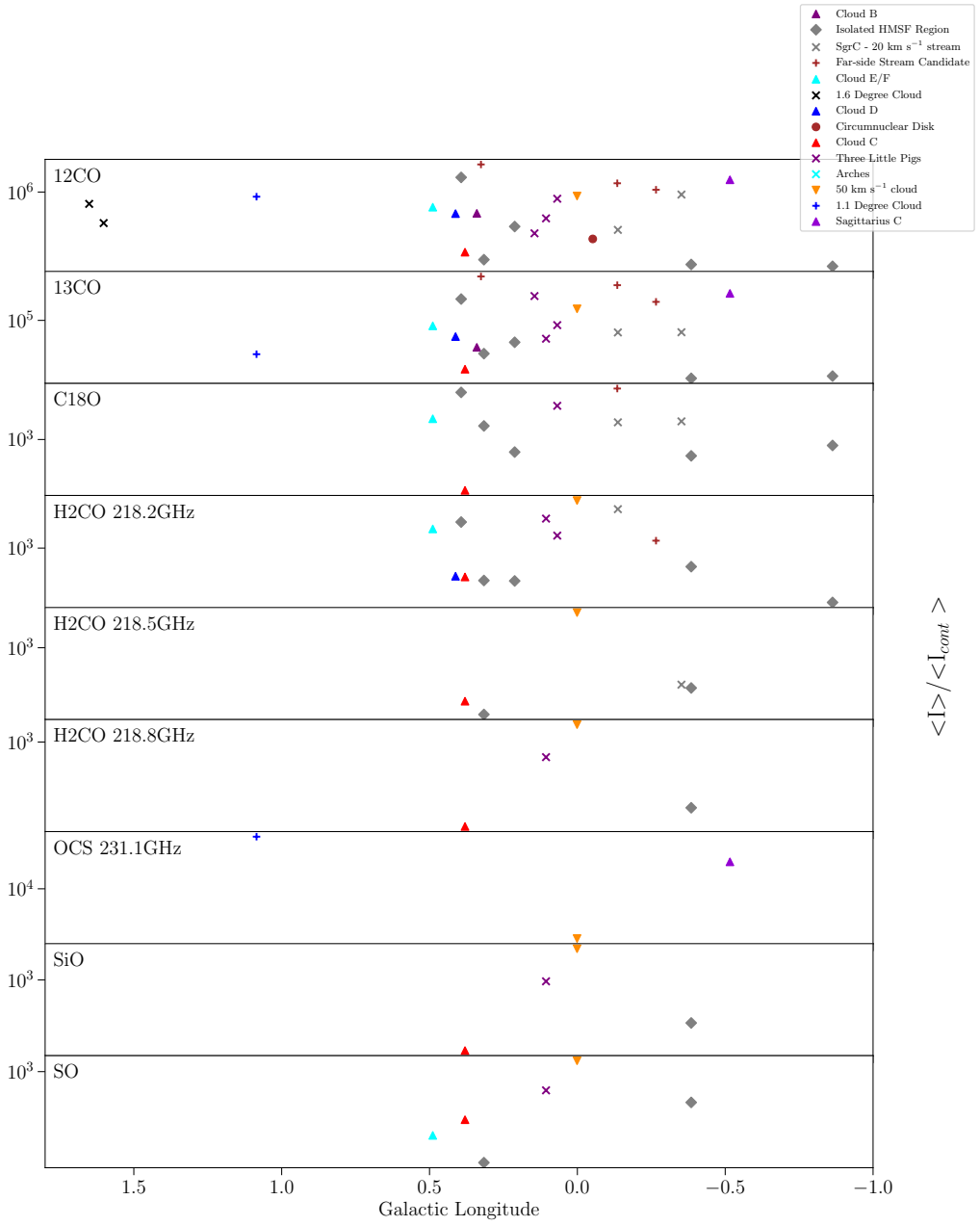

FIGURE 2.20: Normalized integrated intensity ratios for each observed transition in each region compared to the 230 GHz continuum.

increased shocks in the gas). This substantiates previous observations from Mills & Battersby (2017b) who found a similar trend towards the Galactic Centre in a number of molecular species, a trend that was further enforced by HC_3N observations by Mills et al. (2018b) who found an increase in the dense gas fraction inwards of R $\lesssim$ 140 pc.

Finally, we can compare the line ratios of the CMZoom sources in the Galactic Centre with the isolated high mass star-forming (HMSF) regions in the survey. These lie along our line of sight towards the CMZ but are actually located in the disk, providing an useful control sample.

Perhaps surprisingly, the line brightness ratios of the isolated HMSF regions are indistinguishable from the Galactic Centre sources. This is in direct contrast to observations of clouds in the Galactic Centre and the Galactic disk on $\gtrsim$ pc scales, which show very different emission line ratios. Specifically, Galactic Centre clouds ubiquitously show bright emission from dense gas tracers (e.g. NH_3, N_2H^+, HCO^+) across the whole extent of the cloud, while in disk clouds, emission from these dense gas tracers is confined to core ($\lesssim$0.1 pc) scales. The similarity of the line ratios between the Galactic Centre and disk sources in the CMZoom survey data suggests that the physical conditions are much more similar in these two locations on sub-pc scales than on cloud scales. This has important implications for understanding the similarities and differences in the processes controlling star formation between the two environments.

2.6 Line properties of 230 GHz continuum sources

We now investigate the detection statistics and line properties of the CMZoom 230 GHz continuum sources using the fits to the spectra for each of the main individual transitions targeted in the CMZoom survey (see Table 2.1).

2.6.1 Detection statistics of brightest lines and identification of primary kinematic tracer

Table 2.3 shows the detection statistics for each of the key tracers discussed in Table 2.1. We note here that the complete number of cores in our dataset differs substantially from the complete robust catalog presented in Paper II, as we have left several larger mosaics

Molecule	Rest Frequency (GHz)	Quantum Number	Upper Energy Level (K)	Tracer	Detection Percentage
^{12}CO	230.53800000	J=2-1	16.59608	Dense Gas	96
^{13}CO	220.39868420	J=2-1	15.86618	Dense Gas	96
C^{18}O	219.56035410	J=2-1	15.8058	Dense Gas	58
H_2CO	218.22219200	3(0,3)-2(0,2)	20.9564	Dense Gas	82
H_2CO	218.47563200	3(2,2)-2(2,1)	68.0937	Dense Gas	36
H_2CO	218.76006600	3(2,1)-2(2,0)	68.11081	Dense Gas	39
SiO	217.10498000	5-4	31.25889	Protostellar outflows & shocks	39
OCS	218.90335550	18-17	99.81016	Shocks	15
OCS	231.06099340	19-18	110.89923	Shocks	13
SO	219.94944200	6-5	34.9847	Shocks	60

TABLE 2.3: Summary of 10 key transitions targeted by the CMZoom survey with the percentage of cores investigated in this paper that show emission in that transition.

– including Sagittarius B2 – out of this analysis until additional steps can be made to suitably clean these. Of the remaining regions, ^{12}CO and ^{13}CO are detected in 96% of all cores. However, all ^{12}CO and most ^{13}CO data suffer from severe image artefacts so they are not reliable tracers for determining the kinematics of the cores. We ignore these transitions in the kinematic analysis from here on.

After ^{12}CO and ^{13}CO, C^{18}O and the lowest energy H_2CO transition are the next most often detected, being found in 58% and 82% of all cores, respectively. As summarised in Table 2.3, the images of these transitions do not suffer from imaging artefacts and the line profiles are generally well fit with single or multiple Gaussian components. The emission from both of these transitions should therefore provide robust information about the core kinematics. Given the prevalence of the lower transition of H_2CO and the fewer deviations in line profiles from that well described by a single Gaussian component, we opt to use H_2CO as our fiducial tracer of the core kinematics.

Figure 2.21 shows the mass-radius relation for all cores included in this analysis, with circles indicating cores with a H_2CO (218.2 GHz) detection. These cores represent 88.8% of the total mass of cores that have been included in this analysis. As such, using this transition as our fiducial tracer provides significant coverage across the whole survey.

2.6.2 Analysis of core velocities

Figure 2.22 shows a histogram of the V_{LSR} difference for each core between H_2CO and all other lines detected detected towards that core. The black dashed line shows the best-fit Gaussian to all data within a V_{LSR} difference $\Delta V_{LSR} \leq 5\,\mathrm{km\,s^{-1}}$. The small mean and dispersion of $-0.29\,\mathrm{km\,s^{-1}}$ and $1.98\,\mathrm{km\,s^{-1}}$, respectively, gives confidence that the observed V_{LSR} for cores is robust. There are 30 cores with $\Delta V_{LSR} > 5\,\mathrm{km\,s^{-1}}$ which lie in 9 regions throughout the survey. Of these 30 cores, 12 of them belong to

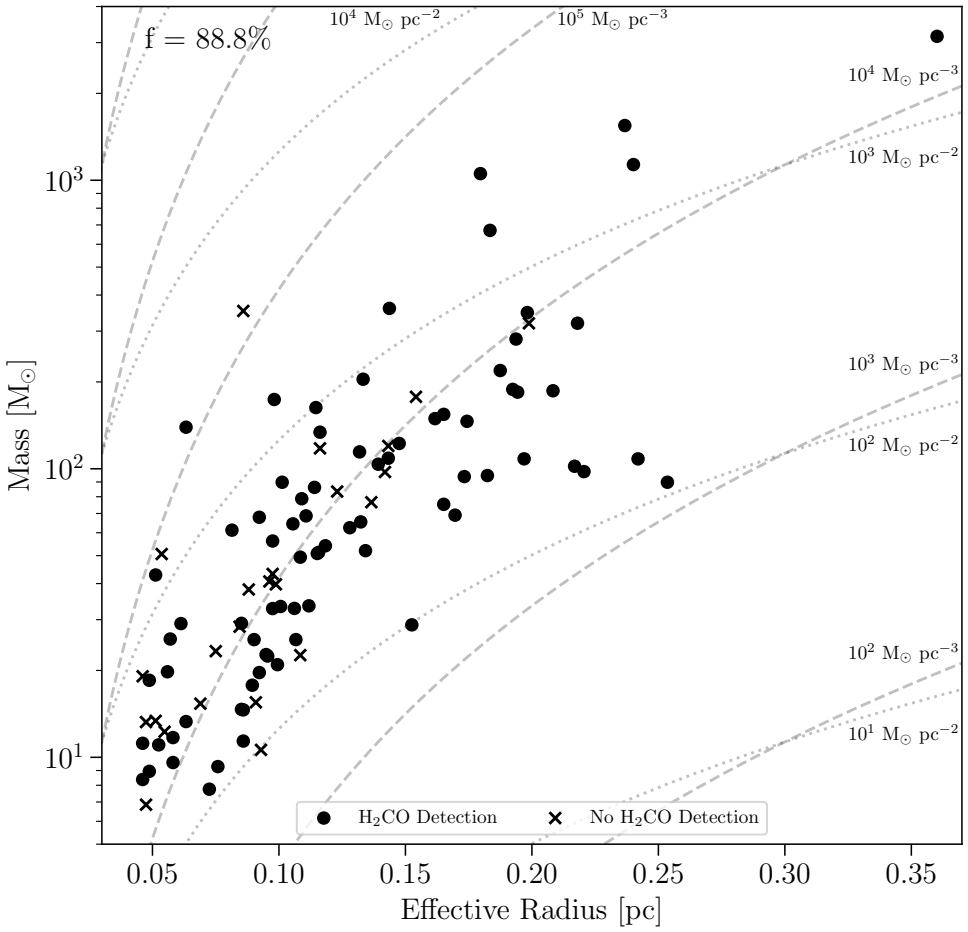

FIGURE 2.21: Mass vs effective radius relation with markers indicating cores with a H_2CO (218.2 GHz) detection. The number in the top-left corner states that cores with H_2CO (218.2 GHz) detections account for 88.8% of the mass of all cores in this work. The dashed lines are lines of constant volume density, while dotted lines indicate lines of constant column density.

G359.889−0.093, 5 to G0.001−0.058 and 4 to G0.068−0.075 – i.e. they lie very close in project to the Galactic centre. This is the most complicated part of position-position-velocity space, with multiple, physically distinct components along the line of sight, so these V_{LSR} offsets are not unexpected as these regions are experiencing significant shear and velocity gradients across them.

We then seek to understand how these core V_{LSR} values compare to the observed velocities of their parent clouds on larger scales. In order to determine a representative velocity range for each parent cloud, we use the catalogue of Walker et al. (in prep.),

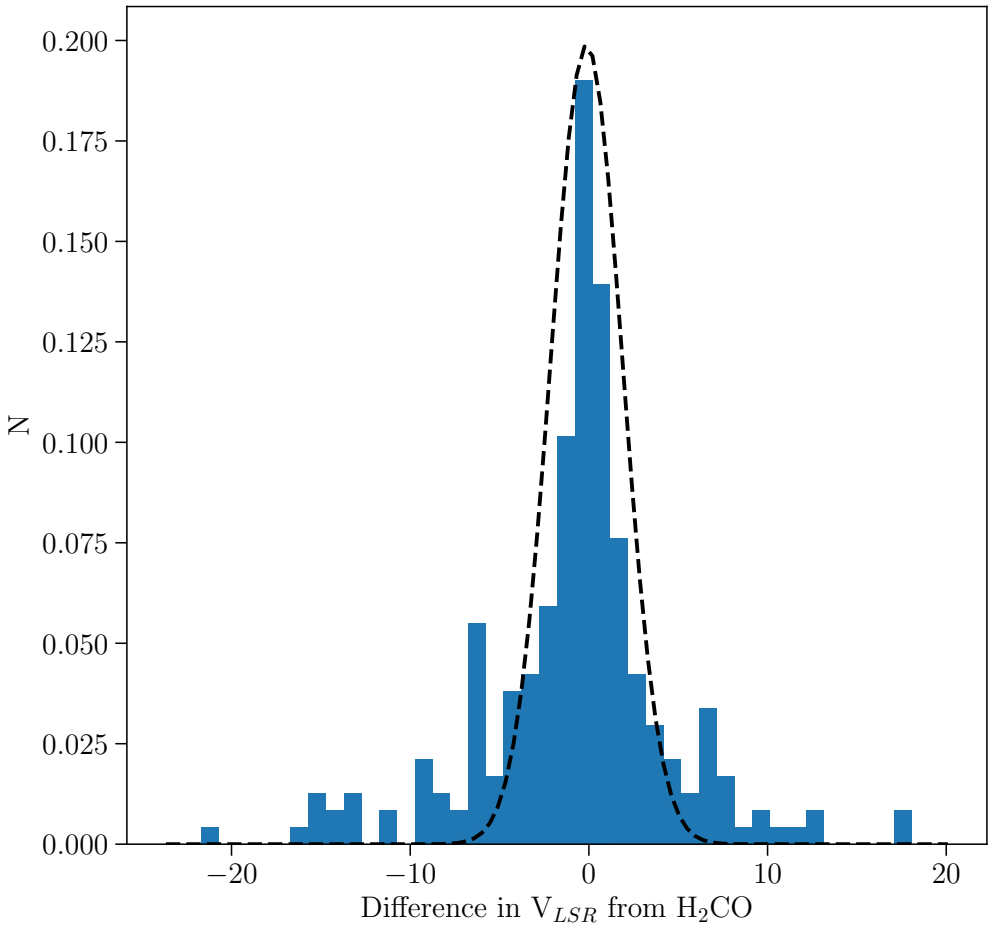

FIGURE 2.22: Histogram of the V_{LSR} difference of each key transition when compared to the lower transition of H_2CO for every core.

who extracted spatially averaged spectra for each cloud from single-dish data in the literature.

Figure 2.23 compares the full-width half maximum (FWHM) of the Walker et al. (in prep.) single-dish observations to the range of observed core velocities within the same cloud, using only the core velocities measured for the 10 key transitions described in Table 2.1. The dashed line shows the one-to-one relation between those velocities. In general, we would expect the range of core velocities within a cloud to be similar to or smaller than the cloud's FWHM if the cores lie within the parent cloud, i.e. points should lie below the one-to-one line. As expected, most of the regions satisfy this criteria.

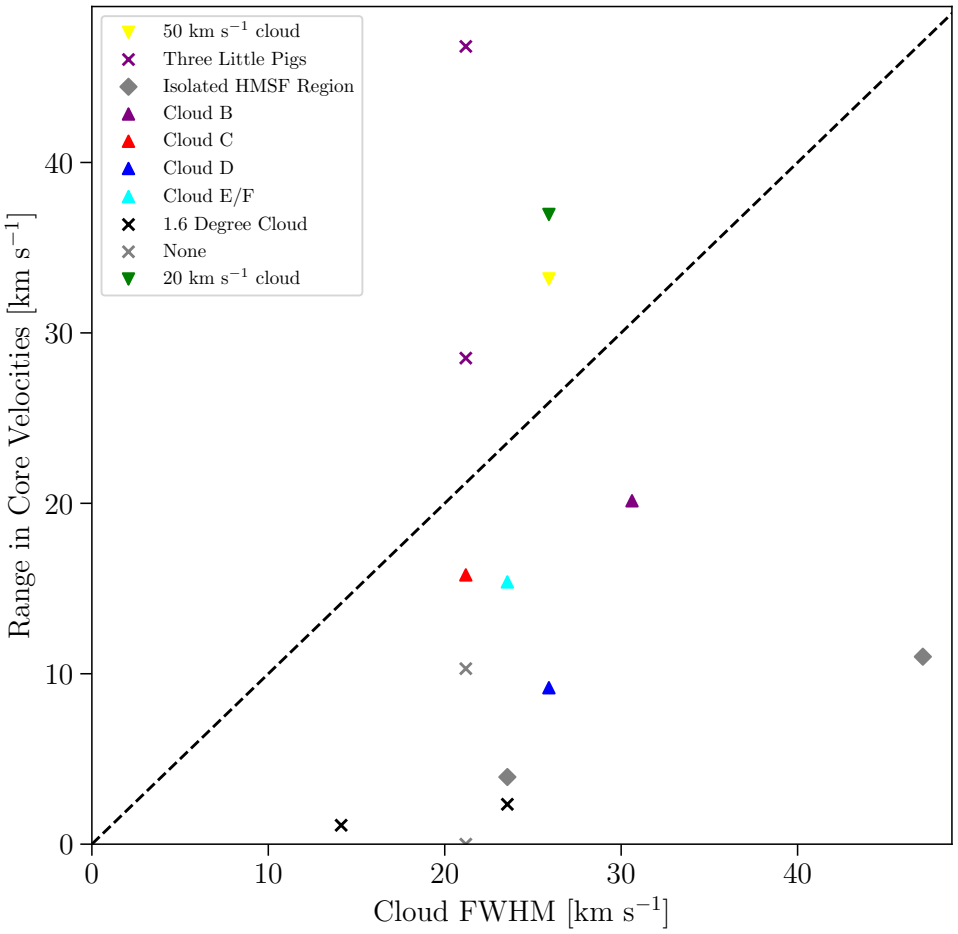

FIGURE 2.23: Comparison of the range in core velocities of the 10 key transitions targeted by the survey as measured by *scousepy* to the observed FWHM of the cloud. The dashed line shows the one-to-one line. The majority of cores fall below the dashed line, as expected if these cores are distributed within the cloud. In the main text we discuss each of the clouds which lie above the dashed line.

Two of the four regions that do not meet this criteria are the 20- and 50- km s^{-1} clouds. This is somewhat expected, firstly as these clouds are composed of large mosaics (67 and 24 pointings, respectively). Secondly, these clouds have large velocity gradients across them, causing the core velocities on one side of the region to differ significantly from the other side.

The 'Three Little Pigs' clouds that lie above the one-to-one line, however, are small and do not have large velocity gradients across them. The region farthest above the one-to-one line – 'G0.068-0.075' – contains 12 dense cores identified by Paper II. To try

and understand the much larger than expected range in core velocities, we inspect the individual spectra for this region in detail.

Figure 2.24 shows the spectra extracted from each spectral cube of the most massive core (G0.068-0.075a) in which ^{13}CO, C^{18}O, H_2CO (218.2 GHz) and SiO all peak at $\sim 20\,\mathrm{km\,s^{-1}}$, differing from the average V_{LSR} of the remaining cores within the cloud by $\sim 30\,\mathrm{km\,s^{-1}}$. Figure 2.25 shows the same spectra for the second most massive core in the cloud, in which these key transitions peak well within the shaded region indicating the cloud's velocity dispersion. Since this is the case for all cores other than 'a', it suggests that this core may not be contained within the cloud, and instead may be unassociated with the cloud indentified in Walker et al (in prep.). Further work is required to understand the nature and location along the line of sight of core 'a'.

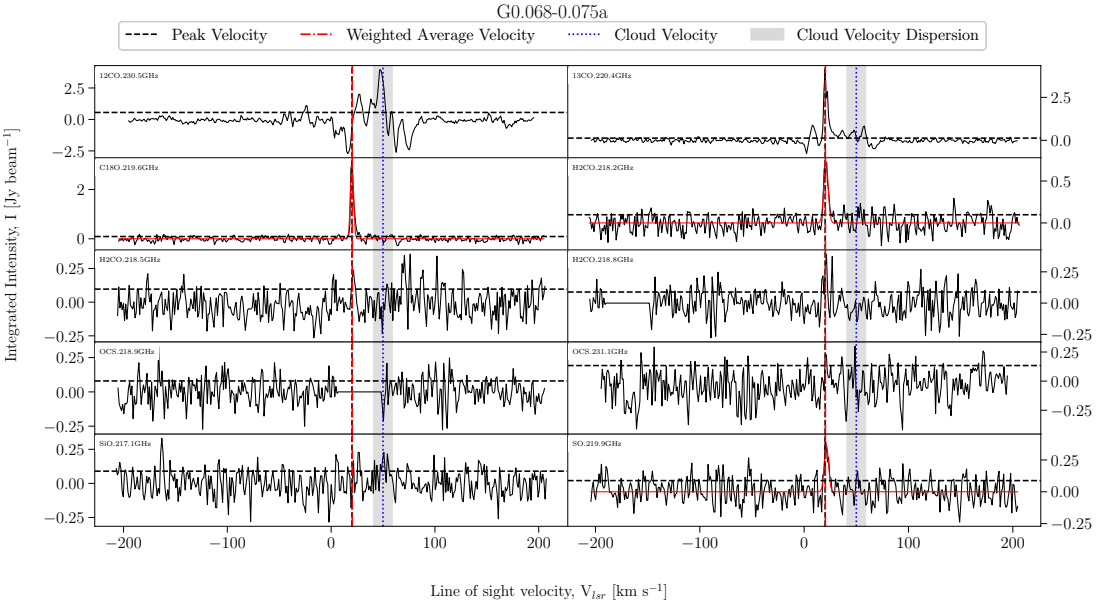

FIGURE 2.24: Fitted spectra for dendrogram leaf G0.068-0.075a, with scouse fits overlaid in red, cloud velocity and velocity dispersions are indicated by the blue dashed line and grey shaded area, respectively.

The fourth cloud above the dashed line, 'G0.106-0.082', contains multiple, broad velocity components in the spectra (Figure 2.26). The peak of the CMZoom emission sits within the shaded region showing the cloud's velocity dispersion. However, additional velocity components in most of the transitions lie outside this range. It seems likely that the Walker et al. (in prep.) catalogue only derived the cloud velocity and velocity dispersion from one of these two velocity components. The third Little Pigs cloud is not present as it had no detection in any of the 10 key transitions.

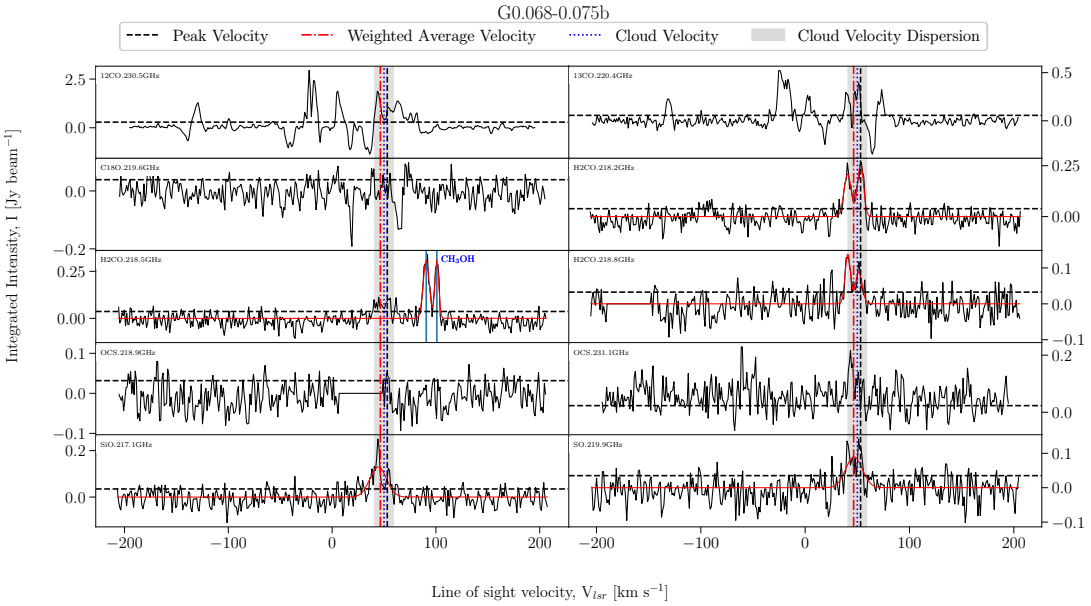

FIGURE 2.25: Fitted spectra for dendrogram leaf G0.068-0.075b, with scouse fits overlaid in red, cloud velocity and velocity dispersions are indicated by the blue dashed line and grey shaded area, respectively.

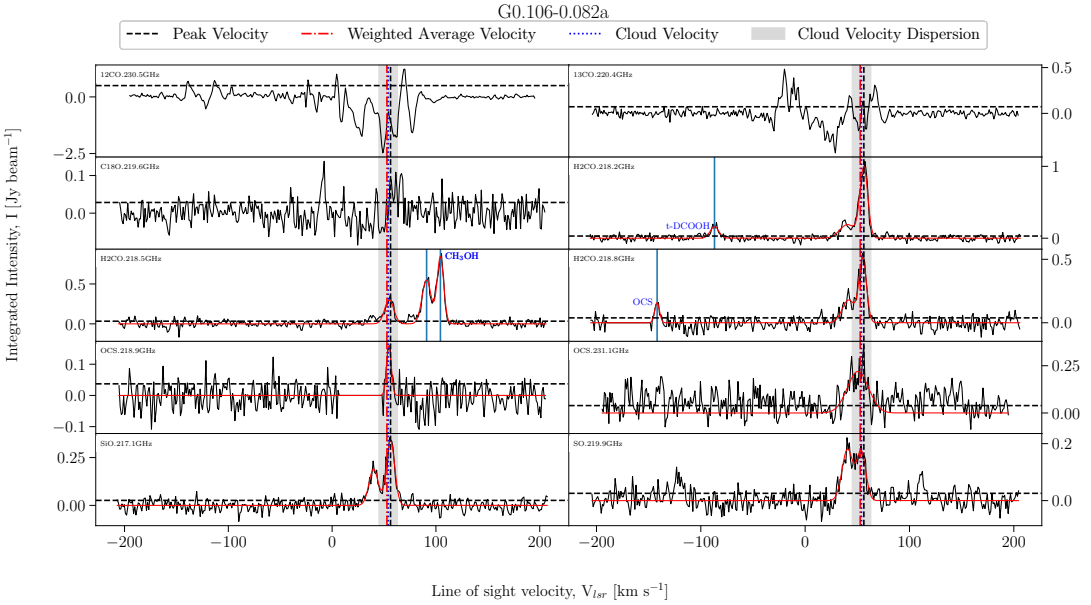

FIGURE 2.26: Fitted spectra for dendrogram leaf G0.106-0.082a, with scouse fits overlaid in red, cloud velocity and velocity dispersions are indicated by the blue dashed line and grey shaded area, respectively.

2.6.3 Core velocity dispersions

Figure 2.27 shows a histogram of the velocity dispersion difference for each core between H_2CO and all other lines detected towards that core. The black dashed line shows the best-fit Gaussian to all data within $\Delta\sigma \leq 4\,\mathrm{km\,s^{-1}}$. The small mean and dispersion of $0.15\,\mathrm{km\,s^{-1}}$ and $1.41\,\mathrm{km\,s^{-1}}$, respectively, gives confidence that the observed velocity dispersion for the cores are robust. There are 10 cores with $\Delta\sigma > 4\,\mathrm{km\,s^{-1}}$ from 4 different regions. Of these 10 cores, 3 belong to G0.001−0.058, 3 to G0.068−0.075, 2 to G0.106−0.082 and 2 to G359.889−0.093. We note that most cores with $\Delta\sigma > 4\,\mathrm{km\,s^{-1}}$ also have $\Delta V_{LSR} > 5\,\mathrm{km\,s^{-1}}$, likely a result of either multiple velocity components being averaged together or poorer fit results from lower signal-to-noise spectra.

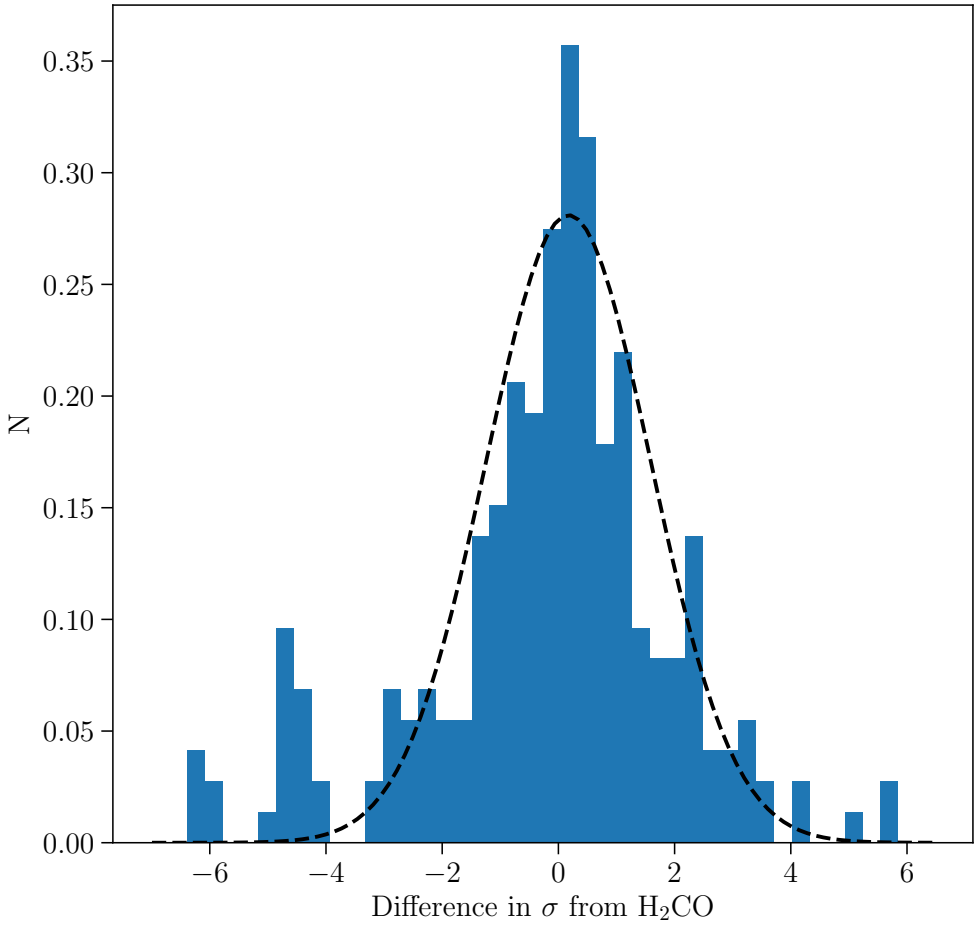

FIGURE 2.27: Histogram of the V_{LSR} difference of each key transition when compared to the lower transition of H_2CO for every core.

2.6.4 Number of lines detected per core

Figure 2.28 shows the relation between the observed continuum flux of each core and the number of spectral lines detected. There is a slightly upward trend showing that the brighter cores tend to have more lines detected. Three of the six observed dense cores within cloud 'b' have no detected emission lines despite having continuum fluxes of $\gtrsim$0.2 Jy. All other cores with such high continuum fluxes have $\geq$9 detected lines. These 'line-deficient, continuum-bright' cores are interesting sources to followup as potential precursors to totally metal stars that have been predicted to exist (Hopkins, 2014).

Conversely, cores in the 'Three Little Pigs' clouds, and to a lesser extent the 50 km s^{-1} cloud, stand out as having a large number of lines detected at low continuum flux levels. We note that in Figure 2.33, the cores in both of these clouds lie in the same portion of external pressure vs gas surface density space, and have a similar (low) fraction of star forming cores, with only one or two ambigious tracers of star formation activity. We speculate that the large number of lines detected in cores at low continuum flux levels in the 'Three Little Pigs' clouds and 50 km s^{-1} cloud may be the result of shocks in the high pressure gas beginning to compress the gas and instigate star formation. Further work is needed to test this hypothesis.

2.6.5 Correlations between the emission from different transitions

We now investigate how well the emission from the 10 key different transitions correlate with each other. Figure 2.29 shows the Pearson correlation coefficient matrix for the measured amplitudes of the detected emission from these lines. The larger the correlation coefficient shown in each grid cell, the stronger the correlation between the two lines in that row and column. Negative values indicate the emission in the lines is anti-correlated. The correlation coefficient of 1.0 along the diagonal of the matrix shows the auto-correlation of the emission from each line with itself.

We begin by looking at the correlations between the three main 'groups' of transitions – the CO isotopologues, the H_2CO transitions tracing dense gas, and the shock tracers – before investigating the correlations between transitions in different groups.

Unsurprisingly, emission from the three CO isotopologues are well correlated. The imaging artefacts in the ^{12}CO and ^{13}CO datacubes may well contribute to a lower correlation

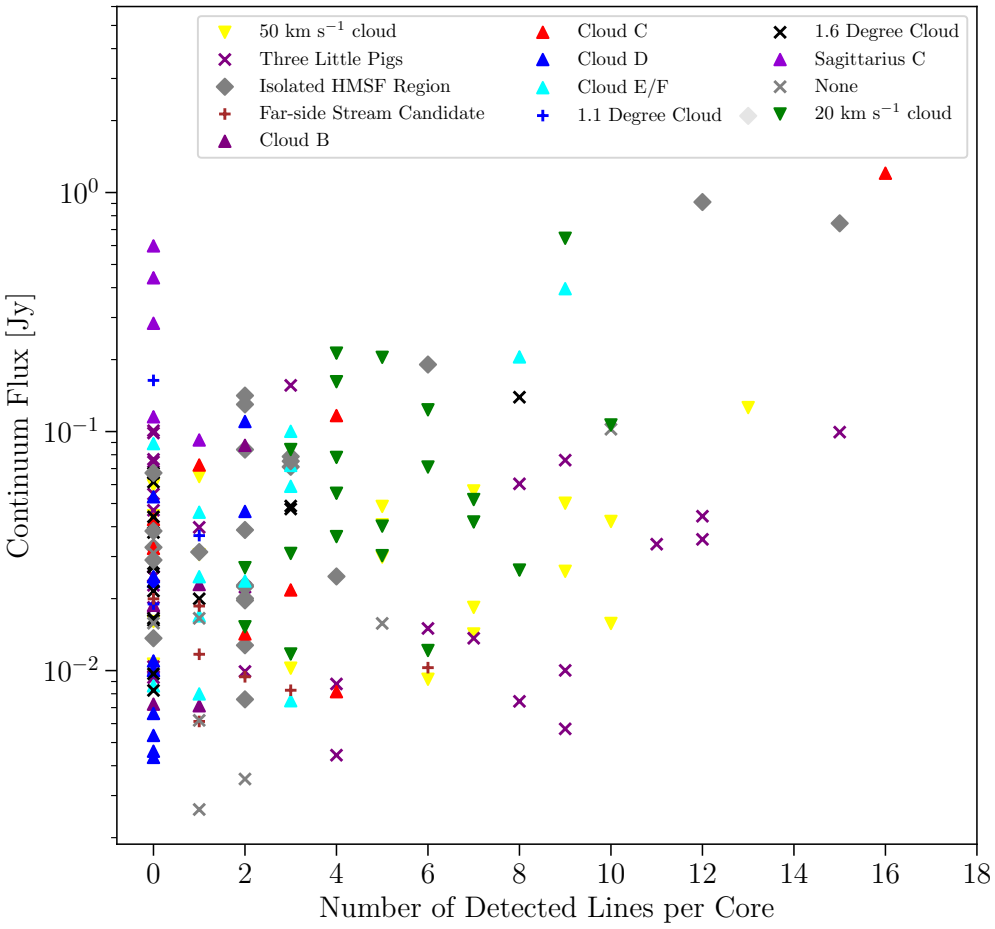

FIGURE 2.28: Comparison of the total continuum flux of each dense core to the number of total detected lines within the core. A general upwards trend implying that the brighter cores tend to have more line complexity.

coefficient between these transitions than may have been expected. Again unsurprisingly, the three H_2CO transitions are also well correlated, with the lowest two energy levels having the highest correlation coefficient of all line pairs. Emission from the SiO, SO and OCS transitions are all well correlated too. As these transitions trace emission from shocks, these correlation makes sense.

We then turn to comparing correlations between transitions in different groups. The emission from ^{12}CO and ^{13}CO is almost completely uncorrelated (and sometimes even slightly anti-correlated) with the emission from all the other transitions. The only stark exception to this is that emission from ^{13}CO is well correlated with emission from the

lowest energy level of H_2CO.

The $C^{18}O$ emission only shows a very weak correlation with most of the other non-CO transitions. Again the notable exception to this is that the $C^{18}O$ emission is well correlated with the lower energy transition of H_2CO. The increasing correlation between the CO isotopologues with the lower energy transition of H_2CO, from ^{12}CO to ^{13}CO to $C^{18}O$, suggests that these transitions are increasingly better tracers of denser gas, as expected given their relative abundances

Comparing the H_2CO transitions with the shock tracers, there is a clear trend of increased correlation with increasing H_2CO transition energy for all shock tracers. This suggests there is a relation between regions containing dense gas with higher excitation conditions and the prevalence and strength of shocks. Such regions might be expected where there are the convergent points of large-scale, supersonic, colliding gas flows or increased star formation activity.

Summarising the results of the correlation matrix analysis, we conclude that: (i) ^{12}CO (and to a lesser extent ^{13}CO) is a poor tracer of the dense gas; (ii) the $C^{18}O$ and lowest energy H_2CO transition are the most robust tracers of the dense gas; (iii) the higher energy H_2CO transitions and the shock tracers are all consistently pinpointing regions with elevated shocks and/or star formation activity.

2.7 Analysis

In this section we use the results of the line fitting and conclusions in Section 2.6 to determine the likely virial state of the continuum cores (§ 2.7.1) and its relation to their star forming potential (§ 2.7.2), then search for signs of proto-stellar outflows (§ 2.7.3) and intermediate-mass black holes (§ 2.7.4) in the CMZoom line data.

2.7.1 Determining the virial state of the compact continuum sources

As described above, H_2CO (218.2 GHz) was used to determine the kinematic properties for the cores within Paper II's dendrogram catalog due to its prevalence throughout the survey and typically being a bright line with a Gaussian profile and a single velocity

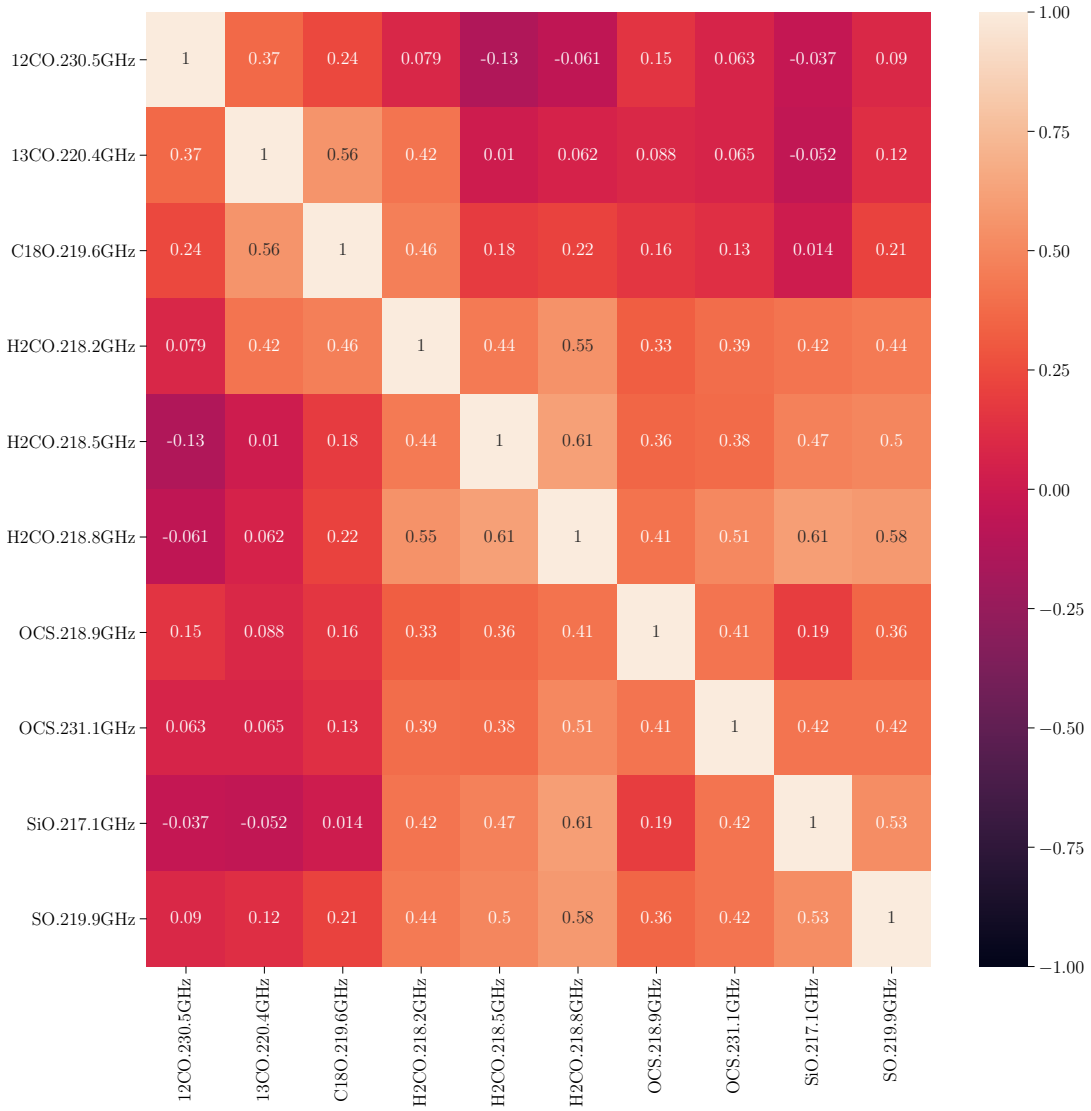

FIGURE 2.29: Correlation matrix showing the correlation coefficients between the amplitude of Gaussian peaks fit by *scousepy* for the 10 key transitions targeted by the survey.

component. Using the line fit parameters for this transition, we calculated the virial parameter, α, using the observed velocity dispersion (σ_{obs}), by considering a core's kinetic energy support against its own self gravity through,

$$\alpha = \frac{5\sigma^2 R}{GM},$$

where σ is the velocity dispersion, R and M are the radius and mass of the dendrogram core derived in Paper II, and G is the gravitational constant. The constant '5' comes from the assumption that these cores are uniform spheres. We also calculated the virial parameter using the corrected velocity dispersion (σ_{int}) by subtracting the channel width (σ_{inst}) in quadrature from the observed velocity dispersion, $\sigma_{int} = \sqrt{\sigma_{obs} - \sigma_{inst}}$.

Figure 2.30 shows the distribution of virial parameters as a function of core mass and core velocity dispersion. Using this form of the virial analysis, only six (out of 103) of the more high-mass cores are virially bound based on observed velocity dispersions, and four are virially bound based on the corrected velocity dispersion. $94 - 96\%$ of cores in the survey are gravitationally unbound when only considering a core's kinetic energy support against its own self gravity.

To explore if this is a physical representation of the core population within the CMZ or a result of the limited velocity resolution of the survey, we first repeated the analysis in Figure 2.30 after correcting for the instrumental velocity resolution (blue crosses in Fig 2.30). The velocity dispersion of most cores are significantly larger than the channel width, so the virial ratios >1 for the majority of cores are not affected by the instrumental velocity resolution.

We then determined what velocity dispersion each core would need to have for it to be gravitationally bound, i.e. to have $\alpha = 1$. Figure 2.31 shows a histogram of these '$\alpha = 1$' velocity dispersions compared to the measured velocity dispersions of the cores. This shows that in order to unambiguously determine the virial state of those cores with σ close to the channel width requires re-observing them with an instrumental velocity resolution of $\sim 0.1\,\mathrm{km\,s^{-1}}$. We highlight these low velocity dispersion sources as particularly interesting to follow-up in the search for potential sites of star formation activity with the CMZ.

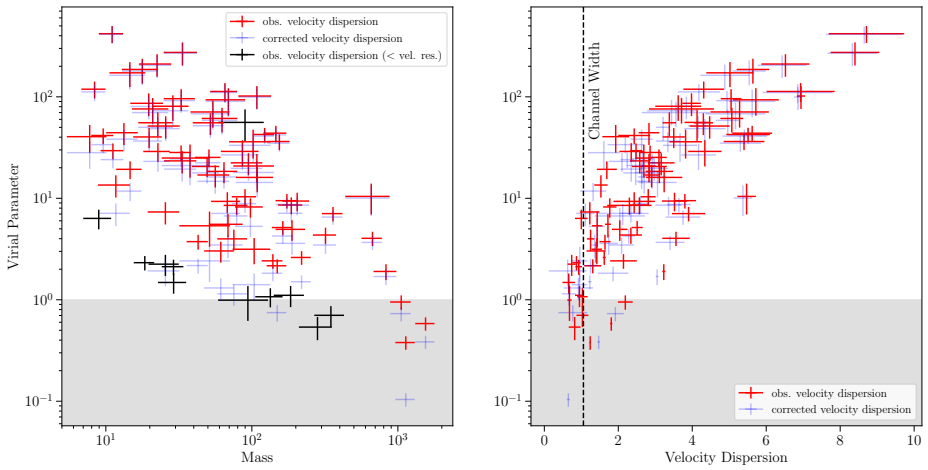

FIGURE 2.30: Virial parameters as a function of dendrogram core mass [left] and observed velocity dispersion [right]. The red crosses show the observed velocity dispersion, the blue crosses show the velocity dispersion corrected for the instrumental velocity resolution. The black crosses in the left panel show those measurements for which the fit result for the velocity dispersion is lower than the channel width, and thus cannot be corrected for the instrumental velocity resolution. The vertical dashed line in the right panel indicates the channel width of the ASIC data. The shaded grey region represents the condition a core must meet to be virially bound. These plots show that when only considering the support from gas kinetic energy against self-gravity, most of the cores are not gravitationally bound. The fact that the measured linewidths for most cores are larger than the channel width demonstrates that this result is not affected by the velocity resolution of the observations.

Having concluded these high virial ratios are real for the majority of sources, we then seek to understand whether these cores are simply transient overdensities, or longer-lived structures. Previous work on the clouds within the dust ridge by Walker et al. (2018c) and Barnes et al. (2019) found that while dust ridge clouds are gravitationally unbound according to virial metrics comparing the gravitational potential and kinetic energies, the intense pressure observed within the CMZ is sufficient to keep these cores in hydrostatic equilibrium.

In Figure 2.32, we replicate the Figure 4 of Walker et al. (2018c) – which in turn replicated Figure 3 of Field et al. (2011) – for all cores in the CMZoom survey with a detected H_2CO (218.2 GHz) transition. The black curved lines show where cores would be in hydrostatic equilibrium if confined by external pressures described by,

$$V_0^2 = \frac{\sigma^2}{R} = \frac{1}{3}\left(\pi\Gamma G\Sigma + \frac{4P_e}{\Sigma}\right), \tag{2.1}$$

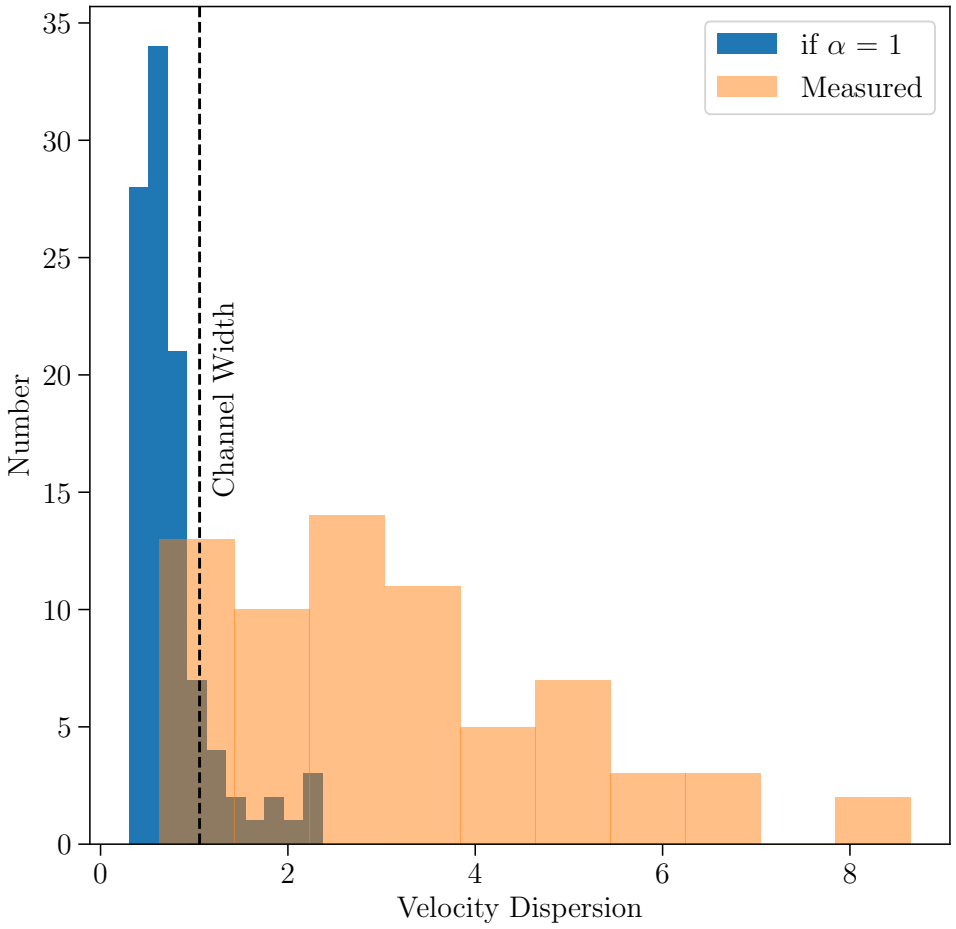

FIGURE 2.31: Histogram of measured velocity dispersions (orange) compared to the velocity dispersion required for every core to be virially bound (blue). The fact that the observed velocity dispersion is larger than the channel width for most of the cores suggests that the CMZoom velocity resolution is not biasing the virial analysis for most cores. A velocity resolution of $\sim$0.1 km s^{-1} would be required to determine if the small number of cores with linewidths comparable to the CMZ velocity resolution are gravitationally bound.

where V_0 is the linewidth-size scaling relation, σ and R are the velocity dispersion and radius of the core, Γ is a form factor related to the density structure (as described by Elmegreen, 1989) and here we adopt $\Gamma = 0.73$ which describes an isothermal sphere at critical mass, Σ is the mass surface density, G is the gravitational constant and P_e is the external pressure. The black dashed line represents the simple virial condition of $\mathrm{P}_e = 0$ as shown in Figure 2.30.

Given the calculated gas pressure in the CMZ of $P_{turb}/k = \mu m_H n \sigma^2/k \sim 10^9\,\mathrm{K\,cm^{-3}}$

(Kruijssen et al., 2014b), Figure 2.32 further enforces the conclusion of Walker et al. (2018c) that while only a small number of these cores are gravitationally bound according to simply virial analysis, the intense pressures found within the CMZ are capable of keeping a large fraction of these cores in hydrostatic equilibrium, so they may still be long-lived structures. The implication of this intermediate conclusion is that the more simplified virial equilibrium analysis does not paint a complete picture of core collapse within more extreme environments, and a more detailed analysis is necessary to understand how star formation proceeds within these environments.

2.7.2 The relation of core gas kinematics to a core's star forming potential

We then seek to understand what role, if any, the kinematic state of the gas plays in setting the star formation potential of the cores. Figure 2.33 repeats Figure 2.32, but with marker colours representing a number of key structures throughout the CMZ. Hatchfield et. al. (in prep) use a number of standard star formation tracer catalogs including methanol masers (Caswell et al., 2010), water masers (Walsh et al., 2014), 24μm point sources (Gutermuth & Heyer, 2015) and 70μm point source (Molinari et al., 2016) catalogs to identify which dense cores within Paper II's catalog may be associated with ongoing star formation. They defined three categories: cores definitely associated with these star formation tracers, cores definitely not associated with these star formation tracers, and an additional category for a small number of cores where it was difficult to determine whether the observed star formation tracer was associated with that core or not. We combined these star formation tracer activities with targeted observations of the 20 km s^{-1} cloud from Lu et al. (2015), who detected a number of deeply embedded H_2O masers towards this cloud. In Figure 2.33, cores with robust associated star formation tracers are marked with a filled circle. Cores with an unclear star formation tracer association are marked with a square. Cores with no star formation tracers are marked with crosses.

We find that all cores below the $P_e = 0$ line, i.e. all cores with $\alpha \leq 1$, are associated with a star formation tracer. As cores move upwards and to the left of the $P_e = 0$ line the fraction of cores with star formation tracers drops.

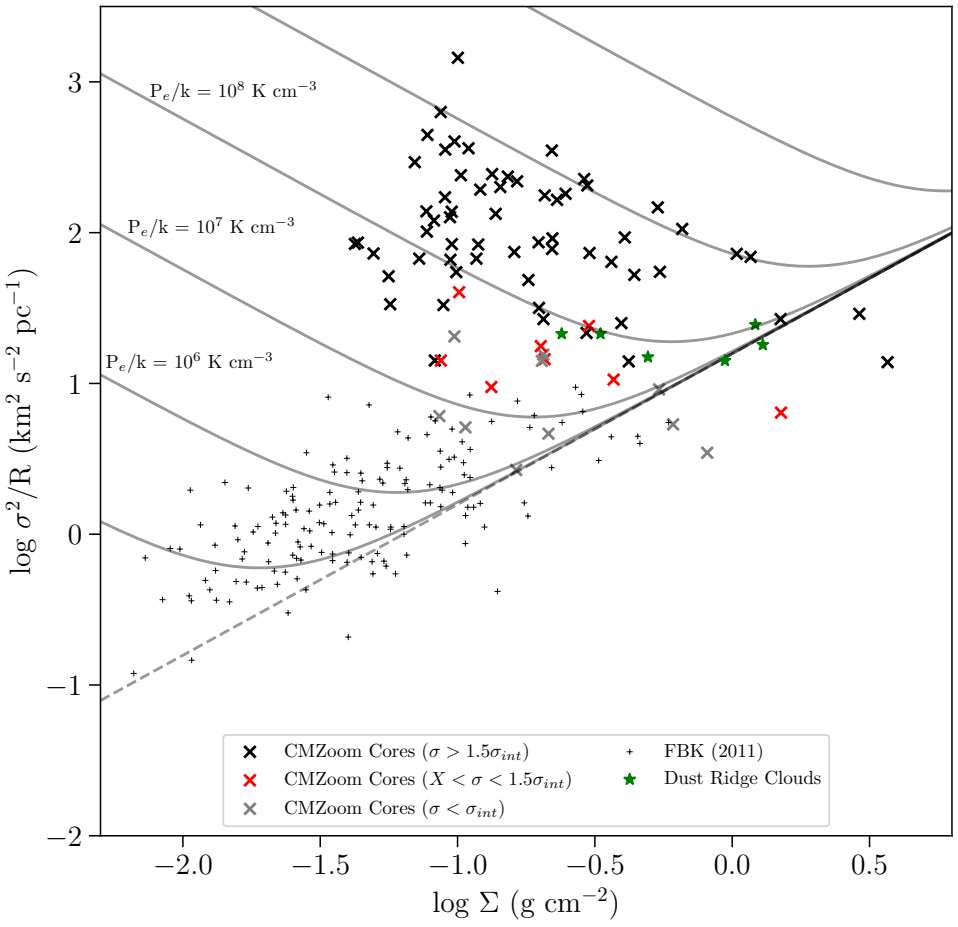

FIGURE 2.32: Comparison of the CMZoom cores shown by crosses, to Galactic Ring Survey clouds (Field et al., 2011) shown by black plus symbols. Grey crosses indicate cores with a velocity dispersion less than the channel width ($\sigma_{int} = 1.2\,\mathrm{km\,s^{-1}}$) of the survey. Red crosses indicate cores with only slightly resolved velocity dispersions between 1 and 1.5 times the channel width. The black crosses indicate lines with a velocity disperion more than 1.5 times the channel width, so are well resolved. Overlaid are green star markers corresponding to Walker et al. (2018c)'s measurements of dust ridge clouds. The dashed line represents virial equilibrium with $P_e = 0$ and the curved lines represent objects in hydrostatic equilibrium at the stated pressure. While few of the CMZoom cores would be self-gravitating with $P_e = 0$, at pressures of $P_e = 10^8$ K km^{-1} the majoriry of these cores would be in hydrostatic equilibrium.

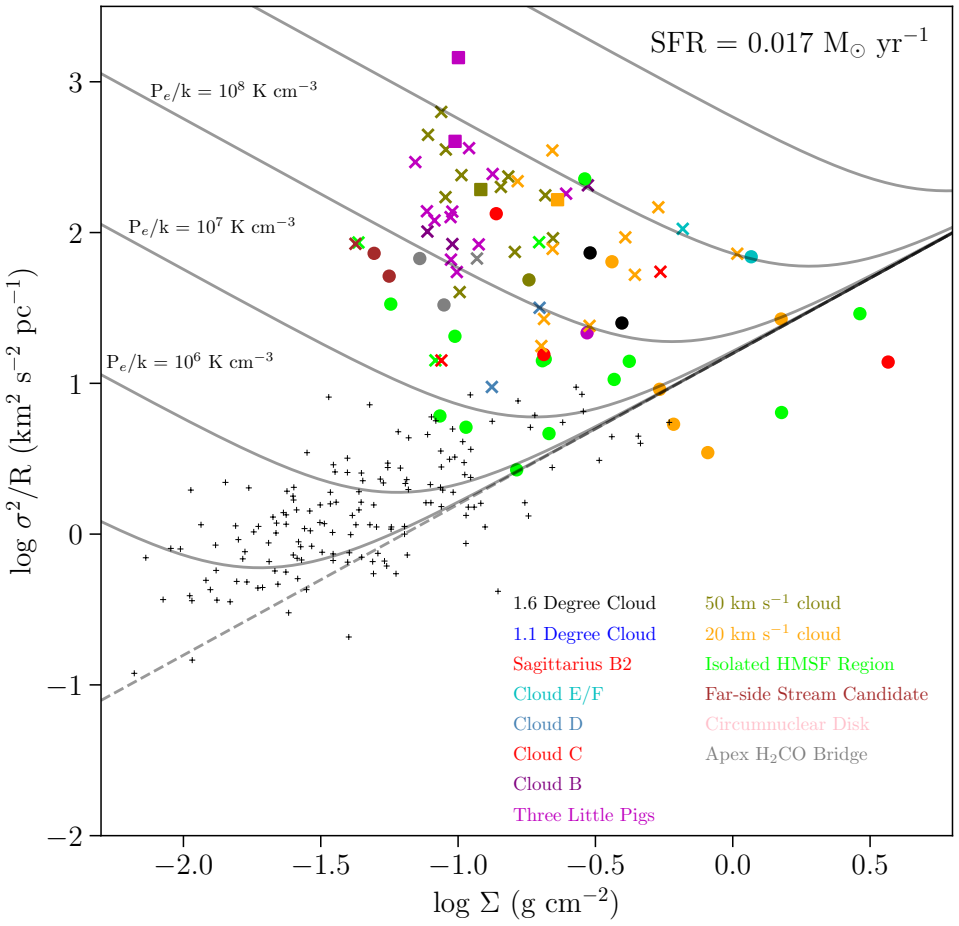

FIGURE 2.33: Figure 2.32 with marker colors indicating different key regions throughout the CMZ. Circles indicate cores that have associated star formation tracers according to Hatchfield et. al. (in prep) or Lu et al. (2015), squares indicate cores with potential star formation tracer association according to Hatchfield et. al. (in prep) and crosses indicate cores with no star formation tracer association. All cores below or close to $P_e = 0$ (shown by the dashed line) are found to be star forming, while the fraction of cores that are star forming drops off quickly against increased pressure or distance above this line. If we take all cores with definite or ambiguous star formation tracers, we estimte a current day star formation rate of 0.017 $M_\odot$ yr^{-1}.

We then try to quantify if there is a combination of physical properties that can be used to determine the likelihood that a given core will be star forming or not. Figure 2.34 shows the fraction of cores that are star forming below lines of constant pressure (left) or as a function of distance from the $P_e = 0$ line (right). The red markers show the fraction of isolated HMSF cores that were found to be associated with star formation tracers, while black markers show isolated HMSF cores in both the definite and ambiguous association star formation tracer groups. Purple markers show the fraction of CMZ cores with definite star formation tracers, while blue markers show both definite and ambiguous star formation tracers.

Figure 2.34 shows the fraction of cores that are star forming below lines of constant pressure (left) or as a function of distance from $P_e = 0$ broken up into two categories. The top panel shows this trend with the cores split up into CMZ cores (blue and purple markers) and isolated HMSF cores (black and red markers) while the bottom panel shows this trend with the cores split up into all cores (black and red markers) and only CMZ cores (blue and purple markers).

All cores below a maximum external pressure of $10^7\,\mathrm{K\,cm^{-3}}$ have associated star formation tracer activity but above $10^7\,\mathrm{K\,cm^{-3}}$ the isolated HMSF cores separate significantly from the population of CMZ cores, plateauing at 80% while the CMZ cores drop to $\sim 30\%$. These isolated HMSF regions were selected due to their potential star formation activity, so it is no surprise that this population of cores differ significantly from CMZ cores. A similar trend occurs as a function of star forming cores against maximum distance from $P_e = 0$, though the CMZoom cores separate from the isolated HMSF regions at a faster rate than as a function of external pressure. This suggests that while the external pressure factors in to whether or not a core will begin to form stars, the proximity of a core to being virially bound provides a more accurate indication of it's star formation activity.

Finally, we use this information on star formation activity and kinematic state of the cores to update the present day star formation rate calculation in Paper II. In that paper the full catalog of dense cores was used to estimate an upper limit on future star formation rates under the assumption that all dense cores would, at some point, begin to form stars. Assuming a Kroupa IMF and a star forming efficiency of 10%, we use the mass and free fall times estimated for each core in Paper II to estimate a current day star

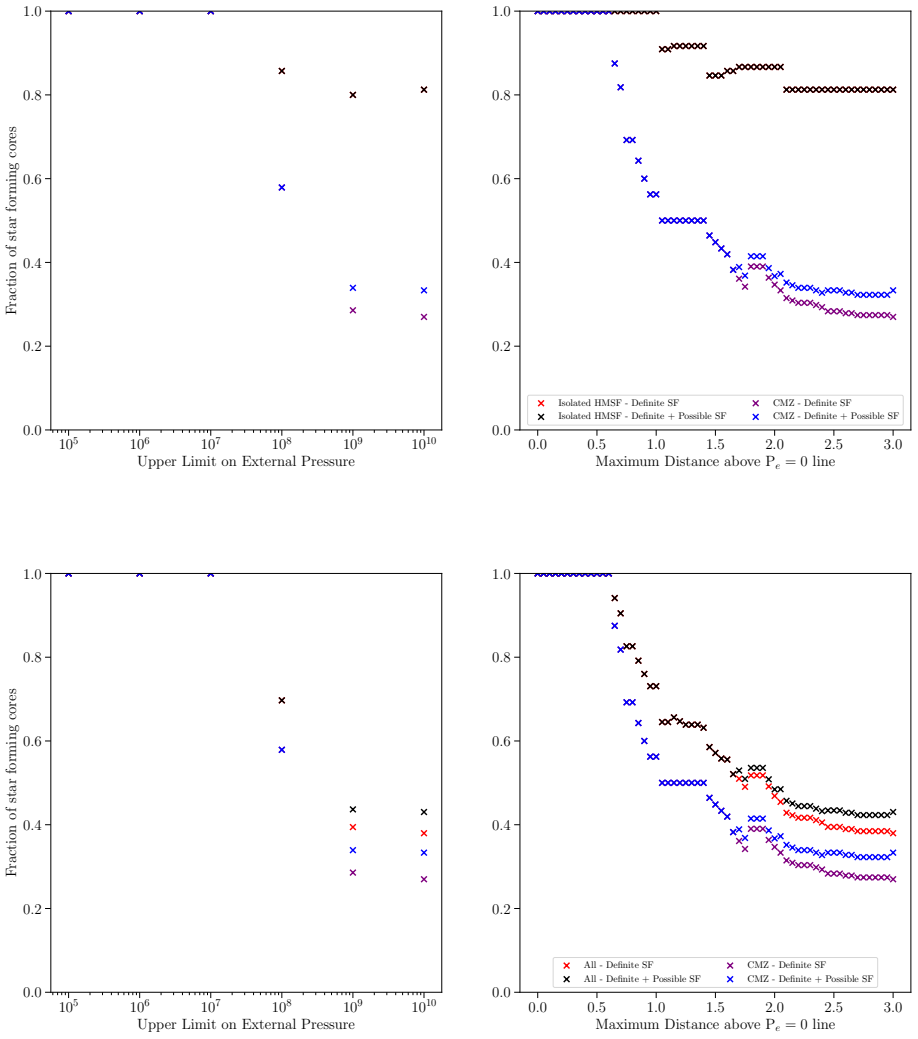

FIGURE 2.34: [Top] Fraction of cores that are star forming as a function of upper limit on the external pressure [left] or maximum distance above the $P_e = 0$ line [right]. Red markers indicate isolated HMSF cores with definite star formation tracers, black indicates isolated HMSF cores with definitive or potential star formation tracers, purple markers indicate CMZ cores that have definite star formation tracers and blue indicates cores with definite or possible star formation tracers. [Bottom] Fraction of cores that are star forming as a function of upper limit on the external pressure [left] or maximum distance from $P_e = 0$ line [right]. Red markers indicate all cores with definite star formation tracers, black indicates all cores with definitive or potential star formation tracers, purple markers indicate CMZ cores that have definitive star formation tracers and blue indicates cores with definitive or possible star formation tracers.

formation rate of 0.017 $M_\odot$ yr^{-1} if we take only those cores which have observed H_2CO (218.2 GHz) emission and a definite or ambiguous associated star formation tracer. This drops to 0.009 $M_\odot$ yr^{-1} if we remove isolated HMSF regions from this sub-sample, as these regions are likely not part of the CMZ. We note again that this sample does not include Sagittarius B2 or the CND due to severe image artefacts. Ginsburg et al. (2018b) uses the estimated age of the Sgr B2 complex ($t = 0.74$ Myr) to infer a star formation rate across the entire cloud of 0.062 $M_\odot$ yr^{-1}, which dominates our estimated SFR from the cores within the rest of the survey.

2.7.3 Searching for proto-stellar outflows

The CMZoom spectral set up was specifically selected to target a number of classic outflow tracers; SiO (Gueth et al., 1998; Codella et al., 2007; Tafalla et al., 2015) and CO. The energies involved in protostellar outflows are sufficiently high enough to vaporize SiO dust grain mantels and while CO is more prevalant and excited at lower temperatures, it has been used to observe protostellar outflows towards high-mass star forming regions in the past (e.g. Beuther et al., 2003).

As the most detected transition within the quality controlled data set, and with the most reliable line profiles, we first used H_2CO (218.2 GHz) to provide a single V_{LSR} for each core. Combining this with the l and b positions from paper II, we generated $\{l, b, V_{LSR}\}$ positions for a large majority of the cores within Paper II's robust catalog. These data were then overlaid on non-primary beam corrected[16] 3D cubes of SiO and the three CO isotopologues within *glue*[17]. Each core was then examined by eye to check for extended structure along the velocity axis. During this process, only two convincing outflows - i.e. an outflow with red- and blue-shifted lobes surrounding the central velocity of the core - were detected in regions G0.380+0.050 and G359.615−0.243 as shown in Figures 2.36 and 2.37.

These two regions were followed up by creating a series of moment maps for SiO and the three CO isotopologues over 10 $km\,s^{-1}$ intervals across the surrounding ± 30 $km\,s^{-1}$ from the core V_{LSR}. Figures 2.36 and 2.37 show these moment maps as contours overlaid on the 230 GHz continuum emission for G0.380+0.050 and G359.615+0.243. While

[16]The increased noise at the edge of the primary beam corrected images obscured the outflow emission.
[17]https://glueviz.org

^{12}CO emission shows evidence of red/blue lobes surrounding the core at 30% of peak brightness, there is no sign of similar outflow morphology in any other transition, despite other work having identified an outflow at this core in SiO emission. The absence of such morphology in SiO is potentially a result of SiO tracing material closer to the jet as opposed to the extended jet structure itself.

The emission in SiO and the three CO isotopologues of 359.615-0.243 all show consistent structures in the form of a significant red lobe to the left of the core. The lack of a strong blue lobe on the opposite side of the core may be the result of sensitivity, opacity or different excitation conditions..

In conclusion, *CMZoom* provides the first systematic, sub-pc-scale search for high mass proto-stellar outflows within the CMZ. We detect only two outflows throughout the survey – one in a known high mass star forming region, and a second in an isolated high mass star forming region – and can therefore rule out a wide-spread population of high-mass stars in the process of forming that has been missed by previous observations, e.g. due to having low luminosity of weak/no cm-continuum emission.

2.7.4 Intermediate Mass Black Holes

In the picture of hierarchical galaxy formation, many intermediate mass black holes (IMBHs) from cannibalised globular clusters and dwarf galaxies, as well as merging stellar mass black holes are expected to be found within the central regions of galaxies like the Milky Way, though their exact origins are at this stage hypothetical. So-called 'high-velocity compact clouds' (HVCCs) – dense gas clouds ($< 5\,$pc) with high brightness temperatures and large velocity dispersions ($\sigma > 50\,\mathrm{km\,s^{-1}}$) (Oka et al., 1998, 2012; Tokuyama et al., 2019) – in the CMZ have been interpreted as the signpost of an intermediate mass black hole (IMBH) passing through a gas cloud and interacting with the gas. As the first sub-pc-scale resolution survey of the dense gas across the whole CMZ, CMZoom is ideally placed to find such HVCCs.

To determine CMZoom's ability to detect such HVCCs we turn to the papers reporting detections of IMBHs through this method. Oka et al. (2016) reported a compact (≤ 1.6 pc) candidate IMBH detected in HCN and SiO with an extremely broad velocity width ($\lesssim$ 100 km s^{-1}). Using the volume density of N(H_2) $\geq 10^{6.5}$ cm $^{-3}$ given by Oka

et al. (2016), we estimate column densities of three of our dense gas tracers – ^{13}CO, C^{18}O and H_2CO, assuming standard abundance ratios ($[^{13}CO]/[H_2] = 2 \times 10^{-6}$, Pineda et al. (2008), $[C^{18}O]/[H_2] = 1.7 \times 10^{-7}$ Frerking et al. (1982) and $[H_2CO]/[H_2] = 10^{-9}$, van der Tak et al. (2000)), though these standard abundances may not apply within the extreme pressures and temperatures of the CMZ. Using these column densities, a kinetic temperature of 60 K and a linewidth of 20 km s^{-1}, we use RADEX (van der Tak et al., 2007) to estimate a brightness temperature for this IMBH candidate lies between $16 - 40$ K for our dense gas tracers.

Assuming a typical beam size of $3'' \times 3''$ at a frequency of 230 GHz we calculate the RMS for each spectra in K, as shown in Figure 2.35, which peaks at ~ 0.2 K. If this brightness temperature range of $16 - 40$ K is representative of IMBH candidates at these transitions, we would expect to easily detect ~ 1 pc features using the *CMZoom* survey. However, even before quality control, we find no spectral components fit with velocity dispersions ≥ 20 km s^{-1} throughout the data. The only exceptions are from protostellar outflows.

In summary, we can rule out the presence of HVCC's or IMBH's within the region covered by this work.

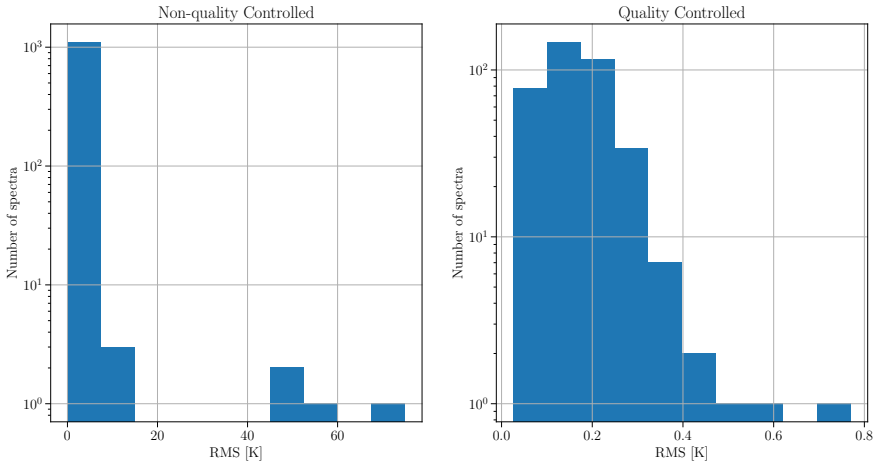

FIGURE 2.35: Histogram of the RMS of every spectra throughout the survey measured in Kelvin. The quality controlled data set peaks at ~ 0.2 K.

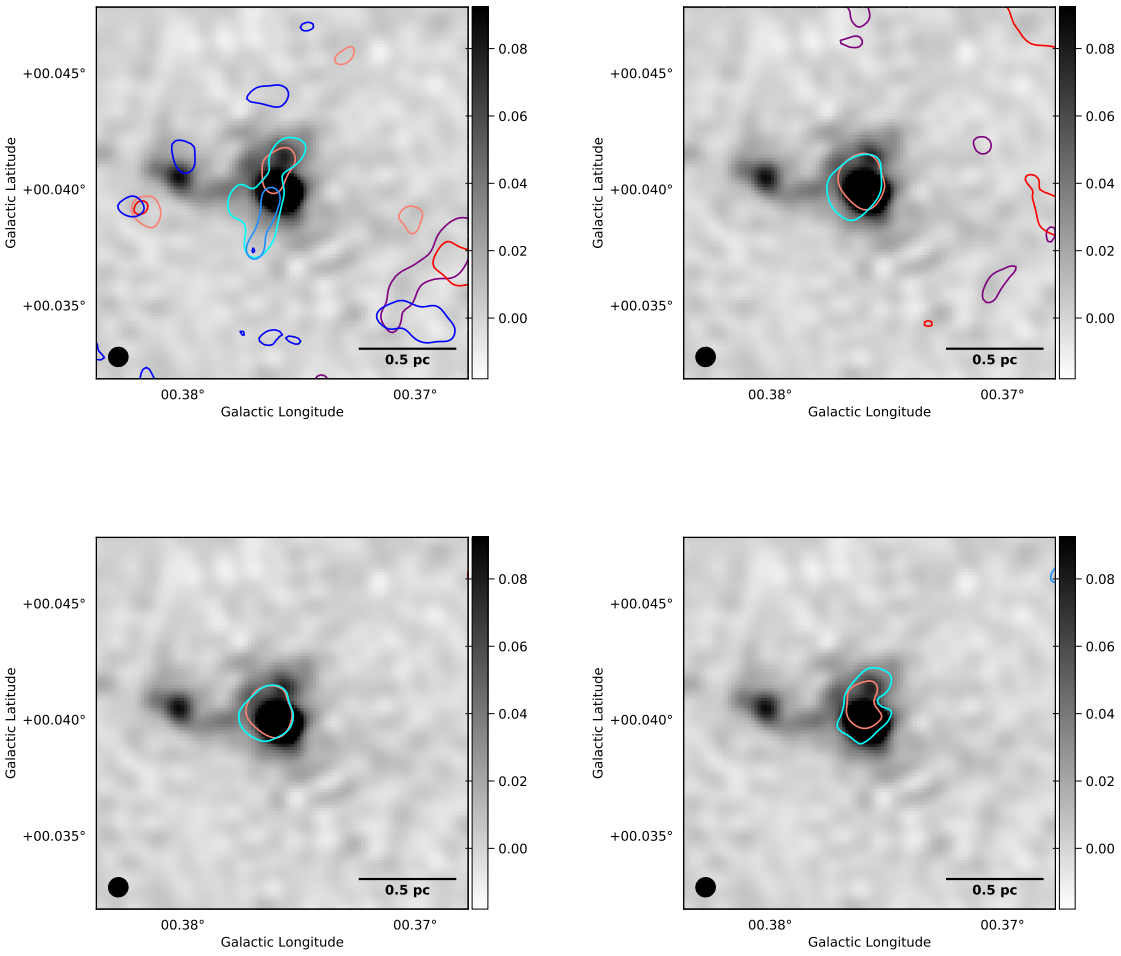

FIGURE 2.36: The grey scale images show the 230 GHz continuum emission centred on the most massive core within G0.380+0.050. The colour bar shows the flux density in Jy. Overlaid are contours of moment maps produced over 10 km s^{-1} intervals from ±30 km s^{-1} from the core's V_{LSR}, for ^{12}CO (top-left), ^{13}CO (top-right), C^{18}O (bottom-left) and SiO (bottom-right).

2.8 Conclusion

We present 216-220 GHz and 228-232 GHz spectral line data from the SMA's Large Program observing the Galactic Centre, *CMZoom*, and the associated data release. This data extends the work of previous papers published from this survey – the 230 GHz dust continuum data release and a dense core catalog.

These data were imaged via a pipeline that is an extension to the previously developed imaging pipeline built for the 230 GHz dust continuum data. During this process, a number of regions – in particular Sagittarius B2 and the Circumnuclear Disk – were found to suffer from severe imaging issues, which prevented these regions from being

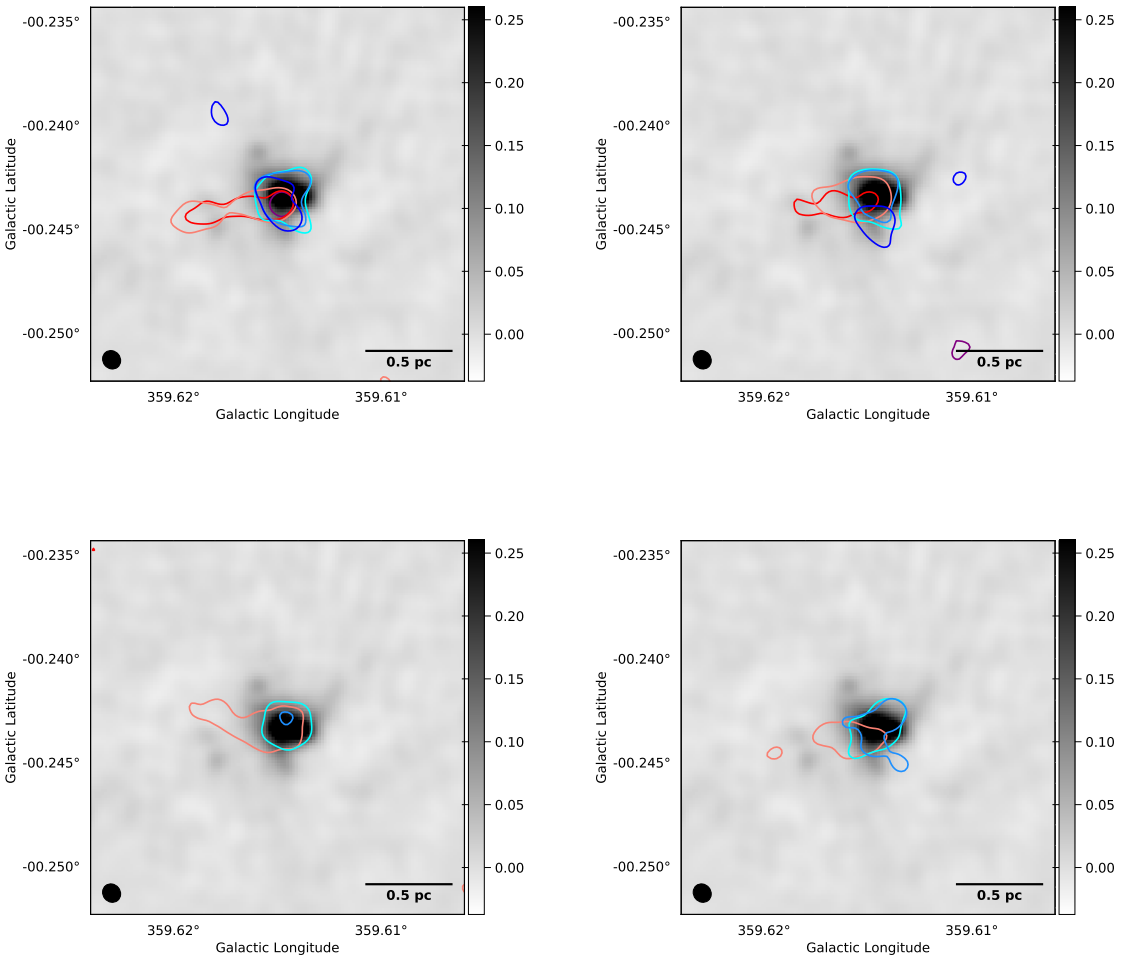

FIGURE 2.37: The grey scale images show the 230 GHz continuum emission centred on the most massive core within G359.615+0.243. The colour bar shows the flux density in Jy. Overlaid are 5σ contours of moment maps produced over 10 km s^{-1} intervals from ±30 km s^{-1} from the core's V_{LSR}, for ^{12}CO (top-left), ^{13}CO (top-right), C^{18}O (bottom-left) and SiO (bottom-right).

analysed. Once imaged, all data were examined by eye to identify both imaging artefacts as well as potentially interesting structures. The quality controlled data were then used to produce moment maps for each cloud, as well as spectra for most dense cores identified by Paper II.

Using *scousepy*, these spectra were fit and then quality controlled to remove spurious fit results before being used to extract kinematic information for a majority of these dense cores and also identify a number of spectral lines beyond the 10 major transitions of dense gas and shocks that were targeted by *CMZoom*.

By measuring the normalized integrated intensity with respect to both C^{18}O and 230 GHz dust continuum, we find that the shock tracers, SiO and SO, as well as the two higher

energy H_2CO transitions increase by several orders of magnitude towards the Galactic Centre. We also find that the population of isolated HMSF cores that were included in the survey due to their association with star formation tracers, but which likely lie outside the Galactic Centre, have indistinguishable line ratios from the CMZ cores. While this approach is unsophisticated and does not take into account complexities such as opacity and excitation, these results suggest that while observations of cloud scale chemistry have indicated stark differences in line emission ratios between the CMZ and the Galactic Disk, these differences diminish when zooming down to the core scale.

We identified H_2CO (218.2 GHz) as the best tracer of core kinematics, due both to the frequency with which it was detected in cores, but also its tendency to be fit by single Gaussian components. Using this transition, we determine a single V_{LSR} and velocity dispersion for every core where H_2CO was detected and calculated a virial parameter for each core. Using a simple virial analysis, only four dense cores were found to be gravitationally bound.

Expanding this analysis to factor in external pressure and compare this to cores identified as having associated star formation tracers, we find most cores appear to be consistent with being in hydrostatic equilibrium given the high external pressure in the CMZ. All cores below a maximum external pressure of $10^7\,\mathrm{K\,cm^3}$ have associated star formation activity. Above this pressure, the fraction of star forming cores drops. We find that the fraction of star forming cores drops even more steeply the farther it lies from virial equilibrium. We conclude that while the external pressure plays a role in determining whether or not a core will begin to form stars, how close a cores is to being gravitationally bound provides a more accurate indication of its star formation activity.

Through visual inspection of the three CO isotopologues and SiO, only two protostellar outflows (in clouds G0.380+0.050 and G359.614+0.243) were detected throughout the entire survey. We can therefore rule out a wide-spread population of high-mass stars in the process of forming that has been missed by previous observations, e.g. due to having low luminosity of weak/no cm-continuum emission

Recent observations of the CMZ have highlighted a number of high-velocity compact clouds (HVCCs) which have been interpreted as candidate intermediate mass black holes (IMBHs). Despite having the sensitivity and resolution to detect such HVCCs, we do not find any evidence for IMBHs within the *CMZoom* survey spectral line data.

Chapter 3

M83

Preface

The work presented in this chapter is taken from Callanan et. al. (submitted). The PI of the ALMA observation was Steven Longmore. Data calibration, reduction and analysis was completed by myself.

3.1 Introduction

Determining how star formation varies with environment is a key step towards understanding how galaxies build their stellar mass over time. Most of what is known about the detailed processes of star formation on proto-stellar core scales comes from observations of star forming regions in the Solar neighbourhood (Molinari et al., 2014). From studies of star formation regions on larger scales within our own Galaxy and external galaxies, we have learned that there exists a strong correlation between star formation rate surface density and gas surface density, although the exact form of this correlation is debated (Kennicutt, 1998b; Bigiel et al., 2008b; Leroy et al., 2008b; Schruba et al., 2011b; Gutermuth et al., 2011b; Lada et al., 2012b; Krumholz & Dekel, 2012b). Such relations are fundamental in the context of galaxy evolution because they dictate the location and rate at which galaxies grow their stellar mass. A major goal of star formation research is to build a bottom-up understanding of how these global star formation relations are shaped by the physics of star formation on proto-stellar scales.

One particularly interesting region in this regard is the Central Molecular Zone (CMZ). This is the largest reservoir of dense molecular gas in the Galaxy, extending to a galactocentric radius of 250 pc. The CMZ contains roughly 5% of our Galaxy's molecular gas (Dahmen et al., 1998a), putting the surface density at two orders of magnitude higher than the Milky Way average, and is subject to some of the most extreme conditions for star formation in our Galaxy. With pressures several orders of magnitude larger than those found in the Galactic disk (Morris & Serabyn, 1996c), temperatures reaching several hundreds of Kelvin (Mills & Morris, 2013a; Ginsburg et al., 2016; Krieger et al., 2017a), and densities of $> 10^4$ cm^{-3} on spatial scales of 1 pc (Longmore et al., 2013d), the properties of the molecular gas found within this region are similar to those in galaxies at redshift $1 < z < 2$ (Kruijssen & Longmore, 2013a). The proximity of this gas to the supermassive black hole (SMBH) Sagitarrius A* and the nuclear star cluster (Genzel et al., 2010a) means it has potentially been exposed to significant active galactic nuclei (AGN) and star formation feedback in the past, despite the SMBH currently being in a quiescent state (Sofue & Handa, 1984; Su et al., 2010). This region of our Galaxy therefore provides a unique laboratory to study the star formation process in an extreme environment, similar to those commonly found in the early Universe.

Studies of the CMZ have advanced our understanding of how extreme environments can impact star formation (Longmore et al., 2014; Ginsburg et al., 2019; Barnes et al., 2019, 2020). Recent and ongoing Galactic plane surveys across the electromagnetic spectrum (Aguirre et al., 2011a; H. E. S. S. Collaboration et al., 2018), large scale surveys of the Galactic Centre such as HOPS (Walsh et al., 2011a), SWAG (Krieger et al., 2017a), CMZoom (Battersby et al., 2020; Hatchfield et al., 2020), CHIMPS2 (Eden et al., 2020), SOFIA/FORCAST (Hankins et al., 2020) and SEDIGISM (Schuller et al., 2021) as well as more targeted observations (Longmore et al., 2012; Henshaw et al., 2016c; Walker et al., 2018a; Ginsburg & Kruijssen, 2018; Henshaw et al., 2019a; Lu et al., 2019, 2020) continue to elucidate how star formation may be affected by these extreme conditions.

However, future progress in this area is hampered by the difficulty in unambiguously constraining the three-dimensional geometry of the gas and young stars (Kruijssen et al., 2015; Henshaw et al., 2016b; Longmore & Kruijssen, 2018). In addition, the CMZ only represents a single snapshot of the star formation/feedback and AGN feeding/feedback baryon cycle, which may vary in time (Kruijssen & Longmore, 2014b; Krumholz & Kruijssen, 2015a; Krumholz et al., 2017; Armillotta et al., 2019b). Both detailed simulations

of gas flows in CMZ-like environments and observations of gas in the CMZ suggest the inflow is clumpy, supporting the notion of high variability with time (Sormani et al., 2015a,b,c, 2018; Sormani & Barnes, 2019a).

Many of these problems can be overcome by studying the centres of other galaxies, with favourable (close to face-on) orientations and varying levels of star formation and AGN activity. In this paper, we look to extend our understanding of star formation in extreme environments and test recent models of baryon cycles in the centres of barred spiral galaxies. To do this, we use high resolution ALMA data to study the distribution of dense gas and young stars in the central few hundred parsecs of the nearby Milky Way-like galaxy, M83 (NGC 5236).

In this paper we will use ALMA observations of dense gas tracers HCN and HCO^+ to measure the kinematics and dense gas properties of the central region of M83, and in turn compare these observations to the CMZ. In section 3.2 we summarize previous observations of the centre of M83. section 3.3 presents the ALMA observations and data reduction. In section 3.4 we derive the physical and kinematic properties of dense gas in the centre of M83 down to the size scale of individual molecular clouds. In section 3.5 we compare the properties of dense gas clouds and young stellar clusters in the centre of M83 and the Milky Way. In section 3.6 we seek to explain the order of magnitude offset in star formation rate between these two galaxy centers and discuss the implications of our findings for understanding star formation and feedback in the centres of galaxies. Finally, we summarise our conclusions in section 3.7.

3.2 The centres of M83 and the CMZ: twins at heart?

The centre of M83 was selected for comparison with the CMZ for four key reasons: (1) M83 is nearby (4.6 Mpc, Table 3.1) allowing us to make comparisons with the CMZ at the scales of individual molecular clouds; (2) it has a similar physical structure, morphology, metallicity and gas/star content as the Milky Way within the central few hundred parsecs (Table 3.2); (3) its moderate inclination of 24° (Talbot et al., 1979) allows for an almost unobscured view of the galactic centre; (4) while the CMZ is currently under-producing stars compared to dense gas relations (Longmore et al., 2013a; Barnes et al., 2017), the centre of M83 is over-producing stars when compared to Lada et al. (2012b, see also

Figure 1.5). This order of magnitude difference in star formation rate, despite having similar stellar and gas properties when averaged on hundred-pc scales, simultaneously provides a key test of star formation theories in extreme environments and of models of baryon cycles in galaxy centres.

As one of the nearest, face on ($i = 24°$), massive ($M_* = 6.4 \times 10^{10}$ $M_\odot$, Lundgren et al., 2004b) spiral galaxies, M83 has been studied in detail across the electromagnetic spectrum: X-ray (Cole et al., 2017), visible (Blair et al., 2014), near-infrared (Williams et al., 2015), mid-infrared (Vogler et al., 2005) and radio (Maddox et al., 2006). Observations of the Brα (4.05 μm) and Brγ (2.17 μm) recombination lines of ionised hydrogen within the circumnuclear region of M83 by Turner et al. (1987) have shown that there is significant dust extinction within the region ($A_\nu \gtrsim 14$ mag), though the dust distribution is observed to be patchy. Sub-arcsecond angular resolution J and K band observations of the circumnuclear region of M83 show two prominent dust lanes (red dotted line in Figure 3.1) spiralling into a circumnuclear dust ring at a galactocentric radius of a few hundred pc. As shown in Figure 3.1, the outer circumnuclear ring (blue dotted line) is connected to an inner circumnuclear ring (purple dotted line) via a narrow inner bar or 'bridge' (green dotted line) perpendicular to the primary stellar bar (Elmegreen et al., 1998). The area between the two rings was identified as being a region of intense star formation. It is hypothesised that these two circumnuclear rings coincide roughly with the locations of the two inner Lindblad resonances (Buta & Combes, 1996).

Harris et al. (2001) identified 45 massive star clusters within the central region of the galaxy, with 90% lying within the outer circumnuclear ring, and used equivalent widths of Hα emission to estimate their ages. As a cluster ages and the hottest, most massive stars in the cluster begin to die, emission of ionizing photons from hydrogen recombination lines decreases steadily. As such, the equivalent width of H α measures the ratio of young ionizing stars and older non-ionizing stars, and as such acts as a good proxy for the age of a cluster. 75% of these clusters above the mass of $2 \times 10^4 M_\odot$ are younger than 10 Myr old, and of the clusters younger than 10 Myr and more massive than $5 \times 10^3 M_\odot$, 70% are between 5-7 Myr. The remaining 25% of clusters above the mass of $2 \times 10^4 M_\odot$ range from 13-47 Myr. Of the 45 clusters, 9 are younger than 5 Myr, though 6 of these have anomalous photometry, potentially caused by dust attenuation. Harris et al. (2001) estimate the catalogue is complete to clusters of mass $\geq 2 \times 10^4 M_\odot$ for ages between $0 - 40$ Myr.

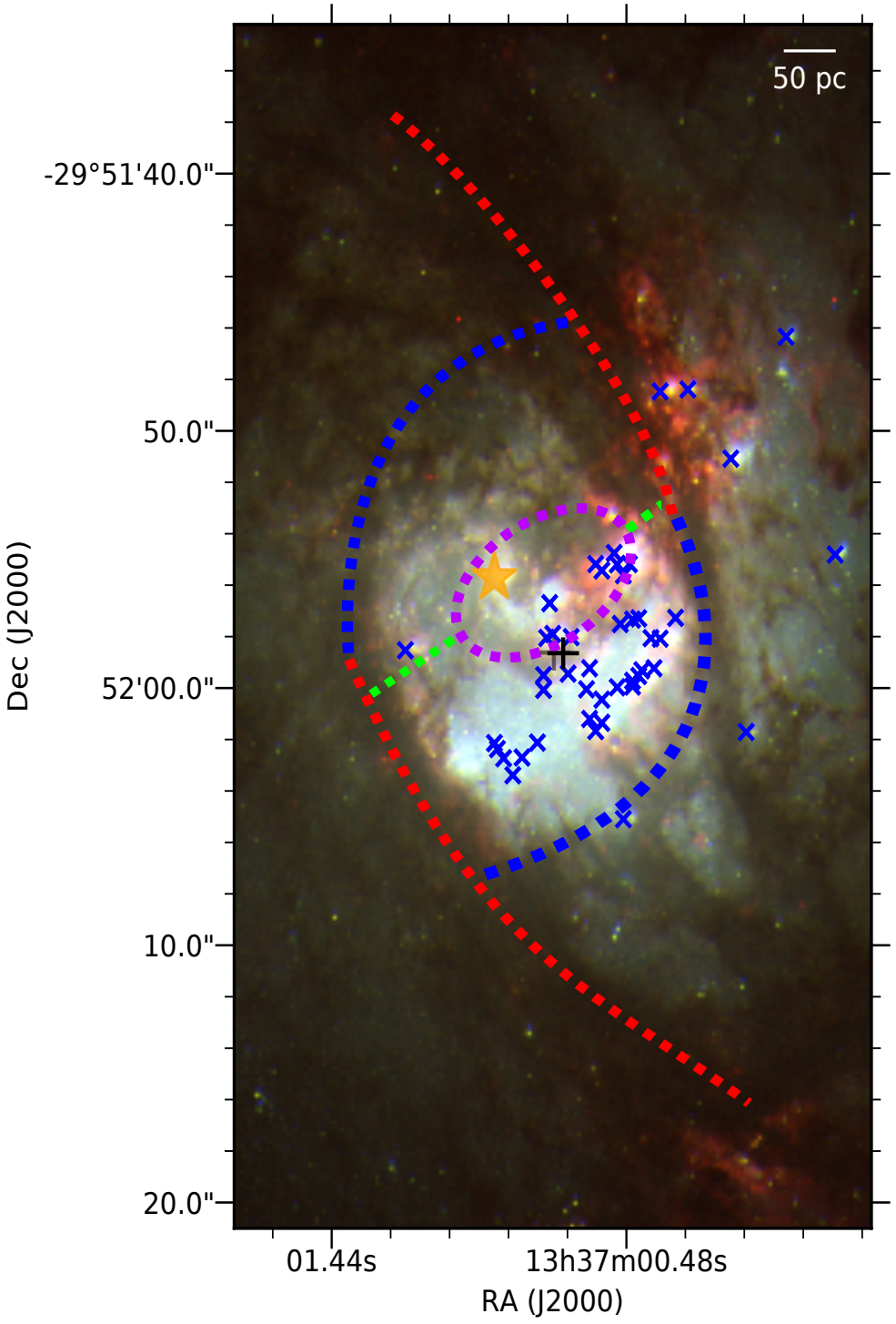

FIGURE 3.1: Hubble Space Telescope three-colour image of the inner 1 kpc × 0.6 kpc of M83 (red = Hα, green = WFPC2 V, blue = WFPC2 B). Also labelled are the massive stellar cluster positions (blue ×) as observed by (Harris et al., 2001) as well as M83's visible nucleus (orange ⋆). The weighted average location of the kinematic centre from Knapen et al. (2010) is shown as a black plus. A schematic of the main structural components observed by Elmegreen et al. (1998) is overlaid and separated by colour. Red represents the dust lanes, blue is the outer circumnuclear ring, purple the inner circumnuclear ring and green represents the narrow bar or 'bridge' connecting these latter two components.

There are two possible explanations for this age distribution of the clusters: (1) there was a burst of cluster formation between 5 and 7 Myr ago, with little formation occurring between 7 and 50 Myr ago; or (2) clusters did form prior to 7 Myr ago but have since dissolved into the field population. The sharp cutoff in the age distribution (Harris et al., 2001) would suggest the former is far more likely (Lamers et al., 2005; Kruijssen et al., 2011). A majority of these star clusters are located within the star formation arc identified by Elmegreen et al. (1998), they are shown as blue crosses in Figure 3.1. The population of clusters is highly asymmetric with respect to the optical nucleus (orange star), in the south-western space between the inner and outer circumnuclear rings.

As the brightest, most compact young stellar systems, young massive clusters (YMCs) are the best tracer of star formation activity in the centre of M83 over the last <10 Myr. Work by Harris et al. (2001) has shown a clear azimuthal age gradient in the population of YMC's in the inner ∼200 pc of M83. The mass of the clouds in the circumnuclear gas stream derived by Freeman et al. (2017) of $\sim 10^4 - 10^6\,M_\odot$ provides the mass reservoir expected from a progenitor to $\sim 10^3 - 10^4\,M_\odot$ stellar clusters, assuming a typical GMC star formation efficiency of ∼10% (Longmore et al., 2014; Kruijssen et al., 2019c; Chevance et al., 2020b).

Sakamoto et al. (2004) confirmed the structure of the gas within the centre of M83, as first observed by Elmegreen et al. (1998), with SMA observations in CO (J=2 − 1) and CO (J=3 − 2) lines, suggesting that the dust lanes and the nuclear rings (red, blue and purple dotted lines in Figure 3.1) are following x_1 and x_2 orbits respectively due to their distance from the centre and orientation to the galactic bar (Athanassoula, 1992). They also found that while the K band isophotal centre lies on the systemic velocity contour, and as a result is likely the dynamical centre, the visible nucleus is offset from this contour. While Sakamoto et al. (2004) suggest this may be evidence of a second, hidden nucleus, Knapen et al. (2010) rule out a hidden nucleus due to a lack of enhancement in optical or near-IR emission among other reasons. They instead conclude that it is more probable that the visible nucleus is the only nucleus of M83 and that the offset of the kinematic centre is due to some extreme past event such as a merger or a galaxy-galaxy interaction. Following this argument, in this paper we focus only on the optical nucleus, illustrated by the star in Figure 3.1.

There are many similarities between the structural components of the gas in the centre

Table 3.1: M83 Characteristics

Parameter	Value	Reference
α_{J2000}	13:37:00.91	(1)
δ_{J2000}	-29:51:55.7	(1)
v_{lsr}	519 km s^{-1}	(2)
RC3 Type	SAB(s)c	(3)
Inclination	24°	(4)
Position Angle	225°	(5)
Distance	4.6 Mpc (1" = 22.3 pc)	(6)

(1) Houghton & Thatte (2008); (2) Meyer et al. (2004); (3) Crowther (2013); (4) Comte (1981); (5) Foyle et al. (2012); (6) Tully et al. (2013);

Table 3.2: CMZ-Inner M83 Comparison

Parameter	CMZ	Inner M83
Gas Content, $M_\odot$	$5 \times 10^{7(1)}$	$5 \times 10^{7(2)}$
Stellar Content $M_\odot$	$10^{9(1)}$	$5 \times 10^{8(3)}$
Circular Velocity, km s^{-1}	$\sim 100^{(4)}$	$\sim 100^{(5)}$
Velocity Dispersion, km s^{-1}	$\sim 20^{(6)}$	$\sim 20^{(5)}$
Gas Surface Density, $M_\odot pc^{-2}$	$10^{2-3(1)}$	$10^{2-3(7)}$
Metallicity	twice solar$^{(8)}$	twice solar$^{(9)}$
Star Formation Rate, $M_\odot yr^{-1}$	$0.08^{(10)}$	$0.8^{(11)}$
SMBH Mass, $M_\odot$	4×10^6	(1-4) $\times 10^6$

A comparison of key physical, chemical and kinematic characteristics of the inner few hundred parsecs of the Milky Way and M83. Every characteristic except the star formation rate is the same to within a factor of a few.
(1) Launhardt et al. (2002); (2) Israel & Baas (2001); (3) Fathi et al. (2008); (4) Mróz et al. (2019); (5) Lundgren et al. (2004b); (6) Shetty et al. (2012); (7) Lundgren et al. (2004a); (8) Le Petit et al. (2016); (9) Gazak et al. (2014); (10) Barnes et al. (2017); (11) Muraoka et al. (2007)

of M83 and the CMZ, particularly comparing the circumnuclear rings and the dust lanes feeding gas into the region. Models seeking to interpret the 3D geometry and kinematics of the dense gas in the CMZ find the data is well fit by a gas stream orbiting the centre at a radius of $\sim$ 100 pc (Molinari et al., 2011a; Kruijssen et al., 2015). The supermassive black hole, Sagittarius A*, is also known to be displaced from the geometric centre of symmetry of this orbit in much the same way we observe the visual nucleus within M83 to be. Sormani & Barnes (2019a) recently proposed that much of the gas in the inner kpc of the Milky Way outside of the $\sim$ 100 pc stream belongs to dust lanes feeding gas into the CMZ, which are analogous to the dust lanes seen in the centre of M83 (see red dashed lines in Figure 3.1).

TABLE 3.3: Observations

Spectral Line	Channel Width [km s^{-1}]	Beam Size [$''$]	Sensitivity [mJy bm^{-1}]
HCN	3.8	(0.49x0.45)	0.47
HCO^+	3.9	(0.51x0.48)	0.48
CS	3.5	(0.51x0.48)	0.28
CCH	5.8	(0.51x0.49)	0.12

3.3 Observations

The data presented in this work are Atacama Large Millimetre Array (ALMA) Cycle 3 observations targeting M83 over three nights between April 18th to September 22nd, 2016 (project ID 2015.1.01177.S, PI: S. Longmore). Observations covered an area of $100'' \times 120''$ centred on the nucleus of M83. The typical cloud scale within the CMZ is $\sim$10 pc (Longmore et al., 2013d; Henshaw et al., 2016c) so an angular resolution of $0.54''$ was selected, corresponding to a physical scale of 12 pc at the distance of M83. Observations were taken in configurations C36-2 and C36-7 to reliably recover spatial scales from $0.54''$ to $25''$ (2.4 pc to 600pc). Callisto and Titan were used as flux calibrators on the first and second nights respectively, and J1427-4206 was observed as a bandpass calibrator on all three nights. The observations consist of 4 spectral windows, centred on 86.7 GHz, 88.5 GHz, 98.6 GHz and 100.5 GHz, each with 1.875 GHz of total bandwidth. These spectral windows were chosen to include ground state rotational transitions of bright, dense gas tracers: HCN $(1-0)$, HCO^+ $(1-0)$, and CS $(2-1)$.

The data were calibrated using the standard ALMA pipeline. Visual inspection of the calibrated visibilities showed that no further steps beyond the pipeline reduction were needed before imaging. The observations were then concatenated to generate a final calibrated dataset using the **C**ommon **A**stronomy **S**oftware **A**pplications (CASA) package, version 4.3 (McMullin et al., 2007), which was then used to image the data.

A preliminary clean of each spectral window was performed using CASA's *clean* task to allow for easier identification of key lines within each spectral window. These cleans were performed in an uninteractive mode, with an averaging over every 10 channels. Continuum subtraction was then performed on these datacubes by highlighting line-free channels within all four spectral windows within the *uvcontsub* task in CASA. Cleaning of the continuum was done in an interactive mode using a Briggs weighting with a robust

parameter of 0.5 and primary beam correction. An image of the 95 GHz continuum is shown in the top left panel of Figure 3.2.

Four lines were detected in the first phase of data reduction: HCN $(1-0)$, HCO^+ $(1-0)$, CS $(2-1)$ and CCH (N = 1 - 0). Interactive cleaning was performed on each of those lines, cleaning down to the level of 2.5σ (intensity of 5 mJy/beam) with a cell size of $0.15''$.

Figure 3.2 shows the integrated intensity, intensity weighted velocity and intensity weighted velocity dispersion maps of HCN $(1-0)$, and Figure A.235 shows the channel maps of the emission. The morphology and velocity structure of the HCO^+ $(1-0)$ emission (Figures A.234 & A.236) is very similar to that of the HCN $(1-0)$. This similarity provides confidence in the robustness of these lines as tracers of the dense gas morphology and kinematics. The CS and CCH transitions are much weaker than the HCN $(1-0)$ and HCO^+ $(1-0)$ lines (Figure A.237). Since we are primarily interested in the kinematics of the gas, and both HCN $(1-0)$ and HCO^+ $(1-0)$ trace the same structure and kinematics, the following analysis therefore focuses on HCN $(1-0)$.

3.4 Deriving gas properties at individual molecular cloud scales

3.4.1 Dense gas morphology

The general structure of the dense gas traced by HCN $(1-0)$ and HCO^+ $(1-0)$ emission is similar to that reported in previous observations at J- and K-band by Elmegreen et al. (1998) and CO by Sakamoto et al. (2004) (see Figures 3.2 & A.235). Two streams of gas from the north and south of the maps tracing the dust lanes in the HST map are connected to M83's outer circumnuclear ring which in turn is connected to the inner circumnuclear ring by a narrow inner bar.

3.4.2 Continuum Emission and Spectral Index Maps

In order to derive the physical properties of the dense gas clouds we first need to assess the contribution to the flux which may come from free-free emission. The continuum

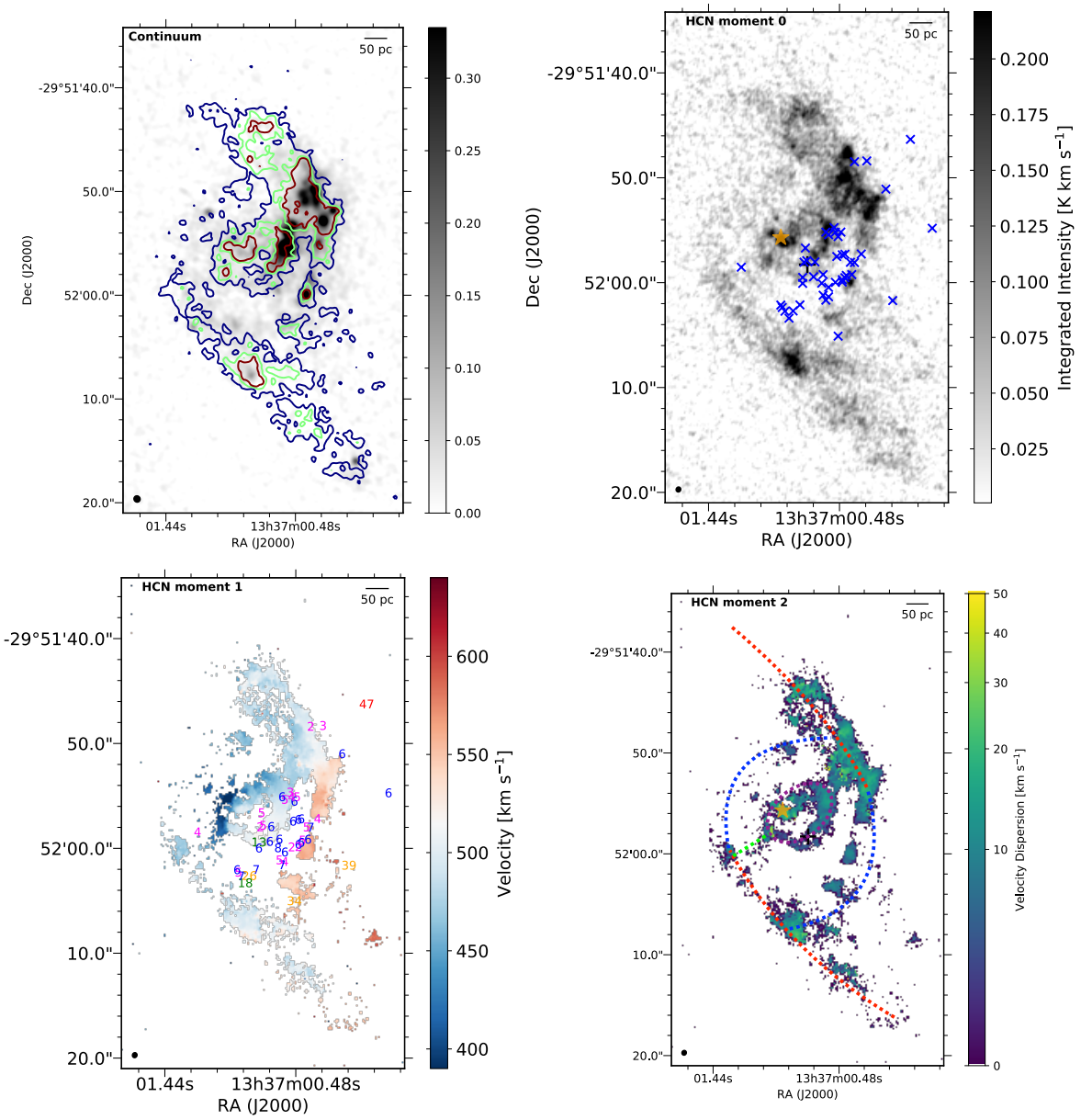

FIGURE 3.2: [Top Left] ALMA 95 GHz continuum emission map produced by averaging all line-free channels over the four spectral windows. HCN $(1-0)$ integrated intensity contours are overlaid at (30, 60, 90) K km s^{-1}. There is a reasonable correlation between the continuum emission and the brightest HCN $(1-0)$ emission. [Top Right] Integrated intensity map of HCN $(1-0)$. Blue crosses show positions of massive stellar clusters as found by Harris et al. (2001). The orange star indicates the visual centre of M83. [Bottom Left] First order moment (intensity weighted velocity) map of HCN $(1-0)$. Here we replot the clusters with their corresponding cluster age. [Bottom Right] Second order moment (intensity weighted velocity dispersion) map of HCN $(1-0)$. In all panels the synthesised beam is shown as the filled ellipse in the bottom left corner.

emission is mostly confined to the northern dust lane and the western side of the circumnuclear ring (Upper Left panel of Figure 3.2). To determine the source of this continuum emission we derive the continuum spectral index, i.e. the dependence of radiative flux density on frequency within each spectral window, for each pixel across the map. We do this by generating maps of the continuum emission using only the lowest and highest frequency spectral windows (spw1 and spw3) centred at 86.7 GHz and 100.5 GHz, respectively, masking all pixels with emission less than five times the RMS noise level in each image, and then determining the flux density ratio between these maps. Figure 3.3 shows the spectral index of this continuum emission, with contours of HCN and Hα emission overlaid.

As shown in Figure 3.3, the spectral index of the continuum emission in the circumnuclear ring and at the southern part of the northern dust lane vary between $0-2$, and $3-4$, respectively. Although there is scatter due to a combination of the uncertainty in flux measurements and the small frequency range over which the spectral index is calculated, the spectral index of continuum emission in the circumnuclear ring is consistent with free-free emission from gas photoionised by young, high-mass stars (which lies between -0.1 and 2 for optically thin and thick emission, respectively; Dyson & Williams, 1997; Kurtz, 2005). We therefore conclude that there are embedded (i.e., recently formed) high-mass stars in this region.

The spectral index of the continuum emission at the bottom of the dust lane is consistent with that expected from thermal dust emission. We postulate that this comes from warm dust that has been heated by embedded star formation activity at this location, which is at an early evolutionary stage before free-free emission from young high-mass stars begins to dominate.

3.4.3 Dense gas kinematics

Figure 3.4 shows a 2D histogram of the velocity dispersion per pixel determined by **S**emi-automated multi-**CO**mponent **U**niversel **S**pectral-line fitting **E**ngine (SCOUSE; Henshaw et al., 2016a) with respect to galactocentric radius as measured from the visible nucleus (indicated by the orange star in Figure 3.1). The spread in the measured velocity dispersions at all galactocentric radii is substantially larger than the uncertainty in individual measurements (typically $\sim 1\,\mathrm{kms}^{-1}$). There are some clear trends in the

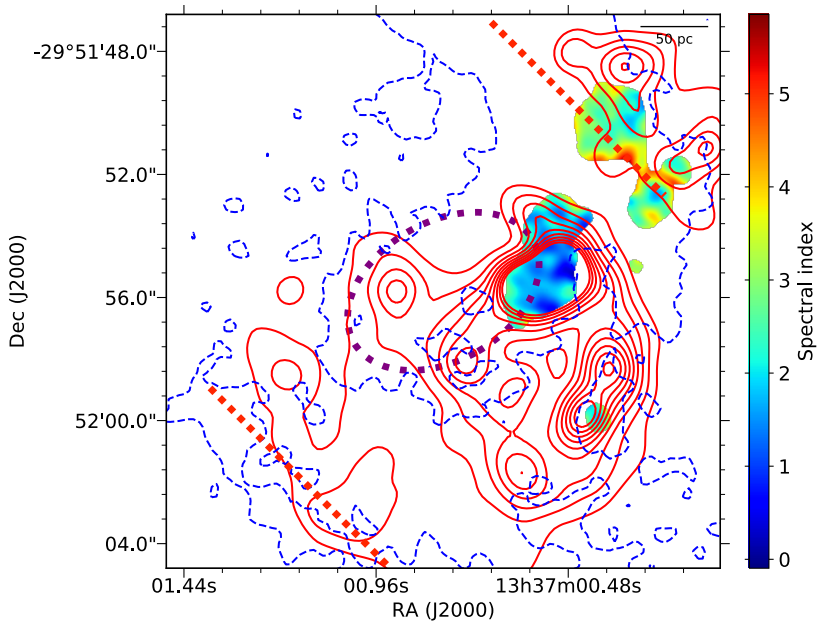

FIGURE 3.3: Spectral index map calculated from the flux density ratio at 86.5 GHz and 100.5 GHz after masking each continuum image to a threshold of 5σ. For spatial context Hα contours (red) and the HCN $(1-0)$ emission (blue) at a level of 10 K are overlaid. The circumnuclear ring and the dust lanes are denoted by the purple dotted ellipse and red dotted lines respectively. Each contour is smoothed with a gaussian kernel of 3x3 pixels. The purple ellipse and red lines indicate the inner circumnuclear ring and dust lanes respectively. The continuum emission associated with the 100 pc circumnuclear ring has a spectral index of $0-2$, as expected from free-free emission of gas photoionised by high mass stars. This region of the ring is associated with star formation, as well as a large fraction of the clusters associated with the high intensity Hα emission, as is expected for a region with young, high-mass stars.

range of the measured velocity dispersions with galactocentric radius. The velocity dispersion decreases within increasing galactocentric radius from the galactic centre to ~ 130 pc, where it reaches a minimum that differs from the mean velocity dispersion of 19 km s^{-1} by 2.8σ. It then increases to around $\sim 200-250$ pc before decreasing again towards a radius of 400 pc. We discuss the possible origin of this in Section 5.

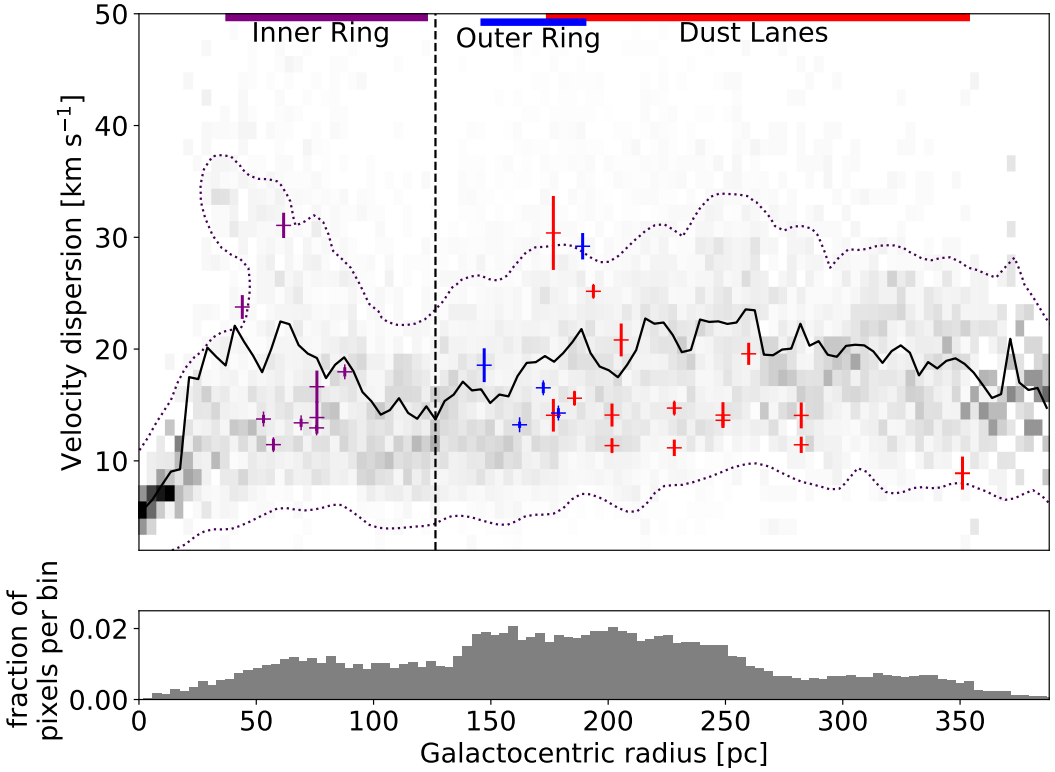

FIGURE 3.4: Top: Velocity dispersion as a function of galactocentric radius. The background shows a 2D histogram of the maximum velocity dispersion per line of sight calculated via SCOUSE against galactocentric radius. The solid line shows the average velocity dispersion per radial bin. The dotted contours above and below this show a value of 0.02 of the normalized histogram for each 12 pc bin. These therefore contain approximately 98% of the data. The individual data points show the velocity dispersion measurements from individual peaks shown in Figures A.238 (red), A.239 (blue) and A.240 (purple). The vertical dashed black line pinpoints the minimum of the velocity dispersion at $\sim$ 130 pc. Bottom: Histogram of fraction of total pixels within each galactogentric bin.

3.5 Comparison of dense gas and young stars in the centre of M83 and the Milky Way

We now compare the properties of dense gas and young stars in M83 and the Milky Way at individual cloud scales in order to determine why there is an order of magnitude difference in star formation rate in the inner few hundred pc of both galaxies, when the volume-averaged gas and stellar properties are similar to within a factor two (Table 3.2).

3.5.1 Centre of M83 & MW: similar morphology of gas and young stars

We start with a comparison of morphological structures as a function of radius. Unfortunately, as we sit in the plane of the Galaxy, we do not have a top-down view of the gas and stellar structure in the Milky Way. We therefore rely on observational distance constraints and numerical modelling to convert the position-position-velocity data into a 3D structure (Kruijssen et al., 2015; Henshaw et al., 2016b; Longmore & Kruijssen, 2018).

The properties of gas structures derived in this way are qualitatively very similar to those in M83, with gas falling towards the centre along 'dust lanes' in the bar (Binney et al., 1991; Sormani & Barnes, 2019a) and a circumnuclear gas stream orbiting the centre at a similar galactocentric radius (Molinari et al., 2011a; Kruijssen et al., 2015, 2019a; Dale et al., 2019b). It has been known for a long time that the dense gas mass distribution in the inner few hundred pc of the Milky Way is highly asymmetric, with three-quarters of ^{13}CO and CS emission at positive longitudes (Bally et al., 1988a). We see a similar degree of asymmetry in the distribution of dense gas structure in M83. A significant fraction of the gas is in-falling from the northern dust lane, with roughly two-thirds of the gas within the inner circumnuclear ring found on the western side. This asymmetry was predicted in simulations of the CMZ by Sormani et al. (2018), who highlighted M83 as an example of an external galaxy showing similar structure, though this was largely time dependent within the simulations.

Outside of the nuclear cluster in the inner few pc of the Milky Way, the 3D structure of young, high-mass stars and stellar clusters is even more difficult to ascertain than in the gas (Longmore & Kruijssen, 2018). However, it is clear that the recent star formation activity in the CMZ is constrained to the inner $\sim$150 pc – the same galactocentric radius range of recent star formation in M83.

As the 3D structures of both dense gas and young stars in the inner few hundred pc of the Milky Way and M83 are similar to within the constraints provided by current Milky Way models, we conclude that differences in morphology cannot explain the order of magnitude difference in star formation rate within the inner kpc of both galaxies.

3.5.2 Centre of M83 & MW: galactocentric trends in velocity dispersion

Returning now to Figure 3.4, we compare the dependence of velocity dispersion with galactocentic radius. Due to our relative position to the centre of our Galaxy, we do not have a face-on view of the velocity dispersion with galactocentric radius. Therefore, we compare to recent 1D models of gas inflows in the inner few hundred parsecs of barred spiral galaxies.

These models predict a relationship between the gas velocity dispersion and galactocentric radius that depends on the rotation curve of the galaxy (Krumholz & Kruijssen, 2015a; Krumholz et al., 2017). For galaxies with a rotation curve like the Milky Way, these models predict that the gas velocity dispersion should increase monotonically with decreasing galactocentric radius while the rotation curve is flat, and then decrease sharply as the rotation curve transitions to more solid body like rotation. In the Milky Way, this transition occurs at a galactocentric radius of $\sim 100 - 200\,\mathrm{pc}$ (Krumholz & Kruijssen, 2015a). No direct predictions have been made for the relationship between the gas velocity dispersion and galactocentric radius of M83, due to the unavailability in the literature of a rotation curve at sufficiently high spatial resolution. However, given the similarity in the properties of the gas and stellar distribution in the inner few hundred pc of both galaxies, it seems reasonable to expect a similar qualitative trend in M83 as that predicted for the Milky Way (Sormani et al., 2018).

Due to the 1D nature of the Krumholz & Kruijssen (2015a) and Krumholz et al. (2017) gas inflow models, each galactocentric radius bin only has a single velocity dispersion assigned to it by definition. Therefore, a direct comparison with Figure 3.4 is non-trivial. Nevertheless, we note that the sharp drop in the mean and range of the measured velocity dispersion occurs at the same galactocentric radius at which recent star formation has occured ($\sim$100$-$200 pc). Though it is not sufficiently high resolution for a direct prediction of this relationship, comparing this location with M83's velocity curve (Fathi et al., 2008) does show a correspondence between the minimum velocity dispersion and the turnover in the velocity curve at roughly ~ 130 pc.

The coincidence of the minimum in gas velocity dispersion and maximum in star formation activity at the radius where the velocity curve turns over is consistent with the

predictions of the 1D dynamical models (Krumholz & Kruijssen, 2015a; Krumholz et al., 2017). Sormani & Li (2020) recently tested whether the formation of nuclear rings *requires* a shear minimum, by performing numerical simulations of barred potentials with a flat rotation curve (i.e. without a shear minimum). They find that a nuclear ring forms in their simulations regardless, demonstrating that a shear minimum is not a necessary condition. However, by adopting a flat rotation curve they do not address the main point of the prediction by 1D dynamical models, which is that in the presence of a shear minimum, the location of the nuclear ring would correlate with the position of the shear minimum. The shear rate is easily calculated from a sufficiently high resolution rotation curve using

$$\frac{A}{\omega} = \frac{1}{2}\left(1 - \frac{R}{V}\frac{dV}{dR}\right) \tag{3.1}$$

where A is the first Oort constant, ω is the angular velocity and V is the measured V_{los} at the radius R. Thus, a shear minimum is easily obtainable in the presence of a detailed rotation curve and combining this with further modelling of the M83 gravitational potential is needed for a quantitative comparison to the model predictions, but is beyond the scope of the current paper.

3.5.3 Centre of M83 & MW: similar average dense gas properties

Table 3.4 shows the dense ($n_H = 10^4$ cm^{-3}) gas properties in the centre of the Milky Way and M83, averaged over the main morphological components for the mass, and on the size-scales of individual molecular clouds (∼12 pc) within those morphological components for the velocity dispersion. The total mass of gas, the velocity dispersion, and the orbital period of the circumnuclear gas streams in M83 and the Milky Way are similar to within a factor of 2. The mass of gas within the circumnuclear ring area of M83 is calculated using $M_{\rm dense} = \alpha_{\rm HCN} L_{\rm HCN}$, where $\alpha_{\rm HCN}$ is a conversion factor, which we took to be $\alpha_{\rm HCN} = 14$ M$_\odot$ / K km s^{-1} pc^2 (Onus et al., 2018). While $\alpha_{\rm HCN}$ can vary significantly, we assume it to be the same in both galactic centre environments. $L_{\rm HCN}$ is given by multiplying the integrated brightness temperature by the area of the pixel.

X-ray studies of M83 suggest that the AGN is either highly obscured, or emitting at a very low luminosity (Yukita et al., 2016). If obscuration is not the cause, this puts

TABLE 3.4: Gas properties of CMZ and M83's circumnuclear ring.

Galaxy	Mass, $M_\odot$	Velocity dispersion, km s^{-1}	Orbital Myr	Period,	Rotational Velocity, km s^{-1}
Milky Way	$7 \times 10^{7(1)}$	$17^{(2)}$	$3.1^{(3)}$		$150^{(4)}$
M83	6.5×10^7	15	3.7		120

Comparison of several key dense gas properties within the central circumnuclear rings of Milky Way and M83. Properties for M83 are derived from our HCN data. The velocity dispersion in both cases was calculated on the same scale of 12 pc, using the linewidth-size relation from Shetty et al. (2012). (1) - Molinari et al. (2011a); (2) - Shetty et al. (2012); (3) - Kruijssen et al. (2015); (4) - Langer et al. (2017)

the AGN at a similar level of emission as Sgr A*, which is the faintest SMBH known (Sabha et al., 2010). Ferrari et al. (2013) estimates the mass of the optical nucleus to be $(1-4) \times 10^6$ $M_\odot$, putting it well within the range of the highly accurately known mass of Sgr A* at 4×10^6 $M_\odot$ Boehle et al. (2016).

We conclude that neither the average properties of dense gas, nor AGN activity, can explain the order of magnitude difference in star formation rate in the inner few hundred pc of the Milky Way and M83.

3.5.4 Comparison of SFR measurements

We now compare SFR measurements in the same regions of both galaxies to make sure the magnitude, spatial area, and timescales probed by the SFR measurements are as consistent as possible.

The SFR in the centre of the Milky Way has been studied in detail by Barnes et al. (2017) using all available diagnostics and data in the literature. They find that all measurements are consistent with the SFR in the inner 500 pc of the Milky Way being $\sim 0.08\,M_\odot\,yr^{-1}$ for the last ~ 5 Myr.

We could find no similar compilation of nuclear SFR measurements for M83, so performed a literature search of recently reported SFR estimates. The most directly comparable SFR measurement with Barnes et al. (2017) in terms of area is that of Muraoka et al. (2007). They used 6 cm continuum emission to infer a SFR in the inner 500 pc of M83 of $0.8\,M_\odot\,yr^{-1}$. The assumption used to convert the measured 6 cm continuum

luminosity to a SFR is that all of the flux is non-thermal emission from supernova remnants. If true, the representative timescale probed by this SFR measurement will be related to the supernovae responsible for generating the emission, as discussed below.

However, cm continuum emission can also arise from free-free emission caused by the ionising luminosity of high mass stars. The representative timescale for free-free emission is only a few Myr, so much shorter than the timescale for non-thermal emission. Given that we are interested in the potential variability of M83's SFR, it is important to associate the correct timescale to the 6 cm continuum SFR measurement. In their review on this topic, Kennicutt & Evans (2012) state that the non-thermal emission should overwhelmingly dominate the integrated radio emission at frequencies ≤ 5 GHz (wavelengths $\geq$6 cm). This suggests that the SNe timescale is the correct one to use.

To determine a more accurate representative SFR timescale, we consider two effects: the timescales over which synchrotron-producing cosmic ray (CR) electrons are injected, and the timescales over which they persist once created. On the former, SNe will start anywhere between 3 and 9 Myr post-star formation (e.g. Leitherer et al., 2014), depending on exactly which stars succeed in blowing up and which fail and collapse directly to a black hole. For super-solar metallicity, where winds are expected to be more efficient and thus envelope loss makes it easier for the stars to explode, the timescale is probably closer to the younger end of the possible range, though with significant uncertainty. The SN explosions will continue until $\sim$40 Myr, with a fairly flat rate between the beginning and end. Thus to first order the rate of CR electron injection represents an average of the SFR over the past $\sim 5 - 40$ Myr.

On the latter question of persistence times, the synchrotron cooling timescale for electrons with a critical frequency ν_c is

$$\sim 1\mathrm{Gyr} \times \ (B/\mu\mathrm{G})^{-3/2}(\nu_\mathrm{c}/\mathrm{GHz})^{-1/2} \tag{3.2}$$

where B is the magnetic field (Condon, 1992). In the absence of a direct measurement of the magnetic field strength in the centre of M83, we take the Solar neighbourhood mean of $\sim 5\,\mu$G as a likely lower limit, which sets an analogous lower limit on the cooling time. For $\nu_c = 5$ GHz and $B = 5\,\mu$G, the corresponding cooling time is 40 Myr. Increasing the magnetic field strength by an order of magnitude to a more likely value of $50\,\mu$G would reduce the cooling timescale to $\sim$1 Myr. The cooling time is therefore comparable to

or shorter than the SN delay time. We therefore take the SFR based on synchrotron emission as representing an average over a timescale of order tens of Myr, making it comparable to FUV (0-10-100 Myr; Kennicutt & Evans, 2012), for example, as a SFR indicator.

Inverse Compton (IC) losses also set a limit on the CR electron lifetime that is probably much shorter than the upper limit of 40 Myr. The IC loss time is equal to the magnetic loss time multiplied by the ratio U_B / U_R, where U_B = magnetic energy density and U_R = radiation energy density. In the Solar neighbourhood, IC and synchotron loss times are about the same, but the SFR per unit area, and thus the radiation intensity, must be much higher in the centre of M83. Therefore, even assuming that the B field is no stronger than in the Solar neighbourhood, the CR loss time must be well under 40 Myr as a result of IC losses. A zeroth-order estimate would be that the IC loss time just scales as the inverse of the SFR per unit area.

Other measurements of M83's nuclear SFR are determined over larger areas, so less directly comparable to Barnes et al. (2017). The most recent measurements are from Hong et al. (2011), and Foyle et al. (2012), who determined SFRs of 0.8 and 0.7 $M_\odot\,yr^{-1}$, respectively, for the inner ∼800 pc of M83 using Hα emission. The slight difference in their SFR values is due to the use of different corrections to account for dust obscuration. Hα emission traces star formation over the last $3 - 10$ Myr (Kennicutt & Evans, 2012; Haydon et al., 2020).

Based on the above measurements, we conclude that the SFR in the centre of M83 is ∼0.8 $M_\odot$ yr^{-1} averaged on several to tens of Myr timescales. This is an order of magnitude larger than the SFR in the centre of the Milky way over the last ∼5 Myr.

3.6 Conundrum: broken star formation theories or extreme time variability?

The conclusions of the previous section bring us to an interesting, intermediate result. We have shown that the morphology, total gas mass reservoir, and average properties of gas in that reservoir are the same in both galaxies, and yet the star formation rate differs by an order of magnitude. This means that from the time probed by the star formation

rate measurements (up to $5-7$ Myr for the young stellar clusters), either (i) the star formation efficiency per unit mass of dense gas varies by an order of magnitude between the galaxies, or, (ii) the star formation rate has varied by the same amount. Scenario (i) causes severe problems for theories of star formation, as one implicit assumption of all theories is that parcels of gas with similar properties should produce similar stellar populations. Given the extreme variation in star formation rate over a short period of time, scenario (ii) provides strong constraints on the time variability of feeding and feedback, with important implications for the baryon cycles in galactic centres.

We now try to distinguish between these possibilities by focusing in detail on the properties of dense gas and young stars in the inner $\sim$150 pc of both galaxies, where all the current star formation activity is located.

The inner circumnuclear ring is the main morphological component of both galaxies containing all the recent star formation activity in the central regions. The relationship between the dense gas and young stars in the Milky Way's circumnuclear gas stream has been investigated in detail on the size scales of individual molecular clouds and stellar clusters (Molinari et al., 2011a; Longmore et al., 2013d; Barnes et al., 2017). Using the above data and analysis, we can now compare the properties of gas and young stars on similar scales in M83.

Below we first investigate the likelihood that the gas we are observing within M83's circumnuclear ring exists in a stable orbit (§3.6.1). We then study variations in kinematic properties of the gas in the ring (§3.6.2), its gravitational stability (§3.6.3), and how this might be affected by the galactic gravitational potential (§3.6.4). Next we compare the properties of the gas with the surrounding young stellar cluster population to see if they may be causally related (§3.6.5), and understand what this means for the implied star formation rate as a function of time (§3.6.6). Finally, in §3.6.7, we try and bring all this information together to understand whether the comparison of gas and young stars in the Milky Way and M83's nuclear regions implies broken star formation theories or extreme time variability.

3.6.1 Orbital stability within M83's circumnuclear ring

Before approaching this conundrum, it is important to assess whether the gas in the circumnuclear ring is in a stable orbit around the centre. Given the offset nucleus, the suggestion that the galaxy may have undergone a recent interaction, and evidence of an $m = 1$ perturbation, i.e. lopsidedness, it is plausible that the gas in the circumnuclear ring is strongly dynamically disturbed and not in a stable orbit. However, several lines of reasoning suggest the gas has been in stable orbits for at least an orbital time.

Figure 3.5 shows the HCN channel map of gas in the circumnuclear ring. The observations show that the gas morphology, density and kinematics vary smoothly and trace the gas in a ring around the nucleus in PPV space. To investigate whether this observed velocity structure is consistent with gas orbiting the centre, we constructed elliptical orbits in the x-y plane (inclination = 0°, position angle = 0°) of model galaxies, and then transformed the position and velocity vectors to M83's inclination (24°) and position angle (45°) using 3×3 rotation matrices.

The left panel of Figure 3.6 shows the observed orientation of the circumnuclear ring and the location of the visible nucleus in red. The black ellipse and cross show the geometry of the ellipse and nucleus when de-projected into M83's x-y plane. Using this geometry, we constructed models of gas on the elliptical orbit assuming the conservation of angular momentum. Once the circular velocity at one point on the ellipse has been specified, the velocity at every other point on the ellipse is known because the velocity times the radius is constant. We created a face-on galaxy with elliptical Keplerian orbits and then projected that using a matrix transform with the observed inclination and position angle of M83 to transform the projection of the ellipses and corresponding projected velocities. We then took the line of sight component of the velocities as a function of position around the orbit as we would see the gas velocity on that orbit from Earth. The orbits constructed in this way are closed and are assumed to remain closed for the small number of orbits we are interested in. As the orbital time of a few Myr is much smaller than the dynamical time of the bar, we have not worried about the effect of the rotating bar frame.

The centre and right panels of Figure 3.6 show the V_{LSR} of the HCO^+ and HCN emission determined from the SCOUSE fitting for all pixels in the ellipse used to define the circumnuclear ring. These observed velocities are plotted as a function of azimuthal

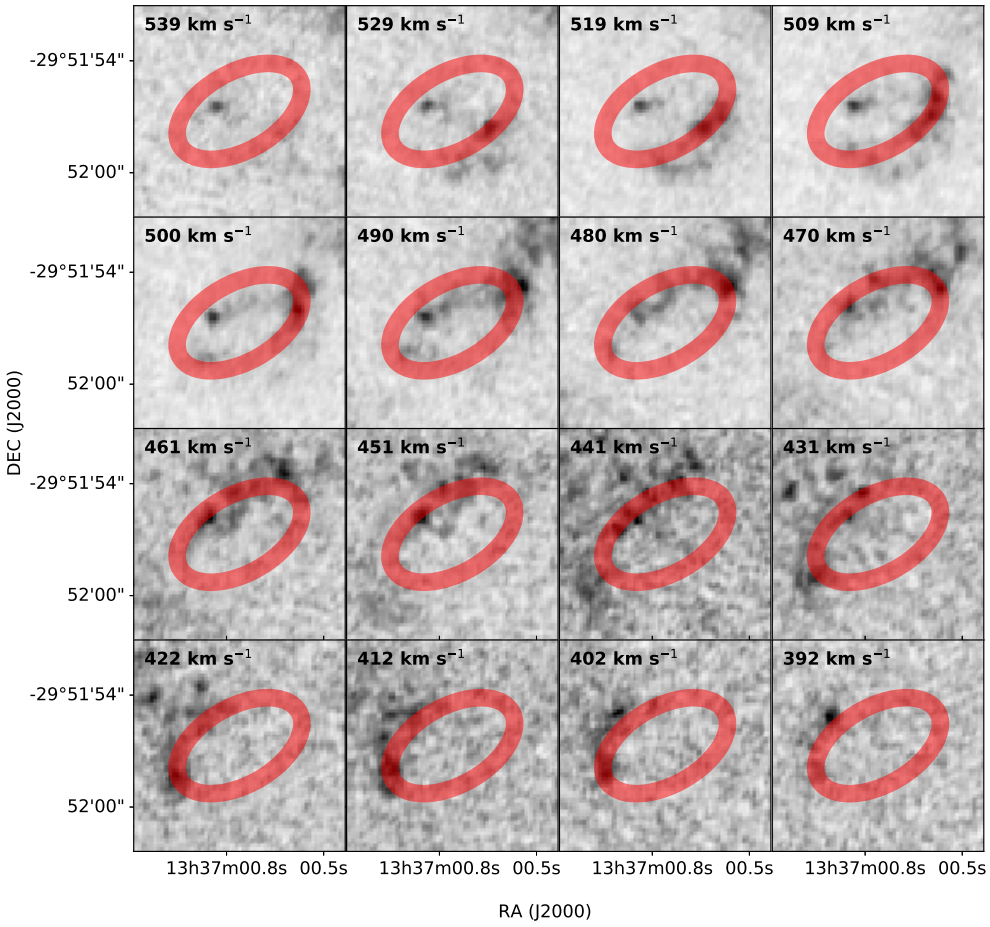

FIGURE 3.5: Channel maps of HCN $(1-0)$ emission, with every $\sim$10 km s^{-1} averaged together between 392 km s^{-1} and 539 km s^{-1}. The central velocity of each velocity bin is shown.

angle around the ring. The dashed black lines show the line-of-sight velocity as a function of azimuthal angle from the models of gas on the elliptical orbits described above, when projected to M83's inclination and position angle. The dashed lines in the centre and right panels of Figure 3.6 show the expected velocity structure when using the centre of the ellipse and the location of the visible nucleus in the x-y plane, respectively, to define the zero radius location.

Figure 3.6 demonstrates that the observed velocity structure in M83's circumnuclear ring can be reasonably well reproduced by elliptical orbits moving under the conservation of angular momentum for models where the radius equals zero location is defined either at the centre of the ellipse or the location of the visible nucleus. The scatter on the observed V_{LSR} as a function of azimuthal angle is too large to immediately distinguish

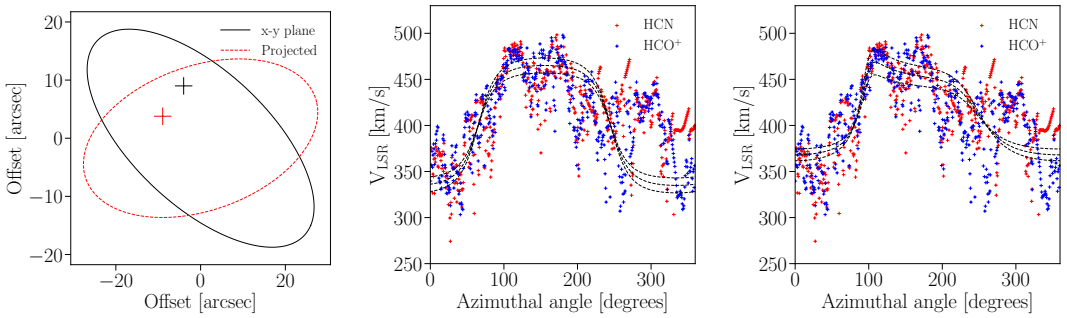

FIGURE 3.6: [Left] The observed orientation of the circumnuclear ring and location of the visible nucleus (red), and the ellipse and location of nucleus when de-projected into the x-y plane of the galaxy (black) using the known inclination and position angles of M83. [Centre] V_{LSR} of the HCO^+ (blue crosses) and HCN (red crosses) emission determined from the SCOUSE fitting for all pixels in the ellipse used to define the circumnuclear ring. These observed velocities are plotted as a function of azimuthal angle around the ring. The dashed black lines show the expected line-of-sight velocity as a function of azimuth determined from models of gas on elliptical orbits in the galaxy's x-y plane when projected to M83's inclination and position angle. For the centre panel, the zero radius point is defined as the centre of the ellipse, and the circular velocity at semi-major axis is 140, 160, and 180 kms^{-1}, respectively, for the dashed lines with increasing velocity amplitude. [Right] Same as the centre panel, but with the zero radius point defined as the location of the visible nucleus, and the circular velocity at semi-major axis of 80, 100, and 120 kms^{-1}, respectively, for the dashed lines with increasing velocity amplitude.

which model best fits the data.

The fact that the velocity structure in M83's circumnuclear ring is consistent with gas moving on stable orbits suggests that the potential must be stable enough that it is not wildly varying on the orbital timescale. If the gas kinematics were deeply disturbed one would not expect to see a closed ring of gas. We can conclude it is likely that the gas is orbiting stably around the kinematic centre.

Another possibility is that the bar potential is preventing stable orbits from existing over the galactocentric radii encompassing the circumnuclear ring. In general, gas in a bar potential should only be able to orbit without self-colliding if it is on an x_1 or an x_2 orbit, and there is a range of galactocentric radii where no such orbits exist. Given the above considerations, and the fact that the bar potential does not prevent the existence of closed, non-intersecting orbits, it seems plausible that the inner circumnuclear ring does in fact follow an x_2 orbit, and the exterior dust lanes are in the forbidden zone where no such orbits exist.

3.6.2 Variation in kinematic properties within M83's circumnuclear gas ring

While studying individual peaks around the circumnuclear gas ring gives us an insight into trends within the gas, it does not provide a complete picture.

To study how the gas evolves along the ring in M83, as opposed to within individual intensity peaks, we deproject the inner circumnuclear ring into cylindrical polar coordinates and average the polar image of the ring per azimuthal angle bin. As we are considering both radial and azimuthal trends, we also consider the azimuthal profile around the ellipse which has been defined in Figure 3.7 and average the velocity dispersion and integrated intensity over a region of $1''$ surrounding each pixel along this ellipse. This is because the deprojection method will blend together the radial bins across the entire ring, removing the subtleties of any potential radial trends. Figure 3.7 shows the variation in velocity dispersion and integrated brightness temperature with galactocentric radius for HCN $(1-0)$ and HCO^+ $(1-0)$ respectively. The shaded regions show the uncertainty on the velocity dispersion and integrated brightness temperature calculated by SCOUSE. These two transitions follow qualitatively similar trends, which gives confidence that the observed trends are accurately tracing the underlying gas kinematics. The observed velocity dispersion reaches a maximum at pericentre and a minimum at roughly 70pc for both transitions. While the average velocity dispersion appears to decrease with increasing distance from the optical nucleus, there are significant variations within this trend that appear unrelated to distance.

We then investigate whether there are any trends with azimuthal angle of the gas as it orbits the centre. Figure 3.8 shows the evolution of brightness temperature and velocity dispersion around the circumnuclear gas ring as a function of azimuthal angle.

Focusing first on the integrated intensity, we see a significant peak at apocentre, and several local peaks around pericentre. By eye, the distribution of the peaks throughout the integrated intensity curve appears quasi-regular despite the peaks themselves showing considerable variation in brightness.

We calculate the structure function of the integrated intensity (Henshaw et al., 2020) to determine if there is a preferred separation between the observed peaks. The structure function of order p is given by $SF \equiv \langle |I(x) - I(x+d)|^p \rangle$ averaged in this case over

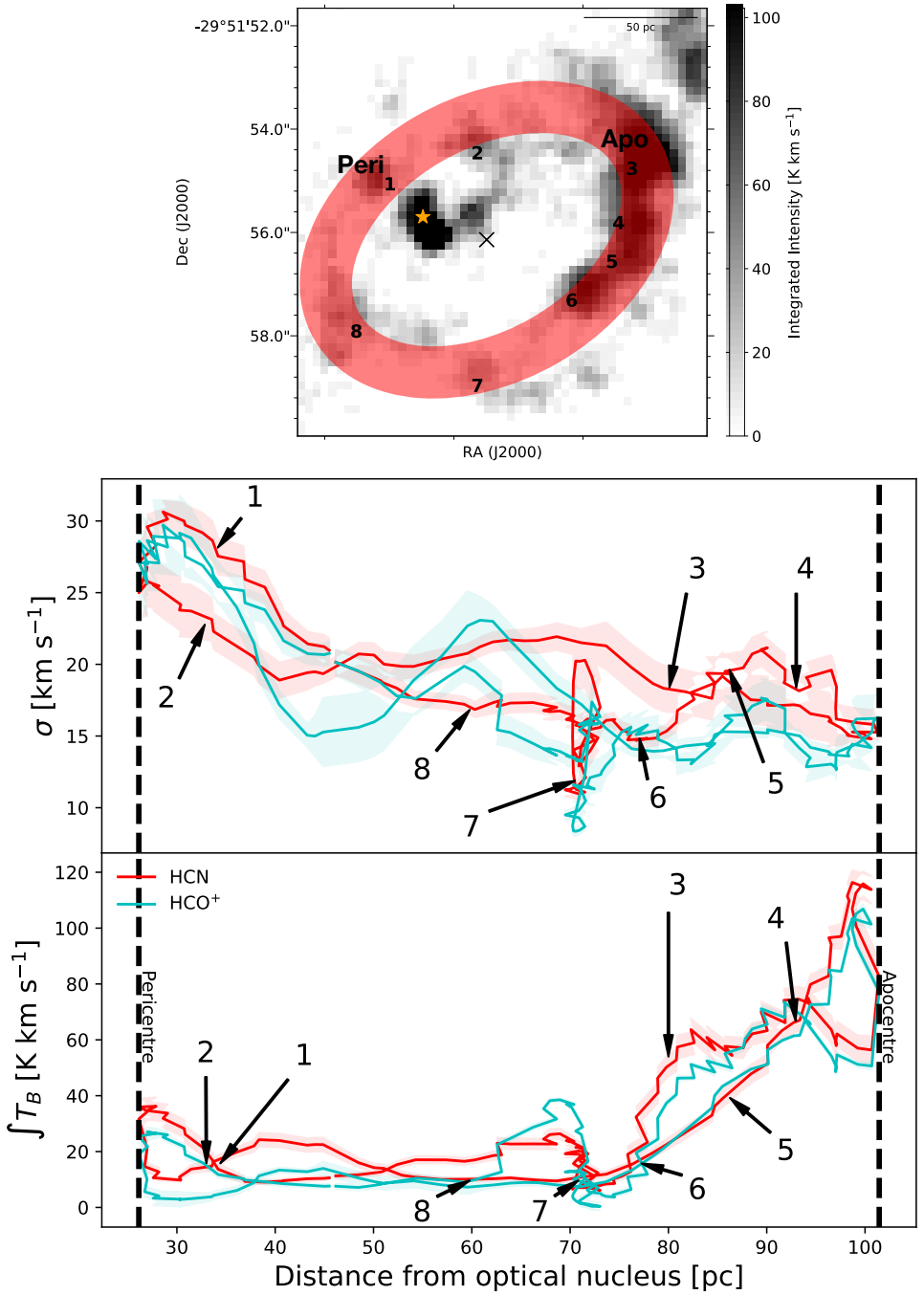

FIGURE 3.7: [Top]: Integrated brightness temperature map. The manually generated ellipse is shown in red. The numbers indicate the positions for which individual spectra were taken (see Figure A.240). The orange star is the nucleus and the black cross is the centre of the fitted ellipse. [Middle]: Variation in velocity dispersion as a function of distance from the optical nucleus around the circumnuclear ring for HCN $(1-0)$ (red) and HCO^+ $(1-0)$ (blue). We do this around the circumnuclear ring to avoid averaging the two sides of the ellipse together. [Bottom]: Variation in brightness temperature as a function of radius for the same two lines. The shaded regions denote the 1σ uncertainty in velocity dispersion and brightness temperature. The positions of the spectra shown in Figure A.240 are labelled.

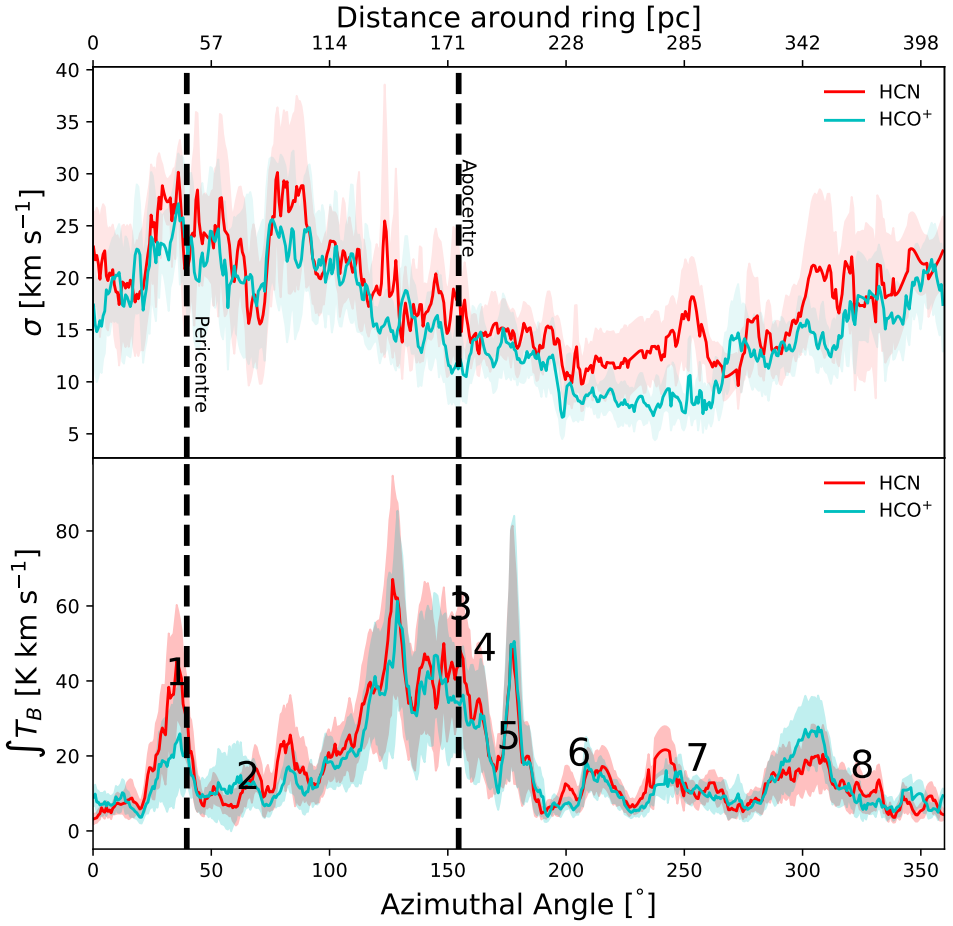

FIGURE 3.8: Variation of velocity dispersion (top) and integrated brightness temperature (bottom) associated with the inner circumnuclear ring as a function of azimuthal angle, going clockwise from left to right. HCN emission is shown in red while HCO^+ is shown in blue. The shaded regions shows the standard deviation per azimuthal angle bin. The positions of the spectra shown in Figure A.240 are labelled, as are the positions of pericentre and apocentre with respect to visible nucleus of M83, represented by the vertical shaded region and dashed line respectively. These are separated by less than 180° due to the focus of the ellipse being slightly displaced from the visible nucleus of M83. The shaded region corresponds to the 2σ uncertainty in pericenter due to the uncertainty in the position of the visible nucleus derived by Díaz et al. (2006) of 0.15″ or $\sim$ 4 pc. The upper x-axis shows the distance around the inner circumnuclear ring, assuming an ellipse with a semimajor axis of 50 pc.

azimuthal angle, where I is the intensity (in this example), measured at a location $x+d$ relative to position x. We do this only for integrated intensity as we are interested only in the spacing between clouds. In the following, we compute the first-order structure function and so $p = 1$. Structure functions are traditionally used in studies of the interstellar medium to measure the scale-dependence of certain quantities (e.g. velocity; Padoan et al., 2002; Heyer & Brunt, 2004). However, a property of the structure function, exploited mainly in time series analysis (Cordes & Downs, 1985; Lachowicz et al., 2006) but more recently in studies of the ISM (Henshaw et al., 2020), is its sensitivity to periodicity in data. The structure function of a periodic quantity will display a local minimum at the location of the corresponding wavelength.

We compute the structure function at 0.5° increments in azimuth around the ellipse. This is to prevent any possible bias introduced by, for example, starting our measurement at a position which happens to intersect one of the intensity peaks. In Figure 3.9 we display the mean structure function measured at each location and the 1σ dispersion about the mean. A clear dip in the profile of the structure function is observed at $d \approx 100\,\mathrm{pc}$. Visual inspection of the left hand panel of Figure 3.9 confirms that the most prominent peaks are indeed spaced by approximately $\sim 100\,\mathrm{pc}$.

3.6.3 M83's circumnuclear gas ring: unstable to gravitational collapse?

We now investigate what might cause this quasi-regular spacing in the gas properties. Kim & Moon (2016) model the gravitational instability of rotating isothermal rings at the centres of barred galaxies, like M83, to understand their star formation potential. They argue that rings with smaller α are typically more unstable, though this instability is suppressed if the angular frequency Ω is larger than the critical frequency. Using the observed circumnuclear ring radius ($\sim$100 pc), circular velocity ($\sim$75 kms^{-1}), mass ($\sim 5 \times 10^8\,\mathrm{M}_\odot$) and velocity dispersion (17 kms^{-1}, see below) we calculate the Kim & Moon (2016) α (virial parameter) and $\hat{\Omega}_0$ (critical angular frequency) parameters for M83's circumnuclear gas ring, as given by

$$\alpha = 0.01 \left(\frac{c_s}{10\ \mathrm{km\ s^{-1}}}\right)^2 \left(\frac{M_g}{4 \times 10^8\ \mathrm{M_\odot}}\right)^{-1} \left(\frac{R_0}{1\ \mathrm{kpc}}\right),$$

and

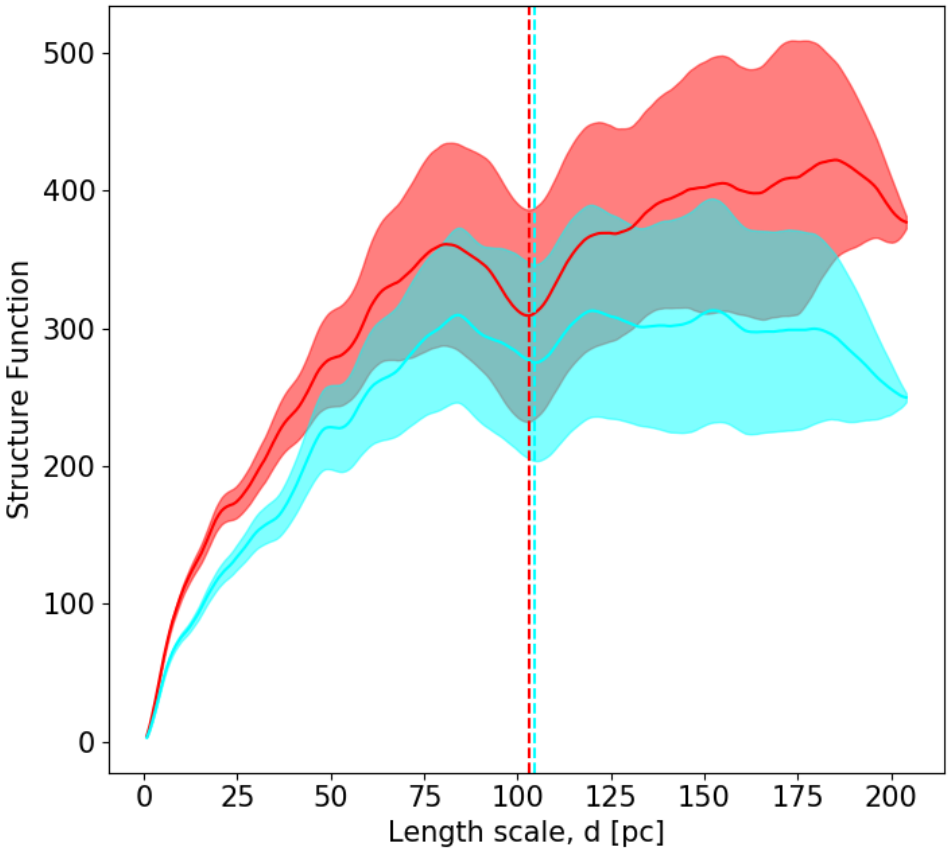

FIGURE 3.9: The structure functions computed when varying the zero point in azimuth in steps of 0.5°. The blue line shows the average structure function and the shaded region shows the variation in structure function when changing the zero point. The dashed line shows the location of the minimum at 100 pc. The colours in both correspond to the same transitions as Figures 3.7 and 3.8.

$$\hat{\Omega}_0 = 2.1 \left(\frac{v_{\rm rot}}{200 \text{ km s}^{-1}} \right) \left(\frac{M_g}{4 \times 10^8 \text{ M}_\odot} \right)^{-0.5} \left(\frac{R_0}{1 \text{ kpc}} \right)^{0.5}$$

to be 0.023 and 0.7, respectively. Given their definitions of α and $\hat{\Omega}_0$, this places the ring in the regime of being marginally unstable against gravitational collapse (Kim & Moon, 2016, Fig. 12). In this model, the growth rate of the instabilities is always close to $\sim 0.81(G\rho_c)^{0.5}$, where ρ_c is the central density of the ring. For reasonable values of ρ_c ($> 10^2\,\text{cm}^{-3}$), the instabilities are expected to develop within an orbital period and produce around ∼10 approximately evenly spaced clumps. Given the circumference of M83's circumnuclear gas ring, the clumps should be separated by ∼60 pc. Considering

the idealised nature of the Kim & Moon (2016) model (e.g. uniform density, circular orbits) the similarity with the predicted clump spacing suggests gravitational instabilities are a plausible explanation for the observed quasi-regular gas spacing.

To investigate this further, we also consider families of physical models which have been constructed to understand what determines the spacing of gas fragments within a filament (Chandrasekhar & Fermi, 1953; Nagasawa, 1987; Inutsuka & Miyama, 1992; Nakamura et al., 1993; Tomisaka, 1995, 1996). The most simplistic model is the "sausage" instability (Nagasawa, 1987), in which the fragment spacing within filaments is roughly equal to the wavelength of the fastest growing unstable mode of the fluid instability. For isothermal cylinders of finite radius R, this wavelength depends on the ratio between the cylinder radius and the isothermal scale height $H = c_s \left(4\pi G \rho_c\right)^{-1/2}$, where c_s is the sound speed, G is the gravitational constant and ρ_c is the gas mass density at $R = 0$, where R is the radius of the filament or cylinder. In the case that the radius of the filament is much larger than the scale height, this wavelength is $\lambda_{\rm max} = 22H$. Taking $\lambda_{\rm max}$ to be the scale length determined in the previous section, we calculate a scale height of $\sim 4.5\,$pc.

As the gas kinematics in the circumnuclear ring are dominated by non-thermal motions, we instead use the average velocity dispersion around the ring in place of the sound speed to determine the required density. However, we first must ensure that this velocity dispersion is not significantly impacted by velocity gradients within the circumnuclear ring. We approximate the total measured velocity dispersion, $\sigma_{\rm tot}$, as the convolution of two Gaussians: the first, $\sigma_{\rm int}$, corresponding to the intrinsic velocity dispersion of the gas; the second, $\sigma_{\rm orb}$, is the contribution to the observed velocity dispersion caused by the local velocity gradients along the orbit. The magnitude and relative contribution of $\sigma_{\rm orb}$ to $\sigma_{\rm tot}$ will increase as the aperture over which the velocity dispersion is measured increases. To quantify the magnitude of $\sigma_{\rm orb}$ as a function of size scale, we first calculated the velocity gradient around the orbit at the highest, intrinsic angular resolution of the observations ($\sim$12 pc). We found a linear fit with a gradient of $\pm$ 3 km s^{-1} pc^{-1} provides a good approximation of the orbit. Using this gradient we can determine $\sigma_{\rm orb}$ as a function of size scale by averaging over the required size scale and determining the intrinsic velocity dispersion as $\sigma_{\rm int} = \sqrt{\sigma^2_{\rm TOT} - \sigma^2_{\rm orb}}$. We find that the contribution of the orbital velocity gradient to the total velocity dispersion is negligible – even averaging over a spatial scale of $\sim$ 30 pc the quadrature-subtracted velocity dispersion only contributes

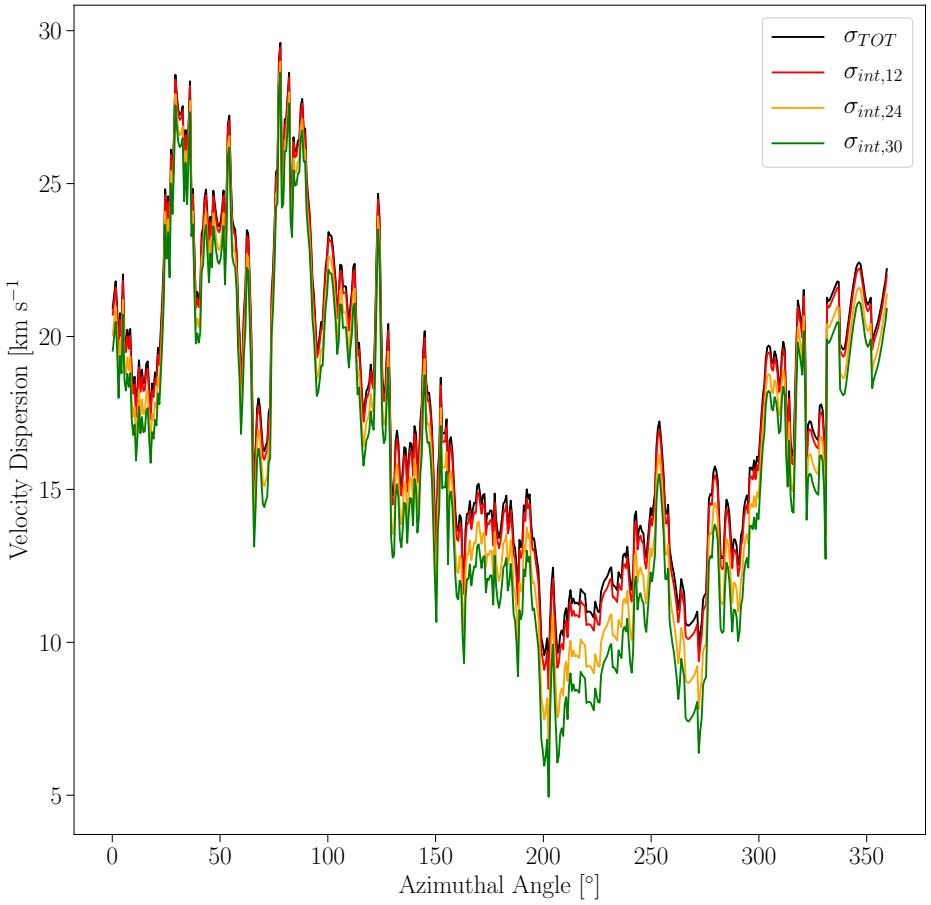

FIGURE 3.10: Intrinsic velocity dispersions compared to the observed velocity dispersion (black line) when averaging over spatial scales of 12 (red), 24 (orange) and 30 pc (green). At scales of 12 pc, the difference between the intrinsic and observed velocity dispersion is negligible.

$\sim$25% to the total velocity dispersion. Figure 3.10 shows the difference in intrinsic velocity dispersion when subtracting the orbital velocity gradient in quadrature on spatial scales of 12, 24 and 30 pc. As we determine the velocity dispersion at a size scale of $\sim 12\,\mathrm{pc}$ we conclude that the observed velocity dispersion is not impacted significantly by the orbital velocity gradient. As such we use $\sigma_{\mathrm{int}} = 17\,\mathrm{kms}^{-1}$ to calculate a critical density of $n = 4 \times 10^3\,\mathrm{cm}^{-3}$.

While this critical density is broadly consistent with those measured on large scales in the CMZ and M83 which suggests that the gas could be subject to this instability, this is an over simplistic scenario for several reasons. Firstly, this model deals with a

cylinder of infinite length, instead of a rotating ring. Additionally, while the model is in isolation, the rotating stream has gas being fed in at both extremes by the dust lanes further out. Finally, the displacement of the nucleus from the centre of the ring may produce additional perturbations within the gas in the ring.

For these reasons, we consider other possible mechanisms of gas fragmentation. It is possible that the observed fragment separation is a result of the 'wiggle' instability (Wada & Koda, 2004; Kim et al., 2012; Henshaw et al., 2020), seen in hydrostatic simulations of galactic centres (Sormani et al., 2015a; Ridley et al., 2017). It is also plausible that the turbulence produces this quasi-periodicity somewhat sporadically, and we are merely observing it here by chance.

Although the observed fragmentation length is intriguing, more realistic analytical models or dedicated simulations are required to understand its origin.

3.6.4 M83's circumnuclear gas ring properties: shaped by the gravitational potential?

We now seek to understand what may be causing the variations in integrated brightness temperature and velocity dispersion of HCN $(1-0)$ and HCO^+ $(1-0)$ along the circumnuclear ring.

In the absence of any numerical simulations with time-dependent chemistry, we make the assumption that the abundance of HCN $(1-0)$ and HCO^+ $(1-0)$ are constant throughout the circumnuclear ring. We see that the HCN $(1-0)$ and HCO^+ $(1-0)$ emission is well resolved, with the smallest cloud being 80% larger than the beam size, so beam dilution should not be a major issue. Therefore, variations in integrated intensity can be a result of a change in excitation conditions, opacity, column density of material, or a combination of all three.

If the emission were optically thick we would expect the line brightness temperature to equal the excitation temperature and the line profiles to become self-absorbed and non Gaussian. Given the brightness temperature of the spectra is <5K and the line shape is roughly Gaussian, we conclude opacity is not a serious issue at the scales probed by these observations. The variation in integrated intensity is therefore due to an increase in excitation conditions, column density, or volume density.

One potential explanation for the trends in integrated intensity and velocity dispersion is that we are witnessing conservation of mass flux as the gas orbits the galactic centre. Azimuthally, due to the elliptical orbit, as the gas moves further away from the nucleus it slows down and will tend to 'pile up' at apocentre as it spends more time at that location. Radially, however, pileup occurs where the density of orbital streamlines is the highest, which is at pericenter. Assuming the HCO^+ $(1-0)$ and HCN $(1-0)$ integrated brightness temperature traces the dense gas mass on scales of ~ 10 pc (as discussed by Mills & Battersby, 2017a), we would expect to observe a correlation between brightness temperature and radius. The bottom panel of Figure 3.7 shows that indeed the highest brightness temperature emission is at largest radii. However, the sudden increase in brightness temperature between position 2 and 3 (apocentre) and much slower drop off in brightness temperature from apocentre to position 5 and 6 is not consistent with the picture of orbital pile-up, which would require azimuthal symmetry.

Another potential explanation could be that the trend in velocity dispersion and integrated intensity is simply due to the clouds having a similar virial state, and clouds with a larger column density (brighter HCO^+ $(1-0)$ and HCN $(1-0)$ emission) will have larger velocity dispersions. A comparison of the two panels of Figure 3.7 shows there is an anti-correlation between brightness temperature and velocity dispersion at both peri- and apocentre; while the velocity dispersion peaks at the smaller radii, the integrated intensity peaks closer to apocenter.

Returning to Figure 3.8, it is interesting to note that the location of the sharp rise in integrated intensity at apocentre in the circumnuclear ring's orbit also corresponds to the location at which the circumnuclear ring and the 'bridge' intersect (see Figure 3.1). One explanation for the increase in integrated intensity close to apocentre would therefore be that this is the location at which gas from the dust lanes is deposited onto the circumnuclear gas ring though the 'bridge'. In this scenario, the increased integrated intensity would then be due to an increase in column or volume density from the new material being added on to the ring.

However, several lines of evidence argue against this scenario. Firstly, if substantial quantities of gas were being deposited at the bridge-ring intersection we would expect to see a sudden jump in the integrated intensity of the ring at the intersection point. Figure 3.8 shows the integrated intensity increases steadily in azimuthal angle from

significantly before the intersection point (number 3). In addition, the total mass of dense gas in the whole bridge inferred from the HCN $(1-0)$ and HCO^+ $(1-0)$ integrated intensity emission is much smaller than the increase in integrated intensity seen in the circumnuclear ring at the bridge-ring intersection point. If the current mass in the bridge region is representative of the time-averaged mass flow, then if mass *is* transferred to the ring through the bridge, it is at a much smaller rate than can explain the increase in integrated intensity. The lack of extinction at this bridge suggests that the gas is not simply being transferred to the ring at lower densities.

Secondly, if substantial quantities of gas were being deposited at the bridge-ring intersection we would expect to see signs of this in the gas kinematics in the form of multiple spectral components, or broad line emission. Figure A.240 shows that the one location with unambiguous multiple velocity components is indeed at the bridge-ring intersection point. However, this is the *opposite* intersection point from where we see the increase in integrated intensity. At the other intersection point (number 3) with the maximum integrated intensity, Figure 3.8 shows that in fact the velocity dispersion is closest to its minimum value.

An alternative explanation for the observed variation in gas properties is that the clouds in the circumnuclear gas stream are being shaped by the external gravitational potential. 3D hydrodynamical simulations of gas clouds orbiting the centre of the Milky Way at a similar galactocentric radius show that a combination of the background potential and eccentric orbital motion shape the morphological and kinematic evolution of the clouds (Kruijssen et al., 2019a). Specifically, strong shear, tidal and geometric deformation, and the passage through the orbital pericentre affect the cloud sizes, column densities, velocity dispersions, line-of-sight velocity gradients, angular momenta, and kinematic complexity. Although such simulations have not been run for gas clouds in the circumnuclear gas stream of M83, the similarity of the inner few hundred parsec of M83 and the Milky Way make it plausible that M83's external potential will exhibit similar behavior.

Furthermore, we note a strong increase in velocity dispersion around pericentre passage, with a maximum of $\sim$30 $\mathrm{km s^{-1}}$ at the location of position 1. The simulations of Kruijssen et al. (2015), Kruijssen et al. (2019a) and Dale et al. (2019b) show that additional turbulence driven by motion in the shearing potential, which reaches a maximum as

clouds move through pericentre, may be responsible for increasing the velocity dispersion. As the clouds pass pericentre, the rate of turbulent energy injection slows down, and the energy is expected to dissipate on a crossing time. While the impact of pericentre passage in these simulations is quite small, they are based on the gravitational potential of the CMZ. To determine how significant this effect is in M83, simulations would have to be run using a model of M83's gravitational potential.

From the observed galactocentric radius and velocity dispersion (Table A.2) the crossing time for the cloud nearest pericentre (position 1) is $\sim$0.4 Myr. Given the previously calculated orbital period of the inner ring of 3.1 Myr and assuming a fixed orbital velocity, the cloud will have moved $\sim$50 pc along the orbit by the time it has dissipated the additional energy. The cloud at position 2 lies $\sim$50 pc along the orbit and the velocity dispersion has dropped from $\sim$30 kms^{-1} to $\sim$20 kms^{-1}. These qualitative trends are consistent with that expected from the injection and dissipation of turbulent energy. However, care does need to be taken when comparing these observations with the simulations. The velocity dispersions reported in the simulations are determined from a viewing angle looking through the disk mid-plane, whereas our observations view the galaxy from above.

Given that the predominant age of clusters sits well within the most likely timeframe within which SNe will likely start (3 - 9 Myr; Leitherer et al., 2014), we consider the likelihood of the energy liberated in these events being enough to impact the gas flow, perhaps even disrupting the ring entirely. Using 3D hydrodynamical simulations to understand how SNe affect surrounding molecular gas clouds, Rogers & Pittard (2013) found that the energy released from SNe primarily escape from the region along lower density channels. While the very edges of their dense molecular clouds were ablated, the majority of the gas in their dense clouds were resistant to this process. Applying this to the centre of M83, this would imply that the energy from the SNe, which explode in a low density environment offset from the ring, will likely escape with minimal impact on the ring itself. However, the combined affect of many SNe may play an important role in the longer term star formation cycle, e.g. by making it more difficult for gas to enter the circumnuclear stream.

3.6.5 M83's circumnuclear gas ring: cradle for the observed stellar clusters?

We now look in more detail into the stellar clusters, and how trends observed in the gas may have imprinted onto the cluster population.

The Kruijssen et al. (2019a) simulations show that the transformative dynamical changes to the clouds as they orbit can lead to cloud collapse and star formation. This can generate an evolutionary progression of cloud collapse with a common starting point, which either marks the time of accretion onto the tidally-compressive region or of the most recent pericentre passage. Such an evolutionary progression should leave an imprint on the age distribution of recently formed stars as a function of their position with respect to the gas clouds. Specifically, they should exhibit an age gradient that increases with distance travelled from the common starting point for star formation (e.g. pericentre passage or the circumnuclear ring-bridge intersection point).

If the gas in the circumnuclear ring is to form stars, the imprint of the ∼100 pc spacing in the gas should also be observable in the distribution of young stars (at least until they are disrupted by galactic dynamics). Returning to the distribution of YMC's in Figure 3.1, there are too few clusters in Harris et al. (2001) to do a rigorous spatial clustering analysis. However, it is interesting to note that by-eye there are a few groups of clusters which are clearly separated from other groups by around 100 pc, though we cannot state firmly that this is anything but confirmation bias.

To see if there is any relationship between the YMCs and the gas in the circumnuclear ring, we take the ages[1] of the stellar clusters with galactocentric radius less than 220 pc and plot them in azimuth in the same way as for the gas[2]. Figure 3.11 shows that there is a linear relation between cluster age and azimuthal angle. We thus confirm the similar age gradient within these clusters reported by Harris et al. (2001) and Knapen et al. (2010).

[1] We note that there are discrepancies between the cluster ages in Table 2 and Fig. 11 of Harris et al. (2001). We use the values in Table 2 but the results are robust when using either values.

[2] In doing this, we have checked for local outliers (i.e. with ages vastly different from the neighbouring clusters) and verified if these could be caused by age degeneracies in the colour-colour space used to determine the ages (Harris et al., 2001, Fig. 6). For discrepant cluster ages that can be explained by this degeneracy, we have set the ages to that of their neighbours.

We then used Bayesian analysis to determine the uncertainty on the line fit by constructing a model with three parameters: the gradient (m), intercept (b) and fractional error on the age uncertainty (f). Including parameter f allows the modelling to take into account the fact that the age uncertainties are not reported in Harris et al. (2001), so any uncertainties we choose may be over-/under-estimates. We assume flat priors in all three parameters in the ranges, $0.0 < m < 0.5$, $0.0 < b < 10.0$, and $-3.5 < \log(f) < 1.0$. We used the python package EMCEE (Foreman-Mackey et al., 2013) to sample the posterior probability distribution. The initial positions of the posterior distribution sampling chains (or 'walkers') were drawn from a narrow Gaussian centred on the maximum likelihood solution. After initialising the positions of 32 'walkers' across the posterior distribution in this way, we used EMCEE to let the 'walkers' independently sample the posterior distribution in 5000 Markov chain Monte Carlo (MCMC) steps. The autocorrelation time (how long it takes each 'walker' to lose its memory of where it started, and hence begin fairly sampling the posterior distribution) was ∼40 steps. We therefore discarded the first 120 steps of each 'walker' (commonly known as a 'burn-in' time) to ensure the remaining steps sampling the posterior distribution were not affected by the choice of initial 'walker' location.

Figure 3.11 shows the results of the Bayesian analysis where the cluster age uncertainty was assumed to be 1 Myr. The 16^{th}, 50^{th}, and 84^{th} percentiles of the samples in the marginalized distributions are $m = 0.0259^{+0.0092}_{-0.0096}\,\text{yr}\,\text{degree}^{-1}$, $b = 4.6196^{+0.366}_{-0.364}\,\text{yr}$, and $\log(f) = -1.60^{+0.245}_{-0.2186}$. The resulting angular frequency, Ω, orbital period, and circular velocity, V_{circ}, are 0.673, 9.3 Myr and 79 kms^{-1}, respectively. These values are consistent with the observed gas rotation curve at the galactocentric radius range of the ring and clusters (Lundgren et al., 2004b). We repeated the analysis varying the age uncertainty on the clusters from 0.1 Myr to 4 Myr. While the additional fractional error on the age uncertainty (f) increased as our assumed age uncertainty decreased, the values of m and b changed very little. We conclude that our results are robust against the unknown uncertainty on the cluster ages.

Extrapolating this relation back in azimuth to where the cluster age equals zero suggests that the progenitor clouds from which these clusters formed began collapsing at a common point. A natural explanation for this is that some event may be responsible for triggering star formation. The azimuthal angle at this 'cluster age equals zero' point

is $-178°$, where $0°$ is defined as directly West (to the right) of the center. The uncertainties on the line fit translate to large (tens of degrees) uncertainties on this 'cluster age equals zero' angle. However, it is constrained to lie in the quadrant of the orbit in which the circumnuclear gas stream passes closest to the bottom of the gravitational potential. If the YMCs formed in the circumnuclear gas stream, their age gradient is consistent with their formation having been triggered by pericentre passage. A similar scenario has been proposed for star formation in the circumnuclear stream of the Milky Way (e.g. Longmore et al., 2013d; Kruijssen et al., 2015, 2019a; Jeffreson et al., 2018). An important source of uncertainty arises in the $t = 0$ point due to intrinsic uncertainty in the rotation curve and its derivation. These uncertainties are propagated into the conversion from phase angle to time. As the clusters have likely gone through one orbital cycle, small uncertainties in the rotation curve will lead to larger errors when traced back to the $t = 0$ point.

If pericentre passage triggers star formation in the circumnuclear ring, star formation is expected to occur over the next (few) free-fall time(s) along the orbit. Taking a density of $n \sim 10^{4-5}$ cm^{-3}, we find a free-fall time of 0.03 - 0.3 Myr, with the higher end of this range closely matching the free-fall times of clouds found in the CMZ (Kruijssen et al., 2015).Given the orbital velocity, the orbital position corresponding to a few free fall times places the star formation at the following apocentre and beyond (locations 3, 4, 5 and 6). Figure 3.2 shows that these positions coincide with the continuum source in the circumnuclear ring with spectral indices consistent with free-free emission from young, high-mass stars.

The locations in the circumnuclear stream with the brightest continuum emission coincide with the brightest HCN $(1-0)$ and HCO$^+$ $(1-0)$ integrated intensity emission. If the clouds at these positions have embedded star formation, as implied by the continuum emission, their densities and temperatures will be higher than in quiescent clouds. These conditions will result in brighter line emission, explaining the increased HCN $(1-0)$ and HCO$^+$ $(1-0)$ integrated intensity at these locations. The resulting feedback from young stars will eventually disperse the remaining gas, potentially explaining the lack of HCN $(1-0)$ and HCO$^+$ $(1-0)$ at position 7 and beyond and the bright Hα emission at this location shown in Figure 3.3.

The only other location outside the circumnuclear gas ring that is both near enough

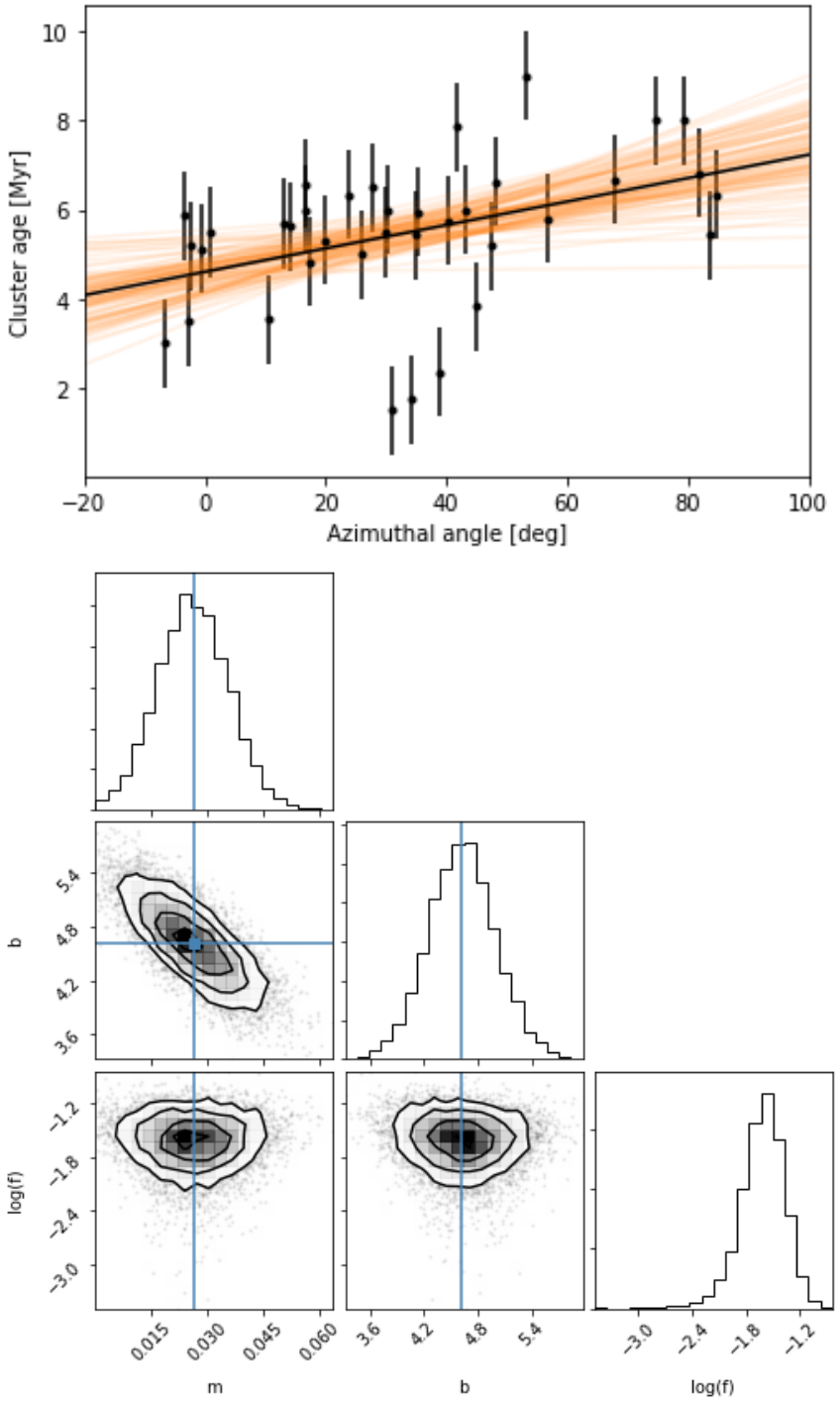

FIGURE 3.11: [Top] Ages of the massive star clusters observed by Harris et al. (2001) [black dots] as a function of azimuthal angle around the circumnuclear ring. Error bars show a representative 1 Myr uncertainty in cluster ages. The black line shows the result of Bayesian fitting of a straight line to the data points. The orange lines show opacity-weighted, randomly selected fits from the posterior probability distribution to provide a visual assessment of the line parameter uncertainties. [Bottom] Corner plot showing 1D and 2D projections of the posterior probability distribution parameters, where m is the gradient, b is the intercept, and f is the fractional uncertainty in the cluster ages (see text for details). The blue horizontal and vertical lines show the best-fit m and b from least squares minimisation.

to the stellar clusters, and has a large enough gas reservoir to form stellar clusters, is the southern end of the western dust lane. In simulations of gas flows in barred spiral galaxies, individual gas streams can collide at these locations (Sormani et al., 2015a). The resulting strong shocks can lead to increased gas density – a natural location for star and cluster formation. In this scenario, the continuum emission peaks at the end of the dust lane with spectral indices consistent with those of thermal dust emission would represent the youngest sites of star formation activity, as their continuum is not yet dominated by free-free emission. It is interesting to note that there is then a linear increase in star formation age from this location, through the free-free continuum sources at the western end of the circumnuclear gas ring to the well-known age gradient in the clusters.

3.6.6 Comparison of the dense gas and young stars with the Milky Way

Regardless of the causal relationship between the circumnuclear gas ring, the southern end of the dust lane, and the stellar clusters, the observed properties of the dense gas along M83's circumnuclear ring are remarkably similar to those of the circumnuclear gas stream in the Milky Way. The total mass, mass distribution of clouds, orbital velocity, galactocentric radius and gas velocity dispersion are the same within the observational uncertainties (Table 3.4). In addition, when comparing the gas velocity dispersion, column density and star formation activity as a function of azimuth around the ring, the magnitude of change in these properties in both galaxies is similar when the azimuth angle is measured from pericentre passage with the bottom of the galactic gravitational potential. Indeed, an observer located at the same distance from the centre of M83, and at the same angle with respect to M83's stellar bar as the Sun is in the Milky Way, would have a strikingly similar view of the gas and stars at their galactic centre as we do of ours. Even the observed locations and mean masses of M83's stellar clusters (few $10^4\,M_\odot$) are similar to the distribution of the 24 micron sources in the centre of the Milky Way.

Having conducted a detailed comparison of gas and young stars at similar spatial scales in both galaxies, the only significant difference we can find in these properties between the two galactic centres is the number, location and age distribution of the young stellar

clusters. The inner 200 pc of the Milky Way contains two clusters (Arches and Quintuplet, Portegies Zwart et al., 2010) and a distributed population of either very young or evolved high-mass stars (e.g. '24μm point sources', Yusef-Zadeh et al., 2008). On the other hand, in the same galactocentric radius range, M83 has 45 clusters of similar mass.

However, when we separate the clusters by age, a very different picture emerges. As mentioned in the introduction, the age distribution of clusters in M83 has a very strong peak at ages of 5-7 Myr (Harris et al., 2001). If we only select clusters with a similar age range as the Arches and Quintuplet in the Milky Way ($\lesssim$4 Myr), the number of clusters is roughly similar. Unfortunately it is particularly difficult to age such young clusters accurately, so a direct comparison is difficult, but we estimate that the centre of M83 only has a factor $\sim$2 more clusters in the age range $\lesssim$4 Myr than the centre of the Milky Way.

Regarding the relative location of the clusters in the centre of the two galaxies, while most of the current star formation within the CMZ is occurring within the circumnuclear stream, the clusters in the centre of M83 are primarily distributed outside of the circumnuclear ring. While there is little to no current star formation at similar galactocentric radii in the CMZ, we note that there is a well known population of 24μm point sources (Yusef-Zadeh et al., 2008), which are thought to be related to a previous generation of star formation, at the same galactocentric radii range as the clusters in the centre of M83. Therefore, the galactocentric radii range of star formation over the last $\sim$10 Myr appears similar in the centre of both galaxies and M83 contains a large population of clusters aged between 5-7 Myr in the inner few hundred pc that are missing in the Milky Way.

3.6.7 Resolution of the conundrum: time variability in the SFR, not broken star formation theories

We now return to the conundrum posed at the beginning of this section and the original motivation for comparing the dense gas and young stellar populations in the centres of the two galaxies: what is causing the order of magnitude difference in star formation rate when the dense gas properties are almost indistinguishable?

The resolution of this conundrum, as also indicated by Harris et al. (2001), is that the conundrum disappears almost completely when only the most recent SF (i.e within the last 4 Myr) and the current properties of the gas are considered. This implies that the SFR is strongly variable with time, and causes one to overestimate the SFR in M83 when using more standard estimates. While this result may seem obvious in hindsight, there are several important implications.

Firstly, it gives confidence that gas clouds with similar properties produce similar stellar populations, a key assumption of all star formation theories. The ∼Myr timescale for star formation to occur corresponds to several free-fall times at the average cloud density. This is often invoked as a natural time for star formation in gas clouds. It follows from the above points that what we are learning about the detailed physical processes shaping star formation in the centre of Milky Way can be directly applied to similar environments in nearby galaxies.

The second implication is that M83 had a burst of star formation 5-7 Myr ago. This possibility was previously pointed out in the original young massive cluster survey by Harris et al. (2001). However, they were careful to make clear that they couldn't rule out an alternative possibility, that the elevated star formation episode had continued for much longer than 7 Myr, and that the reason older clusters were not detectable in their data was due to disruption.

Given the remarkable similarity between the present-day properties of the gas, the youngest stellar clusters in the centres of the two galaxies and the SF estimates from free-free emission, it is far more likely that the elevated star formation episode had a very short duration, and that the present-day conditions are much more representative of the time-averaged conditions for both galaxies.

If true, this suggests that galaxies like the Milky Way and M83 have a duty cycle for star formation. For much of the time they have a relatively low star formation rate, consistent with observations that show most nearby galaxy centres have much lower than average dense gas star formation efficiency (Usero et al., 2015). The comparison of M83 and the Milky Way suggests that these periods of quiescence are punctuated by short episodes lasting for a few Myr where the star formation rate can increase by between one and two orders of magnitude. The young massive cluster population in M83 suggests that the star formation rate was an order of magnitude higher than average for

a period of a few Myr. The relatively short starburst duration means finding a galaxy in this phase is statistically unlikely, so observational examples will be rare and large galaxy samples are needed to overcome this problem. Previous studies of star-forming nuclear rings by Allard et al. (2006a) and Sarzi et al. (2007) found strong evidence of this episodic star formation cycle. Krumholz & Kruijssen (2015b) model the evolution of gas in the centre of a barred galaxy and predict a timescale of 10-20 Myr for this process of gas accumulation and star formation. If we assume a starburst event lasts roughly ~ 1 Myr, this timeline suggests we would expect $5 - 10\%$ of galaxies to be in this burst phase at any given time.

The galaxy NGC 253 is particular interesting in this regard. Much like M83 and the Milky Way, NGC-253 also contains a circumnuclear gas ring with a similar radius (Leroy et al., 2018). Recent observations have shown that NGC 253 has 14 extremely young (<1 Myr old) super star clusters, which contain the bulk of the nuclear star formation activity. We postulate that 5-7 Myr ago M83 went through a starburst phase qualitatively similar to that currently observed in NGC 253, which produced the majority of the clusters we see today in M83's centre.

If the centre of the Milky Way, NGC 253 and M83 represent the quiescent, starburst, and post-starburst phase, respectively, of a commomly shared duty cycle, future detailed comparison of their gas properties and young stellar populations will help understand key aspects of the duty cycle. For example, what controls the duration of quiescence between starbursts? What eventually triggers and then ends the starburst? What controls the increased magnitude in star formation? Is there any link between star formation and feedback to feeding of the central supermassive black holes?

Finally, we point out that the interpretation of a duty cycle with a long period of quiescence punctuated by short, extremely intense star formation episodes has important implications for the mass flows and energy cycles in galaxy centres, and thus galaxy evolution. As star formation is highly localised in both space and time, the resulting feedback will be much more efficient at driving galactic-scale nuclear outflows (e.g. the outflow currently being driven in NGC 253, Krieger et al., 2019; Zschaechner et al., 2018) than the same star formation integrated over the whole duty cycle.

3.7 Conclusion

Using ALMA Band 3 HCN $(1-0)$ and HCO^+ $(1-0)$ observations we have studied the distribution and kinematics of the dense gas on $\sim$10 pc scales in the inner few hundred parsec of the nearby spiral galaxy M83. The HCN and HCO^+ emission closely traces the previously known molecular gas features and dust absorption features. Visual inspection of the HCN and HCO^+ data cubes show that multiple velocity components in the spectra are prevalent, especially at the end of the dust lanes. We used SCOUSE to perform multi-component spectral line fitting of the HCN and HCO^+ line profiles. The resulting fits from both lines are remarkably similar, giving confidence in the robustness of these transitions to trace the dense gas distribution and kinematics accurately.

We find that the range in the measured velocity dispersion varies considerably with galactocentric radius. The drop in velocity dispersion at the same radius range containing all the recent star formation activity and the turn over in the rotation curve qualitatively matches the predictions of recent 1D models of gas transport and star formation in the centres of galaxies (Krumholz & Kruijssen, 2015a; Krumholz et al., 2017).

The gas in the inner circumnuclear gas ring (galactocentric radii $\lesssim$120 pc) shows strong variations in HCN and HCO^+ velocity dispersion and integrated intensity. When averaged in azimuth around the ring, the integrated intensity emission shows quasi-periodic behaviour with a spacing between the oscillations of $\sim$100 pc. Given the absence of an analytical model for the stability of orbiting gas in a circumnuclear ring, we use this to estimate the density required to produce an instability of this length in a self-gravitating cylinder, which was calculated to be 4×10^3 cm^{-3}. This is in reasonable agreement with the density of the CMZ and M83 measured at this scale, given the sources of error in this calculation.

The variation in the HCN and HCO^+ velocity dispersion and integrated intensity around the circumnuclear gas stream is consistent with a scenario in which a combination of an eccentric orbit through an axisymmetric potential is shaping the gas properties. Specifically, there is a strong increase in the velocity dispersion of gas at pericentre passage, consistent with the expectation of additional turbulence being added to the gas driven by motion in the shearing potential, which reaches a maximum at pericentre. The velocity dispersion peaks and then quickly drops off between pericentre and apocentre returning

to the average value after approximately a crossing time, consistent with expectations of turbulence dissipation. The apocentre also corresponds to the peak in the HCN and HCO^+ integrated intensity emission, corresponding to an increase in the column density and/or excitation conditions. The detection of free-free continuum emission towards this location is consistent with these clouds containing embedded, recently formed, high mass stars.

Comparing the properties of the gas in the circumnuclear ring with the age and location of the nearby young massive clusters, we find a linear age gradient of the clusters with azimuthal angle around the galactic centre, suggesting there is a common location for their formation. If the clusters formed in the circumnuclear gas ring, their ages are consistent with the common location for the onset of star formation being close to pericentre passage at the bottom of the galactic gravitational potential. Though we note that the uncertainty in this location as a result of the rotation curve and its derivation is considerable, especially over more than one orbital cycle.

We put forward a scenario to explain the observed properties of the gas in the circumnuclear gas stream and the surrounding young massive clusters. In this scenario, gas in the circumnuclear stream is undergoing gravitational instabilities which determines the spacing and mass of individual clouds around the ring. A combination of the external gravitational potential and eccentric orbit then shape the gas properties, compressing the gas and adding turbulent energy into the gas as it approaches pericentre. The gas then dissipates its turbulent energy on a crossing time and begins to form stars. Over the next ∼Myr, feedback from the newly formed stars disperses the remaining molecular gas, leaving the observed young massive clusters.

Finally we show that the only way to reconcile the order of magnitude difference in SFRs between the two galaxies given their remarkably similar dense gas properties is with time variability. Isolating the youngest (<4 Myr old) stellar populations, the inferred SFRs of both galaxies agree within a factor ∼2. This has important implications for interpreting observations of galaxy centres and understanding their mass flows and energy cycles.

M83's young massive cluster population suggests the SFR must have been an order of magnitude higher $5-7$ Myr ago. The comparison of observed SFR with present day gas properties is therefore highly misleading, and highlights the danger of interpreting dense gas vs SFR relations to understand the physics of star formation in galaxy centres. In

addition, M83's 'starburst' phase was highly localised, both spatially and temporally, greatly increasing the feedback efficiency and ability to drive galactic-scale outflows.

Krumholz & Kruijssen (2015b) propose that this star formation cycle is likely controlled by the timescales over which gas is drawn inwards into galactic regions by the galactic bar. As the gas is transported inwards of the inner Lindblad resonance, turbulence gets injected by acoustic instabilities which keep the gas somewhat stable and thus star formation is unable to begin. At the rotation curve turnover, this support against collapse disappears, leading to an extreme star formation event. While the 3D hydrodynamical simulation presented by Armillotta et al. (2019a) suggest that these star formation cycles are not due to variations in gas inflow rates but instead due to variations in the gas depletion/star formation efficiencies, Sormani et al. (2020) finds the inverse to be true.

This cycle is likely restricted to galactic centres as some mechanism is required that allows for large amounts of gas build up, prevents star formation during this build up and then leads to a significant conversion from gas to stars in a short period of time. In the centre of galaxies, this mechanism is the galactic bar driving unsteady gas inflow into the centre with turbulence driving. However, they are still vital for understanding the evolution of a galaxy as a whole. This highly dynamic nature of star formation and feedback cycles in galaxy centres means (i) modeling and interpreting observations must avoid averaging over large spatial areas or timescales, and (ii) understanding the multi-scale processes controlling these cycles requires comparing snapshots of galaxies in different evolutionary stages.

Chapter 4

Conclusions and Future Work

The work presented in Chapter 2 of this thesis merely scratches the surface of the breadth and depth of the potential scientific output of the CMZoom survey. Due to time/computational constraints, only a fraction of the full CMZoom survey was imaged, with the observations taken using the ASIC correlator being the sole focus. During the several year period of the survey, the SMA was updating from this correlator to the SWARM correlator, which covered a larger frequency bandwidth with a higher spectral resolution. While the data from the ASIC correlator are still very powerful in probing the chemical complexity of the region and determining kinematic properties of individual dense cores, the higher spectral resolution would immensely improve the capabilities of the survey to probe a number of open questions regarding the virial equilibrium of a number of cores with velocity dispersions lower than the instrumental channel width of ASIC. However, due to the timescale over which the correlators were updated during the observing schedule, the SWARM data does not have as large spatial coverage as the ASIC data.

Even before utilising this SWARM data, there is still a wealth of potential work using just the ASIC data. Due to a number of unpreventable imaging artefacting, we opted to remove a couple of key regions from the analysis during this work, primarily Sagittarius (Sgr) B2. This is a vast complex of gas that contains a bulk of the modern day star formation within the CMZ, several large protoclusters that contain a large number of high-mass YSOs and compact H II regions. Recent work by Ginsburg et al. (2018b) identified a significant population of high-mass protostellar cores contained within Sgr

B2, a large fraction of which do not belong to the previously known large protoclusters, implying that a majority of the cloud is going through a star burst and not just these cluster. The column densities of the gas for which these clusters reside do support a similar threshold as proposed by Lada et al. (2010), however the vast reservoir of gas above this threshold that has no YSOs adds to this picture of some other factor required to explain star formation in these extreme environments. By adding these YSO sources to the analysis done in Chapter 2, we would expect a similar conclusion to be drawn - that of a population of cores that aren't virially bound according to simple virial analysis but appear to be gravitationally bound as a result of the intense pressures within the CMZ, implying that these gas pressures are vital in controlling star formation in galactic centre regions.

Given the complexity and prevalence of some of the key transitions throughout the survey region (specifically ^{12}CO and ^{13}CO), the next important step is to combine these data with single dish data where possible. This process of feathering in single dish observations will allow us to better capture the large-scale emission and will mitigate numerous issues that arise due to the prevalence of these CO isotopologues, both spatially and spectrally. Using *scousepy*, dozens of unique lines were identified and fit across the region. Using this range in molecular transitions, we can calculate core temperatures and densities using radiative transfer codes to paint a clearer picture of the counterplay between dust, radiation and molecular lines within the CMZ.

One unanswered question regarding star formation within the CMZ is if there is a particular mechanism that triggers its onset, with recent predictions suggesting that passage through the bottom of the gravitational potential – i.e. past Sagittarius A* – triggers cloud collapse and in turn, the formation of protostellar cores. An upcoming paper from Hatchfield et. al. (in prep) will investigate star formation tracer activity for each of the dendrogram leaves, which combined with the spectral line data, will help test this prediction. With a complete catalog of dense cores, star formation tracer associations and measurements of virial parameters, we can begin to combine these data with orbital models to test this prediction. If passage past Sagittarius A* is in fact the trigger, we would expect to see cores approaching this position in the orbit to have lower virial parameters and cores beyond this position to have increasing numbers of masers, 24μm and 70 μm sources. Estimates of ages from regions of known star formation could further add to this orbital model.

We identified three cores within cloud 'b' with no detected lines but continuum fluxes equivalent to that of cores with ≥ 9 detected lines. This lack of spectral line emission is a key prediction for precursor pre-stellar cores of 'totally metal' stars, a rare (1 in 10^4) population of stars with metallicities of Z $\sim$ 1 that have been predicted to exist (Hopkins, 2014). These cores are therefore interesting candidates as sites of possible formation for this hypothetical stellar population, which would represent a brand new pathway for stellar evolution.

While two proto-stellar outflows were detected as spatially resolved structures throughout the survey, there are a number of spectra that show line wings typically representative of an outflow. Additionally, a number of possible outflows were detected in by-eye examinations of integrated intensity moment maps. Following these sources up with higher spectral and spatial resolution observations with ALMA may highlight a handful of proto-stellar outflows that the CMZoom survey was only marginally sensitive to. Although this won't change the results of Chapter 2 (that there is no hidden population of very young high-mass star forming regions that have been missed by previous surveys), given the rarity of cores with any star formation activity in the CMZ, any additional sources will be useful to follow up.

The work presented in Chapter 3 sets the framework for a powerful exploration into the extreme conditions of extragalactic centres and the behaviour of gas and dust therein. While the selection criteria for this method is necessarily quite strict, requiring Milky Way-like galaxies with low inclination angles that are sufficiently close enough to study kinematics down to the scales of individual clouds. By repeating this analysis across a larger number of galaxies, both starbursting galaxies or otherwise, we can start to paint a more full picture of this potential 10 Myr star formation cycle within galactic centres and gain a better understanding of the processes of star formation within these unique regions.

Appendix A

Appendix

A.1 Appendix 1: CMZoom Moment Maps

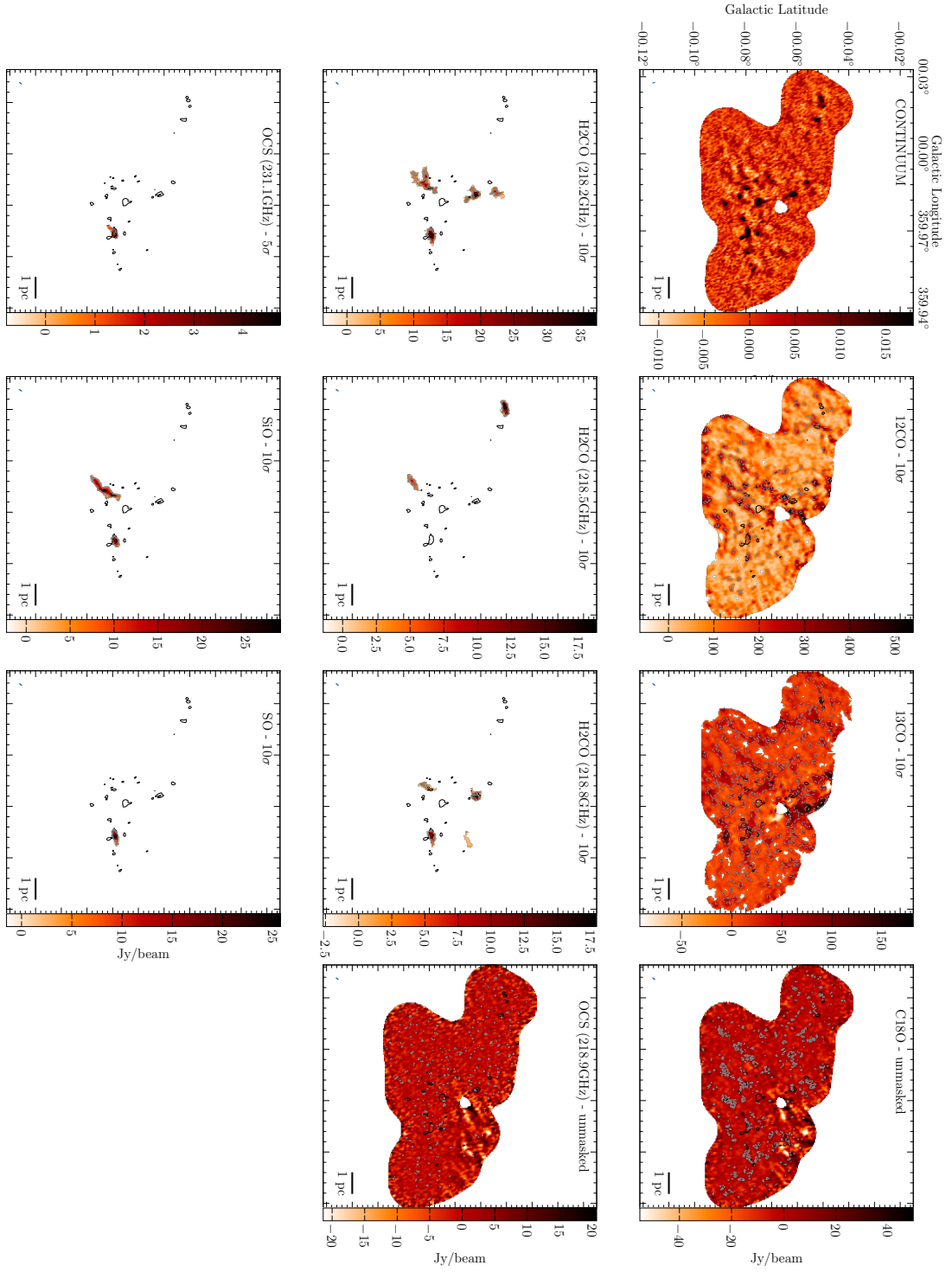

FIGURE A.1: G0.001-0.058 integrated intensity moment maps

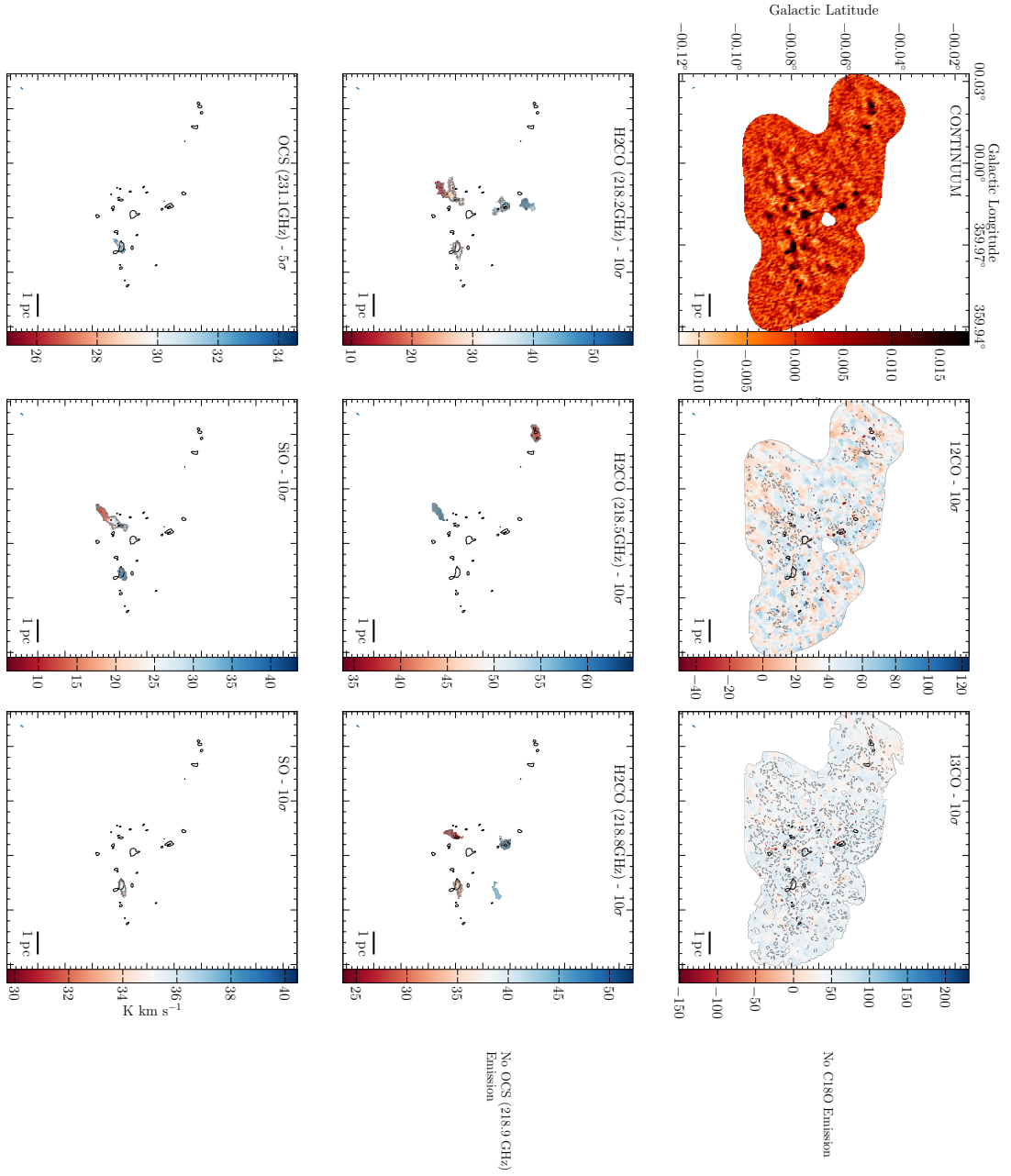

FIGURE A.2: G0.001-0.058 V_{LSR} moment maps

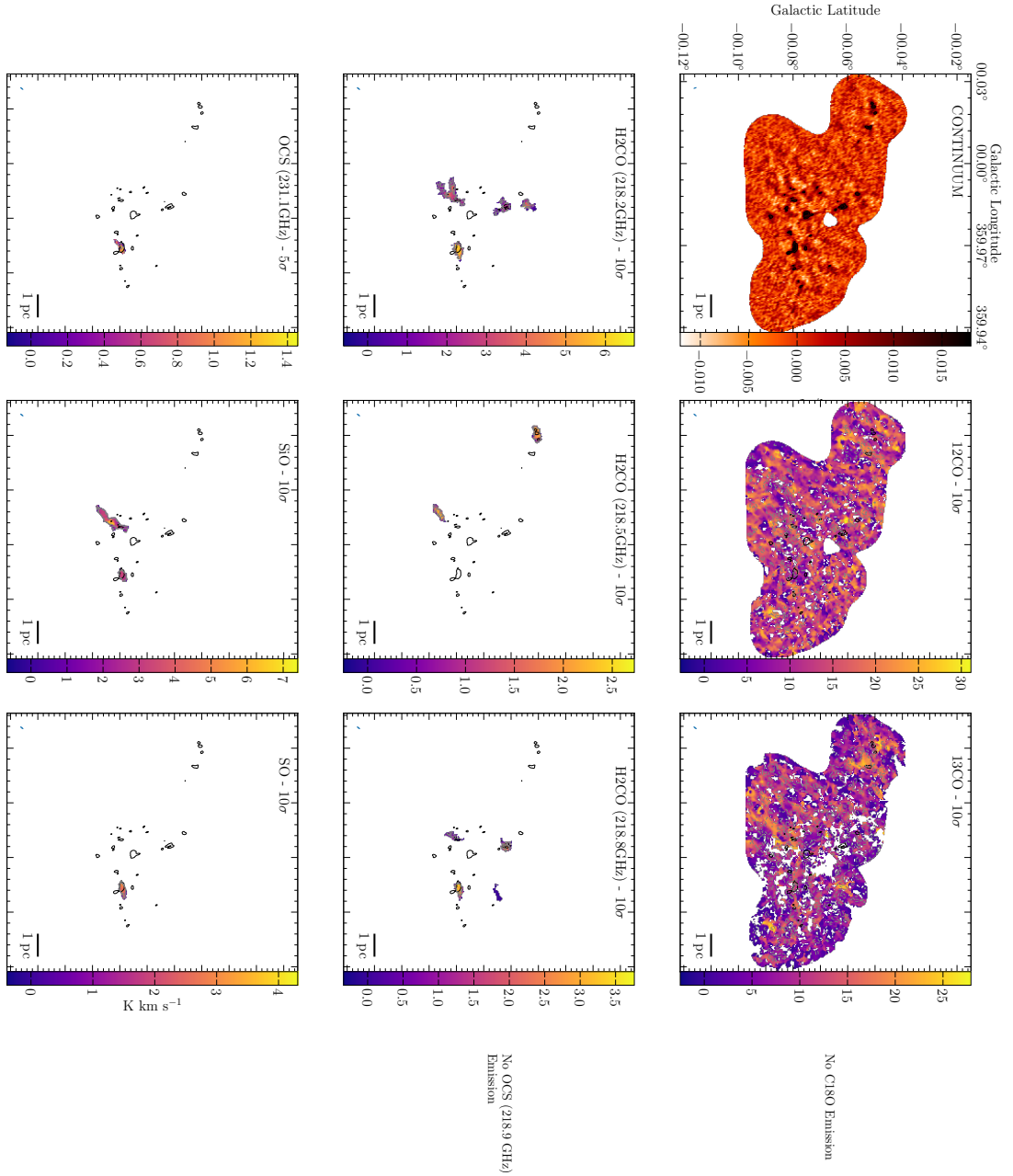

FIGURE A.3: G0.001-0.058 velocity dispersion moment maps

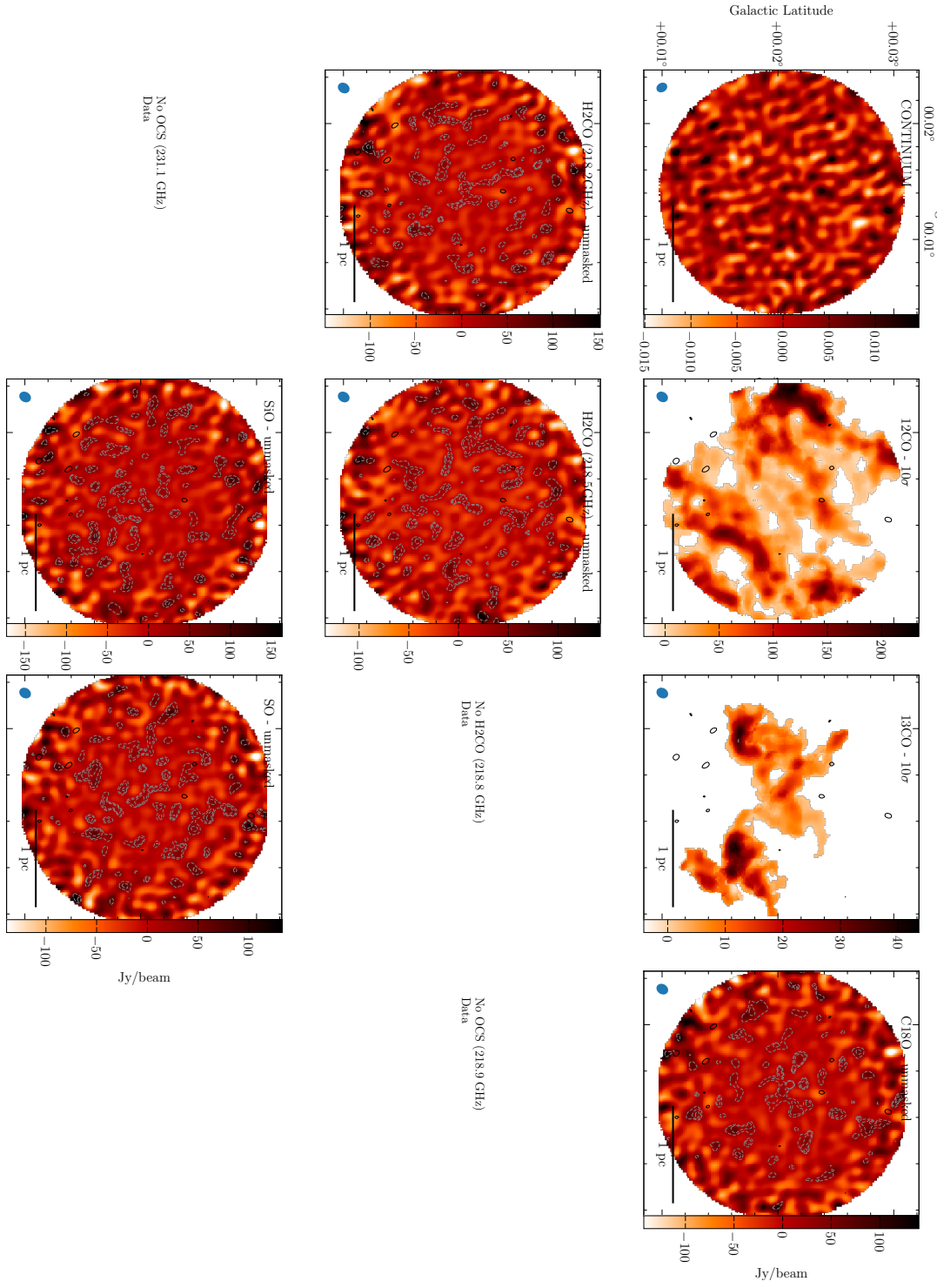

FIGURE A.4: G0.014+0.021 integrated intensity moment maps

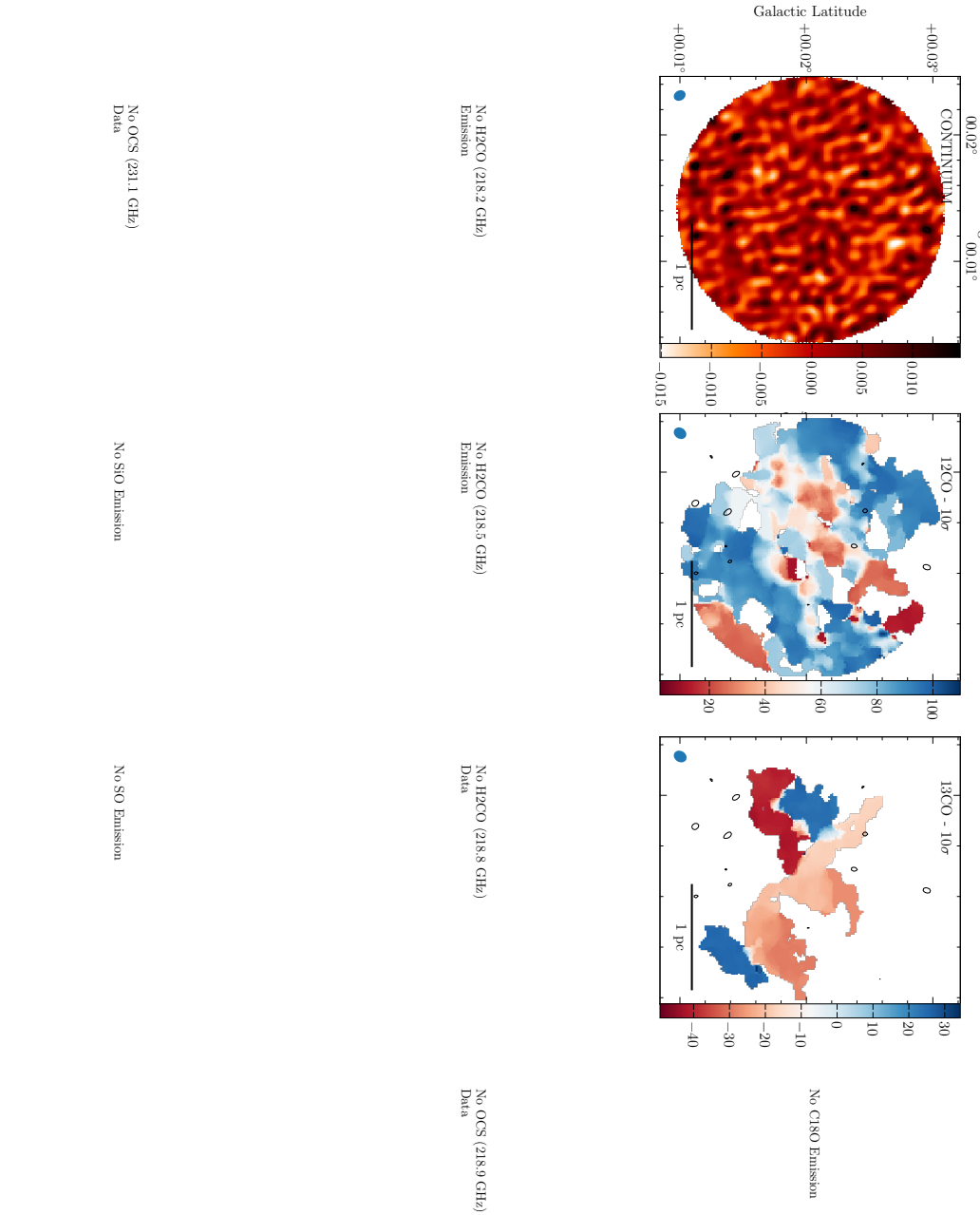

FIGURE A.5: G0.014+0.021 V_{LSR} moment maps

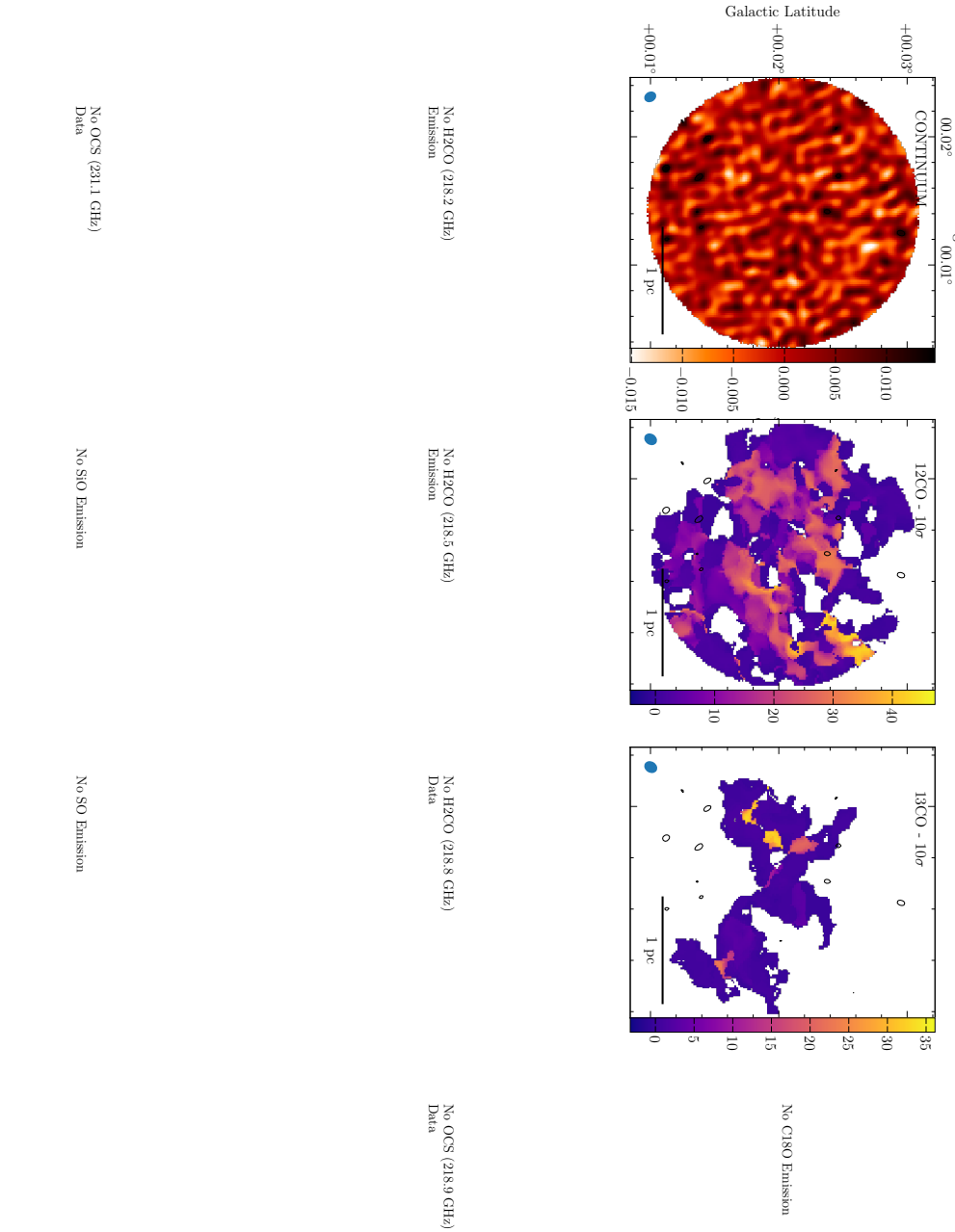

FIGURE A.6: G0.014+0.021 velocity dispersion moment maps

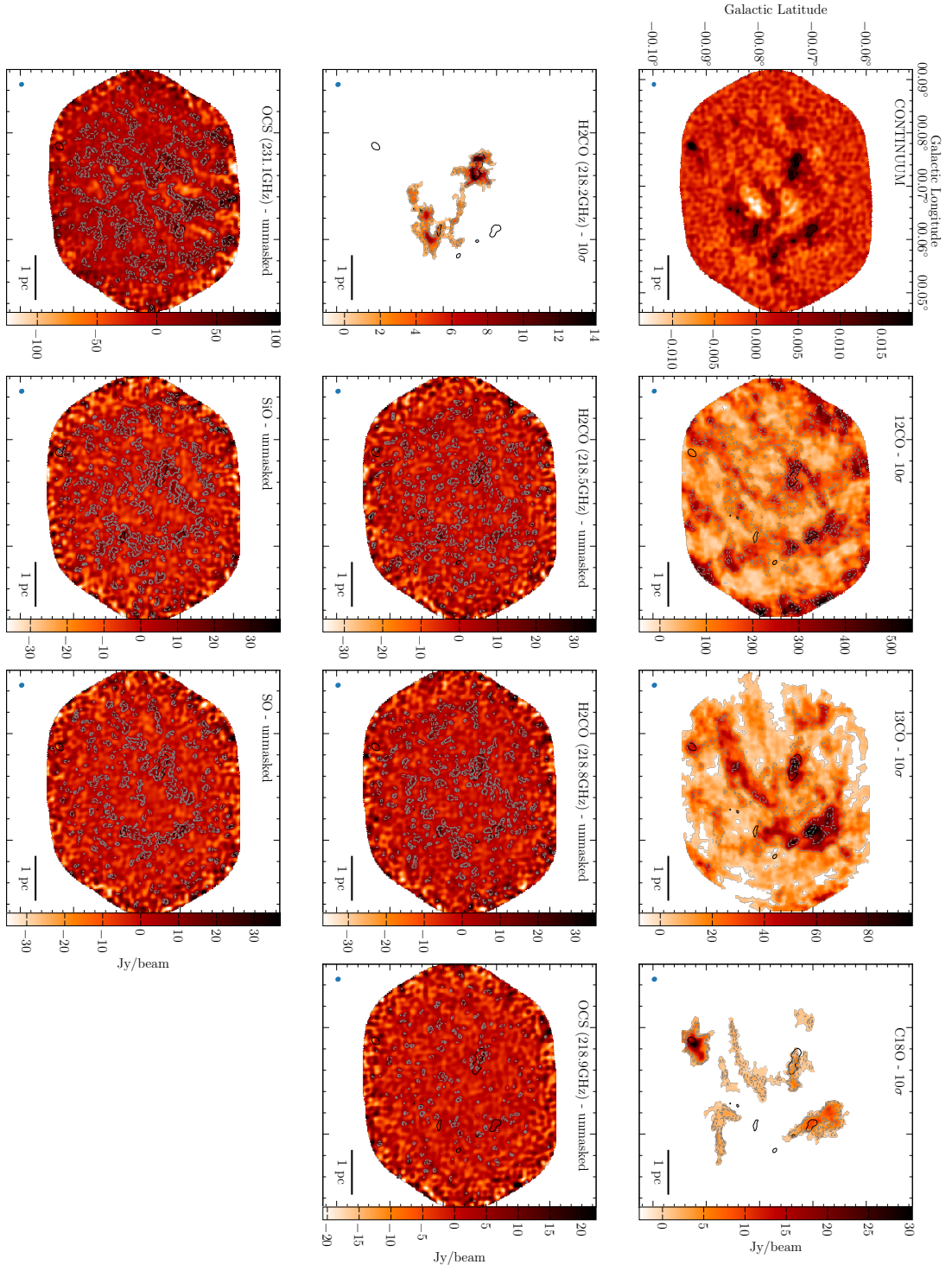

FIGURE A.7: G0.068-0.075 integrated intensity moment maps

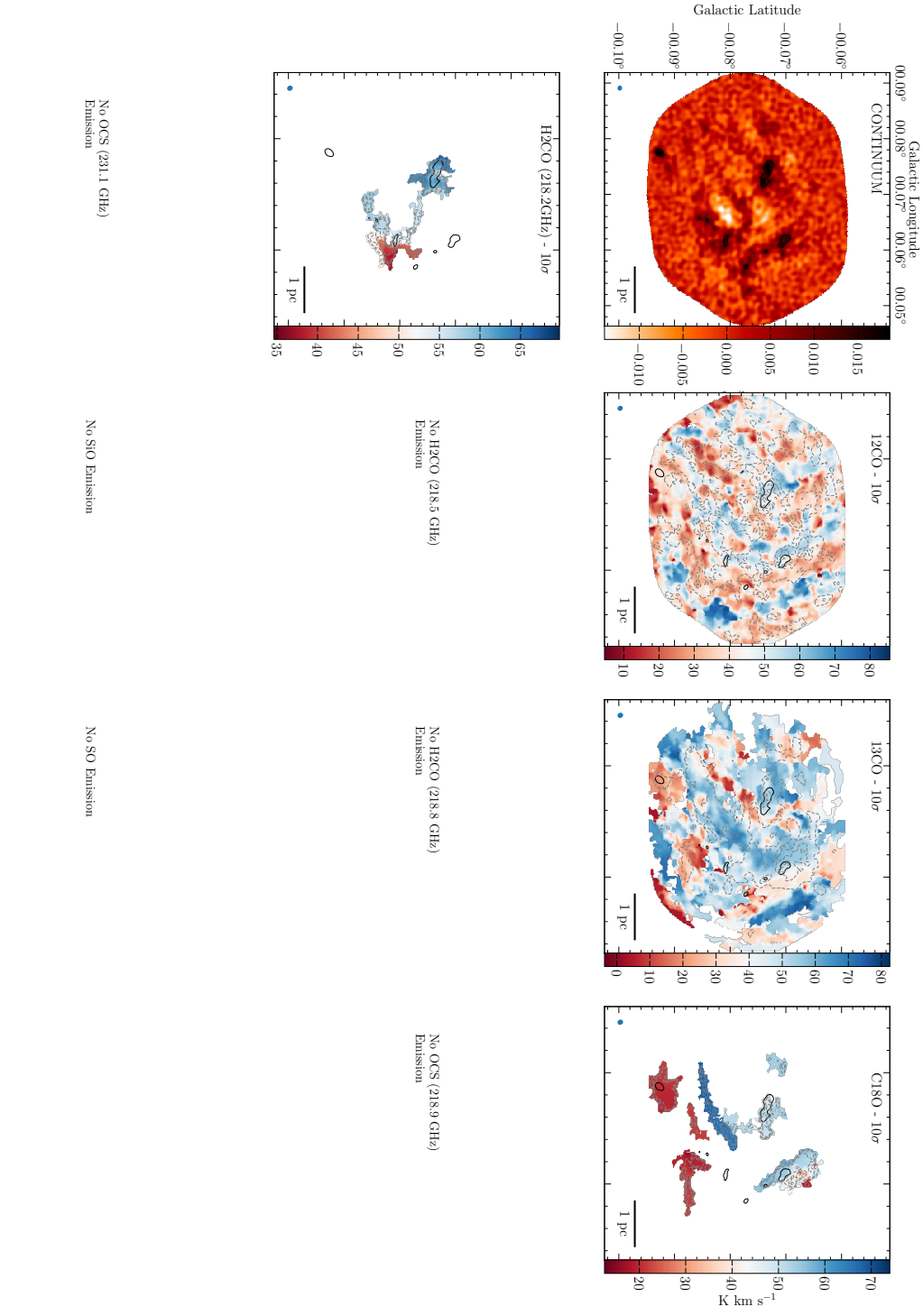

FIGURE A.8: G0.068-0.075 V_{LSR} moment maps

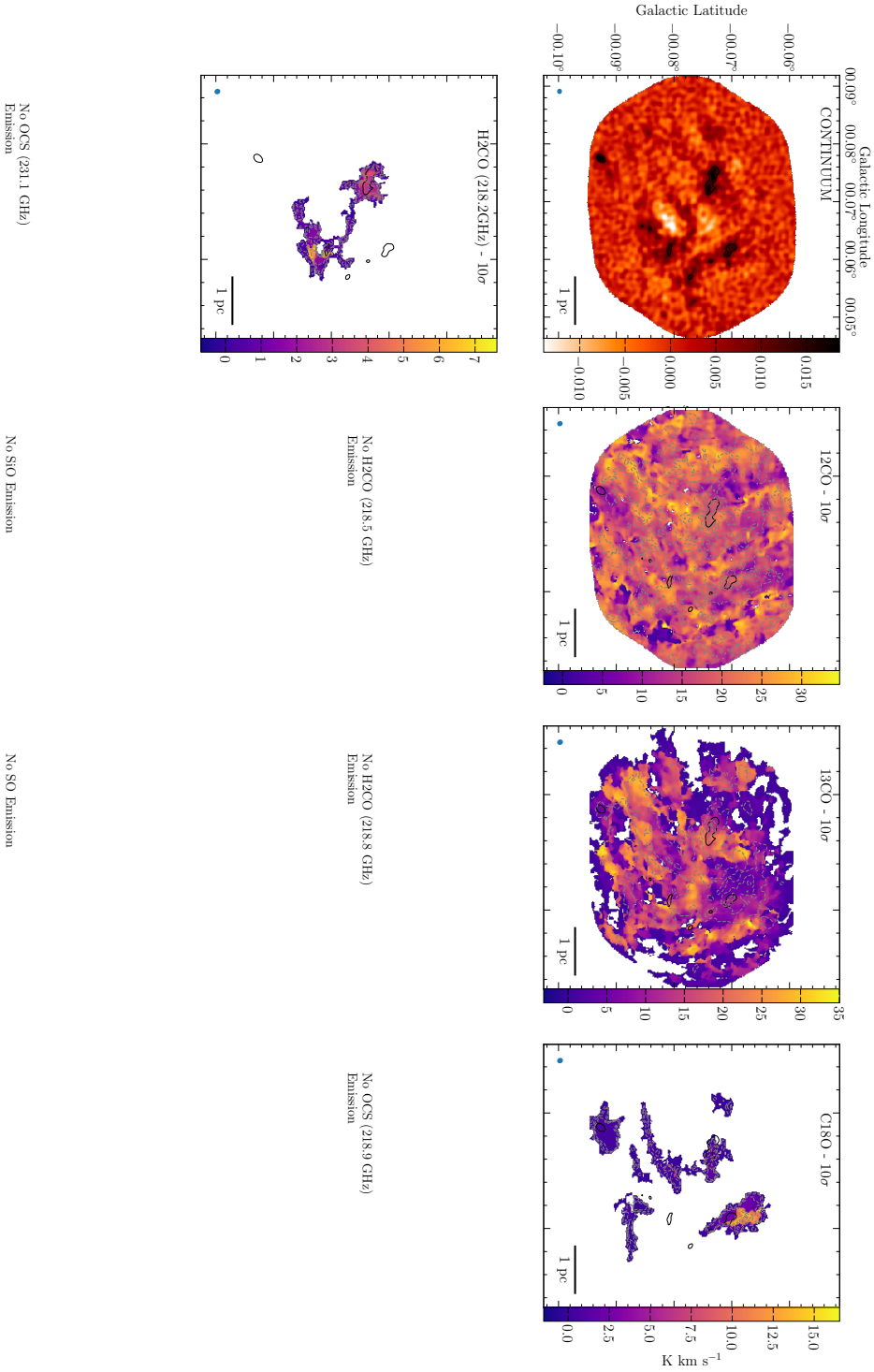

FIGURE A.9: G0.068-0.075 velocity dispersion moment maps

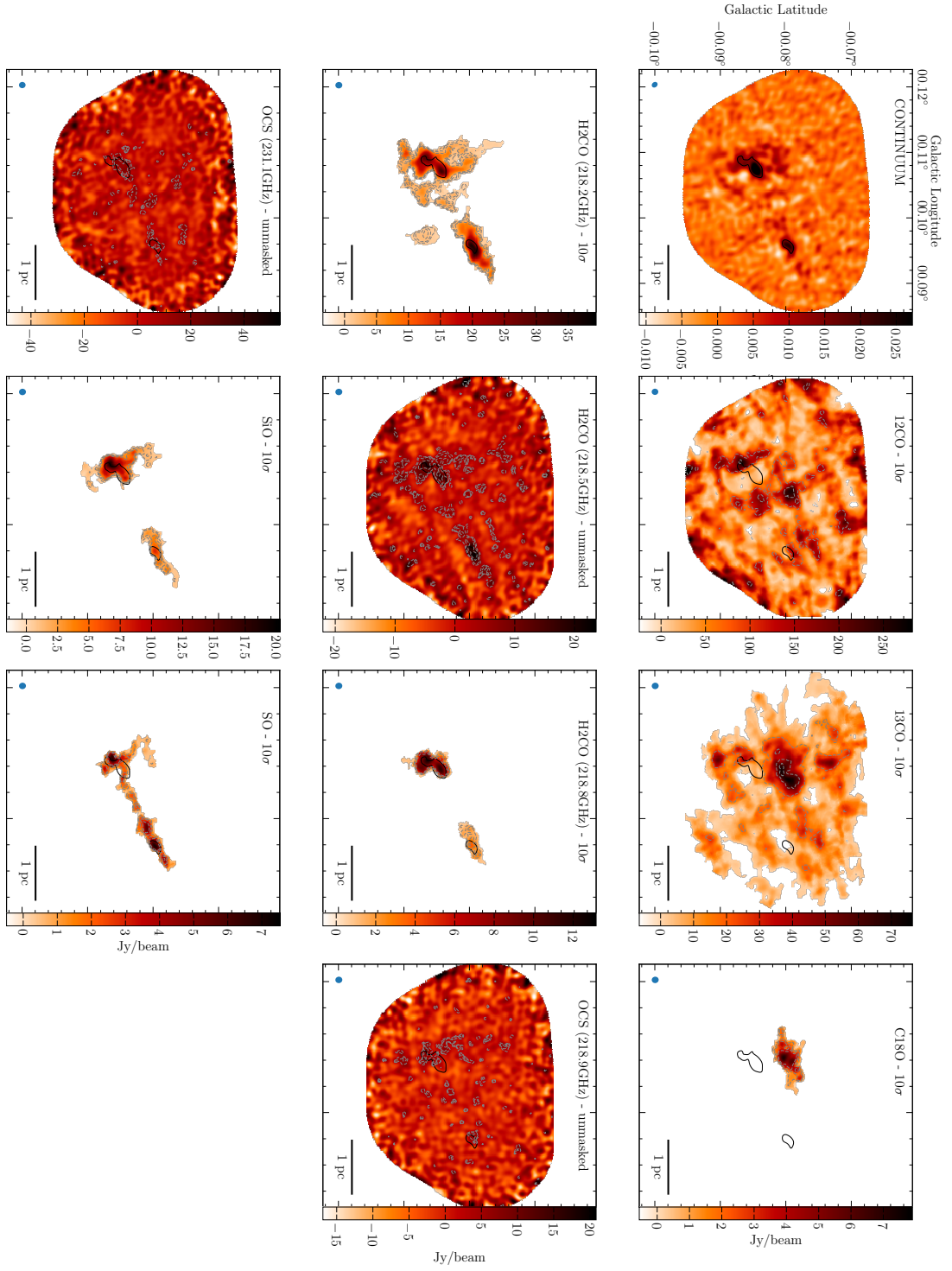

FIGURE A.10: G0.106-0.082 integrated intensity moment maps

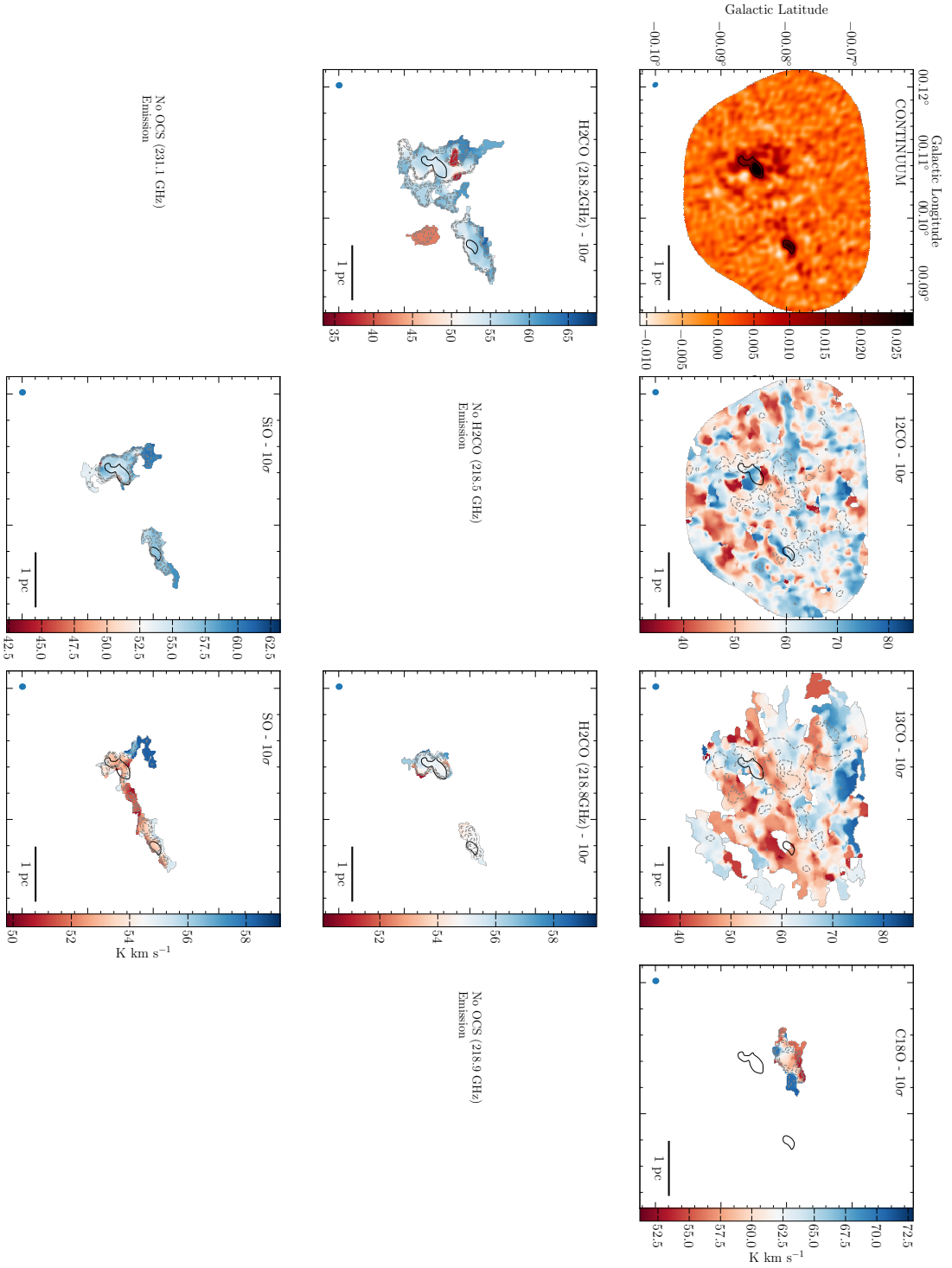

FIGURE A.11: G0.106-0.082 V_{LSR} moment maps

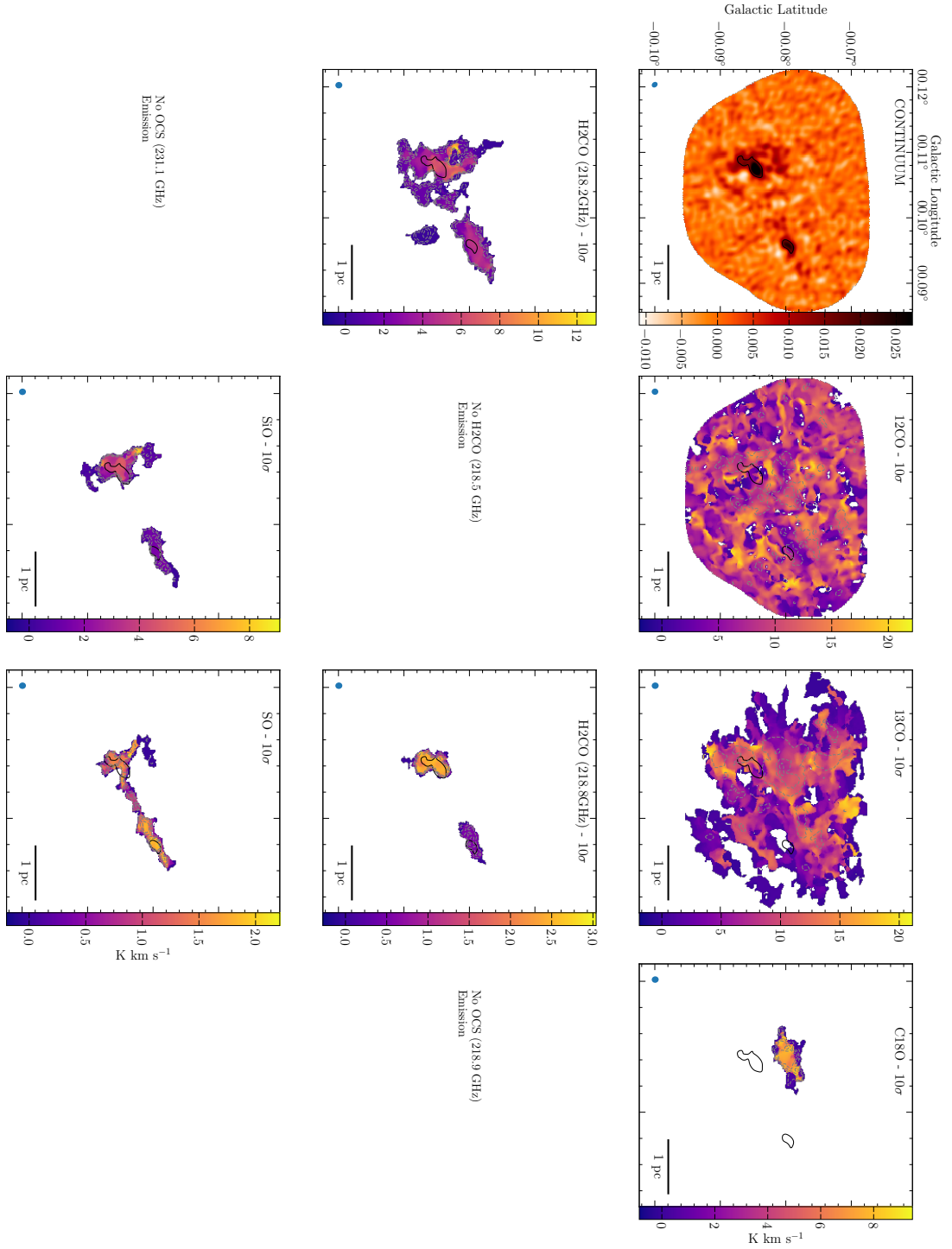

FIGURE A.12: G0.106-0.082 velocity dispersion moment maps

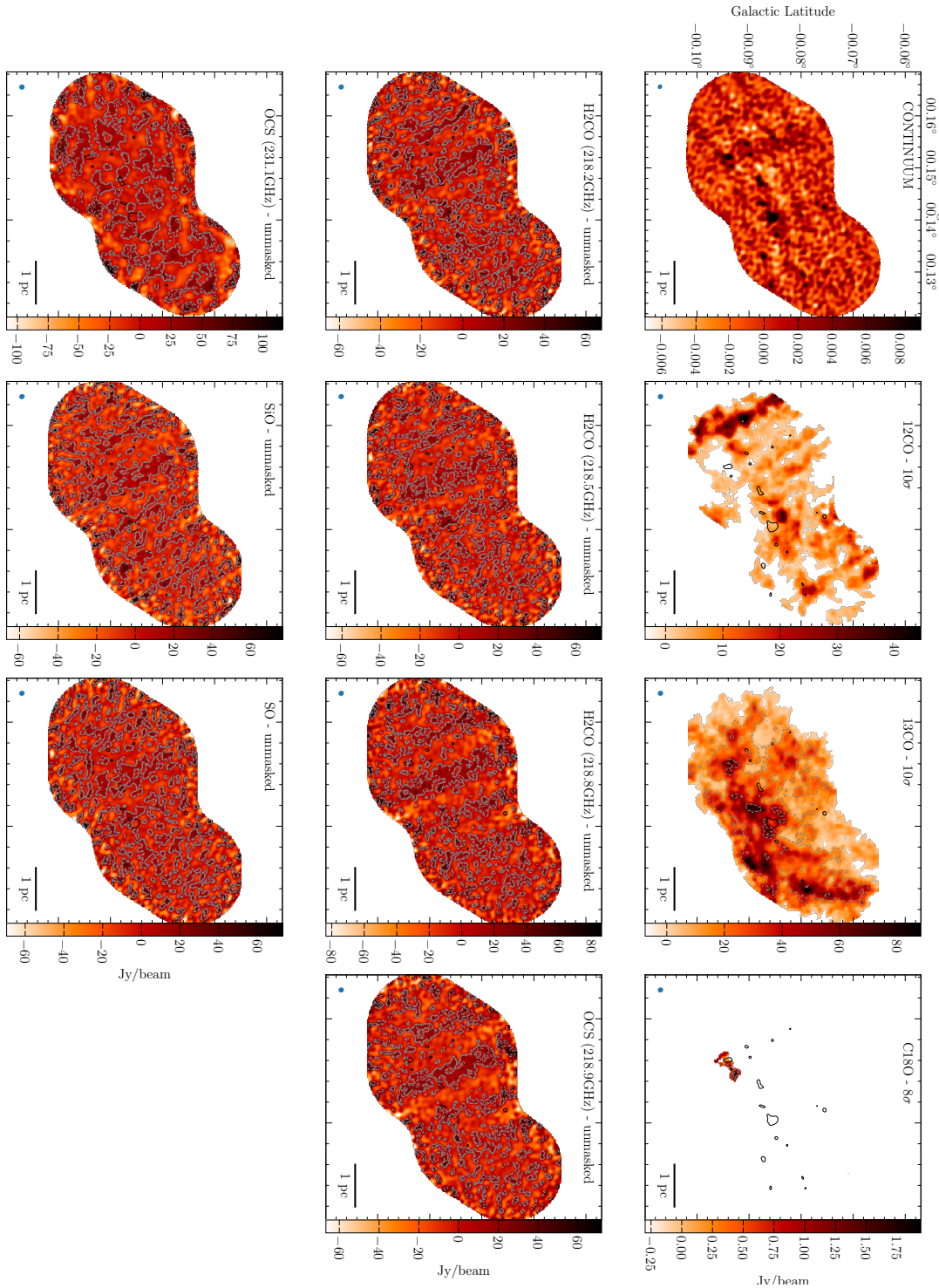

FIGURE A.13: G0.145-0.086 integrated intensity maps moment maps

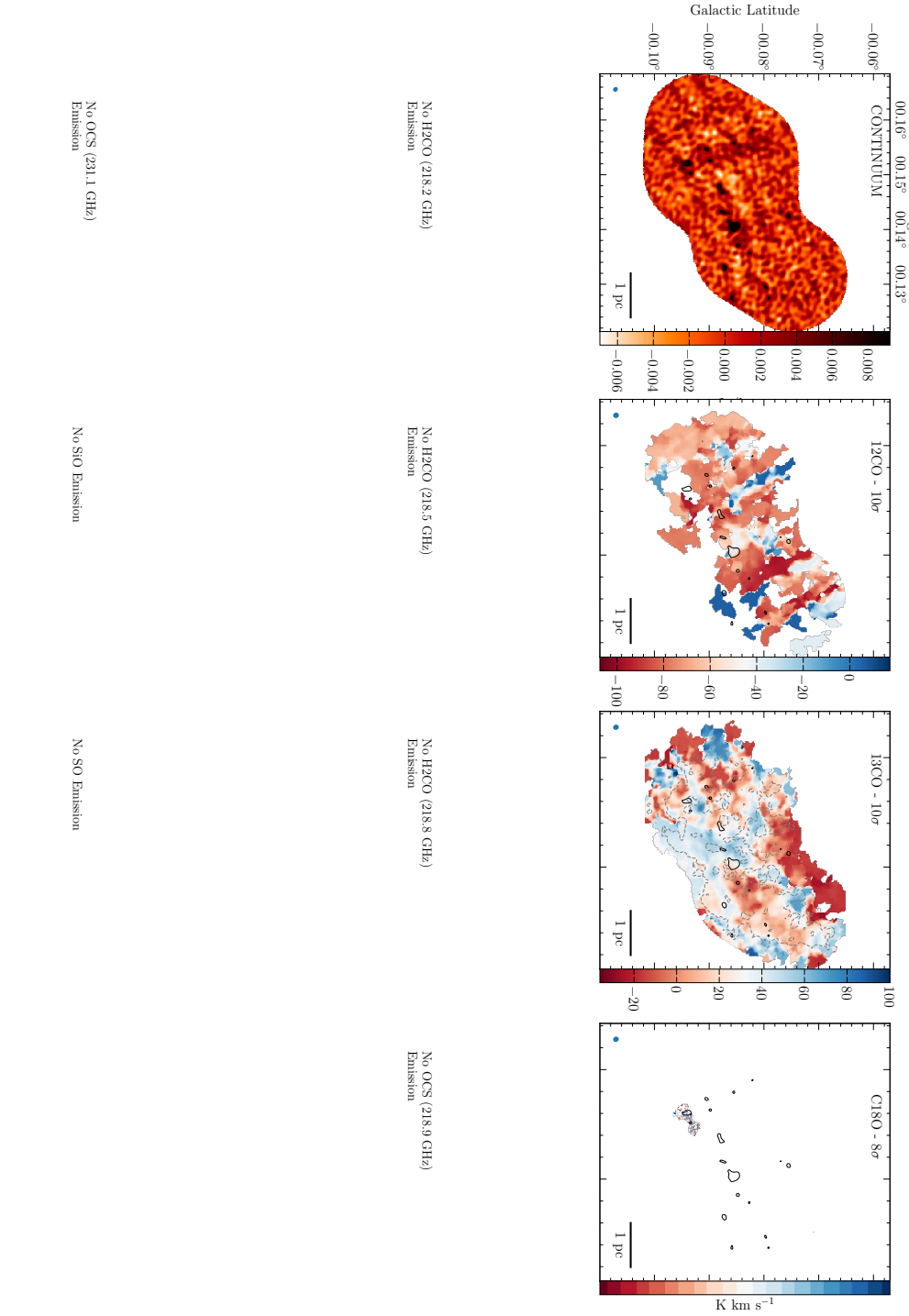

FIGURE A.14: G0.145-0.086 V_{LSR} moment maps

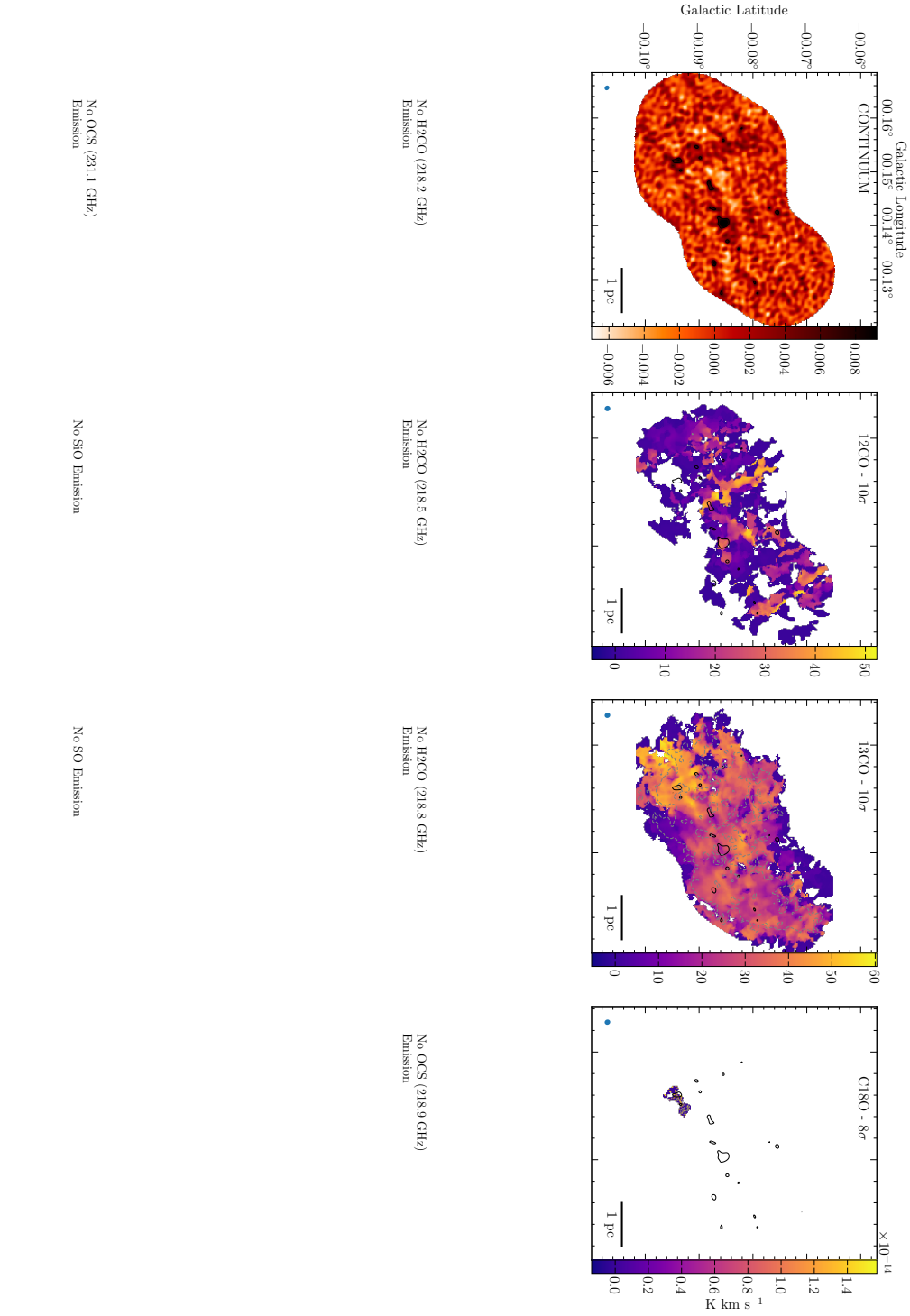

FIGURE A.15: G0.145-0.086 velocity dispersion moment maps

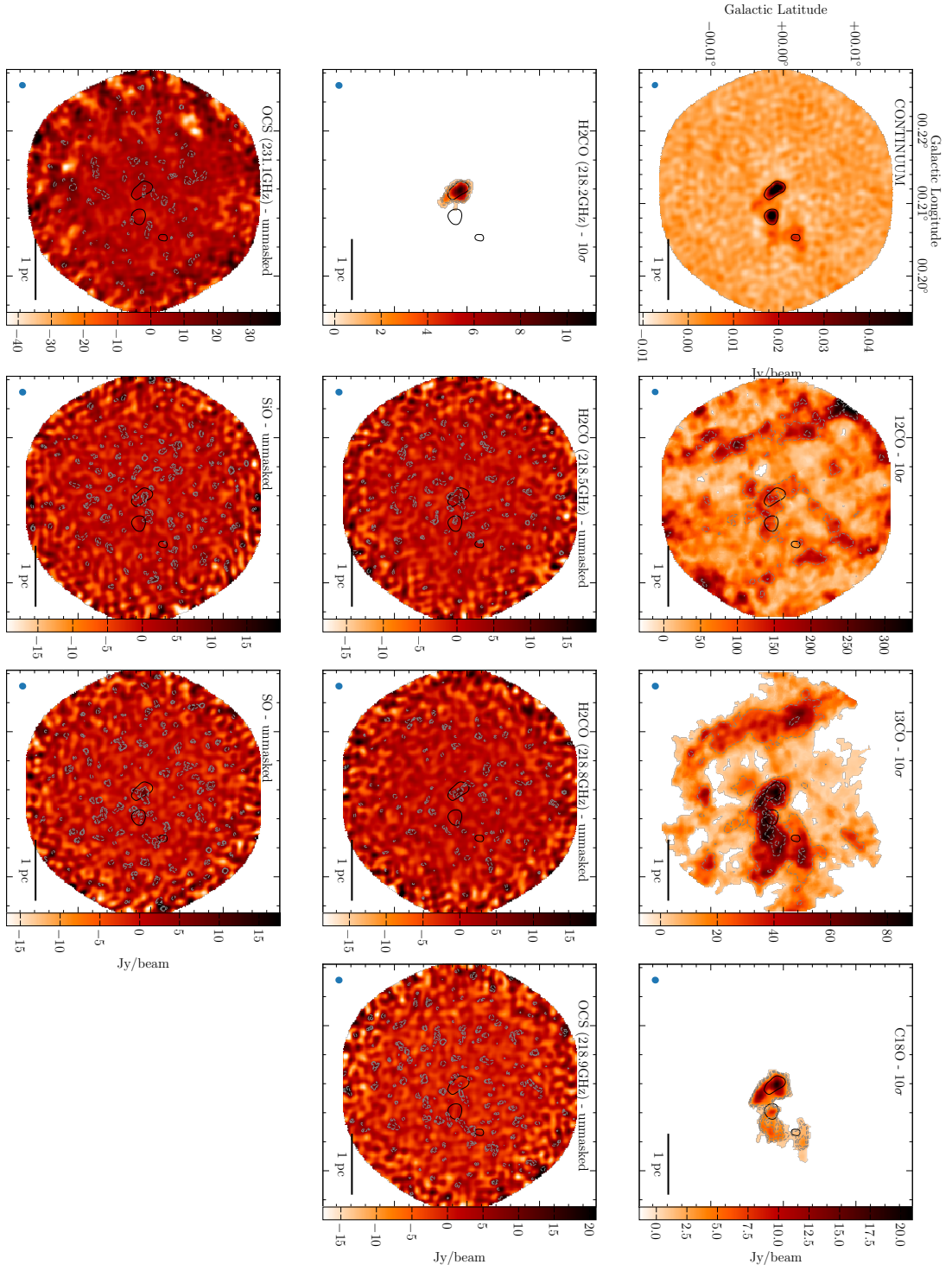

FIGURE A.16: G0.212-0.001 integrated intensity moment maps

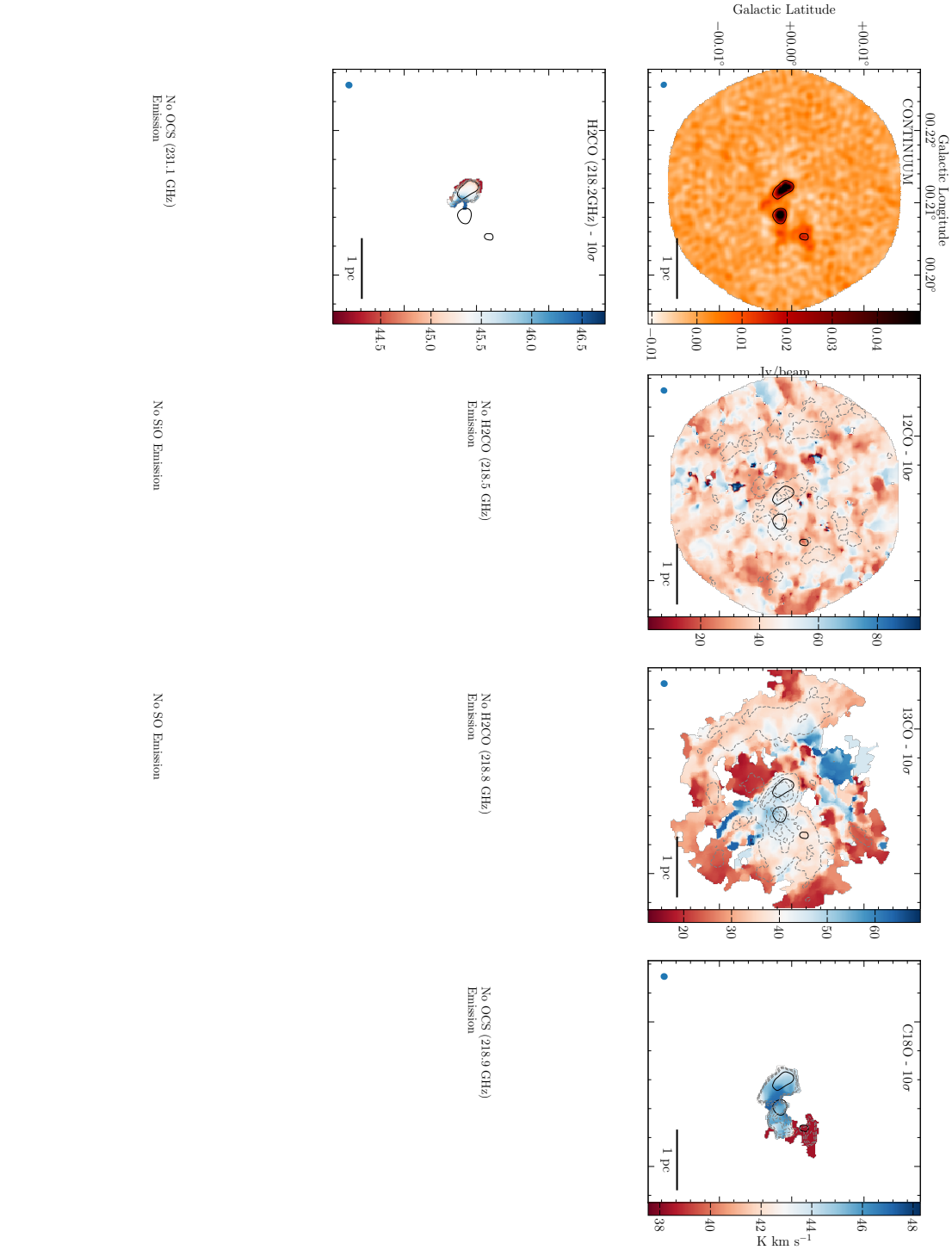

FIGURE A.17: G0.212-0.001 V_{LSR} moment maps

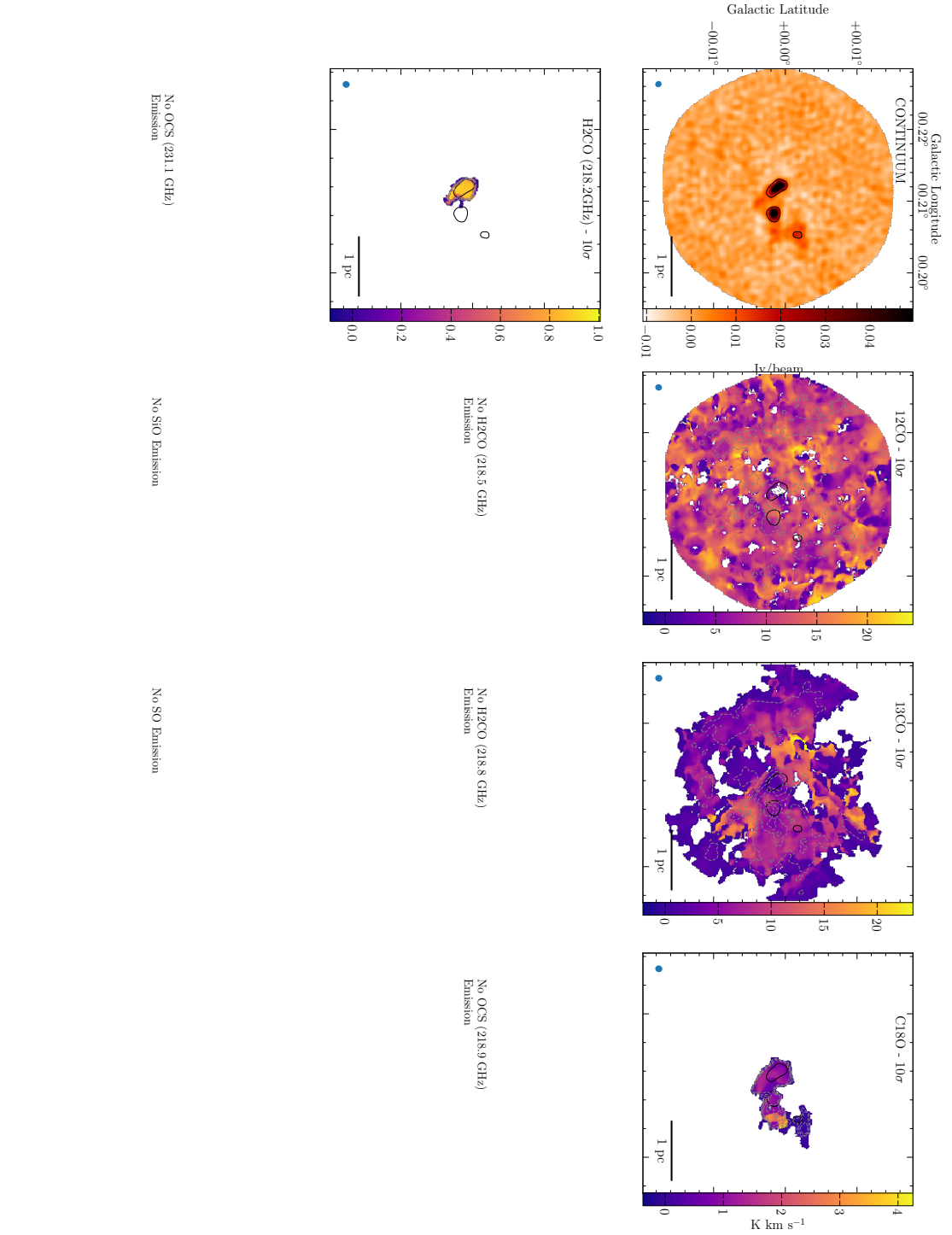

FIGURE A.18: G0.212-0.001 velocity dispersion moment maps

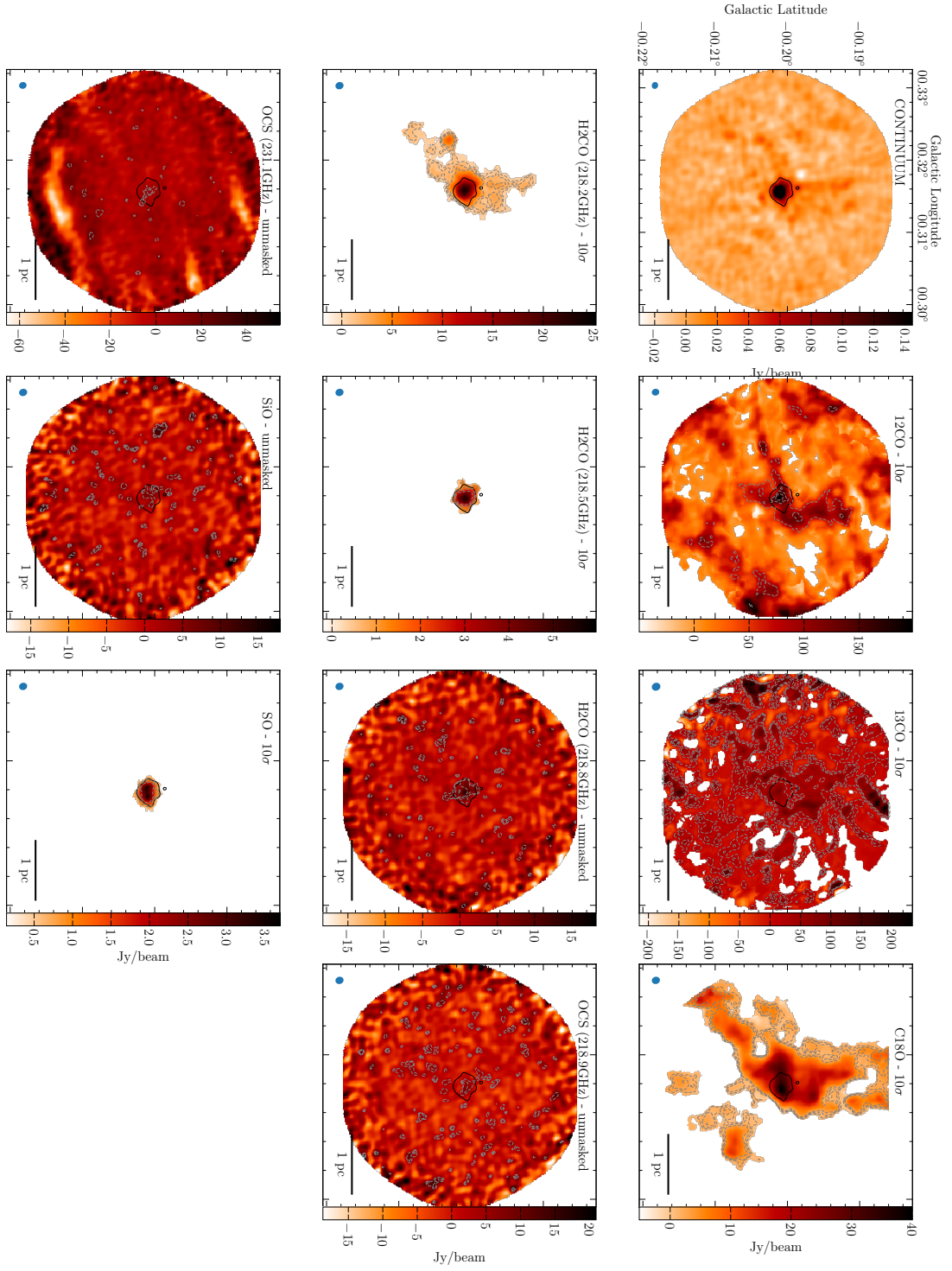

FIGURE A.19: G0.316-0.201 integrated intensity moment maps

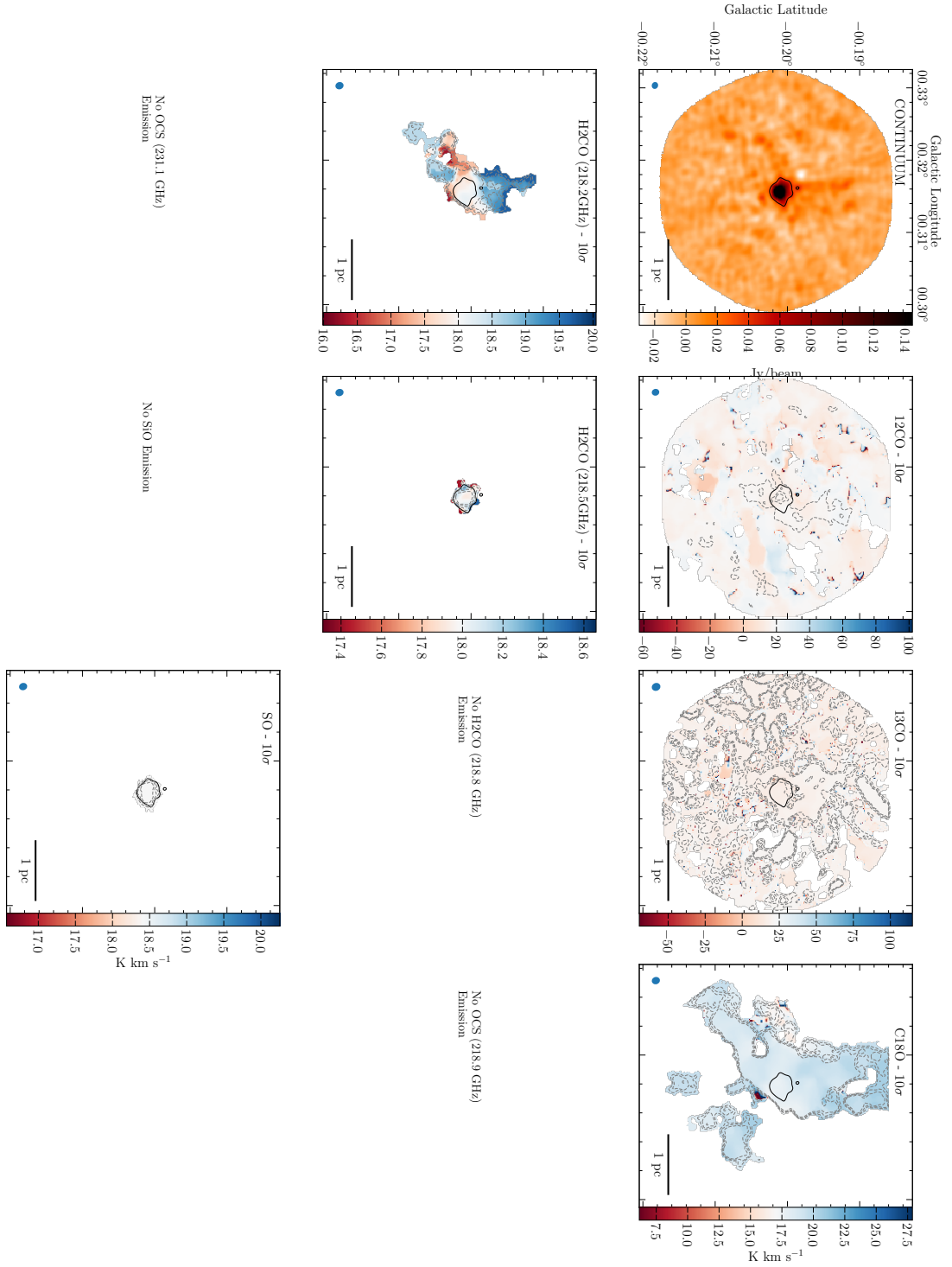

FIGURE A.20: G0.316-0.201 V_{LSR} moment maps

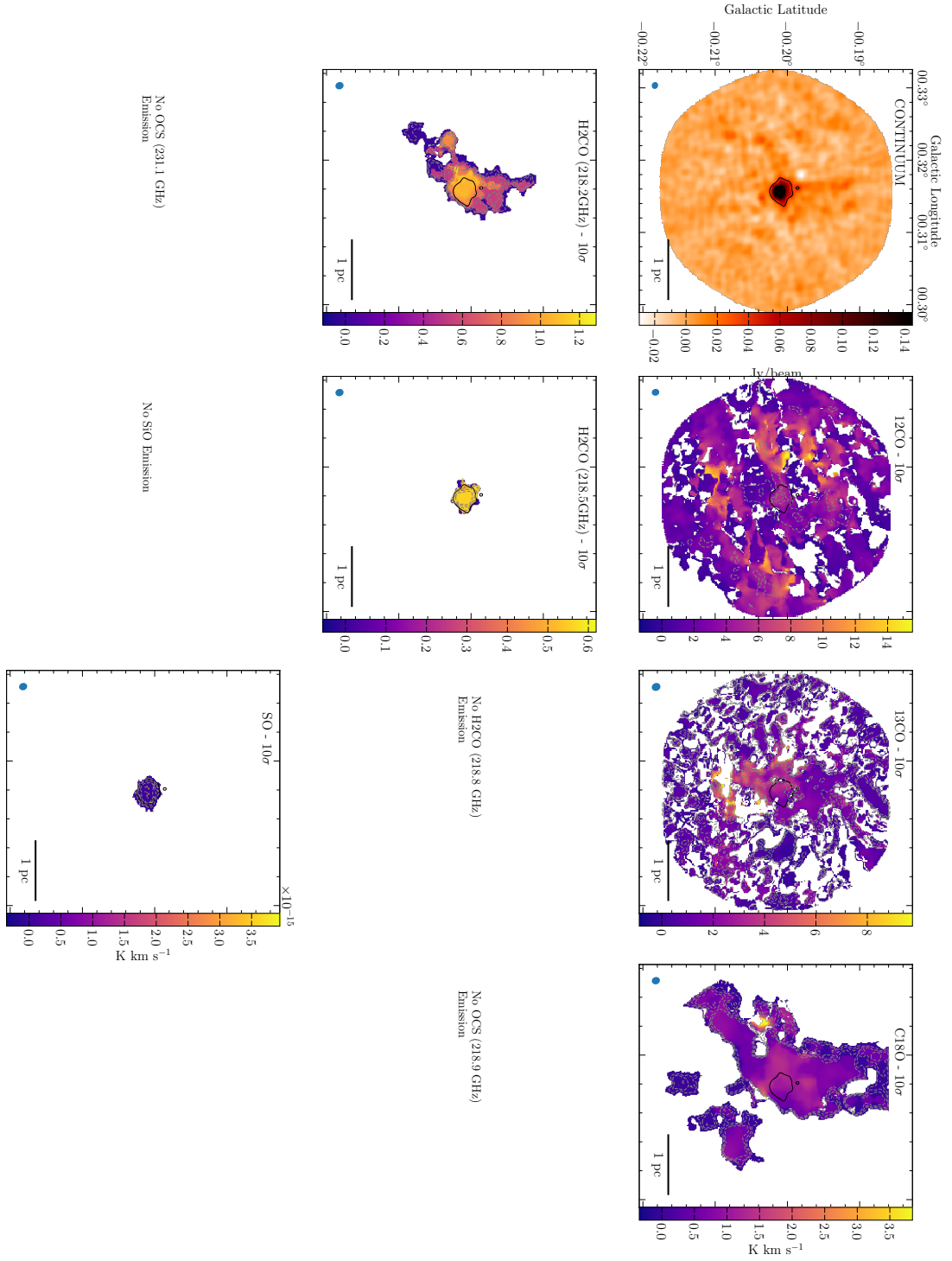

FIGURE A.21: G0.316-0.201 velocity dispersion moment maps

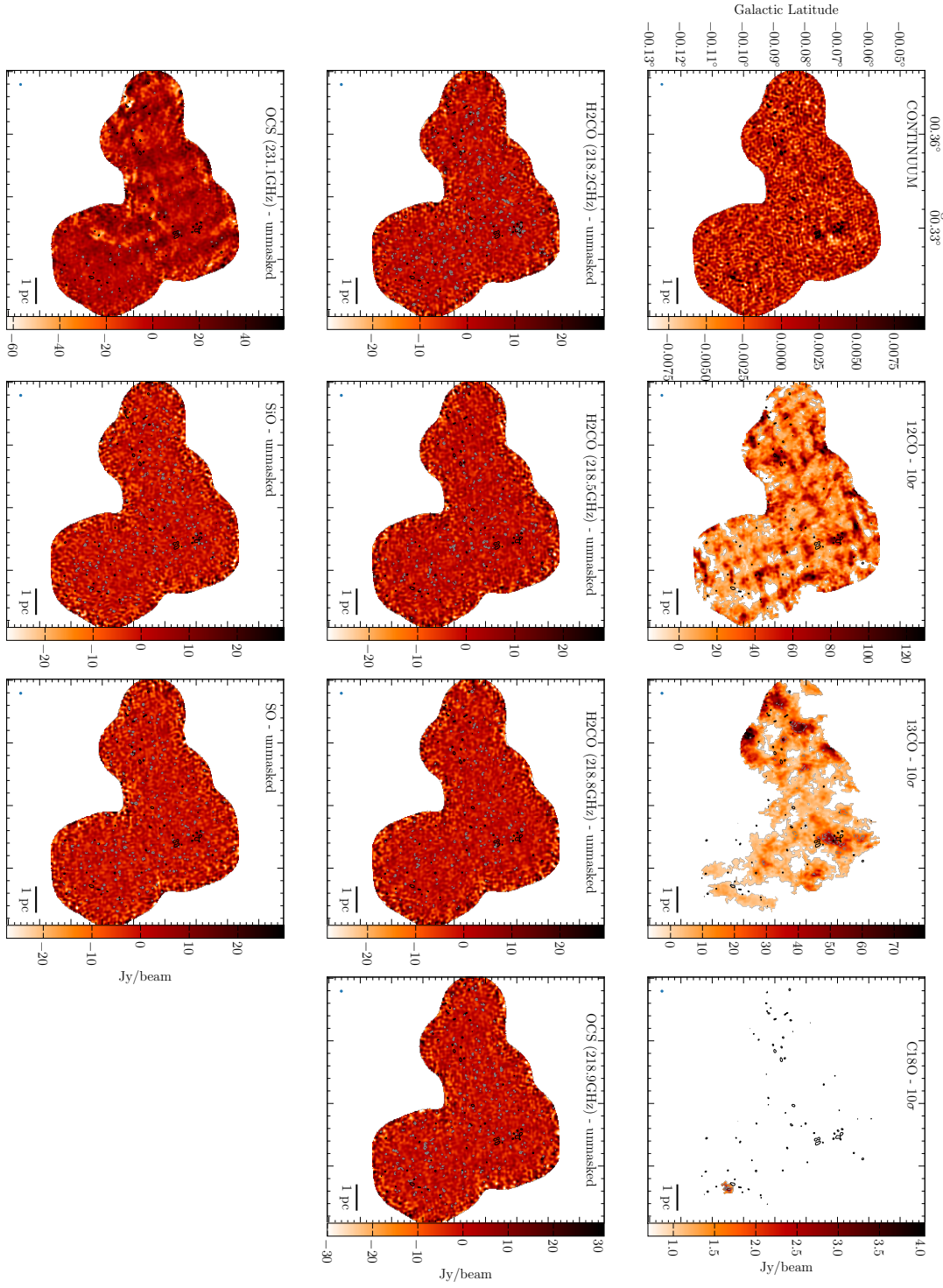

FIGURE A.22: G0.326-0.085 integrated intensity moment maps

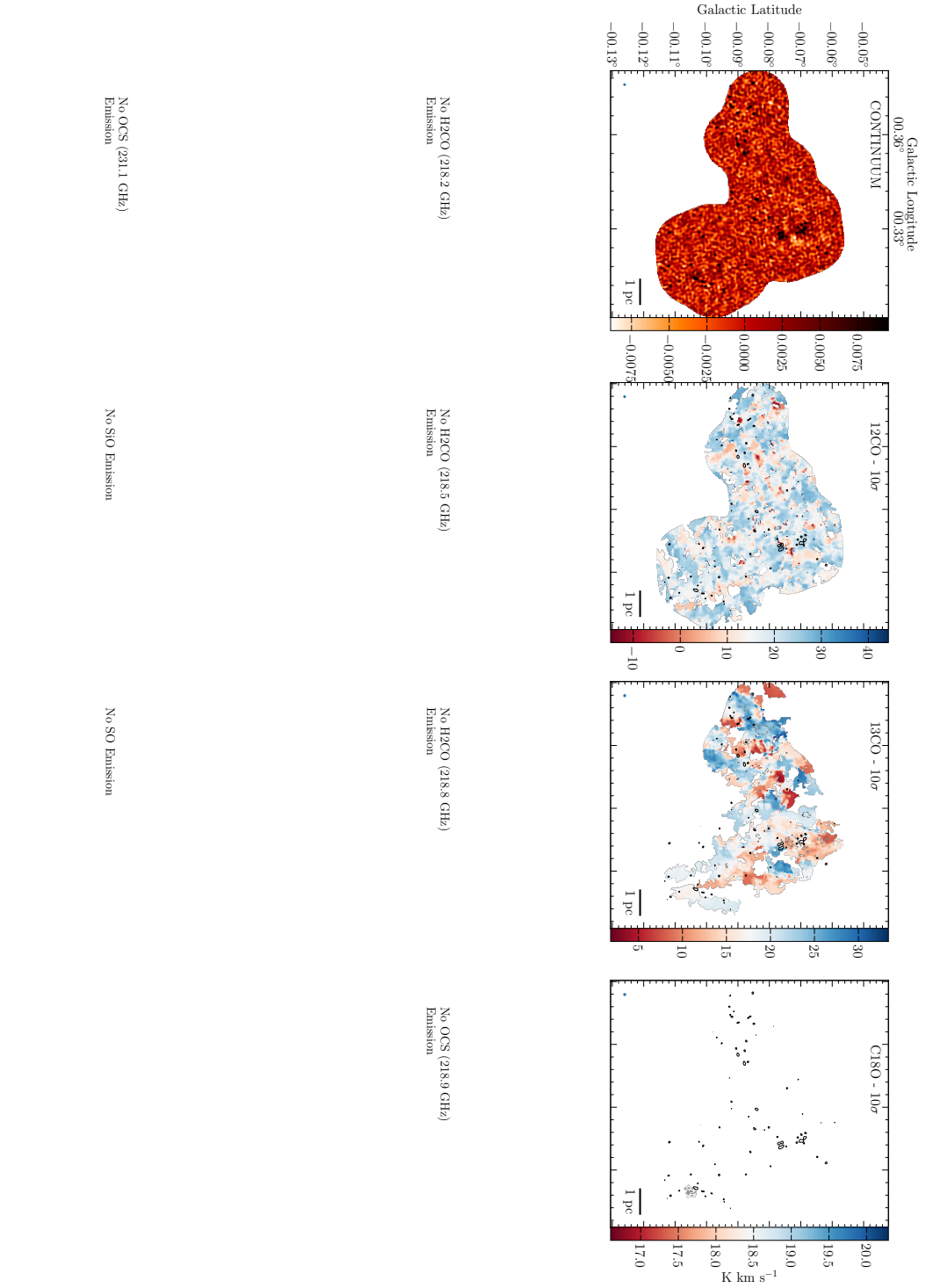

FIGURE A.23: G0.326-0.085 V_{LSR} moment maps

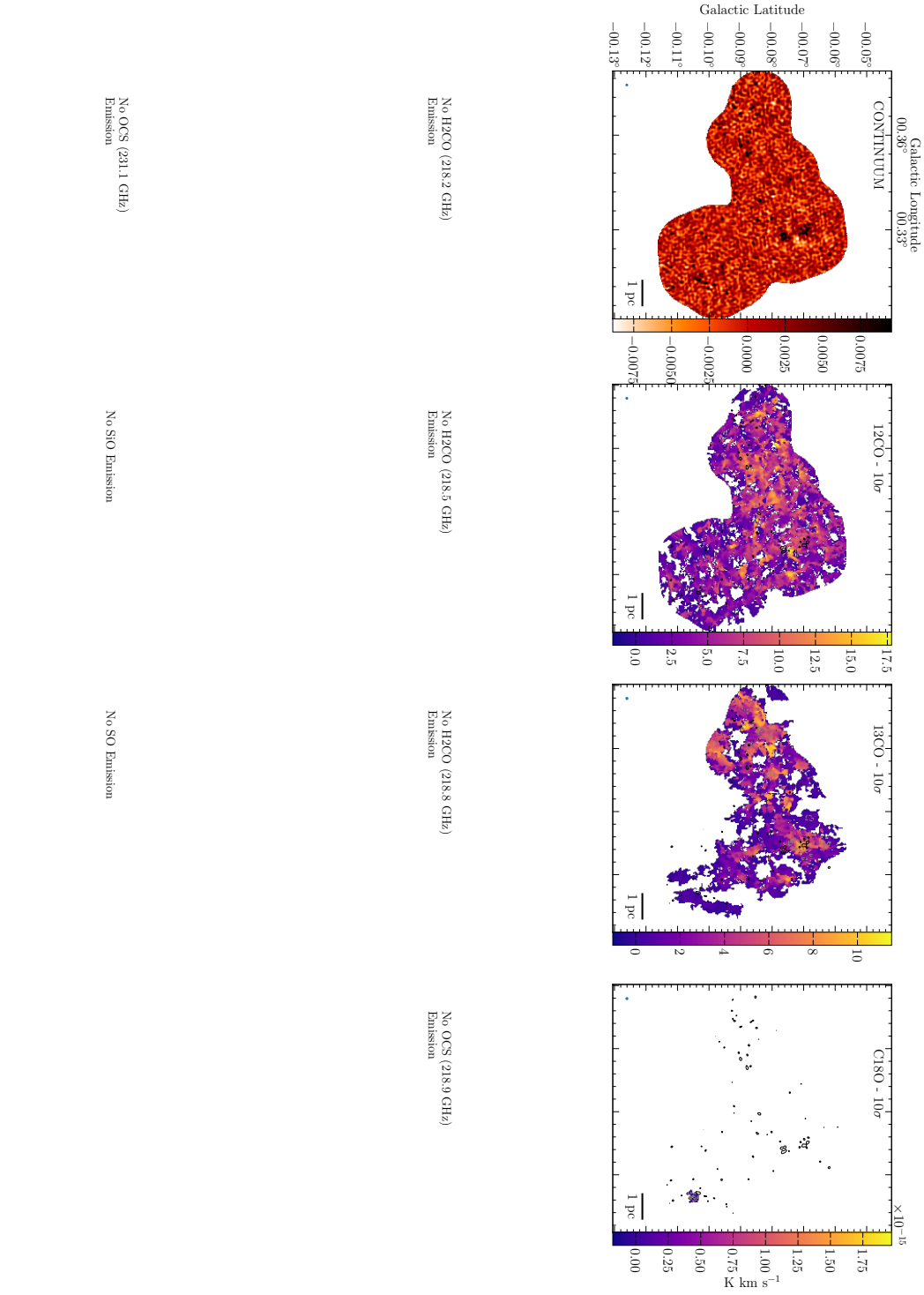

FIGURE A.24: G0.326-0.085 velocity dispersion moment maps

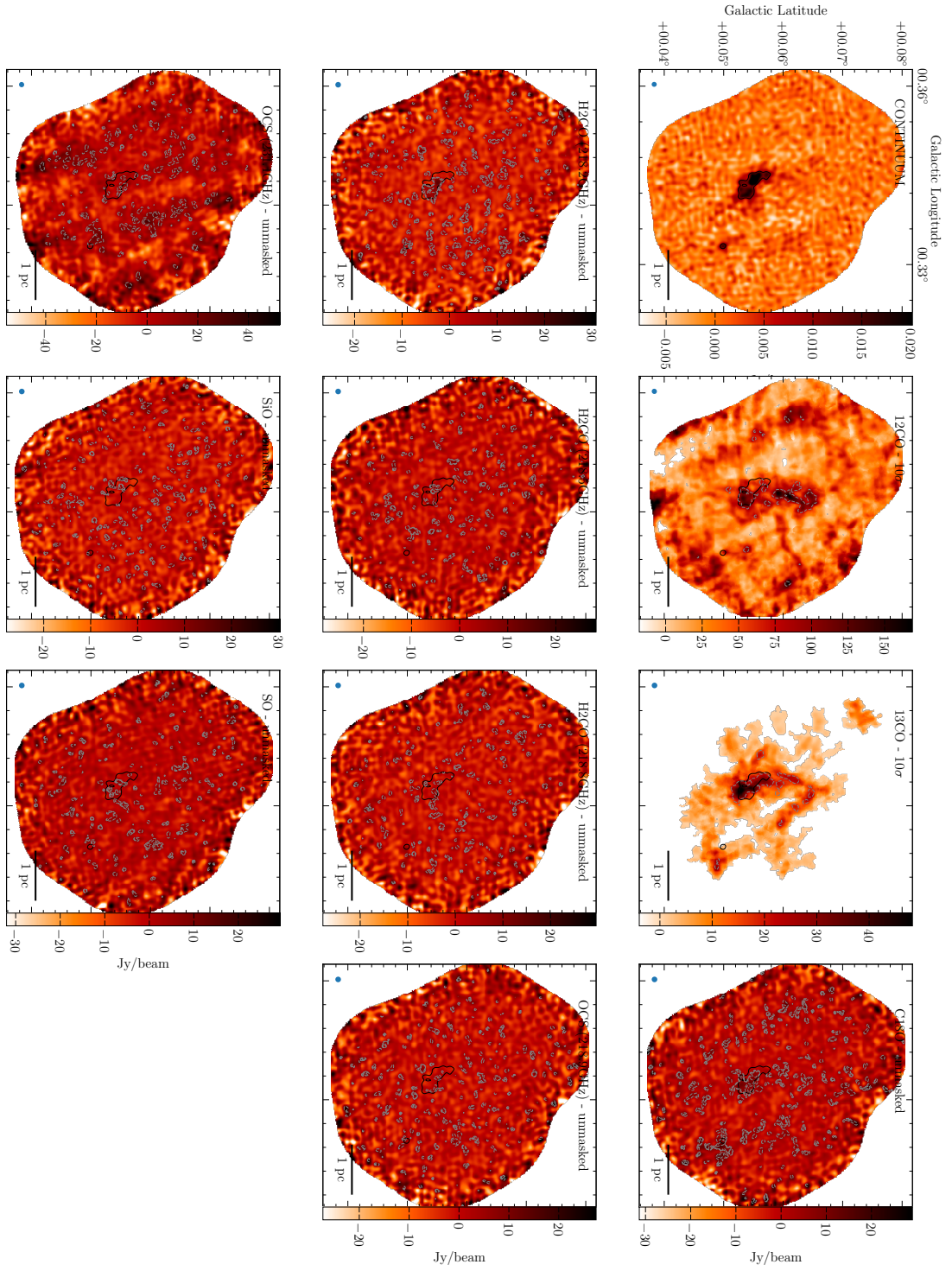

FIGURE A.25: G0.340-0.055 integrated intensity moment maps

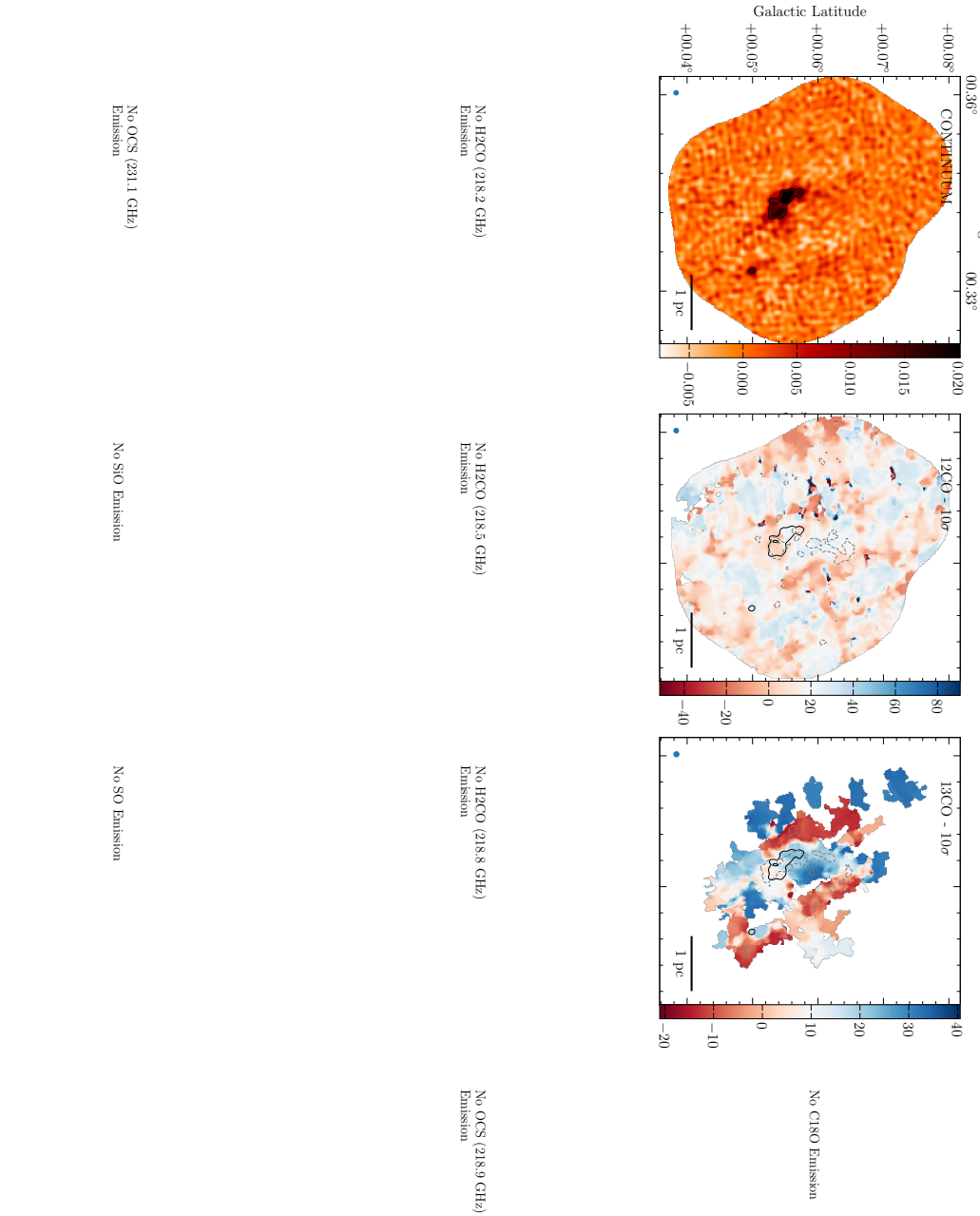

FIGURE A.26: G0.340-0.055 V_{LSR} moment maps

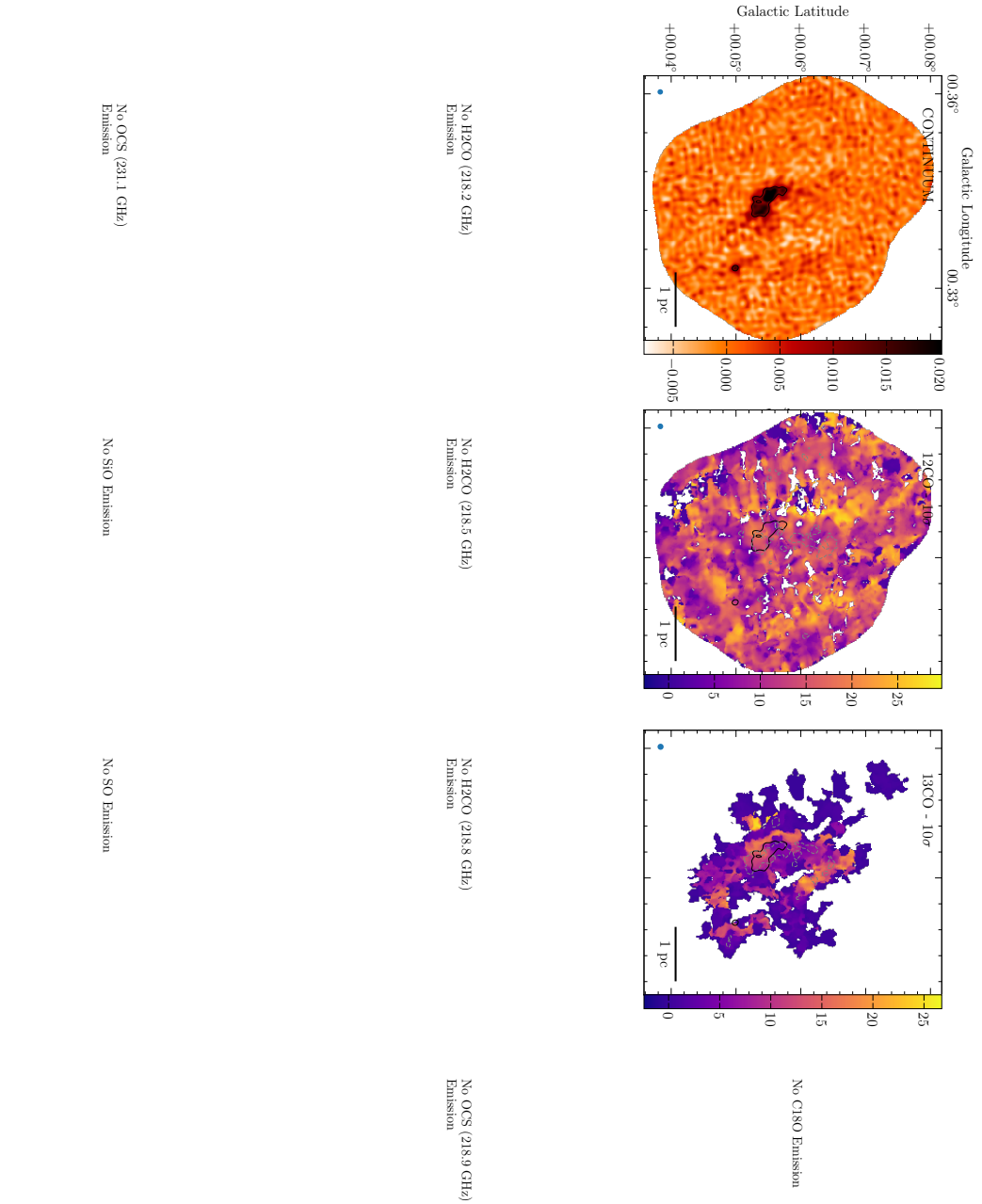

FIGURE A.27: G0.340-0.055 velocity dispersion moment maps

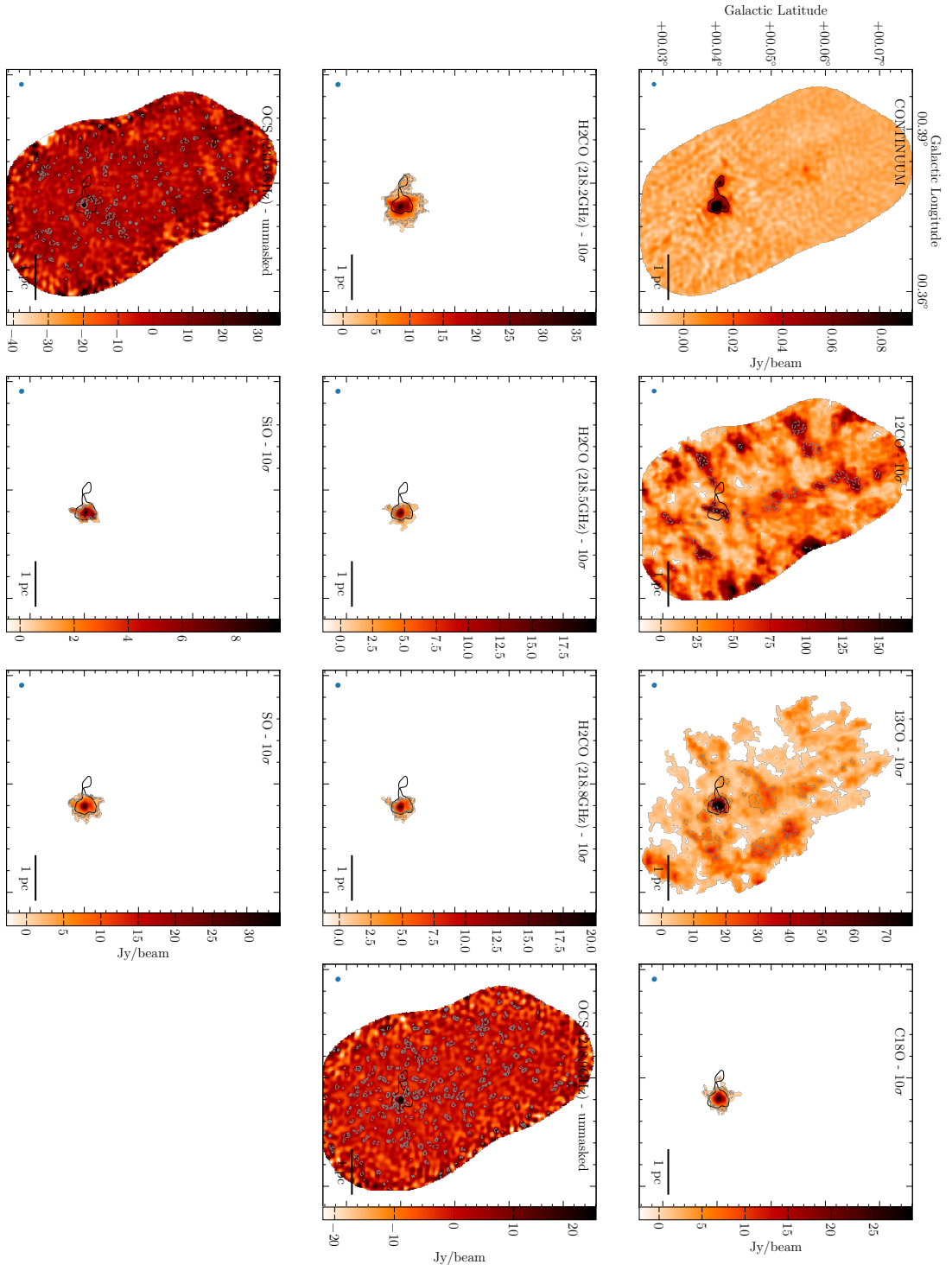

FIGURE A.28: G0.380+0.050 integrated intensity moment maps

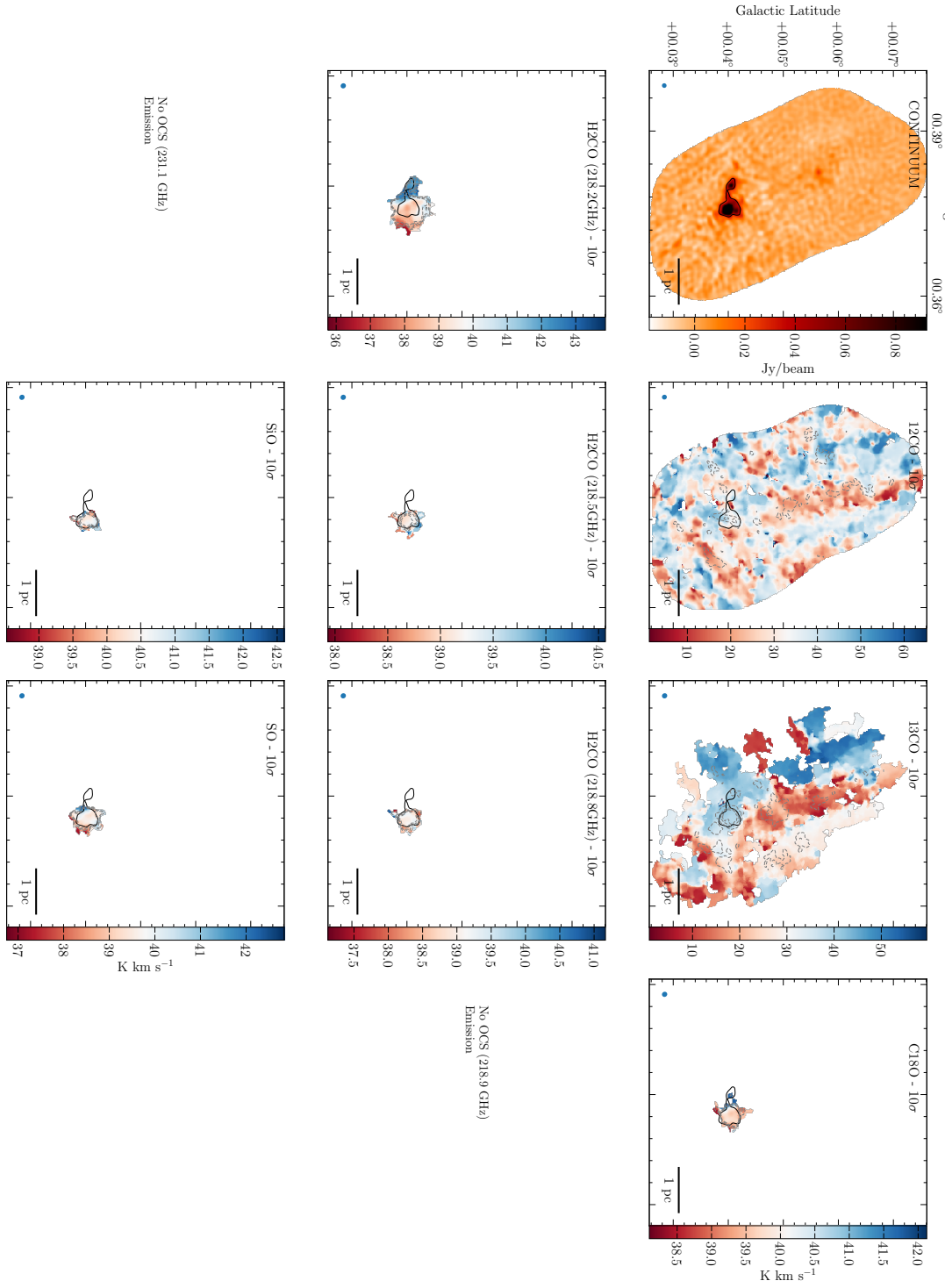

FIGURE A.29: G0.380+0.050 V_{LSR} moment maps

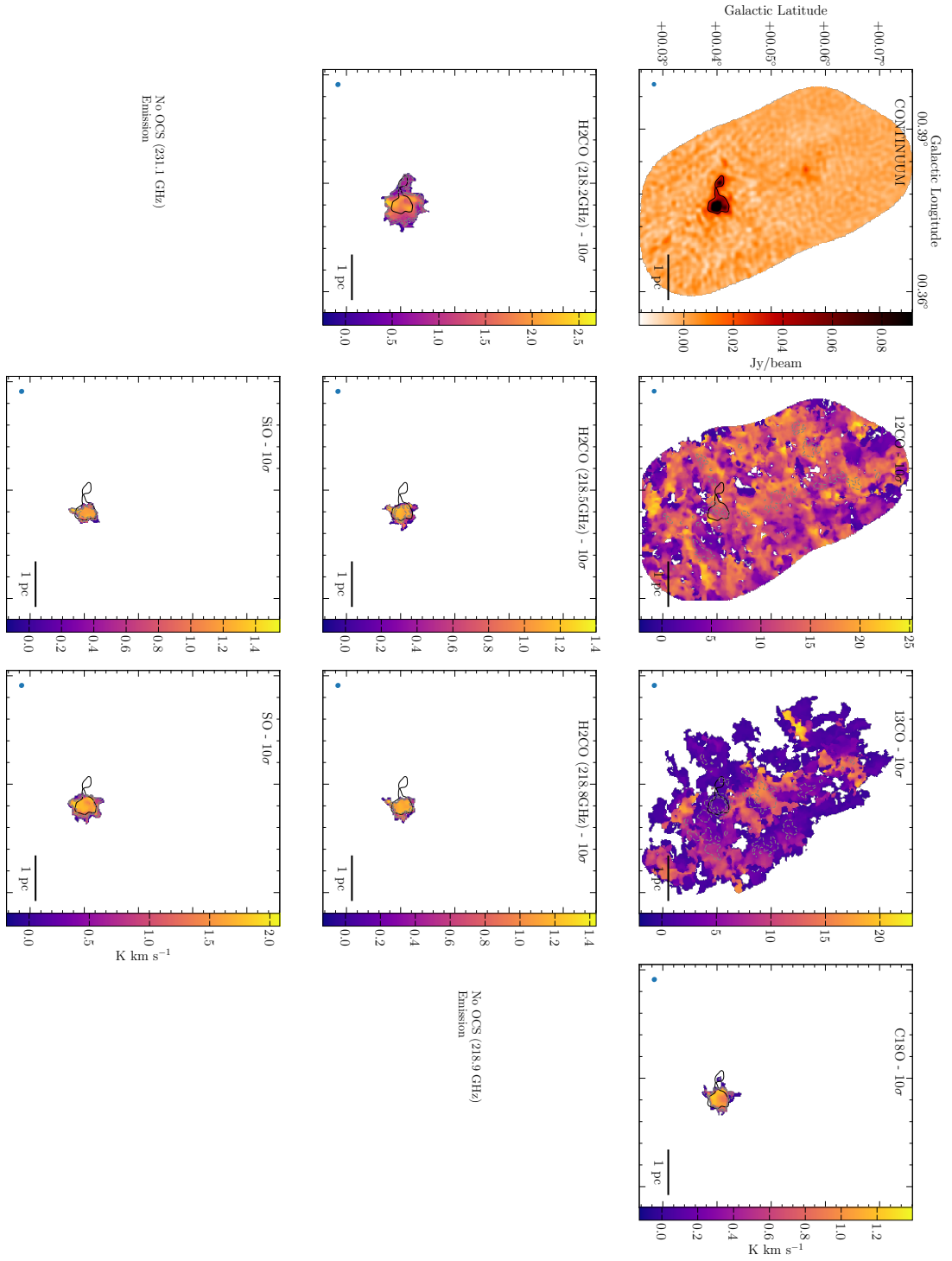

FIGURE A.30: G0.380+0.050 velocity dispersion moment maps

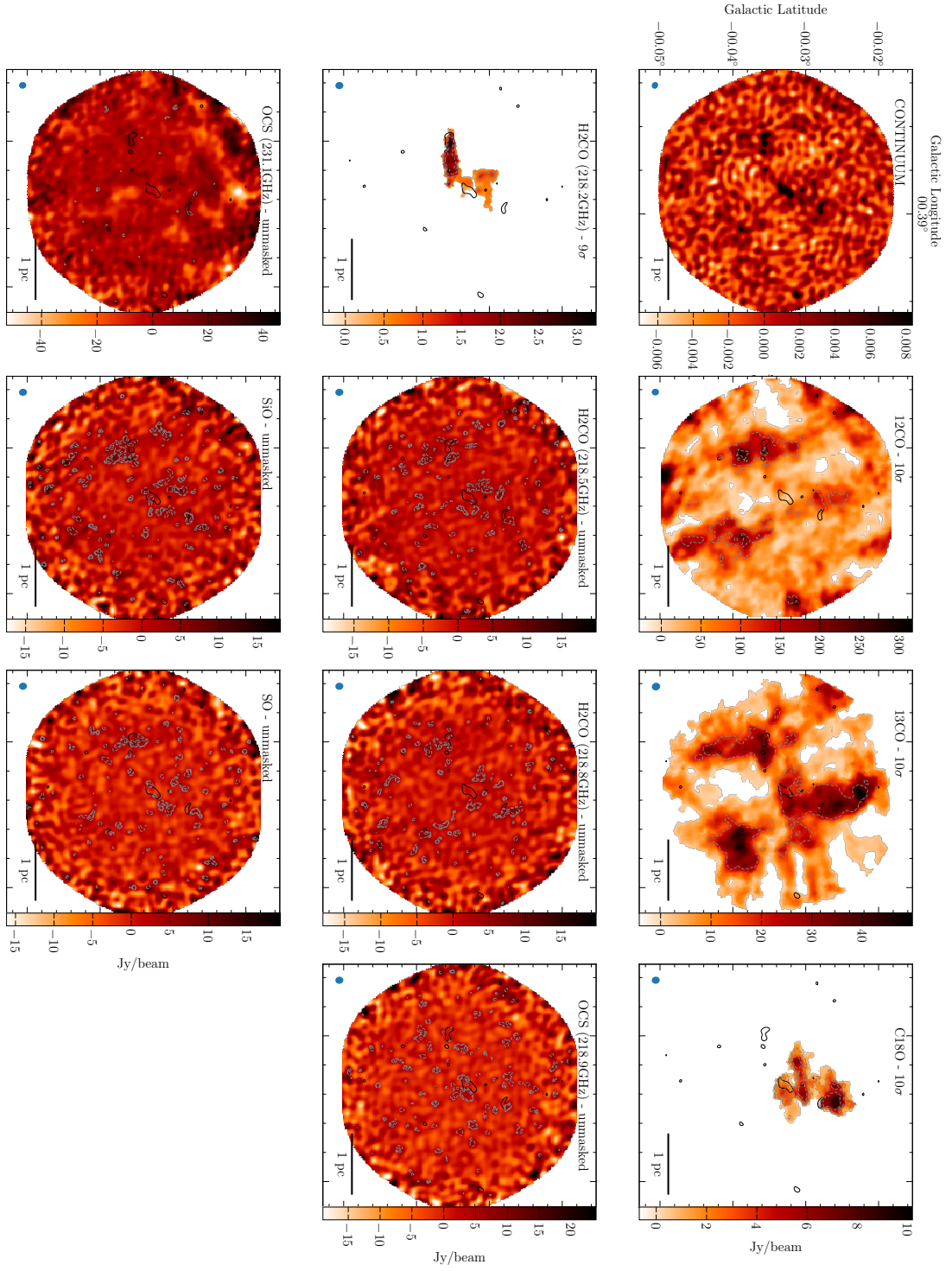

FIGURE A.31: G0.393-0.034 integrated intensity moment maps

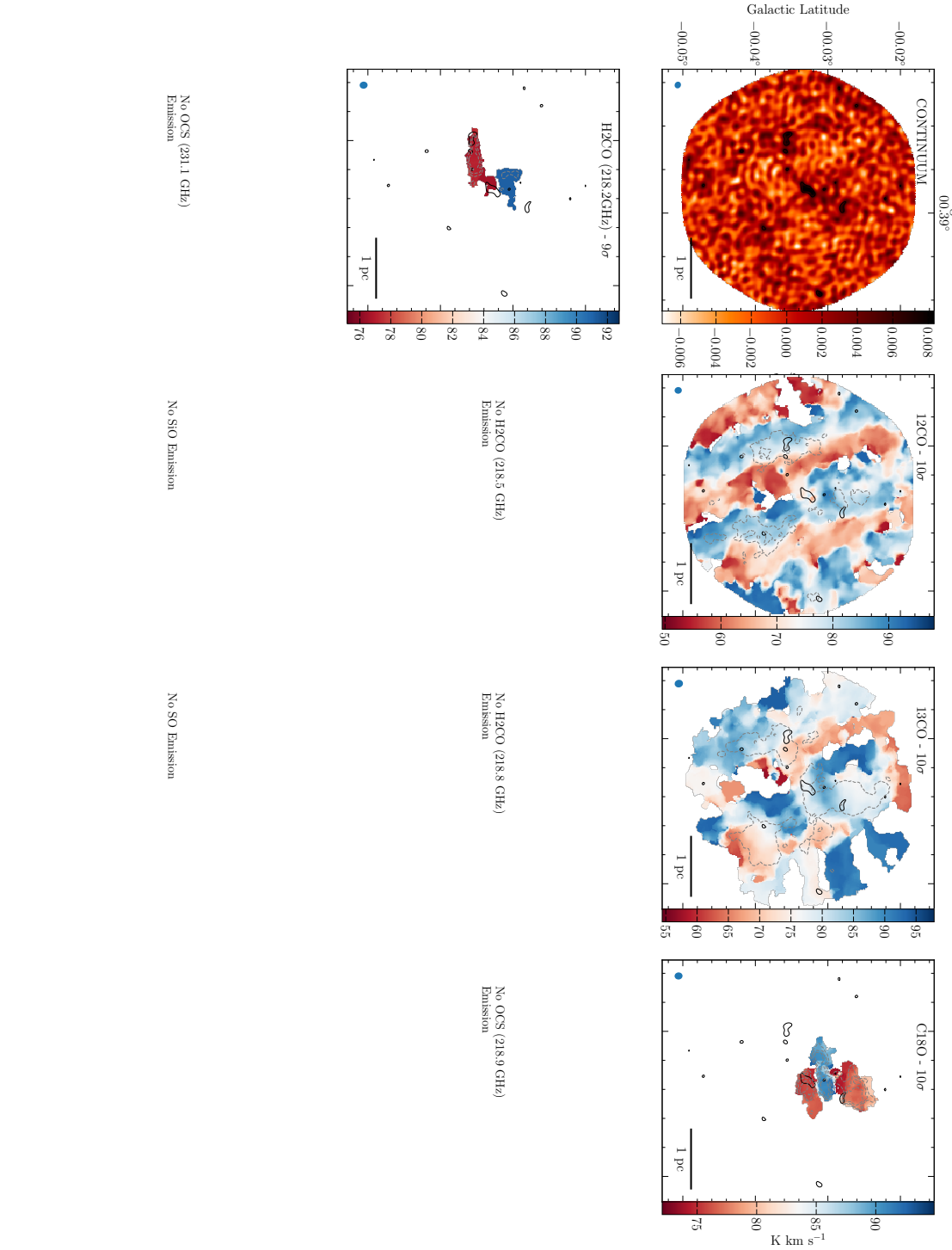

FIGURE A.32: G0.393-0.034 V_{LSR} moment maps

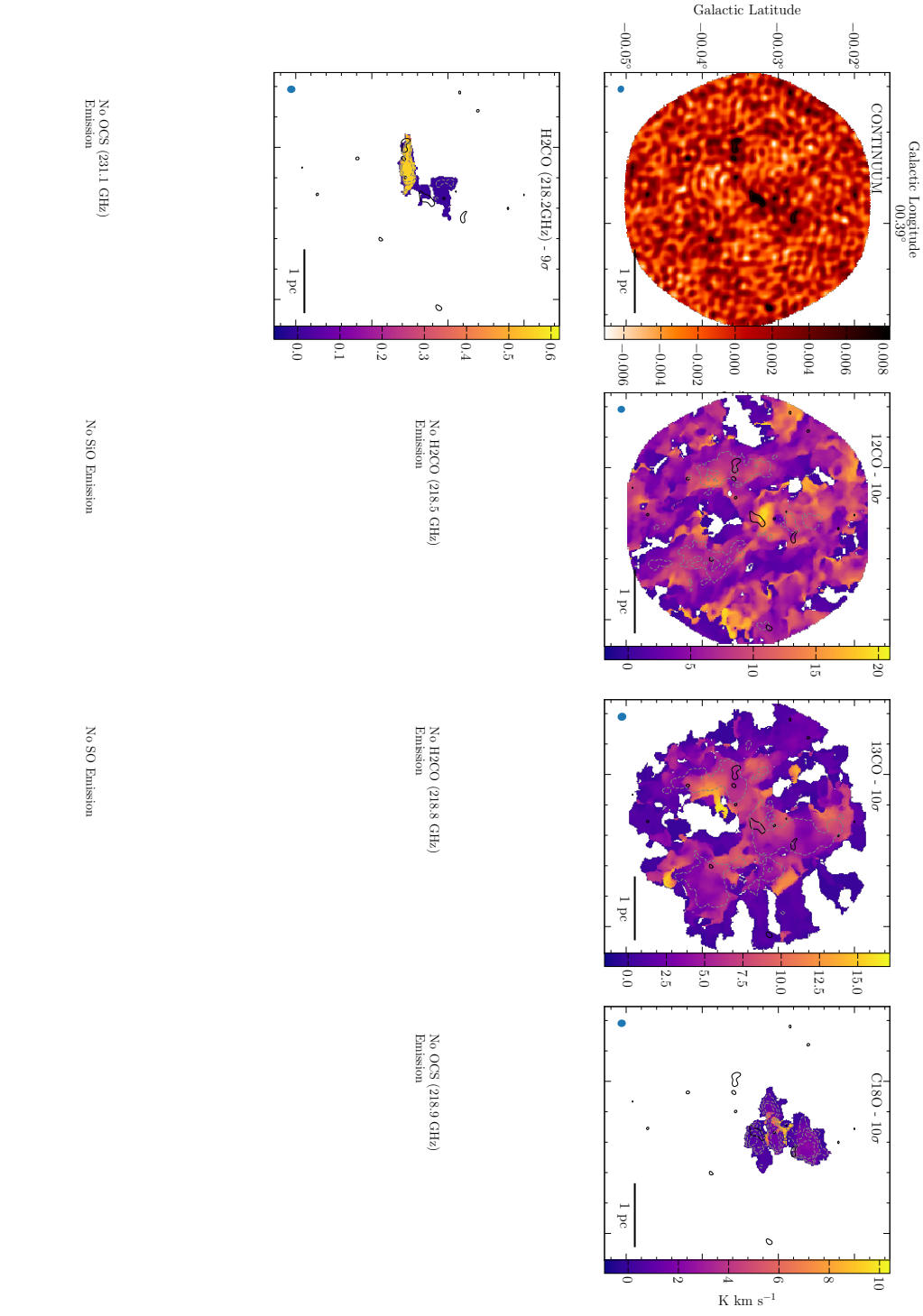

FIGURE A.33: G0.393-0.034 velocity dispersion moment maps

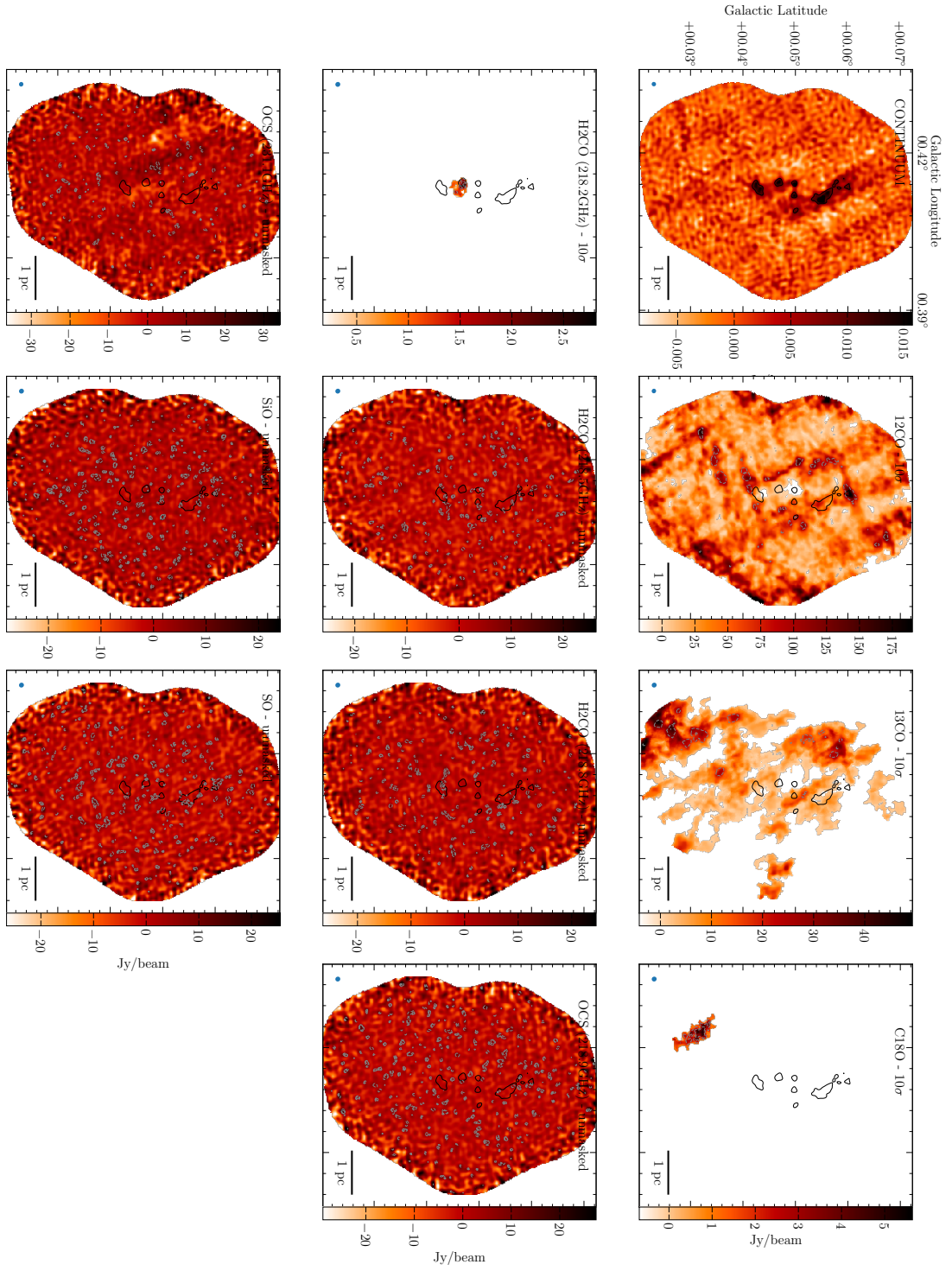

FIGURE A.34: G0.412+0.052 integrated intensity moment maps

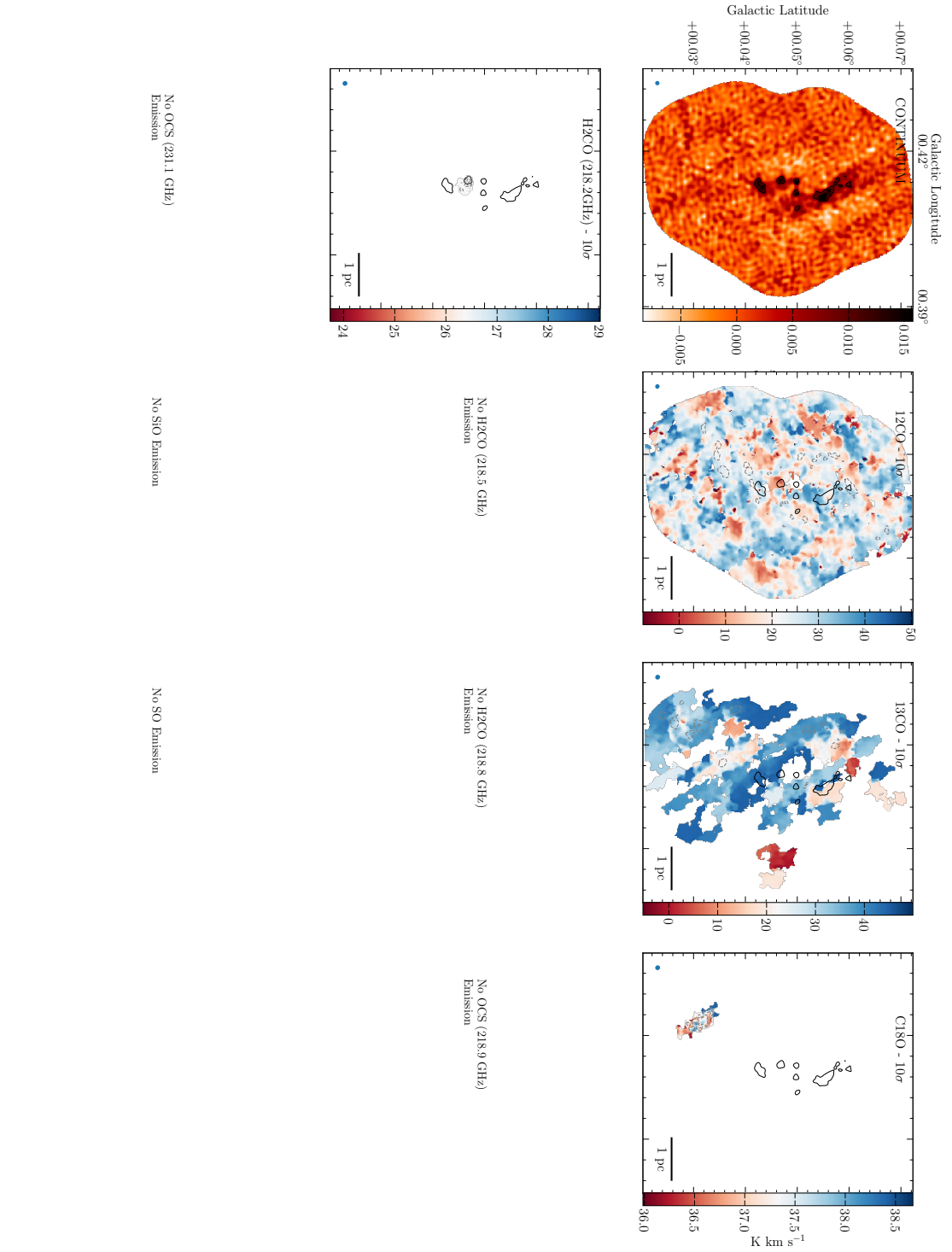

FIGURE A.35: G0.412+0.052 V_{LSR} moment maps

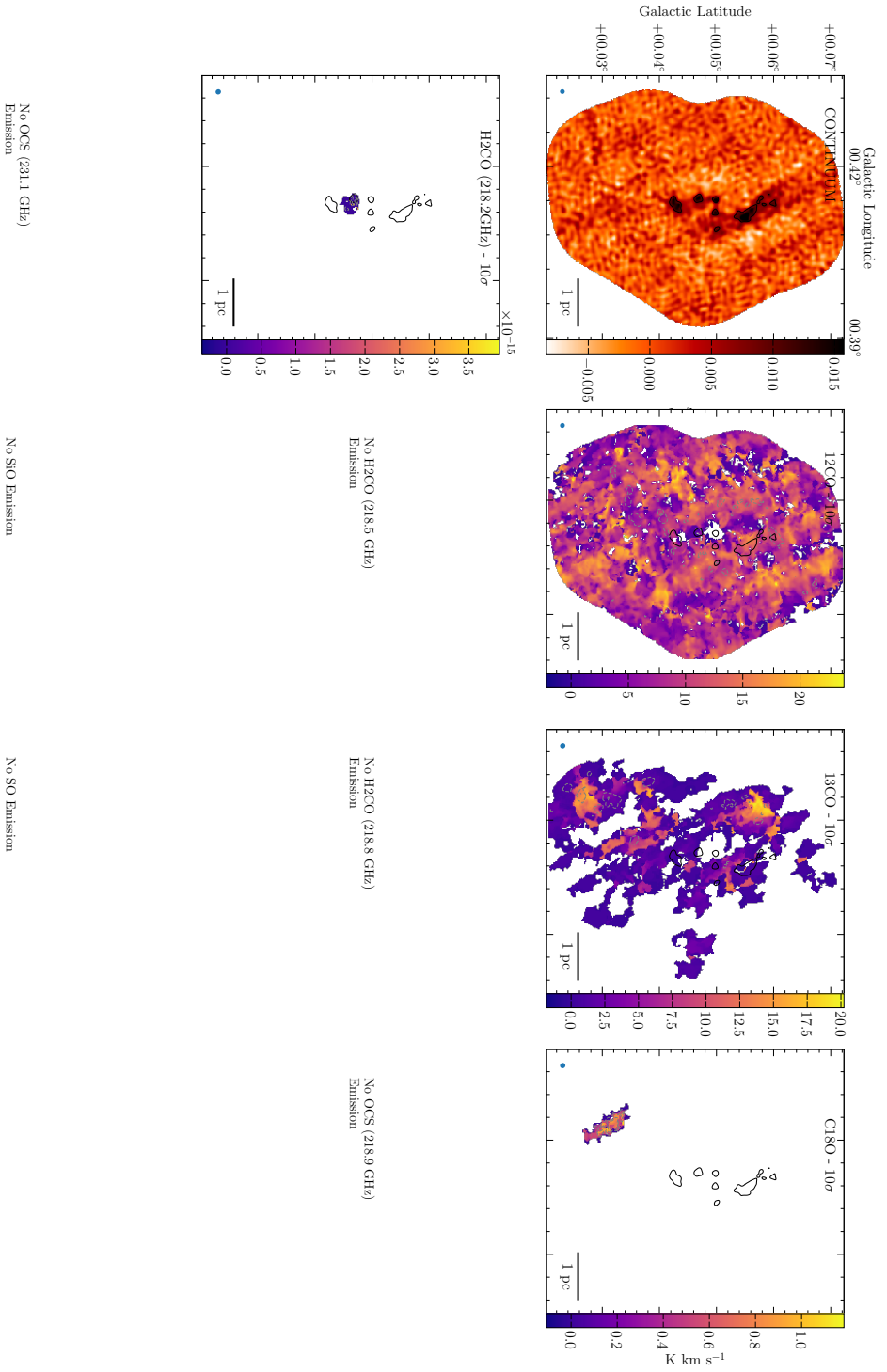

FIGURE A.36: G0.412+0.052 velocity dispersion moment maps

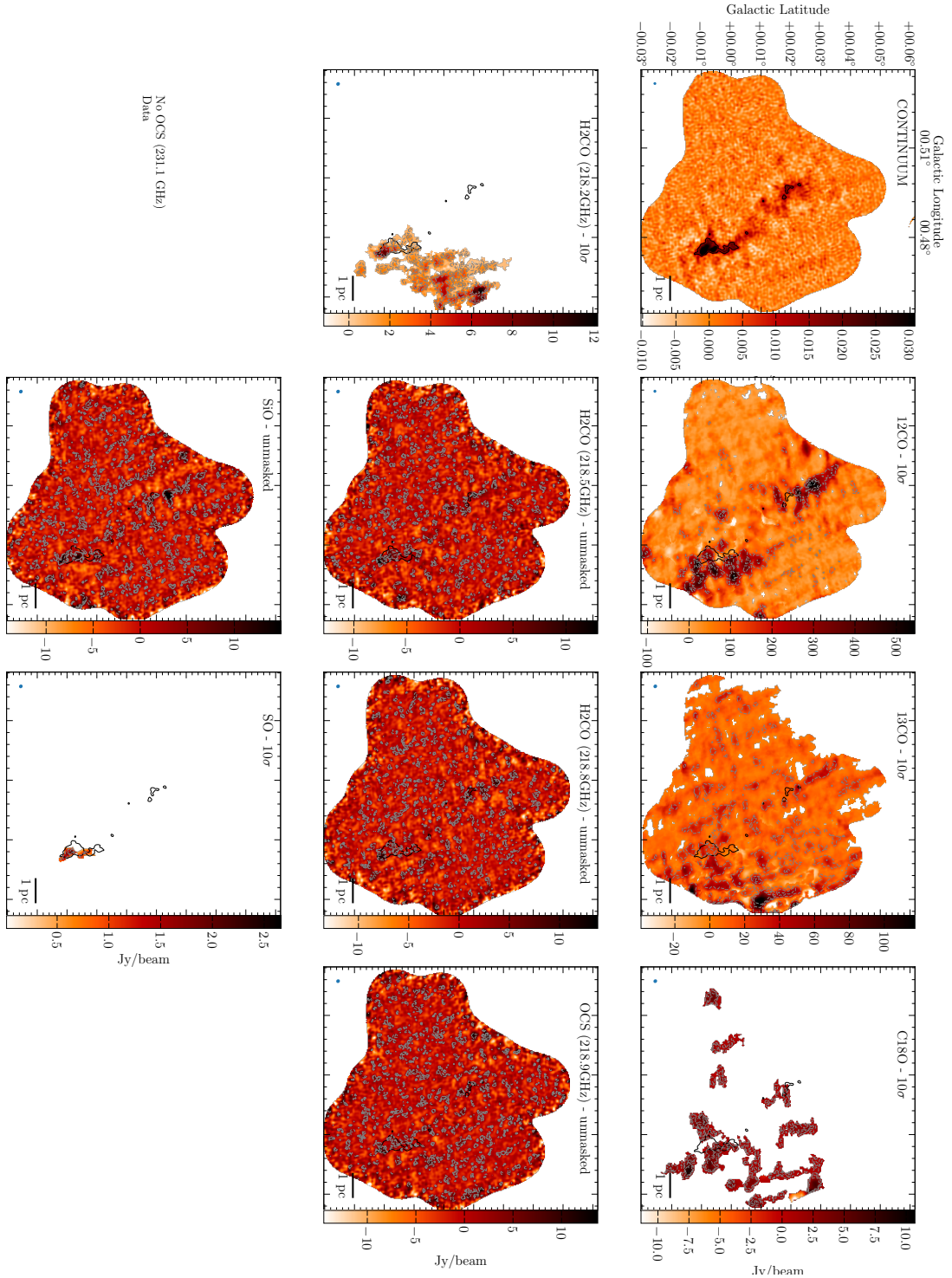

FIGURE A.37: G0.489+0.010 integrated intensity moment maps

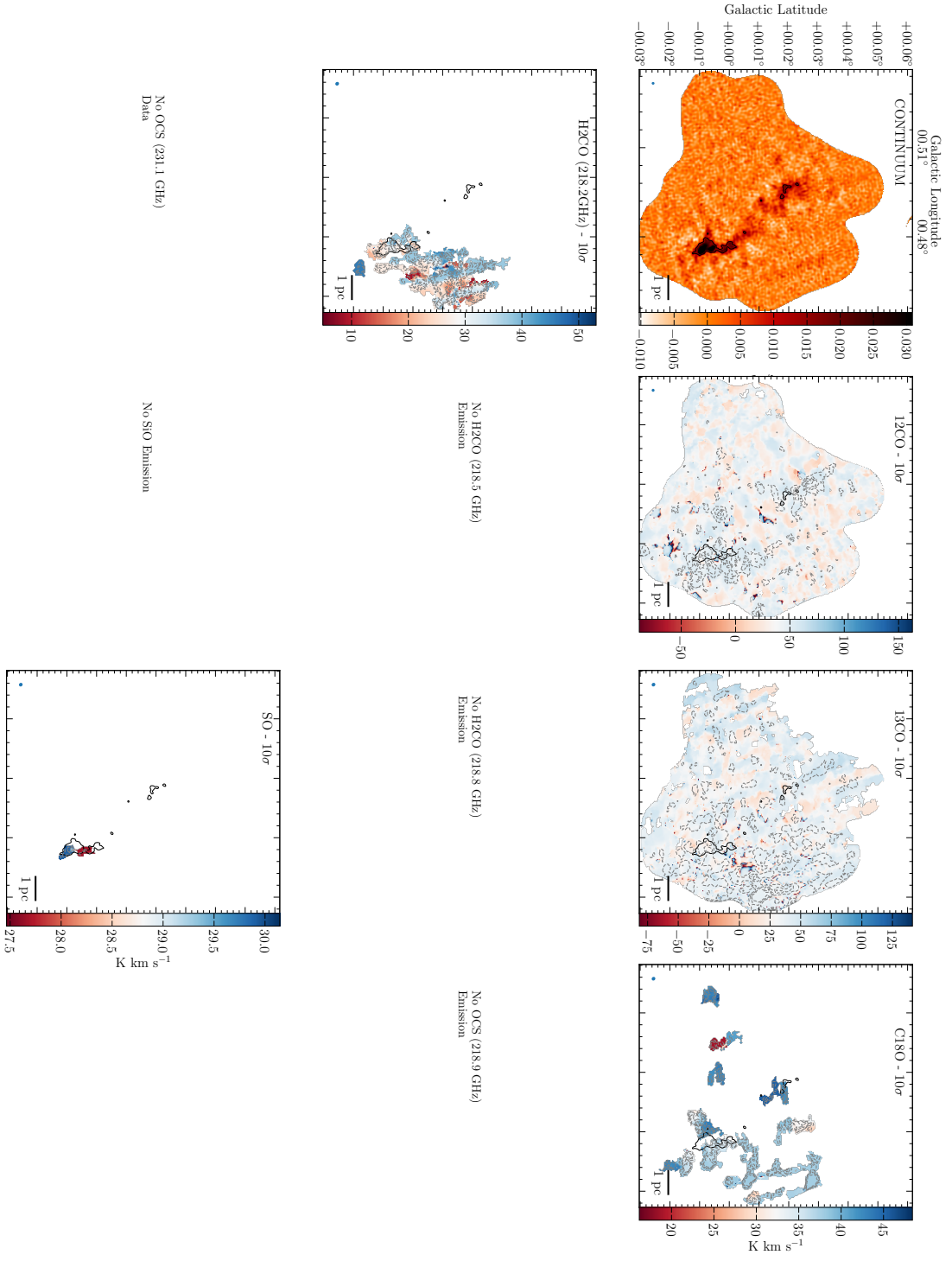

FIGURE A.38: G0.489+0.010 V_{LSR} moment maps

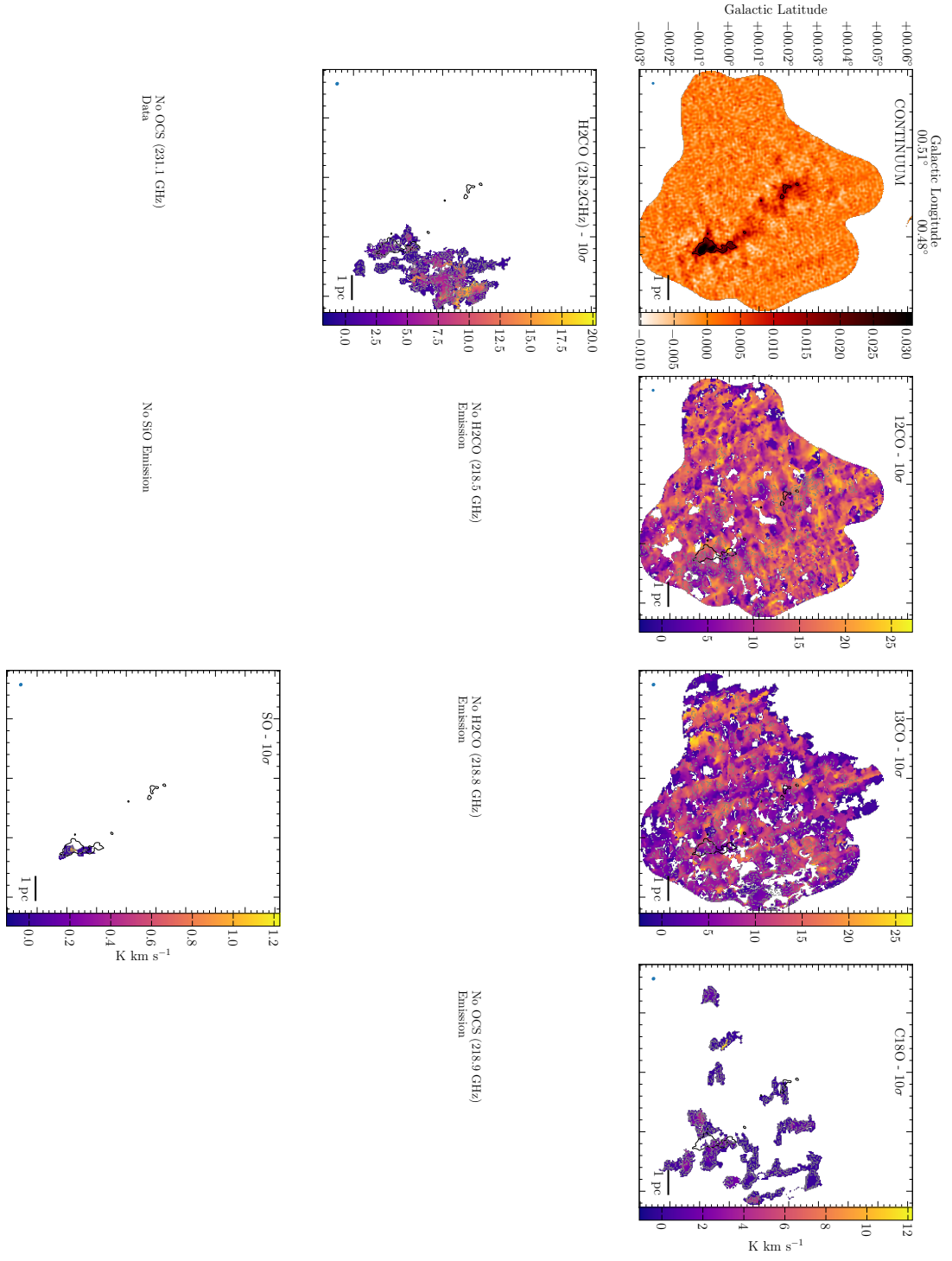

FIGURE A.39: G0.489+0.010 velocity dispersion moment maps

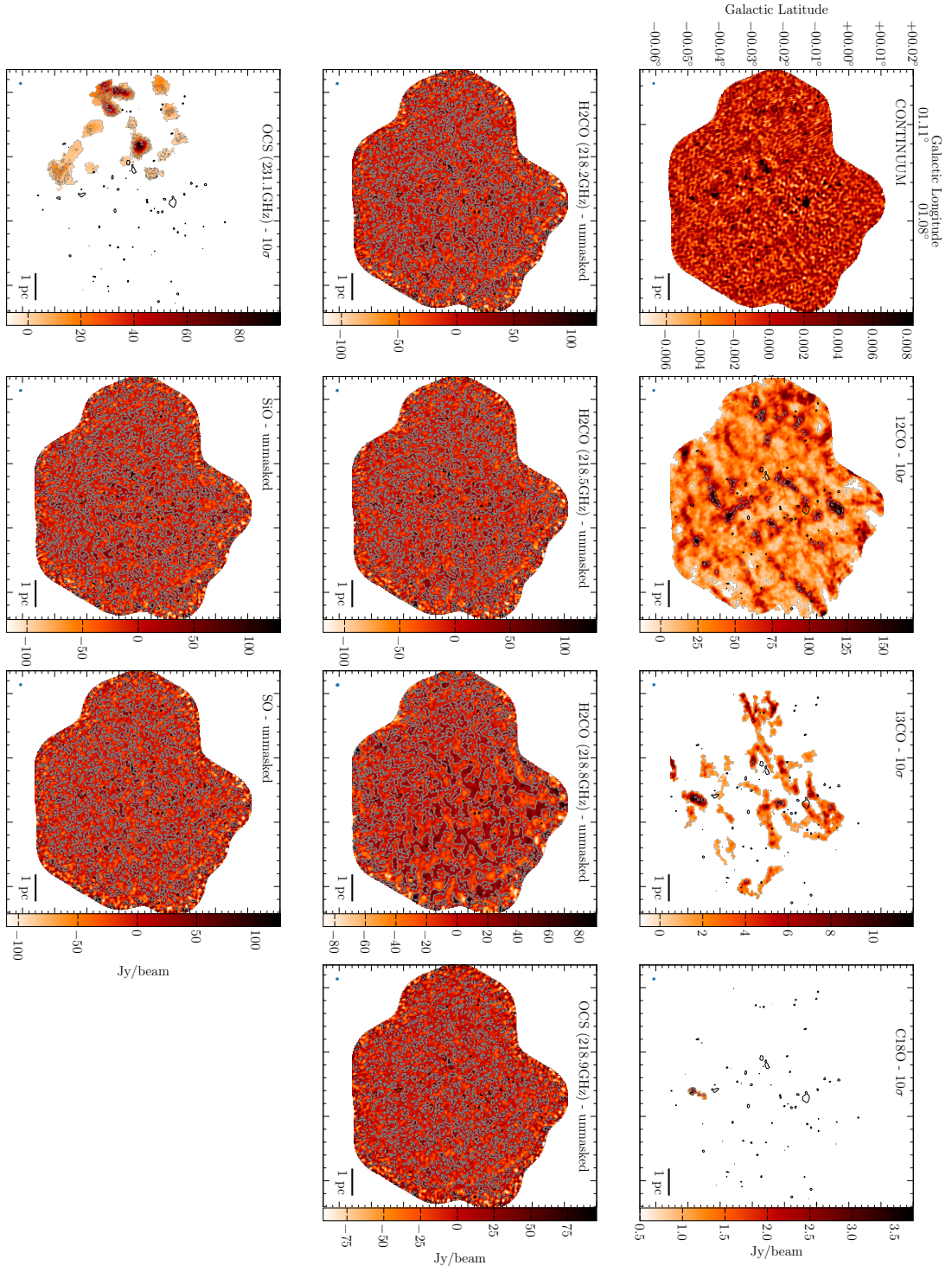

FIGURE A.40: G1.085-0.027 integrated intensity moment maps

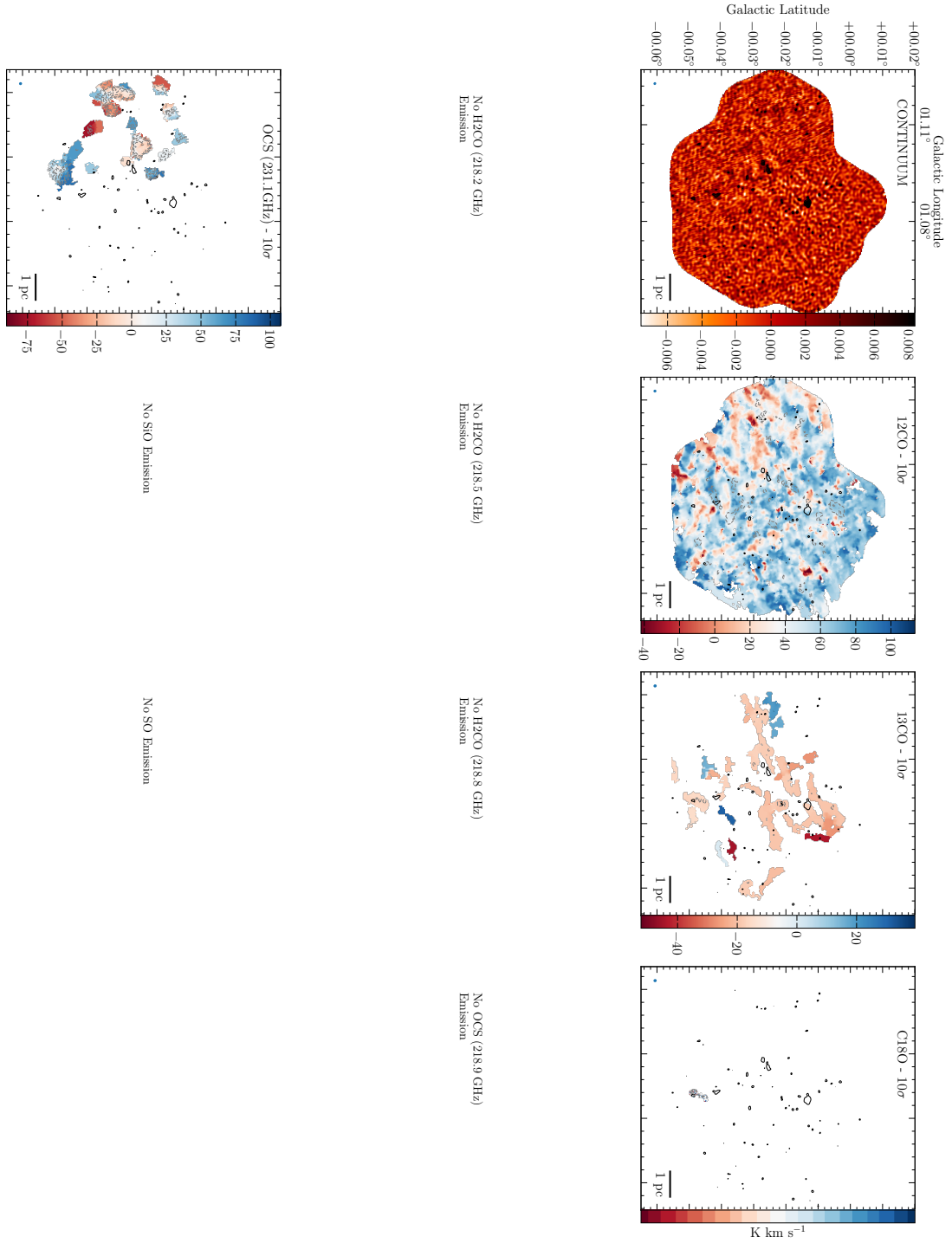

FIGURE A.41: G1.085-0.027 V_{LSR} moment maps

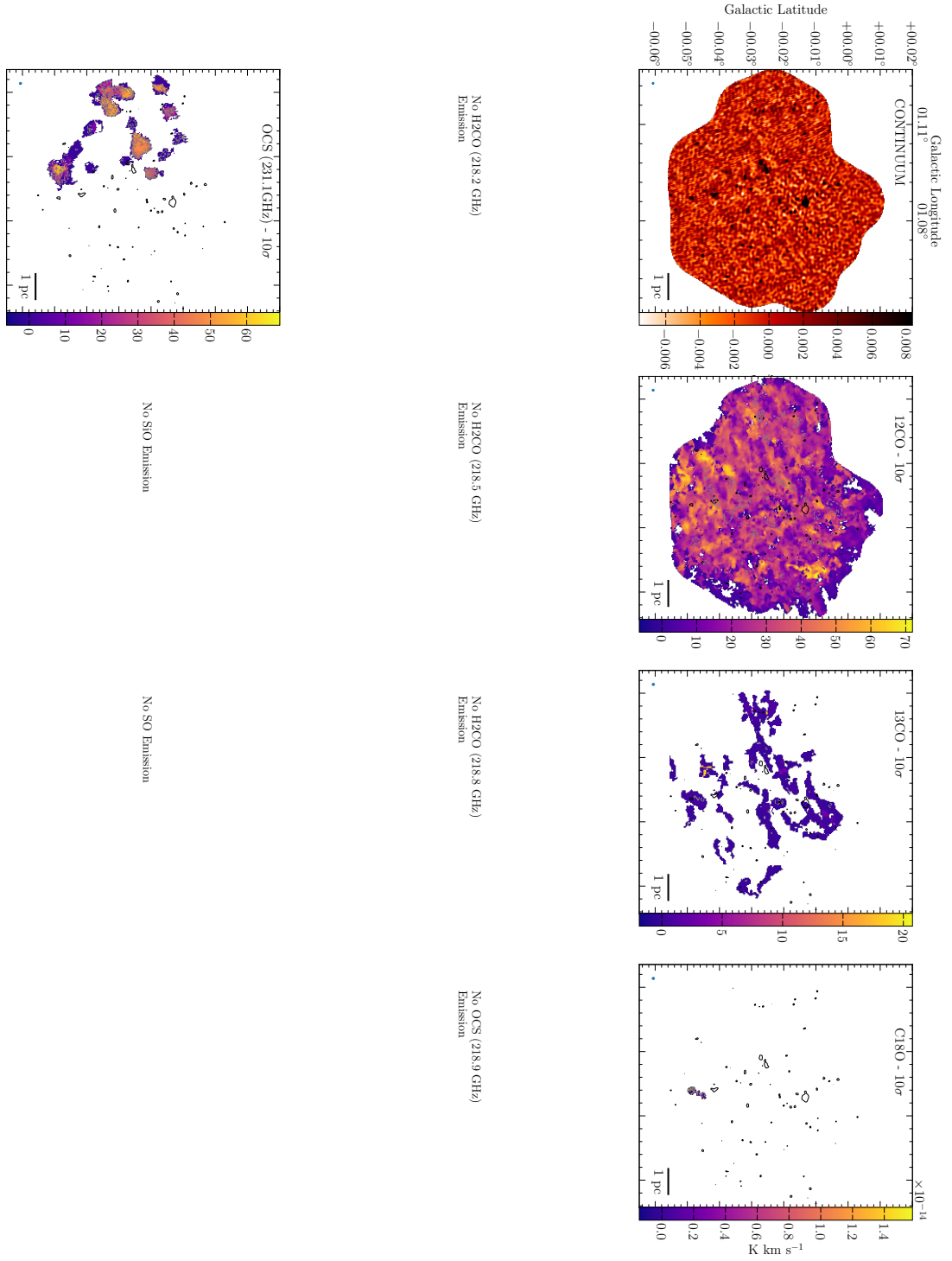

FIGURE A.42: G1.085-0.027 velocity dispersion moment maps

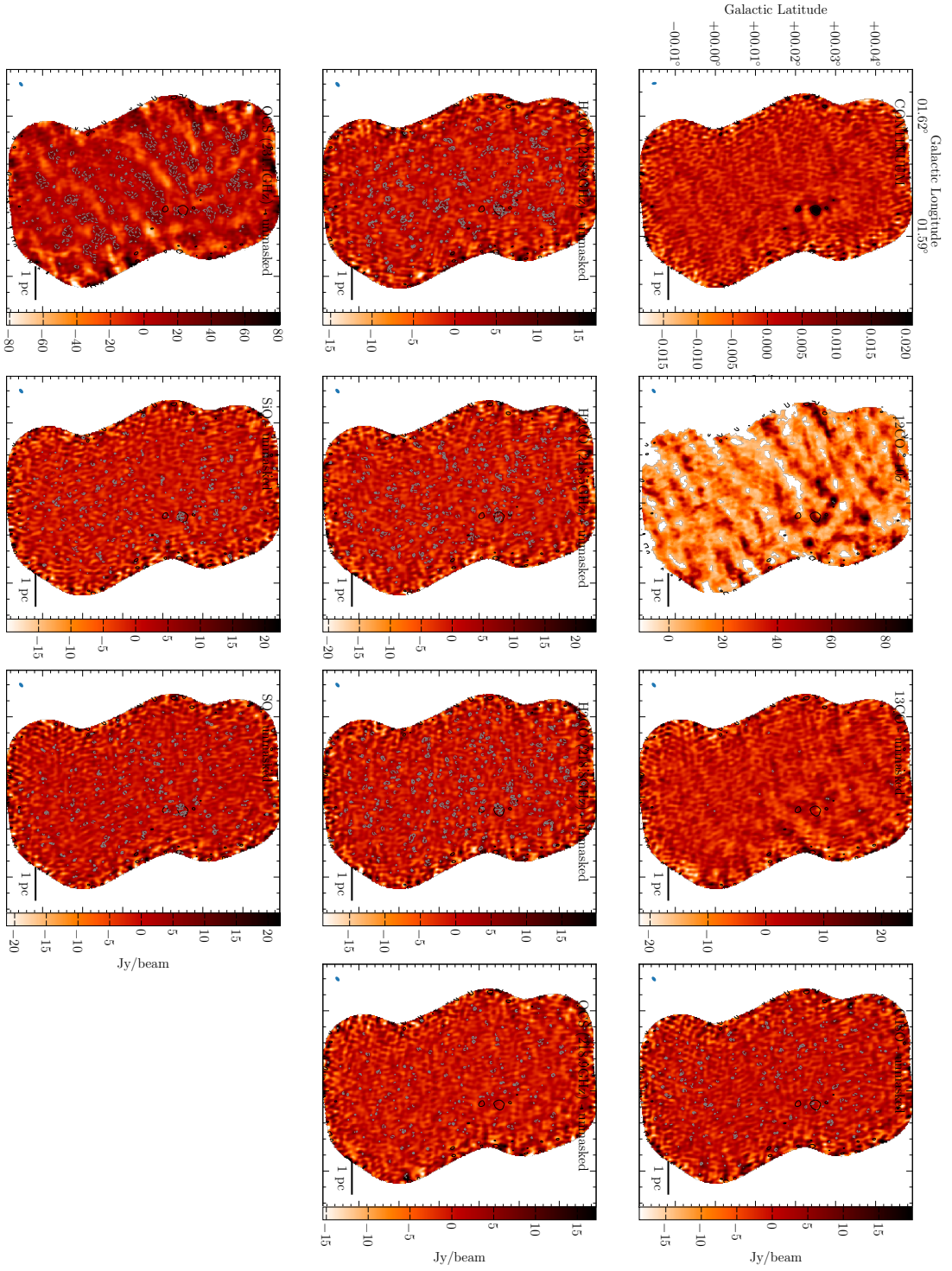

FIGURE A.43: G1.602+0.018 integrated intensity moment maps

FIGURE A.44: G1.602+0.018 V_{LSR} moment maps

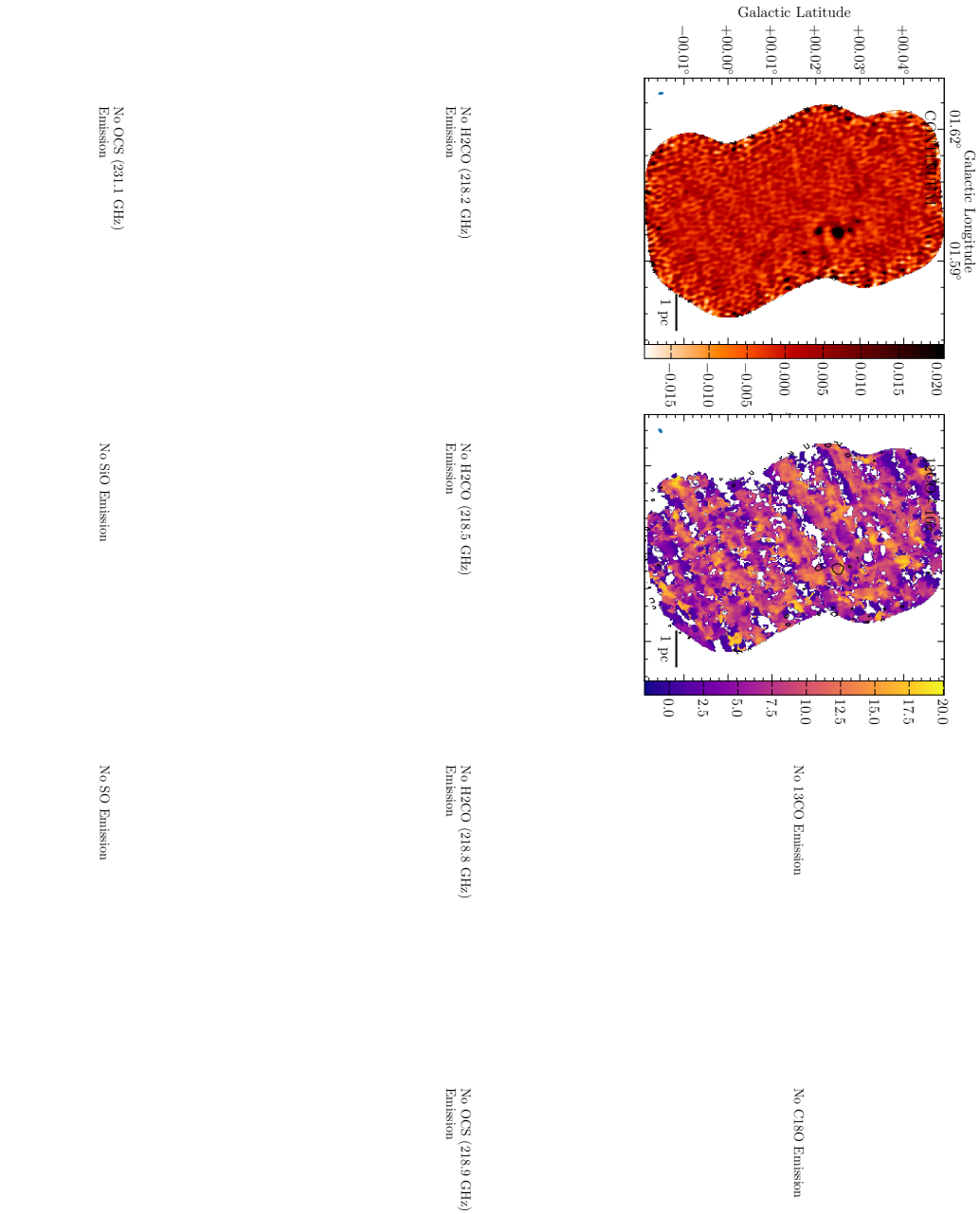

FIGURE A.45: G1.602+0.018 velocity dispersion moment maps

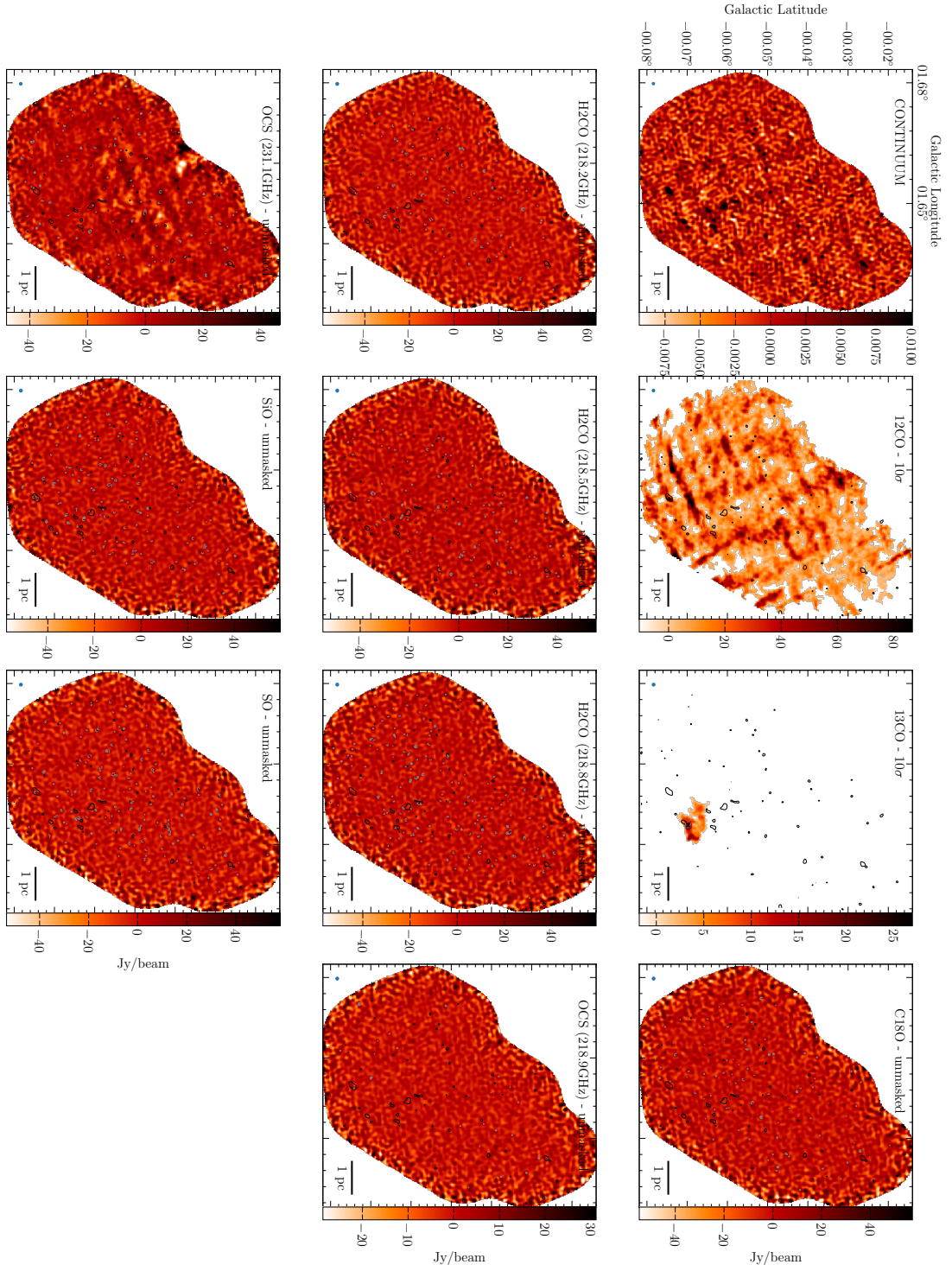

FIGURE A.46: G1.651-0.050 integrated intensity moment maps

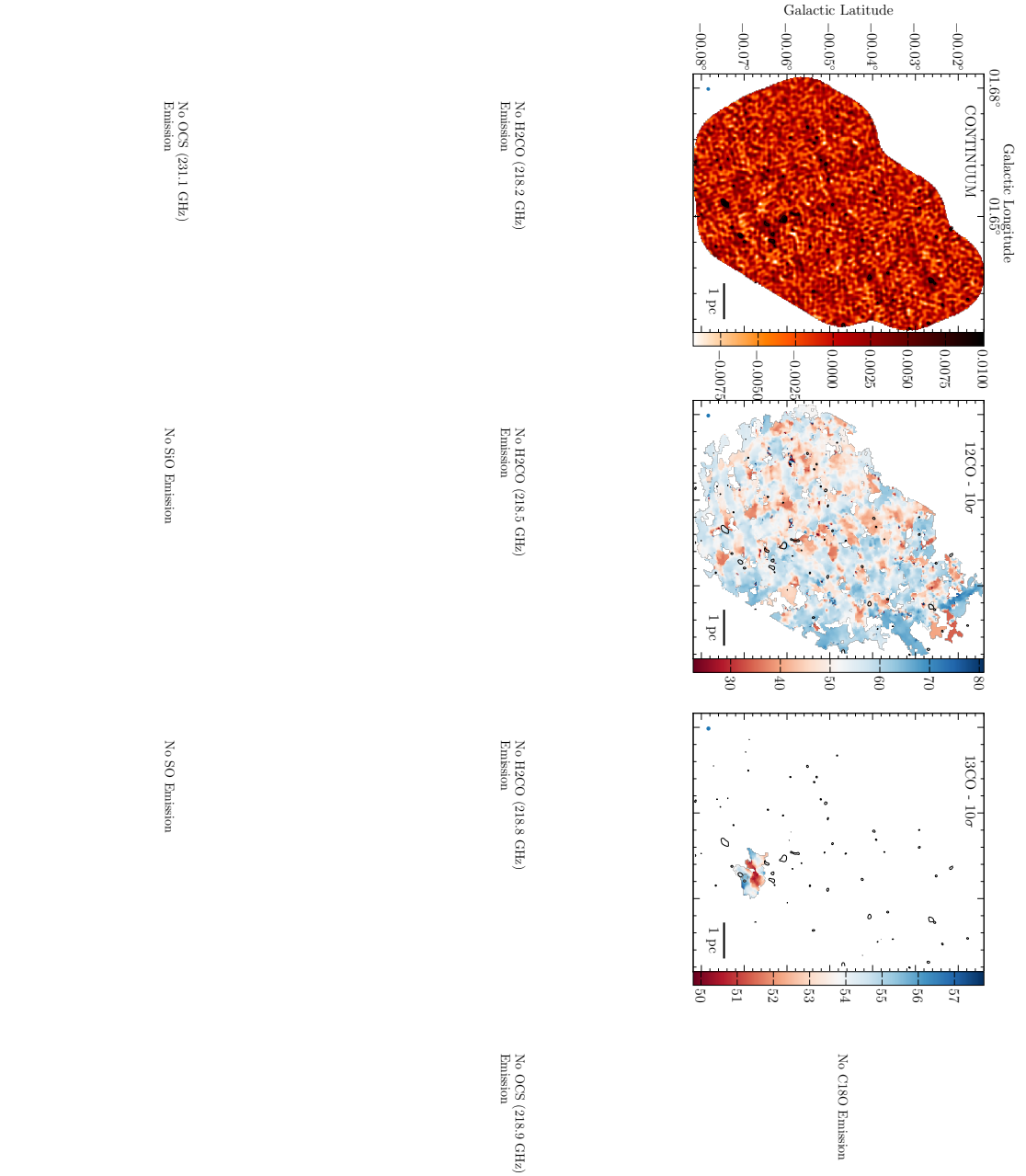

FIGURE A.47: G1.651-0.050 V_{LSR} moment maps

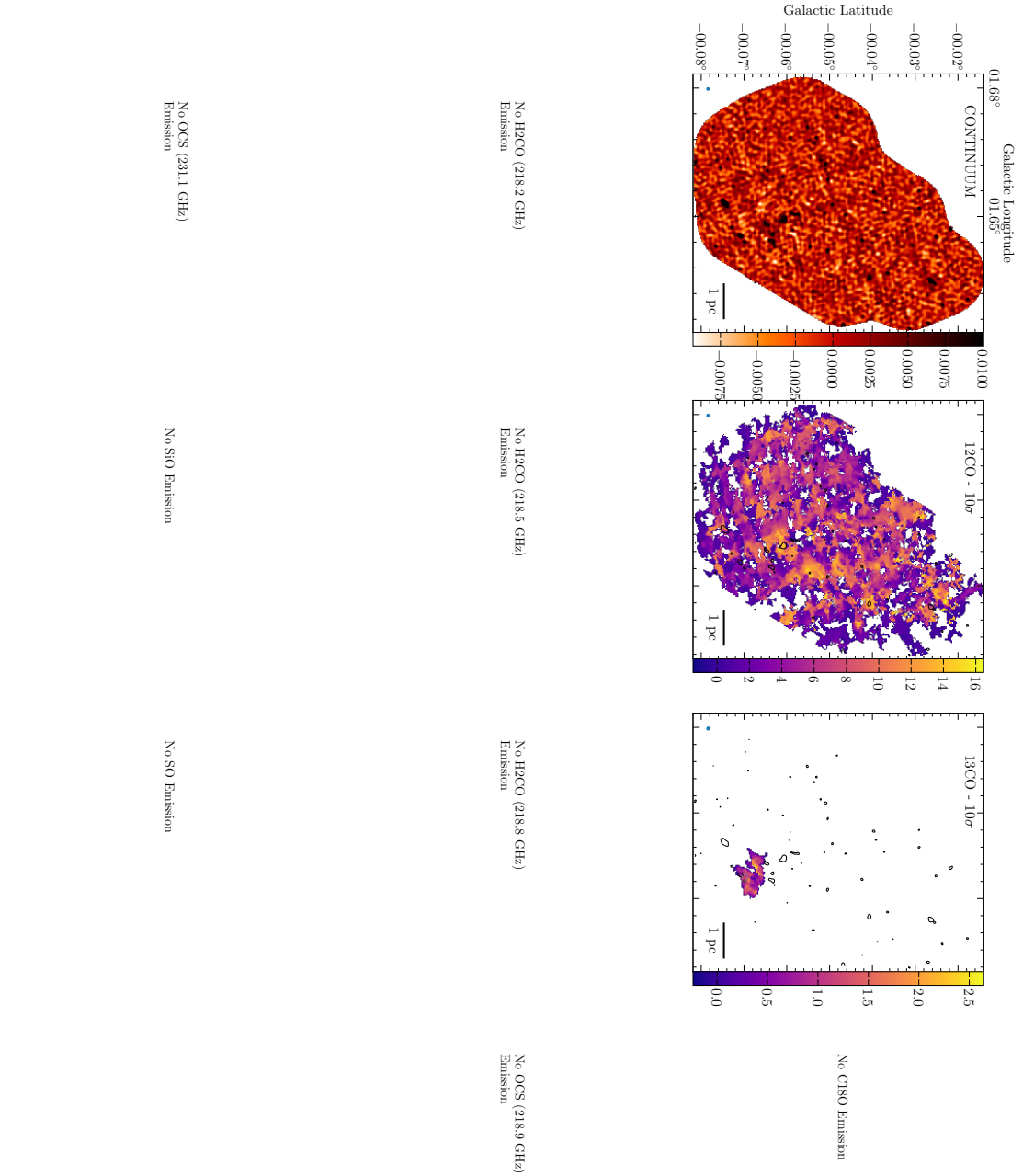

FIGURE A.48: G1.651-0.050 velocity dispersion moment maps

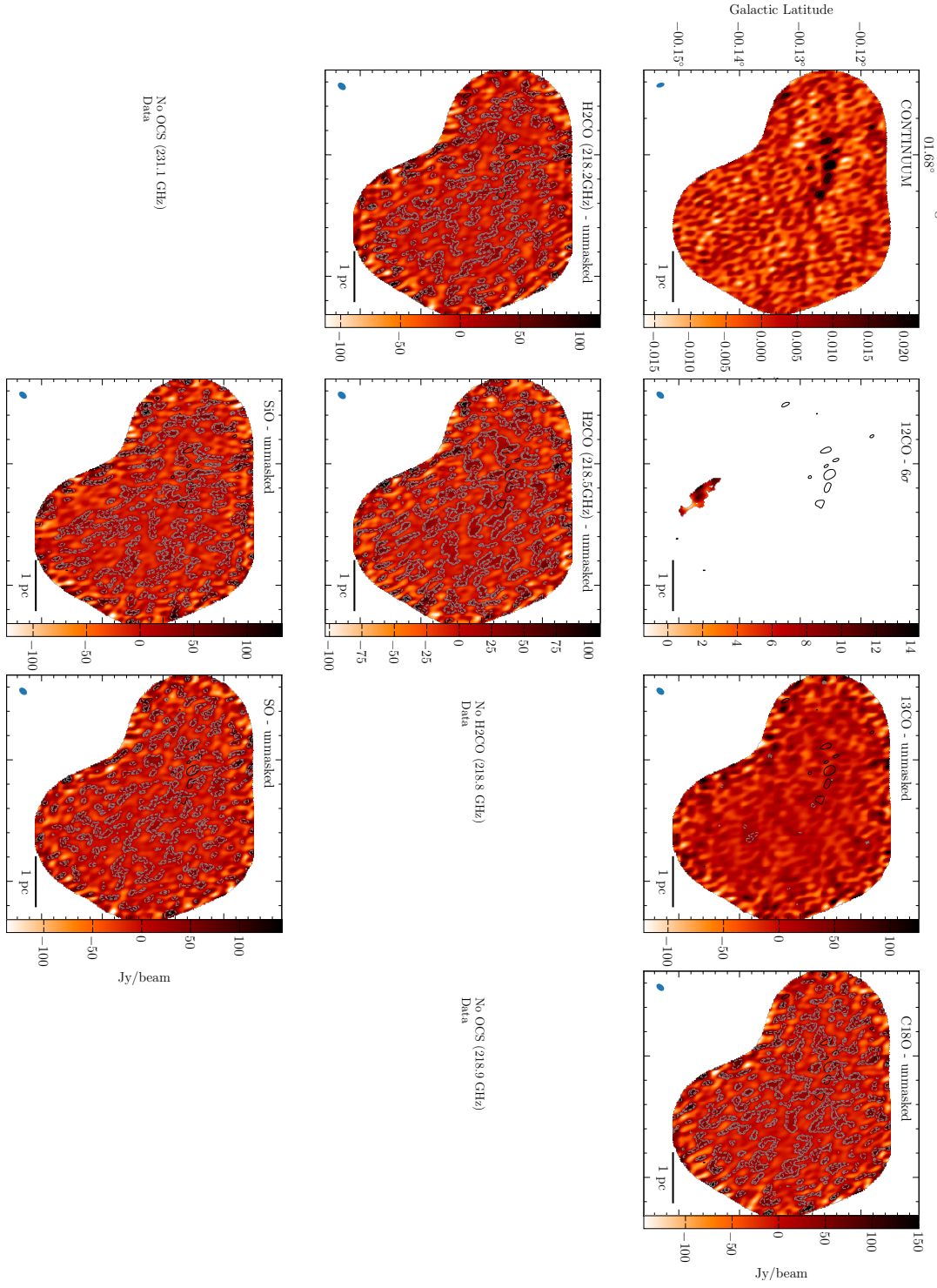

FIGURE A.49: G1.670-0.130 integrated intensity moment maps

FIGURE A.50: G1.670-0.130 V_{LSR} moment maps

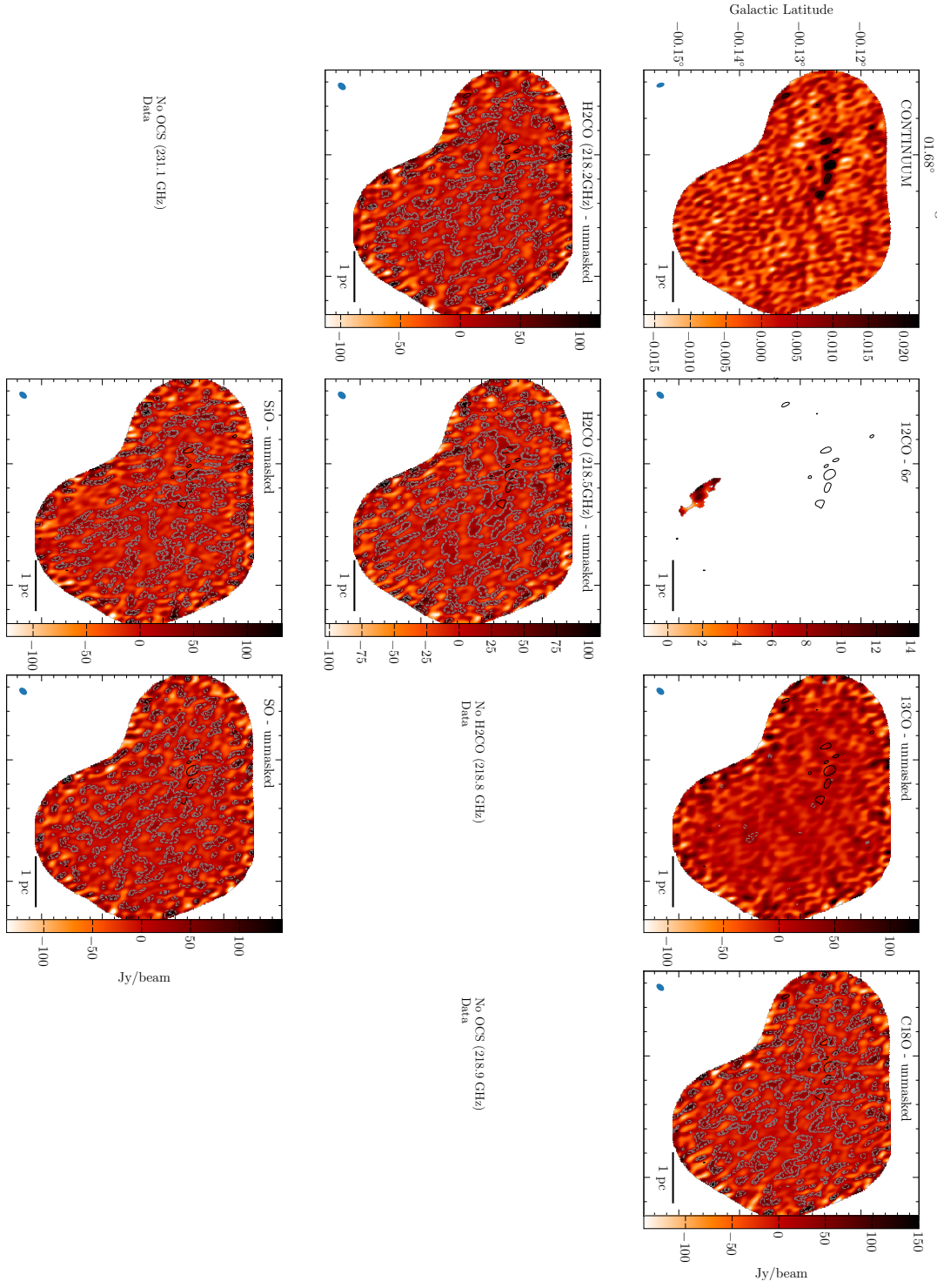

FIGURE A.51: G1.670-0.130 velocity dispersion moment maps

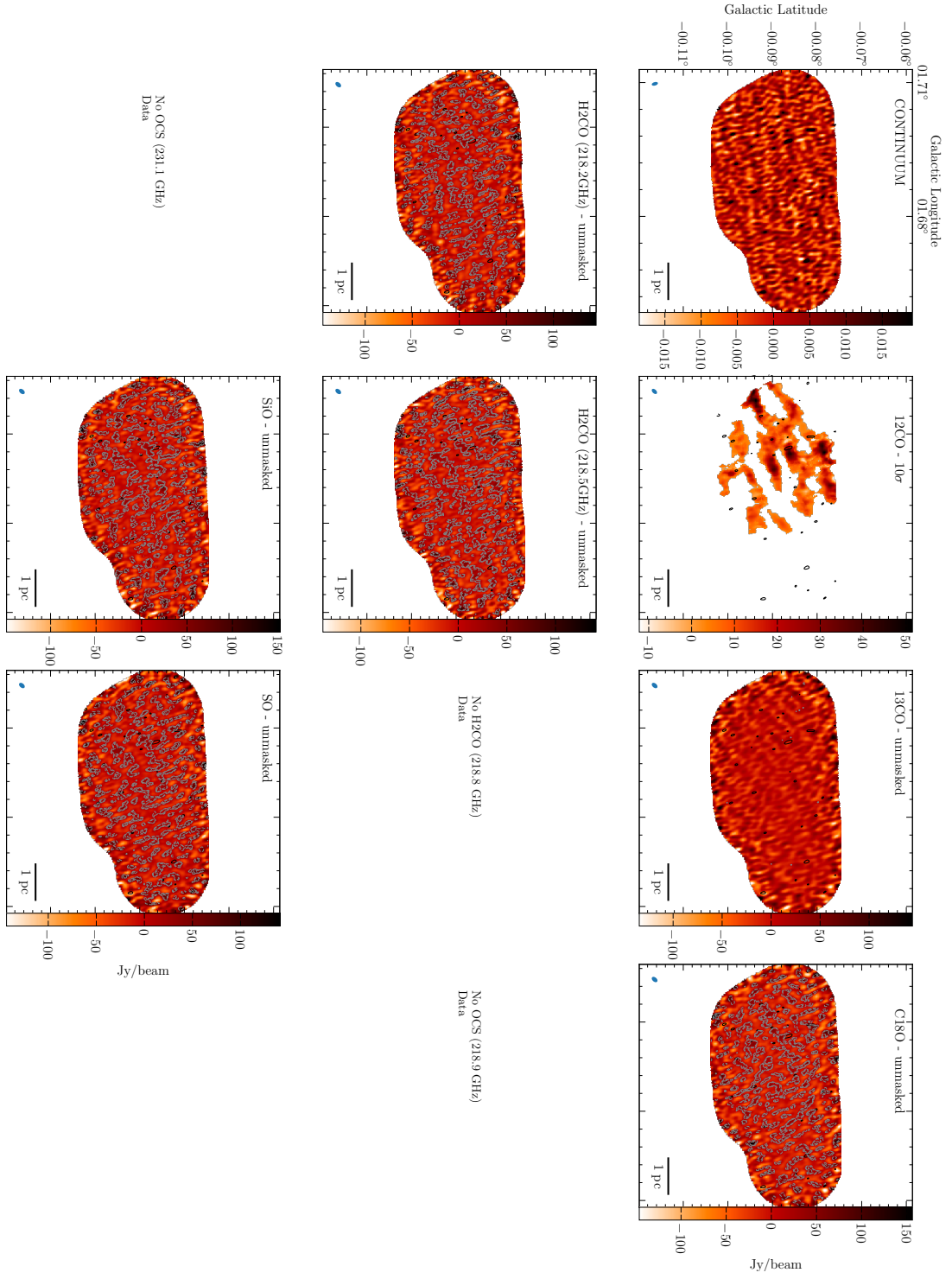

FIGURE A.52: G1.683-0.089 integrated intensity moment maps

FIGURE A.53: G1.683-0.089 V_{LSR} moment maps

FIGURE A.54: G1.683-0.089 velocity dispersion moment maps

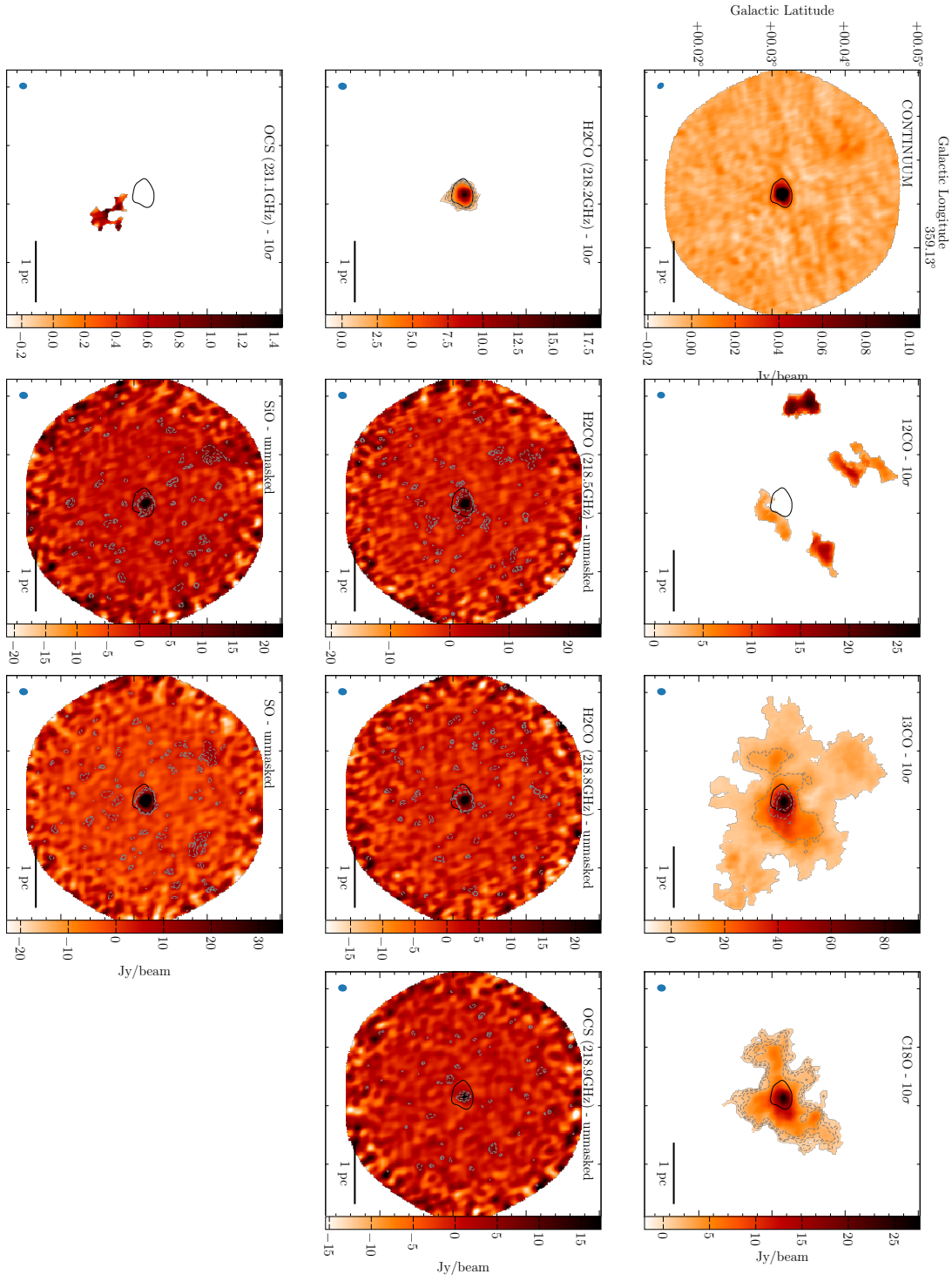

FIGURE A.55: G359.137+0.031 integrated intensity moment maps

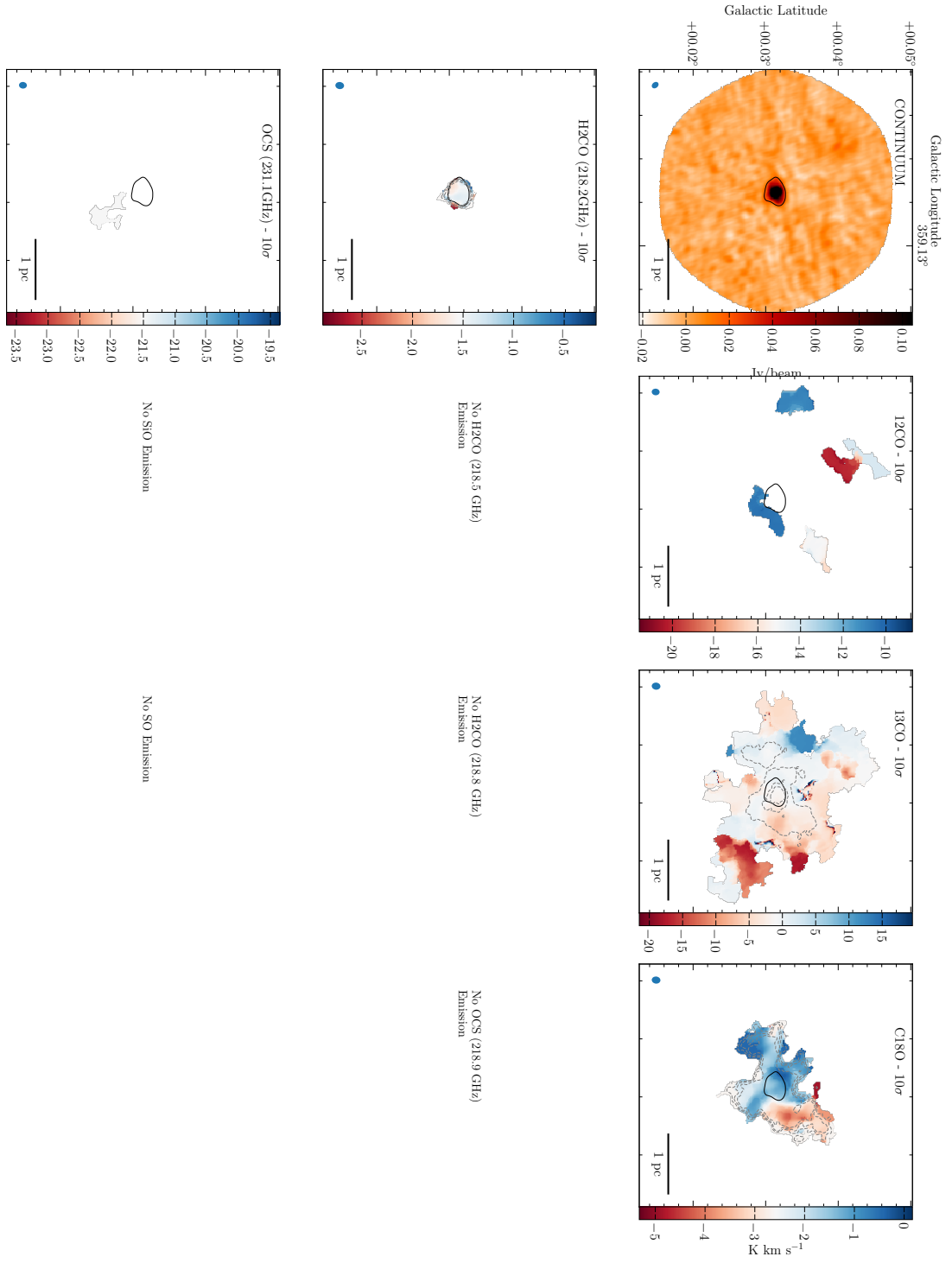

FIGURE A.56: G359.137+0.031 V_{LSR} moment maps

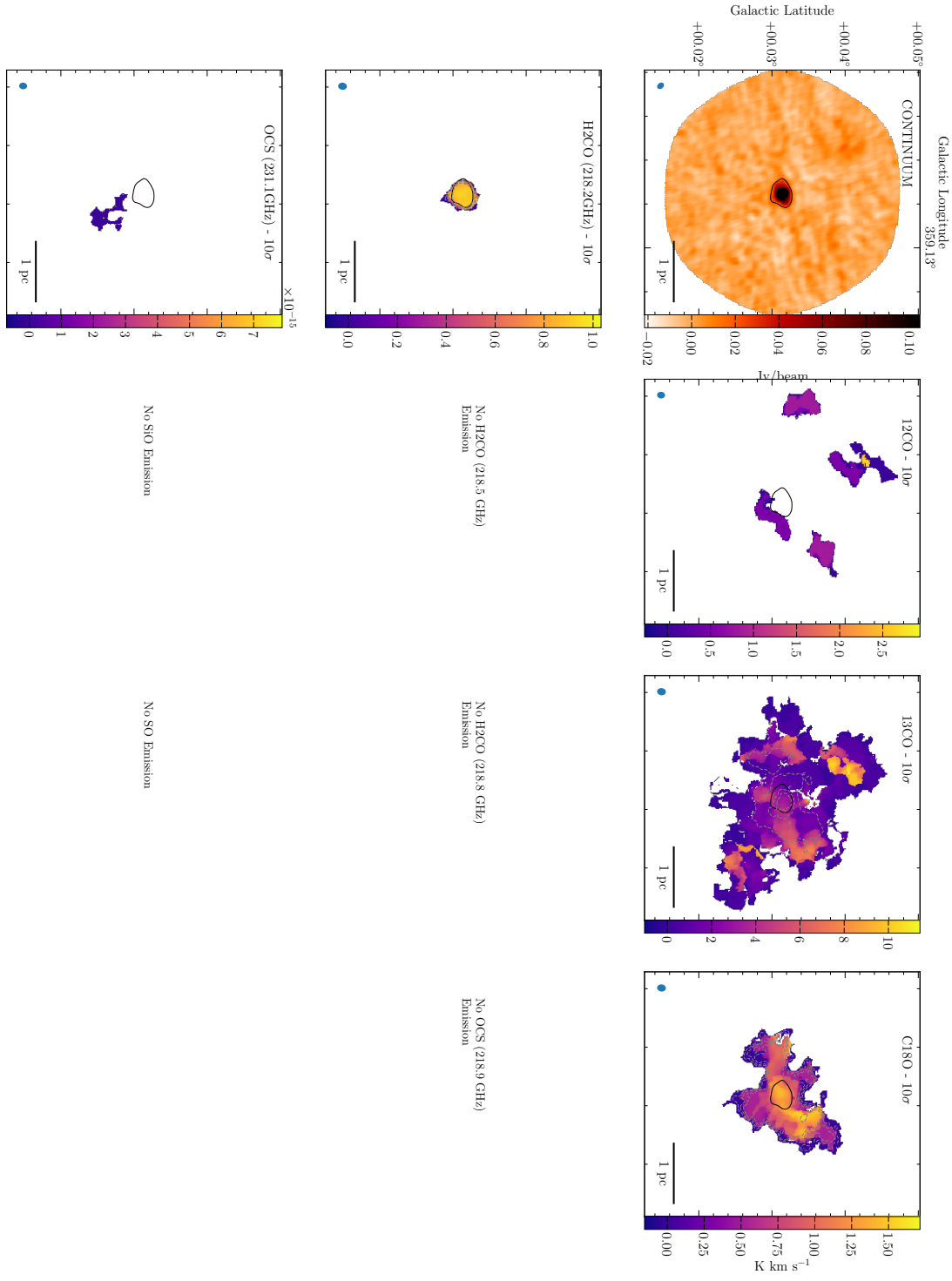

FIGURE A.57: G359.137+0.031 velocity dispersion moment maps

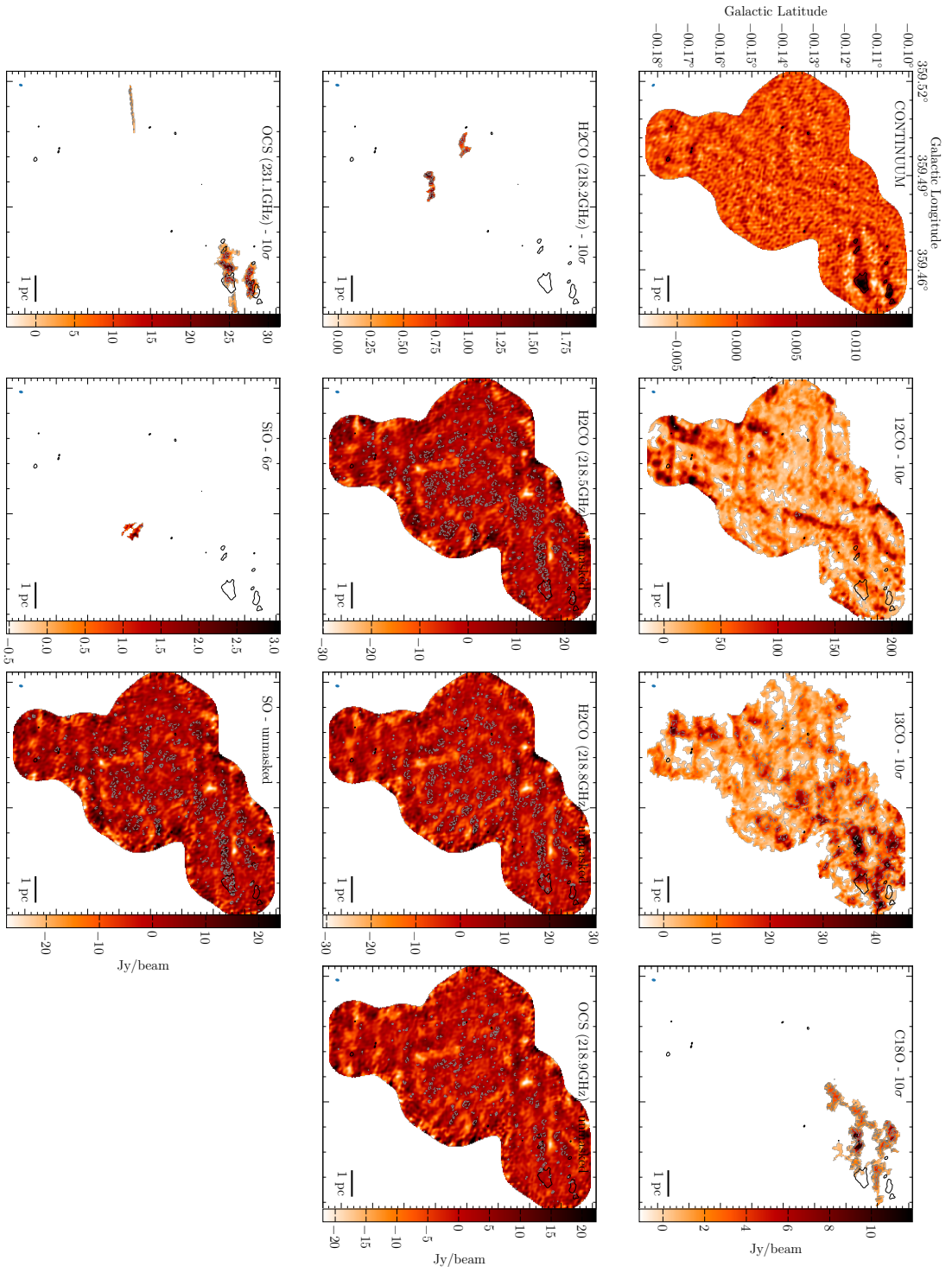

FIGURE A.58: G359.484-0.132 integrated intensity moment maps

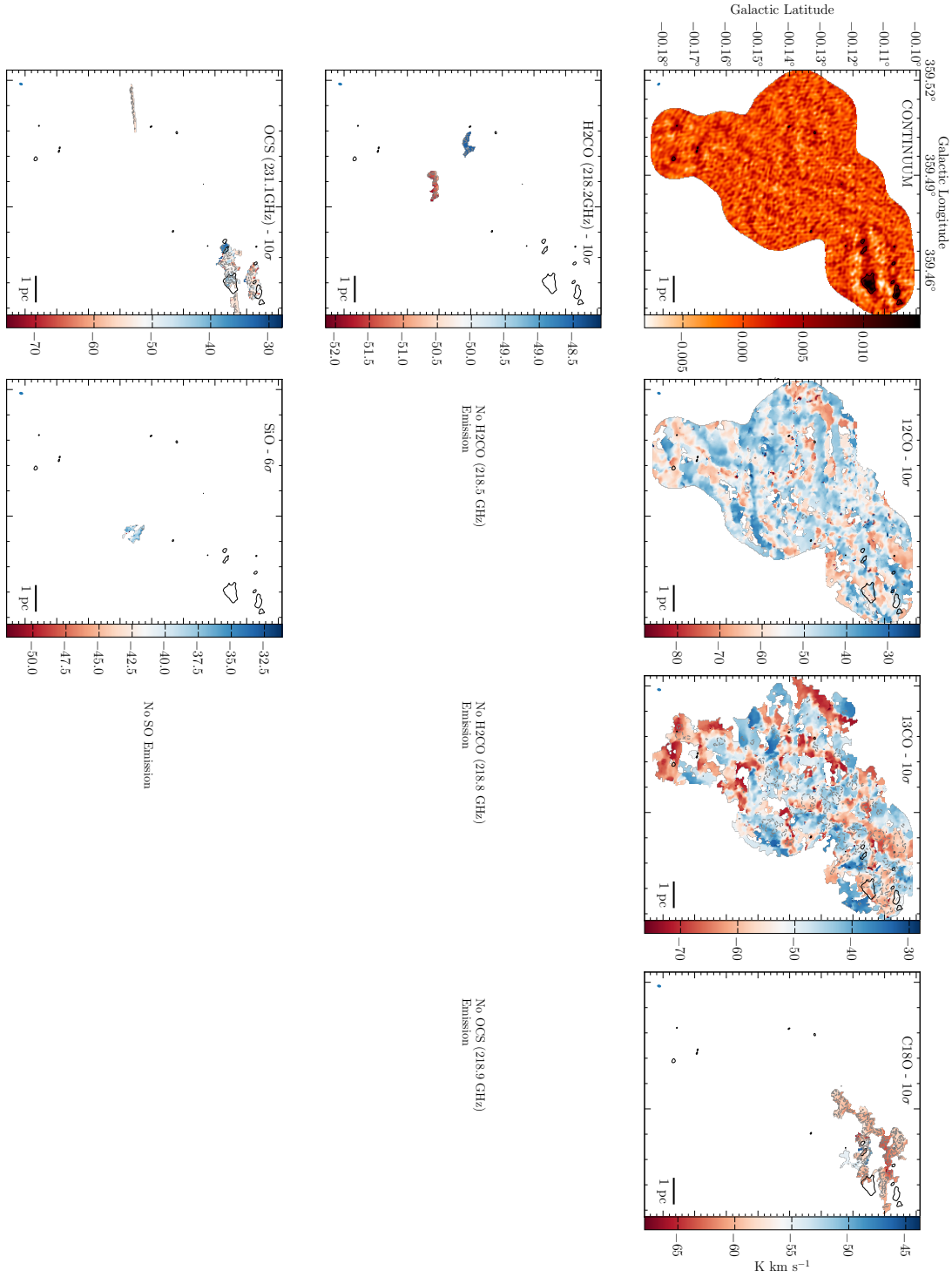

FIGURE A.59: G359.484-0.132 V_{LSR} moment maps

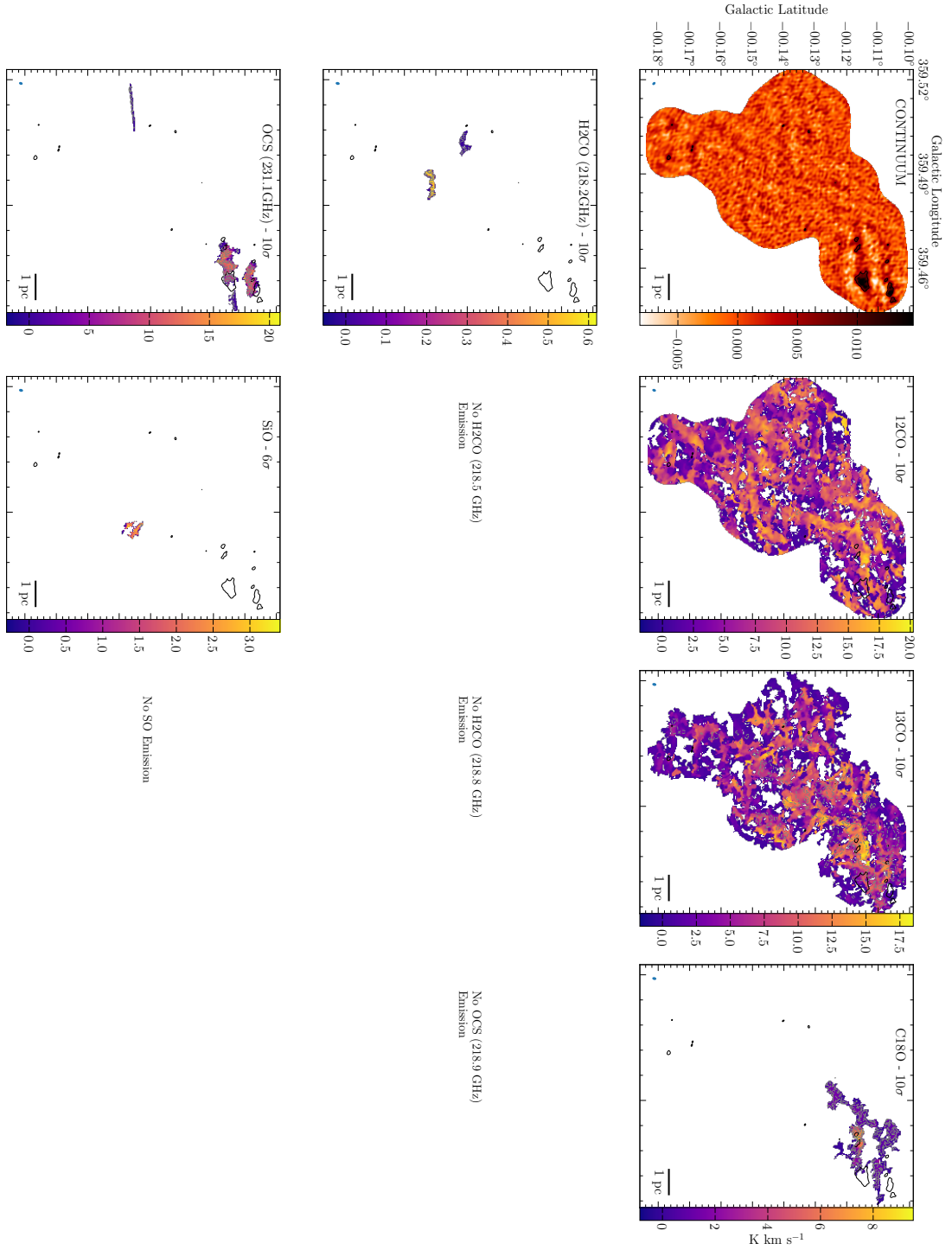

FIGURE A.60: G359.484-0.132 velocity dispersion moment maps

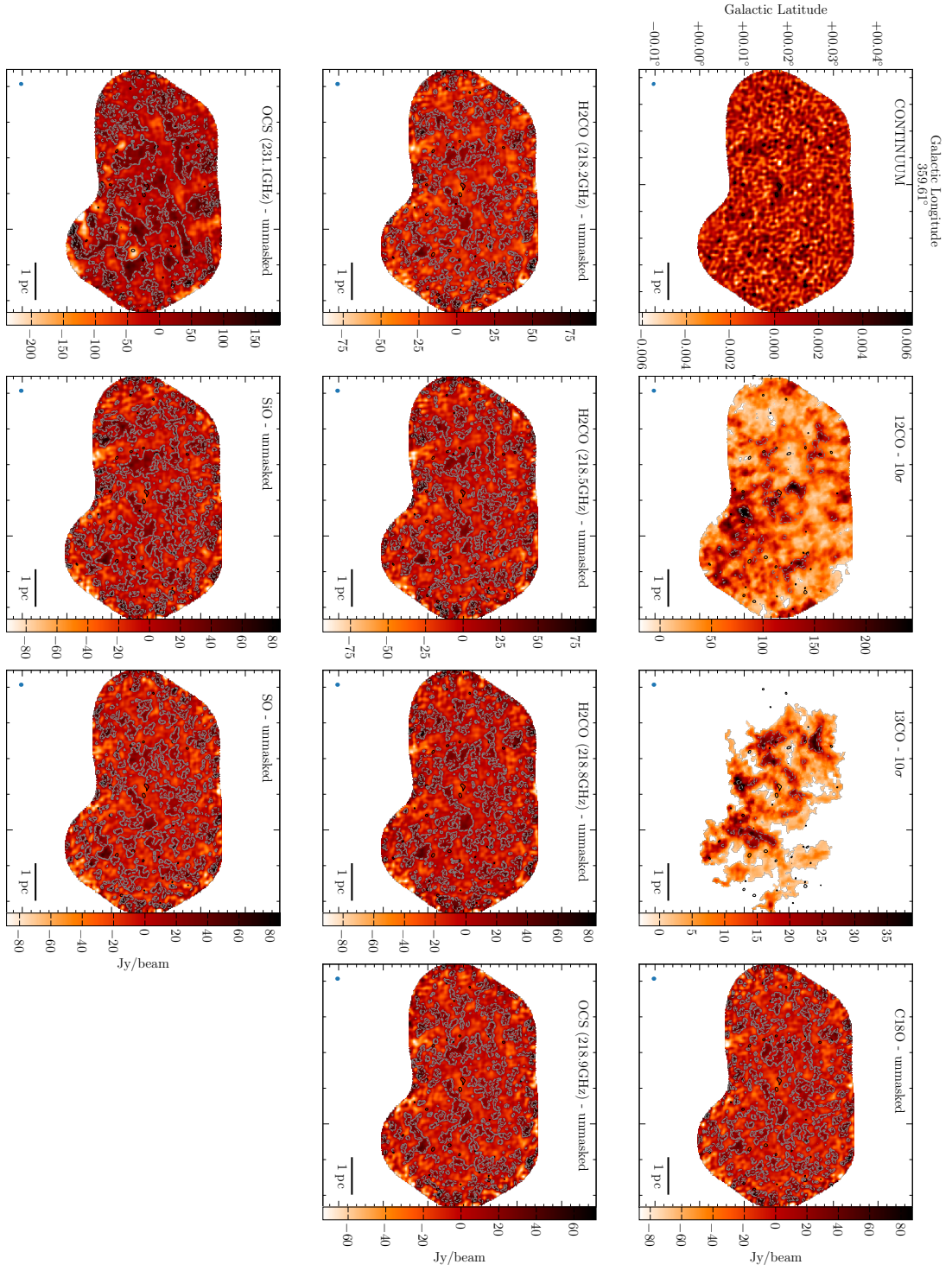

FIGURE A.61: G359.611+0.018 integrated intensity moment maps

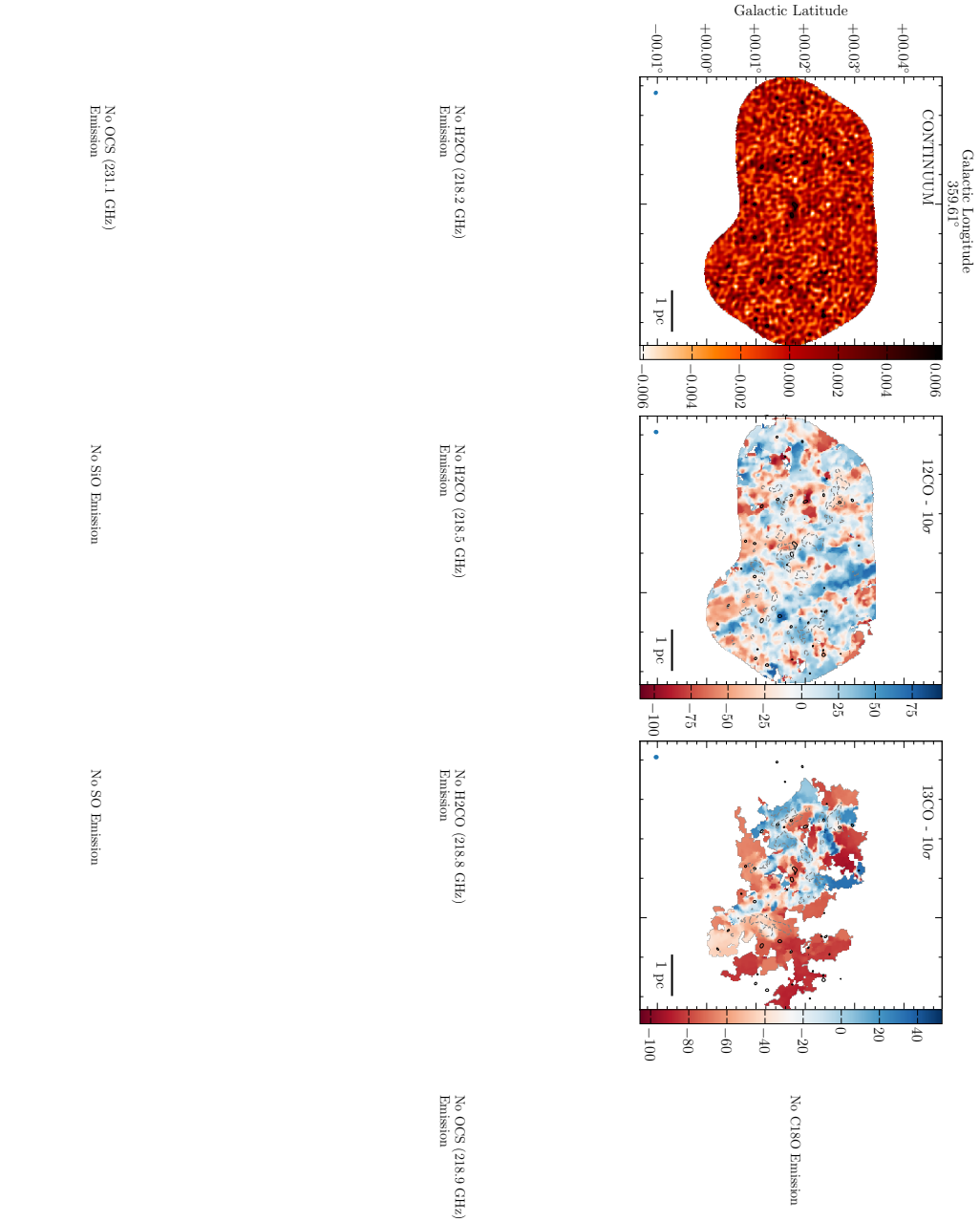

FIGURE A.62: G359.611+0.018 V_{LSR} moment maps

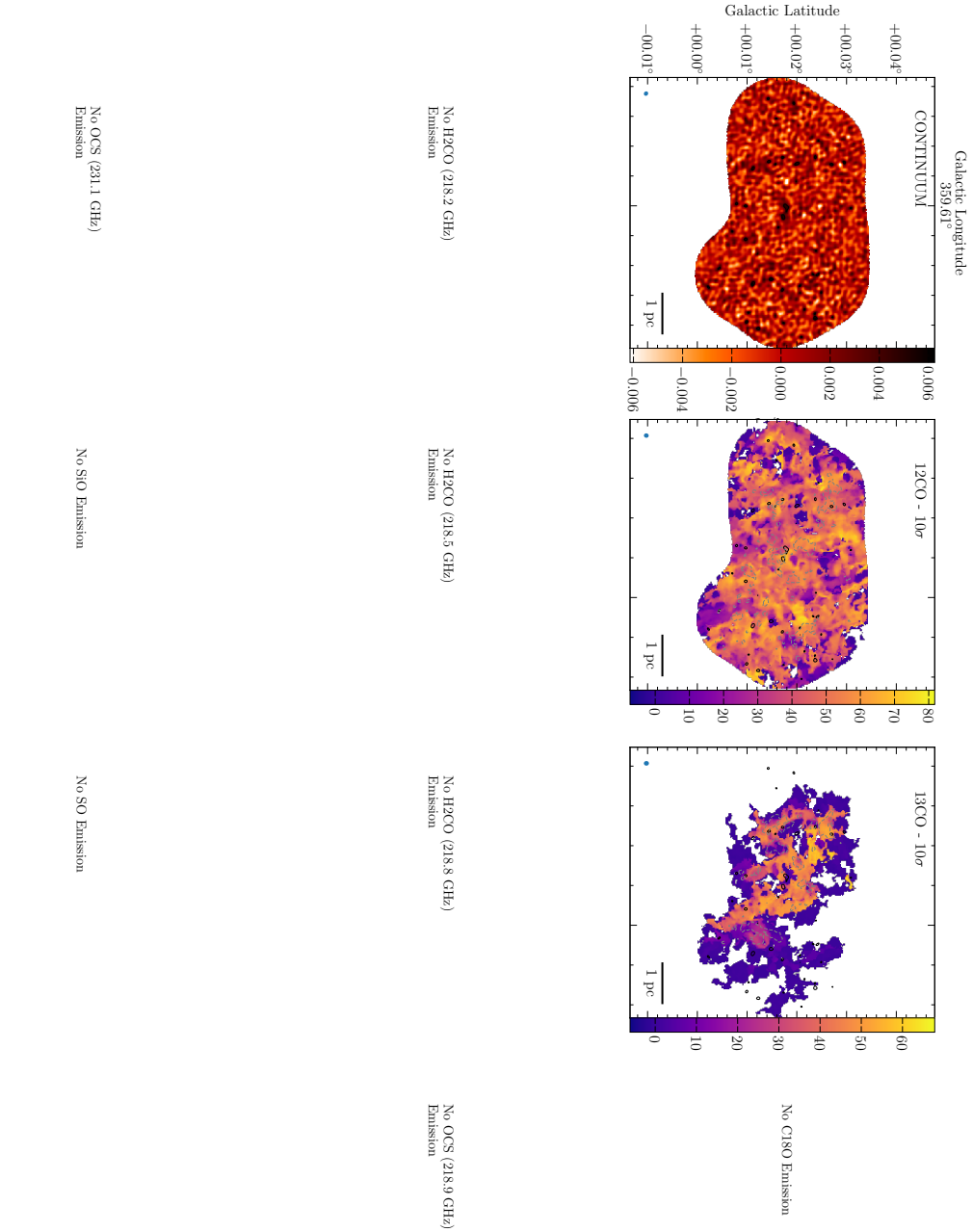

FIGURE A.63: G359.611+0.018 velocity dispersion moment maps

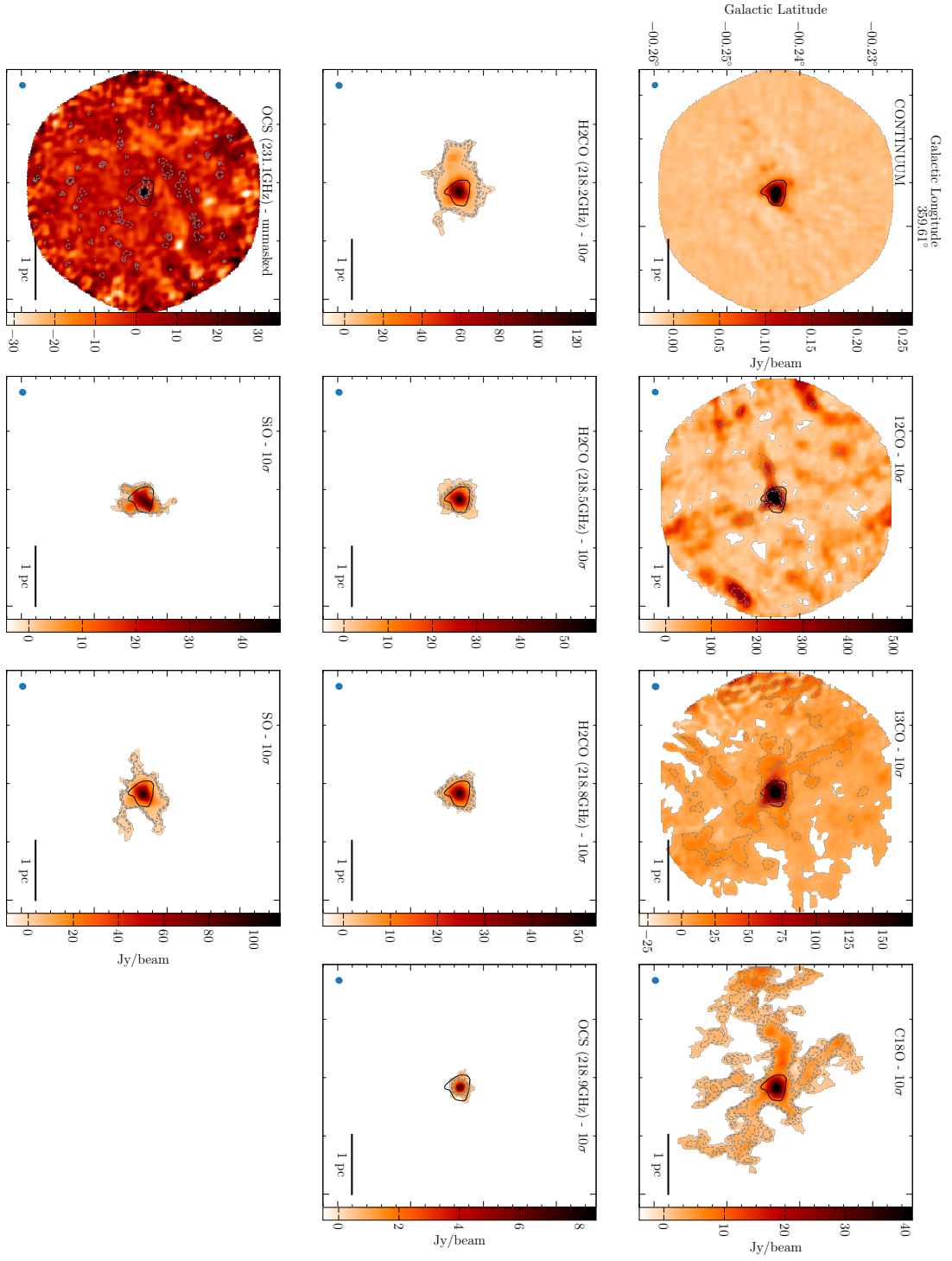

FIGURE A.64: G359.615-0.243 integrated intensity moment maps

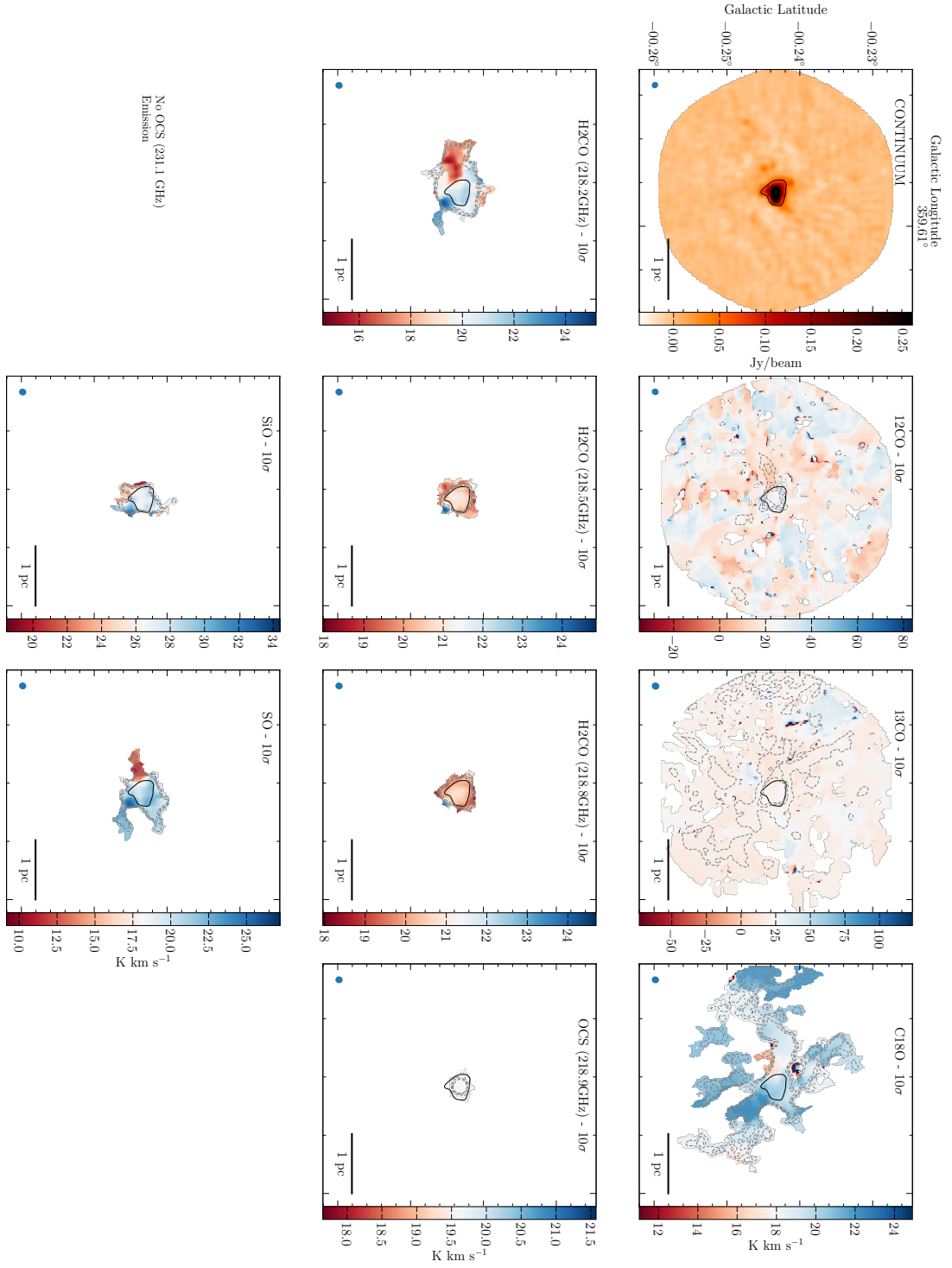

FIGURE A.65: G359.615-0.243 V_{LSR} moment maps

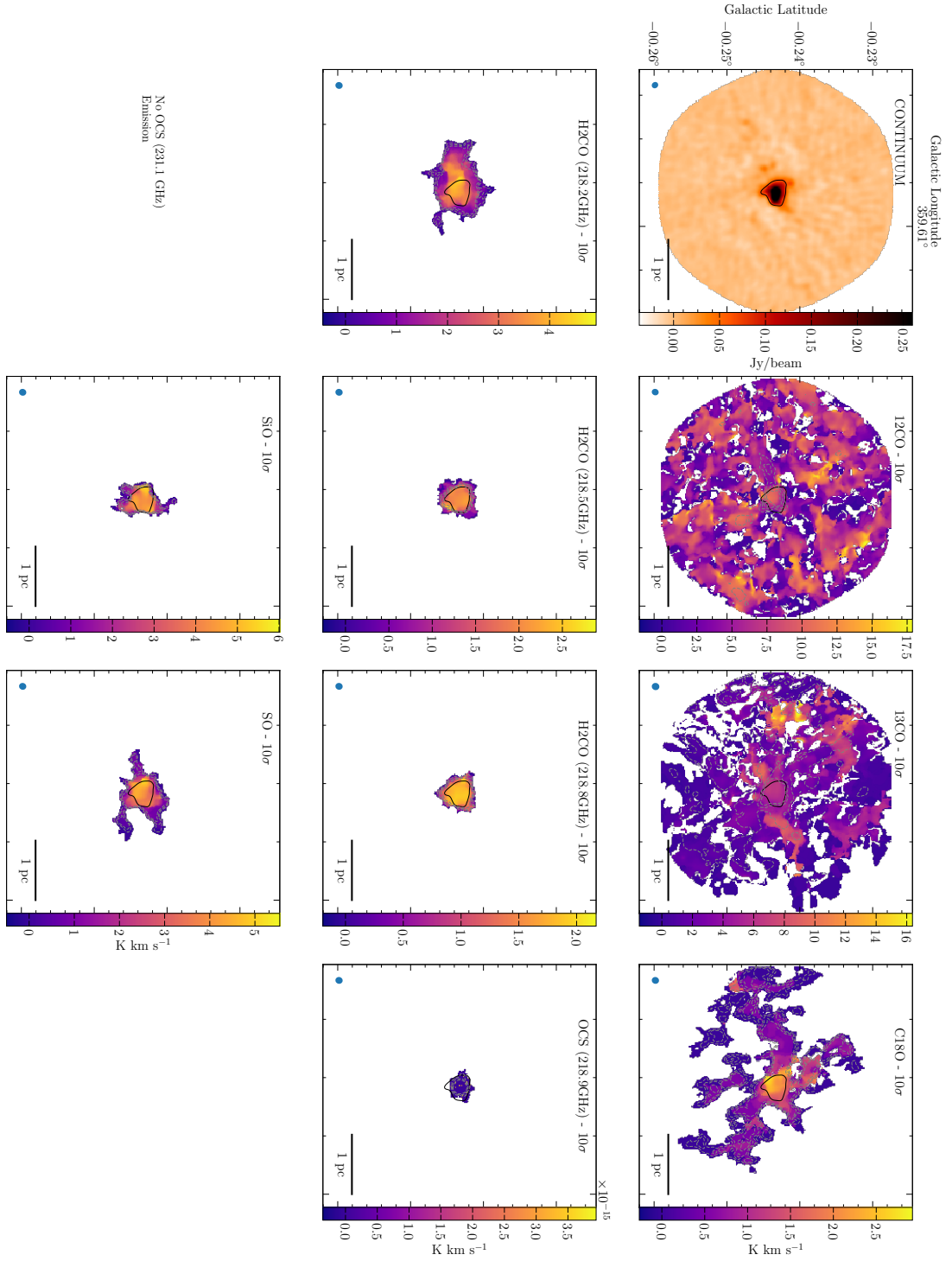

FIGURE A.66: G359.615-0.243 velocity dispersion moment maps

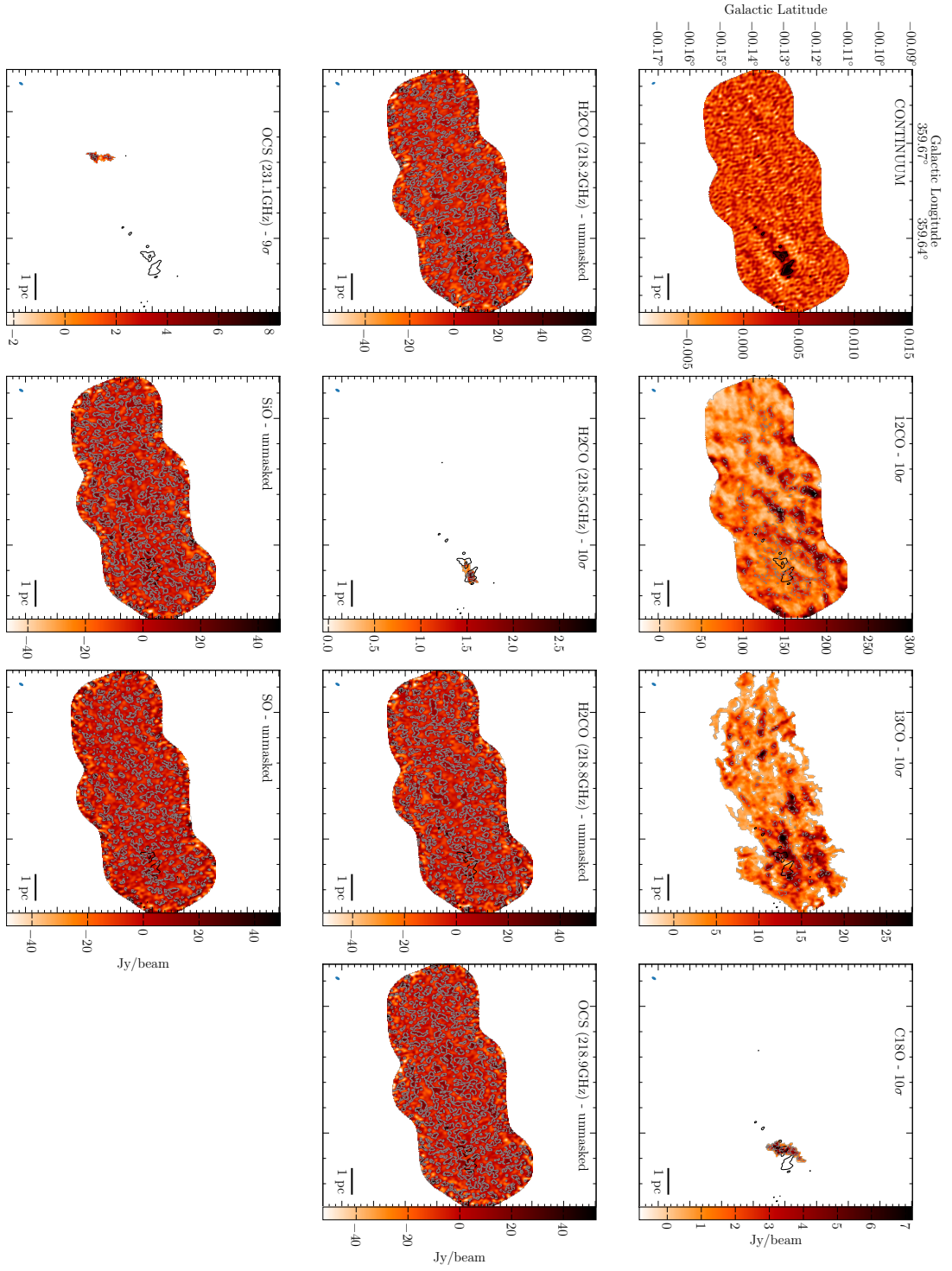

FIGURE A.67: G359.648-0.133 integrated intensity moment maps

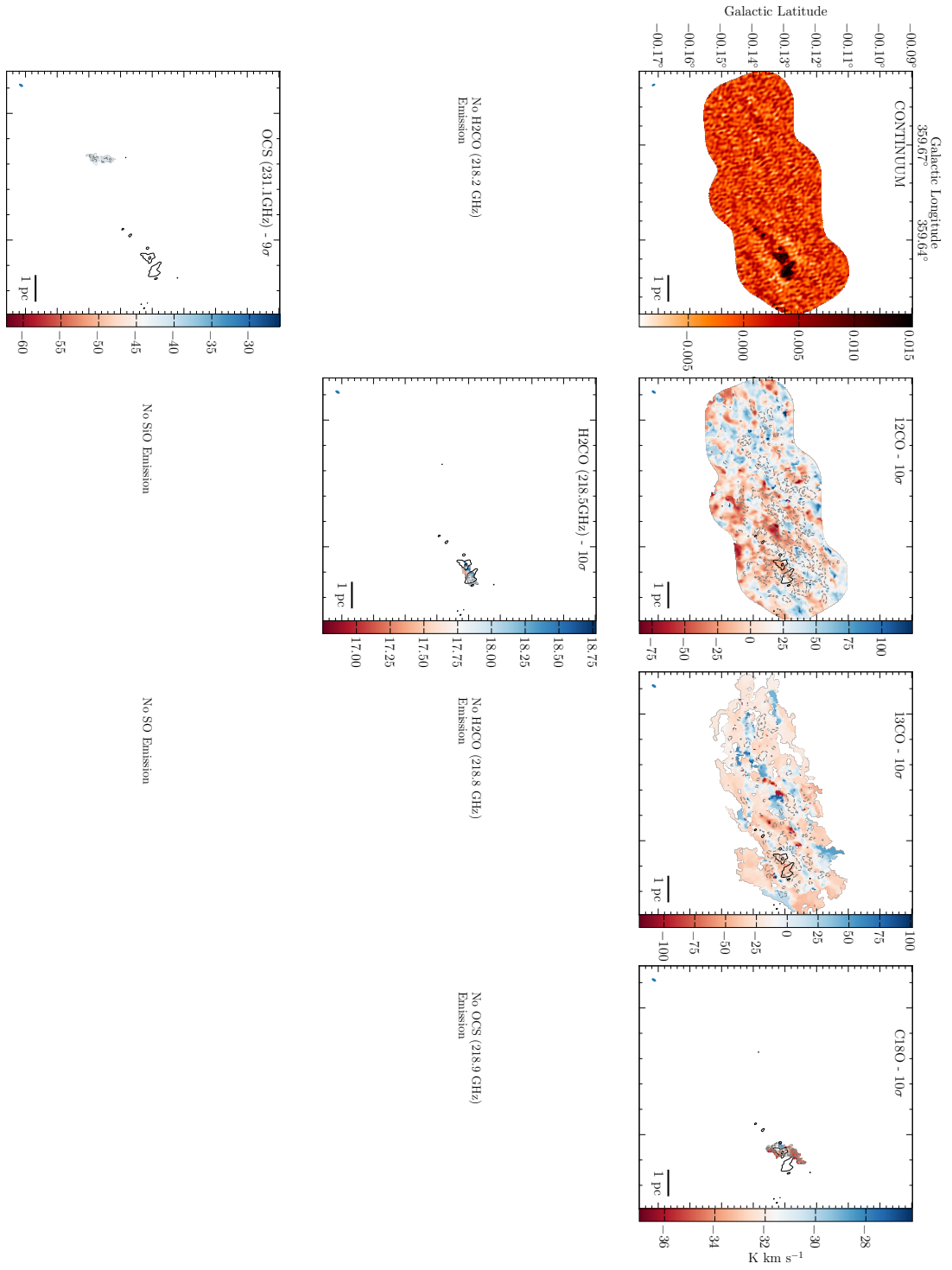

FIGURE A.68: G359.648-0.133 V_{LSR} moment maps

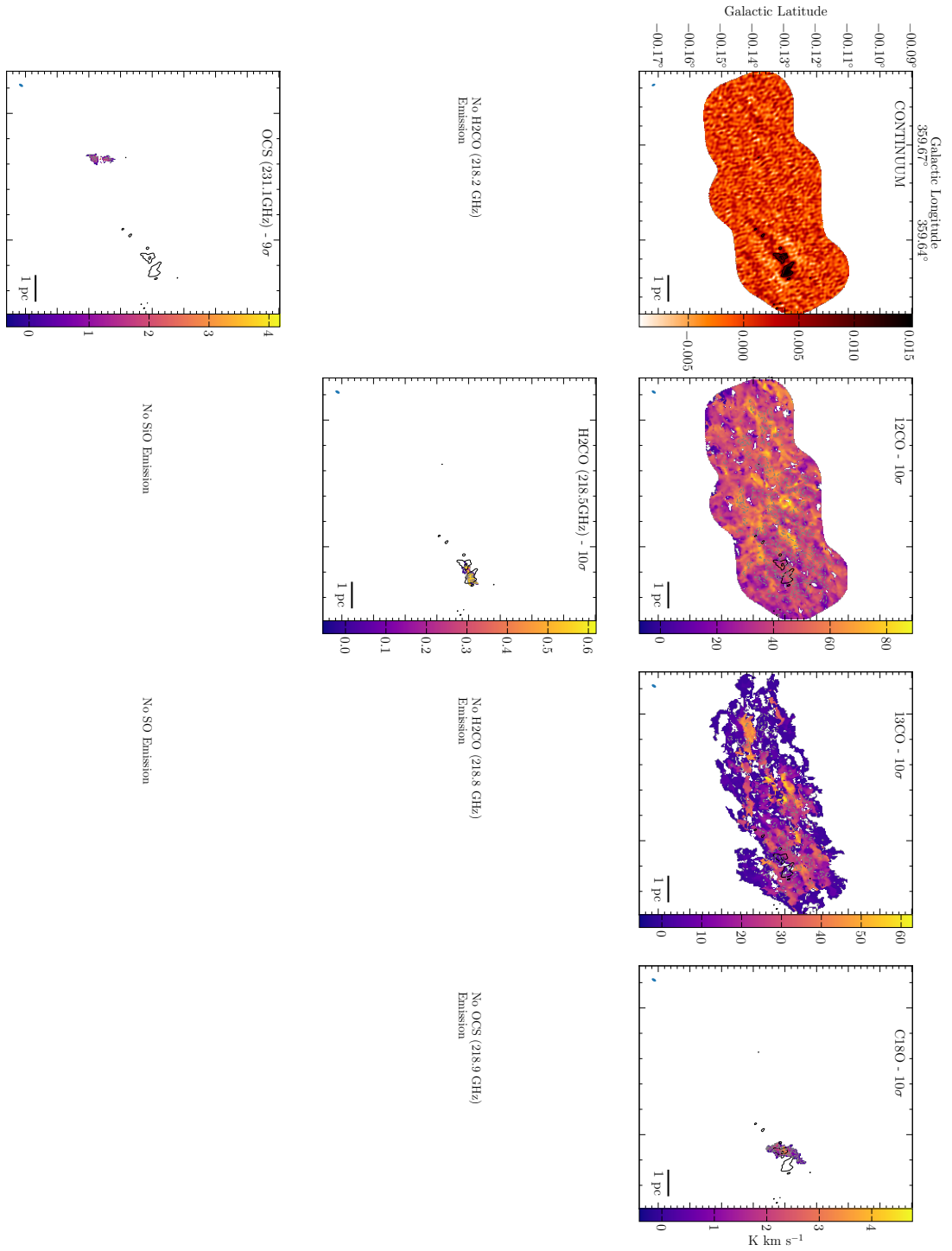

FIGURE A.69: G359.648-0.133 velocity dispersion moment maps

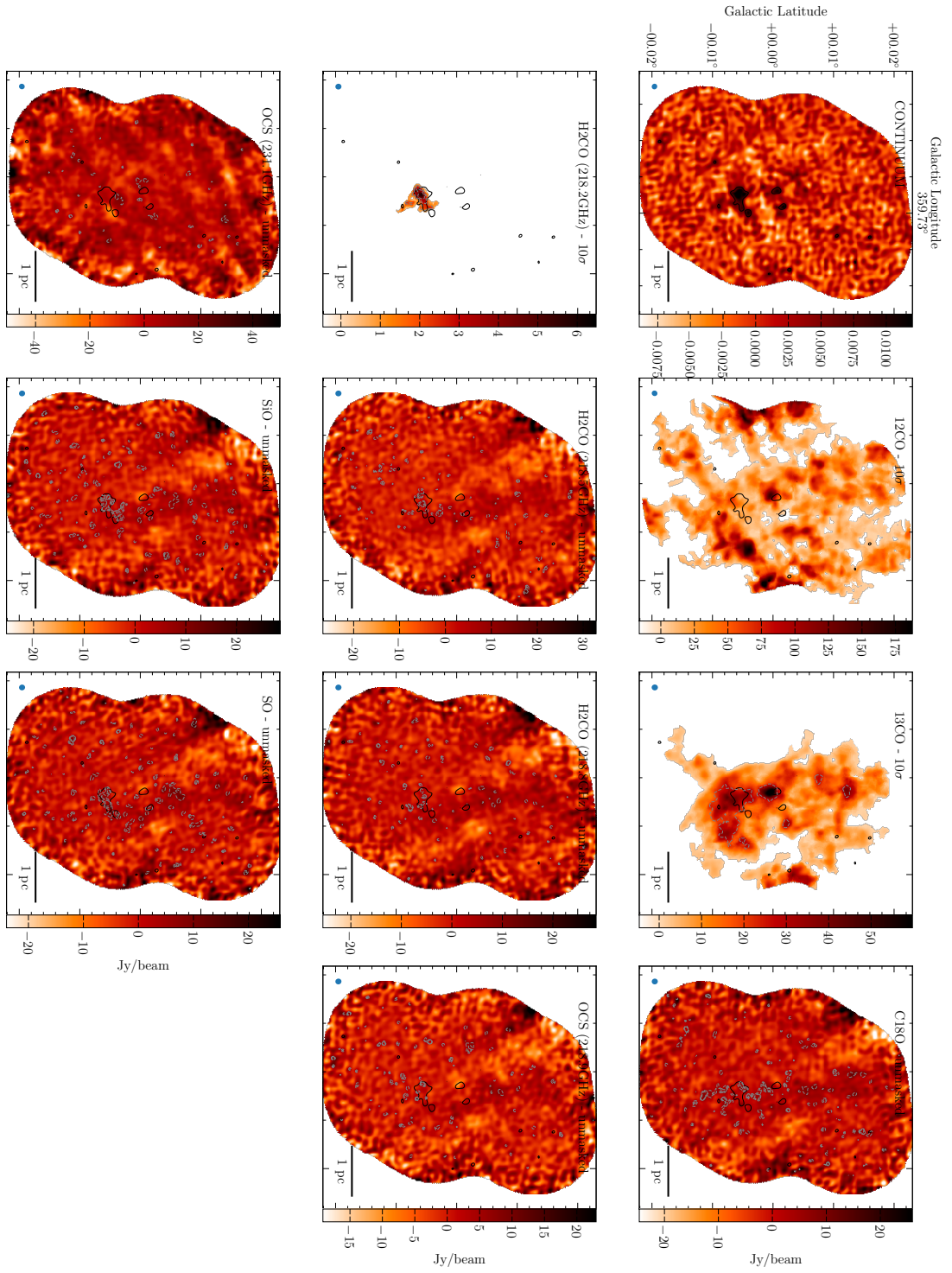

FIGURE A.70: G359.734+0.002 integrated intensity moment maps

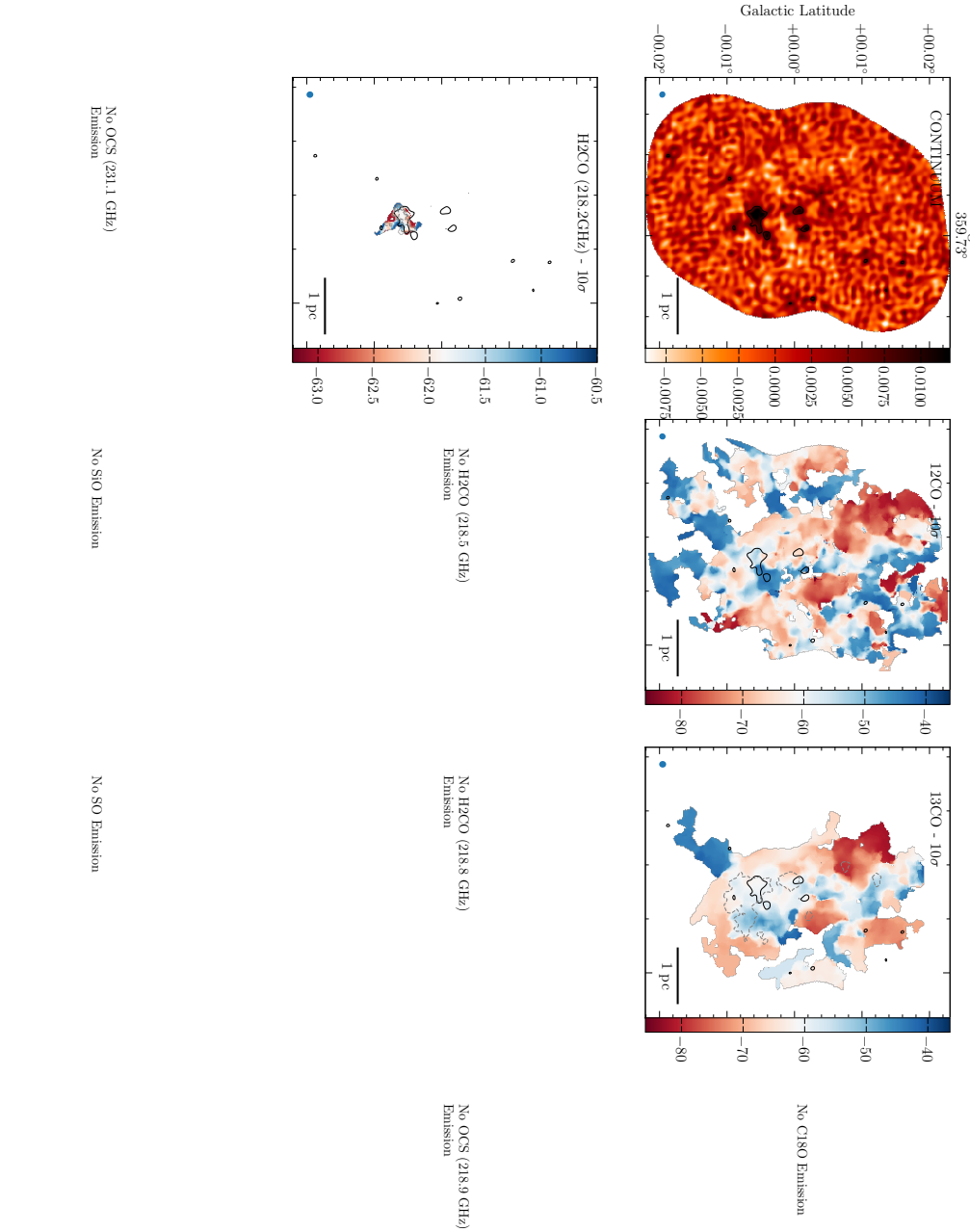

FIGURE A.71: G359.734+0.002 V_{LSR} moment maps

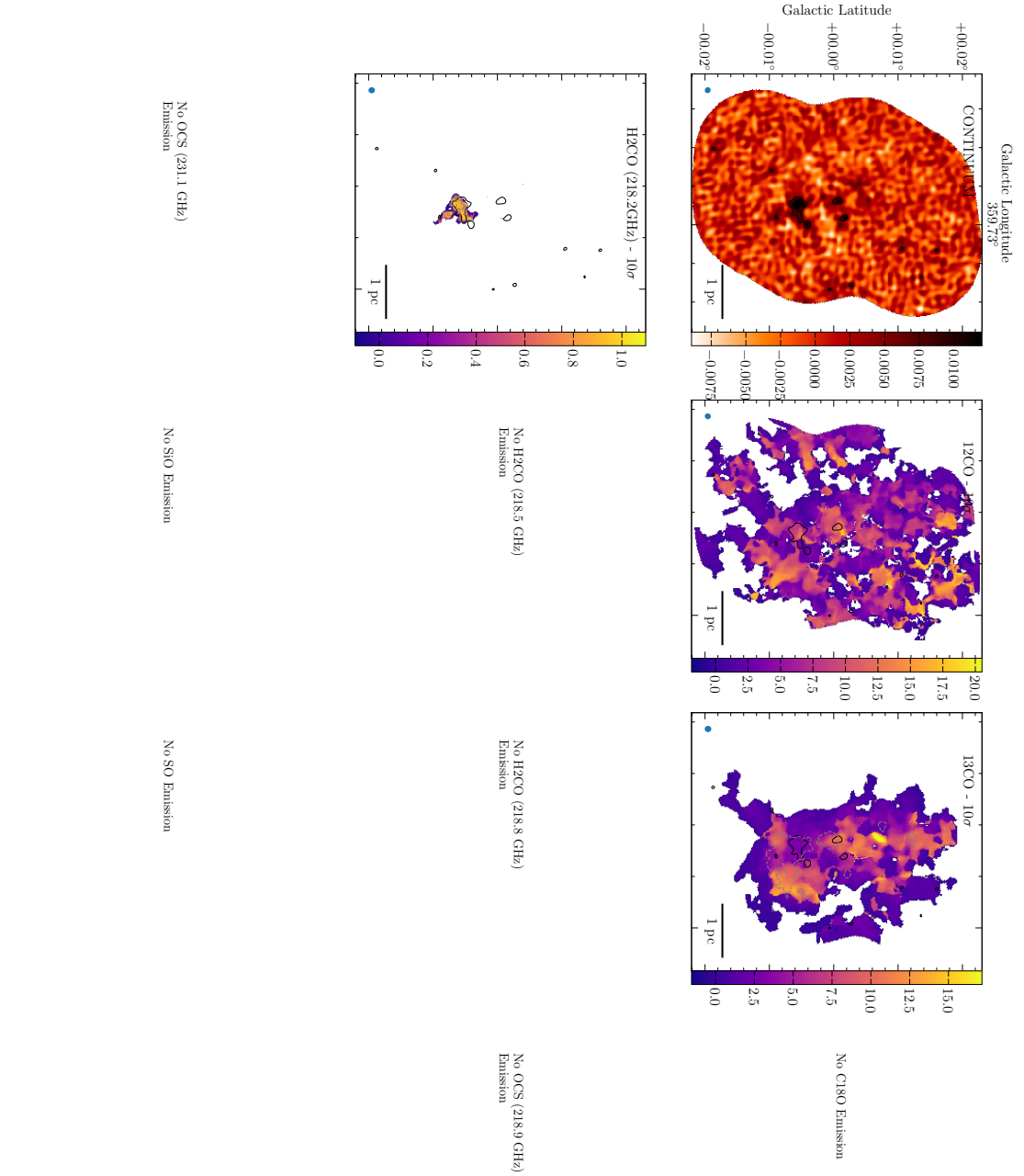

FIGURE A.72: G359.734+0.002 velocity dispersion moment maps

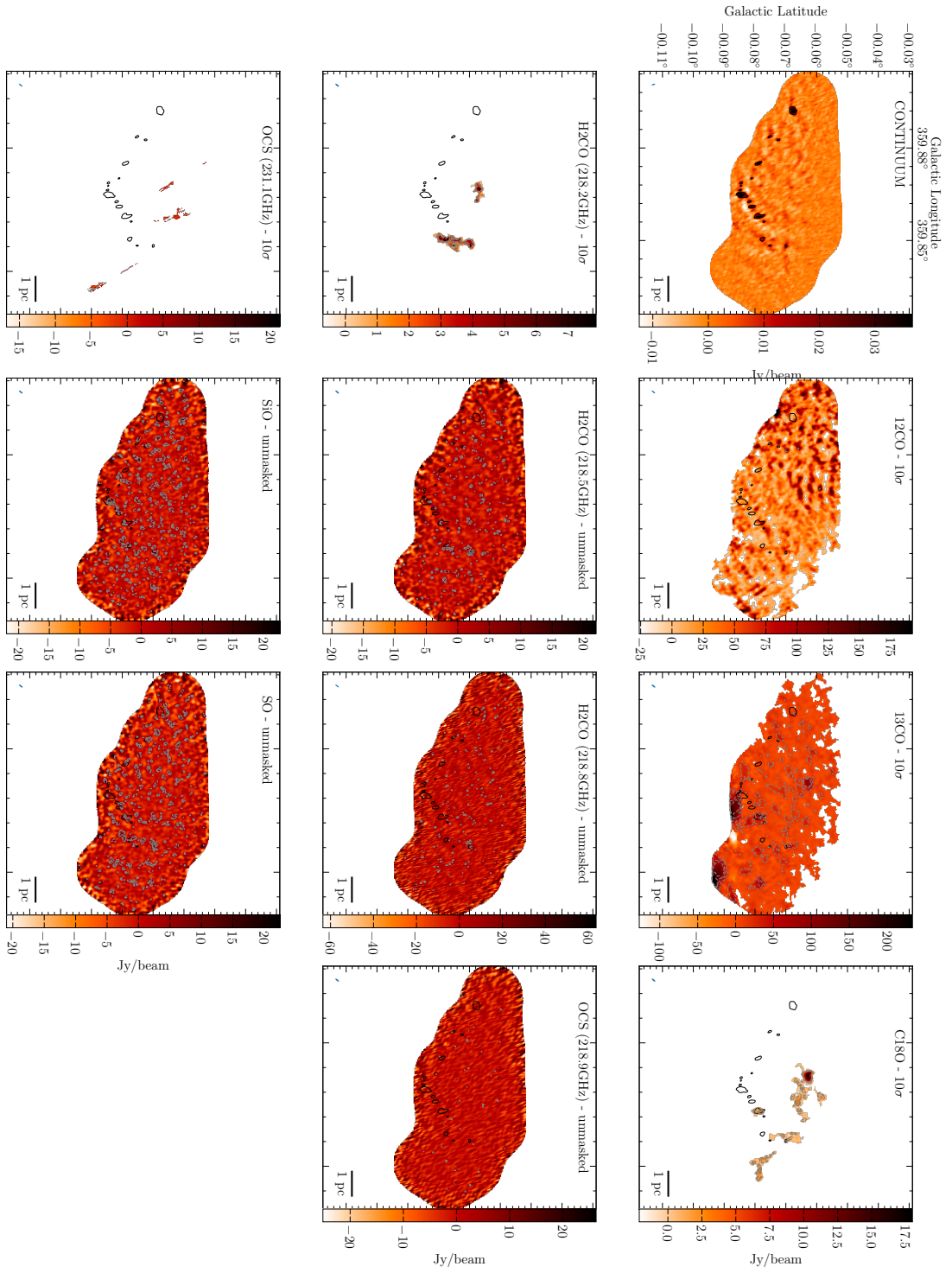

FIGURE A.73: G359.863-0.069 integrated intensity moment maps

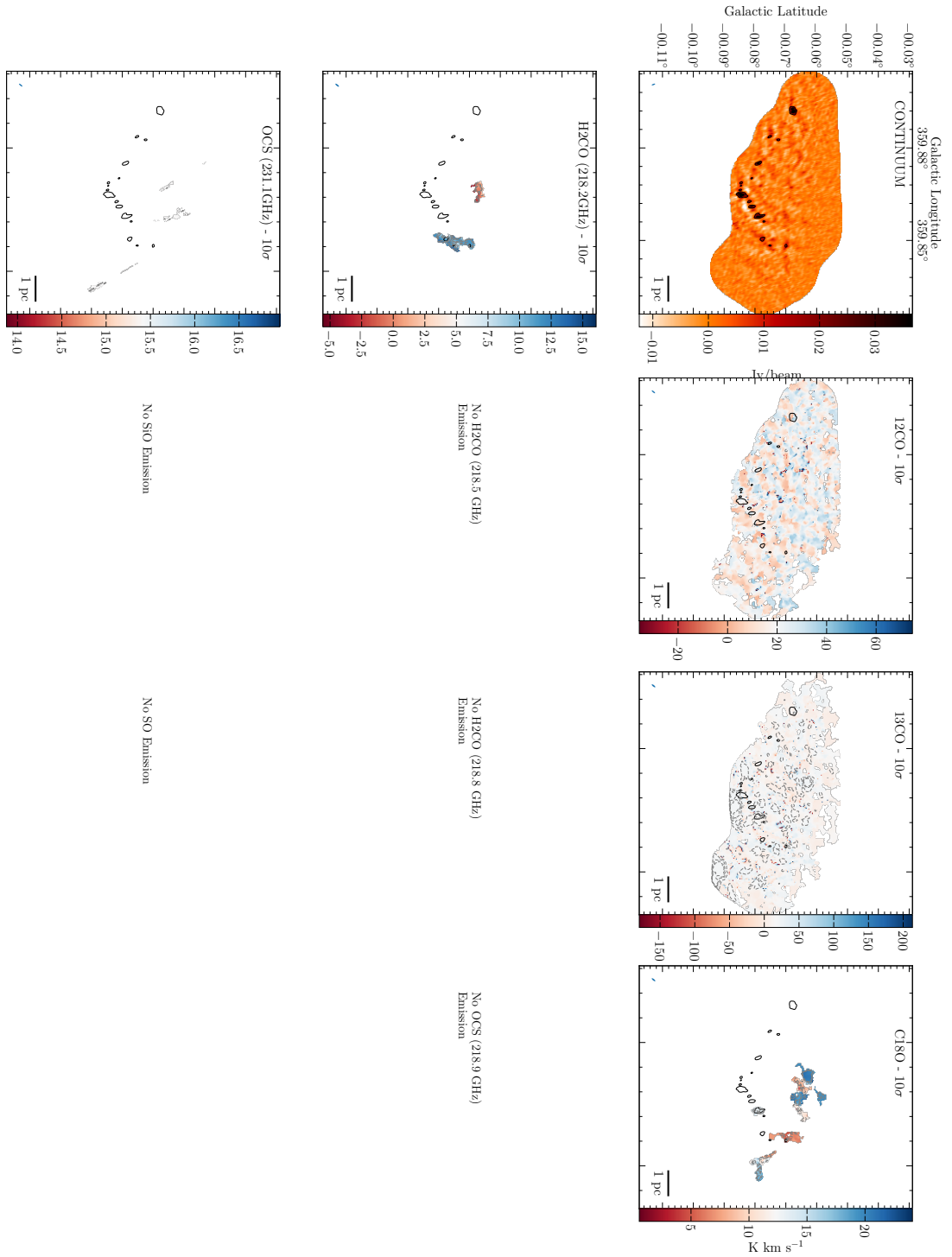

FIGURE A.74: G359.863-0.069 V_{LSR} moment maps

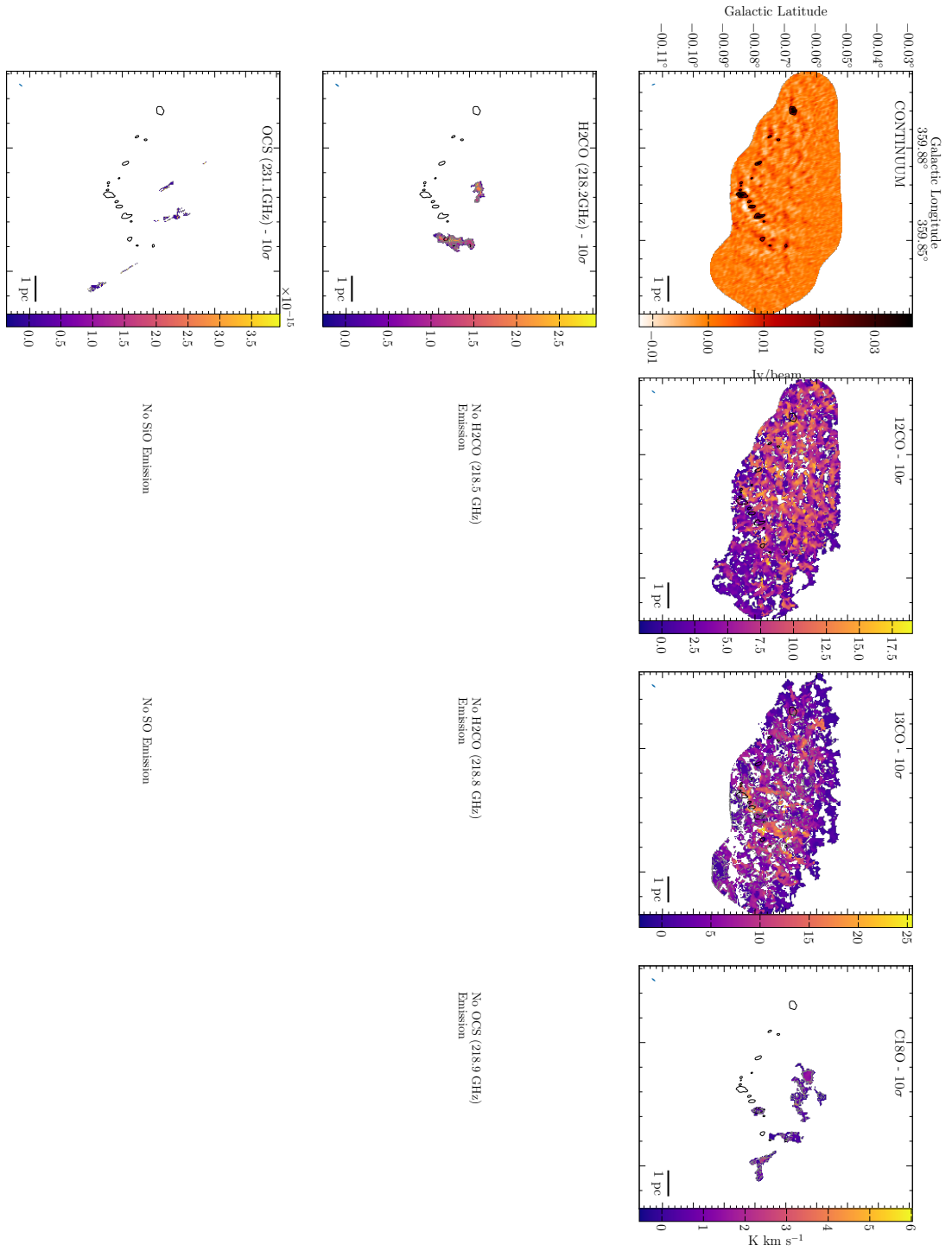

FIGURE A.75: G359.863-0.069 velocity dispersion moment maps

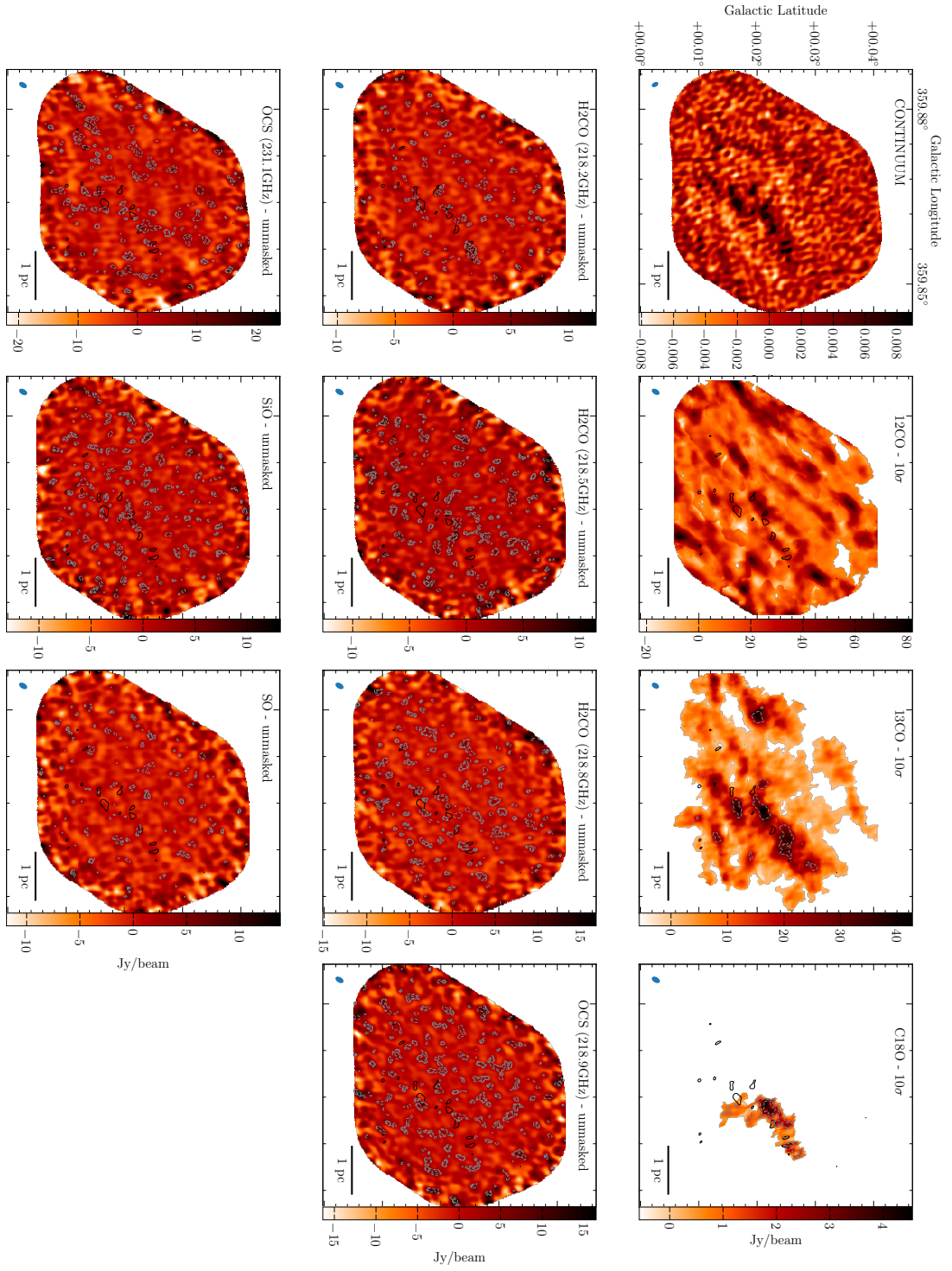

FIGURE A.76: G359.865+0.022 integrated intensity moment maps

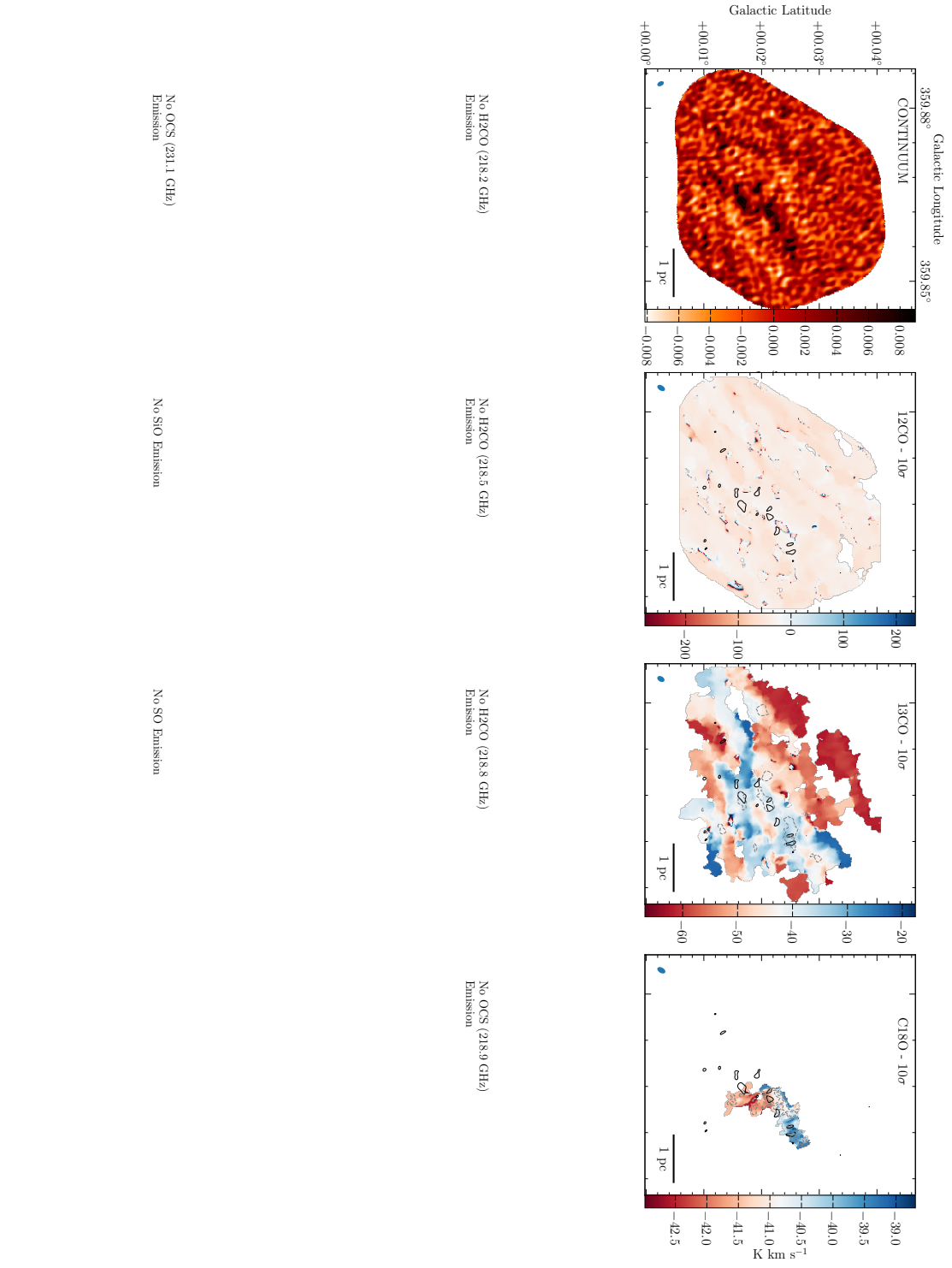

FIGURE A.77: G359.865+0.022 V_{LSR} moment maps

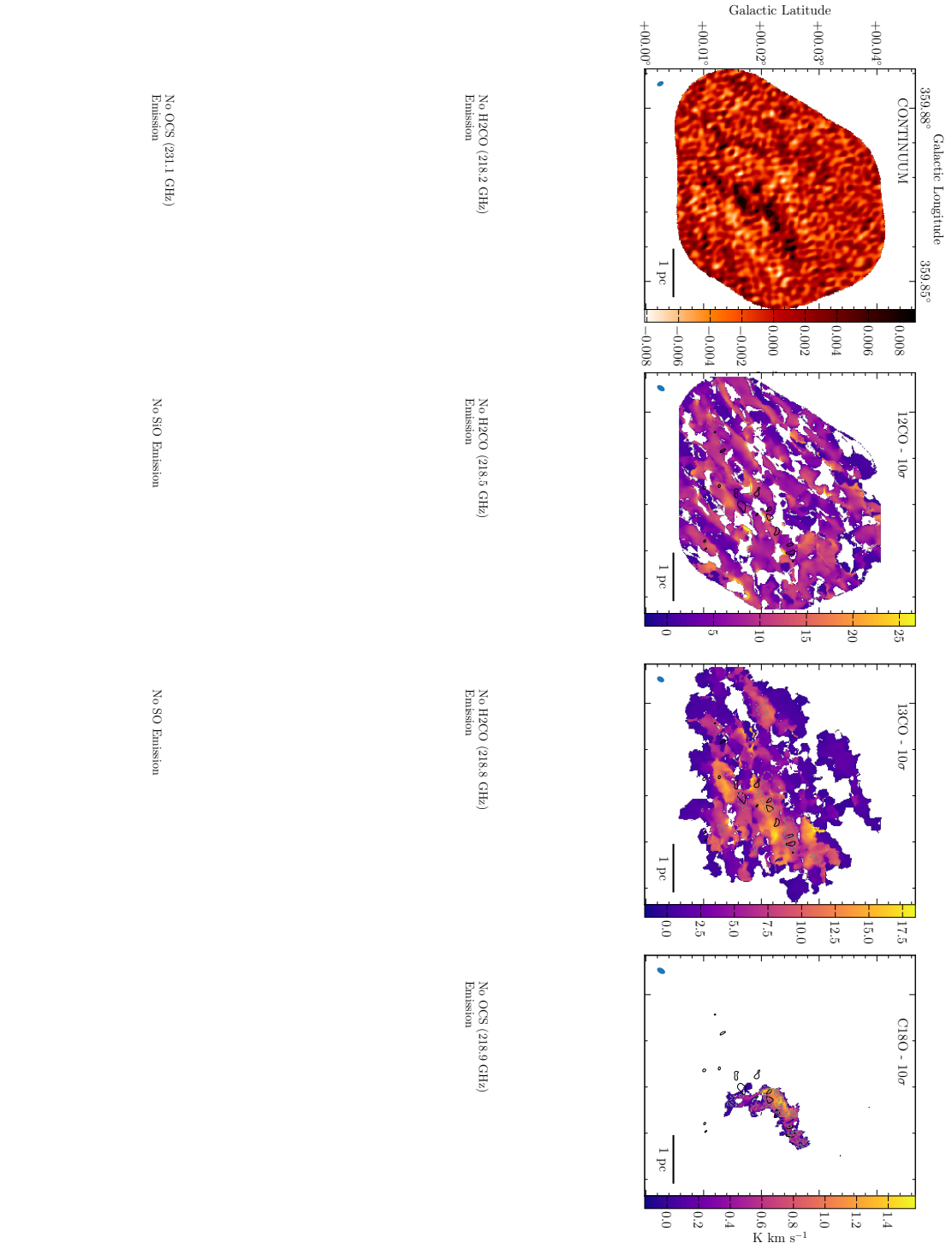

FIGURE A.78: G359.865+0.022 velocity dispersion moment maps

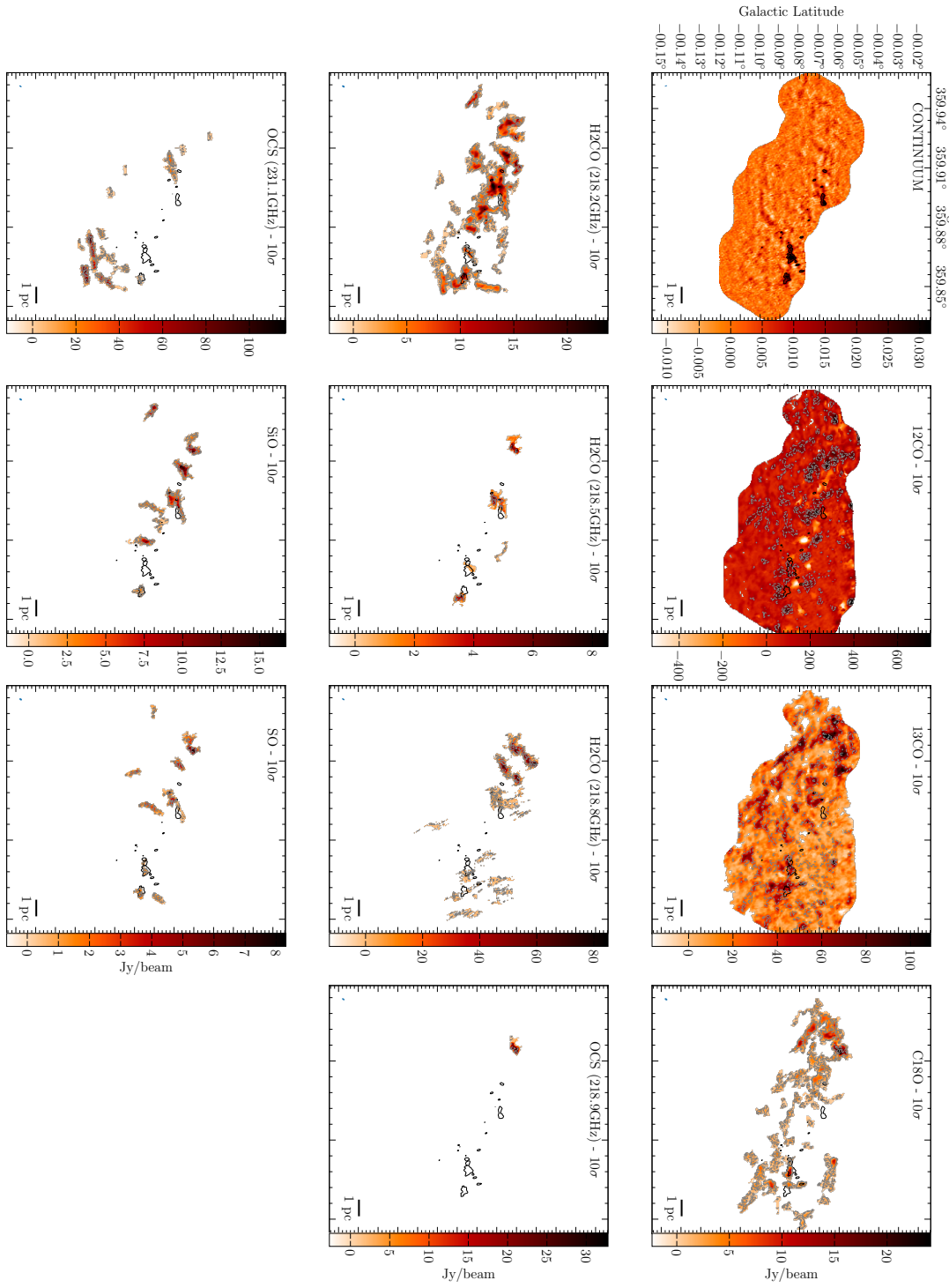

FIGURE A.79: G359.889-0.093 integrated intensity moment maps

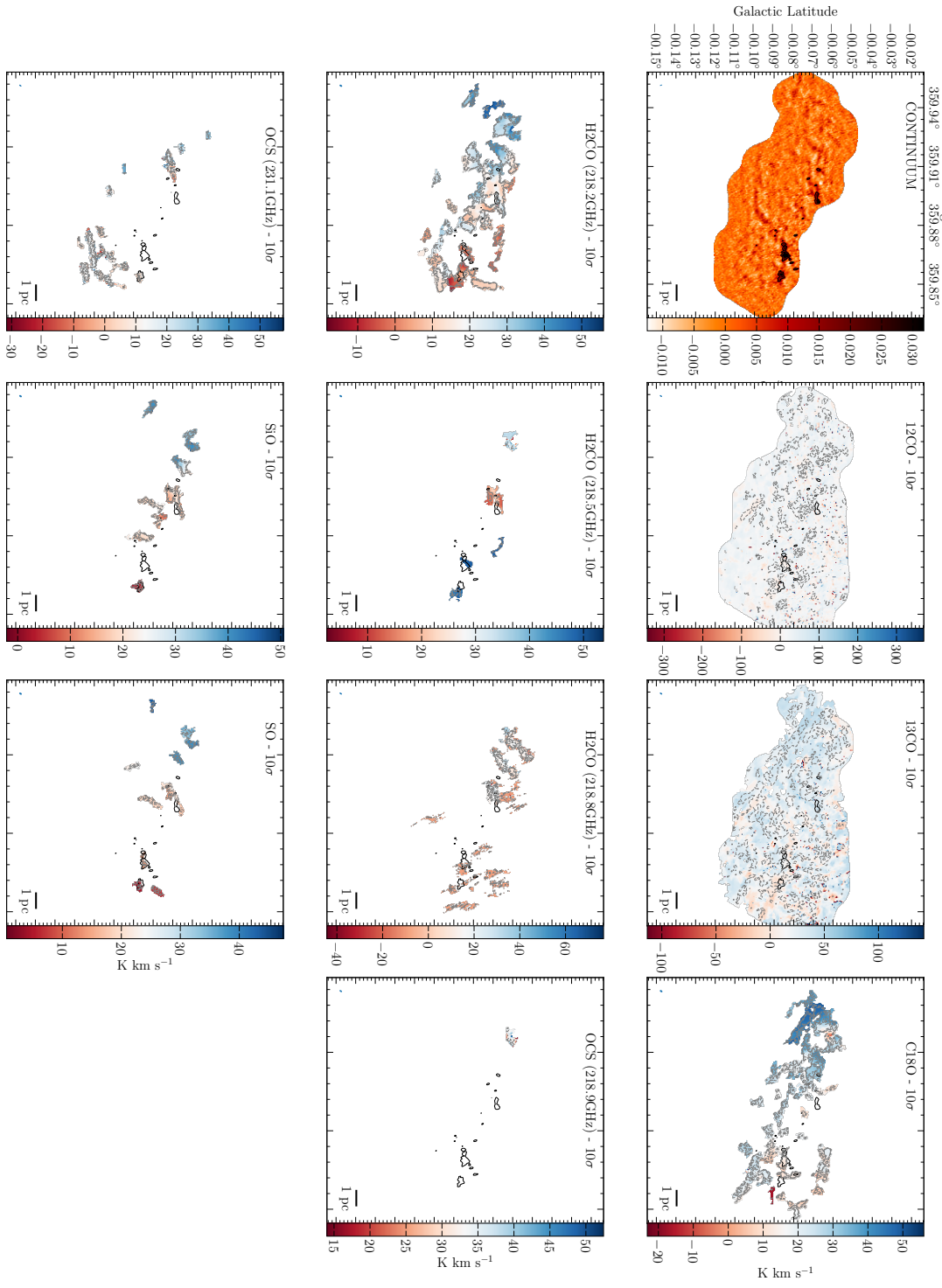

FIGURE A.80: G359.889-0.093 V_{LSR} moment maps

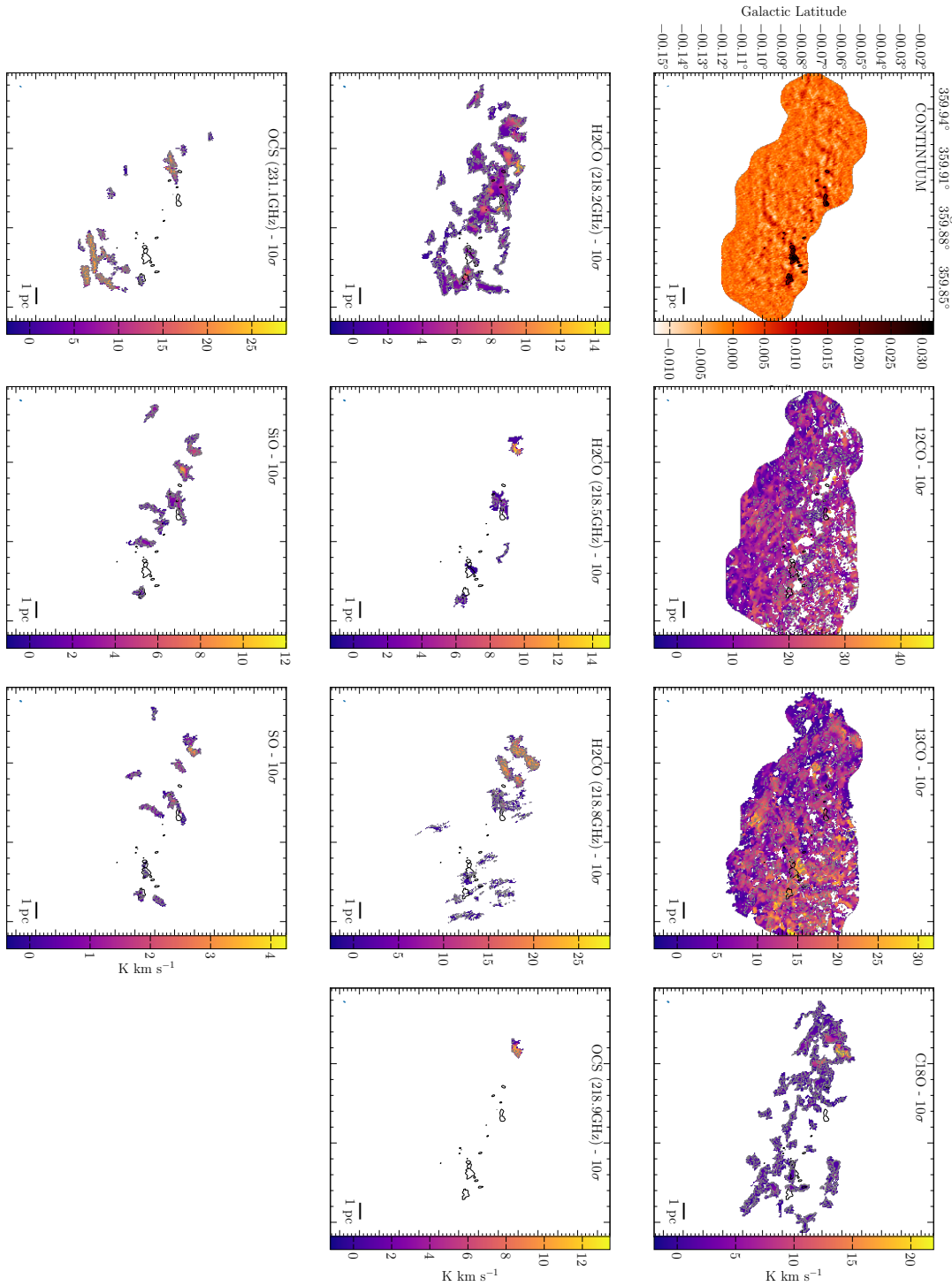

FIGURE A.81: G359.889-0.093 velocity dispersion moment maps

A.2 Appendix 2: CMZoom Spectra Fitting Parameters

Leaf	Transition	Detected	Number of Comps	Comp.	Amplitude	Velocity	Width	RMS
G0.001-0.058a	12CO (230.5GHz)	Y	4	1	3.99 ± 0.16	92.48 ± 0.35	6.76 ± 6.76	0.32
G0.001-0.058a	12CO (230.5GHz)	Y	4	3	1.56 ± 0.18	43.14 ± 0.41	3.09 ± 3.09	0.32
G0.001-0.058a	12CO (230.5GHz)	Y	4	4	5.66 ± 0.18	20.75 ± 0.11	3.19 ± 3.19	0.32
G0.001-0.058a	13CO (220.4GHz)	Y	4	1	0.57 ± 0.05	94.76 ± 0.67	6.46 ± 6.46	0.12
G0.001-0.058a	13CO (220.4GHz)	Y	4	2	1.35 ± 0.18	59.3 ± 0.1	0.75 ± 0.75	0.12
G0.001-0.058a	13CO (220.4GHz)	Y	4	3	1.85 ± 0.16	51.5 ± 0.07	0.81 ± 0.81	0.12
G0.001-0.058a	13CO (220.4GHz)	Y	4	4	0.54 ± 0.04	30.73 ± 0.93	10.44 ± 10.44	0.12
G0.001-0.058a	C18O (219.6GHz)	Y	1	1	0.15 ± 0.02	30.71 ± 1.03	6.36 ± 6.36	0.06
G0.001-0.058a	H2CO (218.2GHz)	Y	3	1	0.44 ± 0.02	38.62 ± 0.88	6.09 ± 6.09	0.04
G0.001-0.058a	H2CO (218.2GHz)	Y	3	2	0.55 ± 0.04	25.14 ± 0.55	4.72 ± 4.72	0.04
G0.001-0.058a	H2CO (218.5GHz)	Y	2	1	1.33 ± 0.02	82.2 ± 0.11	6.47 ± 6.47	0.04
G0.001-0.058a	H2CO (218.5GHz)	Y	2	2	0.31 ± 0.02	36.32 ± 0.55	9.55 ± 9.55	0.04
G0.001-0.058a	H2CO (218.8GHz)	Y	1	1	0.37 ± 0.01	33.5 ± 0.33	7.39 ± 7.39	0.04
G0.001-0.058a	OCS (218.9GHz)	N	0	0	0.0 ± 0.0	0.0 ± 0.0	0.0 ± 0.0	0.04
G0.001-0.058a	OCS (231.1GHz)	Y	2	1	0.32 ± 0.02	32.67 ± 0.47	7.15 ± 7.15	0.05
G0.001-0.058a	SO (219.9GHz)	Y	3	1	0.18 ± 0.02	91.63 ± 0.52	3.39 ± 3.39	0.04
G0.001-0.058a	SO (219.9GHz)	Y	3	2	0.67 ± 0.02	33.84 ± 0.19	6.39 ± 6.39	0.04
G0.001-0.058a	SiO (217.1GHz)	Y	1	1	0.56 ± 0.02	34.63 ± 0.22	6.89 ± 6.89	0.04
G0.001-0.058b	12CO (230.5GHz)	N	0	0	0.0 ± 0.0	0.0 ± 0.0	0.0 ± 0.0	0.71
G0.001-0.058b	13CO (220.4GHz)	N	0	0	0.0 ± 0.0	0.0 ± 0.0	0.0 ± 0.0	0.29
G0.001-0.058b	C18O (219.6GHz)	N	0	0	0.0 ± 0.0	0.0 ± 0.0	0.0 ± 0.0	0.09
G0.001-0.058b	H2CO (218.2GHz)	Y	1	1	0.23 ± 0.05	37.28 ± 0.6	2.3 ± 2.3	0.08
G0.001-0.058b	H2CO (218.5GHz)	N	0	0	0.0 ± 0.0	0.0 ± 0.0	0.0 ± 0.0	0.06
G0.001-0.058b	H2CO (218.8GHz)	N	0	0	0.0 ± 0.0	0.0 ± 0.0	0.0 ± 0.0	0.06
G0.001-0.058b	OCS (218.9GHz)	N	0	0	0.0 ± 0.0	0.0 ± 0.0	0.0 ± 0.0	0.05
G0.001-0.058b	OCS (231.1GHz)	N	0	0	0.0 ± 0.0	0.0 ± 0.0	0.0 ± 0.0	0.1
G0.001-0.058b	SO (219.9GHz)	N	0	0	0.0 ± 0.0	0.0 ± 0.0	0.0 ± 0.0	0.07
G0.001-0.058b	SiO (217.1GHz)	N	0	0	0.0 ± 0.0	0.0 ± 0.0	0.0 ± 0.0	0.06
G0.001-0.058c	12CO (230.5GHz)	Y	2	1	1.43 ± 0.08	61.82 ± 0.29	4.55 ± 4.55	0.12
G0.001-0.058c	12CO (230.5GHz)	Y	2	2	2.4 ± 0.07	16.58 ± 0.2	6.3 ± 6.3	0.12
G0.001-0.058c	13CO (220.4GHz)	Y	3	1	0.55 ± 0.03	67.48 ± 0.3	3.83 ± 3.83	0.05
G0.001-0.058c	13CO (220.4GHz)	Y	3	2	1.53 ± 0.07	59.47 ± 0.05	1.1 ± 1.1	0.05
G0.001-0.058c	13CO (220.4GHz)	Y	3	3	0.3 ± 0.03	19.61 ± 0.56	5.03 ± 5.03	0.05
G0.001-0.058c	C18O (219.6GHz)	N	0	0	0.0 ± 0.0	0.0 ± 0.0	0.0 ± 0.0	0.04
G0.001-0.058c	H2CO (218.2GHz)	Y	4	1	0.08 ± 0.02	71.93 ± 1.05	3.25 ± 3.25	0.04
G0.001-0.058c	H2CO (218.2GHz)	Y	4	2	0.24 ± 0.02	51.16 ± 0.52	5.92 ± 5.92	0.04
G0.001-0.058c	H2CO (218.2GHz)	Y	4	3	0.21 ± 0.02	31.19 ± 0.57	5.29 ± 5.29	0.04
G0.001-0.058c	H2CO (218.5GHz)	Y	2	1	0.36 ± 0.02	94.86 ± 0.26	5.39 ± 5.39	0.03
G0.001-0.058c	H2CO (218.5GHz)	Y	2	2	0.14 ± 0.01	48.35 ± 0.76	6.39 ± 6.39	0.03
G0.001-0.058c	H2CO (218.8GHz)	Y	1	1	0.08 ± 0.01	45.34 ± 1.95	17.93 ± 17.93	0.03
G0.001-0.058c	OCS (218.9GHz)	N	0	0	0.0 ± 0.0	0.0 ± 0.0	0.0 ± 0.0	0.03
G0.001-0.058c	OCS (231.1GHz)	N	0	0	0.0 ± 0.0	0.0 ± 0.0	0.0 ± 0.0	0.04
G0.001-0.058c	SO (219.9GHz)	Y	1	1	0.33 ± 0.01	46.98 ± 0.28	5.55 ± 5.55	0.03
G0.001-0.058c	SiO (217.1GHz)	Y	1	1	0.14 ± 0.01	47.27 ± 0.95	10.45 ± 10.45	0.03
G0.001-0.058d	12CO (230.5GHz)	Y	2	1	1.44 ± 0.14	76.4 ± 0.71	5.07 ± 5.07	0.3
G0.001-0.058d	12CO (230.5GHz)	Y	2	2	0.82 ± 0.15	61.8 ± 1.09	3.9 ± 3.9	0.3
G0.001-0.058d	13CO (220.4GHz)	Y	1	1	0.45 ± 0.05	64.03 ± 0.62	4.93 ± 4.93	0.1
G0.001-0.058d	C18O (219.6GHz)	N	0	0	0.0 ± 0.0	0.0 ± 0.0	0.0 ± 0.0	0.05
G0.001-0.058d	H2CO (218.2GHz)	N	0	0	0.0 ± 0.0	0.0 ± 0.0	0.0 ± 0.0	0.05
G0.001-0.058d	H2CO (218.5GHz)	N	0	0	0.0 ± 0.0	0.0 ± 0.0	0.0 ± 0.0	0.04
G0.001-0.058d	H2CO (218.8GHz)	N	0	0	0.0 ± 0.0	0.0 ± 0.0	0.0 ± 0.0	0.04
G0.001-0.058d	OCS (218.9GHz)	N	0	0	0.0 ± 0.0	0.0 ± 0.0	0.0 ± 0.0	0.04
G0.001-0.058d	OCS (231.1GHz)	N	0	0	0.0 ± 0.0	0.0 ± 0.0	0.0 ± 0.0	0.08
G0.001-0.058d	SO (219.9GHz)	N	0	0	0.0 ± 0.0	0.0 ± 0.0	0.0 ± 0.0	0.04
G0.001-0.058d	SiO (217.1GHz)	N	0	0	0.0 ± 0.0	0.0 ± 0.0	0.0 ± 0.0	0.04
G0.001-0.058e	12CO (230.5GHz)	Y	1	1	5.74 ± 0.59	54.66 ± 0.41	3.43 ± 3.43	1.0
G0.001-0.058e	13CO (220.4GHz)	Y	2	1	3.16 ± 0.1	51.81 ± 0.14	3.86 ± 3.86	0.18
G0.001-0.058e	C18O (219.6GHz)	Y	1	1	0.45 ± 0.08	49.39 ± 0.44	2.14 ± 2.14	0.12
G0.001-0.058e	H2CO (218.2GHz)	Y	2	1	0.61 ± 0.06	41.04 ± 0.38	3.11 ± 3.11	0.11
G0.001-0.058e	H2CO (218.5GHz)	Y	2	1	0.79 ± 0.04	99.35 ± 0.33	6.36 ± 6.36	0.09
G0.001-0.058e	H2CO (218.5GHz)	Y	2	2	0.29 ± 0.03	52.59 ± 0.96	7.17 ± 7.17	0.09
G0.001-0.058e	H2CO (218.8GHz)	Y	1	1	0.26 ± 0.03	53.85 ± 0.93	6.3 ± 6.3	0.08
G0.001-0.058e	OCS (218.9GHz)	N	0	0	0.0 ± 0.0	0.0 ± 0.0	0.0 ± 0.0	0.06
G0.001-0.058e	OCS (231.1GHz)	N	0	0	0.0 ± 0.0	0.0 ± 0.0	0.0 ± 0.0	0.11
G0.001-0.058e	SO (219.9GHz)	Y	1	1	0.58 ± 0.05	50.07 ± 0.54	5.92 ± 5.92	0.11
G0.001-0.058e	SiO (217.1GHz)	Y	3	1	0.11 ± 0.03	85.62 ± 2.17	5.79 ± 5.79	0.08
G0.001-0.058e	SiO (217.1GHz)	Y	3	2	0.39 ± 0.03	54.71 ± 0.67	7.69 ± 7.69	0.08
G0.001-0.058f	12CO (230.5GHz)	N	0	0	0.0 ± 0.0	0.0 ± 0.0	0.0 ± 0.0	0.56
G0.001-0.058f	13CO (220.4GHz)	Y	1	1	0.66 ± 0.11	31.99 ± 1.34	7.13 ± 7.13	0.29
G0.001-0.058f	C18O (219.6GHz)	N	0	0	0.0 ± 0.0	0.0 ± 0.0	0.0 ± 0.0	0.09
G0.001-0.058f	H2CO (218.2GHz)	Y	2	1	0.62 ± 0.03	42.35 ± 0.31	5.07 ± 5.07	0.08
G0.001-0.058f	H2CO (218.5GHz)	Y	2	1	0.62 ± 0.03	91.67 ± 0.2	3.18 ± 3.18	0.07
G0.001-0.058f	H2CO (218.5GHz)	Y	2	2	0.18 ± 0.03	41.75 ± 0.85	4.8 ± 4.8	0.07
G0.001-0.058f	H2CO (218.8GHz)	N	0	0	0.0 ± 0.0	0.0 ± 0.0	0.0 ± 0.0	0.06
G0.001-0.058f	OCS (218.9GHz)	N	0	0	0.0 ± 0.0	0.0 ± 0.0	0.0 ± 0.0	0.05
G0.001-0.058f	OCS (231.1GHz)	N	0	0	0.0 ± 0.0	0.0 ± 0.0	0.0 ± 0.0	0.07
G0.001-0.058f	SO (219.9GHz)	N	0	0	0.0 ± 0.0	0.0 ± 0.0	0.0 ± 0.0	0.07
G0.001-0.058f	SiO (217.1GHz)	Y	1	1	0.29 ± 0.03	42.52 ± 0.53	5.03 ± 5.03	0.06
G0.001-0.058g	12CO (230.5GHz)	N	0	0	0.0 ± 0.0	0.0 ± 0.0	0.0 ± 0.0	0.85
G0.001-0.058g	13CO (220.4GHz)	Y	1	1	1.45 ± 0.16	47.28 ± 0.42	3.22 ± 3.22	0.3
G0.001-0.058g	C18O (219.6GHz)	Y	1	1	0.27 ± 0.05	46.22 ± 0.62	3.17 ± 3.17	0.08
G0.001-0.058g	H2CO (218.2GHz)	Y	2	1	0.26 ± 0.03	44.88 ± 0.79	5.28 ± 5.28	0.08
G0.001-0.058g	H2CO (218.5GHz)	Y	2	1	1.14 ± 0.04	97.24 ± 0.12	3.35 ± 3.35	0.07
G0.001-0.058g	H2CO (218.5GHz)	Y	2	2	0.35 ± 0.04	48.79 ± 0.37	2.9 ± 2.9	0.07

Continued on next page

Table A.1 – *Continued from previous page*

Leaf	Transition	Detected	Number of Comps	Comp.	Amplitude	Velocity	Width	RMS
G0.001-0.058g	H2CO (218.8GHz)	Y	2	1	0.29 ± 0.05	47.45 ± 0.34	1.87 ± 1.87	0.06
G0.001-0.058g	OCS (218.9GHz)	Y	1	1	0.35 ± 0.05	46.91 ± 0.29	1.95 ± 1.95	0.06
G0.001-0.058g	OCS (231.1GHz)	N	0	0	0.0 ± 0.0	0.0 ± 0.0	0.0 ± 0.0	0.07
G0.001-0.058g	SO (219.9GHz)	Y	1	1	0.75 ± 0.04	47.87 ± 0.23	3.66 ± 3.66	0.08
G0.001-0.058g	SiO (217.1GHz)	Y	1	1	0.29 ± 0.03	49.79 ± 0.56	4.56 ± 4.56	0.06
G0.001-0.058h	12CO (230.5GHz)	N	0	0	0.0 ± 0.0	0.0 ± 0.0	0.0 ± 0.0	0.82
G0.001-0.058h	13CO (220.4GHz)	Y	1	1	1.57 ± 0.08	58.03 ± 0.18	3.16 ± 3.16	0.13
G0.001-0.058h	C18O (219.6GHz)	N	0	0	0.0 ± 0.0	0.0 ± 0.0	0.0 ± 0.0	0.09
G0.001-0.058h	H2CO (218.2GHz)	N	0	0	0.0 ± 0.0	0.0 ± 0.0	0.0 ± 0.0	0.1
G0.001-0.058h	H2CO (218.5GHz)	N	0	0	0.0 ± 0.0	0.0 ± 0.0	0.0 ± 0.0	0.11
G0.001-0.058h	H2CO (218.8GHz)	N	0	0	0.0 ± 0.0	0.0 ± 0.0	0.0 ± 0.0	0.07
G0.001-0.058h	OCS (218.9GHz)	N	0	0	0.0 ± 0.0	0.0 ± 0.0	0.0 ± 0.0	0.06
G0.001-0.058h	OCS (231.1GHz)	N	0	0	0.0 ± 0.0	0.0 ± 0.0	0.0 ± 0.0	0.07
G0.001-0.058h	SO (219.9GHz)	N	0	0	0.0 ± 0.0	0.0 ± 0.0	0.0 ± 0.0	0.09
G0.001-0.058h	SiO (217.1GHz)	N	0	0	0.0 ± 0.0	0.0 ± 0.0	0.0 ± 0.0	0.08
G0.001-0.058i	12CO (230.5GHz)	Y	1	1	3.07 ± 0.24	11.78 ± 0.56	6.1 ± 6.1	0.45
G0.001-0.058i	13CO (220.4GHz)	Y	5	1	3.11 ± 0.11	75.79 ± 0.08	1.84 ± 1.84	0.15
G0.001-0.058i	13CO (220.4GHz)	Y	5	2	0.81 ± 0.1	36.91 ± 0.34	2.38 ± 2.38	0.15
G0.001-0.058i	13CO (220.4GHz)	Y	5	3	0.86 ± 0.11	21.13 ± 0.3	2.07 ± 2.07	0.15
G0.001-0.058i	13CO (220.4GHz)	Y	5	4	1.15 ± 0.08	7.77 ± 0.29	3.65 ± 3.65	0.15
G0.001-0.058i	C18O (219.6GHz)	Y	2	1	0.45 ± 0.05	75.9 ± 0.24	1.7 ± 1.7	0.07
G0.001-0.058i	H2CO (218.2GHz)	Y	1	1	0.55 ± 0.06	76.35 ± 0.18	1.51 ± 1.51	0.06
G0.001-0.058i	H2CO (218.5GHz)	N	0	0	0.0 ± 0.0	0.0 ± 0.0	0.0 ± 0.0	0.05
G0.001-0.058i	H2CO (218.8GHz)	N	0	0	0.0 ± 0.0	0.0 ± 0.0	0.0 ± 0.0	0.05
G0.001-0.058i	OCS (218.9GHz)	N	0	0	0.0 ± 0.0	0.0 ± 0.0	0.0 ± 0.0	0.05
G0.001-0.058i	OCS (231.1GHz)	N	0	0	0.0 ± 0.0	0.0 ± 0.0	0.0 ± 0.0	0.06
G0.001-0.058i	SO (219.9GHz)	N	0	0	0.0 ± 0.0	0.0 ± 0.0	0.0 ± 0.0	0.05
G0.001-0.058i	SiO (217.1GHz)	Y	1	1	0.21 ± 0.05	5.26 ± 0.36	1.24 ± 1.24	0.06
G0.001-0.058j	12CO (230.5GHz)	Y	1	1	3.66 ± 0.38	29.05 ± 0.23	1.93 ± 1.93	0.56
G0.001-0.058j	13CO (220.4GHz)	N	0	0	0.0 ± 0.0	0.0 ± 0.0	0.0 ± 0.0	0.21
G0.001-0.058j	C18O (219.6GHz)	N	0	0	0.0 ± 0.0	0.0 ± 0.0	0.0 ± 0.0	0.1
G0.001-0.058j	H2CO (218.2GHz)	N	0	0	0.0 ± 0.0	0.0 ± 0.0	0.0 ± 0.0	0.12
G0.001-0.058j	H2CO (218.5GHz)	Y	1	1	0.37 ± 0.05	96.78 ± 0.55	3.82 ± 3.82	0.09
G0.001-0.058j	H2CO (218.8GHz)	N	0	0	0.0 ± 0.0	0.0 ± 0.0	0.0 ± 0.0	0.07
G0.001-0.058j	OCS (218.9GHz)	N	0	0	0.0 ± 0.0	0.0 ± 0.0	0.0 ± 0.0	0.08
G0.001-0.058j	OCS (231.1GHz)	N	0	0	0.0 ± 0.0	0.0 ± 0.0	0.0 ± 0.0	0.11
G0.001-0.058j	SO (219.9GHz)	N	0	0	0.0 ± 0.0	0.0 ± 0.0	0.0 ± 0.0	0.09
G0.001-0.058j	SiO (217.1GHz)	N	0	0	0.0 ± 0.0	0.0 ± 0.0	0.0 ± 0.0	0.08
G0.001-0.058k	12CO (230.5GHz)	Y	1	1	3.54 ± 0.38	28.27 ± 0.29	2.31 ± 2.31	0.46
G0.001-0.058k	13CO (220.4GHz)	Y	1	1	1.21 ± 0.06	38.77 ± 0.3	5.11 ± 5.11	0.11
G0.001-0.058k	C18O (219.6GHz)	Y	1	1	0.37 ± 0.03	42.48 ± 0.6	7.27 ± 7.27	0.07
G0.001-0.058k	H2CO (218.2GHz)	Y	1	1	0.34 ± 0.02	33.44 ± 0.66	8.4 ± 8.4	0.07
G0.001-0.058k	H2CO (218.5GHz)	Y	2	1	0.21 ± 0.02	80.9 ± 0.69	5.49 ± 5.49	0.06
G0.001-0.058k	H2CO (218.5GHz)	Y	2	2	0.14 ± 0.02	37.03 ± 1.18	7.32 ± 7.32	0.06
G0.001-0.058k	H2CO (218.8GHz)	N	0	0	0.0 ± 0.0	0.0 ± 0.0	0.0 ± 0.0	0.06
G0.001-0.058k	OCS (218.9GHz)	N	0	0	0.0 ± 0.0	0.0 ± 0.0	0.0 ± 0.0	0.06
G0.001-0.058k	OCS (231.1GHz)	N	0	0	0.0 ± 0.0	0.0 ± 0.0	0.0 ± 0.0	0.07
G0.001-0.058k	SO (219.9GHz)	Y	1	1	0.24 ± 0.02	35.33 ± 0.8	8.73 ± 8.73	0.06
G0.001-0.058k	SiO (217.1GHz)	N	0	0	0.0 ± 0.0	0.0 ± 0.0	0.0 ± 0.0	0.06
G0.001-0.058l	13CO (220.4GHz)	Y	4	1	0.38 ± 0.07	69.96 ± 0.31	1.51 ± 1.51	0.08
G0.001-0.058l	13CO (220.4GHz)	Y	4	2	0.73 ± 0.05	61.42 ± 0.21	2.62 ± 2.62	0.08
G0.001-0.058l	13CO (220.4GHz)	Y	4	3	1.32 ± 0.07	48.89 ± 0.08	1.45 ± 1.45	0.08
G0.001-0.058l	13CO (220.4GHz)	Y	4	4	0.26 ± 0.05	33.26 ± 0.61	2.93 ± 2.93	0.08
G0.001-0.058l	C18O (219.6GHz)	Y	1	1	0.15 ± 0.02	52.7 ± 1.48	8.52 ± 8.52	0.06
G0.001-0.058l	H2CO (218.2GHz)	Y	2	1	0.55 ± 0.03	28.57 ± 0.28	5.05 ± 5.05	0.05
G0.001-0.058l	H2CO (218.5GHz)	Y	2	1	0.53 ± 0.02	77.11 ± 0.26	4.99 ± 4.99	0.05
G0.001-0.058l	H2CO (218.5GHz)	Y	2	2	0.17 ± 0.02	26.09 ± 0.74	4.56 ± 4.56	0.05
G0.001-0.058l	H2CO (218.8GHz)	Y	1	1	0.21 ± 0.02	26.7 ± 0.54	4.12 ± 4.12	0.05
G0.001-0.058l	OCS (218.9GHz)	N	0	0	0.0 ± 0.0	0.0 ± 0.0	0.0 ± 0.0	0.05
G0.001-0.058l	OCS (231.1GHz)	N	0	0	0.0 ± 0.0	0.0 ± 0.0	0.0 ± 0.0	0.06
G0.001-0.058l	SO (219.9GHz)	Y	2	1	0.27 ± 0.03	56.86 ± 0.49	3.9 ± 3.9	0.05
G0.001-0.058l	SO (219.9GHz)	Y	2	2	0.52 ± 0.03	29.11 ± 0.28	4.96 ± 4.96	0.05
G0.001-0.058l	SiO (217.1GHz)	Y	1	1	0.5 ± 0.02	29.56 ± 0.27	5.0 ± 5.0	0.05
G0.001-0.058m	12CO (230.5GHz)	Y	1	1	4.59 ± 0.39	37.81 ± 0.2	2.07 ± 2.07	0.43
G0.001-0.058m	13CO (220.4GHz)	N	0	0	0.0 ± 0.0	0.0 ± 0.0	0.0 ± 0.0	0.26
G0.001-0.058m	C18O (219.6GHz)	Y	1	1	0.28 ± 0.04	42.98 ± 0.49	3.0 ± 3.0	0.07
G0.001-0.058m	H2CO (218.2GHz)	Y	2	1	0.3 ± 0.03	45.38 ± 0.65	6.46 ± 6.46	0.07
G0.001-0.058m	H2CO (218.2GHz)	Y	2	2	0.19 ± 0.05	21.27 ± 0.57	2.05 ± 2.05	0.07
G0.001-0.058m	H2CO (218.5GHz)	Y	2	1	0.31 ± 0.03	99.6 ± 0.41	4.01 ± 4.01	0.06
G0.001-0.058m	H2CO (218.5GHz)	Y	2	2	0.15 ± 0.02	48.5 ± 1.04	6.02 ± 6.02	0.06
G0.001-0.058m	H2CO (218.8GHz)	N	0	0	0.0 ± 0.0	0.0 ± 0.0	0.0 ± 0.0	0.05
G0.001-0.058m	OCS (218.9GHz)	N	0	0	0.0 ± 0.0	0.0 ± 0.0	0.0 ± 0.0	0.05
G0.001-0.058m	OCS (231.1GHz)	N	0	0	0.0 ± 0.0	0.0 ± 0.0	0.0 ± 0.0	0.05
G0.001-0.058m	SO (219.9GHz)	Y	1	1	0.3 ± 0.02	45.83 ± 0.57	6.49 ± 6.49	0.05
G0.001-0.058m	SiO (217.1GHz)	Y	1	1	0.24 ± 0.02	44.34 ± 0.74	8.63 ± 8.63	0.05
G0.001-0.058n	12CO (230.5GHz)	N	0	0	0.0 ± 0.0	0.0 ± 0.0	0.0 ± 0.0	0.78
G0.001-0.058n	13CO (220.4GHz)	N	0	0	0.0 ± 0.0	0.0 ± 0.0	0.0 ± 0.0	0.22
G0.001-0.058n	H2CO (218.2GHz)	Y	1	1	0.65 ± 0.04	26.38 ± 0.29	3.98 ± 3.98	0.07
G0.001-0.058n	H2CO (218.5GHz)	Y	3	1	0.14 ± 0.03	116.36 ± 0.93	4.03 ± 4.03	0.06
G0.001-0.058n	H2CO (218.5GHz)	Y	3	2	0.64 ± 0.03	74.86 ± 0.18	3.29 ± 3.29	0.06
G0.001-0.058n	H2CO (218.5GHz)	Y	3	3	0.14 ± 0.03	25.87 ± 0.88	3.86 ± 3.86	0.06
G0.001-0.058n	H2CO (218.8GHz)	Y	2	1	0.11 ± 0.02	66.81 ± 1.19	4.48 ± 4.48	0.05
G0.001-0.058n	H2CO (218.8GHz)	Y	2	2	0.25 ± 0.03	25.84 ± 0.38	2.65 ± 2.65	0.05
G0.001-0.058n	OCS (218.9GHz)	N	0	0	0.0 ± 0.0	0.0 ± 0.0	0.0 ± 0.0	0.05
G0.001-0.058n	OCS (231.1GHz)	Y	1	1	0.27 ± 0.05	27.88 ± 0.39	1.73 ± 1.73	0.07
G0.001-0.058n	SO (219.9GHz)	Y	2	1	0.21 ± 0.04	66.08 ± 0.59	3.09 ± 3.09	0.07
G0.001-0.058n	SO (219.9GHz)	Y	2	2	0.47 ± 0.04	26.14 ± 0.26	2.91 ± 2.91	0.07

Continued on next page

Table A.1 – *Continued from previous page*

Leaf	Transition	Detected	Number of Comps	Comp.	Amplitude	Velocity	Width	RMS
G0.001-0.058n	SiO (217.1GHz)	Y	1	1	0.44 ± 0.03	27.7 ± 0.26	3.48 ± 3.48	0.06
G0.001-0.058o	12CO (230.5GHz)	Y	1	1	1.72 ± 0.21	36.33 ± 0.83	5.85 ± 5.85	0.41
G0.001-0.058o	13CO (220.4GHz)	Y	2	1	1.3 ± 0.06	65.49 ± 0.2	3.81 ± 3.81	0.11
G0.001-0.058o	13CO (220.4GHz)	Y	2	2	0.48 ± 0.07	30.88 ± 0.43	2.41 ± 2.41	0.11
G0.001-0.058o	C18O (219.6GHz)	N	0	0	0.0 ± 0.0	0.0 ± 0.0	0.0 ± 0.0	0.08
G0.001-0.058o	H2CO (218.2GHz)	N	0	0	0.0 ± 0.0	0.0 ± 0.0	0.0 ± 0.0	0.07
G0.001-0.058o	H2CO (218.5GHz)	N	0	0	0.0 ± 0.0	0.0 ± 0.0	0.0 ± 0.0	0.06
G0.001-0.058o	H2CO (218.8GHz)	N	0	0	0.0 ± 0.0	0.0 ± 0.0	0.0 ± 0.0	0.05
G0.001-0.058o	OCS (218.9GHz)	N	0	0	0.0 ± 0.0	0.0 ± 0.0	0.0 ± 0.0	0.05
G0.001-0.058o	OCS (231.1GHz)	N	0	0	0.0 ± 0.0	0.0 ± 0.0	0.0 ± 0.0	0.06
G0.001-0.058o	SO (219.9GHz)	N	0	0	0.0 ± 0.0	0.0 ± 0.0	0.0 ± 0.0	0.06
G0.001-0.058o	SiO (217.1GHz)	N	0	0	0.0 ± 0.0	0.0 ± 0.0	0.0 ± 0.0	0.06
G0.001-0.058p	12CO (230.5GHz)	Y	1	1	6.7 ± 0.26	25.63 ± 0.16	3.7 ± 3.7	0.41
G0.001-0.058p	13CO (220.4GHz)	N	0	0	0.0 ± 0.0	0.0 ± 0.0	0.0 ± 0.0	0.14
G0.001-0.058p	C18O (219.6GHz)	N	0	0	0.0 ± 0.0	0.0 ± 0.0	0.0 ± 0.0	0.08
G0.001-0.058p	H2CO (218.2GHz)	Y	2	1	0.48 ± 0.03	21.54 ± 0.44	5.64 ± 5.64	0.08
G0.001-0.058p	H2CO (218.5GHz)	Y	1	1	0.77 ± 0.03	72.97 ± 0.2	5.07 ± 5.07	0.05
G0.001-0.058p	H2CO (218.8GHz)	Y	1	1	0.23 ± 0.02	22.8 ± 0.64	6.26 ± 6.26	0.05
G0.001-0.058p	OCS (218.9GHz)	N	0	0	0.0 ± 0.0	0.0 ± 0.0	0.0 ± 0.0	0.05
G0.001-0.058p	OCS (231.1GHz)	Y	1	1	0.42 ± 0.04	24.69 ± 0.32	2.61 ± 2.61	0.08
G0.001-0.058p	SO (219.9GHz)	Y	1	1	0.63 ± 0.03	24.17 ± 0.3	5.52 ± 5.52	0.07
G0.001-0.058p	SiO (217.1GHz)	Y	1	1	0.54 ± 0.02	24.42 ± 0.32	8.4 ± 8.4	0.05
G0.001-0.058q	12CO (230.5GHz)	Y	3	1	1.79 ± 0.12	51.2 ± 0.93	11.59 ± 11.59	0.32
G0.001-0.058q	12CO (230.5GHz)	Y	3	2	7.05 ± 0.23	17.86 ± 0.13	3.32 ± 3.32	0.32
G0.001-0.058q	13CO (220.4GHz)	Y	4	1	1.68 ± 0.11	59.56 ± 0.11	1.49 ± 1.49	0.12
G0.001-0.058q	13CO (220.4GHz)	Y	4	2	0.62 ± 0.07	39.08 ± 0.5	4.02 ± 4.02	0.12
G0.001-0.058q	13CO (220.4GHz)	Y	4	3	0.58 ± 0.07	18.58 ± 0.51	3.78 ± 3.78	0.12
G0.001-0.058q	C18O (219.6GHz)	N	0	0	0.0 ± 0.0	0.0 ± 0.0	0.0 ± 0.0	0.1
G0.001-0.058q	H2CO (218.2GHz)	Y	1	1	0.29 ± 0.03	28.29 ± 1.56	15.11 ± 15.11	0.1
G0.001-0.058q	H2CO (218.5GHz)	N	0	0	0.0 ± 0.0	0.0 ± 0.0	0.0 ± 0.0	0.09
G0.001-0.058q	H2CO (218.8GHz)	N	0	0	0.0 ± 0.0	0.0 ± 0.0	0.0 ± 0.0	0.07
G0.001-0.058q	OCS (218.9GHz)	N	0	0	0.0 ± 0.0	0.0 ± 0.0	0.0 ± 0.0	0.06
G0.001-0.058q	OCS (231.1GHz)	N	0	0	0.0 ± 0.0	0.0 ± 0.0	0.0 ± 0.0	0.1
G0.001-0.058q	SO (219.9GHz)	N	0	0	0.0 ± 0.0	0.0 ± 0.0	0.0 ± 0.0	0.09
G0.001-0.058q	SiO (217.1GHz)	N	0	0	0.0 ± 0.0	0.0 ± 0.0	0.0 ± 0.0	0.08
G0.001-0.058r	12CO (230.5GHz)	Y	4	1	3.04 ± 0.14	103.53 ± 0.34	6.48 ± 6.48	0.22
G0.001-0.058r	12CO (230.5GHz)	Y	4	2	4.02 ± 0.21	74.74 ± 0.17	2.74 ± 2.74	0.22
G0.001-0.058r	12CO (230.5GHz)	Y	4	3	1.89 ± 0.15	49.2 ± 0.51	5.71 ± 5.71	0.22
G0.001-0.058r	12CO (230.5GHz)	Y	4	4	6.75 ± 0.18	19.79 ± 0.12	3.65 ± 3.65	0.22
G0.001-0.058r	13CO (220.4GHz)	Y	7	1	0.72 ± 0.09	102.0 ± 0.2	1.57 ± 1.57	0.08
G0.001-0.058r	13CO (220.4GHz)	Y	7	2	0.34 ± 0.06	101.7 ± 0.98	8.54 ± 8.54	0.08
G0.001-0.058r	13CO (220.4GHz)	Y	7	3	0.95 ± 0.05	69.76 ± 0.27	4.36 ± 4.36	0.08
G0.001-0.058r	13CO (220.4GHz)	Y	7	4	1.97 ± 0.07	58.95 ± 0.08	1.74 ± 1.74	0.08
G0.001-0.058r	13CO (220.4GHz)	Y	7	5	1.09 ± 0.1	51.08 ± 0.1	0.99 ± 0.99	0.08
G0.001-0.058r	13CO (220.4GHz)	Y	7	6	0.59 ± 0.06	27.32 ± 0.45	2.7 ± 2.7	0.08
G0.001-0.058r	13CO (220.4GHz)	Y	7	7	0.33 ± 0.05	17.04 ± 1.0	4.13 ± 4.13	0.08
G0.001-0.058r	C18O (219.6GHz)	N	0	0	0.0 ± 0.0	0.0 ± 0.0	0.0 ± 0.0	0.1
G0.001-0.058r	H2CO (218.2GHz)	Y	1	1	0.21 ± 0.02	32.89 ± 2.53	20.29 ± 20.29	0.09
G0.001-0.058r	H2CO (218.5GHz)	Y	3	1	0.33 ± 0.03	92.72 ± 1.13	7.17 ± 7.17	0.07
G0.001-0.058r	H2CO (218.5GHz)	Y	3	2	0.51 ± 0.05	77.22 ± 0.48	3.87 ± 3.87	0.07
G0.001-0.058r	H2CO (218.5GHz)	Y	3	3	0.17 ± 0.03	42.81 ± 1.54	8.86 ± 8.86	0.07
G0.001-0.058r	H2CO (218.8GHz)	N	0	0	0.0 ± 0.0	0.0 ± 0.0	0.0 ± 0.0	0.08
G0.001-0.058r	OCS (218.9GHz)	N	0	0	0.0 ± 0.0	0.0 ± 0.0	0.0 ± 0.0	0.08
G0.001-0.058r	OCS (231.1GHz)	N	0	0	0.0 ± 0.0	0.0 ± 0.0	0.0 ± 0.0	0.11
G0.001-0.058r	SO (219.9GHz)	Y	2	1	0.12 ± 0.02	98.35 ± 3.58	17.45 ± 17.45	0.08
G0.001-0.058r	SO (219.9GHz)	Y	2	2	0.36 ± 0.03	38.74 ± 0.98	11.66 ± 11.66	0.08
G0.001-0.058r	SiO (217.1GHz)	N	0	0	0.0 ± 0.0	0.0 ± 0.0	0.0 ± 0.0	0.07
G0.001-0.058s	12CO (230.5GHz)	N	0	0	0.0 ± 0.0	0.0 ± 0.0	0.0 ± 0.0	0.5
G0.001-0.058s	13CO (220.4GHz)	Y	3	1	0.61 ± 0.07	60.96 ± 0.47	3.49 ± 3.49	0.13
G0.001-0.058s	13CO (220.4GHz)	Y	3	2	1.0 ± 0.07	38.41 ± 0.29	3.53 ± 3.53	0.13
G0.001-0.058s	13CO (220.4GHz)	Y	3	3	0.56 ± 0.09	16.96 ± 0.42	2.31 ± 2.31	0.13
G0.001-0.058s	C18O (219.6GHz)	N	0	0	0.0 ± 0.0	0.0 ± 0.0	0.0 ± 0.0	0.12
G0.001-0.058s	H2CO (218.2GHz)	Y	1	1	0.88 ± 0.09	38.24 ± 0.18	1.53 ± 1.53	0.11
G0.001-0.058s	H2CO (218.5GHz)	Y	2	1	0.6 ± 0.05	88.35 ± 0.34	3.39 ± 3.39	0.1
G0.001-0.058s	H2CO (218.5GHz)	Y	2	2	0.43 ± 0.08	37.08 ± 0.31	1.43 ± 1.43	0.1
G0.001-0.058s	H2CO (218.8GHz)	Y	2	1	0.23 ± 0.06	53.48 ± 0.58	2.03 ± 2.03	0.08
G0.001-0.058s	H2CO (218.8GHz)	Y	2	2	0.29 ± 0.05	39.24 ± 0.53	2.75 ± 2.75	0.08
G0.001-0.058s	OCS (218.9GHz)	N	0	0	0.0 ± 0.0	0.0 ± 0.0	0.0 ± 0.0	0.08
G0.001-0.058s	OCS (231.1GHz)	N	0	0	0.0 ± 0.0	0.0 ± 0.0	0.0 ± 0.0	0.1
G0.001-0.058s	SO (219.9GHz)	Y	1	1	0.65 ± 0.06	38.8 ± 0.3	2.69 ± 2.69	0.11
G0.001-0.058s	SiO (217.1GHz)	N	0	0	0.0 ± 0.0	0.0 ± 0.0	0.0 ± 0.0	0.1
G0.068-0.075a	12CO (230.5GHz)	Y	1	1	3.99 ± 0.34	47.65 ± 0.28	2.79 ± 2.79	0.56
G0.068-0.075a	13CO (220.4GHz)	Y	1	1	3.57 ± 0.14	20.73 ± 0.09	1.97 ± 1.97	0.13
G0.068-0.075a	C18O (219.6GHz)	Y	1	1	3.12 ± 0.09	20.11 ± 0.05	1.45 ± 1.45	0.09
G0.068-0.075a	H2CO (218.2GHz)	Y	1	1	0.75 ± 0.07	20.91 ± 0.21	2.04 ± 2.04	0.1
G0.068-0.075a	H2CO (218.5GHz)	N	0	0	0.0 ± 0.0	0.0 ± 0.0	0.0 ± 0.0	0.1
G0.068-0.075a	H2CO (218.8GHz)	N	0	0	0.0 ± 0.0	0.0 ± 0.0	0.0 ± 0.0	0.09
G0.068-0.075a	OCS (218.9GHz)	N	0	0	0.0 ± 0.0	0.0 ± 0.0	0.0 ± 0.0	0.08
G0.068-0.075a	OCS (231.1GHz)	N	0	0	0.0 ± 0.0	0.0 ± 0.0	0.0 ± 0.0	0.13
G0.068-0.075a	SO (219.9GHz)	Y	1	1	0.37 ± 0.06	21.37 ± 0.38	2.0 ± 2.0	0.09
G0.068-0.075a	SiO (217.1GHz)	N	0	0	0.0 ± 0.0	0.0 ± 0.0	0.0 ± 0.0	0.09
G0.068-0.075b	12CO (230.5GHz)	Y	2	1	1.14 ± 0.13	59.81 ± 1.5	11.04 ± 11.04	0.29
G0.068-0.075b	12CO (230.5GHz)	Y	2	2	1.76 ± 0.29	6.28 ± 0.46	2.45 ± 2.45	0.29
G0.068-0.075b	13CO (220.4GHz)	Y	5	1	0.28 ± 0.04	73.07 ± 0.4	2.32 ± 2.32	0.06
G0.068-0.075b	13CO (220.4GHz)	Y	5	2	0.23 ± 0.03	45.85 ± 0.81	6.38 ± 6.38	0.06
G0.068-0.075b	13CO (220.4GHz)	Y	5	3	0.24 ± 0.04	3.16 ± 0.51	2.78 ± 2.78	0.06
G0.068-0.075b	C18O (219.6GHz)	N	0	0	0.0 ± 0.0	0.0 ± 0.0	0.0 ± 0.0	0.04

Continued on next page

Table A.1 – *Continued from previous page*

Leaf	Transition	Detected	Number of Comps	Comp.	Amplitude	Velocity	Width	RMS
G0.068-0.075b	H2CO (218.2GHz)	Y	2	1	0.26 ± 0.02	53.13 ± 0.29	2.83 ± 2.83	0.04
G0.068-0.075b	H2CO (218.2GHz)	Y	2	2	0.21 ± 0.02	40.77 ± 0.39	3.48 ± 3.48	0.04
G0.068-0.075b	H2CO (218.5GHz)	Y	3	1	0.31 ± 0.02	100.89 ± 0.17	1.82 ± 1.82	0.04
G0.068-0.075b	H2CO (218.5GHz)	Y	3	2	0.31 ± 0.02	90.65 ± 0.21	2.89 ± 2.89	0.04
G0.068-0.075b	H2CO (218.5GHz)	Y	3	3	0.08 ± 0.01	49.52 ± 1.33	8.31 ± 8.31	0.04
G0.068-0.075b	H2CO (218.8GHz)	Y	2	1	0.09 ± 0.02	51.46 ± 0.74	3.2 ± 3.2	0.03
G0.068-0.075b	H2CO (218.8GHz)	Y	2	2	0.14 ± 0.02	40.89 ± 0.43	2.5 ± 2.5	0.03
G0.068-0.075b	OCS (218.9GHz)	N	0	0	0.0 ± 0.0	0.0 ± 0.0	0.0 ± 0.0	0.03
G0.068-0.075b	OCS (231.1GHz)	Y	3	1	0.15 ± 0.03	43.65 ± 0.48	2.02 ± 2.02	0.02
G0.068-0.075b	SO (219.9GHz)	Y	2	1	0.09 ± 0.01	48.93 ± 1.52	6.91 ± 6.91	0.04
G0.068-0.075b	SO (219.9GHz)	Y	2	2	0.1 ± 0.03	40.71 ± 0.41	1.11 ± 1.11	0.04
G0.068-0.075b	SiO (217.1GHz)	Y	1	1	0.13 ± 0.01	44.4 ± 0.86	8.03 ± 8.03	0.03
G0.068-0.075c	12CO (230.5GHz)	Y	3	1	5.31 ± 0.28	62.38 ± 0.28	4.34 ± 4.34	0.53
G0.068-0.075c	12CO (230.5GHz)	Y	3	2	2.82 ± 0.33	76.6 ± 0.45	3.16 ± 3.16	0.53
G0.068-0.075c	12CO (230.5GHz)	Y	3	3	7.18 ± 0.33	39.24 ± 0.16	3.13 ± 3.13	0.53
G0.068-0.075c	13CO (220.4GHz)	Y	2	1	0.89 ± 0.04	69.05 ± 0.33	6.82 ± 6.82	0.07
G0.068-0.075c	13CO (220.4GHz)	Y	2	2	2.03 ± 0.05	42.66 ± 0.12	4.41 ± 4.41	0.07
G0.068-0.075c	C18O (219.6GHz)	Y	2	1	0.16 ± 0.02	66.92 ± 0.92	8.03 ± 8.03	0.04
G0.068-0.075c	C18O (219.6GHz)	Y	2	2	0.48 ± 0.02	44.36 ± 0.21	3.7 ± 3.7	0.04
G0.068-0.075c	H2CO (218.2GHz)	Y	2	1	0.31 ± 0.02	60.56 ± 0.8	6.55 ± 6.55	0.04
G0.068-0.075c	H2CO (218.2GHz)	Y	2	2	0.21 ± 0.02	41.21 ± 1.29	7.32 ± 7.32	0.04
G0.068-0.075c	H2CO (218.5GHz)	Y	3	1	0.33 ± 0.03	112.07 ± 0.3	2.67 ± 2.67	0.05
G0.068-0.075c	H2CO (218.5GHz)	Y	3	2	0.3 ± 0.02	95.79 ± 0.51	6.41 ± 6.41	0.05
G0.068-0.075c	H2CO (218.5GHz)	Y	3	3	0.14 ± 0.01	51.41 ± 1.46	12.26 ± 12.26	0.05
G0.068-0.075c	H2CO (218.8GHz)	Y	1	1	0.15 ± 0.01	49.54 ± 1.15	11.37 ± 11.37	0.04
G0.068-0.075c	OCS (218.9GHz)	N	0	0	0.0 ± 0.0	0.0 ± 0.0	0.0 ± 0.0	0.04
G0.068-0.075c	OCS (231.1GHz)	Y	1	1	0.22 ± 0.03	44.26 ± 0.62	4.18 ± 4.18	0.05
G0.068-0.075c	SO (219.9GHz)	Y	3	1	0.17 ± 0.03	63.53 ± 0.41	1.7 ± 1.7	0.05
G0.068-0.075c	SO (219.9GHz)	Y	3	2	0.19 ± 0.03	44.98 ± 0.47	2.83 ± 2.83	0.05
G0.068-0.075c	SiO (217.1GHz)	Y	1	1	0.17 ± 0.01	46.32 ± 0.94	9.72 ± 9.72	0.05
G0.068-0.075d	12CO (230.5GHz)	Y	2	1	6.36 ± 0.26	58.29 ± 0.27	5.67 ± 5.67	0.58
G0.068-0.075d	12CO (230.5GHz)	Y	2	2	1.71 ± 0.22	17.97 ± 1.19	8.11 ± 8.11	0.58
G0.068-0.075d	13CO (220.4GHz)	Y	5	1	0.62 ± 0.04	61.02 ± 1.37	9.33 ± 9.33	0.08
G0.068-0.075d	13CO (220.4GHz)	Y	5	2	0.93 ± 0.11	48.03 ± 0.27	2.8 ± 2.8	0.08
G0.068-0.075d	13CO (220.4GHz)	Y	5	3	0.61 ± 0.08	10.04 ± 0.36	2.31 ± 2.31	0.08
G0.068-0.075d	C18O (219.6GHz)	Y	2	1	0.37 ± 0.03	50.25 ± 0.27	2.72 ± 2.72	0.05
G0.068-0.075d	H2CO (218.2GHz)	Y	2	1	0.53 ± 0.03	61.28 ± 0.2	3.53 ± 3.53	0.05
G0.068-0.075d	H2CO (218.2GHz)	Y	2	2	0.42 ± 0.03	47.93 ± 0.22	2.68 ± 2.68	0.05
G0.068-0.075d	H2CO (218.5GHz)	Y	4	1	0.38 ± 0.03	107.69 ± 0.33	3.83 ± 3.83	0.06
G0.068-0.075d	H2CO (218.5GHz)	Y	4	2	0.37 ± 0.04	97.09 ± 0.23	1.86 ± 1.86	0.06
G0.068-0.075d	H2CO (218.5GHz)	Y	4	3	0.18 ± 0.03	59.04 ± 0.6	3.18 ± 3.18	0.06
G0.068-0.075d	H2CO (218.5GHz)	Y	4	4	0.26 ± 0.05	47.39 ± 0.24	1.16 ± 1.16	0.06
G0.068-0.075d	H2CO (218.8GHz)	Y	2	1	0.18 ± 0.02	58.59 ± 0.72	4.65 ± 4.65	0.05
G0.068-0.075d	H2CO (218.8GHz)	Y	2	2	0.18 ± 0.04	47.72 ± 0.41	1.67 ± 1.67	0.05
G0.068-0.075d	OCS (218.9GHz)	N	0	0	0.0 ± 0.0	0.0 ± 0.0	0.0 ± 0.0	0.05
G0.068-0.075d	OCS (231.1GHz)	N	0	0	0.0 ± 0.0	0.0 ± 0.0	0.0 ± 0.0	0.05
G0.068-0.075d	SO (219.9GHz)	Y	2	1	0.22 ± 0.03	59.03 ± 0.5	3.63 ± 3.63	0.05
G0.068-0.075d	SO (219.9GHz)	Y	2	2	0.29 ± 0.03	48.16 ± 0.3	2.1 ± 2.1	0.05
G0.068-0.075d	SiO (217.1GHz)	Y	1	1	0.23 ± 0.02	55.59 ± 0.62	6.26 ± 6.26	0.05
G0.068-0.075e	12CO (230.5GHz)	N	0	0	0.0 ± 0.0	0.0 ± 0.0	0.0 ± 0.0	0.39
G0.068-0.075e	13CO (220.4GHz)	N	0	0	0.0 ± 0.0	0.0 ± 0.0	0.0 ± 0.0	0.12
G0.068-0.075e	C18O (219.6GHz)	N	0	0	0.0 ± 0.0	0.0 ± 0.0	0.0 ± 0.0	0.06
G0.068-0.075e	H2CO (218.2GHz)	Y	1	1	0.42 ± 0.04	57.5 ± 0.26	2.58 ± 2.58	0.06
G0.068-0.075e	H2CO (218.5GHz)	Y	1	1	0.47 ± 0.04	104.13 ± 0.25	2.56 ± 2.56	0.06
G0.068-0.075e	H2CO (218.8GHz)	N	0	0	0.0 ± 0.0	0.0 ± 0.0	0.0 ± 0.0	0.05
G0.068-0.075e	OCS (218.9GHz)	N	0	0	0.0 ± 0.0	0.0 ± 0.0	0.0 ± 0.0	0.05
G0.068-0.075e	OCS (231.1GHz)	N	0	0	0.0 ± 0.0	0.0 ± 0.0	0.0 ± 0.0	0.07
G0.068-0.075e	SO (219.9GHz)	N	0	0	0.0 ± 0.0	0.0 ± 0.0	0.0 ± 0.0	0.06
G0.068-0.075e	SiO (217.1GHz)	N	0	0	0.0 ± 0.0	0.0 ± 0.0	0.0 ± 0.0	0.06
G0.068-0.075f	12CO (230.5GHz)	Y	1	1	3.2 ± 0.31	67.32 ± 0.42	3.84 ± 3.84	0.47
G0.068-0.075f	13CO (220.4GHz)	Y	5	1	0.69 ± 0.07	69.71 ± 0.17	1.37 ± 1.37	0.09
G0.068-0.075f	13CO (220.4GHz)	Y	5	2	0.71 ± 0.06	34.94 ± 0.22	2.45 ± 2.45	0.09
G0.068-0.075f	13CO (220.4GHz)	Y	5	3	0.29 ± 0.06	5.48 ± 0.54	2.49 ± 2.49	0.09
G0.068-0.075f	C18O (219.6GHz)	N	0	0	0.0 ± 0.0	0.0 ± 0.0	0.0 ± 0.0	0.06
G0.068-0.075f	H2CO (218.2GHz)	Y	1	1	0.73 ± 0.03	38.27 ± 0.18	3.38 ± 3.38	0.06
G0.068-0.075f	H2CO (218.5GHz)	Y	2	1	0.72 ± 0.05	88.45 ± 0.15	1.93 ± 1.93	0.07
G0.068-0.075f	H2CO (218.5GHz)	Y	2	2	0.27 ± 0.04	38.04 ± 0.46	2.55 ± 2.55	0.07
G0.068-0.075f	H2CO (218.8GHz)	Y	1	1	0.25 ± 0.04	38.14 ± 0.41	2.24 ± 2.24	0.06
G0.068-0.075f	OCS (218.9GHz)	N	0	0	0.0 ± 0.0	0.0 ± 0.0	0.0 ± 0.0	0.06
G0.068-0.075f	OCS (231.1GHz)	N	0	0	0.0 ± 0.0	0.0 ± 0.0	0.0 ± 0.0	0.07
G0.068-0.075f	SO (219.9GHz)	Y	1	1	0.23 ± 0.04	37.9 ± 0.48	2.43 ± 2.43	0.06
G0.068-0.075f	SiO (217.1GHz)	Y	1	1	0.37 ± 0.04	39.47 ± 0.34	3.01 ± 3.01	0.06
G0.068-0.075g	12CO (230.5GHz)	Y	5	1	2.07 ± 0.23	84.78 ± 0.31	2.37 ± 2.37	0.32
G0.068-0.075g	12CO (230.5GHz)	Y	5	2	9.67 ± 0.19	55.86 ± 0.08	3.66 ± 3.66	0.32
G0.068-0.075g	12CO (230.5GHz)	Y	5	3	4.51 ± 0.21	31.57 ± 0.16	3.08 ± 3.08	0.32
G0.068-0.075g	12CO (230.5GHz)	Y	5	4	4.6 ± 0.23	15.0 ± 0.14	2.56 ± 2.56	0.32
G0.068-0.075g	13CO (220.4GHz)	Y	2	1	1.71 ± 0.07	53.93 ± 0.2	4.33 ± 4.33	0.1
G0.068-0.075g	13CO (220.4GHz)	Y	2	2	2.97 ± 0.11	30.7 ± 0.07	1.62 ± 1.62	0.1
G0.068-0.075g	C18O (219.6GHz)	Y	2	1	0.3 ± 0.03	54.86 ± 0.4	3.69 ± 3.69	0.06
G0.068-0.075g	C18O (219.6GHz)	Y	2	2	0.29 ± 0.04	29.92 ± 0.28	1.72 ± 1.72	0.06
G0.068-0.075g	H2CO (218.2GHz)	Y	1	1	0.14 ± 0.03	49.0 ± 0.88	3.71 ± 3.71	0.06
G0.068-0.075g	H2CO (218.5GHz)	Y	1	1	0.28 ± 0.03	96.64 ± 0.47	3.66 ± 3.66	0.06
G0.068-0.075g	H2CO (218.8GHz)	Y	1	1	0.14 ± 0.03	51.17 ± 0.76	3.78 ± 3.78	0.05
G0.068-0.075g	OCS (218.9GHz)	N	0	0	0.0 ± 0.0	0.0 ± 0.0	0.0 ± 0.0	0.05
G0.068-0.075g	OCS (231.1GHz)	N	0	0	0.0 ± 0.0	0.0 ± 0.0	0.0 ± 0.0	0.09
G0.068-0.075g	SO (219.9GHz)	Y	1	1	0.21 ± 0.02	49.5 ± 0.65	5.13 ± 5.13	0.05
G0.068-0.075g	SiO (217.1GHz)	Y	1	1	0.23 ± 0.03	49.96 ± 0.41	3.21 ± 3.21	0.05

Continued on next page

Table A.1 – *Continued from previous page*

Leaf	Transition	Detected	Number of Comps	Comp.	Amplitude	Velocity	Width	RMS
G0.068-0.075h	13CO (220.4GHz)	Y	5	1	0.35 ± 0.08	59.55 ± 0.94	3.48 ± 3.48	0.16
G0.068-0.075h	13CO (220.4GHz)	Y	5	3	0.62 ± 0.11	6.98 ± 0.42	2.14 ± 2.14	0.16
G0.068-0.075h	C18O (219.6GHz)	N	0	0	0.0 ± 0.0	0.0 ± 0.0	0.0 ± 0.0	0.07
G0.068-0.075h	H2CO (218.2GHz)	N	0	0	0.0 ± 0.0	0.0 ± 0.0	0.0 ± 0.0	0.07
G0.068-0.075h	H2CO (218.5GHz)	Y	1	1	1.8 ± 0.06	87.49 ± 0.07	1.87 ± 1.87	0.08
G0.068-0.075h	H2CO (218.8GHz)	Y	1	1	0.26 ± 0.08	135.11 ± 0.31	0.66 ± 0.66	0.07
G0.068-0.075h	OCS (218.9GHz)	N	0	0	0.0 ± 0.0	0.0 ± 0.0	0.0 ± 0.0	0.07
G0.068-0.075h	OCS (231.1GHz)	N	0	0	0.0 ± 0.0	0.0 ± 0.0	0.0 ± 0.0	0.1
G0.068-0.075h	SO (219.9GHz)	Y	1	1	0.47 ± 0.05	37.91 ± 0.26	2.01 ± 2.01	0.08
G0.068-0.075h	SiO (217.1GHz)	N	0	0	0.0 ± 0.0	0.0 ± 0.0	0.0 ± 0.0	0.07
G0.068-0.075i	12CO (230.5GHz)	N	0	0	0.0 ± 0.0	0.0 ± 0.0	0.0 ± 0.0	0.74
G0.068-0.075i	13CO (220.4GHz)	Y	2	1	0.75 ± 0.1	41.21 ± 0.29	1.81 ± 1.81	0.15
G0.068-0.075i	C18O (219.6GHz)	N	0	0	0.0 ± 0.0	0.0 ± 0.0	0.0 ± 0.0	0.07
G0.068-0.075i	H2CO (218.2GHz)	Y	1	1	0.57 ± 0.05	56.7 ± 0.28	2.83 ± 2.83	0.08
G0.068-0.075i	H2CO (218.5GHz)	Y	1	1	0.64 ± 0.05	103.26 ± 0.26	3.05 ± 3.05	0.08
G0.068-0.075i	H2CO (218.8GHz)	Y	1	1	0.33 ± 0.05	55.02 ± 0.4	2.34 ± 2.34	0.08
G0.068-0.075i	OCS (218.9GHz)	N	0	0	0.0 ± 0.0	0.0 ± 0.0	0.0 ± 0.0	0.07
G0.068-0.075i	OCS (231.1GHz)	N	0	0	0.0 ± 0.0	0.0 ± 0.0	0.0 ± 0.0	0.1
G0.068-0.075i	SO (219.9GHz)	N	0	0	0.0 ± 0.0	0.0 ± 0.0	0.0 ± 0.0	0.08
G0.068-0.075i	SiO (217.1GHz)	Y	1	1	0.28 ± 0.04	57.74 ± 0.55	3.48 ± 3.48	0.08
G0.068-0.075j	12CO (230.5GHz)	Y	2	1	10.14 ± 0.32	56.4 ± 0.17	4.72 ± 4.72	0.56
G0.068-0.075j	12CO (230.5GHz)	Y	2	2	5.97 ± 0.39	12.72 ± 0.24	3.18 ± 3.18	0.56
G0.068-0.075j	13CO (220.4GHz)	Y	2	1	2.97 ± 0.07	54.13 ± 0.14	5.29 ± 5.29	0.13
G0.068-0.075j	13CO (220.4GHz)	Y	2	2	2.03 ± 0.13	35.1 ± 0.11	1.56 ± 1.56	0.13
G0.068-0.075j	C18O (219.6GHz)	Y	1	1	0.54 ± 0.04	53.71 ± 0.35	4.58 ± 4.58	0.07
G0.068-0.075j	H2CO (218.2GHz)	N	0	0	0.0 ± 0.0	0.0 ± 0.0	0.0 ± 0.0	0.06
G0.068-0.075j	H2CO (218.5GHz)	Y	2	1	0.55 ± 0.04	96.59 ± 0.36	4.27 ± 4.27	0.08
G0.068-0.075j	H2CO (218.5GHz)	Y	2	2	0.25 ± 0.03	49.7 ± 0.95	5.92 ± 5.92	0.08
G0.068-0.075j	H2CO (218.8GHz)	N	0	0	0.0 ± 0.0	0.0 ± 0.0	0.0 ± 0.0	0.07
G0.068-0.075j	OCS (218.9GHz)	N	0	0	0.0 ± 0.0	0.0 ± 0.0	0.0 ± 0.0	0.07
G0.068-0.075j	OCS (231.1GHz)	Y	2	1	0.24 ± 0.07	137.7 ± 0.8	2.43 ± 2.43	0.12
G0.068-0.075j	OCS (231.1GHz)	Y	2	2	0.36 ± 0.06	49.09 ± 0.59	3.12 ± 3.12	0.12
G0.068-0.075j	SO (219.9GHz)	Y	1	1	0.46 ± 0.05	48.61 ± 0.42	3.53 ± 3.53	0.08
G0.068-0.075j	SiO (217.1GHz)	Y	1	1	0.39 ± 0.05	47.65 ± 0.41	2.86 ± 2.86	0.08
G0.068-0.075k	12CO (230.5GHz)	Y	1	1	9.05 ± 0.31	56.04 ± 0.24	6.2 ± 6.2	0.55
G0.068-0.075k	13CO (220.4GHz)	Y	3	1	2.66 ± 0.07	53.36 ± 0.16	5.53 ± 5.53	0.16
G0.068-0.075k	13CO (220.4GHz)	Y	3	2	3.17 ± 0.13	35.07 ± 0.07	1.57 ± 1.57	0.16
G0.068-0.075k	C18O (219.6GHz)	Y	3	1	0.49 ± 0.04	53.19 ± 0.43	4.26 ± 4.26	0.1
G0.068-0.075k	C18O (219.6GHz)	Y	3	2	0.39 ± 0.07	35.05 ± 0.31	1.39 ± 1.39	0.1
G0.068-0.075k	C18O (219.6GHz)	Y	3	3	0.32 ± 0.1	19.66 ± 0.28	0.87 ± 0.87	0.1
G0.068-0.075k	H2CO (218.2GHz)	Y	2	1	0.35 ± 0.04	47.4 ± 0.55	4.31 ± 4.31	0.09
G0.068-0.075k	H2CO (218.5GHz)	Y	1	1	0.51 ± 0.04	97.39 ± 0.45	5.1 ± 5.1	0.09
G0.068-0.075k	H2CO (218.8GHz)	Y	1	1	0.24 ± 0.04	48.44 ± 0.73	3.48 ± 3.48	0.08
G0.068-0.075k	OCS (218.9GHz)	N	0	0	0.0 ± 0.0	0.0 ± 0.0	0.0 ± 0.0	0.08
G0.068-0.075k	OCS (231.1GHz)	N	0	0	0.0 ± 0.0	0.0 ± 0.0	0.0 ± 0.0	0.12
G0.068-0.075k	SO (219.9GHz)	Y	1	1	0.51 ± 0.04	48.84 ± 0.4	4.35 ± 4.35	0.09
G0.068-0.075k	SiO (217.1GHz)	Y	1	1	0.31 ± 0.03	49.43 ± 0.82	6.74 ± 6.74	0.09
G0.068-0.075l	12CO (230.5GHz)	N	0	0	0.0 ± 0.0	0.0 ± 0.0	0.0 ± 0.0	0.63
G0.068-0.075l	C18O (219.6GHz)	N	0	0	0.0 ± 0.0	0.0 ± 0.0	0.0 ± 0.0	0.08
G0.068-0.075l	H2CO (218.2GHz)	N	0	0	0.0 ± 0.0	0.0 ± 0.0	0.0 ± 0.0	0.09
G0.068-0.075l	H2CO (218.5GHz)	Y	2	1	1.28 ± 0.06	88.4 ± 0.12	2.18 ± 2.18	0.1
G0.068-0.075l	H2CO (218.5GHz)	Y	2	2	0.44 ± 0.07	38.96 ± 0.32	1.79 ± 1.79	0.1
G0.068-0.075l	H2CO (218.8GHz)	Y	1	1	0.26 ± 0.05	37.67 ± 0.56	2.58 ± 2.58	0.08
G0.068-0.075l	OCS (218.9GHz)	N	0	0	0.0 ± 0.0	0.0 ± 0.0	0.0 ± 0.0	0.08
G0.068-0.075l	OCS (231.1GHz)	N	0	0	0.0 ± 0.0	0.0 ± 0.0	0.0 ± 0.0	0.15
G0.068-0.075l	SO (219.9GHz)	N	0	0	0.0 ± 0.0	0.0 ± 0.0	0.0 ± 0.0	0.09
G0.068-0.075l	SiO (217.1GHz)	N	0	0	0.0 ± 0.0	0.0 ± 0.0	0.0 ± 0.0	0.09
G0.070-0.035a	12CO (230.5GHz)	N	0	0	0.0 ± 0.0	0.0 ± 0.0	0.0 ± 0.0	0.5
G0.070-0.035a	13CO (220.4GHz)	Y	1	1	2.51 ± 0.26	30.14 ± 0.4	3.35 ± 3.35	0.5
G0.070-0.035a	H2CO (218.2GHz)	Y	2	1	0.36 ± 0.02	59.02 ± 0.16	2.83 ± 2.83	0.03
G0.070-0.035a	H2CO (218.2GHz)	Y	2	2	0.37 ± 0.08	43.2 ± 0.3	0.44 ± 0.44	0.03
G0.070-0.035a	H2CO (218.5GHz)	Y	1	1	0.33 ± 0.02	105.03 ± 0.25	3.34 ± 3.34	0.03
G0.070-0.035a	H2CO (218.8GHz)	Y	2	1	0.1 ± 0.01	57.03 ± 0.64	4.14 ± 4.14	0.03
G0.070-0.035a	OCS (218.9GHz)	Y	1	1	0.09 ± 0.02	55.73 ± 0.53	2.57 ± 2.57	0.03
G0.070-0.035a	OCS (231.1GHz)	Y	1	1	0.09 ± 0.02	55.73 ± 0.53	2.57 ± 2.57	0.03
G0.070-0.035a	SO (219.9GHz)	Y	1	1	0.3 ± 0.04	51.97 ± 0.17	1.06 ± 1.06	0.04
G0.070-0.035b	12CO (230.5GHz)	Y	1	1	6.5 ± 0.57	56.09 ± 0.2	1.92 ± 1.92	0.51
G0.070-0.035b	13CO (220.4GHz)	Y	2	1	6.5 ± 0.37	56.09 ± 0.13	1.92 ± 1.92	0.51
G0.070-0.035b	H2CO (218.2GHz)	Y	1	1	0.36 ± 0.04	61.67 ± 0.44	3.82 ± 3.82	0.07
G0.070-0.035b	H2CO (218.5GHz)	Y	2	1	0.49 ± 0.04	109.13 ± 0.27	2.65 ± 2.65	0.07
G0.070-0.035b	H2CO (218.5GHz)	Y	2	2	0.38 ± 0.05	98.49 ± 0.3	2.04 ± 2.04	0.07
G0.070-0.035b	H2CO (218.8GHz)	N	0	0	0.0 ± 0.0	0.0 ± 0.0	0.0 ± 0.0	0.07
G0.070-0.035b	OCS (218.9GHz)	N	0	0	0.0 ± 0.0	0.0 ± 0.0	0.0 ± 0.0	0.07
G0.070-0.035b	OCS (231.1GHz)	N	0	0	0.0 ± 0.0	0.0 ± 0.0	0.0 ± 0.0	0.07
G0.070-0.035b	SO (219.9GHz)	N	0	0	0.0 ± 0.0	0.0 ± 0.0	0.0 ± 0.0	0.07
G0.070-0.035c	12CO (230.5GHz)	N	0	0	0.0 ± 0.0	0.0 ± 0.0	0.0 ± 0.0	1.56
G0.070-0.035c	13CO (220.4GHz)	N	0	0	0.0 ± 0.0	0.0 ± 0.0	0.0 ± 0.0	1.56
G0.070-0.035c	H2CO (218.2GHz)	Y	2	1	0.44 ± 0.03	60.78 ± 0.42	5.7 ± 5.7	0.07
G0.070-0.035c	H2CO (218.2GHz)	Y	2	2	0.62 ± 0.07	40.1 ± 0.12	0.93 ± 0.93	0.07
G0.070-0.035c	H2CO (218.5GHz)	Y	2	1	0.62 ± 0.02	102.11 ± 0.2	6.76 ± 6.76	0.03
G0.070-0.035c	H2CO (218.5GHz)	Y	2	2	0.14 ± 0.01	52.92 ± 1.07	10.51 ± 10.51	0.03
G0.070-0.035c	H2CO (218.8GHz)	Y	2	1	0.13 ± 0.01	54.18 ± 0.79	8.76 ± 8.76	0.03
G0.070-0.035c	OCS (218.9GHz)	Y	1	1	0.1 ± 0.01	53.34 ± 0.85	8.56 ± 8.56	0.03
G0.070-0.035c	OCS (231.1GHz)	Y	1	1	0.1 ± 0.01	53.34 ± 0.85	8.56 ± 8.56	0.03
G0.070-0.035c	SO (219.9GHz)	Y	2	1	1.06 ± 0.07	49.43 ± 0.09	1.17 ± 1.17	0.07
G0.070-0.035c	SO (219.9GHz)	Y	2	2	0.37 ± 0.05	41.28 ± 0.34	2.09 ± 2.09	0.07
G0.070-0.035c	SiO (217.1GHz)	Y	2	2	0.35 ± 0.02	52.64 ± 0.72	9.93 ± 9.93	0.04

Continued on next page

Table A.1 – *Continued from previous page*

Leaf	Transition	Detected	Number of Comps	Comp.	Amplitude	Velocity	Width	RMS
G0.070-0.035d	12CO (230.5GHz)	N	0	0	0.0 ± 0.0	0.0 ± 0.0	0.0 ± 0.0	20.79
G0.070-0.035d	13CO (220.4GHz)	N	0	0	0.0 ± 0.0	0.0 ± 0.0	0.0 ± 0.0	20.79
G0.070-0.035d	C18O (219.6GHz)	Y	2	1	0.36 ± 0.04	29.79 ± 0.54	4.86 ± 4.86	0.08
G0.070-0.035d	H2CO (218.5GHz)	Y	2	1	1.85 ± 0.12	38.78 ± 0.28	3.85 ± 3.85	0.24
G0.070-0.035d	H2CO (218.8GHz)	N	0	0	0.0 ± 0.0	0.0 ± 0.0	0.0 ± 0.0	0.26
G0.070-0.035d	OCS (218.9GHz)	N	0	0	0.0 ± 0.0	0.0 ± 0.0	0.0 ± 0.0	0.23
G0.070-0.035d	OCS (231.1GHz)	N	0	0	0.0 ± 0.0	0.0 ± 0.0	0.0 ± 0.0	0.23
G0.070-0.035d	SO (219.9GHz)	N	0	0	0.0 ± 0.0	0.0 ± 0.0	0.0 ± 0.0	6.11
G0.070-0.035d	SiO (217.1GHz)	N	0	0	0.0 ± 0.0	0.0 ± 0.0	0.0 ± 0.0	7.14
G0.070-0.035e	12CO (230.5GHz)	N	0	0	0.0 ± 0.0	0.0 ± 0.0	0.0 ± 0.0	19.93
G0.070-0.035e	13CO (220.4GHz)	N	0	0	0.0 ± 0.0	0.0 ± 0.0	0.0 ± 0.0	19.93
G0.070-0.035e	C18O (219.6GHz)	Y	4	1	0.29 ± 0.05	24.05 ± 0.57	3.11 ± 3.11	0.08
G0.070-0.035e	H2CO (218.5GHz)	Y	1	1	1.75 ± 0.11	39.98 ± 0.26	3.64 ± 3.64	0.19
G0.070-0.035e	OCS (218.9GHz)	Y	3	1	0.72 ± 0.09	187.42 ± 0.61	4.44 ± 4.44	0.18
G0.070-0.035e	OCS (231.1GHz)	N	0	0	0.0 ± 0.0	0.0 ± 0.0	0.0 ± 0.0	0.18
G0.070-0.035e	SO (219.9GHz)	N	0	0	0.0 ± 0.0	0.0 ± 0.0	0.0 ± 0.0	5.34
G0.070-0.035e	SiO (217.1GHz)	N	0	0	0.0 ± 0.0	0.0 ± 0.0	0.0 ± 0.0	24.17
G0.106-0.082a	12CO (230.5GHz)	N	0	0	0.0 ± 0.0	0.0 ± 0.0	0.0 ± 0.0	0.5
G0.106-0.082a	C18O (219.6GHz)	N	0	0	0.0 ± 0.0	0.0 ± 0.0	0.0 ± 0.0	0.03
G0.106-0.082a	H2CO (218.2GHz)	Y	3	1	0.98 ± 0.02	56.28 ± 0.11	3.74 ± 3.74	0.03
G0.106-0.082a	H2CO (218.2GHz)	Y	3	2	0.19 ± 0.01	40.7 ± 0.92	7.51 ± 7.51	0.03
G0.106-0.082a	H2CO (218.5GHz)	Y	3	1	0.84 ± 0.02	104.33 ± 0.11	3.19 ± 3.19	0.03
G0.106-0.082a	H2CO (218.5GHz)	Y	3	2	0.55 ± 0.02	91.02 ± 0.2	4.43 ± 4.43	0.03
G0.106-0.082a	H2CO (218.5GHz)	Y	3	3	0.3 ± 0.02	55.02 ± 0.31	4.46 ± 4.46	0.03
G0.106-0.082a	H2CO (218.8GHz)	Y	3	1	0.5 ± 0.02	55.27 ± 0.24	3.52 ± 3.52	0.04
G0.106-0.082a	H2CO (218.8GHz)	Y	3	2	0.18 ± 0.02	41.76 ± 0.99	6.14 ± 6.14	0.04
G0.106-0.082a	OCS (218.9GHz)	Y	2	1	0.16 ± 0.02	54.72 ± 0.38	2.24 ± 2.24	0.04
G0.106-0.082a	OCS (231.1GHz)	Y	1	1	0.22 ± 0.02	50.62 ± 1.23	10.2 ± 10.2	0.04
G0.106-0.082a	SO (219.9GHz)	Y	2	1	0.17 ± 0.02	53.82 ± 0.83	4.32 ± 4.32	0.03
G0.106-0.082a	SO (219.9GHz)	Y	2	2	0.18 ± 0.01	40.57 ± 0.87	5.14 ± 5.14	0.03
G0.106-0.082a	SiO (217.1GHz)	Y	2	1	0.34 ± 0.01	56.28 ± 0.18	3.98 ± 3.98	0.03
G0.106-0.082a	SiO (217.1GHz)	Y	2	2	0.19 ± 0.01	39.99 ± 0.36	4.53 ± 4.53	0.03
G0.106-0.082b	12CO (230.5GHz)	Y	1	1	3.53 ± 0.29	58.64 ± 0.27	2.9 ± 2.9	0.5
G0.106-0.082b	C18O (219.6GHz)	N	0	0	0.0 ± 0.0	0.0 ± 0.0	0.0 ± 0.0	0.04
G0.106-0.082b	H2CO (218.2GHz)	Y	2	1	0.9 ± 0.01	56.56 ± 0.11	6.94 ± 6.94	0.03
G0.106-0.082b	H2CO (218.5GHz)	Y	2	1	0.95 ± 0.01	104.77 ± 0.1	5.59 ± 5.59	0.03
G0.106-0.082b	H2CO (218.5GHz)	Y	2	2	0.37 ± 0.01	56.17 ± 0.28	6.42 ± 6.42	0.03
G0.106-0.082b	H2CO (218.8GHz)	Y	1	1	0.48 ± 0.02	55.97 ± 0.27	6.82 ± 6.82	0.04
G0.106-0.082b	OCS (218.9GHz)	N	0	0	0.0 ± 0.0	0.0 ± 0.0	0.0 ± 0.0	0.04
G0.106-0.082b	OCS (231.1GHz)	N	0	0	0.0 ± 0.0	0.0 ± 0.0	0.0 ± 0.0	0.05
G0.106-0.082b	SO (219.9GHz)	Y	2	1	0.3 ± 0.01	55.05 ± 0.27	6.55 ± 6.55	0.02
G0.106-0.082b	SiO (217.1GHz)	Y	1	1	0.4 ± 0.01	58.43 ± 0.2	6.52 ± 6.52	0.02
G0.106-0.082c	12CO (230.5GHz)	Y	3	1	2.55 ± 0.2	83.21 ± 0.37	4.1 ± 4.1	0.35
G0.106-0.082c	12CO (230.5GHz)	Y	3	2	5.78 ± 0.21	58.56 ± 0.16	3.78 ± 3.78	0.35
G0.106-0.082c	13CO (220.4GHz)	Y	4	1	0.33 ± 0.02	74.01 ± 0.7	11.11 ± 11.11	0.05
G0.106-0.082c	13CO (220.4GHz)	Y	4	2	0.67 ± 0.04	55.47 ± 0.12	1.63 ± 1.63	0.05
G0.106-0.082c	13CO (220.4GHz)	Y	4	3	0.43 ± 0.04	3.76 ± 0.21	2.24 ± 2.24	0.05
G0.106-0.082c	C18O (219.6GHz)	Y	1	1	0.1 ± 0.02	57.79 ± 1.19	6.1 ± 6.1	0.04
G0.106-0.082c	H2CO (218.2GHz)	Y	3	1	1.08 ± 0.02	56.08 ± 0.12	5.07 ± 5.07	0.04
G0.106-0.082c	H2CO (218.2GHz)	Y	3	2	0.28 ± 0.02	40.64 ± 0.39	3.52 ± 3.52	0.04
G0.106-0.082c	H2CO (218.5GHz)	Y	2	1	0.89 ± 0.03	103.74 ± 0.15	4.27 ± 4.27	0.04
G0.106-0.082c	H2CO (218.5GHz)	Y	2	2	0.37 ± 0.02	54.6 ± 0.46	6.6 ± 6.6	0.04
G0.106-0.082c	H2CO (218.8GHz)	Y	2	1	0.63 ± 0.03	54.63 ± 0.27	5.2 ± 5.2	0.05
G0.106-0.082c	OCS (218.9GHz)	Y	1	1	0.33 ± 0.03	54.88 ± 0.34	3.15 ± 3.15	0.05
G0.106-0.082c	OCS (231.1GHz)	Y	1	1	0.31 ± 0.04	53.97 ± 0.65	3.98 ± 3.98	0.1
G0.106-0.082c	SO (219.9GHz)	Y	1	1	0.36 ± 0.02	54.05 ± 0.39	6.72 ± 6.72	0.04
G0.106-0.082c	SiO (217.1GHz)	Y	1	1	0.59 ± 0.02	56.25 ± 0.21	5.94 ± 5.94	0.04
G0.106-0.082d	12CO (230.5GHz)	Y	5	1	2.33 ± 0.15	77.22 ± 0.28	3.68 ± 3.68	0.22
G0.106-0.082d	12CO (230.5GHz)	Y	5	2	3.56 ± 0.18	61.34 ± 0.16	2.59 ± 2.59	0.22
G0.106-0.082d	12CO (230.5GHz)	Y	5	3	2.91 ± 0.15	48.47 ± 0.23	3.83 ± 3.83	0.22
G0.106-0.082d	12CO (230.5GHz)	Y	5	4	2.17 ± 0.12	17.48 ± 0.4	6.44 ± 6.44	0.22
G0.106-0.082d	13CO (220.4GHz)	Y	3	1	1.63 ± 0.07	59.15 ± 0.11	2.29 ± 2.29	0.09
G0.106-0.082d	13CO (220.4GHz)	Y	3	2	0.62 ± 0.06	34.2 ± 0.34	3.21 ± 3.21	0.09
G0.106-0.082d	C18O (219.6GHz)	Y	2	1	0.23 ± 0.04	59.08 ± 0.36	1.82 ± 1.82	0.05
G0.106-0.082d	C18O (219.6GHz)	Y	2	2	0.11 ± 0.03	32.68 ± 1.02	3.77 ± 3.77	0.05
G0.106-0.082d	H2CO (218.2GHz)	Y	3	1	0.3 ± 0.03	61.2 ± 0.36	3.03 ± 3.03	0.05
G0.106-0.082d	H2CO (218.2GHz)	Y	3	2	0.18 ± 0.02	39.38 ± 0.89	7.01 ± 7.01	0.05
G0.106-0.082d	H2CO (218.5GHz)	Y	1	1	0.37 ± 0.02	103.42 ± 0.38	5.02 ± 5.02	0.05
G0.106-0.082d	H2CO (218.8GHz)	Y	4	1	0.22 ± 0.04	60.12 ± 0.54	2.16 ± 2.16	0.07
G0.106-0.082d	H2CO (218.8GHz)	Y	4	2	0.18 ± 0.05	53.14 ± 0.59	1.6 ± 1.6	0.07
G0.106-0.082d	H2CO (218.8GHz)	Y	4	3	0.11 ± 0.03	41.73 ± 1.43	4.45 ± 4.45	0.07
G0.106-0.082d	OCS (218.9GHz)	Y	1	1	0.19 ± 0.03	56.24 ± 0.78	4.58 ± 4.58	0.06
G0.106-0.082d	OCS (231.1GHz)	N	0	0	0.0 ± 0.0	0.0 ± 0.0	0.0 ± 0.0	0.1
G0.106-0.082d	SO (219.9GHz)	Y	1	1	0.16 ± 0.01	49.39 ± 1.21	11.23 ± 11.23	0.05
G0.106-0.082d	SiO (217.1GHz)	Y	1	1	0.19 ± 0.01	38.07 ± 1.42	19.84 ± 19.84	0.04
G0.145-0.086a	12CO (230.5GHz)	N	0	0	0.0 ± 0.0	0.0 ± 0.0	0.0 ± 0.0	0.13
G0.145-0.086a	13CO (220.4GHz)	Y	3	1	0.26 ± 0.03	83.11 ± 0.83	5.9 ± 5.9	0.06
G0.145-0.086a	13CO (220.4GHz)	Y	3	2	0.56 ± 0.04	36.8 ± 0.29	3.22 ± 3.22	0.06
G0.145-0.086a	13CO (220.4GHz)	Y	3	3	1.76 ± 0.05	15.72 ± 0.08	2.59 ± 2.59	0.06
G0.145-0.086a	C18O (219.6GHz)	N	0	0	0.0 ± 0.0	0.0 ± 0.0	0.0 ± 0.0	0.04
G0.145-0.086a	H2CO (218.5GHz)	N	0	0	0.0 ± 0.0	0.0 ± 0.0	0.0 ± 0.0	0.04
G0.145-0.086a	H2CO (218.8GHz)	N	0	0	0.0 ± 0.0	0.0 ± 0.0	0.0 ± 0.0	0.05
G0.145-0.086a	OCS (218.9GHz)	N	0	0	0.0 ± 0.0	0.0 ± 0.0	0.0 ± 0.0	0.05
G0.145-0.086a	OCS (231.1GHz)	N	0	0	0.0 ± 0.0	0.0 ± 0.0	0.0 ± 0.0	0.07
G0.145-0.086a	SO (219.9GHz)	N	0	0	0.0 ± 0.0	0.0 ± 0.0	0.0 ± 0.0	0.03
G0.145-0.086a	SiO (217.1GHz)	N	0	0	0.0 ± 0.0	0.0 ± 0.0	0.0 ± 0.0	0.04
G0.145-0.086b	13CO (220.4GHz)	Y	1	1	0.8 ± 0.05	27.85 ± 0.35	5.27 ± 5.27	0.09

Continued on next page

Table A.1 – *Continued from previous page*

Leaf	Transition	Detected	Number of Comps	Comp.	Amplitude	Velocity	Width	RMS
G0.145-0.086b	C18O (219.6GHz)	N	0	0	0.0 ± 0.0	0.0 ± 0.0	0.0 ± 0.0	0.04
G0.145-0.086b	H2CO (218.2GHz)	N	0	0	0.0 ± 0.0	0.0 ± 0.0	0.0 ± 0.0	0.04
G0.145-0.086b	H2CO (218.5GHz)	N	0	0	0.0 ± 0.0	0.0 ± 0.0	0.0 ± 0.0	0.04
G0.145-0.086b	H2CO (218.8GHz)	N	0	0	0.0 ± 0.0	0.0 ± 0.0	0.0 ± 0.0	0.05
G0.145-0.086b	OCS (218.9GHz)	N	0	0	0.0 ± 0.0	0.0 ± 0.0	0.0 ± 0.0	0.05
G0.145-0.086b	OCS (231.1GHz)	N	0	0	0.0 ± 0.0	0.0 ± 0.0	0.0 ± 0.0	0.07
G0.145-0.086b	SO (219.9GHz)	N	0	0	0.0 ± 0.0	0.0 ± 0.0	0.0 ± 0.0	0.03
G0.145-0.086b	SiO (217.1GHz)	N	0	0	0.0 ± 0.0	0.0 ± 0.0	0.0 ± 0.0	0.03
G0.212-0.001a	12CO (230.5GHz)	Y	1	1	6.62 ± 0.25	43.54 ± 0.1	2.21 ± 2.21	0.36
G0.212-0.001a	13CO (220.4GHz)	Y	1	1	6.52 ± 0.08	44.62 ± 0.03	1.79 ± 1.79	0.09
G0.212-0.001a	C18O (219.6GHz)	Y	1	1	1.46 ± 0.03	44.48 ± 0.03	1.44 ± 1.44	0.03
G0.212-0.001a	H2CO (218.2GHz)	Y	1	1	0.87 ± 0.02	44.93 ± 0.04	1.62 ± 1.62	0.02
G0.212-0.001a	H2CO (218.5GHz)	Y	2	1	0.23 ± 0.02	94.22 ± 0.16	1.78 ± 1.78	0.02
G0.212-0.001a	H2CO (218.5GHz)	Y	2	2	0.13 ± 0.01	44.86 ± 0.35	2.81 ± 2.81	0.02
G0.212-0.001a	H2CO (218.8GHz)	Y	1	1	0.15 ± 0.02	45.23 ± 0.28	2.03 ± 2.03	0.03
G0.212-0.001a	OCS (218.9GHz)	N	0	0	0.0 ± 0.0	0.0 ± 0.0	0.0 ± 0.0	0.02
G0.212-0.001a	OCS (231.1GHz)	N	0	0	0.0 ± 0.0	0.0 ± 0.0	0.0 ± 0.0	0.03
G0.212-0.001a	SO (219.9GHz)	Y	1	1	0.13 ± 0.01	44.57 ± 0.28	2.28 ± 2.28	0.02
G0.212-0.001a	SiO (217.1GHz)	N	0	0	0.0 ± 0.0	0.0 ± 0.0	0.0 ± 0.0	0.02
G0.212-0.001b	12CO (230.5GHz)	Y	2	1	1.79 ± 0.3	61.78 ± 0.35	1.82 ± 1.82	0.36
G0.212-0.001b	12CO (230.5GHz)	Y	2	2	2.82 ± 0.26	49.2 ± 0.25	2.37 ± 2.37	0.36
G0.212-0.001b	13CO (220.4GHz)	Y	4	1	0.57 ± 0.05	83.17 ± 0.15	1.4 ± 1.4	0.06
G0.212-0.001b	13CO (220.4GHz)	Y	4	2	0.28 ± 0.06	53.81 ± 0.33	1.35 ± 1.35	0.06
G0.212-0.001b	13CO (220.4GHz)	Y	4	3	0.28 ± 0.03	61.52 ± 0.67	3.97 ± 3.97	0.06
G0.212-0.001b	13CO (220.4GHz)	Y	4	4	3.88 ± 0.05	45.95 ± 0.03	1.93 ± 1.93	0.06
G0.212-0.001b	C18O (219.6GHz)	Y	1	1	0.56 ± 0.03	45.27 ± 0.09	1.39 ± 1.39	0.03
G0.212-0.001b	H2CO (218.2GHz)	Y	1	1	0.17 ± 0.03	44.57 ± 0.23	1.31 ± 1.31	0.03
G0.212-0.001b	H2CO (218.5GHz)	N	0	0	0.0 ± 0.0	0.0 ± 0.0	0.0 ± 0.0	0.03
G0.212-0.001b	H2CO (218.8GHz)	N	0	0	0.0 ± 0.0	0.0 ± 0.0	0.0 ± 0.0	0.03
G0.212-0.001b	OCS (218.9GHz)	N	0	0	0.0 ± 0.0	0.0 ± 0.0	0.0 ± 0.0	0.03
G0.212-0.001b	OCS (231.1GHz)	N	0	0	0.0 ± 0.0	0.0 ± 0.0	0.0 ± 0.0	0.04
G0.212-0.001b	SO (219.9GHz)	N	0	0	0.0 ± 0.0	0.0 ± 0.0	0.0 ± 0.0	0.02
G0.212-0.001b	SiO (217.1GHz)	N	0	0	0.0 ± 0.0	0.0 ± 0.0	0.0 ± 0.0	0.03
G0.212-0.001c	12CO (230.5GHz)	Y	2	1	0.65 ± 0.14	49.75 ± 0.66	3.24 ± 3.24	0.19
G0.212-0.001c	12CO (230.5GHz)	Y	2	2	0.83 ± 0.06	32.02 ± 1.41	10.99 ± 10.99	0.19
G0.212-0.001c	13CO (220.4GHz)	Y	1	1	2.6 ± 0.08	37.85 ± 0.06	1.72 ± 1.72	0.04
G0.212-0.001c	C18O (219.6GHz)	Y	1	1	0.58 ± 0.03	37.96 ± 0.05	0.73 ± 0.73	0.03
G0.212-0.001c	H2CO (218.2GHz)	Y	1	1	0.21 ± 0.02	37.42 ± 0.18	1.77 ± 1.77	0.03
G0.212-0.001c	H2CO (218.5GHz)	N	0	0	0.0 ± 0.0	0.0 ± 0.0	0.0 ± 0.0	0.03
G0.212-0.001c	H2CO (218.8GHz)	N	0	0	0.0 ± 0.0	0.0 ± 0.0	0.0 ± 0.0	0.03
G0.212-0.001c	OCS (218.9GHz)	N	0	0	0.0 ± 0.0	0.0 ± 0.0	0.0 ± 0.0	0.02
G0.212-0.001c	OCS (231.1GHz)	N	0	0	0.0 ± 0.0	0.0 ± 0.0	0.0 ± 0.0	0.03
G0.212-0.001c	SO (219.9GHz)	N	0	0	0.0 ± 0.0	0.0 ± 0.0	0.0 ± 0.0	0.02
G0.212-0.001c	SiO (217.1GHz)	N	0	0	0.0 ± 0.0	0.0 ± 0.0	0.0 ± 0.0	0.03
G0.212-0.001d	12CO (230.5GHz)	Y	1	1	1.78 ± 0.24	39.85 ± 0.48	3.14 ± 3.14	0.33
G0.212-0.001d	13CO (220.4GHz)	Y	3	1	0.65 ± 0.07	65.69 ± 0.16	1.23 ± 1.23	0.07
G0.212-0.001d	13CO (220.4GHz)	Y	3	2	4.46 ± 0.08	45.66 ± 0.03	1.26 ± 1.26	0.07
G0.212-0.001d	13CO (220.4GHz)	Y	3	3	1.87 ± 0.05	39.66 ± 0.12	2.96 ± 2.96	0.07
G0.212-0.001d	C18O (219.6GHz)	Y	2	1	0.68 ± 0.05	45.6 ± 0.09	1.13 ± 1.13	0.05
G0.212-0.001d	C18O (219.6GHz)	Y	2	2	0.28 ± 0.03	38.65 ± 0.29	2.09 ± 2.09	0.05
G0.212-0.001d	H2CO (218.2GHz)	N	0	0	0.0 ± 0.0	0.0 ± 0.0	0.0 ± 0.0	0.05
G0.212-0.001d	H2CO (218.5GHz)	N	0	0	0.0 ± 0.0	0.0 ± 0.0	0.0 ± 0.0	0.04
G0.212-0.001d	H2CO (218.8GHz)	N	0	0	0.0 ± 0.0	0.0 ± 0.0	0.0 ± 0.0	0.05
G0.212-0.001d	OCS (218.9GHz)	N	0	0	0.0 ± 0.0	0.0 ± 0.0	0.0 ± 0.0	0.05
G0.212-0.001d	OCS (231.1GHz)	N	0	0	0.0 ± 0.0	0.0 ± 0.0	0.0 ± 0.0	0.05
G0.212-0.001d	SO (219.9GHz)	N	0	0	0.0 ± 0.0	0.0 ± 0.0	0.0 ± 0.0	0.04
G0.212-0.001d	SiO (217.1GHz)	N	0	0	0.0 ± 0.0	0.0 ± 0.0	0.0 ± 0.0	0.04
G0.212-0.001e	12CO (230.5GHz)	Y	1	1	9.5 ± 0.43	44.54 ± 0.09	1.74 ± 1.74	0.48
G0.212-0.001e	13CO (220.4GHz)	Y	1	1	6.22 ± 0.1	45.01 ± 0.04	1.9 ± 1.9	0.1
G0.212-0.001e	C18O (219.6GHz)	Y	1	1	1.2 ± 0.04	44.79 ± 0.07	1.94 ± 1.94	0.05
G0.212-0.001e	H2CO (218.2GHz)	Y	1	1	0.27 ± 0.04	44.97 ± 0.27	1.69 ± 1.69	0.05
G0.212-0.001e	H2CO (218.5GHz)	N	0	0	0.0 ± 0.0	0.0 ± 0.0	0.0 ± 0.0	0.05
G0.212-0.001e	H2CO (218.8GHz)	N	0	0	0.0 ± 0.0	0.0 ± 0.0	0.0 ± 0.0	0.04
G0.212-0.001e	OCS (218.9GHz)	N	0	0	0.0 ± 0.0	0.0 ± 0.0	0.0 ± 0.0	0.05
G0.212-0.001e	OCS (231.1GHz)	N	0	0	0.0 ± 0.0	0.0 ± 0.0	0.0 ± 0.0	0.06
G0.212-0.001e	SO (219.9GHz)	N	0	0	0.0 ± 0.0	0.0 ± 0.0	0.0 ± 0.0	0.04
G0.212-0.001e	SiO (217.1GHz)	N	0	0	0.0 ± 0.0	0.0 ± 0.0	0.0 ± 0.0	0.05
G0.316-0.201a	12CO (230.5GHz)	Y	1	1	6.48 ± 0.16	15.58 ± 0.1	3.5 ± 3.5	0.15
G0.316-0.201a	13CO (220.4GHz)	Y	1	1	8.02 ± 0.11	16.79 ± 0.03	1.61 ± 1.61	0.05
G0.316-0.201a	C18O (219.6GHz)	Y	1	1	5.79 ± 0.03	17.48 ± 0.01	1.13 ± 1.13	0.03
G0.316-0.201a	H2CO (218.2GHz)	Y	2	1	2.52 ± 0.03	17.5 ± 0.02	1.24 ± 1.24	0.03
G0.316-0.201a	H2CO (218.5GHz)	Y	2	1	0.72 ± 0.03	66.76 ± 0.07	1.62 ± 1.62	0.03
G0.316-0.201a	H2CO (218.5GHz)	Y	2	2	0.75 ± 0.03	17.7 ± 0.06	1.27 ± 1.27	0.03
G0.316-0.201a	H2CO (218.8GHz)	Y	1	1	0.64 ± 0.03	17.79 ± 0.09	1.71 ± 1.71	0.03
G0.316-0.201a	OCS (218.9GHz)	Y	1	1	0.16 ± 0.02	17.34 ± 0.31	1.83 ± 1.83	0.03
G0.316-0.201a	OCS (231.1GHz)	Y	2	1	0.17 ± 0.02	18.61 ± 0.33	2.14 ± 2.14	0.03
G0.316-0.201a	SO (219.9GHz)	Y	4	1	0.14 ± 0.02	73.59 ± 0.33	1.67 ± 1.67	0.03
G0.316-0.201a	SO (219.9GHz)	Y	4	2	0.95 ± 0.03	17.72 ± 0.04	1.1 ± 1.1	0.03
G0.316-0.201b	12CO (230.5GHz)	Y	2	1	8.75 ± 0.45	21.83 ± 0.03	0.69 ± 0.69	0.18
G0.316-0.201b	13CO (220.4GHz)	Y	1	1	2.57 ± 0.09	19.09 ± 0.08	1.9 ± 1.9	0.07
G0.316-0.201b	C18O (219.6GHz)	Y	1	1	2.35 ± 0.06	18.57 ± 0.03	0.97 ± 0.97	0.06
G0.316-0.201b	H2CO (218.5GHz)	N	0	0	0.0 ± 0.0	0.0 ± 0.0	0.0 ± 0.0	0.06
G0.316-0.201b	H2CO (218.8GHz)	N	0	0	0.0 ± 0.0	0.0 ± 0.0	0.0 ± 0.0	0.06
G0.316-0.201b	OCS (218.9GHz)	N	0	0	0.0 ± 0.0	0.0 ± 0.0	0.0 ± 0.0	0.06
G0.316-0.201b	OCS (231.1GHz)	N	0	0	0.0 ± 0.0	0.0 ± 0.0	0.0 ± 0.0	0.05
G0.316-0.201b	SO (219.9GHz)	N	0	0	0.0 ± 0.0	0.0 ± 0.0	0.0 ± 0.0	0.06
G0.316-0.201b	SiO (217.1GHz)	N	0	0	0.0 ± 0.0	0.0 ± 0.0	0.0 ± 0.0	0.05

Continued on next page

Table A.1 – *Continued from previous page*

Leaf	Transition	Detected	Number of Comps	Comp.	Amplitude	Velocity	Width	RMS
G0.316-0.201c	12CO (230.5GHz)	Y	1	1	6.28 ± 0.25	18.12 ± 0.08	1.72 ± 1.72	0.25
G0.316-0.201c	13CO (220.4GHz)	Y	1	1	7.28 ± 0.26	18.4 ± 0.07	1.7 ± 1.7	0.1
G0.316-0.201c	C18O (219.6GHz)	Y	1	1	2.84 ± 0.07	18.38 ± 0.03	1.07 ± 1.07	0.07
G0.316-0.201c	H2CO (218.2GHz)	Y	1	1	0.67 ± 0.06	18.16 ± 0.14	1.42 ± 1.42	0.07
G0.316-0.201c	H2CO (218.5GHz)	N	0	0	0.0 ± 0.0	0.0 ± 0.0	0.0 ± 0.0	0.08
G0.316-0.201c	H2CO (218.8GHz)	N	0	0	0.0 ± 0.0	0.0 ± 0.0	0.0 ± 0.0	0.07
G0.316-0.201c	OCS (218.9GHz)	N	0	0	0.0 ± 0.0	0.0 ± 0.0	0.0 ± 0.0	0.07
G0.316-0.201c	OCS (231.1GHz)	N	0	0	0.0 ± 0.0	0.0 ± 0.0	0.0 ± 0.0	0.12
G0.316-0.201c	SO (219.9GHz)	Y	1	1	0.45 ± 0.06	18.92 ± 0.21	1.36 ± 1.36	0.07
G0.316-0.201c	SiO (217.1GHz)	N	0	0	0.0 ± 0.0	0.0 ± 0.0	0.0 ± 0.0	0.07
G0.316-0.201d	12CO (230.5GHz)	Y	1	1	7.49 ± 0.19	20.88 ± 0.04	1.53 ± 1.53	0.19
G0.316-0.201d	13CO (220.4GHz)	Y	1	1	5.87 ± 0.17	19.96 ± 0.06	1.72 ± 1.72	0.08
G0.316-0.201d	C18O (219.6GHz)	Y	1	1	2.15 ± 0.08	18.97 ± 0.04	0.67 ± 0.67	0.07
G0.316-0.201d	H2CO (218.2GHz)	Y	1	1	0.81 ± 0.06	19.11 ± 0.08	0.68 ± 0.68	0.06
G0.316-0.201d	H2CO (218.5GHz)	N	0	0	0.0 ± 0.0	0.0 ± 0.0	0.0 ± 0.0	0.07
G0.316-0.201d	H2CO (218.8GHz)	N	0	0	0.0 ± 0.0	0.0 ± 0.0	0.0 ± 0.0	0.08
G0.316-0.201d	OCS (218.9GHz)	N	0	0	0.0 ± 0.0	0.0 ± 0.0	0.0 ± 0.0	0.07
G0.316-0.201d	OCS (231.1GHz)	N	0	0	0.0 ± 0.0	0.0 ± 0.0	0.0 ± 0.0	0.06
G0.316-0.201d	SO (219.9GHz)	Y	1	1	0.23 ± 0.04	19.28 ± 0.41	1.83 ± 1.83	0.06
G0.316-0.201d	SiO (217.1GHz)	N	0	0	0.0 ± 0.0	0.0 ± 0.0	0.0 ± 0.0	0.07
G0.316-0.201e	12CO (230.5GHz)	Y	2	1	3.15 ± 0.31	23.5 ± 0.25	2.21 ± 2.21	0.33
G0.316-0.201e	12CO (230.5GHz)	Y	2	2	2.15 ± 0.16	5.04 ± 0.76	8.6 ± 8.6	0.33
G0.316-0.201e	13CO (220.4GHz)	Y	1	1	15.63 ± 0.67	19.02 ± 0.02	0.59 ± 0.59	0.08
G0.316-0.201e	H2CO (218.2GHz)	Y	1	1	0.7 ± 0.04	17.89 ± 0.2	2.9 ± 2.9	0.07
G0.316-0.201e	H2CO (218.5GHz)	Y	1	1	0.3 ± 0.04	67.36 ± 0.63	4.46 ± 4.46	0.08
G0.316-0.201e	H2CO (218.8GHz)	N	0	0	0.0 ± 0.0	0.0 ± 0.0	0.0 ± 0.0	0.08
G0.316-0.201e	OCS (218.9GHz)	N	0	0	0.0 ± 0.0	0.0 ± 0.0	0.0 ± 0.0	0.08
G0.316-0.201e	OCS (231.1GHz)	N	0	0	0.0 ± 0.0	0.0 ± 0.0	0.0 ± 0.0	0.08
G0.316-0.201e	SO (219.9GHz)	N	0	0	0.0 ± 0.0	0.0 ± 0.0	0.0 ± 0.0	0.07
G0.316-0.201e	SiO (217.1GHz)	N	0	0	0.0 ± 0.0	0.0 ± 0.0	0.0 ± 0.0	0.08
G0.316-0.201f	12CO (230.5GHz)	Y	1	1	8.79 ± 0.3	18.75 ± 0.08	1.97 ± 1.97	0.21
G0.316-0.201f	13CO (220.4GHz)	N	0	0	0.0 ± 0.0	0.0 ± 0.0	0.0 ± 0.0	0.36
G0.316-0.201f	H2CO (218.2GHz)	N	0	0	0.0 ± 0.0	0.0 ± 0.0	0.0 ± 0.0	0.06
G0.316-0.201f	H2CO (218.5GHz)	N	0	0	0.0 ± 0.0	0.0 ± 0.0	0.0 ± 0.0	0.07
G0.316-0.201f	H2CO (218.8GHz)	N	0	0	0.0 ± 0.0	0.0 ± 0.0	0.0 ± 0.0	0.07
G0.316-0.201f	OCS (218.9GHz)	N	0	0	0.0 ± 0.0	0.0 ± 0.0	0.0 ± 0.0	0.06
G0.316-0.201f	OCS (231.1GHz)	N	0	0	0.0 ± 0.0	0.0 ± 0.0	0.0 ± 0.0	0.08
G0.316-0.201f	SO (219.9GHz)	N	0	0	0.0 ± 0.0	0.0 ± 0.0	0.0 ± 0.0	0.06
G0.316-0.201f	SiO (217.1GHz)	N	0	0	0.0 ± 0.0	0.0 ± 0.0	0.0 ± 0.0	0.07
G0.316-0.201g	12CO (230.5GHz)	Y	1	1	7.6 ± 0.19	14.58 ± 0.05	1.62 ± 1.62	0.2
G0.316-0.201g	13CO (220.4GHz)	N	0	0	0.0 ± 0.0	0.0 ± 0.0	0.0 ± 0.0	0.3
G0.316-0.201g	C18O (219.6GHz)	Y	1	1	0.32 ± 0.06	16.56 ± 0.85	4.0 ± 4.0	0.09
G0.316-0.201g	H2CO (218.2GHz)	N	0	0	0.0 ± 0.0	0.0 ± 0.0	0.0 ± 0.0	0.06
G0.316-0.201g	H2CO (218.5GHz)	N	0	0	0.0 ± 0.0	0.0 ± 0.0	0.0 ± 0.0	0.06
G0.316-0.201g	H2CO (218.8GHz)	N	0	0	0.0 ± 0.0	0.0 ± 0.0	0.0 ± 0.0	0.06
G0.316-0.201g	OCS (218.9GHz)	N	0	0	0.0 ± 0.0	0.0 ± 0.0	0.0 ± 0.0	0.06
G0.316-0.201g	OCS (231.1GHz)	N	0	0	0.0 ± 0.0	0.0 ± 0.0	0.0 ± 0.0	0.08
G0.316-0.201g	SO (219.9GHz)	N	0	0	0.0 ± 0.0	0.0 ± 0.0	0.0 ± 0.0	0.06
G0.316-0.201g	SiO (217.1GHz)	N	0	0	0.0 ± 0.0	0.0 ± 0.0	0.0 ± 0.0	0.07
G0.316-0.201h	12CO (230.5GHz)	Y	1	1	13.24 ± 0.64	20.72 ± 0.02	0.67 ± 0.67	0.34
G0.316-0.201h	13CO (220.4GHz)	Y	1	1	7.06 ± 0.18	18.41 ± 0.04	1.41 ± 1.41	0.1
G0.316-0.201h	C18O (219.6GHz)	Y	1	1	4.79 ± 0.07	18.96 ± 0.02	0.82 ± 0.82	0.07
G0.316-0.201h	H2CO (218.2GHz)	Y	1	1	0.84 ± 0.17	18.64 ± 0.07	0.66 ± 0.66	0.07
G0.316-0.201h	H2CO (218.5GHz)	N	0	0	0.0 ± 0.0	0.0 ± 0.0	0.0 ± 0.0	0.08
G0.316-0.201h	H2CO (218.8GHz)	N	0	0	0.0 ± 0.0	0.0 ± 0.0	0.0 ± 0.0	0.08
G0.316-0.201h	OCS (218.9GHz)	N	0	0	0.0 ± 0.0	0.0 ± 0.0	0.0 ± 0.0	0.07
G0.316-0.201h	OCS (231.1GHz)	N	0	0	0.0 ± 0.0	0.0 ± 0.0	0.0 ± 0.0	0.1
G0.316-0.201h	SO (219.9GHz)	N	0	0	0.0 ± 0.0	0.0 ± 0.0	0.0 ± 0.0	0.08
G0.316-0.201h	SiO (217.1GHz)	N	0	0	0.0 ± 0.0	0.0 ± 0.0	0.0 ± 0.0	0.08
G0.316-0.201i	12CO (230.5GHz)	N	0	0	0.0 ± 0.0	0.0 ± 0.0	0.0 ± 0.0	0.42
G0.316-0.201i	13CO (220.4GHz)	Y	1	1	2.36 ± 0.13	18.68 ± 0.19	2.94 ± 2.94	0.09
G0.316-0.201i	C18O (219.6GHz)	Y	1	1	2.82 ± 0.08	18.56 ± 0.04	1.3 ± 1.3	0.08
G0.316-0.201i	H2CO (218.2GHz)	Y	1	1	0.92 ± 0.08	18.14 ± 0.1	0.93 ± 0.93	0.08
G0.316-0.201i	H2CO (218.5GHz)	N	0	0	0.0 ± 0.0	0.0 ± 0.0	0.0 ± 0.0	0.08
G0.316-0.201i	H2CO (218.8GHz)	N	0	0	0.0 ± 0.0	0.0 ± 0.0	0.0 ± 0.0	0.08
G0.316-0.201i	OCS (218.9GHz)	N	0	0	0.0 ± 0.0	0.0 ± 0.0	0.0 ± 0.0	0.08
G0.316-0.201i	OCS (231.1GHz)	N	0	0	0.0 ± 0.0	0.0 ± 0.0	0.0 ± 0.0	0.11
G0.316-0.201i	SO (219.9GHz)	N	0	0	0.0 ± 0.0	0.0 ± 0.0	0.0 ± 0.0	0.07
G0.316-0.201i	SiO (217.1GHz)	N	0	0	0.0 ± 0.0	0.0 ± 0.0	0.0 ± 0.0	0.08
G0.316-0.201j	12CO (230.5GHz)	Y	1	1	12.5 ± 0.34	14.18 ± 0.04	1.3 ± 1.3	0.34
G0.316-0.201j	13CO (220.4GHz)	Y	1	1	7.96 ± 0.15	17.65 ± 0.06	2.61 ± 2.61	0.09
G0.316-0.201j	C18O (219.6GHz)	Y	1	1	4.46 ± 0.07	18.31 ± 0.02	1.11 ± 1.11	0.06
G0.316-0.201j	H2CO (218.2GHz)	Y	1	1	0.8 ± 0.09	18.47 ± 0.08	0.74 ± 0.74	0.06
G0.316-0.201j	H2CO (218.5GHz)	N	0	0	0.0 ± 0.0	0.0 ± 0.0	0.0 ± 0.0	0.07
G0.316-0.201j	H2CO (218.8GHz)	N	0	0	0.0 ± 0.0	0.0 ± 0.0	0.0 ± 0.0	0.07
G0.316-0.201j	OCS (218.9GHz)	N	0	0	0.0 ± 0.0	0.0 ± 0.0	0.0 ± 0.0	0.07
G0.316-0.201j	OCS (231.1GHz)	N	0	0	0.0 ± 0.0	0.0 ± 0.0	0.0 ± 0.0	0.1
G0.316-0.201j	SO (219.9GHz)	N	0	0	0.0 ± 0.0	0.0 ± 0.0	0.0 ± 0.0	0.07
G0.316-0.201j	SiO (217.1GHz)	N	0	0	0.0 ± 0.0	0.0 ± 0.0	0.0 ± 0.0	0.07
G0.316-0.201k	12CO (230.5GHz)	Y	1	1	11.01 ± 0.28	18.16 ± 0.05	1.86 ± 1.86	0.29
G0.316-0.201k	C18O (219.6GHz)	N	0	0	0.0 ± 0.0	0.0 ± 0.0	0.0 ± 0.0	0.08
G0.316-0.201k	H2CO (218.2GHz)	N	0	0	0.0 ± 0.0	0.0 ± 0.0	0.0 ± 0.0	0.08
G0.316-0.201k	H2CO (218.5GHz)	N	0	0	0.0 ± 0.0	0.0 ± 0.0	0.0 ± 0.0	0.09
G0.316-0.201k	H2CO (218.8GHz)	N	0	0	0.0 ± 0.0	0.0 ± 0.0	0.0 ± 0.0	0.09
G0.316-0.201k	OCS (218.9GHz)	N	0	0	0.0 ± 0.0	0.0 ± 0.0	0.0 ± 0.0	0.08
G0.316-0.201k	OCS (231.1GHz)	N	0	0	0.0 ± 0.0	0.0 ± 0.0	0.0 ± 0.0	0.05
G0.316-0.201k	SO (219.9GHz)	N	0	0	0.0 ± 0.0	0.0 ± 0.0	0.0 ± 0.0	0.09

Continued on next page

Table A.1 – *Continued from previous page*

Leaf	Transition	Detected	Number of Comps	Comp.	Amplitude	Velocity	Width	RMS
G0.316-0.201k	SiO (217.1GHz)	N	0	0	0.0 ± 0.0	0.0 ± 0.0	0.0 ± 0.0	0.09
G0.316-0.201l	12CO (230.5GHz)	Y	1	1	7.59 ± 0.28	16.75 ± 0.17	3.92 ± 3.92	0.19
G0.316-0.201l	13CO (220.4GHz)	Y	1	1	9.24 ± 0.19	16.73 ± 0.03	1.41 ± 1.41	0.12
G0.316-0.201l	C18O (219.6GHz)	Y	1	1	3.35 ± 0.12	17.34 ± 0.02	0.78 ± 0.78	0.09
G0.316-0.201l	H2CO (218.2GHz)	Y	1	1	0.56 ± 0.08	17.37 ± 0.16	1.0 ± 1.0	0.08
G0.316-0.201l	H2CO (218.5GHz)	N	0	0	0.0 ± 0.0	0.0 ± 0.0	0.0 ± 0.0	0.09
G0.316-0.201l	H2CO (218.8GHz)	N	0	0	0.0 ± 0.0	0.0 ± 0.0	0.0 ± 0.0	0.09
G0.316-0.201l	OCS (218.9GHz)	N	0	0	0.0 ± 0.0	0.0 ± 0.0	0.0 ± 0.0	0.09
G0.316-0.201l	OCS (231.1GHz)	N	0	0	0.0 ± 0.0	0.0 ± 0.0	0.0 ± 0.0	0.11
G0.316-0.201l	SO (219.9GHz)	N	0	0	0.0 ± 0.0	0.0 ± 0.0	0.0 ± 0.0	0.08
G0.316-0.201l	SiO (217.1GHz)	N	0	0	0.0 ± 0.0	0.0 ± 0.0	0.0 ± 0.0	0.1
G0.326-0.085a	12CO (230.5GHz)	Y	3	1	2.51 ± 0.29	79.57 ± 0.25	1.85 ± 1.85	0.31
G0.326-0.085a	12CO (230.5GHz)	Y	3	2	2.33 ± 0.15	31.89 ± 0.53	7.38 ± 7.38	0.31
G0.326-0.085a	12CO (230.5GHz)	Y	3	3	1.41 ± 0.31	60.43 ± 0.42	1.66 ± 1.66	0.31
G0.326-0.085a	13CO (220.4GHz)	Y	6	1	1.93 ± 0.09	90.64 ± 0.09	1.59 ± 1.59	0.11
G0.326-0.085a	13CO (220.4GHz)	Y	6	2	0.9 ± 0.07	80.83 ± 0.25	2.68 ± 2.68	0.11
G0.326-0.085a	13CO (220.4GHz)	Y	6	3	0.68 ± 0.08	61.83 ± 0.28	1.94 ± 1.94	0.11
G0.326-0.085a	13CO (220.4GHz)	Y	6	4	1.53 ± 0.07	33.17 ± 0.15	2.89 ± 2.89	0.11
G0.326-0.085a	13CO (220.4GHz)	Y	6	5	0.63 ± 0.12	20.77 ± 0.21	0.95 ± 0.95	0.11
G0.326-0.085a	13CO (220.4GHz)	Y	6	6	1.57 ± 0.09	9.89 ± 0.11	1.81 ± 1.81	0.11
G0.326-0.085a	C18O (219.6GHz)	N	0	0	0.0 ± 0.0	0.0 ± 0.0	0.0 ± 0.0	0.08
G0.326-0.085a	H2CO (218.2GHz)	Y	1	1	0.56 ± 0.13	9.32 ± 0.21	0.6 ± 0.6	0.09
G0.326-0.085a	H2CO (218.5GHz)	N	0	0	0.0 ± 0.0	0.0 ± 0.0	0.0 ± 0.0	0.09
G0.326-0.085a	H2CO (218.8GHz)	N	0	0	0.0 ± 0.0	0.0 ± 0.0	0.0 ± 0.0	0.09
G0.326-0.085a	OCS (218.9GHz)	N	0	0	0.0 ± 0.0	0.0 ± 0.0	0.0 ± 0.0	0.09
G0.326-0.085a	OCS (231.1GHz)	N	0	0	0.0 ± 0.0	0.0 ± 0.0	0.0 ± 0.0	0.09
G0.326-0.085a	SO (219.9GHz)	N	0	0	0.0 ± 0.0	0.0 ± 0.0	0.0 ± 0.0	0.09
G0.326-0.085a	SiO (217.1GHz)	N	0	0	0.0 ± 0.0	0.0 ± 0.0	0.0 ± 0.0	0.08
G0.326-0.085b	12CO (230.5GHz)	Y	6	1	2.01 ± 0.3	110.12 ± 0.3	1.75 ± 1.75	0.29
G0.326-0.085b	12CO (230.5GHz)	Y	6	4	2.65 ± 0.26	39.67 ± 0.31	3.48 ± 3.48	0.29
G0.326-0.085b	12CO (230.5GHz)	Y	6	5	3.1 ± 0.31	25.3 ± 0.18	1.67 ± 1.67	0.29
G0.326-0.085b	12CO (230.5GHz)	Y	6	6	0.89 ± 0.22	37.59 ± 2.48	18.64 ± 18.64	0.29
G0.326-0.085b	13CO (220.4GHz)	Y	8	1	0.88 ± 0.09	108.88 ± 0.2	1.72 ± 1.72	0.11
G0.326-0.085b	13CO (220.4GHz)	Y	8	2	0.41 ± 0.07	89.84 ± 0.58	2.98 ± 2.98	0.11
G0.326-0.085b	13CO (220.4GHz)	Y	8	3	0.52 ± 0.11	64.85 ± 0.29	1.18 ± 1.18	0.11
G0.326-0.085b	13CO (220.4GHz)	Y	8	4	0.44 ± 0.22	39.45 ± 0.5	1.65 ± 1.65	0.11
G0.326-0.085b	13CO (220.4GHz)	Y	8	5	0.61 ± 0.07	33.62 ± 1.36	4.01 ± 4.01	0.11
G0.326-0.085b	13CO (220.4GHz)	Y	8	6	0.67 ± 0.1	15.94 ± 0.27	1.62 ± 1.62	0.11
G0.326-0.085b	13CO (220.4GHz)	Y	8	7	0.8 ± 0.11	10.59 ± 0.2	1.12 ± 1.12	0.11
G0.326-0.085b	C18O (219.6GHz)	N	0	0	0.0 ± 0.0	0.0 ± 0.0	0.0 ± 0.0	0.09
G0.326-0.085b	H2CO (218.2GHz)	Y	1	1	0.46 ± 0.07	10.18 ± 0.36	1.93 ± 1.93	0.09
G0.326-0.085b	H2CO (218.5GHz)	N	0	0	0.0 ± 0.0	0.0 ± 0.0	0.0 ± 0.0	0.09
G0.326-0.085b	H2CO (218.8GHz)	N	0	0	0.0 ± 0.0	0.0 ± 0.0	0.0 ± 0.0	0.1
G0.326-0.085b	OCS (218.9GHz)	N	0	0	0.0 ± 0.0	0.0 ± 0.0	0.0 ± 0.0	0.09
G0.326-0.085b	OCS (231.1GHz)	N	0	0	0.0 ± 0.0	0.0 ± 0.0	0.0 ± 0.0	0.11
G0.326-0.085b	SO (219.9GHz)	N	0	0	0.0 ± 0.0	0.0 ± 0.0	0.0 ± 0.0	0.1
G0.326-0.085b	SiO (217.1GHz)	N	0	0	0.0 ± 0.0	0.0 ± 0.0	0.0 ± 0.0	0.09
G0.340+0.055a	12CO (230.5GHz)	Y	3	1	1.62 ± 0.12	81.93 ± 0.38	4.36 ± 4.36	0.21
G0.340+0.055a	12CO (230.5GHz)	Y	3	2	1.68 ± 0.14	25.96 ± 0.34	3.61 ± 3.61	0.21
G0.340+0.055a	13CO (220.4GHz)	Y	2	1	0.83 ± 0.03	21.45 ± 0.23	5.12 ± 5.12	0.05
G0.340+0.055a	C18O (219.6GHz)	Y	1	1	0.15 ± 0.02	20.86 ± 0.76	4.92 ± 4.92	0.04
G0.340+0.055a	H2CO (218.2GHz)	Y	1	1	0.21 ± 0.02	23.3 ± 0.59	5.51 ± 5.51	0.05
G0.340+0.055a	H2CO (218.5GHz)	N	0	0	0.0 ± 0.0	0.0 ± 0.0	0.0 ± 0.0	0.04
G0.340+0.055a	H2CO (218.8GHz)	N	0	0	0.0 ± 0.0	0.0 ± 0.0	0.0 ± 0.0	0.05
G0.340+0.055a	OCS (218.9GHz)	N	0	0	0.0 ± 0.0	0.0 ± 0.0	0.0 ± 0.0	0.04
G0.340+0.055a	OCS (231.1GHz)	N	0	0	0.0 ± 0.0	0.0 ± 0.0	0.0 ± 0.0	0.03
G0.340+0.055a	SO (219.9GHz)	N	0	0	0.0 ± 0.0	0.0 ± 0.0	0.0 ± 0.0	0.04
G0.340+0.055a	SiO (217.1GHz)	N	0	0	0.0 ± 0.0	0.0 ± 0.0	0.0 ± 0.0	0.04
G0.340+0.055b	12CO (230.5GHz)	Y	2	1	2.07 ± 0.1	91.06 ± 0.38	6.7 ± 6.7	0.23
G0.340+0.055b	12CO (230.5GHz)	Y	2	2	2.84 ± 0.22	20.63 ± 0.13	1.43 ± 1.43	0.23
G0.340+0.055b	13CO (220.4GHz)	Y	3	1	0.26 ± 0.03	94.55 ± 0.73	6.45 ± 6.45	0.07
G0.340+0.055b	13CO (220.4GHz)	Y	3	2	0.47 ± 0.04	20.42 ± 0.25	2.49 ± 2.49	0.07
G0.340+0.055b	C18O (219.6GHz)	N	0	0	0.0 ± 0.0	0.0 ± 0.0	0.0 ± 0.0	0.06
G0.340+0.055b	H2CO (218.2GHz)	N	0	0	0.0 ± 0.0	0.0 ± 0.0	0.0 ± 0.0	0.05
G0.340+0.055b	H2CO (218.5GHz)	N	0	0	0.0 ± 0.0	0.0 ± 0.0	0.0 ± 0.0	0.06
G0.340+0.055b	H2CO (218.8GHz)	N	0	0	0.0 ± 0.0	0.0 ± 0.0	0.0 ± 0.0	0.06
G0.340+0.055b	OCS (218.9GHz)	N	0	0	0.0 ± 0.0	0.0 ± 0.0	0.0 ± 0.0	0.06
G0.340+0.055b	OCS (231.1GHz)	N	0	0	0.0 ± 0.0	0.0 ± 0.0	0.0 ± 0.0	0.05
G0.340+0.055b	SO (219.9GHz)	N	0	0	0.0 ± 0.0	0.0 ± 0.0	0.0 ± 0.0	0.06
G0.340+0.055b	SiO (217.1GHz)	N	0	0	0.0 ± 0.0	0.0 ± 0.0	0.0 ± 0.0	0.05
G0.340+0.055c	12CO (230.5GHz)	Y	4	1	1.79 ± 0.25	53.54 ± 0.27	1.67 ± 1.67	0.28
G0.340+0.055c	12CO (230.5GHz)	Y	4	2	2.54 ± 0.15	14.7 ± 0.31	4.54 ± 4.54	0.28
G0.340+0.055c	13CO (220.4GHz)	Y	3	1	0.42 ± 0.04	16.15 ± 1.26	5.43 ± 5.43	0.07
G0.340+0.055c	13CO (220.4GHz)	Y	3	2	0.55 ± 0.05	2.66 ± 0.86	4.69 ± 4.69	0.07
G0.340+0.055c	C18O (219.6GHz)	Y	1	1	0.11 ± 0.02	6.48 ± 2.26	11.97 ± 11.97	0.06
G0.340+0.055c	H2CO (218.2GHz)	Y	1	1	0.38 ± 0.03	17.83 ± 0.3	2.86 ± 2.86	0.05
G0.340+0.055c	H2CO (218.5GHz)	N	0	0	0.0 ± 0.0	0.0 ± 0.0	0.0 ± 0.0	0.05
G0.340+0.055c	H2CO (218.8GHz)	N	0	0	0.0 ± 0.0	0.0 ± 0.0	0.0 ± 0.0	0.06
G0.340+0.055c	OCS (218.9GHz)	N	0	0	0.0 ± 0.0	0.0 ± 0.0	0.0 ± 0.0	0.05
G0.340+0.055c	OCS (231.1GHz)	N	0	0	0.0 ± 0.0	0.0 ± 0.0	0.0 ± 0.0	0.06
G0.340+0.055c	SO (219.9GHz)	N	0	0	0.0 ± 0.0	0.0 ± 0.0	0.0 ± 0.0	0.06
G0.340+0.055c	SiO (217.1GHz)	N	0	0	0.0 ± 0.0	0.0 ± 0.0	0.0 ± 0.0	0.05
G0.340+0.055d	12CO (230.5GHz)	Y	3	1	1.08 ± 0.09	91.88 ± 0.76	8.09 ± 8.09	0.22
G0.340+0.055d	12CO (230.5GHz)	Y	3	2	2.32 ± 0.18	27.48 ± 0.17	1.95 ± 1.95	0.22
G0.340+0.055d	13CO (220.4GHz)	Y	1	1	0.9 ± 0.04	22.32 ± 0.25	4.79 ± 4.79	0.08
G0.340+0.055d	C18O (219.6GHz)	N	0	0	0.0 ± 0.0	0.0 ± 0.0	0.0 ± 0.0	0.07
G0.340+0.055d	H2CO (218.2GHz)	N	0	0	0.0 ± 0.0	0.0 ± 0.0	0.0 ± 0.0	0.06

Continued on next page

Table A.1 – *Continued from previous page*

Leaf	Transition	Detected	Number of Comps	Comp.	Amplitude	Velocity	Width	RMS
G0.340+0.055d	H2CO (218.5GHz)	N	0	0	0.0 ± 0.0	0.0 ± 0.0	0.0 ± 0.0	0.07
G0.340+0.055d	H2CO (218.8GHz)	N	0	0	0.0 ± 0.0	0.0 ± 0.0	0.0 ± 0.0	0.06
G0.340+0.055d	OCS (218.9GHz)	N	0	0	0.0 ± 0.0	0.0 ± 0.0	0.0 ± 0.0	0.06
G0.340+0.055d	OCS (231.1GHz)	N	0	0	0.0 ± 0.0	0.0 ± 0.0	0.0 ± 0.0	0.05
G0.340+0.055d	SO (219.9GHz)	N	0	0	0.0 ± 0.0	0.0 ± 0.0	0.0 ± 0.0	0.06
G0.340+0.055d	SiO (217.1GHz)	N	0	0	0.0 ± 0.0	0.0 ± 0.0	0.0 ± 0.0	0.06
G0.340+0.055e	13CO (220.4GHz)	Y	3	1	0.45 ± 0.07	95.39 ± 0.56	3.12 ± 3.12	0.1
G0.340+0.055e	13CO (220.4GHz)	Y	3	2	0.89 ± 0.04	10.74 ± 0.48	8.7 ± 8.7	0.1
G0.340+0.055e	C18O (219.6GHz)	N	0	0	0.0 ± 0.0	0.0 ± 0.0	0.0 ± 0.0	0.08
G0.340+0.055e	H2CO (218.2GHz)	Y	1	1	0.33 ± 0.05	3.15 ± 0.43	2.43 ± 2.43	0.08
G0.340+0.055e	H2CO (218.5GHz)	N	0	0	0.0 ± 0.0	0.0 ± 0.0	0.0 ± 0.0	0.08
G0.340+0.055e	H2CO (218.8GHz)	N	0	0	0.0 ± 0.0	0.0 ± 0.0	0.0 ± 0.0	0.09
G0.340+0.055e	OCS (218.9GHz)	N	0	0	0.0 ± 0.0	0.0 ± 0.0	0.0 ± 0.0	0.08
G0.340+0.055e	OCS (231.1GHz)	N	0	0	0.0 ± 0.0	0.0 ± 0.0	0.0 ± 0.0	0.08
G0.340+0.055e	SO (219.9GHz)	N	0	0	0.0 ± 0.0	0.0 ± 0.0	0.0 ± 0.0	0.09
G0.340+0.055e	SiO (217.1GHz)	N	0	0	0.0 ± 0.0	0.0 ± 0.0	0.0 ± 0.0	0.07
G0.340+0.055f	12CO (230.5GHz)	Y	3	1	2.08 ± 0.21	98.18 ± 0.39	3.4 ± 3.4	0.36
G0.340+0.055f	12CO (230.5GHz)	Y	3	2	2.59 ± 0.23	27.93 ± 0.28	2.69 ± 2.69	0.36
G0.340+0.055f	13CO (220.4GHz)	Y	3	1	0.69 ± 0.08	96.62 ± 0.3	2.24 ± 2.24	0.09
G0.340+0.055f	13CO (220.4GHz)	Y	3	3	0.63 ± 0.04	19.8 ± 0.82	8.75 ± 8.75	0.09
G0.340+0.055f	C18O (219.6GHz)	N	0	0	0.0 ± 0.0	0.0 ± 0.0	0.0 ± 0.0	0.08
G0.340+0.055f	H2CO (218.2GHz)	Y	3	1	0.24 ± 0.14	159.33 ± 0.68	0.5 ± 0.5	0.07
G0.340+0.055f	H2CO (218.2GHz)	Y	3	2	0.23 ± 0.06	59.77 ± 0.4	1.27 ± 1.27	0.07
G0.340+0.055f	H2CO (218.2GHz)	Y	3	3	0.3 ± 0.06	1.2 ± 0.33	1.49 ± 1.49	0.07
G0.340+0.055f	H2CO (218.5GHz)	N	0	0	0.0 ± 0.0	0.0 ± 0.0	0.0 ± 0.0	0.08
G0.340+0.055f	H2CO (218.8GHz)	N	0	0	0.0 ± 0.0	0.0 ± 0.0	0.0 ± 0.0	0.08
G0.340+0.055f	OCS (218.9GHz)	N	0	0	0.0 ± 0.0	0.0 ± 0.0	0.0 ± 0.0	0.08
G0.340+0.055f	OCS (231.1GHz)	N	0	0	0.0 ± 0.0	0.0 ± 0.0	0.0 ± 0.0	0.07
G0.340+0.055f	SO (219.9GHz)	N	0	0	0.0 ± 0.0	0.0 ± 0.0	0.0 ± 0.0	0.09
G0.340+0.055f	SiO (217.1GHz)	N	0	0	0.0 ± 0.0	0.0 ± 0.0	0.0 ± 0.0	0.08
G0.380+0.050a	12CO (230.5GHz)	Y	1	1	2.89 ± 0.11	42.48 ± 0.11	2.46 ± 2.46	0.14
G0.380+0.050a	13CO (220.4GHz)	Y	1	1	4.8 ± 0.03	38.79 ± 0.02	1.86 ± 1.86	0.04
G0.380+0.050a	C18O (219.6GHz)	Y	1	1	1.57 ± 0.02	38.96 ± 0.02	1.43 ± 1.43	0.02
G0.380+0.050a	H2CO (218.2GHz)	Y	2	1	1.9 ± 0.03	38.14 ± 0.03	1.81 ± 1.81	0.02
G0.380+0.050a	H2CO (218.5GHz)	Y	2	1	1.54 ± 0.02	87.95 ± 0.03	1.95 ± 1.95	0.02
G0.380+0.050a	H2CO (218.5GHz)	Y	2	2	0.76 ± 0.02	38.57 ± 0.06	1.76 ± 1.76	0.02
G0.380+0.050a	H2CO (218.8GHz)	Y	2	1	0.77 ± 0.02	38.43 ± 0.05	1.94 ± 1.94	0.02
G0.380+0.050a	OCS (218.9GHz)	Y	3	1	0.04 ± 0.01	96.24 ± 1.8	7.8 ± 7.8	0.02
G0.380+0.050a	OCS (218.9GHz)	Y	3	2	0.39 ± 0.01	38.64 ± 0.09	2.51 ± 2.51	0.02
G0.380+0.050a	OCS (231.1GHz)	Y	2	1	0.33 ± 0.01	38.75 ± 0.15	2.99 ± 2.99	0.03
G0.380+0.050a	SO (219.9GHz)	Y	3	1	0.18 ± 0.02	95.17 ± 0.25	2.01 ± 2.01	0.02
G0.380+0.050a	SO (219.9GHz)	Y	3	2	1.02 ± 0.02	38.95 ± 0.05	2.5 ± 2.5	0.02
G0.380+0.050a	SiO (217.1GHz)	Y	2	1	0.45 ± 0.01	39.8 ± 0.1	2.9 ± 2.9	0.02
G0.380+0.050b	12CO (230.5GHz)	Y	3	1	0.76 ± 0.06	88.53 ± 0.66	7.18 ± 7.18	0.15
G0.380+0.050b	12CO (230.5GHz)	Y	3	2	0.81 ± 0.08	22.51 ± 0.44	3.7 ± 3.7	0.15
G0.380+0.050b	13CO (220.4GHz)	Y	2	1	0.82 ± 0.04	40.27 ± 0.11	2.02 ± 2.02	0.05
G0.380+0.050b	C18O (219.6GHz)	N	0	0	0.0 ± 0.0	0.0 ± 0.0	0.0 ± 0.0	0.04
G0.380+0.050b	H2CO (218.2GHz)	Y	1	1	0.48 ± 0.02	41.11 ± 0.15	2.51 ± 2.51	0.04
G0.380+0.050b	H2CO (218.5GHz)	Y	1	1	0.33 ± 0.03	89.53 ± 0.21	1.9 ± 1.9	0.04
G0.380+0.050b	H2CO (218.8GHz)	N	0	0	0.0 ± 0.0	0.0 ± 0.0	0.0 ± 0.0	0.05
G0.380+0.050b	OCS (218.9GHz)	N	0	0	0.0 ± 0.0	0.0 ± 0.0	0.0 ± 0.0	0.04
G0.380+0.050b	OCS (231.1GHz)	N	0	0	0.0 ± 0.0	0.0 ± 0.0	0.0 ± 0.0	0.04
G0.380+0.050b	SO (219.9GHz)	Y	2	1	0.14 ± 0.04	84.9 ± 0.34	1.01 ± 1.01	0.04
G0.380+0.050b	SO (219.9GHz)	Y	2	2	0.21 ± 0.03	40.12 ± 0.28	1.69 ± 1.69	0.04
G0.380+0.050b	SiO (217.1GHz)	Y	2	1	0.1 ± 0.03	41.8 ± 0.74	2.38 ± 2.38	0.04
G0.380+0.050b	SiO (217.1GHz)	Y	2	2	0.03 ± 0.01	57.21 ± 8.56	33.88 ± 33.88	0.04
G0.380+0.050c	12CO (230.5GHz)	N	0	0	0.0 ± 0.0	0.0 ± 0.0	0.0 ± 0.0	0.45
G0.380+0.050c	13CO (220.4GHz)	Y	1	1	0.39 ± 0.06	21.83 ± 0.97	5.1 ± 5.1	0.14
G0.380+0.050c	C18O (219.6GHz)	Y	1	1	0.33 ± 0.07	26.48 ± 0.93	4.04 ± 4.04	0.13
G0.380+0.050c	H2CO (218.2GHz)	N	0	0	0.0 ± 0.0	0.0 ± 0.0	0.0 ± 0.0	0.15
G0.380+0.050c	H2CO (218.5GHz)	N	0	0	0.0 ± 0.0	0.0 ± 0.0	0.0 ± 0.0	0.14
G0.380+0.050c	H2CO (218.8GHz)	N	0	0	0.0 ± 0.0	0.0 ± 0.0	0.0 ± 0.0	0.13
G0.380+0.050c	OCS (218.9GHz)	N	0	0	0.0 ± 0.0	0.0 ± 0.0	0.0 ± 0.0	0.12
G0.380+0.050c	OCS (231.1GHz)	N	0	0	0.0 ± 0.0	0.0 ± 0.0	0.0 ± 0.0	0.14
G0.380+0.050c	SO (219.9GHz)	N	0	0	0.0 ± 0.0	0.0 ± 0.0	0.0 ± 0.0	0.12
G0.380+0.050c	SiO (217.1GHz)	N	0	0	0.0 ± 0.0	0.0 ± 0.0	0.0 ± 0.0	0.12
G0.380+0.050d	12CO (230.5GHz)	Y	1	1	2.55 ± 0.26	43.46 ± 0.27	2.34 ± 2.34	0.33
G0.380+0.050d	13CO (220.4GHz)	N	0	0	0.0 ± 0.0	0.0 ± 0.0	0.0 ± 0.0	0.13
G0.380+0.050d	C18O (219.6GHz)	N	0	0	0.0 ± 0.0	0.0 ± 0.0	0.0 ± 0.0	0.12
G0.380+0.050d	H2CO (218.2GHz)	N	0	0	0.0 ± 0.0	0.0 ± 0.0	0.0 ± 0.0	0.11
G0.380+0.050d	H2CO (218.5GHz)	N	0	0	0.0 ± 0.0	0.0 ± 0.0	0.0 ± 0.0	0.13
G0.380+0.050d	H2CO (218.8GHz)	N	0	0	0.0 ± 0.0	0.0 ± 0.0	0.0 ± 0.0	0.11
G0.380+0.050d	OCS (218.9GHz)	N	0	0	0.0 ± 0.0	0.0 ± 0.0	0.0 ± 0.0	0.11
G0.380+0.050d	OCS (231.1GHz)	N	0	0	0.0 ± 0.0	0.0 ± 0.0	0.0 ± 0.0	0.16
G0.380+0.050d	SO (219.9GHz)	N	0	0	0.0 ± 0.0	0.0 ± 0.0	0.0 ± 0.0	0.11
G0.380+0.050d	SiO (217.1GHz)	N	0	0	0.0 ± 0.0	0.0 ± 0.0	0.0 ± 0.0	0.11
G0.380+0.050e	12CO (230.5GHz)	N	0	0	0.0 ± 0.0	0.0 ± 0.0	0.0 ± 0.0	0.33
G0.380+0.050e	13CO (220.4GHz)	Y	3	1	0.33 ± 0.04	34.04 ± 0.58	4.49 ± 4.49	0.07
G0.380+0.050e	C18O (219.6GHz)	Y	1	1	0.1 ± 0.03	34.86 ± 0.88	2.13 ± 2.13	0.05
G0.380+0.050e	H2CO (218.2GHz)	N	0	0	0.0 ± 0.0	0.0 ± 0.0	0.0 ± 0.0	0.05
G0.380+0.050e	H2CO (218.5GHz)	N	0	0	0.0 ± 0.0	0.0 ± 0.0	0.0 ± 0.0	0.05
G0.380+0.050e	H2CO (218.8GHz)	N	0	0	0.0 ± 0.0	0.0 ± 0.0	0.0 ± 0.0	0.05
G0.380+0.050e	OCS (218.9GHz)	N	0	0	0.0 ± 0.0	0.0 ± 0.0	0.0 ± 0.0	0.05
G0.380+0.050e	OCS (231.1GHz)	N	0	0	0.0 ± 0.0	0.0 ± 0.0	0.0 ± 0.0	0.06
G0.380+0.050e	SO (219.9GHz)	N	0	0	0.0 ± 0.0	0.0 ± 0.0	0.0 ± 0.0	0.05
G0.380+0.050e	SiO (217.1GHz)	N	0	0	0.0 ± 0.0	0.0 ± 0.0	0.0 ± 0.0	0.05
G0.380+0.050f	12CO (230.5GHz)	N	0	0	0.0 ± 0.0	0.0 ± 0.0	0.0 ± 0.0	0.23

Continued on next page

Table A.1 – *Continued from previous page*

Leaf	Transition	Detected	Number of Comps	Comp.	Amplitude	Velocity	Width	RMS
G0.380+0.050f	13CO (220.4GHz)	Y	1	1	0.95 ± 0.06	39.88 ± 0.09	1.28 ± 1.28	0.06
G0.380+0.050f	C18O (219.6GHz)	Y	1	1	0.14 ± 0.02	39.27 ± 0.93	6.6 ± 6.6	0.04
G0.380+0.050f	H2CO (218.2GHz)	Y	1	1	0.2 ± 0.04	31.98 ± 0.26	1.23 ± 1.23	0.03
G0.380+0.050f	H2CO (218.5GHz)	N	0	0	0.0 ± 0.0	0.0 ± 0.0	0.0 ± 0.0	0.04
G0.380+0.050f	H2CO (218.8GHz)	N	0	0	0.0 ± 0.0	0.0 ± 0.0	0.0 ± 0.0	0.04
G0.380+0.050f	OCS (218.9GHz)	N	0	0	0.0 ± 0.0	0.0 ± 0.0	0.0 ± 0.0	0.04
G0.380+0.050f	OCS (231.1GHz)	N	0	0	0.0 ± 0.0	0.0 ± 0.0	0.0 ± 0.0	0.04
G0.380+0.050f	SO (219.9GHz)	N	0	0	0.0 ± 0.0	0.0 ± 0.0	0.0 ± 0.0	0.04
G0.380+0.050f	SiO (217.1GHz)	N	0	0	0.0 ± 0.0	0.0 ± 0.0	0.0 ± 0.0	0.04
G0.380+0.050g	12CO (230.5GHz)	N	0	0	0.0 ± 0.0	0.0 ± 0.0	0.0 ± 0.0	0.23
G0.380+0.050g	13CO (220.4GHz)	Y	3	1	1.99 ± 0.09	41.47 ± 0.06	1.12 ± 1.12	0.1
G0.380+0.050g	13CO (220.4GHz)	Y	3	2	0.28 ± 0.04	13.69 ± 0.89	5.57 ± 5.57	0.1
G0.380+0.050g	C18O (219.6GHz)	N	0	0	0.0 ± 0.0	0.0 ± 0.0	0.0 ± 0.0	0.07
G0.380+0.050g	H2CO (218.2GHz)	Y	1	1	0.69 ± 0.08	42.28 ± 0.1	0.87 ± 0.87	0.07
G0.380+0.050g	H2CO (218.5GHz)	Y	1	1	0.34 ± 0.07	90.64 ± 0.23	0.96 ± 0.96	0.07
G0.380+0.050g	H2CO (218.8GHz)	N	0	0	0.0 ± 0.0	0.0 ± 0.0	0.0 ± 0.0	0.07
G0.380+0.050g	OCS (218.9GHz)	N	0	0	0.0 ± 0.0	0.0 ± 0.0	0.0 ± 0.0	0.07
G0.380+0.050g	OCS (231.1GHz)	N	0	0	0.0 ± 0.0	0.0 ± 0.0	0.0 ± 0.0	0.08
G0.380+0.050g	SO (219.9GHz)	N	0	0	0.0 ± 0.0	0.0 ± 0.0	0.0 ± 0.0	0.06
G0.380+0.050g	SiO (217.1GHz)	N	0	0	0.0 ± 0.0	0.0 ± 0.0	0.0 ± 0.0	0.07
G0.380+0.050h	12CO (230.5GHz)	Y	1	1	2.27 ± 0.13	46.65 ± 0.17	2.58 ± 2.58	0.17
G0.380+0.050h	13CO (220.4GHz)	Y	2	1	1.62 ± 0.08	38.62 ± 0.06	1.06 ± 1.06	0.07
G0.380+0.050h	13CO (220.4GHz)	Y	2	2	0.52 ± 0.06	2.93 ± 0.25	1.89 ± 1.89	0.07
G0.380+0.050h	C18O (219.6GHz)	Y	1	1	0.41 ± 0.07	38.84 ± 0.16	0.79 ± 0.79	0.06
G0.380+0.050h	H2CO (218.2GHz)	Y	1	1	0.76 ± 0.04	38.65 ± 0.16	2.48 ± 2.48	0.06
G0.380+0.050h	H2CO (218.5GHz)	Y	1	1	0.55 ± 0.06	87.91 ± 0.2	1.7 ± 1.7	0.07
G0.380+0.050h	H2CO (218.8GHz)	Y	1	1	0.31 ± 0.06	37.73 ± 0.26	1.08 ± 1.08	0.06
G0.380+0.050h	OCS (218.9GHz)	N	0	0	0.0 ± 0.0	0.0 ± 0.0	0.0 ± 0.0	0.06
G0.380+0.050h	OCS (231.1GHz)	N	0	0	0.0 ± 0.0	0.0 ± 0.0	0.0 ± 0.0	0.08
G0.380+0.050h	SO (219.9GHz)	N	0	0	0.0 ± 0.0	0.0 ± 0.0	0.0 ± 0.0	0.07
G0.380+0.050h	SiO (217.1GHz)	N	0	0	0.0 ± 0.0	0.0 ± 0.0	0.0 ± 0.0	0.06
G0.393-0.034a	12CO (230.5GHz)	Y	2	1	4.47 ± 0.16	98.94 ± 0.17	4.01 ± 4.01	0.28
G0.393-0.034a	12CO (230.5GHz)	Y	2	2	2.45 ± 0.15	45.39 ± 0.32	4.52 ± 4.52	0.28
G0.393-0.034a	13CO (220.4GHz)	Y	3	1	1.17 ± 0.04	96.93 ± 0.18	4.46 ± 4.46	0.08
G0.393-0.034a	13CO (220.4GHz)	Y	3	2	1.98 ± 0.06	75.08 ± 0.07	1.99 ± 1.99	0.08
G0.393-0.034a	13CO (220.4GHz)	Y	3	3	0.63 ± 0.04	45.88 ± 0.32	4.02 ± 4.02	0.08
G0.393-0.034a	C18O (219.6GHz)	Y	2	1	0.2 ± 0.03	97.51 ± 0.37	2.01 ± 2.01	0.05
G0.393-0.034a	C18O (219.6GHz)	Y	2	2	0.51 ± 0.04	74.9 ± 0.13	1.48 ± 1.48	0.05
G0.393-0.034a	H2CO (218.2GHz)	Y	2	1	0.11 ± 0.02	97.16 ± 0.93	4.89 ± 4.89	0.04
G0.393-0.034a	H2CO (218.2GHz)	Y	2	2	0.22 ± 0.03	76.19 ± 0.32	2.35 ± 2.35	0.04
G0.393-0.034a	H2CO (218.5GHz)	N	0	0	0.0 ± 0.0	0.0 ± 0.0	0.0 ± 0.0	0.05
G0.393-0.034a	H2CO (218.8GHz)	N	0	0	0.0 ± 0.0	0.0 ± 0.0	0.0 ± 0.0	0.05
G0.393-0.034a	OCS (218.9GHz)	N	0	0	0.0 ± 0.0	0.0 ± 0.0	0.0 ± 0.0	0.05
G0.393-0.034a	OCS (231.1GHz)	N	0	0	0.0 ± 0.0	0.0 ± 0.0	0.0 ± 0.0	0.07
G0.393-0.034a	SO (219.9GHz)	N	0	0	0.0 ± 0.0	0.0 ± 0.0	0.0 ± 0.0	0.04
G0.393-0.034a	SiO (217.1GHz)	N	0	0	0.0 ± 0.0	0.0 ± 0.0	0.0 ± 0.0	0.04
G0.412+0.052a	12CO (230.5GHz)	Y	3	1	1.01 ± 0.06	43.11 ± 0.42	6.37 ± 6.37	0.09
G0.412+0.052a	13CO (220.4GHz)	Y	2	1	0.39 ± 0.03	47.84 ± 0.22	2.49 ± 2.49	0.04
G0.412+0.052a	13CO (220.4GHz)	Y	2	2	0.47 ± 0.04	16.61 ± 0.13	1.22 ± 1.22	0.04
G0.412+0.052a	C18O (219.6GHz)	N	0	0	0.0 ± 0.0	0.0 ± 0.0	0.0 ± 0.0	0.03
G0.412+0.052a	H2CO (218.2GHz)	Y	1	1	0.22 ± 0.02	16.52 ± 0.26	2.57 ± 2.57	0.03
G0.412+0.052a	H2CO (218.5GHz)	Y	1	1	0.21 ± 0.02	65.29 ± 0.26	1.93 ± 1.93	0.03
G0.412+0.052a	H2CO (218.8GHz)	N	0	0	0.0 ± 0.0	0.0 ± 0.0	0.0 ± 0.0	0.03
G0.412+0.052a	OCS (218.9GHz)	N	0	0	0.0 ± 0.0	0.0 ± 0.0	0.0 ± 0.0	0.03
G0.412+0.052a	OCS (231.1GHz)	N	0	0	0.0 ± 0.0	0.0 ± 0.0	0.0 ± 0.0	0.03
G0.412+0.052a	SO (219.9GHz)	N	0	0	0.0 ± 0.0	0.0 ± 0.0	0.0 ± 0.0	0.03
G0.412+0.052a	SiO (217.1GHz)	N	0	0	0.0 ± 0.0	0.0 ± 0.0	0.0 ± 0.0	0.03
G0.412+0.052b	12CO (230.5GHz)	Y	1	1	1.24 ± 0.08	14.84 ± 0.53	7.21 ± 7.21	0.18
G0.412+0.052b	C18O (219.6GHz)	N	0	0	0.0 ± 0.0	0.0 ± 0.0	0.0 ± 0.0	0.04
G0.412+0.052b	H2CO (218.2GHz)	N	0	0	0.0 ± 0.0	0.0 ± 0.0	0.0 ± 0.0	0.03
G0.412+0.052b	H2CO (218.5GHz)	N	0	0	0.0 ± 0.0	0.0 ± 0.0	0.0 ± 0.0	0.03
G0.412+0.052b	H2CO (218.8GHz)	N	0	0	0.0 ± 0.0	0.0 ± 0.0	0.0 ± 0.0	0.04
G0.412+0.052b	OCS (218.9GHz)	N	0	0	0.0 ± 0.0	0.0 ± 0.0	0.0 ± 0.0	0.04
G0.412+0.052b	OCS (231.1GHz)	N	0	0	0.0 ± 0.0	0.0 ± 0.0	0.0 ± 0.0	0.03
G0.412+0.052b	SO (219.9GHz)	N	0	0	0.0 ± 0.0	0.0 ± 0.0	0.0 ± 0.0	0.04
G0.412+0.052b	SiO (217.1GHz)	N	0	0	0.0 ± 0.0	0.0 ± 0.0	0.0 ± 0.0	0.03
G0.412+0.052c	12CO (230.5GHz)	N	0	0	0.0 ± 0.0	0.0 ± 0.0	0.0 ± 0.0	0.31
G0.412+0.052c	13CO (220.4GHz)	Y	1	1	0.5 ± 0.05	48.73 ± 0.23	2.15 ± 2.15	0.06
G0.412+0.052c	C18O (219.6GHz)	N	0	0	0.0 ± 0.0	0.0 ± 0.0	0.0 ± 0.0	0.04
G0.412+0.052c	H2CO (218.2GHz)	Y	1	1	0.5 ± 0.04	25.7 ± 0.1	1.25 ± 1.25	0.04
G0.412+0.052c	H2CO (218.5GHz)	Y	1	1	0.28 ± 0.02	75.68 ± 0.25	2.58 ± 2.58	0.04
G0.412+0.052c	H2CO (218.8GHz)	N	0	0	0.0 ± 0.0	0.0 ± 0.0	0.0 ± 0.0	0.04
G0.412+0.052c	OCS (218.9GHz)	N	0	0	0.0 ± 0.0	0.0 ± 0.0	0.0 ± 0.0	0.04
G0.412+0.052c	OCS (231.1GHz)	N	0	0	0.0 ± 0.0	0.0 ± 0.0	0.0 ± 0.0	0.07
G0.412+0.052c	SO (219.9GHz)	N	0	0	0.0 ± 0.0	0.0 ± 0.0	0.0 ± 0.0	0.04
G0.412+0.052c	SiO (217.1GHz)	N	0	0	0.0 ± 0.0	0.0 ± 0.0	0.0 ± 0.0	0.03
G0.412+0.052d	12CO (230.5GHz)	Y	2	1	1.43 ± 0.16	55.05 ± 0.39	2.97 ± 2.97	0.25
G0.412+0.052d	12CO (230.5GHz)	Y	2	2	1.65 ± 0.15	33.75 ± 0.37	3.46 ± 3.46	0.25
G0.412+0.052d	13CO (220.4GHz)	Y	3	1	0.47 ± 0.07	50.95 ± 0.25	1.57 ± 1.57	0.07
G0.412+0.052d	13CO (220.4GHz)	Y	3	2	0.68 ± 0.04	35.29 ± 0.26	3.42 ± 3.42	0.07
G0.412+0.052d	C18O (219.6GHz)	N	0	0	0.0 ± 0.0	0.0 ± 0.0	0.0 ± 0.0	0.05
G0.412+0.052d	H2CO (218.2GHz)	N	0	0	0.0 ± 0.0	0.0 ± 0.0	0.0 ± 0.0	0.05
G0.412+0.052d	H2CO (218.5GHz)	N	0	0	0.0 ± 0.0	0.0 ± 0.0	0.0 ± 0.0	0.04
G0.412+0.052d	H2CO (218.8GHz)	N	0	0	0.0 ± 0.0	0.0 ± 0.0	0.0 ± 0.0	0.05
G0.412+0.052d	OCS (218.9GHz)	N	0	0	0.0 ± 0.0	0.0 ± 0.0	0.0 ± 0.0	0.05
G0.412+0.052d	OCS (231.1GHz)	N	0	0	0.0 ± 0.0	0.0 ± 0.0	0.0 ± 0.0	0.05
G0.412+0.052d	SO (219.9GHz)	N	0	0	0.0 ± 0.0	0.0 ± 0.0	0.0 ± 0.0	0.05

Continued on next page

Table A.1 – *Continued from previous page*

Leaf	Transition	Detected	Number of Comps	Comp.	Amplitude	Velocity	Width	RMS
G0.412+0.052d	SiO (217.1GHz)	N	0	0	0.0 ± 0.0	0.0 ± 0.0	0.0 ± 0.0	0.04
G0.412+0.052e	12CO (230.5GHz)	N	0	0	0.0 ± 0.0	0.0 ± 0.0	0.0 ± 0.0	0.43
G0.412+0.052e	13CO (220.4GHz)	Y	1	1	1.06 ± 0.07	50.36 ± 0.11	1.48 ± 1.48	0.07
G0.412+0.052e	C18O (219.6GHz)	N	0	0	0.0 ± 0.0	0.0 ± 0.0	0.0 ± 0.0	0.06
G0.412+0.052e	H2CO (218.2GHz)	N	0	0	0.0 ± 0.0	0.0 ± 0.0	0.0 ± 0.0	0.06
G0.412+0.052e	H2CO (218.5GHz)	N	0	0	0.0 ± 0.0	0.0 ± 0.0	0.0 ± 0.0	0.06
G0.412+0.052e	H2CO (218.8GHz)	N	0	0	0.0 ± 0.0	0.0 ± 0.0	0.0 ± 0.0	0.05
G0.412+0.052e	OCS (218.9GHz)	N	0	0	0.0 ± 0.0	0.0 ± 0.0	0.0 ± 0.0	0.05
G0.412+0.052e	OCS (231.1GHz)	N	0	0	0.0 ± 0.0	0.0 ± 0.0	0.0 ± 0.0	0.06
G0.412+0.052e	SO (219.9GHz)	N	0	0	0.0 ± 0.0	0.0 ± 0.0	0.0 ± 0.0	0.06
G0.412+0.052e	SiO (217.1GHz)	N	0	0	0.0 ± 0.0	0.0 ± 0.0	0.0 ± 0.0	0.05
G0.412+0.052f	12CO (230.5GHz)	Y	1	1	0.76 ± 0.06	46.83 ± 1.6	16.89 ± 16.89	0.18
G0.412+0.052f	13CO (220.4GHz)	Y	3	1	0.61 ± 0.11	38.63 ± 0.19	0.9 ± 0.9	0.11
G0.412+0.052f	C18O (219.6GHz)	N	0	0	0.0 ± 0.0	0.0 ± 0.0	0.0 ± 0.0	0.07
G0.412+0.052f	H2CO (218.2GHz)	N	0	0	0.0 ± 0.0	0.0 ± 0.0	0.0 ± 0.0	0.08
G0.412+0.052f	H2CO (218.5GHz)	N	0	0	0.0 ± 0.0	0.0 ± 0.0	0.0 ± 0.0	0.07
G0.412+0.052f	H2CO (218.8GHz)	N	0	0	0.0 ± 0.0	0.0 ± 0.0	0.0 ± 0.0	0.08
G0.412+0.052f	OCS (218.9GHz)	N	0	0	0.0 ± 0.0	0.0 ± 0.0	0.0 ± 0.0	0.07
G0.412+0.052f	OCS (231.1GHz)	N	0	0	0.0 ± 0.0	0.0 ± 0.0	0.0 ± 0.0	0.08
G0.412+0.052f	SO (219.9GHz)	N	0	0	0.0 ± 0.0	0.0 ± 0.0	0.0 ± 0.0	0.08
G0.412+0.052f	SiO (217.1GHz)	N	0	0	0.0 ± 0.0	0.0 ± 0.0	0.0 ± 0.0	0.06
G0.412+0.052g	12CO (230.5GHz)	N	0	0	0.0 ± 0.0	0.0 ± 0.0	0.0 ± 0.0	0.25
G0.412+0.052g	13CO (220.4GHz)	Y	2	1	0.89 ± 0.09	45.33 ± 0.21	1.85 ± 1.85	0.12
G0.412+0.052g	C18O (219.6GHz)	N	0	0	0.0 ± 0.0	0.0 ± 0.0	0.0 ± 0.0	0.08
G0.412+0.052g	H2CO (218.2GHz)	N	0	0	0.0 ± 0.0	0.0 ± 0.0	0.0 ± 0.0	0.08
G0.412+0.052g	H2CO (218.5GHz)	Y	1	1	0.3 ± 0.07	68.85 ± 0.33	1.16 ± 1.16	0.07
G0.412+0.052g	H2CO (218.8GHz)	N	0	0	0.0 ± 0.0	0.0 ± 0.0	0.0 ± 0.0	0.08
G0.412+0.052g	OCS (218.9GHz)	N	0	0	0.0 ± 0.0	0.0 ± 0.0	0.0 ± 0.0	0.08
G0.412+0.052g	OCS (231.1GHz)	N	0	0	0.0 ± 0.0	0.0 ± 0.0	0.0 ± 0.0	0.08
G0.412+0.052g	SO (219.9GHz)	N	0	0	0.0 ± 0.0	0.0 ± 0.0	0.0 ± 0.0	0.08
G0.412+0.052g	SiO (217.1GHz)	N	0	0	0.0 ± 0.0	0.0 ± 0.0	0.0 ± 0.0	0.07
G0.412+0.052h	12CO (230.5GHz)	N	0	0	0.0 ± 0.0	0.0 ± 0.0	0.0 ± 0.0	0.28
G0.412+0.052h	13CO (220.4GHz)	Y	2	1	1.87 ± 0.1	47.27 ± 0.1	1.63 ± 1.63	0.12
G0.412+0.052h	C18O (219.6GHz)	N	0	0	0.0 ± 0.0	0.0 ± 0.0	0.0 ± 0.0	0.09
G0.412+0.052h	H2CO (218.2GHz)	N	0	0	0.0 ± 0.0	0.0 ± 0.0	0.0 ± 0.0	0.08
G0.412+0.052h	H2CO (218.5GHz)	N	0	0	0.0 ± 0.0	0.0 ± 0.0	0.0 ± 0.0	0.08
G0.412+0.052h	H2CO (218.8GHz)	N	0	0	0.0 ± 0.0	0.0 ± 0.0	0.0 ± 0.0	0.08
G0.412+0.052h	OCS (218.9GHz)	N	0	0	0.0 ± 0.0	0.0 ± 0.0	0.0 ± 0.0	0.08
G0.412+0.052h	OCS (231.1GHz)	N	0	0	0.0 ± 0.0	0.0 ± 0.0	0.0 ± 0.0	0.08
G0.412+0.052h	SO (219.9GHz)	N	0	0	0.0 ± 0.0	0.0 ± 0.0	0.0 ± 0.0	0.07
G0.412+0.052h	SiO (217.1GHz)	N	0	0	0.0 ± 0.0	0.0 ± 0.0	0.0 ± 0.0	0.08
G0.412+0.052i	12CO (230.5GHz)	N	0	0	0.0 ± 0.0	0.0 ± 0.0	0.0 ± 0.0	0.18
G0.412+0.052i	13CO (220.4GHz)	Y	1	1	0.64 ± 0.07	49.08 ± 0.31	2.62 ± 2.62	0.11
G0.412+0.052i	C18O (219.6GHz)	N	0	0	0.0 ± 0.0	0.0 ± 0.0	0.0 ± 0.0	0.08
G0.412+0.052i	H2CO (218.2GHz)	N	0	0	0.0 ± 0.0	0.0 ± 0.0	0.0 ± 0.0	0.08
G0.412+0.052i	H2CO (218.5GHz)	N	0	0	0.0 ± 0.0	0.0 ± 0.0	0.0 ± 0.0	0.09
G0.412+0.052i	H2CO (218.8GHz)	N	0	0	0.0 ± 0.0	0.0 ± 0.0	0.0 ± 0.0	0.08
G0.412+0.052i	OCS (218.9GHz)	N	0	0	0.0 ± 0.0	0.0 ± 0.0	0.0 ± 0.0	0.08
G0.412+0.052i	OCS (231.1GHz)	N	0	0	0.0 ± 0.0	0.0 ± 0.0	0.0 ± 0.0	0.07
G0.412+0.052i	SO (219.9GHz)	N	0	0	0.0 ± 0.0	0.0 ± 0.0	0.0 ± 0.0	0.09
G0.412+0.052i	SiO (217.1GHz)	N	0	0	0.0 ± 0.0	0.0 ± 0.0	0.0 ± 0.0	0.07
G0.412+0.052j	12CO (230.5GHz)	Y	1	1	1.78 ± 0.15	9.95 ± 0.3	2.94 ± 2.94	0.25
G0.412+0.052j	13CO (220.4GHz)	N	0	0	0.0 ± 0.0	0.0 ± 0.0	0.0 ± 0.0	0.11
G0.412+0.052j	C18O (219.6GHz)	N	0	0	0.0 ± 0.0	0.0 ± 0.0	0.0 ± 0.0	0.08
G0.412+0.052j	H2CO (218.2GHz)	N	0	0	0.0 ± 0.0	0.0 ± 0.0	0.0 ± 0.0	0.09
G0.412+0.052j	H2CO (218.5GHz)	N	0	0	0.0 ± 0.0	0.0 ± 0.0	0.0 ± 0.0	0.08
G0.412+0.052j	H2CO (218.8GHz)	N	0	0	0.0 ± 0.0	0.0 ± 0.0	0.0 ± 0.0	0.08
G0.412+0.052j	OCS (218.9GHz)	N	0	0	0.0 ± 0.0	0.0 ± 0.0	0.0 ± 0.0	0.07
G0.412+0.052j	OCS (231.1GHz)	N	0	0	0.0 ± 0.0	0.0 ± 0.0	0.0 ± 0.0	0.09
G0.412+0.052j	SO (219.9GHz)	N	0	0	0.0 ± 0.0	0.0 ± 0.0	0.0 ± 0.0	0.08
G0.412+0.052j	SiO (217.1GHz)	N	0	0	0.0 ± 0.0	0.0 ± 0.0	0.0 ± 0.0	0.07
G0.412+0.052k	12CO (230.5GHz)	Y	4	1	1.49 ± 0.1	56.77 ± 0.38	4.81 ± 4.81	0.16
G0.412+0.052k	12CO (230.5GHz)	Y	4	2	2.52 ± 0.09	34.26 ± 0.27	6.64 ± 6.64	0.16
G0.412+0.052k	12CO (230.5GHz)	Y	4	3	1.53 ± 0.12	12.84 ± 0.3	3.32 ± 3.32	0.16
G0.412+0.052k	13CO (220.4GHz)	N	0	0	0.0 ± 0.0	0.0 ± 0.0	0.0 ± 0.0	0.12
G0.412+0.052k	C18O (219.6GHz)	N	0	0	0.0 ± 0.0	0.0 ± 0.0	0.0 ± 0.0	0.08
G0.412+0.052k	H2CO (218.2GHz)	N	0	0	0.0 ± 0.0	0.0 ± 0.0	0.0 ± 0.0	0.09
G0.412+0.052k	H2CO (218.5GHz)	N	0	0	0.0 ± 0.0	0.0 ± 0.0	0.0 ± 0.0	0.08
G0.412+0.052k	H2CO (218.8GHz)	N	0	0	0.0 ± 0.0	0.0 ± 0.0	0.0 ± 0.0	0.09
G0.412+0.052k	OCS (218.9GHz)	N	0	0	0.0 ± 0.0	0.0 ± 0.0	0.0 ± 0.0	0.08
G0.412+0.052k	OCS (231.1GHz)	N	0	0	0.0 ± 0.0	0.0 ± 0.0	0.0 ± 0.0	0.09
G0.412+0.052k	SO (219.9GHz)	N	0	0	0.0 ± 0.0	0.0 ± 0.0	0.0 ± 0.0	0.08
G0.412+0.052k	SiO (217.1GHz)	N	0	0	0.0 ± 0.0	0.0 ± 0.0	0.0 ± 0.0	0.08
G0.412+0.052l	12CO (230.5GHz)	Y	1	1	1.79 ± 0.14	52.36 ± 0.44	4.79 ± 4.79	0.26
G0.412+0.052l	13CO (220.4GHz)	Y	1	1	0.57 ± 0.06	49.1 ± 0.56	4.46 ± 4.46	0.13
G0.412+0.052l	C18O (219.6GHz)	N	0	0	0.0 ± 0.0	0.0 ± 0.0	0.0 ± 0.0	0.1
G0.412+0.052l	H2CO (218.2GHz)	N	0	0	0.0 ± 0.0	0.0 ± 0.0	0.0 ± 0.0	0.09
G0.412+0.052l	H2CO (218.5GHz)	N	0	0	0.0 ± 0.0	0.0 ± 0.0	0.0 ± 0.0	0.08
G0.412+0.052l	H2CO (218.8GHz)	N	0	0	0.0 ± 0.0	0.0 ± 0.0	0.0 ± 0.0	0.08
G0.412+0.052l	OCS (218.9GHz)	N	0	0	0.0 ± 0.0	0.0 ± 0.0	0.0 ± 0.0	0.08
G0.412+0.052l	OCS (231.1GHz)	N	0	0	0.0 ± 0.0	0.0 ± 0.0	0.0 ± 0.0	0.12
G0.412+0.052l	SO (219.9GHz)	N	0	0	0.0 ± 0.0	0.0 ± 0.0	0.0 ± 0.0	0.1
G0.412+0.052l	SiO (217.1GHz)	N	0	0	0.0 ± 0.0	0.0 ± 0.0	0.0 ± 0.0	0.09
G0.489+0.010a	12CO (230.5GHz)	Y	1	1	4.94 ± 0.73	56.79 ± 1.84	10.7 ± 10.7	1.55
G0.489+0.010a	13CO (220.4GHz)	Y	1	1	33.75 ± 2.13	35.76 ± 0.08	1.06 ± 1.06	2.22
G0.489+0.010a	C18O (219.6GHz)	Y	1	1	1.29 ± 0.08	30.78 ± 0.08	1.15 ± 1.15	0.09
G0.489+0.010a	H2CO (218.5GHz)	Y	2	1	1.43 ± 0.07	79.48 ± 0.15	2.66 ± 2.66	0.09

Continued on next page

Table A.1 – *Continued from previous page*

Leaf	Transition	Detected	Number of Comps	Comp.	Amplitude	Velocity	Width	RMS
G0.489+0.010a	H2CO (218.5GHz)	Y	2	2	0.61 ± 0.08	30.59 ± 0.32	2.18 ± 2.18	0.09
G0.489+0.010a	H2CO (218.8GHz)	Y	2	1	0.59 ± 0.06	30.64 ± 0.27	2.46 ± 2.46	0.09
G0.489+0.010a	OCS (218.9GHz)	Y	1	1	0.37 ± 0.05	30.95 ± 0.45	3.01 ± 3.01	0.08
G0.489+0.010a	SO (219.9GHz)	Y	6	1	0.15 ± 0.12	109.47 ± 0.87	0.75 ± 0.75	0.1
G0.489+0.010a	SO (219.9GHz)	Y	6	5	0.94 ± 0.07	30.72 ± 0.24	2.66 ± 2.66	0.1
G0.489+0.010a	SiO (217.1GHz)	Y	1	1	0.57 ± 0.06	31.77 ± 0.42	3.55 ± 3.55	0.11
G0.489+0.010b	12CO (230.5GHz)	N	0	0	0.0 ± 0.0	0.0 ± 0.0	0.0 ± 0.0	1.7
G0.489+0.010b	13CO (220.4GHz)	N	0	0	0.0 ± 0.0	0.0 ± 0.0	0.0 ± 0.0	1.21
G0.489+0.010b	C18O (219.6GHz)	Y	1	1	2.15 ± 0.1	37.21 ± 0.05	0.66 ± 0.66	0.09
G0.489+0.010b	H2CO (218.5GHz)	Y	2	1	1.24 ± 0.07	77.89 ± 0.15	2.32 ± 2.32	0.11
G0.489+0.010b	H2CO (218.5GHz)	Y	2	2	0.37 ± 0.06	28.73 ± 0.59	2.95 ± 2.95	0.11
G0.489+0.010b	H2CO (218.8GHz)	Y	2	1	0.28 ± 0.04	30.11 ± 0.81	4.45 ± 4.45	0.09
G0.489+0.010b	OCS (218.9GHz)	Y	1	1	0.21 ± 0.04	31.73 ± 1.04	4.63 ± 4.63	0.09
G0.489+0.010b	SO (219.9GHz)	Y	1	1	0.37 ± 0.05	28.79 ± 0.93	6.45 ± 6.45	0.1
G0.489+0.010b	SiO (217.1GHz)	Y	2	1	0.41 ± 0.04	30.38 ± 0.61	5.81 ± 5.81	0.09
G0.489+0.010b	SiO (217.1GHz)	Y	2	2	7.86 ± 0.09	11.88 ± 0.02	0.59 ± 0.59	0.09
G0.489+0.010c	12CO (230.5GHz)	Y	1	1	6.61 ± 1.01	55.86 ± 0.92	5.18 ± 5.18	1.68
G0.489+0.010c	C18O (219.6GHz)	N	0	0	0.0 ± 0.0	0.0 ± 0.0	0.0 ± 0.0	0.1
G0.489+0.010c	H2CO (218.2GHz)	Y	1	1	2.06 ± 0.19	8.45 ± 0.11	0.6 ± 0.6	0.16
G0.489+0.010c	H2CO (218.5GHz)	Y	2	1	0.51 ± 0.06	76.9 ± 0.36	2.94 ± 2.94	0.09
G0.489+0.010c	H2CO (218.8GHz)	N	0	0	0.0 ± 0.0	0.0 ± 0.0	0.0 ± 0.0	0.1
G0.489+0.010c	OCS (218.9GHz)	N	0	0	0.0 ± 0.0	0.0 ± 0.0	0.0 ± 0.0	0.1
G0.489+0.010c	SO (219.9GHz)	Y	1	1	0.48 ± 0.06	28.43 ± 0.43	2.81 ± 2.81	0.11
G0.489+0.010c	SiO (217.1GHz)	N	0	0	0.0 ± 0.0	0.0 ± 0.0	0.0 ± 0.0	0.21
G0.489+0.010d	12CO (230.5GHz)	Y	1	1	10.42 ± 0.98	49.76 ± 0.17	1.6 ± 1.6	0.97
G0.489+0.010d	C18O (219.6GHz)	N	0	0	0.0 ± 0.0	0.0 ± 0.0	0.0 ± 0.0	0.09
G0.489+0.010d	H2CO (218.5GHz)	N	0	0	0.0 ± 0.0	0.0 ± 0.0	0.0 ± 0.0	0.09
G0.489+0.010d	H2CO (218.8GHz)	N	0	0	0.0 ± 0.0	0.0 ± 0.0	0.0 ± 0.0	0.08
G0.489+0.010d	OCS (218.9GHz)	N	0	0	0.0 ± 0.0	0.0 ± 0.0	0.0 ± 0.0	0.09
G0.489+0.010d	SO (219.9GHz)	N	0	0	0.0 ± 0.0	0.0 ± 0.0	0.0 ± 0.0	0.1
G0.489+0.010d	SiO (217.1GHz)	N	0	0	0.0 ± 0.0	0.0 ± 0.0	0.0 ± 0.0	0.09
G0.489+0.010e	12CO (230.5GHz)	N	0	0	0.0 ± 0.0	0.0 ± 0.0	0.0 ± 0.0	0.95
G0.489+0.010e	13CO (220.4GHz)	Y	1	1	1.06 ± 0.11	20.94 ± 0.46	3.75 ± 3.75	0.22
G0.489+0.010e	C18O (219.6GHz)	Y	2	1	0.58 ± 0.06	36.08 ± 0.36	2.86 ± 2.86	0.11
G0.489+0.010e	C18O (219.6GHz)	Y	2	2	0.48 ± 0.07	21.33 ± 0.41	2.58 ± 2.58	0.11
G0.489+0.010e	H2CO (218.2GHz)	N	0	0	0.0 ± 0.0	0.0 ± 0.0	0.0 ± 0.0	0.11
G0.489+0.010e	H2CO (218.5GHz)	Y	1	1	0.62 ± 0.07	82.81 ± 0.34	2.66 ± 2.66	0.11
G0.489+0.010e	H2CO (218.8GHz)	N	0	0	0.0 ± 0.0	0.0 ± 0.0	0.0 ± 0.0	0.1
G0.489+0.010e	OCS (218.9GHz)	N	0	0	0.0 ± 0.0	0.0 ± 0.0	0.0 ± 0.0	0.11
G0.489+0.010e	SO (219.9GHz)	Y	1	1	0.57 ± 0.07	33.63 ± 0.42	3.13 ± 3.13	0.11
G0.489+0.010e	SiO (217.1GHz)	N	0	0	0.0 ± 0.0	0.0 ± 0.0	0.0 ± 0.0	0.1
G0.489+0.010f	12CO (230.5GHz)	Y	2	1	8.12 ± 0.38	46.24 ± 0.15	2.69 ± 2.69	0.47
G0.489+0.010f	12CO (230.5GHz)	Y	2	2	2.53 ± 0.4	27.17 ± 0.45	2.49 ± 2.49	0.47
G0.489+0.010f	13CO (220.4GHz)	Y	2	1	2.26 ± 0.17	42.54 ± 0.12	1.36 ± 1.36	0.17
G0.489+0.010f	13CO (220.4GHz)	Y	2	2	0.95 ± 0.16	27.23 ± 0.3	1.58 ± 1.58	0.17
G0.489+0.010f	C18O (219.6GHz)	Y	1	1	0.88 ± 0.11	42.04 ± 0.13	0.91 ± 0.91	0.1
G0.489+0.010f	H2CO (218.2GHz)	N	0	0	0.0 ± 0.0	0.0 ± 0.0	0.0 ± 0.0	0.1
G0.489+0.010f	H2CO (218.5GHz)	Y	3	1	0.18 ± 0.07	84.13 ± 1.99	8.64 ± 8.64	0.1
G0.489+0.010f	H2CO (218.5GHz)	Y	3	2	0.41 ± 0.09	82.79 ± 0.4	1.81 ± 1.81	0.1
G0.489+0.010f	H2CO (218.5GHz)	Y	3	3	0.3 ± 0.11	2.87 ± 0.38	0.71 ± 0.71	0.1
G0.489+0.010f	H2CO (218.8GHz)	N	0	0	0.0 ± 0.0	0.0 ± 0.0	0.0 ± 0.0	0.1
G0.489+0.010f	OCS (218.9GHz)	N	0	0	0.0 ± 0.0	0.0 ± 0.0	0.0 ± 0.0	0.1
G0.489+0.010f	SO (219.9GHz)	Y	1	1	0.53 ± 0.05	35.57 ± 0.62	5.66 ± 5.66	0.12
G0.489+0.010f	SiO (217.1GHz)	N	0	0	0.0 ± 0.0	0.0 ± 0.0	0.0 ± 0.0	0.1
G0.489+0.010g	12CO (230.5GHz)	Y	1	1	7.02 ± 0.88	44.95 ± 0.21	1.47 ± 1.47	1.03
G0.489+0.010g	13CO (220.4GHz)	Y	1	1	1.65 ± 0.2	42.23 ± 0.18	1.31 ± 1.31	0.21
G0.489+0.010g	C18O (219.6GHz)	N	0	0	0.0 ± 0.0	0.0 ± 0.0	0.0 ± 0.0	0.11
G0.489+0.010g	H2CO (218.2GHz)	N	0	0	0.0 ± 0.0	0.0 ± 0.0	0.0 ± 0.0	0.1
G0.489+0.010g	H2CO (218.5GHz)	N	0	0	0.0 ± 0.0	0.0 ± 0.0	0.0 ± 0.0	0.1
G0.489+0.010g	H2CO (218.8GHz)	N	0	0	0.0 ± 0.0	0.0 ± 0.0	0.0 ± 0.0	0.11
G0.489+0.010g	OCS (218.9GHz)	N	0	0	0.0 ± 0.0	0.0 ± 0.0	0.0 ± 0.0	0.11
G0.489+0.010g	SO (219.9GHz)	N	0	0	0.0 ± 0.0	0.0 ± 0.0	0.0 ± 0.0	0.13
G0.489+0.010g	SiO (217.1GHz)	N	0	0	0.0 ± 0.0	0.0 ± 0.0	0.0 ± 0.0	0.11
G0.489+0.010h	12CO (230.5GHz)	N	0	0	0.0 ± 0.0	0.0 ± 0.0	0.0 ± 0.0	1.58
G0.489+0.010h	13CO (220.4GHz)	Y	2	1	2.22 ± 0.25	43.08 ± 0.11	0.88 ± 0.88	0.23
G0.489+0.010h	13CO (220.4GHz)	Y	2	2	0.78 ± 0.19	1.98 ± 0.4	1.37 ± 1.37	0.23
G0.489+0.010h	C18O (219.6GHz)	Y	1	1	0.54 ± 0.09	42.74 ± 0.21	1.06 ± 1.06	0.1
G0.489+0.010h	H2CO (218.2GHz)	Y	1	1	3.27 ± 0.15	45.31 ± 0.08	0.52 ± 0.52	0.12
G0.489+0.010h	H2CO (218.5GHz)	Y	1	1	0.37 ± 0.06	80.79 ± 0.46	2.46 ± 2.46	0.09
G0.489+0.010h	H2CO (218.8GHz)	N	0	0	0.0 ± 0.0	0.0 ± 0.0	0.0 ± 0.0	0.1
G0.489+0.010h	OCS (218.9GHz)	N	0	0	0.0 ± 0.0	0.0 ± 0.0	0.0 ± 0.0	0.1
G0.489+0.010h	SO (219.9GHz)	N	0	0	0.0 ± 0.0	0.0 ± 0.0	0.0 ± 0.0	0.1
G0.489+0.010h	SiO (217.1GHz)	Y	1	1	3.1 ± 0.11	11.94 ± 0.04	0.69 ± 0.69	0.09
G0.489+0.010i	12CO (230.5GHz)	N	0	0	0.0 ± 0.0	0.0 ± 0.0	0.0 ± 0.0	1.39
G0.489+0.010i	13CO (220.4GHz)	Y	1	1	1.4 ± 0.12	18.02 ± 0.39	3.82 ± 3.82	0.23
G0.489+0.010i	C18O (219.6GHz)	N	0	0	0.0 ± 0.0	0.0 ± 0.0	0.0 ± 0.0	0.11
G0.489+0.010i	H2CO (218.2GHz)	N	0	0	0.0 ± 0.0	0.0 ± 0.0	0.0 ± 0.0	0.13
G0.489+0.010i	H2CO (218.5GHz)	N	0	0	0.0 ± 0.0	0.0 ± 0.0	0.0 ± 0.0	0.12
G0.489+0.010i	H2CO (218.8GHz)	N	0	0	0.0 ± 0.0	0.0 ± 0.0	0.0 ± 0.0	0.12
G0.489+0.010i	OCS (218.9GHz)	N	0	0	0.0 ± 0.0	0.0 ± 0.0	0.0 ± 0.0	0.11
G0.489+0.010i	SO (219.9GHz)	Y	1	1	0.41 ± 0.07	28.58 ± 0.67	3.6 ± 3.6	0.13
G0.489+0.010i	SiO (217.1GHz)	N	0	0	0.0 ± 0.0	0.0 ± 0.0	0.0 ± 0.0	0.11
G0.489+0.010j	12CO (230.5GHz)	Y	3	1	6.51 ± 0.64	88.13 ± 0.35	3.01 ± 3.01	0.85
G0.489+0.010j	12CO (230.5GHz)	Y	3	2	7.74 ± 0.4	64.92 ± 0.56	8.7 ± 8.7	0.85
G0.489+0.010j	12CO (230.5GHz)	Y	3	3	13.35 ± 0.76	47.45 ± 0.15	2.36 ± 2.36	0.85
G0.489+0.010j	13CO (220.4GHz)	Y	2	1	1.94 ± 0.18	88.39 ± 0.21	2.0 ± 2.0	0.22
G0.489+0.010j	13CO (220.4GHz)	Y	2	2	1.39 ± 0.16	46.39 ± 0.33	2.46 ± 2.46	0.22

Continued on next page

Table A.1 – *Continued from previous page*

Leaf	Transition	Detected	Number of Comps	Comp.	Amplitude	Velocity	Width	RMS
G0.489+0.010j	C18O (219.6GHz)	N	0	0	0.0 ± 0.0	0.0 ± 0.0	0.0 ± 0.0	0.11
G0.489+0.010j	H2CO (218.2GHz)	Y	1	1	0.37 ± 0.04	44.5 ± 1.66	12.47 ± 12.47	0.14
G0.489+0.010j	H2CO (218.5GHz)	N	0	0	0.0 ± 0.0	0.0 ± 0.0	0.0 ± 0.0	0.13
G0.489+0.010j	H2CO (218.8GHz)	N	0	0	0.0 ± 0.0	0.0 ± 0.0	0.0 ± 0.0	0.12
G0.489+0.010j	OCS (218.9GHz)	N	0	0	0.0 ± 0.0	0.0 ± 0.0	0.0 ± 0.0	0.14
G0.489+0.010j	SO (219.9GHz)	Y	1	1	0.41 ± 0.03	48.26 ± 1.73	18.37 ± 18.37	0.12
G0.489+0.010j	SiO (217.1GHz)	Y	2	1	0.38 ± 0.08	45.1 ± 0.79	3.75 ± 3.75	0.13
G0.489+0.010j	SiO (217.1GHz)	Y	2	2	0.26 ± 0.05	37.16 ± 2.99	16.38 ± 16.38	0.13
G0.489+0.010k	12CO (230.5GHz)	Y	1	1	5.45 ± 0.38	51.41 ± 0.57	7.09 ± 7.09	1.0
G0.489+0.010k	13CO (220.4GHz)	Y	3	1	0.5 ± 0.1	55.61 ± 1.14	4.79 ± 4.79	0.23
G0.489+0.010k	13CO (220.4GHz)	Y	3	2	1.95 ± 0.18	42.91 ± 0.16	1.52 ± 1.52	0.23
G0.489+0.010k	13CO (220.4GHz)	Y	3	3	1.12 ± 0.14	21.49 ± 0.36	2.54 ± 2.54	0.23
G0.489+0.010k	C18O (219.6GHz)	N	0	0	0.0 ± 0.0	0.0 ± 0.0	0.0 ± 0.0	0.15
G0.489+0.010k	H2CO (218.2GHz)	N	0	0	0.0 ± 0.0	0.0 ± 0.0	0.0 ± 0.0	0.15
G0.489+0.010k	H2CO (218.5GHz)	N	0	0	0.0 ± 0.0	0.0 ± 0.0	0.0 ± 0.0	0.15
G0.489+0.010k	H2CO (218.8GHz)	N	0	0	0.0 ± 0.0	0.0 ± 0.0	0.0 ± 0.0	0.14
G0.489+0.010k	OCS (218.9GHz)	N	0	0	0.0 ± 0.0	0.0 ± 0.0	0.0 ± 0.0	0.13
G0.489+0.010k	SO (219.9GHz)	N	0	0	0.0 ± 0.0	0.0 ± 0.0	0.0 ± 0.0	0.15
G0.489+0.010k	SiO (217.1GHz)	N	0	0	0.0 ± 0.0	0.0 ± 0.0	0.0 ± 0.0	0.15
G0.489+0.010l	12CO (230.5GHz)	Y	2	1	14.32 ± 0.62	48.3 ± 0.19	3.85 ± 3.85	0.95
G0.489+0.010l	12CO (230.5GHz)	Y	2	2	8.39 ± 0.62	14.62 ± 0.33	3.82 ± 3.82	0.95
G0.489+0.010l	13CO (220.4GHz)	Y	3	1	1.92 ± 0.22	88.8 ± 0.2	1.55 ± 1.55	0.27
G0.489+0.010l	13CO (220.4GHz)	Y	3	2	2.96 ± 0.17	45.62 ± 0.17	2.43 ± 2.43	0.27
G0.489+0.010l	13CO (220.4GHz)	Y	3	3	0.85 ± 0.11	13.4 ± 0.95	6.56 ± 6.56	0.27
G0.489+0.010l	C18O (219.6GHz)	N	0	0	0.0 ± 0.0	0.0 ± 0.0	0.0 ± 0.0	0.13
G0.489+0.010l	H2CO (218.2GHz)	Y	1	1	0.57 ± 0.09	44.92 ± 0.51	2.82 ± 2.82	0.15
G0.489+0.010l	H2CO (218.5GHz)	N	0	0	0.0 ± 0.0	0.0 ± 0.0	0.0 ± 0.0	0.16
G0.489+0.010l	H2CO (218.8GHz)	N	0	0	0.0 ± 0.0	0.0 ± 0.0	0.0 ± 0.0	0.14
G0.489+0.010l	OCS (218.9GHz)	N	0	0	0.0 ± 0.0	0.0 ± 0.0	0.0 ± 0.0	0.14
G0.489+0.010l	SO (219.9GHz)	N	0	0	0.0 ± 0.0	0.0 ± 0.0	0.0 ± 0.0	0.16
G0.489+0.010l	SiO (217.1GHz)	N	0	0	0.0 ± 0.0	0.0 ± 0.0	0.0 ± 0.0	0.15
G0.489+0.010m	12CO (230.5GHz)	Y	1	1	5.3 ± 0.71	98.94 ± 1.84	11.9 ± 11.9	1.96
G0.489+0.010m	13CO (220.4GHz)	N	0	0	0.0 ± 0.0	0.0 ± 0.0	0.0 ± 0.0	0.47
G0.489+0.010m	C18O (219.6GHz)	Y	2	1	1.14 ± 0.13	37.26 ± 0.16	1.22 ± 1.22	0.15
G0.489+0.010m	C18O (219.6GHz)	Y	2	2	0.35 ± 0.1	29.78 ± 0.67	1.96 ± 1.96	0.15
G0.489+0.010m	H2CO (218.2GHz)	N	0	0	0.0 ± 0.0	0.0 ± 0.0	0.0 ± 0.0	0.4
G0.489+0.010m	H2CO (218.5GHz)	Y	2	1	1.26 ± 0.12	77.22 ± 0.16	1.45 ± 1.45	0.14
G0.489+0.010m	H2CO (218.8GHz)	N	0	0	0.0 ± 0.0	0.0 ± 0.0	0.0 ± 0.0	0.15
G0.489+0.010m	OCS (218.9GHz)	N	0	0	0.0 ± 0.0	0.0 ± 0.0	0.0 ± 0.0	0.14
G0.489+0.010m	SO (219.9GHz)	Y	2	1	1.17 ± 0.15	162.7 ± 0.24	0.5 ± 0.5	0.14
G0.489+0.010m	SO (219.9GHz)	Y	2	2	1.04 ± 0.11	27.9 ± 0.2	1.62 ± 1.62	0.14
G0.489+0.010m	SiO (217.1GHz)	N	0	0	0.0 ± 0.0	0.0 ± 0.0	0.0 ± 0.0	0.17
G1.085-0.027a	12CO (230.5GHz)	N	0	0	0.0 ± 0.0	0.0 ± 0.0	0.0 ± 0.0	0.16
G1.085-0.027a	C18O (219.6GHz)	N	0	0	0.0 ± 0.0	0.0 ± 0.0	0.0 ± 0.0	0.05
G1.085-0.027a	H2CO (218.2GHz)	N	0	0	0.0 ± 0.0	0.0 ± 0.0	0.0 ± 0.0	0.05
G1.085-0.027a	H2CO (218.5GHz)	N	0	0	0.0 ± 0.0	0.0 ± 0.0	0.0 ± 0.0	0.05
G1.085-0.027a	H2CO (218.8GHz)	N	0	0	0.0 ± 0.0	0.0 ± 0.0	0.0 ± 0.0	0.05
G1.085-0.027a	OCS (218.9GHz)	N	0	0	0.0 ± 0.0	0.0 ± 0.0	0.0 ± 0.0	0.04
G1.085-0.027a	OCS (231.1GHz)	N	0	0	0.0 ± 0.0	0.0 ± 0.0	0.0 ± 0.0	0.05
G1.085-0.027a	SO (219.9GHz)	N	0	0	0.0 ± 0.0	0.0 ± 0.0	0.0 ± 0.0	0.05
G1.085-0.027a	SiO (217.1GHz)	N	0	0	0.0 ± 0.0	0.0 ± 0.0	0.0 ± 0.0	0.05
G1.085-0.027b	12CO (230.5GHz)	N	0	0	0.0 ± 0.0	0.0 ± 0.0	0.0 ± 0.0	0.17
G1.085-0.027b	13CO (220.4GHz)	N	0	0	0.0 ± 0.0	0.0 ± 0.0	0.0 ± 0.0	0.06
G1.085-0.027b	H2CO (218.2GHz)	N	0	0	0.0 ± 0.0	0.0 ± 0.0	0.0 ± 0.0	0.04
G1.085-0.027b	H2CO (218.5GHz)	N	0	0	0.0 ± 0.0	0.0 ± 0.0	0.0 ± 0.0	0.04
G1.085-0.027b	H2CO (218.8GHz)	N	0	0	0.0 ± 0.0	0.0 ± 0.0	0.0 ± 0.0	0.04
G1.085-0.027b	OCS (218.9GHz)	N	0	0	0.0 ± 0.0	0.0 ± 0.0	0.0 ± 0.0	0.04
G1.085-0.027b	OCS (231.1GHz)	N	0	0	0.0 ± 0.0	0.0 ± 0.0	0.0 ± 0.0	0.05
G1.085-0.027b	SO (219.9GHz)	N	0	0	0.0 ± 0.0	0.0 ± 0.0	0.0 ± 0.0	0.03
G1.085-0.027b	SiO (217.1GHz)	N	0	0	0.0 ± 0.0	0.0 ± 0.0	0.0 ± 0.0	0.03
G1.085-0.027c	12CO (230.5GHz)	Y	2	1	1.01 ± 0.12	86.58 ± 0.31	2.23 ± 2.23	0.17
G1.085-0.027c	12CO (230.5GHz)	Y	2	2	1.83 ± 0.1	14.11 ± 0.2	3.14 ± 3.14	0.17
G1.085-0.027c	13CO (220.4GHz)	Y	2	1	0.22 ± 0.03	70.48 ± 1.44	10.78 ± 10.78	0.08
G1.085-0.027c	13CO (220.4GHz)	Y	2	2	0.69 ± 0.05	15.25 ± 0.24	3.01 ± 3.01	0.08
G1.085-0.027c	C18O (219.6GHz)	N	0	0	0.0 ± 0.0	0.0 ± 0.0	0.0 ± 0.0	0.06
G1.085-0.027c	H2CO (218.2GHz)	N	0	0	0.0 ± 0.0	0.0 ± 0.0	0.0 ± 0.0	0.06
G1.085-0.027c	H2CO (218.5GHz)	N	0	0	0.0 ± 0.0	0.0 ± 0.0	0.0 ± 0.0	0.07
G1.085-0.027c	H2CO (218.8GHz)	N	0	0	0.0 ± 0.0	0.0 ± 0.0	0.0 ± 0.0	0.07
G1.085-0.027c	OCS (218.9GHz)	N	0	0	0.0 ± 0.0	0.0 ± 0.0	0.0 ± 0.0	0.05
G1.085-0.027c	OCS (231.1GHz)	N	0	0	0.0 ± 0.0	0.0 ± 0.0	0.0 ± 0.0	0.07
G1.085-0.027c	SO (219.9GHz)	N	0	0	0.0 ± 0.0	0.0 ± 0.0	0.0 ± 0.0	0.06
G1.085-0.027c	SiO (217.1GHz)	N	0	0	0.0 ± 0.0	0.0 ± 0.0	0.0 ± 0.0	0.07
G1.602+0.018a	12CO (230.5GHz)	Y	3	1	1.45 ± 0.12	181.83 ± 0.46	4.97 ± 4.97	0.2
G1.602+0.018a	12CO (230.5GHz)	Y	3	2	0.81 ± 0.07	65.42 ± 1.97	15.73 ± 15.73	0.2
G1.602+0.018a	13CO (220.4GHz)	Y	3	1	0.19 ± 0.02	181.33 ± 0.67	4.42 ± 4.42	0.05
G1.602+0.018a	13CO (220.4GHz)	Y	3	2	0.35 ± 0.03	161.78 ± 0.29	2.92 ± 2.92	0.05
G1.602+0.018a	13CO (220.4GHz)	Y	3	3	0.41 ± 0.04	58.05 ± 0.16	1.3 ± 1.3	0.05
G1.602+0.018a	C18O (219.6GHz)	N	0	0	0.0 ± 0.0	0.0 ± 0.0	0.0 ± 0.0	0.04
G1.602+0.018a	H2CO (218.2GHz)	Y	1	1	0.27 ± 0.03	58.5 ± 0.3	2.34 ± 2.34	0.04
G1.602+0.018a	H2CO (218.5GHz)	Y	2	1	0.58 ± 0.03	106.62 ± 0.12	1.81 ± 1.81	0.04
G1.602+0.018a	H2CO (218.5GHz)	Y	2	2	0.13 ± 0.02	56.53 ± 0.81	4.31 ± 4.31	0.04
G1.602+0.018a	H2CO (218.8GHz)	Y	2	1	0.17 ± 0.11	156.94 ± 0.3	0.62 ± 0.62	0.04
G1.602+0.018a	H2CO (218.8GHz)	Y	2	2	0.14 ± 0.02	57.1 ± 0.61	3.21 ± 3.21	0.04
G1.602+0.018a	OCS (218.9GHz)	N	0	0	0.0 ± 0.0	0.0 ± 0.0	0.0 ± 0.0	0.04
G1.602+0.018a	OCS (231.1GHz)	N	0	0	0.0 ± 0.0	0.0 ± 0.0	0.0 ± 0.0	0.05
G1.602+0.018a	SO (219.9GHz)	Y	1	1	0.2 ± 0.02	58.87 ± 0.38	2.69 ± 2.69	0.04
G1.602+0.018a	SiO (217.1GHz)	Y	1	1	0.18 ± 0.02	58.85 ± 0.49	3.03 ± 3.03	0.04

Continued on next page

Table A.1 – *Continued from previous page*

Leaf	Transition	Detected	Number of Comps	Comp.	Amplitude	Velocity	Width	RMS
G1.602+0.018b	12CO (230.5GHz)	Y	2	1	1.14 ± 0.2	178.43 ± 0.27	1.29 ± 1.29	0.19
G1.602+0.018b	12CO (230.5GHz)	Y	2	2	2.19 ± 0.11	139.48 ± 0.25	4.33 ± 4.33	0.19
G1.602+0.018b	13CO (220.4GHz)	Y	1	1	0.48 ± 0.04	57.92 ± 0.22	2.14 ± 2.14	0.06
G1.602+0.018b	C18O (219.6GHz)	N	0	0	0.0 ± 0.0	0.0 ± 0.0	0.0 ± 0.0	0.05
G1.602+0.018b	H2CO (218.2GHz)	N	0	0	0.0 ± 0.0	0.0 ± 0.0	0.0 ± 0.0	0.06
G1.602+0.018b	H2CO (218.5GHz)	N	0	0	0.0 ± 0.0	0.0 ± 0.0	0.0 ± 0.0	0.05
G1.602+0.018b	H2CO (218.8GHz)	N	0	0	0.0 ± 0.0	0.0 ± 0.0	0.0 ± 0.0	0.05
G1.602+0.018b	OCS (218.9GHz)	N	0	0	0.0 ± 0.0	0.0 ± 0.0	0.0 ± 0.0	0.05
G1.602+0.018b	OCS (231.1GHz)	N	0	0	0.0 ± 0.0	0.0 ± 0.0	0.0 ± 0.0	0.1
G1.602+0.018b	SO (219.9GHz)	N	0	0	0.0 ± 0.0	0.0 ± 0.0	0.0 ± 0.0	0.05
G1.602+0.018b	SiO (217.1GHz)	N	0	0	0.0 ± 0.0	0.0 ± 0.0	0.0 ± 0.0	0.05
G1.602+0.018c	12CO (230.5GHz)	Y	1	1	5.81 ± 0.27	138.64 ± 0.29	5.28 ± 5.28	0.7
G1.602+0.018c	13CO (220.4GHz)	Y	2	1	0.77 ± 0.06	152.03 ± 0.19	2.23 ± 2.23	0.07
G1.602+0.018c	13CO (220.4GHz)	Y	2	2	0.63 ± 0.04	139.42 ± 0.3	3.63 ± 3.63	0.07
G1.602+0.018c	C18O (219.6GHz)	N	0	0	0.0 ± 0.0	0.0 ± 0.0	0.0 ± 0.0	0.06
G1.602+0.018c	H2CO (218.2GHz)	N	0	0	0.0 ± 0.0	0.0 ± 0.0	0.0 ± 0.0	0.06
G1.602+0.018c	H2CO (218.5GHz)	N	0	0	0.0 ± 0.0	0.0 ± 0.0	0.0 ± 0.0	0.05
G1.602+0.018c	H2CO (218.8GHz)	N	0	0	0.0 ± 0.0	0.0 ± 0.0	0.0 ± 0.0	0.06
G1.602+0.018c	OCS (218.9GHz)	N	0	0	0.0 ± 0.0	0.0 ± 0.0	0.0 ± 0.0	0.06
G1.602+0.018c	OCS (231.1GHz)	N	0	0	0.0 ± 0.0	0.0 ± 0.0	0.0 ± 0.0	0.55
G1.602+0.018c	SO (219.9GHz)	N	0	0	0.0 ± 0.0	0.0 ± 0.0	0.0 ± 0.0	0.06
G1.602+0.018c	SiO (217.1GHz)	N	0	0	0.0 ± 0.0	0.0 ± 0.0	0.0 ± 0.0	0.06
G1.602+0.018d	12CO (230.5GHz)	Y	1	1	3.1 ± 0.34	151.26 ± 0.23	1.86 ± 1.86	0.43
G1.602+0.018d	13CO (220.4GHz)	Y	2	1	0.38 ± 0.04	150.32 ± 0.36	2.99 ± 2.99	0.07
G1.602+0.018d	13CO (220.4GHz)	Y	2	2	0.36 ± 0.06	52.67 ± 0.27	1.46 ± 1.46	0.07
G1.602+0.018d	C18O (219.6GHz)	N	0	0	0.0 ± 0.0	0.0 ± 0.0	0.0 ± 0.0	0.06
G1.602+0.018d	H2CO (218.2GHz)	N	0	0	0.0 ± 0.0	0.0 ± 0.0	0.0 ± 0.0	0.06
G1.602+0.018d	H2CO (218.5GHz)	Y	1	1	0.17 ± 0.04	112.93 ± 0.57	2.25 ± 2.25	0.06
G1.602+0.018d	H2CO (218.8GHz)	N	0	0	0.0 ± 0.0	0.0 ± 0.0	0.0 ± 0.0	0.05
G1.602+0.018d	OCS (218.9GHz)	N	0	0	0.0 ± 0.0	0.0 ± 0.0	0.0 ± 0.0	0.05
G1.602+0.018d	OCS (231.1GHz)	N	0	0	0.0 ± 0.0	0.0 ± 0.0	0.0 ± 0.0	0.22
G1.602+0.018d	SO (219.9GHz)	N	0	0	0.0 ± 0.0	0.0 ± 0.0	0.0 ± 0.0	0.06
G1.602+0.018d	SiO (217.1GHz)	N	0	0	0.0 ± 0.0	0.0 ± 0.0	0.0 ± 0.0	0.05
G1.602+0.018e	12CO (230.5GHz)	N	0	0	0.0 ± 0.0	0.0 ± 0.0	0.0 ± 0.0	0.41
G1.602+0.018e	C18O (219.6GHz)	N	0	0	0.0 ± 0.0	0.0 ± 0.0	0.0 ± 0.0	0.07
G1.602+0.018e	H2CO (218.2GHz)	N	0	0	0.0 ± 0.0	0.0 ± 0.0	0.0 ± 0.0	0.07
G1.602+0.018e	H2CO (218.5GHz)	Y	2	1	0.21 ± 0.05	64.16 ± 0.42	1.43 ± 1.43	0.06
G1.602+0.018e	H2CO (218.8GHz)	N	0	0	0.0 ± 0.0	0.0 ± 0.0	0.0 ± 0.0	0.07
G1.602+0.018e	OCS (218.9GHz)	N	0	0	0.0 ± 0.0	0.0 ± 0.0	0.0 ± 0.0	0.07
G1.602+0.018e	OCS (231.1GHz)	N	0	0	0.0 ± 0.0	0.0 ± 0.0	0.0 ± 0.0	0.08
G1.602+0.018e	SO (219.9GHz)	N	0	0	0.0 ± 0.0	0.0 ± 0.0	0.0 ± 0.0	0.07
G1.602+0.018e	SiO (217.1GHz)	N	0	0	0.0 ± 0.0	0.0 ± 0.0	0.0 ± 0.0	0.07
G1.651-0.050a	12CO (230.5GHz)	N	0	0	0.0 ± 0.0	0.0 ± 0.0	0.0 ± 0.0	0.18
G1.651-0.050a	H2CO (218.5GHz)	Y	1	1	0.17 ± 0.04	14.22 ± 0.28	1.17 ± 1.17	0.04
G1.651-0.050a	H2CO (218.8GHz)	N	0	0	0.0 ± 0.0	0.0 ± 0.0	0.0 ± 0.0	0.04
G1.651-0.050a	OCS (218.9GHz)	N	0	0	0.0 ± 0.0	0.0 ± 0.0	0.0 ± 0.0	0.04
G1.651-0.050a	OCS (231.1GHz)	N	0	0	0.0 ± 0.0	0.0 ± 0.0	0.0 ± 0.0	0.05
G1.651-0.050a	SO (219.9GHz)	N	0	0	0.0 ± 0.0	0.0 ± 0.0	0.0 ± 0.0	0.05
G1.651-0.050a	SiO (217.1GHz)	N	0	0	0.0 ± 0.0	0.0 ± 0.0	0.0 ± 0.0	0.04
G1.651-0.050b	12CO (230.5GHz)	Y	2	1	1.2 ± 0.1	181.01 ± 0.34	3.72 ± 3.72	0.17
G1.651-0.050b	12CO (230.5GHz)	Y	2	2	1.98 ± 0.1	60.23 ± 0.2	3.34 ± 3.34	0.17
G1.651-0.050b	13CO (220.4GHz)	Y	1	1	0.53 ± 0.06	52.58 ± 0.21	1.6 ± 1.6	0.08
G1.651-0.050b	C18O (219.6GHz)	N	0	0	0.0 ± 0.0	0.0 ± 0.0	0.0 ± 0.0	0.07
G1.651-0.050b	H2CO (218.2GHz)	Y	3	1	0.09 ± 0.03	178.76 ± 1.75	4.15 ± 4.15	0.07
G1.651-0.050b	H2CO (218.2GHz)	Y	3	2	0.19 ± 0.06	75.88 ± 0.52	1.52 ± 1.52	0.07
G1.651-0.050b	H2CO (218.2GHz)	Y	3	3	0.31 ± 0.04	55.59 ± 0.48	3.24 ± 3.24	0.07
G1.651-0.050b	H2CO (218.5GHz)	Y	2	1	0.29 ± 0.04	102.97 ± 0.43	2.56 ± 2.56	0.07
G1.651-0.050b	H2CO (218.5GHz)	Y	2	2	0.19 ± 0.04	54.48 ± 0.72	3.29 ± 3.29	0.07
G1.651-0.050b	H2CO (218.8GHz)	N	0	0	0.0 ± 0.0	0.0 ± 0.0	0.0 ± 0.0	0.07
G1.651-0.050b	OCS (218.9GHz)	N	0	0	0.0 ± 0.0	0.0 ± 0.0	0.0 ± 0.0	0.07
G1.651-0.050b	OCS (231.1GHz)	N	0	0	0.0 ± 0.0	0.0 ± 0.0	0.0 ± 0.0	0.07
G1.651-0.050b	SO (219.9GHz)	N	0	0	0.0 ± 0.0	0.0 ± 0.0	0.0 ± 0.0	0.07
G1.651-0.050b	SiO (217.1GHz)	N	0	0	0.0 ± 0.0	0.0 ± 0.0	0.0 ± 0.0	0.07
G1.670-0.130a	12CO (230.5GHz)	Y	2	1	1.6 ± 0.14	143.3 ± 0.32	3.17 ± 3.17	0.24
G1.670-0.130a	12CO (230.5GHz)	Y	2	2	1.31 ± 0.09	45.6 ± 0.64	8.47 ± 8.47	0.24
G1.670-0.130a	13CO (220.4GHz)	N	0	0	0.0 ± 0.0	0.0 ± 0.0	0.0 ± 0.0	0.14
G1.670-0.130a	C18O (219.6GHz)	N	0	0	0.0 ± 0.0	0.0 ± 0.0	0.0 ± 0.0	0.11
G1.670-0.130a	H2CO (218.2GHz)	N	0	0	0.0 ± 0.0	0.0 ± 0.0	0.0 ± 0.0	0.13
G1.670-0.130a	H2CO (218.5GHz)	N	0	0	0.0 ± 0.0	0.0 ± 0.0	0.0 ± 0.0	0.11
G1.670-0.130a	SO (219.9GHz)	N	0	0	0.0 ± 0.0	0.0 ± 0.0	0.0 ± 0.0	0.13
G1.670-0.130a	SiO (217.1GHz)	N	0	0	0.0 ± 0.0	0.0 ± 0.0	0.0 ± 0.0	0.14
G1.670-0.130b	12CO (230.5GHz)	N	0	0	0.0 ± 0.0	0.0 ± 0.0	0.0 ± 0.0	0.27
G1.670-0.130b	13CO (220.4GHz)	Y	1	1	0.64 ± 0.13	131.5 ± 0.24	1.01 ± 1.01	0.12
G1.670-0.130b	C18O (219.6GHz)	N	0	0	0.0 ± 0.0	0.0 ± 0.0	0.0 ± 0.0	0.11
G1.670-0.130b	H2CO (218.2GHz)	N	0	0	0.0 ± 0.0	0.0 ± 0.0	0.0 ± 0.0	0.12
G1.670-0.130b	H2CO (218.5GHz)	N	0	0	0.0 ± 0.0	0.0 ± 0.0	0.0 ± 0.0	0.11
G1.670-0.130b	SO (219.9GHz)	N	0	0	0.0 ± 0.0	0.0 ± 0.0	0.0 ± 0.0	0.1
G1.670-0.130b	SiO (217.1GHz)	N	0	0	0.0 ± 0.0	0.0 ± 0.0	0.0 ± 0.0	0.13
G1.670-0.130c	12CO (230.5GHz)	Y	2	1	3.09 ± 0.12	175.85 ± 0.23	5.32 ± 5.32	0.29
G1.670-0.130c	12CO (230.5GHz)	Y	2	2	1.62 ± 0.15	55.71 ± 0.35	3.4 ± 3.4	0.29
G1.670-0.130c	13CO (220.4GHz)	N	0	0	0.0 ± 0.0	0.0 ± 0.0	0.0 ± 0.0	0.15
G1.670-0.130c	C18O (219.6GHz)	N	0	0	0.0 ± 0.0	0.0 ± 0.0	0.0 ± 0.0	0.12
G1.670-0.130c	H2CO (218.2GHz)	N	0	0	0.0 ± 0.0	0.0 ± 0.0	0.0 ± 0.0	0.16
G1.670-0.130c	H2CO (218.5GHz)	N	0	0	0.0 ± 0.0	0.0 ± 0.0	0.0 ± 0.0	0.13
G1.670-0.130c	SO (219.9GHz)	N	0	0	0.0 ± 0.0	0.0 ± 0.0	0.0 ± 0.0	0.14
G1.670-0.130c	SiO (217.1GHz)	N	0	0	0.0 ± 0.0	0.0 ± 0.0	0.0 ± 0.0	0.15
G1.670-0.130d	12CO (230.5GHz)	N	0	0	0.0 ± 0.0	0.0 ± 0.0	0.0 ± 0.0	0.3

Continued on next page

Table A.1 – *Continued from previous page*

Leaf	Transition	Detected	Number of Comps	Comp.	Amplitude	Velocity	Width	RMS
G1.670-0.130d	13CO (220.4GHz)	N	0	0	0.0 ± 0.0	0.0 ± 0.0	0.0 ± 0.0	0.14
G1.670-0.130d	C18O (219.6GHz)	N	0	0	0.0 ± 0.0	0.0 ± 0.0	0.0 ± 0.0	0.12
G1.670-0.130d	H2CO (218.2GHz)	N	0	0	0.0 ± 0.0	0.0 ± 0.0	0.0 ± 0.0	0.14
G1.670-0.130d	H2CO (218.5GHz)	N	0	0	0.0 ± 0.0	0.0 ± 0.0	0.0 ± 0.0	0.13
G1.670-0.130d	SO (219.9GHz)	N	0	0	0.0 ± 0.0	0.0 ± 0.0	0.0 ± 0.0	0.13
G1.670-0.130d	SiO (217.1GHz)	N	0	0	0.0 ± 0.0	0.0 ± 0.0	0.0 ± 0.0	0.14
G1.670-0.130e	12CO (230.5GHz)	Y	1	1	2.2 ± 0.28	35.94 ± 0.24	1.66 ± 1.66	0.32
G1.670-0.130e	13CO (220.4GHz)	N	0	0	0.0 ± 0.0	0.0 ± 0.0	0.0 ± 0.0	0.21
G1.670-0.130e	C18O (219.6GHz)	N	0	0	0.0 ± 0.0	0.0 ± 0.0	0.0 ± 0.0	0.16
G1.670-0.130e	H2CO (218.2GHz)	N	0	0	0.0 ± 0.0	0.0 ± 0.0	0.0 ± 0.0	0.18
G1.670-0.130e	H2CO (218.5GHz)	N	0	0	0.0 ± 0.0	0.0 ± 0.0	0.0 ± 0.0	0.17
G1.670-0.130e	SO (219.9GHz)	N	0	0	0.0 ± 0.0	0.0 ± 0.0	0.0 ± 0.0	0.18
G1.670-0.130e	SiO (217.1GHz)	N	0	0	0.0 ± 0.0	0.0 ± 0.0	0.0 ± 0.0	0.2
G1.670-0.130f	12CO (230.5GHz)	Y	1	1	3.3 ± 0.23	30.58 ± 0.22	2.77 ± 2.77	0.3
G1.670-0.130f	13CO (220.4GHz)	N	0	0	0.0 ± 0.0	0.0 ± 0.0	0.0 ± 0.0	0.19
G1.670-0.130f	C18O (219.6GHz)	N	0	0	0.0 ± 0.0	0.0 ± 0.0	0.0 ± 0.0	0.19
G1.670-0.130f	H2CO (218.2GHz)	N	0	0	0.0 ± 0.0	0.0 ± 0.0	0.0 ± 0.0	0.22
G1.670-0.130f	H2CO (218.5GHz)	N	0	0	0.0 ± 0.0	0.0 ± 0.0	0.0 ± 0.0	0.18
G1.670-0.130f	SO (219.9GHz)	N	0	0	0.0 ± 0.0	0.0 ± 0.0	0.0 ± 0.0	0.2
G1.670-0.130f	SiO (217.1GHz)	N	0	0	0.0 ± 0.0	0.0 ± 0.0	0.0 ± 0.0	0.21
G1.683-0.089a	12CO (230.5GHz)	Y	1	1	4.04 ± 0.49	57.46 ± 0.15	1.08 ± 1.08	0.48
G1.683-0.089a	13CO (220.4GHz)	N	0	0	0.0 ± 0.0	0.0 ± 0.0	0.0 ± 0.0	0.37
G1.683-0.089a	C18O (219.6GHz)	N	0	0	0.0 ± 0.0	0.0 ± 0.0	0.0 ± 0.0	0.34
G1.683-0.089a	H2CO (218.2GHz)	N	0	0	0.0 ± 0.0	0.0 ± 0.0	0.0 ± 0.0	0.38
G1.683-0.089a	H2CO (218.5GHz)	N	0	0	0.0 ± 0.0	0.0 ± 0.0	0.0 ± 0.0	0.32
G1.683-0.089a	SO (219.9GHz)	N	0	0	0.0 ± 0.0	0.0 ± 0.0	0.0 ± 0.0	0.38
G1.683-0.089a	SiO (217.1GHz)	N	0	0	0.0 ± 0.0	0.0 ± 0.0	0.0 ± 0.0	0.39
G1.683-0.089b	12CO (230.5GHz)	N	0	0	0.0 ± 0.0	0.0 ± 0.0	0.0 ± 0.0	0.86
G1.683-0.089b	13CO (220.4GHz)	N	0	0	0.0 ± 0.0	0.0 ± 0.0	0.0 ± 0.0	0.82
G1.683-0.089b	C18O (219.6GHz)	N	0	0	0.0 ± 0.0	0.0 ± 0.0	0.0 ± 0.0	0.75
G1.683-0.089b	H2CO (218.2GHz)	N	0	0	0.0 ± 0.0	0.0 ± 0.0	0.0 ± 0.0	0.72
G1.683-0.089b	H2CO (218.5GHz)	N	0	0	0.0 ± 0.0	0.0 ± 0.0	0.0 ± 0.0	0.67
G1.683-0.089b	SO (219.9GHz)	N	0	0	0.0 ± 0.0	0.0 ± 0.0	0.0 ± 0.0	0.84
G1.683-0.089b	SiO (217.1GHz)	N	0	0	0.0 ± 0.0	0.0 ± 0.0	0.0 ± 0.0	0.76
G359.484-0.132a	12CO (230.5GHz)	N	0	0	0.0 ± 0.0	0.0 ± 0.0	0.0 ± 0.0	0.31
G359.484-0.132a	13CO (220.4GHz)	Y	3	1	0.19 ± 0.03	118.41 ± 0.95	5.13 ± 5.13	0.04
G359.484-0.132a	H2CO (218.5GHz)	Y	2	1	0.96 ± 0.04	47.29 ± 0.09	1.99 ± 1.99	0.03
G359.484-0.132a	OCS (218.9GHz)	Y	3	1	0.51 ± 0.02	194.89 ± 0.09	2.25 ± 2.25	0.02
G359.484-0.132a	OCS (218.9GHz)	Y	3	2	0.11 ± 0.02	56.09 ± 0.32	1.39 ± 1.39	0.02
G359.484-0.132a	OCS (231.1GHz)	N	0	0	0.0 ± 0.0	0.0 ± 0.0	0.0 ± 0.0	0.16
G359.484-0.132a	SO (219.9GHz)	Y	3	1	0.34 ± 0.04	54.75 ± 0.22	1.81 ± 1.81	0.03
G359.484-0.132a	SiO (217.1GHz)	Y	3	1	0.13 ± 0.02	191.93 ± 0.41	2.65 ± 2.65	0.03
G359.484-0.132a	SiO (217.1GHz)	Y	3	2	0.11 ± 0.01	6.18 ± 1.24	16.43 ± 16.43	0.03
G359.484-0.132b	12CO (230.5GHz)	N	0	0	0.0 ± 0.0	0.0 ± 0.0	0.0 ± 0.0	0.74
G359.484-0.132b	13CO (220.4GHz)	N	0	0	0.0 ± 0.0	0.0 ± 0.0	0.0 ± 0.0	0.28
G359.484-0.132b	C18O (219.6GHz)	N	0	0	0.0 ± 0.0	0.0 ± 0.0	0.0 ± 0.0	0.23
G359.484-0.132b	H2CO (218.2GHz)	N	0	0	0.0 ± 0.0	0.0 ± 0.0	0.0 ± 0.0	0.26
G359.484-0.132b	H2CO (218.5GHz)	Y	1	1	0.66 ± 0.16	115.11 ± 0.62	2.22 ± 2.22	0.22
G359.484-0.132b	H2CO (218.8GHz)	Y	1	1	1.51 ± 0.63	148.99 ± 0.3	0.54 ± 0.54	0.23
G359.484-0.132b	OCS (218.9GHz)	N	0	0	0.0 ± 0.0	0.0 ± 0.0	0.0 ± 0.0	0.24
G359.484-0.132b	OCS (231.1GHz)	N	0	0	0.0 ± 0.0	0.0 ± 0.0	0.0 ± 0.0	0.35
G359.484-0.132b	SO (219.9GHz)	N	0	0	0.0 ± 0.0	0.0 ± 0.0	0.0 ± 0.0	0.22
G359.484-0.132b	SiO (217.1GHz)	N	0	0	0.0 ± 0.0	0.0 ± 0.0	0.0 ± 0.0	0.26
G359.484-0.132c	12CO (230.5GHz)	N	0	0	0.0 ± 0.0	0.0 ± 0.0	0.0 ± 0.0	0.57
G359.484-0.132c	C18O (219.6GHz)	N	0	0	0.0 ± 0.0	0.0 ± 0.0	0.0 ± 0.0	0.11
G359.484-0.132c	H2CO (218.2GHz)	N	0	0	0.0 ± 0.0	0.0 ± 0.0	0.0 ± 0.0	0.1
G359.484-0.132c	H2CO (218.5GHz)	N	0	0	0.0 ± 0.0	0.0 ± 0.0	0.0 ± 0.0	0.09
G359.484-0.132c	H2CO (218.8GHz)	N	0	0	0.0 ± 0.0	0.0 ± 0.0	0.0 ± 0.0	0.09
G359.484-0.132c	OCS (218.9GHz)	N	0	0	0.0 ± 0.0	0.0 ± 0.0	0.0 ± 0.0	0.09
G359.484-0.132c	OCS (231.1GHz)	N	0	0	0.0 ± 0.0	0.0 ± 0.0	0.0 ± 0.0	0.27
G359.484-0.132c	SO (219.9GHz)	N	0	0	0.0 ± 0.0	0.0 ± 0.0	0.0 ± 0.0	0.11
G359.484-0.132c	SiO (217.1GHz)	N	0	0	0.0 ± 0.0	0.0 ± 0.0	0.0 ± 0.0	0.09
G359.611+0.018a	12CO (230.5GHz)	Y	2	1	1.68 ± 0.18	27.64 ± 0.33	3.89 ± 3.89	0.14
G359.611+0.018a	12CO (230.5GHz)	Y	2	2	1.5 ± 0.17	27.9 ± 0.71	14.24 ± 14.24	0.14
G359.611+0.018a	13CO (220.4GHz)	Y	1	1	3.04 ± 0.07	20.08 ± 0.12	4.22 ± 4.22	0.02
G359.611+0.018a	C18O (219.6GHz)	Y	1	1	0.99 ± 0.01	19.44 ± 0.04	2.62 ± 2.62	0.01
G359.611+0.018a	H2CO (218.2GHz)	Y	2	1	1.82 ± 0.02	20.12 ± 0.04	3.23 ± 3.23	0.01
G359.611+0.018a	H2CO (218.5GHz)	Y	2	1	1.94 ± 0.02	68.67 ± 0.03	2.18 ± 2.18	0.01
G359.611+0.018a	H2CO (218.5GHz)	Y	2	2	0.97 ± 0.02	19.94 ± 0.06	2.25 ± 2.25	0.01
G359.611+0.018a	H2CO (218.8GHz)	Y	2	1	0.96 ± 0.01	19.82 ± 0.04	2.31 ± 2.31	0.01
G359.611+0.018a	OCS (218.9GHz)	Y	3	1	0.05 ± 0.01	77.51 ± 0.4	2.09 ± 2.09	0.01
G359.611+0.018a	OCS (218.9GHz)	Y	3	2	0.34 ± 0.01	19.36 ± 0.06	2.21 ± 2.21	0.01
G359.611+0.018a	OCS (231.1GHz)	Y	2	1	0.2 ± 0.01	20.11 ± 0.19	2.72 ± 2.72	0.01
G359.611+0.018a	SO (219.9GHz)	Y	3	1	0.18 ± 0.03	75.95 ± 0.33	1.91 ± 1.91	0.01
G359.611+0.018a	SO (219.9GHz)	Y	3	2	1.13 ± 0.02	20.21 ± 0.07	3.63 ± 3.63	0.01
G359.611+0.018a	SiO (217.1GHz)	N	0	0	0.0 ± 0.0	0.0 ± 0.0	0.0 ± 0.0	0.05
G359.611+0.018a	SiO (217.1GHz)	N	0	0	0.0 ± 0.0	0.0 ± 0.0	0.0 ± 0.0	0.05
G359.611+0.018b	12CO (230.5GHz)	Y	1	1	5.41 ± 0.24	11.31 ± 0.18	3.45 ± 3.45	0.41
G359.611+0.018b	13CO (220.4GHz)	Y	1	1	35.48 ± 0.2	21.26 ± 0.01	0.57 ± 0.57	0.06
G359.611+0.018b	C18O (219.6GHz)	N	0	0	0.0 ± 0.0	0.0 ± 0.0	0.0 ± 0.0	0.08
G359.611+0.018b	H2CO (218.2GHz)	Y	1	1	0.44 ± 0.02	16.78 ± 0.25	5.47 ± 5.47	0.03
G359.611+0.018b	H2CO (218.5GHz)	Y	1	1	0.21 ± 0.02	67.2 ± 0.41	4.38 ± 4.38	0.03
G359.611+0.018b	H2CO (218.8GHz)	N	0	0	0.0 ± 0.0	0.0 ± 0.0	0.0 ± 0.0	0.04
G359.611+0.018b	OCS (218.9GHz)	N	0	0	0.0 ± 0.0	0.0 ± 0.0	0.0 ± 0.0	0.03
G359.611+0.018b	OCS (231.1GHz)	N	0	0	0.0 ± 0.0	0.0 ± 0.0	0.0 ± 0.0	0.04
G359.611+0.018b	SO (219.9GHz)	Y	4	1	0.08 ± 0.03	195.66 ± 0.56	1.46 ± 1.46	0.03
G359.611+0.018b	SO (219.9GHz)	Y	4	2	0.06 ± 0.02	60.06 ± 1.14	3.31 ± 3.31	0.03

Continued on next page

Table A.1 – *Continued from previous page*

Leaf	Transition	Detected	Number of Comps	Comp.	Amplitude	Velocity	Width	RMS
G359.611+0.018b	SO (219.9GHz)	Y	4	3	0.15 ± 0.02	9.21 ± 0.42	3.12 ± 3.12	0.03
G359.611+0.018b	SiO (217.1GHz)	N	0	0	0.0 ± 0.0	0.0 ± 0.0	0.0 ± 0.0	0.06
G359.611+0.018c	12CO (230.5GHz)	N	0	0	0.0 ± 0.0	0.0 ± 0.0	0.0 ± 0.0	0.25
G359.611+0.018c	13CO (220.4GHz)	N	0	0	0.0 ± 0.0	0.0 ± 0.0	0.0 ± 0.0	6.82
G359.611+0.018c	H2CO (218.2GHz)	N	0	0	0.0 ± 0.0	0.0 ± 0.0	0.0 ± 0.0	0.04
G359.611+0.018c	H2CO (218.5GHz)	N	0	0	0.0 ± 0.0	0.0 ± 0.0	0.0 ± 0.0	0.04
G359.611+0.018c	H2CO (218.8GHz)	N	0	0	0.0 ± 0.0	0.0 ± 0.0	0.0 ± 0.0	0.04
G359.611+0.018c	OCS (218.9GHz)	N	0	0	0.0 ± 0.0	0.0 ± 0.0	0.0 ± 0.0	0.04
G359.611+0.018c	SO (219.9GHz)	N	0	0	0.0 ± 0.0	0.0 ± 0.0	0.0 ± 0.0	0.04
G359.615-0.243e	12CO (230.5GHz)	Y	1	1	2.62 ± 0.2	86.95 ± 0.82	9.17 ± 9.17	0.65
G359.615-0.243e	13CO (220.4GHz)	N	0	0	0.0 ± 0.0	0.0 ± 0.0	0.0 ± 0.0	0.24
G359.615-0.243e	H2CO (218.8GHz)	N	0	0	0.0 ± 0.0	0.0 ± 0.0	0.0 ± 0.0	0.09
G359.615-0.243e	OCS (218.9GHz)	N	0	0	0.0 ± 0.0	0.0 ± 0.0	0.0 ± 0.0	0.07
G359.615-0.243e	OCS (231.1GHz)	N	0	0	0.0 ± 0.0	0.0 ± 0.0	0.0 ± 0.0	0.1
G359.615-0.243e	SO (219.9GHz)	N	0	0	0.0 ± 0.0	0.0 ± 0.0	0.0 ± 0.0	0.07
G359.615-0.243e	SiO (217.1GHz)	N	0	0	0.0 ± 0.0	0.0 ± 0.0	0.0 ± 0.0	0.07
G359.734+0.002a	12CO (230.5GHz)	N	0	0	0.0 ± 0.0	0.0 ± 0.0	0.0 ± 0.0	0.31
G359.734+0.002a	H2CO (218.5GHz)	Y	2	1	0.41 ± 0.02	17.04 ± 0.15	2.55 ± 2.55	0.03
G359.734+0.002a	OCS (218.9GHz)	Y	1	1	0.15 ± 0.02	164.31 ± 0.43	2.9 ± 2.9	0.03
G359.734+0.002a	OCS (231.1GHz)	N	0	0	0.0 ± 0.0	0.0 ± 0.0	0.0 ± 0.0	0.06
G359.734+0.002a	SO (219.9GHz)	Y	2	1	0.4 ± 0.02	174.04 ± 0.18	2.62 ± 2.62	0.04
G359.734+0.002b	13CO (220.4GHz)	N	0	0	0.0 ± 0.0	0.0 ± 0.0	0.0 ± 0.0	0.24
G359.734+0.002b	C18O (219.6GHz)	N	0	0	0.0 ± 0.0	0.0 ± 0.0	0.0 ± 0.0	0.25
G359.734+0.002b	H2CO (218.2GHz)	N	0	0	0.0 ± 0.0	0.0 ± 0.0	0.0 ± 0.0	0.25
G359.734+0.002b	H2CO (218.5GHz)	N	0	0	0.0 ± 0.0	0.0 ± 0.0	0.0 ± 0.0	0.17
G359.734+0.002b	H2CO (218.8GHz)	N	0	0	0.0 ± 0.0	0.0 ± 0.0	0.0 ± 0.0	0.25
G359.734+0.002b	OCS (218.9GHz)	N	0	0	0.0 ± 0.0	0.0 ± 0.0	0.0 ± 0.0	0.24
G359.734+0.002b	OCS (231.1GHz)	N	0	0	0.0 ± 0.0	0.0 ± 0.0	0.0 ± 0.0	0.3
G359.734+0.002b	SO (219.9GHz)	N	0	0	0.0 ± 0.0	0.0 ± 0.0	0.0 ± 0.0	0.23
G359.734+0.002b	SiO (217.1GHz)	N	0	0	0.0 ± 0.0	0.0 ± 0.0	0.0 ± 0.0	0.17
G359.734+0.002c	H2CO (218.2GHz)	N	0	0	0.0 ± 0.0	0.0 ± 0.0	0.0 ± 0.0	0.08
G359.734+0.002c	H2CO (218.5GHz)	N	0	0	0.0 ± 0.0	0.0 ± 0.0	0.0 ± 0.0	0.06
G359.734+0.002c	H2CO (218.8GHz)	N	0	0	0.0 ± 0.0	0.0 ± 0.0	0.0 ± 0.0	0.08
G359.734+0.002c	OCS (218.9GHz)	N	0	0	0.0 ± 0.0	0.0 ± 0.0	0.0 ± 0.0	0.07
G359.734+0.002c	OCS (231.1GHz)	N	0	0	0.0 ± 0.0	0.0 ± 0.0	0.0 ± 0.0	0.09
G359.734+0.002c	SO (219.9GHz)	N	0	0	0.0 ± 0.0	0.0 ± 0.0	0.0 ± 0.0	0.08
G359.734+0.002c	SiO (217.1GHz)	N	0	0	0.0 ± 0.0	0.0 ± 0.0	0.0 ± 0.0	0.06
G359.734+0.002d	12CO (230.5GHz)	N	0	0	0.0 ± 0.0	0.0 ± 0.0	0.0 ± 0.0	0.48
G359.734+0.002d	H2CO (218.5GHz)	Y	2	1	0.16 ± 0.03	15.74 ± 0.84	3.35 ± 3.35	0.07
G359.734+0.002d	H2CO (218.8GHz)	N	0	0	0.0 ± 0.0	0.0 ± 0.0	0.0 ± 0.0	0.06
G359.734+0.002d	OCS (218.9GHz)	N	0	0	0.0 ± 0.0	0.0 ± 0.0	0.0 ± 0.0	0.07
G359.734+0.002d	OCS (231.1GHz)	N	0	0	0.0 ± 0.0	0.0 ± 0.0	0.0 ± 0.0	0.09
G359.734+0.002d	SO (219.9GHz)	Y	1	1	0.38 ± 0.04	174.18 ± 0.47	4.15 ± 4.15	0.07
G359.734+0.002d	SiO (217.1GHz)	N	0	0	0.0 ± 0.0	0.0 ± 0.0	0.0 ± 0.0	0.06
G359.734+0.002e	12CO (230.5GHz)	N	0	0	0.0 ± 0.0	0.0 ± 0.0	0.0 ± 0.0	0.42
G359.734+0.002e	13CO (220.4GHz)	Y	5	1	0.15 ± 0.04	50.68 ± 0.68	2.26 ± 2.26	0.06
G359.734+0.002e	13CO (220.4GHz)	Y	5	2	0.34 ± 0.04	8.94 ± 0.29	2.12 ± 2.12	0.06
G359.734+0.002e	C18O (219.6GHz)	N	0	0	0.0 ± 0.0	0.0 ± 0.0	0.0 ± 0.0	0.06
G359.734+0.002e	H2CO (218.2GHz)	N	0	0	0.0 ± 0.0	0.0 ± 0.0	0.0 ± 0.0	0.06
G359.734+0.002e	H2CO (218.5GHz)	N	0	0	0.0 ± 0.0	0.0 ± 0.0	0.0 ± 0.0	0.05
G359.734+0.002e	H2CO (218.8GHz)	N	0	0	0.0 ± 0.0	0.0 ± 0.0	0.0 ± 0.0	0.06
G359.734+0.002e	OCS (218.9GHz)	N	0	0	0.0 ± 0.0	0.0 ± 0.0	0.0 ± 0.0	0.06
G359.734+0.002e	OCS (231.1GHz)	N	0	0	0.0 ± 0.0	0.0 ± 0.0	0.0 ± 0.0	0.13
G359.734+0.002e	SO (219.9GHz)	N	0	0	0.0 ± 0.0	0.0 ± 0.0	0.0 ± 0.0	0.05
G359.734+0.002e	SiO (217.1GHz)	N	0	0	0.0 ± 0.0	0.0 ± 0.0	0.0 ± 0.0	0.05
G359.734+0.002f	12CO (230.5GHz)	N	0	0	0.0 ± 0.0	0.0 ± 0.0	0.0 ± 0.0	0.51
G359.734+0.002f	H2CO (218.2GHz)	N	0	0	0.0 ± 0.0	0.0 ± 0.0	0.0 ± 0.0	0.1
G359.734+0.002f	H2CO (218.5GHz)	N	0	0	0.0 ± 0.0	0.0 ± 0.0	0.0 ± 0.0	0.08
G359.734+0.002f	H2CO (218.8GHz)	N	0	0	0.0 ± 0.0	0.0 ± 0.0	0.0 ± 0.0	0.09
G359.734+0.002f	OCS (218.9GHz)	N	0	0	0.0 ± 0.0	0.0 ± 0.0	0.0 ± 0.0	0.09
G359.734+0.002f	OCS (231.1GHz)	N	0	0	0.0 ± 0.0	0.0 ± 0.0	0.0 ± 0.0	0.1
G359.734+0.002f	SO (219.9GHz)	N	0	0	0.0 ± 0.0	0.0 ± 0.0	0.0 ± 0.0	0.1
G359.734+0.002f	SiO (217.1GHz)	N	0	0	0.0 ± 0.0	0.0 ± 0.0	0.0 ± 0.0	0.07
G359.734+0.002g	12CO (230.5GHz)	N	0	0	0.0 ± 0.0	0.0 ± 0.0	0.0 ± 0.0	0.43
G359.734+0.002g	H2CO (218.2GHz)	N	0	0	0.0 ± 0.0	0.0 ± 0.0	0.0 ± 0.0	0.1
G359.734+0.002g	H2CO (218.5GHz)	Y	1	1	0.29 ± 0.05	16.52 ± 0.61	3.35 ± 3.35	0.09
G359.734+0.002g	H2CO (218.8GHz)	N	0	0	0.0 ± 0.0	0.0 ± 0.0	0.0 ± 0.0	0.09
G359.734+0.002g	OCS (218.9GHz)	N	0	0	0.0 ± 0.0	0.0 ± 0.0	0.0 ± 0.0	0.09
G359.734+0.002g	OCS (231.1GHz)	N	0	0	0.0 ± 0.0	0.0 ± 0.0	0.0 ± 0.0	0.12
G359.734+0.002g	SO (219.9GHz)	N	0	0	0.0 ± 0.0	0.0 ± 0.0	0.0 ± 0.0	0.11
G359.734+0.002g	SiO (217.1GHz)	N	0	0	0.0 ± 0.0	0.0 ± 0.0	0.0 ± 0.0	0.09
G359.734+0.002h	13CO (220.4GHz)	N	0	0	0.0 ± 0.0	0.0 ± 0.0	0.0 ± 0.0	0.11
G359.734+0.002h	C18O (219.6GHz)	N	0	0	0.0 ± 0.0	0.0 ± 0.0	0.0 ± 0.0	0.1
G359.734+0.002h	H2CO (218.2GHz)	N	0	0	0.0 ± 0.0	0.0 ± 0.0	0.0 ± 0.0	0.11
G359.734+0.002h	H2CO (218.5GHz)	N	0	0	0.0 ± 0.0	0.0 ± 0.0	0.0 ± 0.0	0.09
G359.734+0.002h	H2CO (218.8GHz)	N	0	0	0.0 ± 0.0	0.0 ± 0.0	0.0 ± 0.0	0.11
G359.734+0.002h	OCS (218.9GHz)	N	0	0	0.0 ± 0.0	0.0 ± 0.0	0.0 ± 0.0	0.1
G359.734+0.002h	OCS (231.1GHz)	N	0	0	0.0 ± 0.0	0.0 ± 0.0	0.0 ± 0.0	0.11
G359.734+0.002h	SO (219.9GHz)	Y	1	1	0.53 ± 0.08	173.45 ± 0.37	2.25 ± 2.25	0.11
G359.734+0.002h	SiO (217.1GHz)	N	0	0	0.0 ± 0.0	0.0 ± 0.0	0.0 ± 0.0	0.09
G359.863-0.069a	13CO (220.4GHz)	N	0	0	0.0 ± 0.0	0.0 ± 0.0	0.0 ± 0.0	0.39
G359.863-0.069a	C18O (219.6GHz)	N	0	0	0.0 ± 0.0	0.0 ± 0.0	0.0 ± 0.0	0.3
G359.863-0.069a	H2CO (218.2GHz)	N	0	0	0.0 ± 0.0	0.0 ± 0.0	0.0 ± 0.0	0.32
G359.863-0.069a	H2CO (218.5GHz)	N	0	0	0.0 ± 0.0	0.0 ± 0.0	0.0 ± 0.0	0.31
G359.863-0.069a	H2CO (218.8GHz)	N	0	0	0.0 ± 0.0	0.0 ± 0.0	0.0 ± 0.0	0.3
G359.863-0.069a	OCS (218.9GHz)	N	0	0	0.0 ± 0.0	0.0 ± 0.0	0.0 ± 0.0	0.29
G359.863-0.069a	OCS (231.1GHz)	N	0	0	0.0 ± 0.0	0.0 ± 0.0	0.0 ± 0.0	0.31

Continued on next page

Table A.1 – *Continued from previous page*

Leaf	Transition	Detected	Number of Comps	Comp.	Amplitude	Velocity	Width	RMS
G359.863-0.069a	SO (219.9GHz)	N	0	0	0.0 ± 0.0	0.0 ± 0.0	0.0 ± 0.0	0.28
G359.863-0.069a	SiO (217.1GHz)	N	0	0	0.0 ± 0.0	0.0 ± 0.0	0.0 ± 0.0	0.25
G359.863-0.069b	12CO (230.5GHz)	Y	1	1	4.81 ± 0.41	58.8 ± 0.21	2.09 ± 2.09	0.52
G359.863-0.069b	13CO (220.4GHz)	Y	5	1	3.55 ± 0.08	59.44 ± 0.05	2.07 ± 2.07	0.1
G359.863-0.069b	C18O (219.6GHz)	Y	1	1	0.32 ± 0.05	60.01 ± 0.38	2.1 ± 2.1	0.07
G359.863-0.069b	H2CO (218.5GHz)	N	0	0	0.0 ± 0.0	0.0 ± 0.0	0.0 ± 0.0	0.07
G359.863-0.069b	H2CO (218.8GHz)	Y	1	1	0.25 ± 0.06	193.67 ± 0.37	1.21 ± 1.21	0.07
G359.863-0.069b	OCS (218.9GHz)	Y	2	1	0.21 ± 0.03	133.94 ± 0.69	3.54 ± 3.54	0.06
G359.863-0.069b	OCS (231.1GHz)	N	0	0	0.0 ± 0.0	0.0 ± 0.0	0.0 ± 0.0	0.06
G359.863-0.069b	SiO (217.1GHz)	N	0	0	0.0 ± 0.0	0.0 ± 0.0	0.0 ± 0.0	0.07
G359.863-0.069c	12CO (230.5GHz)	N	0	0	0.0 ± 0.0	0.0 ± 0.0	0.0 ± 0.0	0.82
G359.863-0.069c	13CO (220.4GHz)	Y	2	1	2.93 ± 0.11	59.97 ± 0.06	1.33 ± 1.33	0.11
G359.863-0.069c	C18O (219.6GHz)	Y	1	1	0.35 ± 0.06	60.21 ± 0.33	1.74 ± 1.74	0.08
G359.863-0.069c	H2CO (218.5GHz)	Y	2	1	0.08 ± 0.02	150.27 ± 3.61	11.99 ± 11.99	0.07
G359.863-0.069c	H2CO (218.8GHz)	N	0	0	0.0 ± 0.0	0.0 ± 0.0	0.0 ± 0.0	0.07
G359.863-0.069c	OCS (218.9GHz)	N	0	0	0.0 ± 0.0	0.0 ± 0.0	0.0 ± 0.0	0.07
G359.863-0.069c	OCS (231.1GHz)	N	0	0	0.0 ± 0.0	0.0 ± 0.0	0.0 ± 0.0	0.15
G359.863-0.069c	SO (219.9GHz)	N	0	0	0.0 ± 0.0	0.0 ± 0.0	0.0 ± 0.0	0.06
G359.863-0.069c	SiO (217.1GHz)	N	0	0	0.0 ± 0.0	0.0 ± 0.0	0.0 ± 0.0	0.07
G359.865+0.022a	12CO (230.5GHz)	Y	1	1	9.94 ± 0.56	68.4 ± 0.39	6.04 ± 6.04	1.34
G359.865+0.022a	C18O (219.6GHz)	N	0	0	0.0 ± 0.0	0.0 ± 0.0	0.0 ± 0.0	0.28
G359.865+0.022a	H2CO (218.2GHz)	N	0	0	0.0 ± 0.0	0.0 ± 0.0	0.0 ± 0.0	0.3
G359.865+0.022a	H2CO (218.5GHz)	N	0	0	0.0 ± 0.0	0.0 ± 0.0	0.0 ± 0.0	0.25
G359.865+0.022a	H2CO (218.8GHz)	N	0	0	0.0 ± 0.0	0.0 ± 0.0	0.0 ± 0.0	0.28
G359.865+0.022a	OCS (218.9GHz)	N	0	0	0.0 ± 0.0	0.0 ± 0.0	0.0 ± 0.0	0.27
G359.865+0.022a	OCS (231.1GHz)	N	0	0	0.0 ± 0.0	0.0 ± 0.0	0.0 ± 0.0	0.42
G359.865+0.022a	SO (219.9GHz)	Y	1	1	1.29 ± 0.33	90.34 ± 0.26	0.81 ± 0.81	0.3
G359.865+0.022a	SiO (217.1GHz)	N	0	0	0.0 ± 0.0	0.0 ± 0.0	0.0 ± 0.0	0.22
G359.865+0.022b	12CO (230.5GHz)	N	0	0	0.0 ± 0.0	0.0 ± 0.0	0.0 ± 0.0	0.38
G359.865+0.022b	13CO (220.4GHz)	Y	4	1	0.93 ± 0.08	53.36 ± 0.44	4.42 ± 4.42	0.15
G359.865+0.022b	H2CO (218.2GHz)	Y	1	1	0.33 ± 0.06	134.55 ± 0.29	1.31 ± 1.31	0.07
G359.865+0.022b	H2CO (218.5GHz)	N	0	0	0.0 ± 0.0	0.0 ± 0.0	0.0 ± 0.0	0.06
G359.865+0.022b	H2CO (218.8GHz)	N	0	0	0.0 ± 0.0	0.0 ± 0.0	0.0 ± 0.0	0.07
G359.865+0.022b	OCS (218.9GHz)	N	0	0	0.0 ± 0.0	0.0 ± 0.0	0.0 ± 0.0	0.07
G359.865+0.022b	OCS (231.1GHz)	N	0	0	0.0 ± 0.0	0.0 ± 0.0	0.0 ± 0.0	0.1
G359.865+0.022b	SO (219.9GHz)	N	0	0	0.0 ± 0.0	0.0 ± 0.0	0.0 ± 0.0	0.07
G359.865+0.022b	SiO (217.1GHz)	N	0	0	0.0 ± 0.0	0.0 ± 0.0	0.0 ± 0.0	0.06
G359.889-0.093a	12CO (230.5GHz)	Y	3	1	1.75 ± 0.41	64.07 ± 0.84	3.1 ± 3.1	0.42
G359.889-0.093a	12CO (230.5GHz)	Y	3	2	2.49 ± 0.35	18.96 ± 0.69	4.31 ± 4.31	0.42
G359.889-0.093a	13CO (220.4GHz)	Y	3	1	0.61 ± 0.07	39.27 ± 0.39	2.92 ± 2.92	0.1
G359.889-0.093a	13CO (220.4GHz)	Y	3	2	1.84 ± 0.08	13.91 ± 0.11	2.19 ± 2.19	0.1
G359.889-0.093a	C18O (219.6GHz)	Y	1	1	1.4 ± 0.04	11.84 ± 0.05	1.39 ± 1.39	0.04
G359.889-0.093a	H2CO (218.2GHz)	Y	2	1	0.5 ± 0.04	16.24 ± 0.19	2.19 ± 2.19	0.05
G359.889-0.093a	H2CO (218.5GHz)	Y	2	1	1.34 ± 0.04	61.09 ± 0.07	2.13 ± 2.13	0.04
G359.889-0.093a	H2CO (218.5GHz)	Y	2	2	0.27 ± 0.04	14.29 ± 0.35	2.33 ± 2.33	0.04
G359.889-0.093a	H2CO (218.8GHz)	Y	1	1	0.25 ± 0.03	14.8 ± 0.38	3.02 ± 3.02	0.05
G359.889-0.093a	OCS (218.9GHz)	N	0	0	0.0 ± 0.0	0.0 ± 0.0	0.0 ± 0.0	0.05
G359.889-0.093a	OCS (231.1GHz)	N	0	0	0.0 ± 0.0	0.0 ± 0.0	0.0 ± 0.0	0.06
G359.889-0.093a	SO (219.9GHz)	Y	2	1	0.76 ± 0.04	13.28 ± 0.13	2.39 ± 2.39	0.05
G359.889-0.093a	SiO (217.1GHz)	Y	2	1	0.24 ± 0.02	16.14 ± 0.49	4.96 ± 4.96	0.04
G359.889-0.093b	12CO (230.5GHz)	N	0	0	0.0 ± 0.0	0.0 ± 0.0	0.0 ± 0.0	1.75
G359.889-0.093b	13CO (220.4GHz)	Y	4	1	1.42 ± 0.14	45.13 ± 0.09	0.72 ± 0.72	0.1
G359.889-0.093b	13CO (220.4GHz)	Y	4	2	1.01 ± 0.07	33.78 ± 0.25	2.76 ± 2.76	0.1
G359.889-0.093b	13CO (220.4GHz)	Y	4	3	0.69 ± 0.07	23.72 ± 0.36	2.71 ± 2.71	0.1
G359.889-0.093b	13CO (220.4GHz)	Y	4	4	0.7 ± 0.08	2.97 ± 0.29	2.23 ± 2.23	0.1
G359.889-0.093b	C18O (219.6GHz)	N	0	0	0.0 ± 0.0	0.0 ± 0.0	0.0 ± 0.0	0.07
G359.889-0.093b	H2CO (218.2GHz)	N	0	0	0.0 ± 0.0	0.0 ± 0.0	0.0 ± 0.0	0.1
G359.889-0.093b	H2CO (218.5GHz)	Y	1	1	1.84 ± 0.06	73.41 ± 0.07	1.89 ± 1.89	0.08
G359.889-0.093b	H2CO (218.8GHz)	N	0	0	0.0 ± 0.0	0.0 ± 0.0	0.0 ± 0.0	0.09
G359.889-0.093b	OCS (218.9GHz)	N	0	0	0.0 ± 0.0	0.0 ± 0.0	0.0 ± 0.0	0.08
G359.889-0.093b	OCS (231.1GHz)	N	0	0	0.0 ± 0.0	0.0 ± 0.0	0.0 ± 0.0	0.11
G359.889-0.093b	SO (219.9GHz)	Y	1	1	0.56 ± 0.06	24.54 ± 0.23	1.81 ± 1.81	0.08
G359.889-0.093b	SiO (217.1GHz)	Y	2	1	0.25 ± 0.07	111.03 ± 0.3	0.87 ± 0.87	0.07
G359.889-0.093b	SiO (217.1GHz)	Y	2	2	0.24 ± 0.04	23.94 ± 0.58	2.92 ± 2.92	0.07
G359.889-0.093c	12CO (230.5GHz)	Y	3	1	2.97 ± 0.23	67.34 ± 0.14	1.49 ± 1.49	0.18
G359.889-0.093c	12CO (230.5GHz)	Y	3	2	5.39 ± 0.29	22.98 ± 0.06	0.99 ± 0.99	0.18
G359.889-0.093c	13CO (220.4GHz)	Y	1	1	3.41 ± 0.06	12.63 ± 0.05	2.66 ± 2.66	0.09
G359.889-0.093c	C18O (219.6GHz)	Y	1	1	0.81 ± 0.02	12.69 ± 0.06	1.79 ± 1.79	0.03
G359.889-0.093c	H2CO (218.2GHz)	Y	1	1	0.24 ± 0.03	6.5 ± 0.16	1.03 ± 1.03	0.03
G359.889-0.093c	H2CO (218.5GHz)	Y	2	1	0.3 ± 0.03	58.29 ± 0.17	1.67 ± 1.67	0.03
G359.889-0.093c	H2CO (218.5GHz)	Y	2	2	0.16 ± 0.03	10.78 ± 0.3	1.59 ± 1.59	0.03
G359.889-0.093c	H2CO (218.8GHz)	Y	1	1	0.16 ± 0.03	9.78 ± 0.29	1.3 ± 1.3	0.04
G359.889-0.093c	OCS (218.9GHz)	N	0	0	0.0 ± 0.0	0.0 ± 0.0	0.0 ± 0.0	0.03
G359.889-0.093c	OCS (231.1GHz)	N	0	0	0.0 ± 0.0	0.0 ± 0.0	0.0 ± 0.0	0.03
G359.889-0.093c	SO (219.9GHz)	N	0	0	0.0 ± 0.0	0.0 ± 0.0	0.0 ± 0.0	0.03
G359.889-0.093c	SiO (217.1GHz)	N	0	0	0.0 ± 0.0	0.0 ± 0.0	0.0 ± 0.0	0.03
G359.889-0.093d	12CO (230.5GHz)	Y	1	1	5.52 ± 0.46	67.39 ± 0.19	1.94 ± 1.94	0.63
G359.889-0.093d	13CO (220.4GHz)	Y	1	1	0.73 ± 0.07	7.66 ± 0.2	1.79 ± 1.79	0.09
G359.889-0.093d	C18O (219.6GHz)	N	0	0	0.0 ± 0.0	0.0 ± 0.0	0.0 ± 0.0	0.03
G359.889-0.093d	H2CO (218.2GHz)	Y	2	1	0.16 ± 0.04	165.14 ± 0.33	0.57 ± 0.57	0.03
G359.889-0.093d	H2CO (218.2GHz)	Y	2	2	0.27 ± 0.04	16.99 ± 0.14	0.82 ± 0.82	0.03
G359.889-0.093d	H2CO (218.5GHz)	Y	1	1	0.16 ± 0.02	60.56 ± 0.74	5.28 ± 5.28	0.04
G359.889-0.093d	H2CO (218.8GHz)	N	0	0	0.0 ± 0.0	0.0 ± 0.0	0.0 ± 0.0	0.04
G359.889-0.093d	OCS (218.9GHz)	N	0	0	0.0 ± 0.0	0.0 ± 0.0	0.0 ± 0.0	0.04
G359.889-0.093d	OCS (231.1GHz)	N	0	0	0.0 ± 0.0	0.0 ± 0.0	0.0 ± 0.0	0.05
G359.889-0.093d	SO (219.9GHz)	N	0	0	0.0 ± 0.0	0.0 ± 0.0	0.0 ± 0.0	0.04
G359.889-0.093d	SiO (217.1GHz)	N	0	0	0.0 ± 0.0	0.0 ± 0.0	0.0 ± 0.0	0.04

Continued on next page

Table A.1 – *Continued from previous page*

Leaf	Transition	Detected	Number of Comps	Comp.	Amplitude	Velocity	Width	RMS
G359.889-0.093e	12CO (230.5GHz)	N	0	0	0.0 ± 0.0	0.0 ± 0.0	0.0 ± 0.0	0.57
G359.889-0.093e	13CO (220.4GHz)	Y	4	1	0.58 ± 0.04	37.4 ± 0.6	6.4 ± 6.4	0.08
G359.889-0.093e	13CO (220.4GHz)	Y	4	2	0.41 ± 0.12	27.2 ± 0.3	0.68 ± 0.68	0.08
G359.889-0.093e	13CO (220.4GHz)	Y	4	3	0.92 ± 0.07	16.18 ± 0.22	2.55 ± 2.55	0.08
G359.889-0.093e	13CO (220.4GHz)	Y	4	4	0.55 ± 0.07	0.49 ± 0.37	2.72 ± 2.72	0.08
G359.889-0.093e	C18O (219.6GHz)	Y	1	1	0.48 ± 0.05	15.56 ± 0.17	1.29 ± 1.29	0.06
G359.889-0.093e	H2CO (218.2GHz)	Y	1	1	0.4 ± 0.03	0.51 ± 0.34	3.52 ± 3.52	0.06
G359.889-0.093e	H2CO (218.5GHz)	Y	1	1	0.71 ± 0.05	63.62 ± 0.13	1.49 ± 1.49	0.06
G359.889-0.093e	H2CO (218.8GHz)	Y	2	1	0.31 ± 0.06	15.27 ± 0.27	1.15 ± 1.15	0.07
G359.889-0.093e	H2CO (218.8GHz)	Y	2	2	0.28 ± 0.04	1.08 ± 0.43	2.36 ± 2.36	0.07
G359.889-0.093e	OCS (218.9GHz)	N	0	0	0.0 ± 0.0	0.0 ± 0.0	0.0 ± 0.0	0.06
G359.889-0.093e	OCS (231.1GHz)	N	0	0	0.0 ± 0.0	0.0 ± 0.0	0.0 ± 0.0	0.13
G359.889-0.093e	SO (219.9GHz)	Y	1	1	0.31 ± 0.06	14.33 ± 0.24	1.12 ± 1.12	0.05
G359.889-0.093e	SiO (217.1GHz)	N	0	0	0.0 ± 0.0	0.0 ± 0.0	0.0 ± 0.0	0.06
G359.889-0.093f	12CO (230.5GHz)	N	0	0	0.0 ± 0.0	0.0 ± 0.0	0.0 ± 0.0	2.17
G359.889-0.093f	13CO (220.4GHz)	Y	2	1	0.65 ± 0.08	27.9 ± 0.75	5.21 ± 5.21	0.18
G359.889-0.093f	H2CO (218.2GHz)	Y	2	1	0.83 ± 0.05	11.91 ± 0.21	3.01 ± 3.01	0.08
G359.889-0.093f	H2CO (218.5GHz)	Y	3	1	1.32 ± 0.05	55.7 ± 0.15	3.7 ± 3.7	0.09
G359.889-0.093f	H2CO (218.5GHz)	Y	3	2	0.47 ± 0.06	44.2 ± 0.31	1.91 ± 1.91	0.09
G359.889-0.093f	H2CO (218.5GHz)	Y	3	3	0.25 ± 0.03	5.93 ± 1.02	6.56 ± 6.56	0.09
G359.889-0.093f	H2CO (218.8GHz)	Y	2	1	0.47 ± 0.04	8.89 ± 0.41	3.89 ± 3.89	0.09
G359.889-0.093f	OCS (218.9GHz)	N	0	0	0.0 ± 0.0	0.0 ± 0.0	0.0 ± 0.0	0.09
G359.889-0.093f	OCS (231.1GHz)	N	0	0	0.0 ± 0.0	0.0 ± 0.0	0.0 ± 0.0	0.09
G359.889-0.093f	SO (219.9GHz)	Y	1	1	0.35 ± 0.04	4.25 ± 0.67	5.1 ± 5.1	0.09
G359.889-0.093f	SiO (217.1GHz)	Y	1	1	0.48 ± 0.03	4.85 ± 0.45	6.03 ± 6.03	0.08
G359.889-0.093g	12CO (230.5GHz)	N	0	0	0.0 ± 0.0	0.0 ± 0.0	0.0 ± 0.0	3.12
G359.889-0.093g	13CO (220.4GHz)	N	0	0	0.0 ± 0.0	0.0 ± 0.0	0.0 ± 0.0	0.13
G359.889-0.093g	C18O (219.6GHz)	N	0	0	0.0 ± 0.0	0.0 ± 0.0	0.0 ± 0.0	0.08
G359.889-0.093g	H2CO (218.2GHz)	Y	1	1	0.55 ± 0.08	29.27 ± 0.36	2.14 ± 2.14	0.11
G359.889-0.093g	H2CO (218.5GHz)	Y	1	1	1.37 ± 0.07	72.72 ± 0.15	2.65 ± 2.65	0.09
G359.889-0.093g	H2CO (218.8GHz)	N	0	0	0.0 ± 0.0	0.0 ± 0.0	0.0 ± 0.0	0.12
G359.889-0.093g	OCS (218.9GHz)	Y	2	1	0.44 ± 0.1	19.87 ± 0.24	0.92 ± 0.92	0.1
G359.889-0.093g	OCS (231.1GHz)	N	0	0	0.0 ± 0.0	0.0 ± 0.0	0.0 ± 0.0	0.14
G359.889-0.093g	SO (219.9GHz)	N	0	0	0.0 ± 0.0	0.0 ± 0.0	0.0 ± 0.0	0.08
G359.889-0.093g	SiO (217.1GHz)	N	0	0	0.0 ± 0.0	0.0 ± 0.0	0.0 ± 0.0	0.07
G359.889-0.093h	12CO (230.5GHz)	N	0	0	0.0 ± 0.0	0.0 ± 0.0	0.0 ± 0.0	1.01
G359.889-0.093h	13CO (220.4GHz)	Y	1	1	0.93 ± 0.14	2.02 ± 0.17	0.99 ± 0.99	0.13
G359.889-0.093h	C18O (219.6GHz)	Y	1	1	0.29 ± 0.05	2.86 ± 0.21	0.95 ± 0.95	0.05
G359.889-0.093h	H2CO (218.2GHz)	Y	1	1	0.45 ± 0.05	12.39 ± 0.14	1.03 ± 1.03	0.05
G359.889-0.093h	H2CO (218.5GHz)	Y	1	1	0.53 ± 0.04	59.14 ± 0.16	1.69 ± 1.69	0.05
G359.889-0.093h	H2CO (218.8GHz)	N	0	0	0.0 ± 0.0	0.0 ± 0.0	0.0 ± 0.0	0.06
G359.889-0.093h	OCS (218.9GHz)	N	0	0	0.0 ± 0.0	0.0 ± 0.0	0.0 ± 0.0	0.06
G359.889-0.093h	OCS (231.1GHz)	N	0	0	0.0 ± 0.0	0.0 ± 0.0	0.0 ± 0.0	0.08
G359.889-0.093h	SO (219.9GHz)	N	0	0	0.0 ± 0.0	0.0 ± 0.0	0.0 ± 0.0	0.05
G359.889-0.093h	SiO (217.1GHz)	Y	1	1	0.19 ± 0.03	11.28 ± 0.62	3.61 ± 3.61	0.05
G359.889-0.093i	12CO (230.5GHz)	N	0	0	0.0 ± 0.0	0.0 ± 0.0	0.0 ± 0.0	1.07
G359.889-0.093i	13CO (220.4GHz)	N	0	0	0.0 ± 0.0	0.0 ± 0.0	0.0 ± 0.0	0.19
G359.889-0.093i	C18O (219.6GHz)	N	0	0	0.0 ± 0.0	0.0 ± 0.0	0.0 ± 0.0	0.06
G359.889-0.093i	H2CO (218.2GHz)	N	0	0	0.0 ± 0.0	0.0 ± 0.0	0.0 ± 0.0	0.09
G359.889-0.093i	H2CO (218.5GHz)	Y	2	1	0.97 ± 0.04	71.19 ± 0.16	3.34 ± 3.34	0.07
G359.889-0.093i	H2CO (218.5GHz)	Y	2	2	0.21 ± 0.04	23.33 ± 0.79	4.01 ± 4.01	0.07
G359.889-0.093i	H2CO (218.8GHz)	Y	2	1	0.21 ± 0.05	25.25 ± 0.88	3.37 ± 3.37	0.09
G359.889-0.093i	OCS (218.9GHz)	Y	1	1	0.21 ± 0.04	23.98 ± 0.75	3.2 ± 3.2	0.08
G359.889-0.093i	SO (219.9GHz)	Y	1	1	0.31 ± 0.04	23.35 ± 0.45	2.97 ± 2.97	0.07
G359.889-0.093i	SiO (217.1GHz)	Y	1	1	0.22 ± 0.03	22.56 ± 0.64	3.65 ± 3.65	0.06
G359.889-0.093j	13CO (220.4GHz)	Y	2	1	0.81 ± 0.1	18.66 ± 0.59	3.97 ± 3.97	0.17
G359.889-0.093j	C18O (219.6GHz)	N	0	0	0.0 ± 0.0	0.0 ± 0.0	0.0 ± 0.0	0.06
G359.889-0.093j	H2CO (218.5GHz)	Y	2	1	1.4 ± 0.05	51.89 ± 0.11	2.66 ± 2.66	0.07
G359.889-0.093j	H2CO (218.5GHz)	Y	2	2	0.36 ± 0.05	2.33 ± 0.39	2.29 ± 2.29	0.07
G359.889-0.093j	H2CO (218.8GHz)	N	0	0	0.0 ± 0.0	0.0 ± 0.0	0.0 ± 0.0	0.08
G359.889-0.093j	OCS (218.9GHz)	N	0	0	0.0 ± 0.0	0.0 ± 0.0	0.0 ± 0.0	0.08
G359.889-0.093j	OCS (231.1GHz)	N	0	0	0.0 ± 0.0	0.0 ± 0.0	0.0 ± 0.0	0.08
G359.889-0.093j	SO (219.9GHz)	Y	1	1	0.48 ± 0.06	3.56 ± 0.25	1.73 ± 1.73	0.07
G359.889-0.093k	12CO (230.5GHz)	Y	2	1	25.13 ± 0.81	23.91 ± 0.06	1.59 ± 1.59	0.46
G359.889-0.093k	12CO (230.5GHz)	Y	2	2	5.23 ± 0.62	7.52 ± 0.37	2.66 ± 2.66	0.46
G359.889-0.093k	13CO (220.4GHz)	Y	3	1	1.48 ± 0.21	56.3 ± 0.1	0.69 ± 0.69	0.11
G359.889-0.093k	13CO (220.4GHz)	Y	3	2	1.65 ± 0.31	25.68 ± 0.1	0.62 ± 0.62	0.11
G359.889-0.093k	13CO (220.4GHz)	Y	3	3	2.1 ± 0.08	8.02 ± 0.13	2.87 ± 2.87	0.11
G359.889-0.093k	C18O (219.6GHz)	N	0	0	0.0 ± 0.0	0.0 ± 0.0	0.0 ± 0.0	0.06
G359.889-0.093k	H2CO (218.2GHz)	Y	2	1	0.43 ± 0.03	17.82 ± 0.66	6.29 ± 6.29	0.07
G359.889-0.093k	H2CO (218.2GHz)	Y	2	2	0.95 ± 0.05	5.39 ± 0.15	2.38 ± 2.38	0.07
G359.889-0.093k	H2CO (218.5GHz)	Y	2	1	0.38 ± 0.05	72.82 ± 0.35	2.37 ± 2.37	0.07
G359.889-0.093k	H2CO (218.5GHz)	Y	2	2	0.42 ± 0.04	57.73 ± 0.42	4.26 ± 4.26	0.07
G359.889-0.093k	H2CO (218.8GHz)	N	0	0	0.0 ± 0.0	0.0 ± 0.0	0.0 ± 0.0	0.08
G359.889-0.093k	OCS (218.9GHz)	N	0	0	0.0 ± 0.0	0.0 ± 0.0	0.0 ± 0.0	0.08
G359.889-0.093k	OCS (231.1GHz)	N	0	0	0.0 ± 0.0	0.0 ± 0.0	0.0 ± 0.0	0.09
G359.889-0.093k	SO (219.9GHz)	Y	2	1	0.43 ± 0.06	24.62 ± 0.27	1.65 ± 1.65	0.07
G359.889-0.093k	SO (219.9GHz)	Y	2	2	0.31 ± 0.04	7.78 ± 0.59	4.27 ± 4.27	0.07
G359.889-0.093k	SiO (217.1GHz)	Y	1	1	0.25 ± 0.02	13.19 ± 0.98	8.66 ± 8.66	0.07
G359.889-0.093l	12CO (230.5GHz)	N	0	0	0.0 ± 0.0	0.0 ± 0.0	0.0 ± 0.0	0.55
G359.889-0.093l	13CO (220.4GHz)	N	0	0	0.0 ± 0.0	0.0 ± 0.0	0.0 ± 0.0	0.17
G359.889-0.093l	C18O (219.6GHz)	Y	1	1	0.53 ± 0.06	3.44 ± 0.1	0.86 ± 0.86	0.05
G359.889-0.093l	H2CO (218.2GHz)	Y	1	1	1.11 ± 0.04	10.11 ± 0.08	1.72 ± 1.72	0.04
G359.889-0.093l	H2CO (218.5GHz)	Y	2	1	1.26 ± 0.04	56.78 ± 0.08	2.16 ± 2.16	0.05
G359.889-0.093l	H2CO (218.5GHz)	Y	2	2	0.36 ± 0.04	8.68 ± 0.3	2.49 ± 2.49	0.05
G359.889-0.093l	H2CO (218.8GHz)	Y	1	1	0.31 ± 0.03	7.67 ± 0.39	3.04 ± 3.04	0.06
G359.889-0.093l	OCS (218.9GHz)	N	0	0	0.0 ± 0.0	0.0 ± 0.0	0.0 ± 0.0	0.05

Continued on next page

Table A.1 – *Continued from previous page*

Leaf	Transition	Detected	Number of Comps	Comp.	Amplitude	Velocity	Width	RMS
G359.889-0.093l	OCS (231.1GHz)	N	0	0	0.0 ± 0.0	0.0 ± 0.0	0.0 ± 0.0	0.1
G359.889-0.093l	SO (219.9GHz)	Y	1	1	0.54 ± 0.05	6.72 ± 0.13	1.15 ± 1.15	0.05
G359.889-0.093l	SiO (217.1GHz)	Y	1	1	0.29 ± 0.04	7.88 ± 0.28	1.94 ± 1.94	0.05
G359.889-0.093m	12CO (230.5GHz)	N	0	0	0.0 ± 0.0	0.0 ± 0.0	0.0 ± 0.0	0.62
G359.889-0.093m	13CO (220.4GHz)	N	0	0	0.0 ± 0.0	0.0 ± 0.0	0.0 ± 0.0	0.12
G359.889-0.093m	C18O (219.6GHz)	N	0	0	0.0 ± 0.0	0.0 ± 0.0	0.0 ± 0.0	0.06
G359.889-0.093m	H2CO (218.2GHz)	Y	3	1	0.19 ± 0.05	1.12 ± 0.51	1.45 ± 1.45	0.06
G359.889-0.093m	H2CO (218.5GHz)	Y	1	1	0.51 ± 0.06	59.28 ± 0.22	1.72 ± 1.72	0.07
G359.889-0.093m	H2CO (218.8GHz)	Y	1	1	0.29 ± 0.06	10.81 ± 0.46	1.91 ± 1.91	0.09
G359.889-0.093m	OCS (218.9GHz)	N	0	0	0.0 ± 0.0	0.0 ± 0.0	0.0 ± 0.0	0.08
G359.889-0.093m	OCS (231.1GHz)	N	0	0	0.0 ± 0.0	0.0 ± 0.0	0.0 ± 0.0	0.1
G359.889-0.093m	SO (219.9GHz)	N	0	0	0.0 ± 0.0	0.0 ± 0.0	0.0 ± 0.0	0.07
G359.889-0.093m	SiO (217.1GHz)	N	0	0	0.0 ± 0.0	0.0 ± 0.0	0.0 ± 0.0	0.07
G359.889-0.093n	12CO (230.5GHz)	N	0	0	0.0 ± 0.0	0.0 ± 0.0	0.0 ± 0.0	1.62
G359.889-0.093n	13CO (220.4GHz)	N	0	0	0.0 ± 0.0	0.0 ± 0.0	0.0 ± 0.0	0.13
G359.889-0.093n	C18O (219.6GHz)	N	0	0	0.0 ± 0.0	0.0 ± 0.0	0.0 ± 0.0	0.08
G359.889-0.093n	H2CO (218.2GHz)	Y	2	1	0.4 ± 0.06	25.55 ± 0.26	1.38 ± 1.38	0.07
G359.889-0.093n	H2CO (218.2GHz)	Y	2	2	0.43 ± 0.06	19.82 ± 0.25	1.43 ± 1.43	0.07
G359.889-0.093n	H2CO (218.5GHz)	Y	1	1	0.88 ± 0.06	71.69 ± 0.15	1.9 ± 1.9	0.08
G359.889-0.093n	H2CO (218.8GHz)	N	0	0	0.0 ± 0.0	0.0 ± 0.0	0.0 ± 0.0	0.09
G359.889-0.093n	OCS (218.9GHz)	N	0	0	0.0 ± 0.0	0.0 ± 0.0	0.0 ± 0.0	0.08
G359.889-0.093n	OCS (231.1GHz)	N	0	0	0.0 ± 0.0	0.0 ± 0.0	0.0 ± 0.0	0.13
G359.889-0.093n	SO (219.9GHz)	Y	2	1	0.31 ± 0.08	78.76 ± 0.31	1.06 ± 1.06	0.08
G359.889-0.093n	SO (219.9GHz)	Y	2	2	0.37 ± 0.06	23.09 ± 0.35	1.93 ± 1.93	0.08
G359.889-0.093n	SiO (217.1GHz)	N	0	0	0.0 ± 0.0	0.0 ± 0.0	0.0 ± 0.0	0.07
G359.889-0.093o	12CO (230.5GHz)	Y	2	1	10.43 ± 0.52	67.72 ± 0.09	1.56 ± 1.56	0.5
G359.889-0.093o	12CO (230.5GHz)	Y	2	2	0.78 ± 0.16	51.87 ± 4.43	17.57 ± 17.57	0.5
G359.889-0.093o	13CO (220.4GHz)	Y	3	1	0.41 ± 0.06	68.17 ± 0.35	2.13 ± 2.13	0.08
G359.889-0.093o	13CO (220.4GHz)	Y	3	2	0.59 ± 0.06	24.49 ± 0.24	2.01 ± 2.01	0.08
G359.889-0.093o	13CO (220.4GHz)	Y	3	3	0.86 ± 0.07	6.21 ± 0.14	1.36 ± 1.36	0.08
G359.889-0.093o	C18O (219.6GHz)	N	0	0	0.0 ± 0.0	0.0 ± 0.0	0.0 ± 0.0	0.05
G359.889-0.093o	H2CO (218.2GHz)	Y	1	1	0.46 ± 0.04	14.81 ± 0.14	1.43 ± 1.43	0.05
G359.889-0.093o	H2CO (218.5GHz)	Y	1	1	0.31 ± 0.03	68.26 ± 0.35	2.68 ± 2.68	0.06
G359.889-0.093o	H2CO (218.8GHz)	N	0	0	0.0 ± 0.0	0.0 ± 0.0	0.0 ± 0.0	0.06
G359.889-0.093o	OCS (218.9GHz)	N	0	0	0.0 ± 0.0	0.0 ± 0.0	0.0 ± 0.0	0.05
G359.889-0.093o	OCS (231.1GHz)	Y	1	1	0.31 ± 0.06	64.21 ± 0.24	1.05 ± 1.05	0.05
G359.889-0.093o	SO (219.9GHz)	N	0	0	0.0 ± 0.0	0.0 ± 0.0	0.0 ± 0.0	0.05
G359.889-0.093o	SiO (217.1GHz)	Y	2	1	0.09 ± 0.03	194.85 ± 0.97	2.36 ± 2.36	0.05
G359.889-0.093o	SiO (217.1GHz)	Y	2	2	0.14 ± 0.03	16.93 ± 0.69	3.14 ± 3.14	0.05
G359.889-0.093p	13CO (220.4GHz)	Y	2	1	2.04 ± 0.09	17.76 ± 0.27	5.59 ± 5.59	0.12
G359.889-0.093p	C18O (219.6GHz)	Y	1	1	0.75 ± 0.06	15.16 ± 0.27	3.04 ± 3.04	0.08
G359.889-0.093p	H2CO (218.2GHz)	N	0	0	0.0 ± 0.0	0.0 ± 0.0	0.0 ± 0.0	0.08
G359.889-0.093p	H2CO (218.5GHz)	Y	1	1	0.83 ± 0.07	63.77 ± 0.21	2.09 ± 2.09	0.09
G359.889-0.093p	H2CO (218.8GHz)	Y	1	1	0.48 ± 0.07	16.33 ± 0.39	2.16 ± 2.16	0.1
G359.889-0.093p	OCS (218.9GHz)	N	0	0	0.0 ± 0.0	0.0 ± 0.0	0.0 ± 0.0	0.09
G359.889-0.093p	OCS (231.1GHz)	N	0	0	0.0 ± 0.0	0.0 ± 0.0	0.0 ± 0.0	0.21
G359.889-0.093p	SO (219.9GHz)	N	0	0	0.0 ± 0.0	0.0 ± 0.0	0.0 ± 0.0	0.09
G359.889-0.093p	SiO (217.1GHz)	N	0	0	0.0 ± 0.0	0.0 ± 0.0	0.0 ± 0.0	0.08
G359.889-0.093q	13CO (220.4GHz)	Y	2	1	0.75 ± 0.08	21.62 ± 0.69	5.42 ± 5.42	0.18
G359.889-0.093q	C18O (219.6GHz)	N	0	0	0.0 ± 0.0	0.0 ± 0.0	0.0 ± 0.0	0.09
G359.889-0.093q	H2CO (218.2GHz)	N	0	0	0.0 ± 0.0	0.0 ± 0.0	0.0 ± 0.0	0.08
G359.889-0.093q	H2CO (218.5GHz)	Y	1	1	0.52 ± 0.05	51.87 ± 0.66	6.15 ± 6.15	0.11
G359.889-0.093q	H2CO (218.8GHz)	N	0	0	0.0 ± 0.0	0.0 ± 0.0	0.0 ± 0.0	0.09
G359.889-0.093q	OCS (218.9GHz)	N	0	0	0.0 ± 0.0	0.0 ± 0.0	0.0 ± 0.0	0.09
G359.889-0.093q	OCS (231.1GHz)	N	0	0	0.0 ± 0.0	0.0 ± 0.0	0.0 ± 0.0	0.14
G359.889-0.093q	SO (219.9GHz)	N	0	0	0.0 ± 0.0	0.0 ± 0.0	0.0 ± 0.0	0.09
G359.889-0.093q	SiO (217.1GHz)	Y	3	2	0.17 ± 0.05	104.04 ± 1.06	2.98 ± 2.98	0.09
G359.889-0.093r	12CO (230.5GHz)	N	0	0	0.0 ± 0.0	0.0 ± 0.0	0.0 ± 0.0	1.91
G359.889-0.093r	13CO (220.4GHz)	Y	2	1	0.8 ± 0.15	35.52 ± 0.74	3.35 ± 3.35	0.28
G359.889-0.093r	13CO (220.4GHz)	Y	2	2	0.74 ± 0.18	22.81 ± 0.68	2.39 ± 2.39	0.28
G359.889-0.093r	C18O (219.6GHz)	N	0	0	0.0 ± 0.0	0.0 ± 0.0	0.0 ± 0.0	0.12
G359.889-0.093r	H2CO (218.2GHz)	Y	2	1	0.98 ± 0.08	11.79 ± 0.15	1.64 ± 1.64	0.11
G359.889-0.093r	H2CO (218.5GHz)	Y	2	1	2.13 ± 0.08	56.41 ± 0.11	2.5 ± 2.5	0.13
G359.889-0.093r	H2CO (218.5GHz)	Y	2	2	0.46 ± 0.07	8.91 ± 0.54	3.01 ± 3.01	0.13
G359.889-0.093r	H2CO (218.8GHz)	Y	1	1	0.52 ± 0.08	9.67 ± 0.45	2.47 ± 2.47	0.14
G359.889-0.093r	OCS (218.9GHz)	N	0	0	0.0 ± 0.0	0.0 ± 0.0	0.0 ± 0.0	0.12
G359.889-0.093r	OCS (231.1GHz)	N	0	0	0.0 ± 0.0	0.0 ± 0.0	0.0 ± 0.0	0.15
G359.889-0.093r	SO (219.9GHz)	Y	1	1	0.44 ± 0.08	6.6 ± 0.49	2.42 ± 2.42	0.12
G359.889-0.093r	SiO (217.1GHz)	Y	1	1	0.37 ± 0.05	7.08 ± 0.59	3.87 ± 3.87	0.1
G359.889-0.093s	12CO (230.5GHz)	N	0	0	0.0 ± 0.0	0.0 ± 0.0	0.0 ± 0.0	2.35
G359.889-0.093s	13CO (220.4GHz)	Y	1	1	1.8 ± 0.1	2.29 ± 0.16	2.51 ± 2.51	0.16
G359.889-0.093s	C18O (219.6GHz)	N	0	0	0.0 ± 0.0	0.0 ± 0.0	0.0 ± 0.0	0.08
G359.889-0.093s	H2CO (218.2GHz)	Y	2	1	0.42 ± 0.04	23.6 ± 0.54	4.47 ± 4.47	0.07

Continued on next page

Table A.1 – *Continued from previous page*

Leaf	Transition	Detected	Number of Comps	Comp.	Amplitude	Velocity	Width	RMS
G359.889-0.093s	H2CO (218.5GHz)	Y	1	1	0.65 ± 0.06	71.54 ± 0.31	2.82 ± 2.82	0.09
G359.889-0.093s	H2CO (218.8GHz)	N	0	0	0.0 ± 0.0	0.0 ± 0.0	0.0 ± 0.0	0.12
G359.889-0.093s	OCS (218.9GHz)	N	0	0	0.0 ± 0.0	0.0 ± 0.0	0.0 ± 0.0	0.09
G359.889-0.093s	OCS (231.1GHz)	N	0	0	0.0 ± 0.0	0.0 ± 0.0	0.0 ± 0.0	0.14
G359.889-0.093s	SO (219.9GHz)	N	0	0	0.0 ± 0.0	0.0 ± 0.0	0.0 ± 0.0	0.08
G359.889-0.093s	SiO (217.1GHz)	N	0	0	0.0 ± 0.0	0.0 ± 0.0	0.0 ± 0.0	0.08
G359.889-0.093t	12CO (230.5GHz)	N	0	0	0.0 ± 0.0	0.0 ± 0.0	0.0 ± 0.0	1.93
G359.889-0.093t	13CO (220.4GHz)	Y	2	1	1.78 ± 0.09	11.41 ± 0.23	3.77 ± 3.77	0.18
G359.889-0.093t	C18O (219.6GHz)	Y	2	1	0.47 ± 0.05	10.73 ± 0.39	3.34 ± 3.34	0.07
G359.889-0.093t	H2CO (218.2GHz)	Y	2	1	0.61 ± 0.05	12.76 ± 0.28	3.12 ± 3.12	0.08
G359.889-0.093t	H2CO (218.5GHz)	Y	1	1	0.34 ± 0.04	54.46 ± 0.92	7.35 ± 7.35	0.1
G359.889-0.093t	H2CO (218.8GHz)	N	0	0	0.0 ± 0.0	0.0 ± 0.0	0.0 ± 0.0	0.11
G359.889-0.093t	OCS (218.9GHz)	N	0	0	0.0 ± 0.0	0.0 ± 0.0	0.0 ± 0.0	0.09
G359.889-0.093t	OCS (231.1GHz)	N	0	0	0.0 ± 0.0	0.0 ± 0.0	0.0 ± 0.0	0.14
G359.889-0.093t	SO (219.9GHz)	N	0	0	0.0 ± 0.0	0.0 ± 0.0	0.0 ± 0.0	0.08
G359.889-0.093t	SiO (217.1GHz)	Y	1	1	0.21 ± 0.03	2.05 ± 1.39	8.1 ± 8.1	0.09
G359.889-0.093u	12CO (230.5GHz)	N	0	0	0.0 ± 0.0	0.0 ± 0.0	0.0 ± 0.0	1.03
G359.889-0.093u	13CO (220.4GHz)	Y	2	1	1.63 ± 0.21	15.36 ± 0.2	1.33 ± 1.33	0.21
G359.889-0.093u	C18O (219.6GHz)	N	0	0	0.0 ± 0.0	0.0 ± 0.0	0.0 ± 0.0	0.1
G359.889-0.093u	H2CO (218.5GHz)	Y	1	1	1.84 ± 0.09	53.42 ± 0.12	2.07 ± 2.07	0.11
G359.889-0.093u	H2CO (218.8GHz)	N	0	0	0.0 ± 0.0	0.0 ± 0.0	0.0 ± 0.0	0.13
G359.889-0.093u	OCS (218.9GHz)	N	0	0	0.0 ± 0.0	0.0 ± 0.0	0.0 ± 0.0	0.11
G359.889-0.093u	OCS (231.1GHz)	N	0	0	0.0 ± 0.0	0.0 ± 0.0	0.0 ± 0.0	0.18
G359.889-0.093u	SO (219.9GHz)	Y	1	1	0.86 ± 0.11	4.73 ± 0.19	1.32 ± 1.32	0.11
G359.889-0.093u	SiO (217.1GHz)	Y	1	1	0.36 ± 0.05	1.94 ± 0.68	4.18 ± 4.18	0.11
G359.948-0.052b	12CO (230.5GHz)	Y	2	1	60.84 ± 1.65	23.48 ± 0.04	1.43 ± 1.43	1.25
G359.948-0.052b	13CO (220.4GHz)	Y	2	1	3.67 ± 0.37	38.74 ± 0.17	1.48 ± 1.48	0.47
G359.948-0.052b	C18O (219.6GHz)	N	0	0	0.0 ± 0.0	0.0 ± 0.0	0.0 ± 0.0	0.14
G359.948-0.052b	H2CO (218.2GHz)	N	0	0	0.0 ± 0.0	0.0 ± 0.0	0.0 ± 0.0	0.07
G359.948-0.052b	H2CO (218.5GHz)	N	0	0	0.0 ± 0.0	0.0 ± 0.0	0.0 ± 0.0	0.14
G359.948-0.052b	H2CO (218.8GHz)	N	0	0	0.0 ± 0.0	0.0 ± 0.0	0.0 ± 0.0	0.04
G359.948-0.052b	OCS (218.9GHz)	Y	10	2	0.57 ± 0.14	180.45 ± 0.34	1.27 ± 1.27	0.07
G359.948-0.052b	OCS (218.9GHz)	Y	10	3	0.31 ± 0.03	140.37 ± 14.59	38.59 ± 38.59	0.07
G359.948-0.052b	OCS (218.9GHz)	Y	10	4	0.25 ± 0.16	77.11 ± 10.15	17.98 ± 17.98	0.07
G359.948-0.052b	OCS (218.9GHz)	Y	10	5	0.23 ± 0.16	46.6 ± 4.8	9.54 ± 9.54	0.07
G359.948-0.052b	OCS (218.9GHz)	Y	10	6	0.52 ± 0.07	22.91 ± 1.14	5.74 ± 5.74	0.07
G359.948-0.052b	OCS (231.1GHz)	N	0	0	0.0 ± 0.0	0.0 ± 0.0	0.0 ± 0.0	0.19
G359.948-0.052b	SO (219.9GHz)	N	0	0	0.0 ± 0.0	0.0 ± 0.0	0.0 ± 0.0	0.16
G359.948-0.052b	SiO (217.1GHz)	N	0	0	0.0 ± 0.0	0.0 ± 0.0	0.0 ± 0.0	0.13
G359.948-0.052h	12CO (230.5GHz)	N	0	0	0.0 ± 0.0	0.0 ± 0.0	0.0 ± 0.0	1.79
G359.948-0.052h	13CO (220.4GHz)	Y	2	1	1.31 ± 0.13	4.56 ± 1.0	8.65 ± 8.65	0.34
G359.948-0.052h	C18O (219.6GHz)	N	0	0	0.0 ± 0.0	0.0 ± 0.0	0.0 ± 0.0	0.22
G359.948-0.052h	H2CO (218.2GHz)	N	0	0	0.0 ± 0.0	0.0 ± 0.0	0.0 ± 0.0	0.16
G359.948-0.052h	H2CO (218.5GHz)	N	0	0	0.0 ± 0.0	0.0 ± 0.0	0.0 ± 0.0	0.16
G359.948-0.052h	H2CO (218.8GHz)	N	0	0	0.0 ± 0.0	0.0 ± 0.0	0.0 ± 0.0	0.12
G359.948-0.052h	OCS (231.1GHz)	N	0	0	0.0 ± 0.0	0.0 ± 0.0	0.0 ± 0.0	0.22
G359.948-0.052h	SO (219.9GHz)	N	0	0	0.0 ± 0.0	0.0 ± 0.0	0.0 ± 0.0	0.23
G359.948-0.052h	SiO (217.1GHz)	N	0	0	0.0 ± 0.0	0.0 ± 0.0	0.0 ± 0.0	0.15
G359.948-0.052m	H2CO (218.5GHz)	N	0	0	0.0 ± 0.0	0.0 ± 0.0	0.0 ± 0.0	0.14
G359.948-0.052m	H2CO (218.8GHz)	N	0	0	0.0 ± 0.0	0.0 ± 0.0	0.0 ± 0.0	0.3
G359.948-0.052m	OCS (218.9GHz)	N	0	0	0.0 ± 0.0	0.0 ± 0.0	0.0 ± 0.0	0.28

A.3 Appendix 3: CMZoom Dendrogram Leaf Spectra

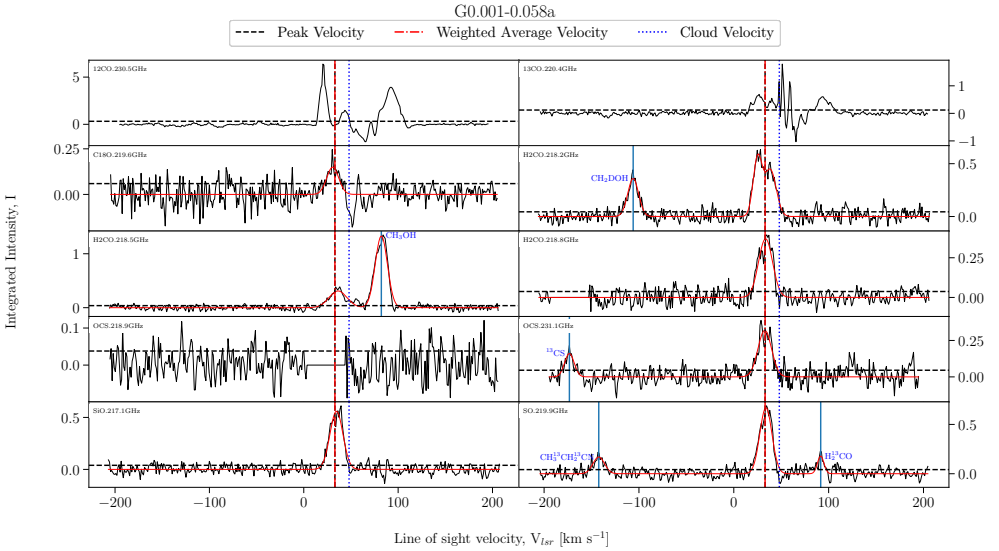

FIGURE A.82: Fitted spectra for dendrogram leaf G0.001-0.058a, with scouse fits overlaid in red.

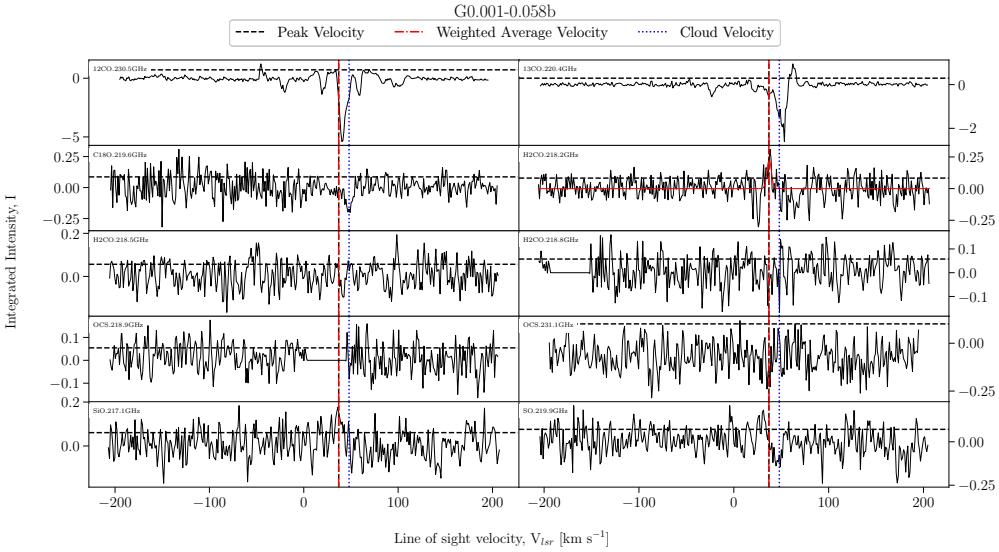

FIGURE A.83: Fitted spectra for dendrogram leaf G0.001-0.058b, with scouse fits overlaid in red.

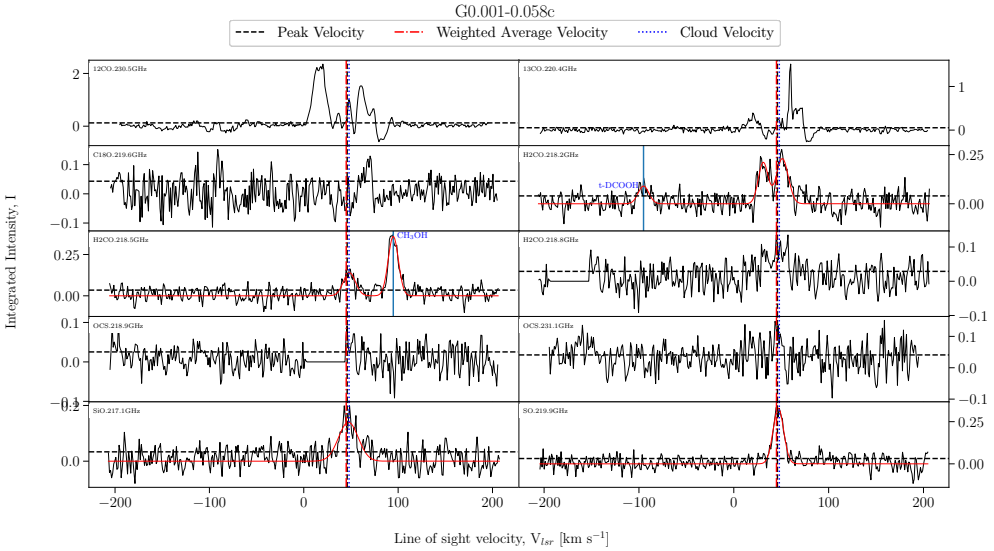

FIGURE A.84: Fitted spectra for dendrogram leaf G0.001-0.058c, with scouse fits overlaid in red.

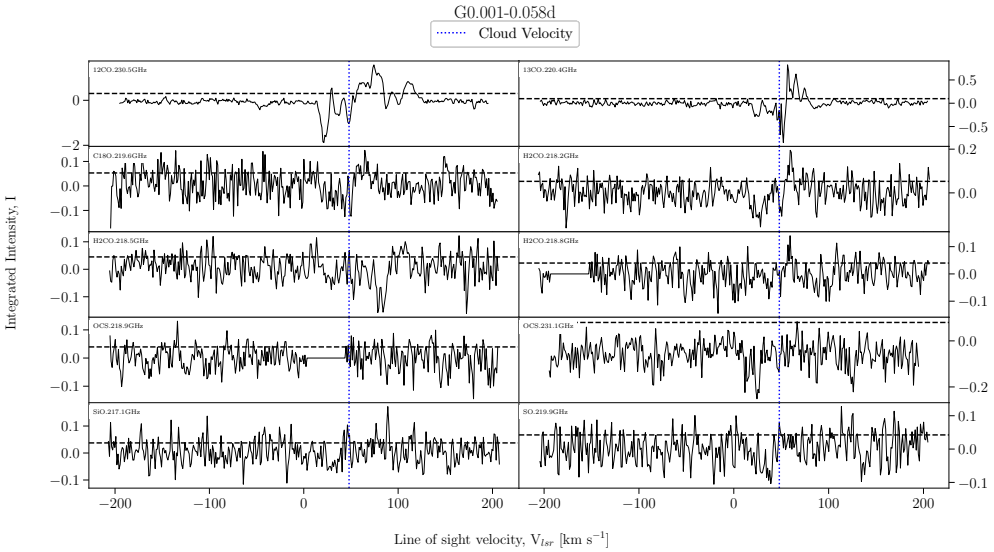

FIGURE A.85: Fitted spectra for dendrogram leaf G0.001-0.058d, with scouse fits overlaid in red.

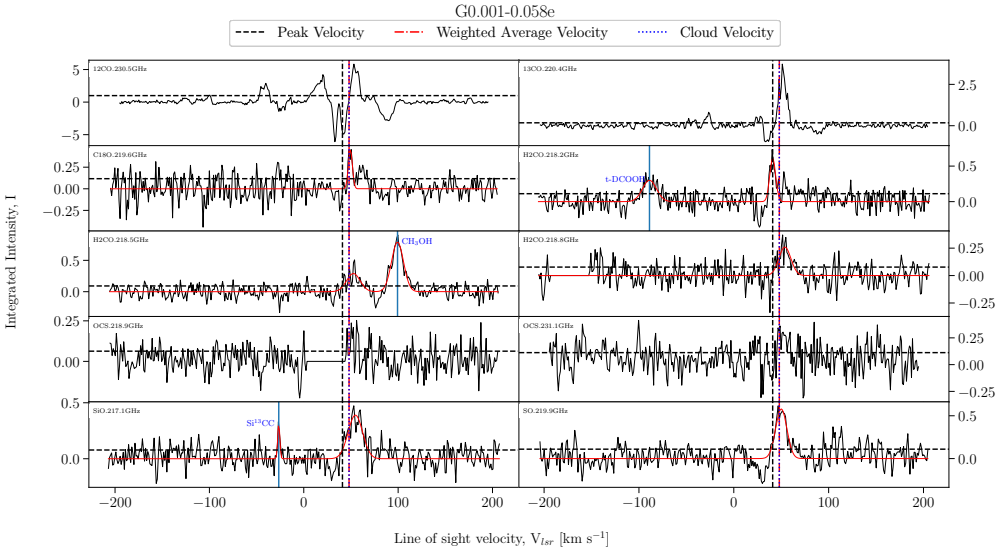

FIGURE A.86: Fitted spectra for dendrogram leaf G0.001-0.058e, with scouse fits overlaid in red.

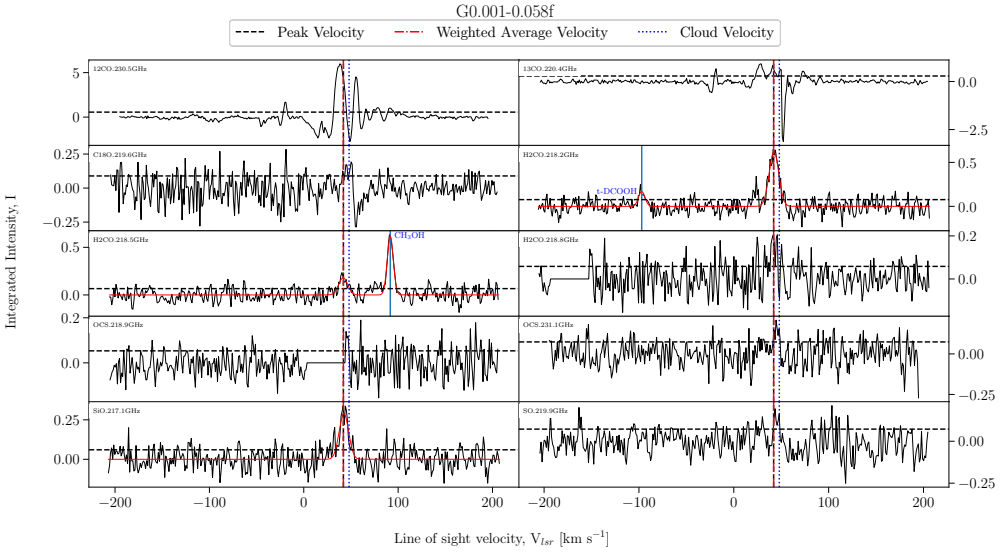

FIGURE A.87: Fitted spectra for dendrogram leaf G0.001-0.058f, with scouse fits overlaid in red.

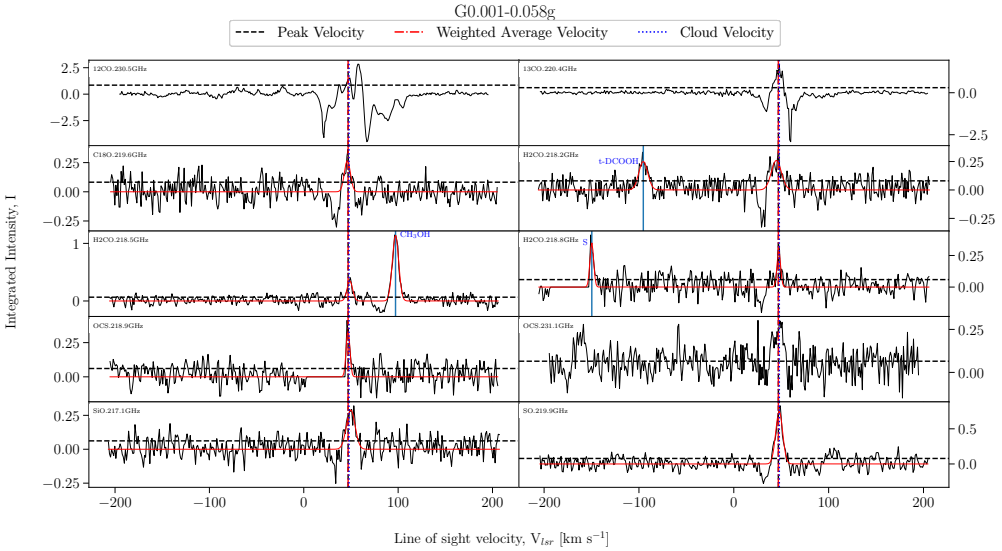

FIGURE A.88: Fitted spectra for dendrogram leaf G0.001-0.058g, with scouse fits overlaid in red.

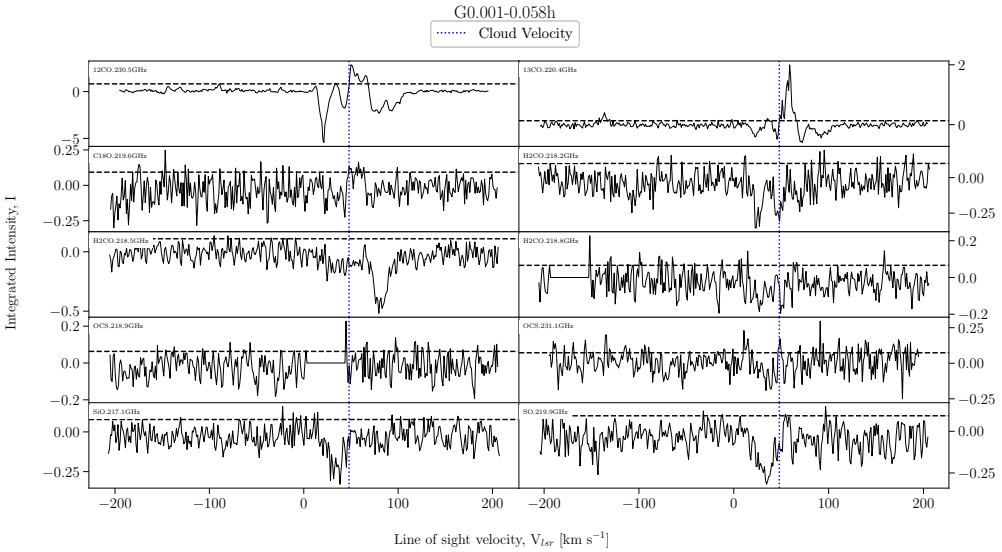

FIGURE A.89: Fitted spectra for dendrogram leaf G0.001-0.058h, with scouse fits overlaid in red.

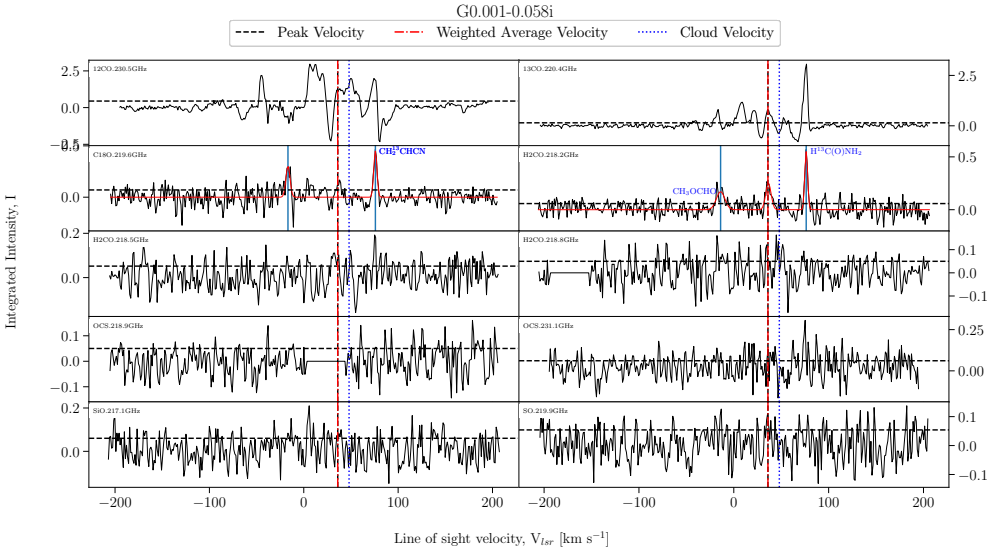

FIGURE A.90: Fitted spectra for dendrogram leaf G0.001-0.058i, with scouse fits overlaid in red.

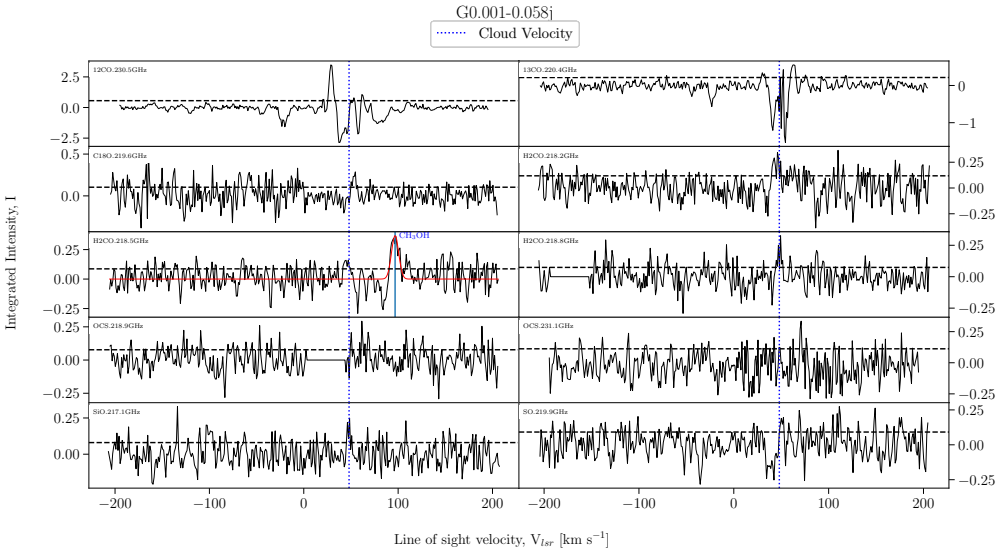

FIGURE A.91: Fitted spectra for dendrogram leaf G0.001-0.058j, with scouse fits overlaid in red.

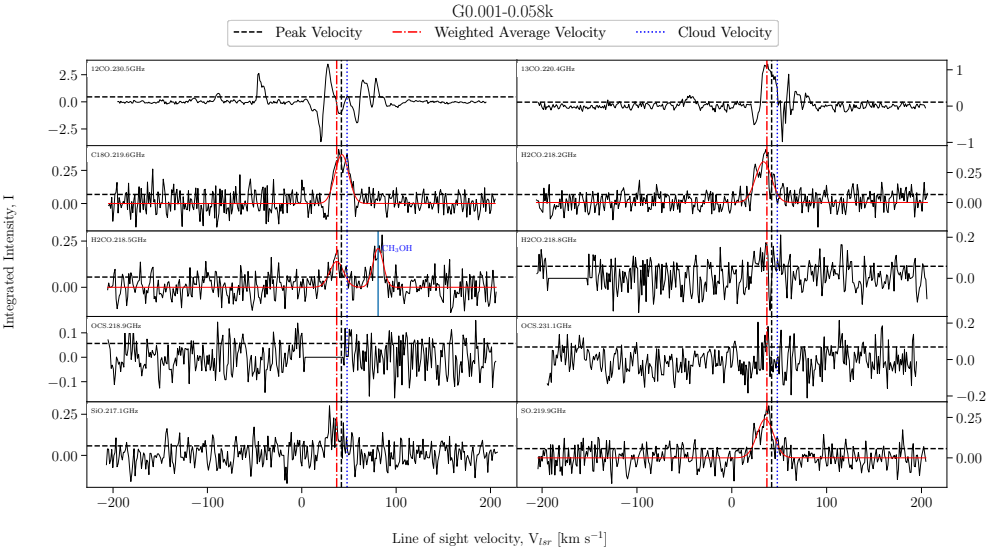

FIGURE A.92: Fitted spectra for dendrogram leaf G0.001-0.058k, with scouse fits overlaid in red.

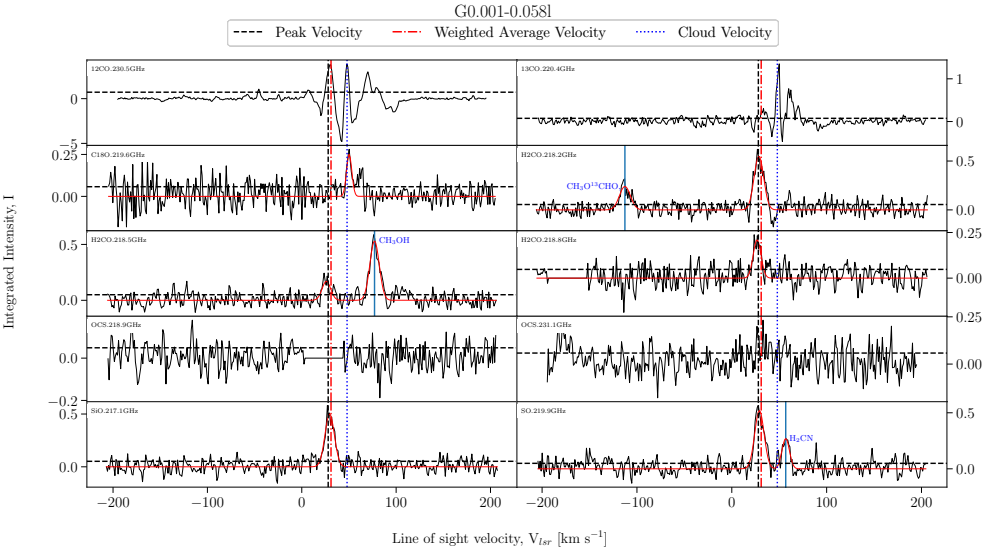

FIGURE A.93: Fitted spectra for dendrogram leaf G0.001-0.058l, with scouse fits overlaid in red.

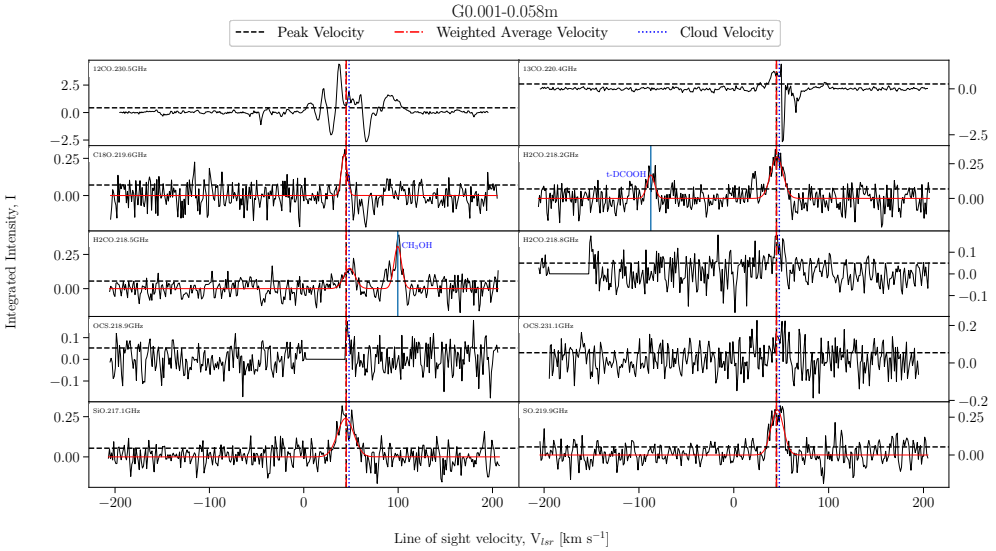

FIGURE A.94: Fitted spectra for dendrogram leaf G0.001-0.058m, with scouse fits overlaid in red.

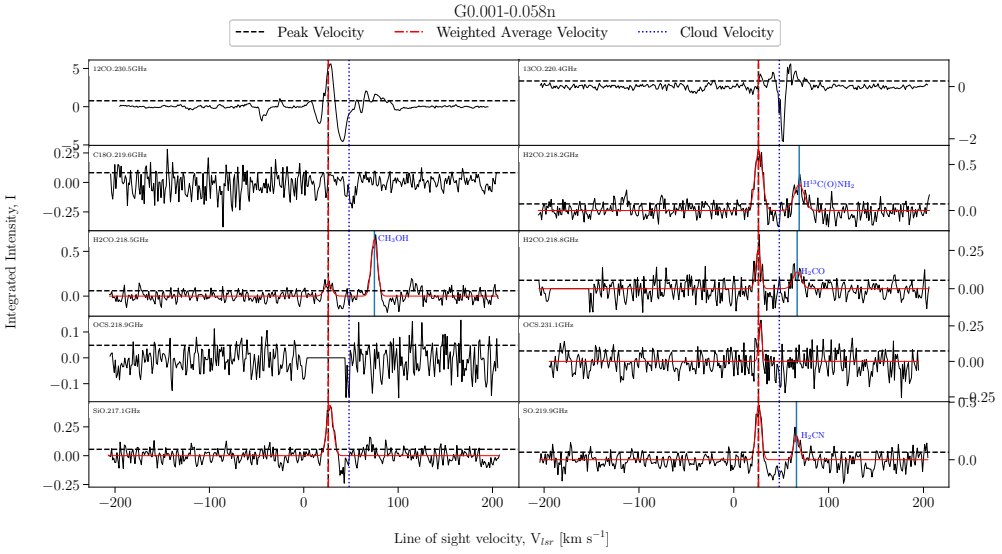

FIGURE A.95: Fitted spectra for dendrogram leaf G0.001-0.058n, with scouse fits overlaid in red.

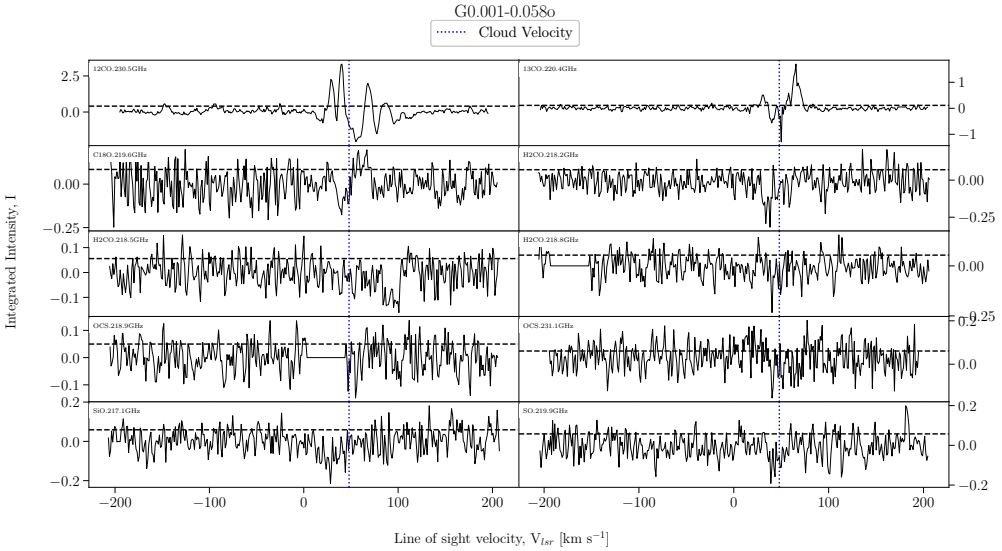

FIGURE A.96: Fitted spectra for dendrogram leaf G0.001-0.058o, with scouse fits overlaid in red.

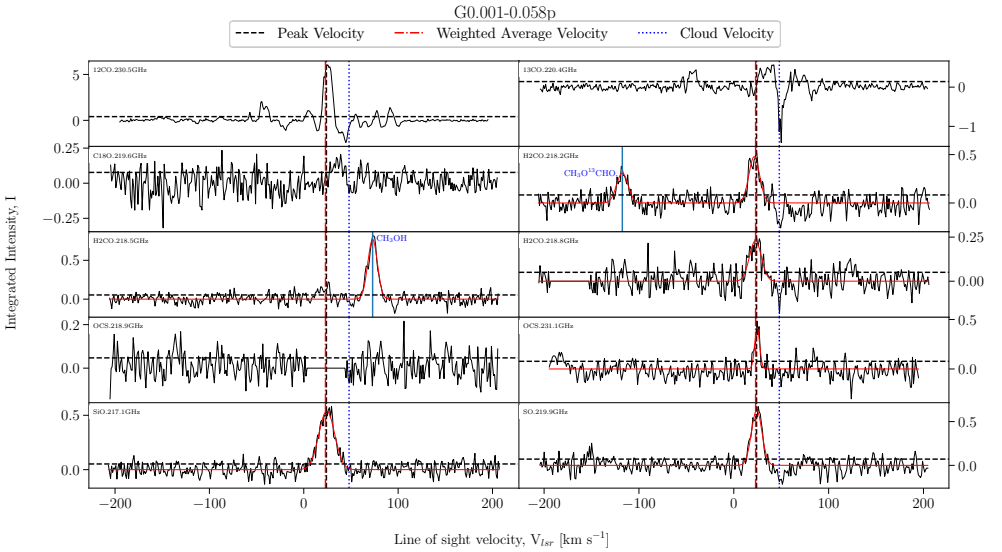

FIGURE A.97: Fitted spectra for dendrogram leaf G0.001-0.058p, with scouse fits overlaid in red.

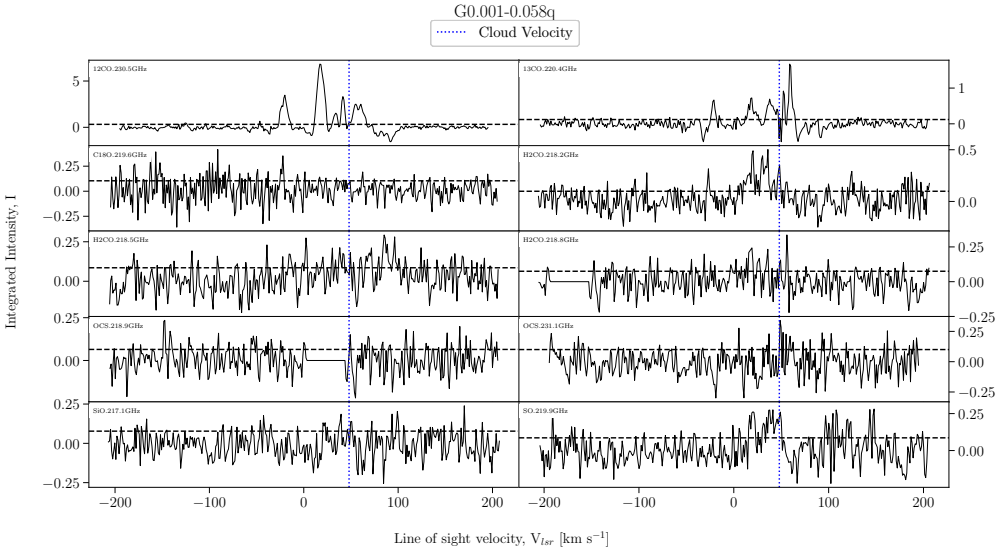

FIGURE A.98: Fitted spectra for dendrogram leaf G0.001-0.058q, with scouse fits overlaid in red.

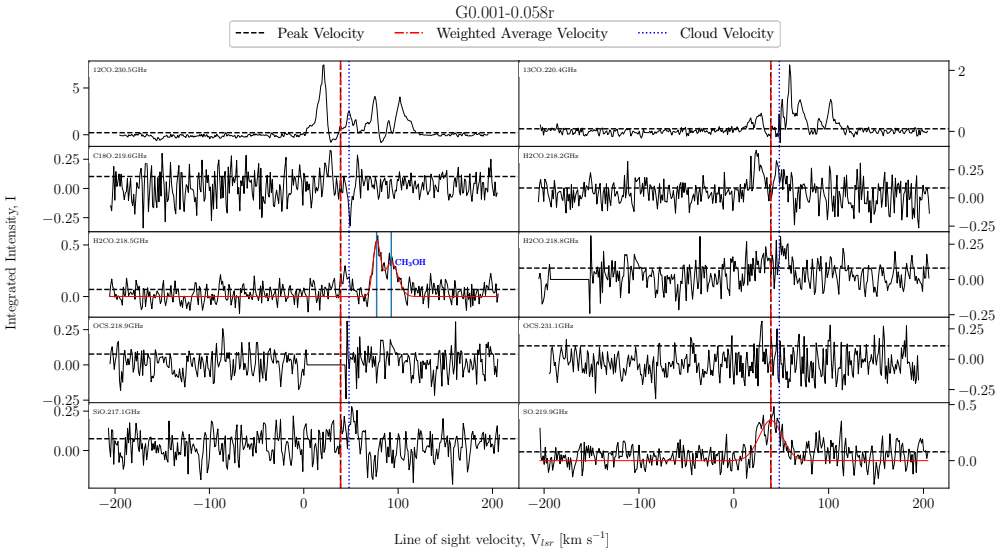

FIGURE A.99: Fitted spectra for dendrogram leaf G0.001-0.058r, with scouse fits overlaid in red.

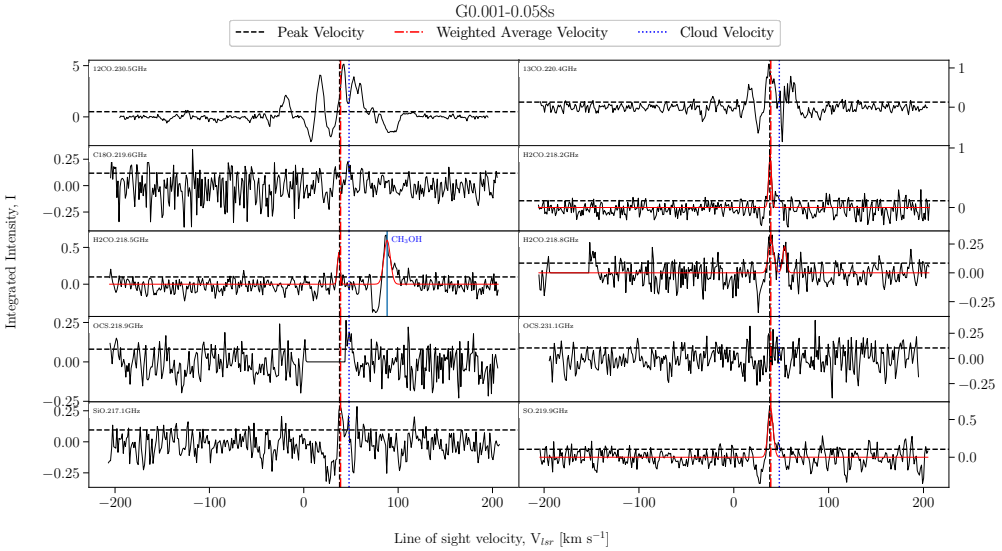

FIGURE A.100: Fitted spectra for dendrogram leaf G0.001-0.058s, with scouse fits overlaid in red.

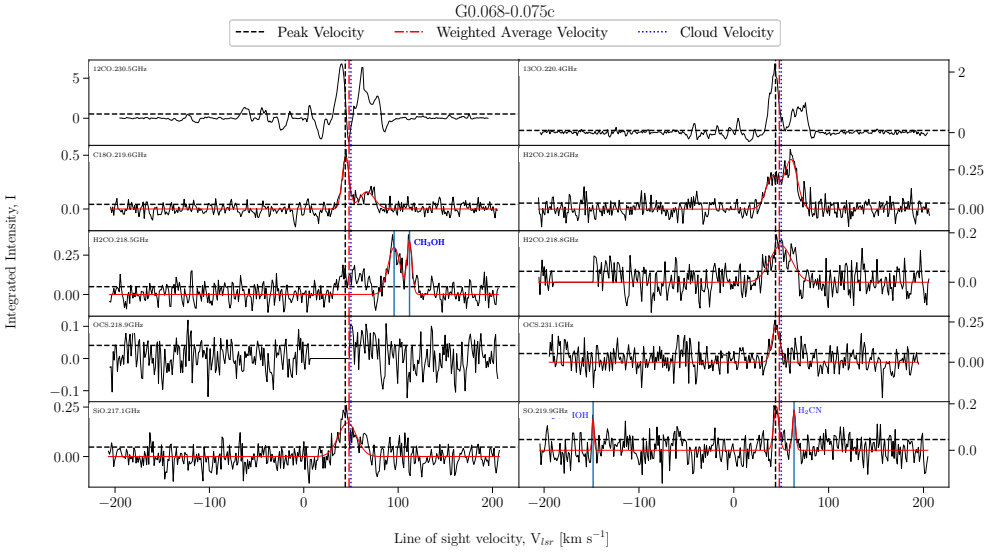

FIGURE A.101: Fitted spectra for dendrogram leaf G0.068-0.075c, with scouse fits overlaid in red.

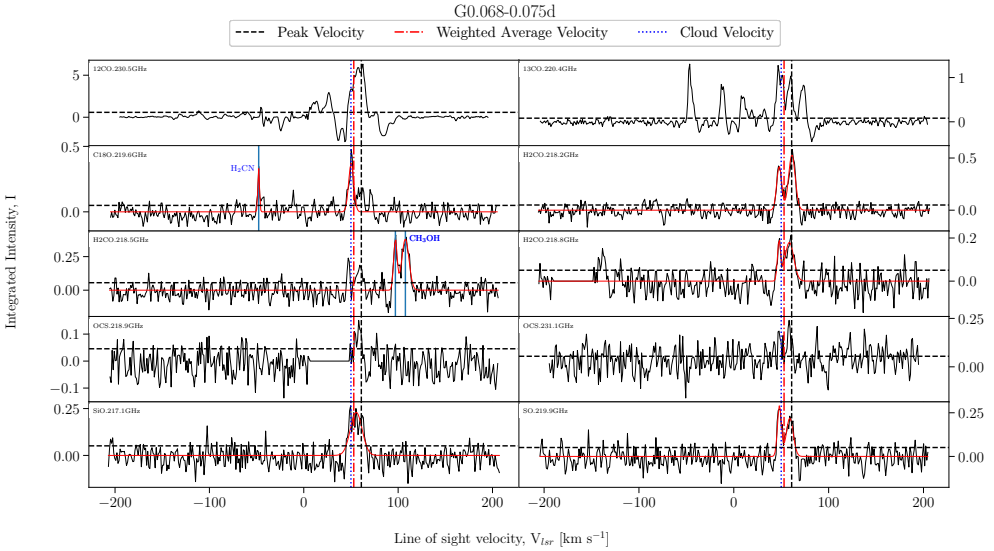

FIGURE A.102: Fitted spectra for dendrogram leaf G0.068-0.075d, with scouse fits overlaid in red.

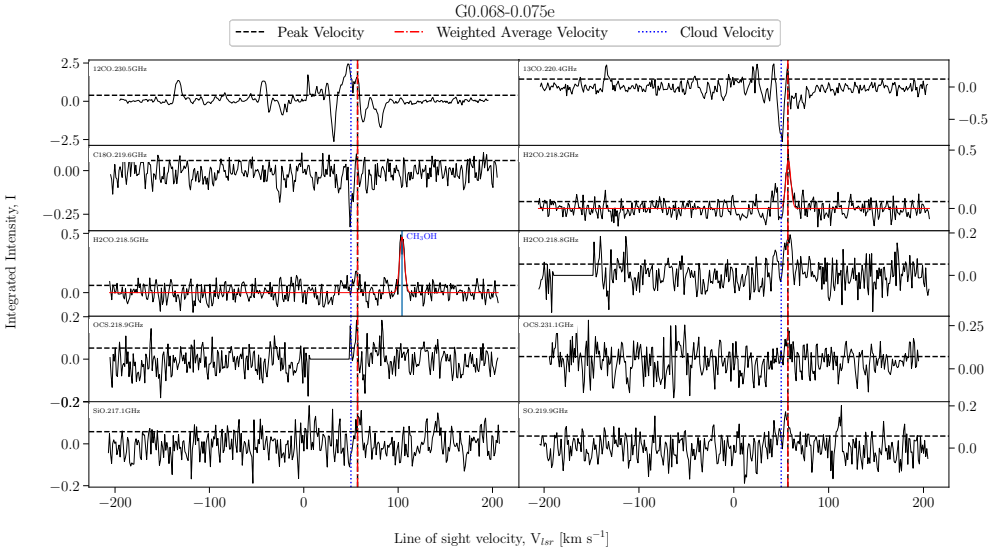

FIGURE A.103: Fitted spectra for dendrogram leaf G0.068-0.075e, with scouse fits overlaid in red.

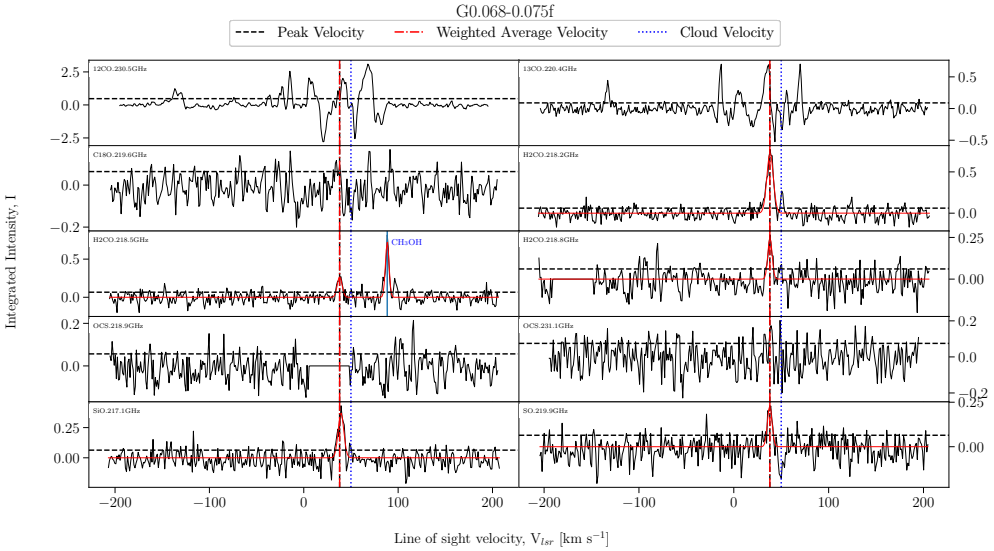

FIGURE A.104: Fitted spectra for dendrogram leaf G0.068-0.075f, with scouse fits overlaid in red.

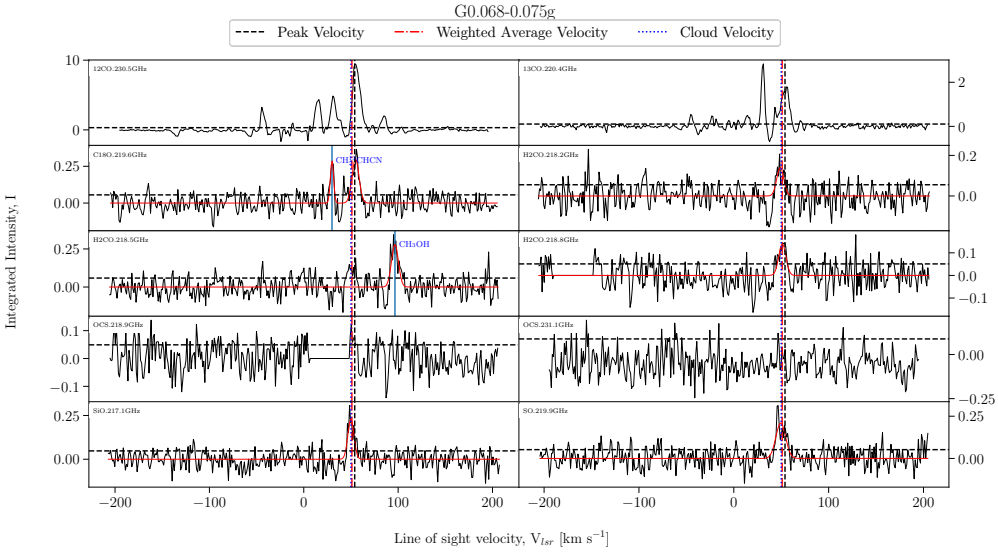

FIGURE A.105: Fitted spectra for dendrogram leaf G0.068-0.075g, with scouse fits overlaid in red.

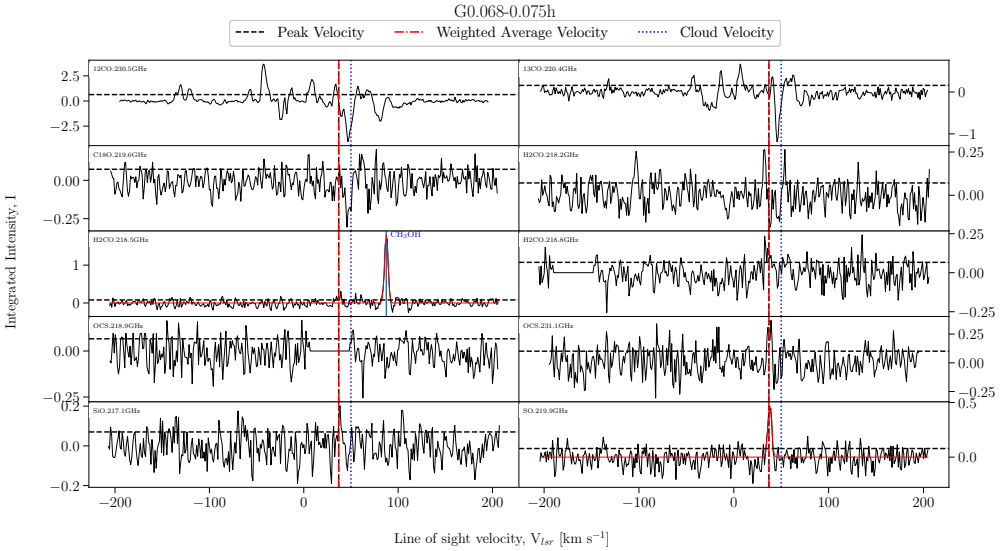

FIGURE A.106: Fitted spectra for dendrogram leaf G0.068-0.075h, with scouse fits overlaid in red.

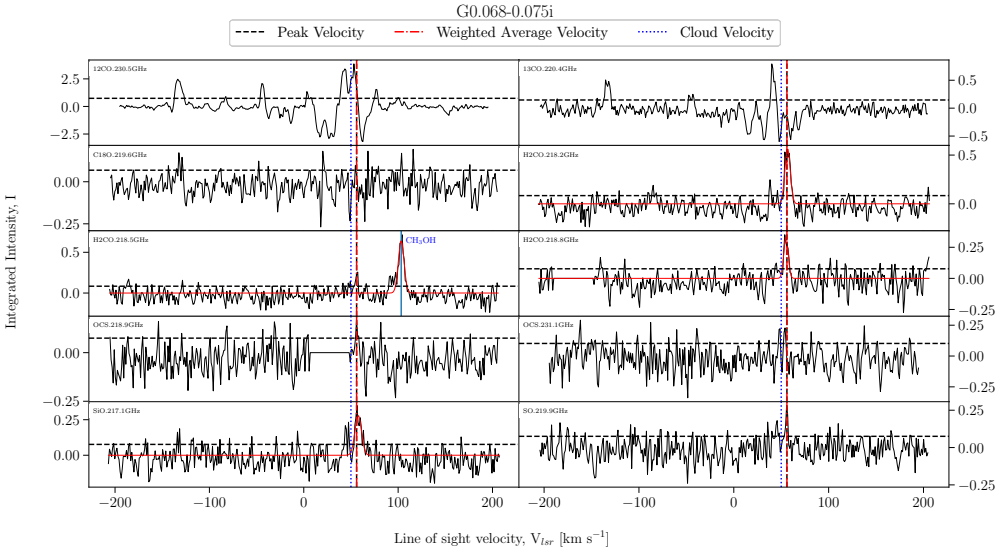

FIGURE A.107: Fitted spectra for dendrogram leaf G0.068-0.075i, with scouse fits overlaid in red.

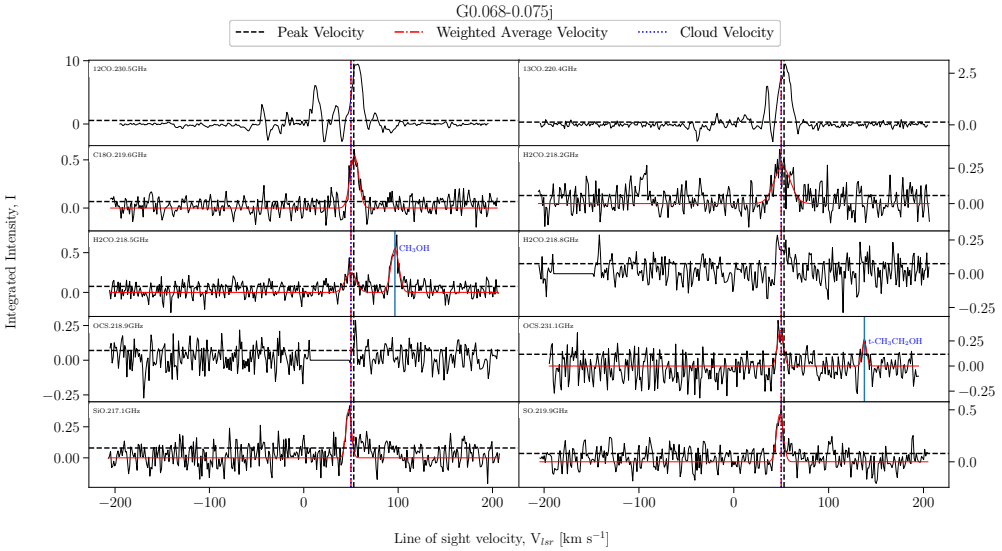

FIGURE A.108: Fitted spectra for dendrogram leaf G0.068-0.075j, with scouse fits overlaid in red.

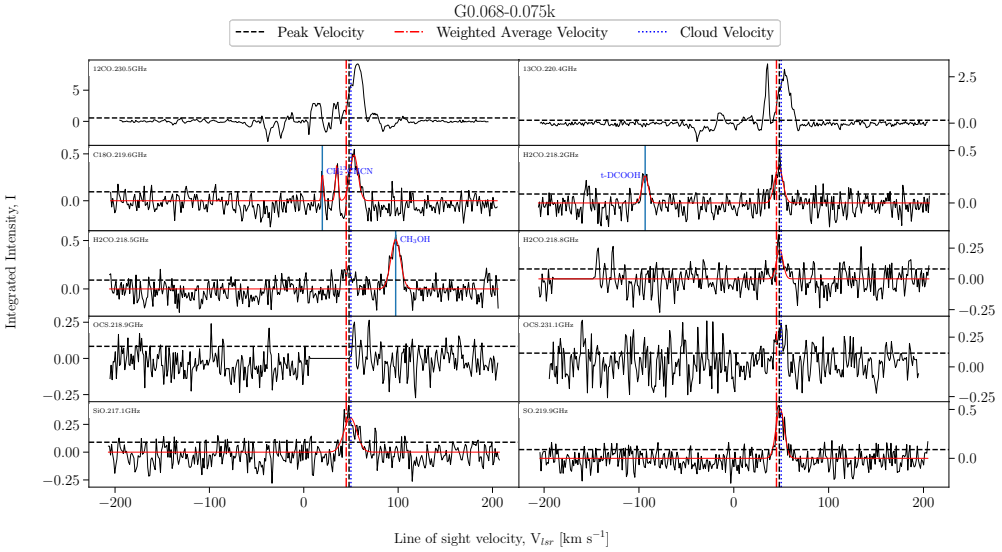

FIGURE A.109: Fitted spectra for dendrogram leaf G0.068-0.075k, with scouse fits overlaid in red.

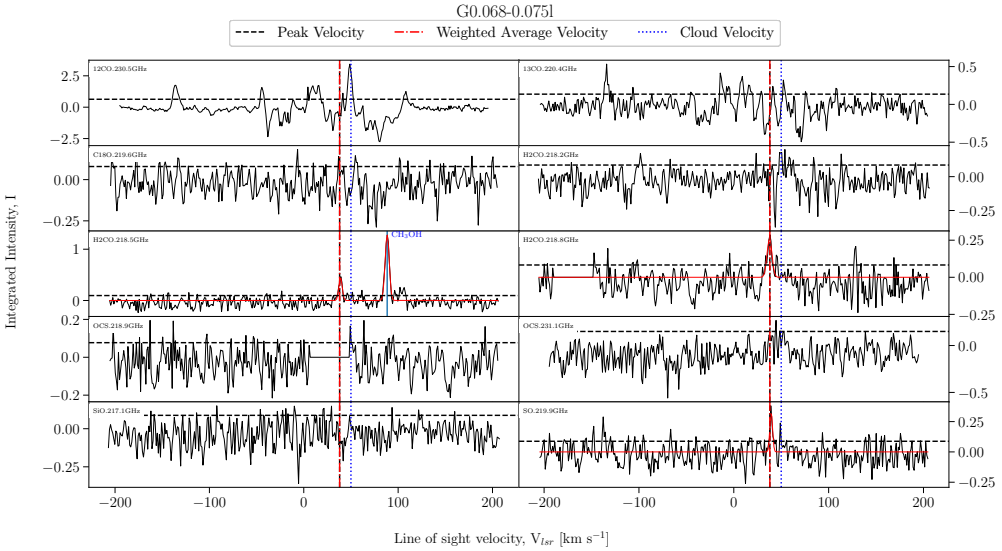

FIGURE A.110: Fitted spectra for dendrogram leaf G0.068-0.075l, with scouse fits overlaid in red.

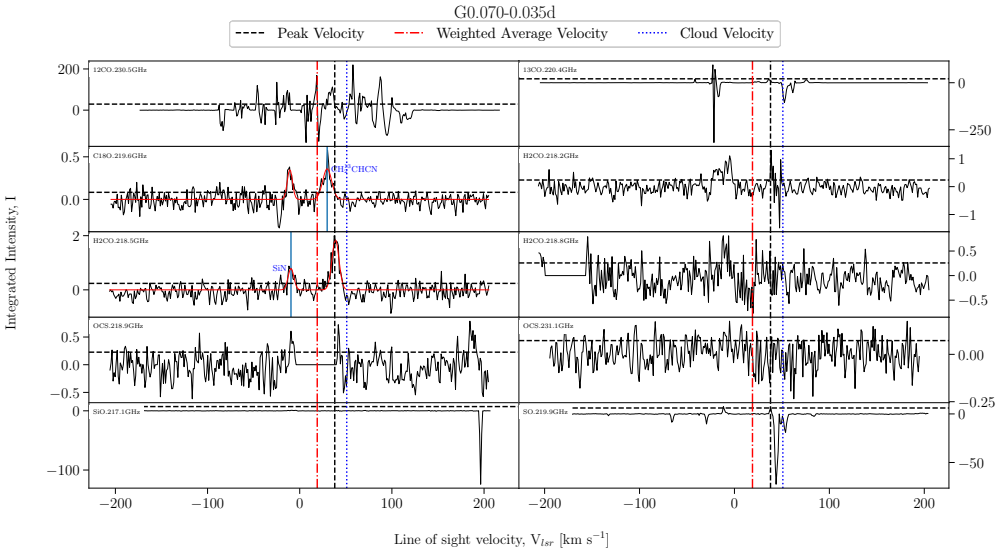

FIGURE A.111: Fitted spectra for dendrogram leaf G0.070-0.035d, with scouse fits overlaid in red.

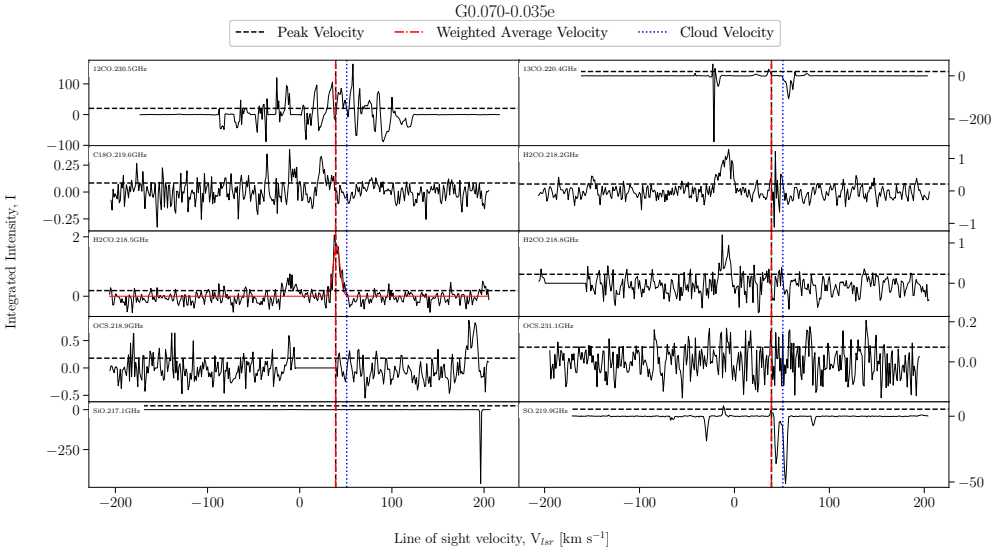

FIGURE A.112: Fitted spectra for dendrogram leaf G0.070-0.035e, with scouse fits overlaid in red.

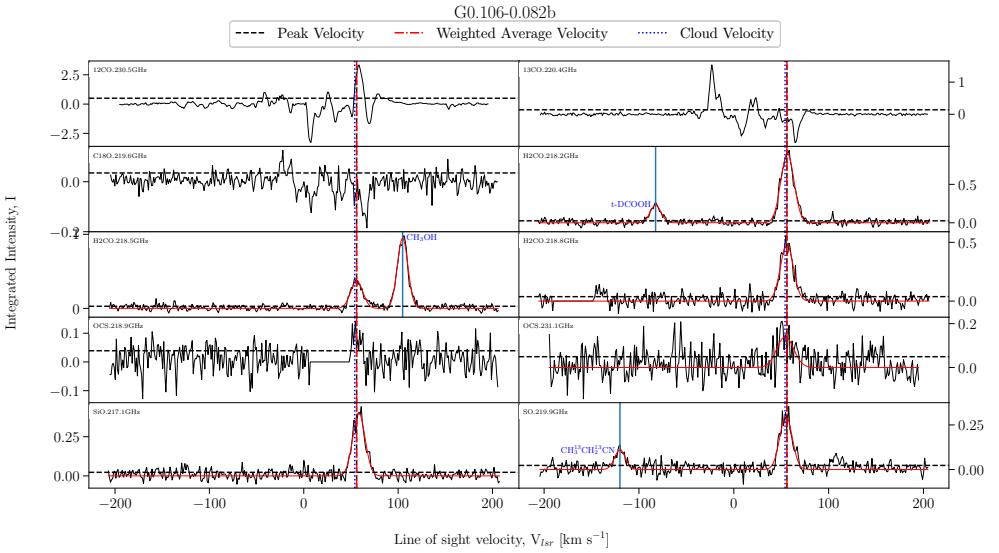

FIGURE A.113: Fitted spectra for dendrogram leaf G0.106-0.082b, with scouse fits overlaid in red.

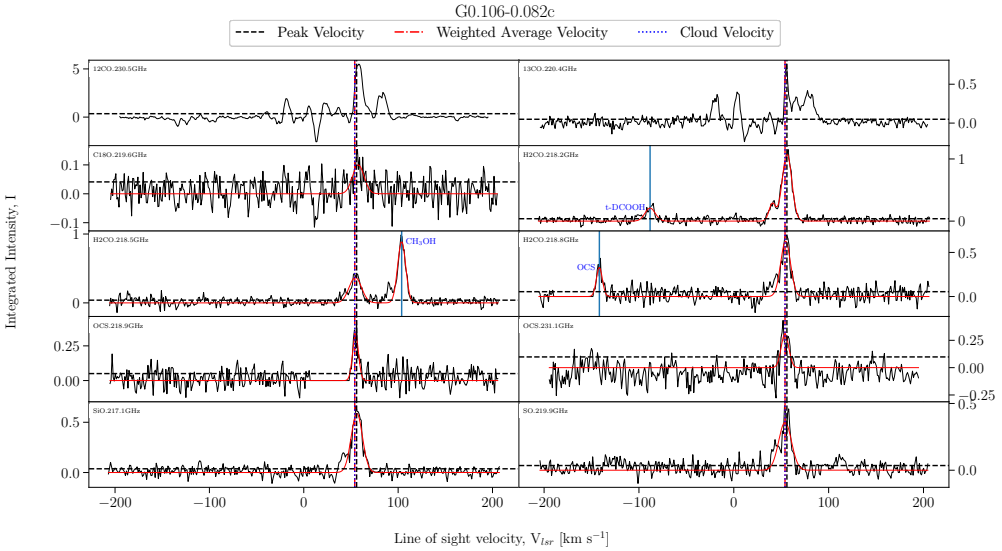

FIGURE A.114: Fitted spectra for dendrogram leaf G0.106-0.082c, with scouse fits overlaid in red.

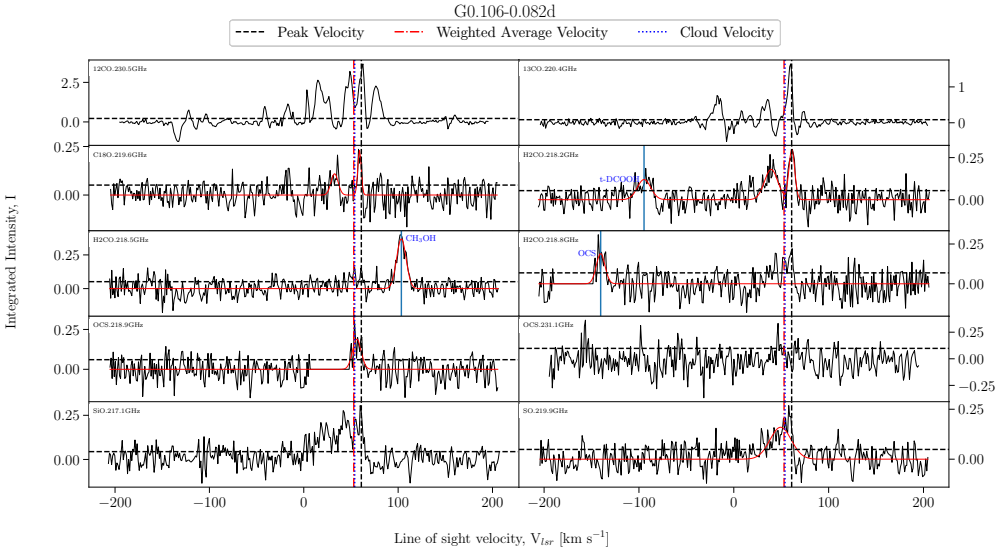

FIGURE A.115: Fitted spectra for dendrogram leaf G0.106-0.082d, with scouse fits overlaid in red.

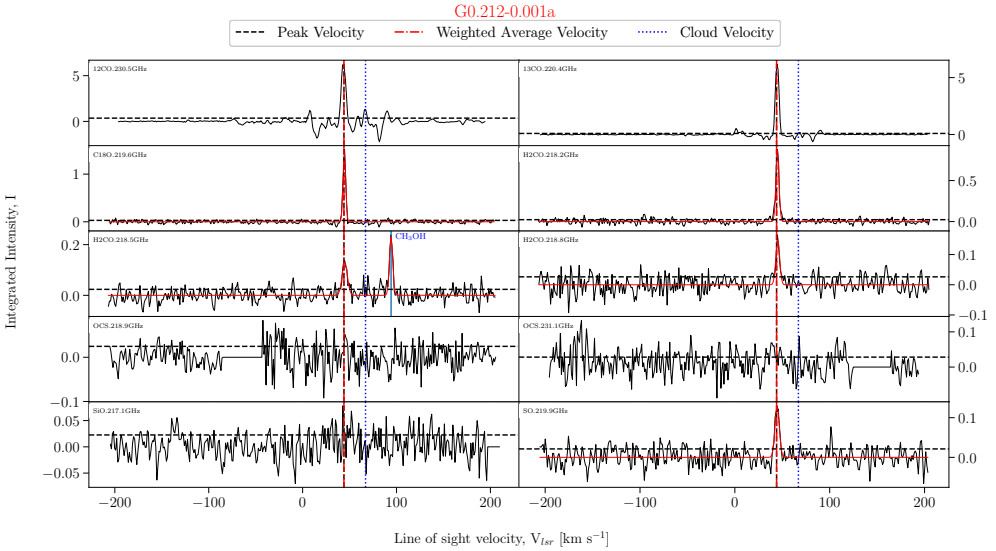

FIGURE A.116: Fitted spectra for dendrogram leaf G0.212-0.001a, with scouse fits overlaid in red.

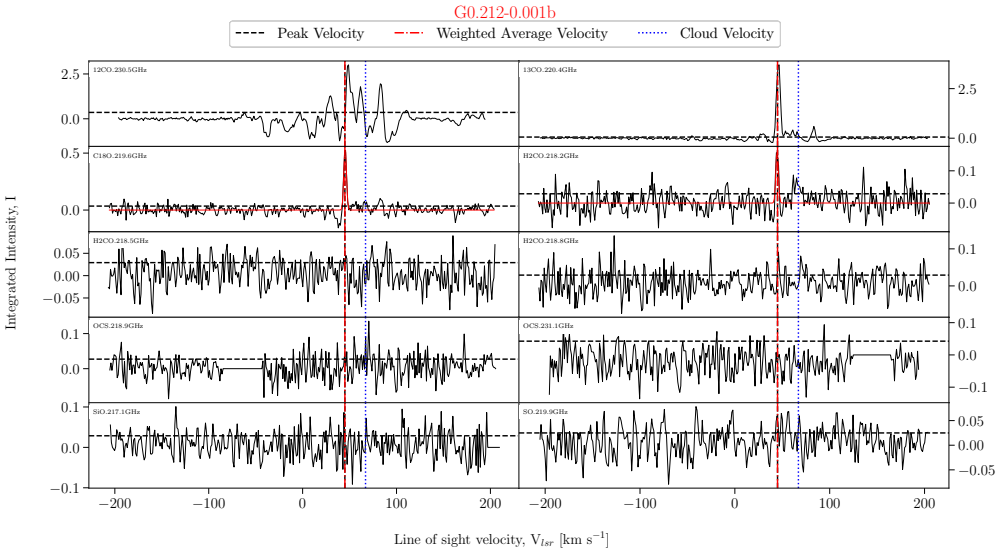

FIGURE A.117: Fitted spectra for dendrogram leaf G0.212-0.001b, with scouse fits overlaid in red.

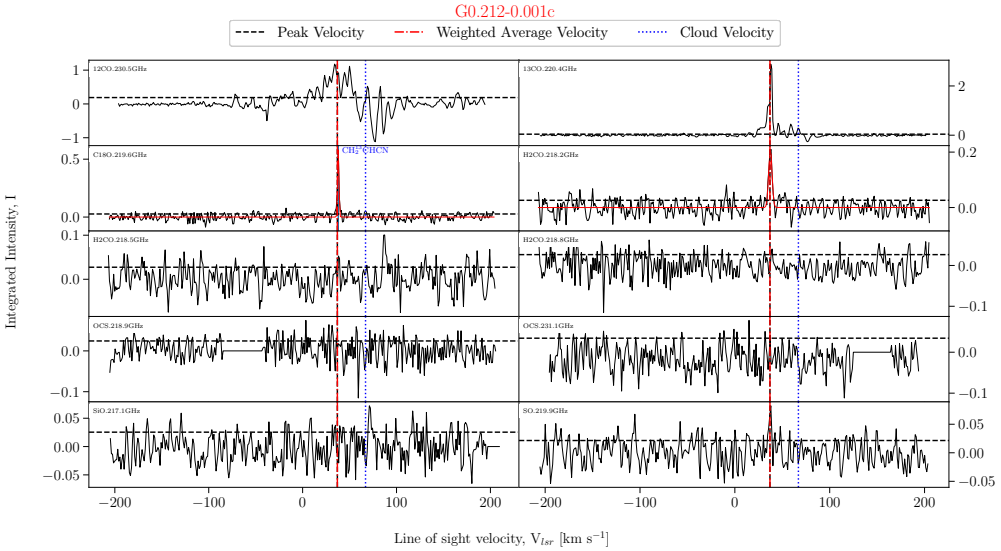

FIGURE A.118: Fitted spectra for dendrogram leaf G0.212-0.001c, with scouse fits overlaid in red.

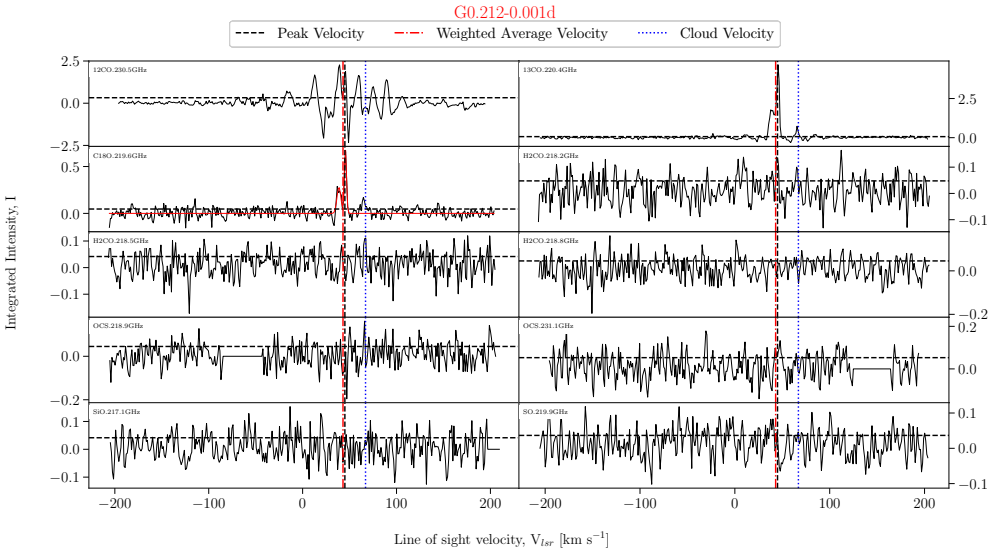

FIGURE A.119: Fitted spectra for dendrogram leaf G0.212-0.001d, with scouse fits overlaid in red.

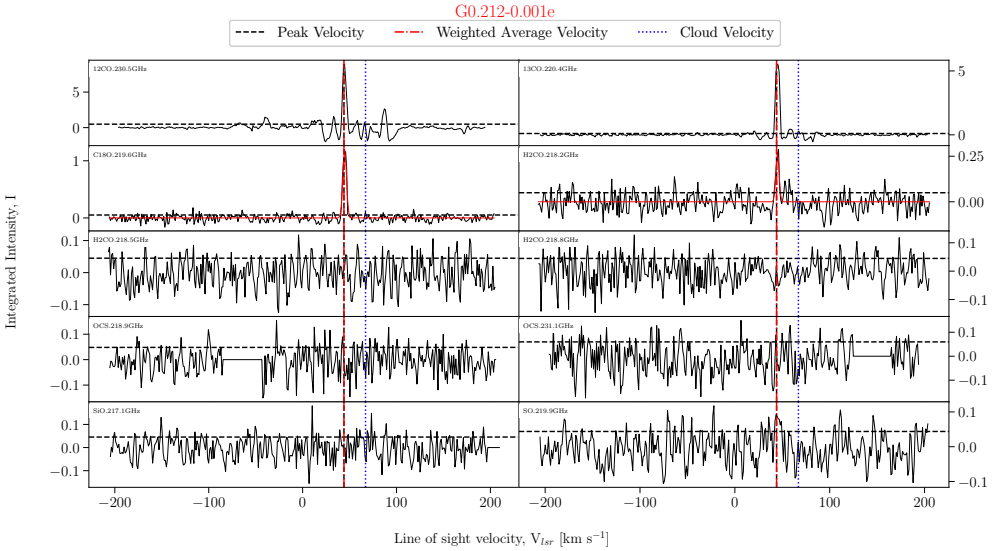

FIGURE A.120: Fitted spectra for dendrogram leaf G0.212-0.001e, with scouse fits overlaid in red.

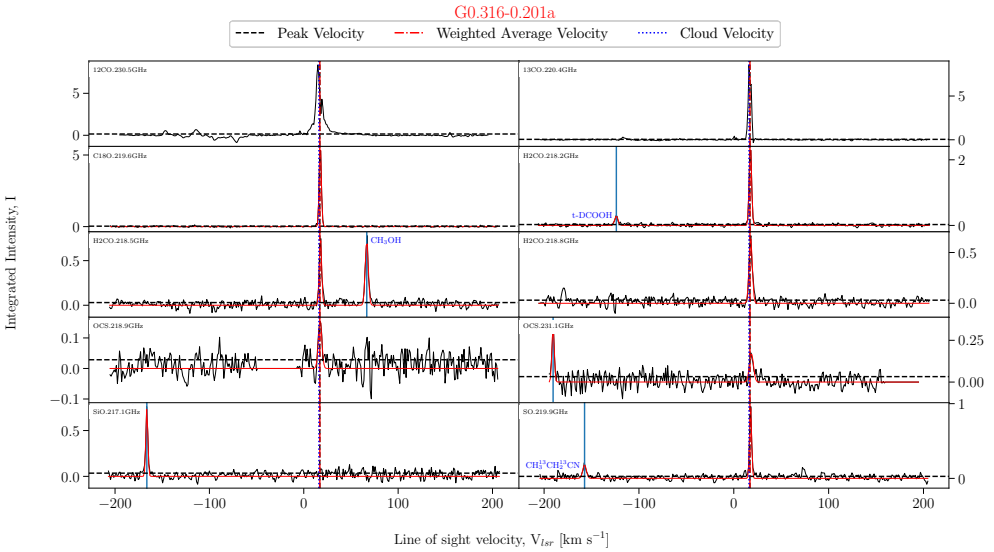

FIGURE A.121: Fitted spectra for dendrogram leaf G0.316-0.201a, with scouse fits overlaid in red.

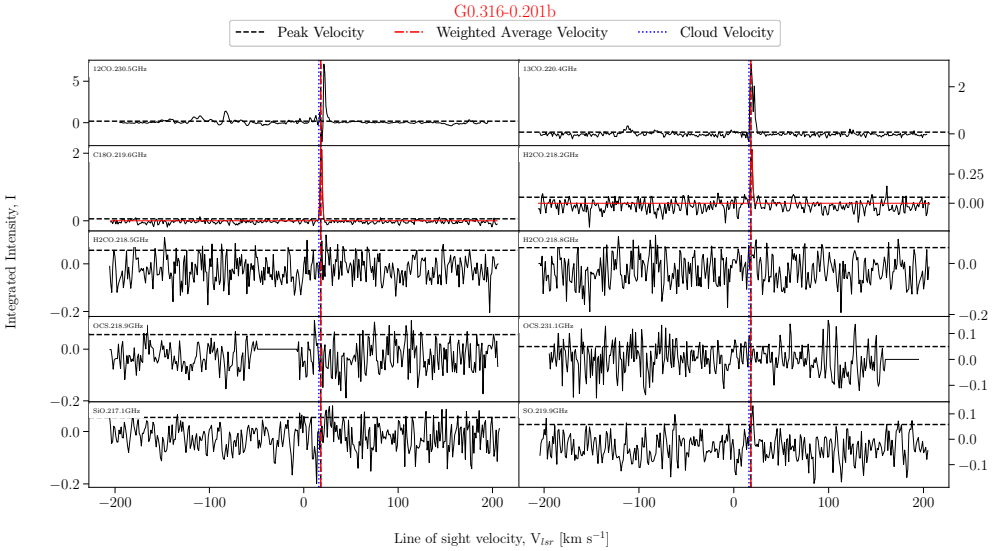

FIGURE A.122: Fitted spectra for dendrogram leaf G0.316-0.201b, with scouse fits overlaid in red.

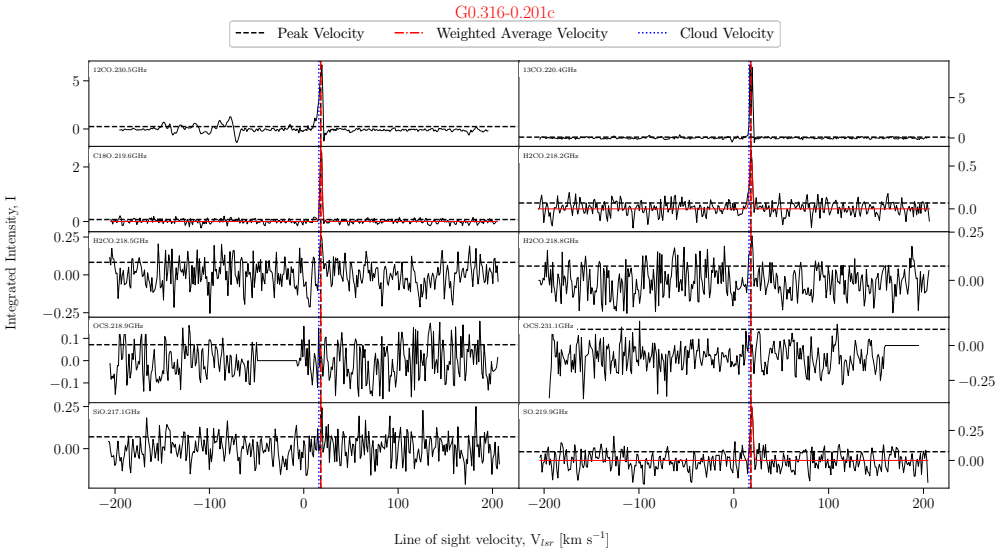

FIGURE A.123: Fitted spectra for dendrogram leaf G0.316-0.201c, with scouse fits overlaid in red.

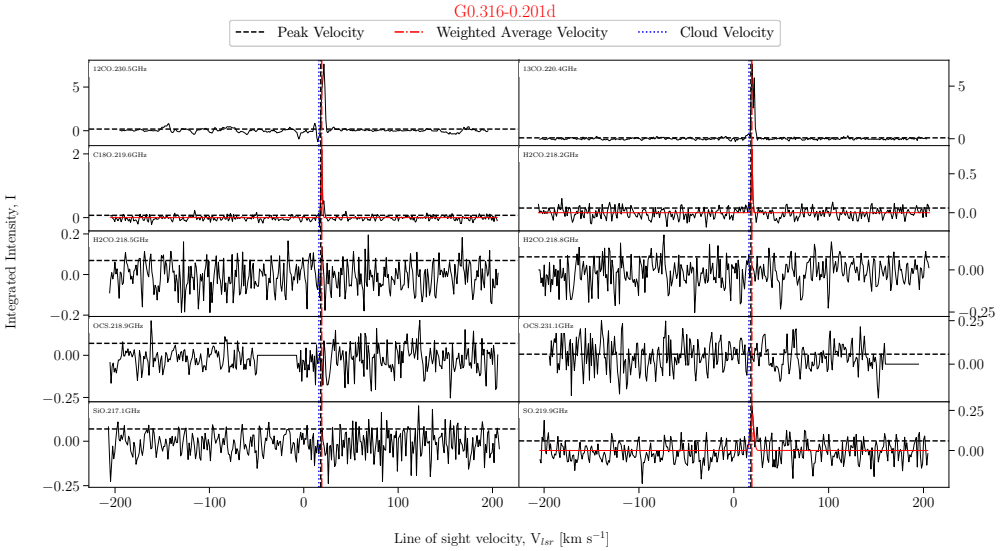

FIGURE A.124: Fitted spectra for dendrogram leaf G0.316-0.201d, with scouse fits overlaid in red.

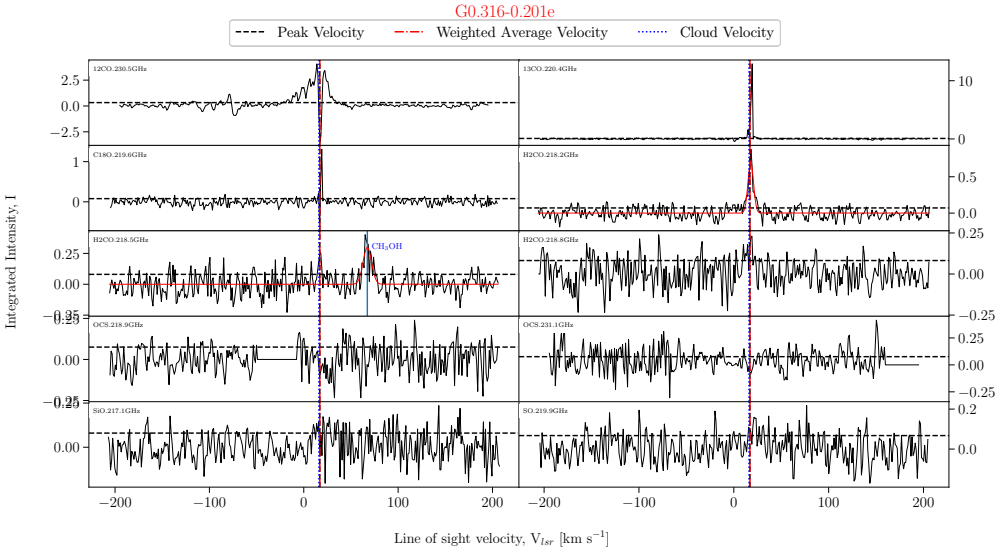

FIGURE A.125: Fitted spectra for dendrogram leaf G0.316-0.201e, with scouse fits overlaid in red.

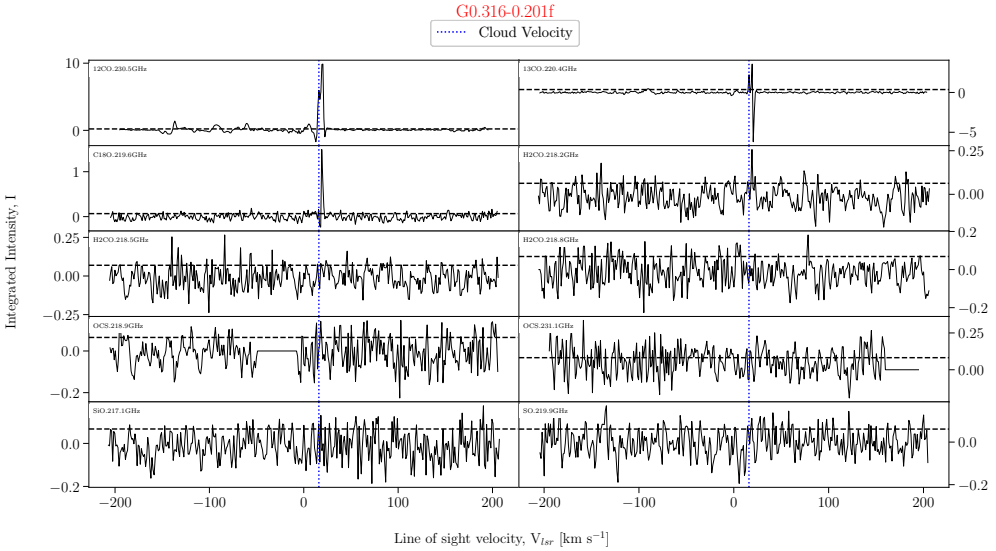

FIGURE A.126: Fitted spectra for dendrogram leaf G0.316-0.201f, with scouse fits overlaid in red.

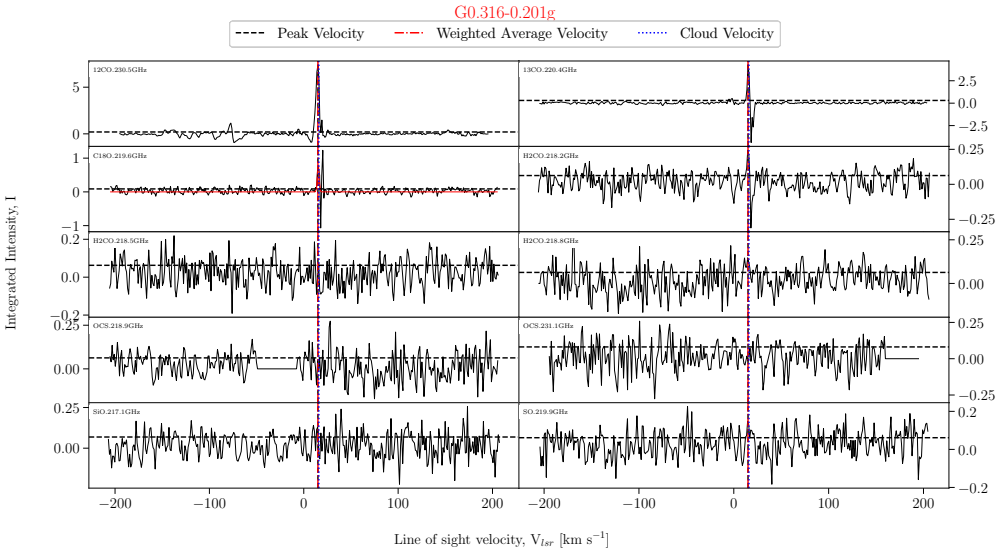

FIGURE A.127: Fitted spectra for dendrogram leaf G0.316-0.201g, with scouse fits overlaid in red.

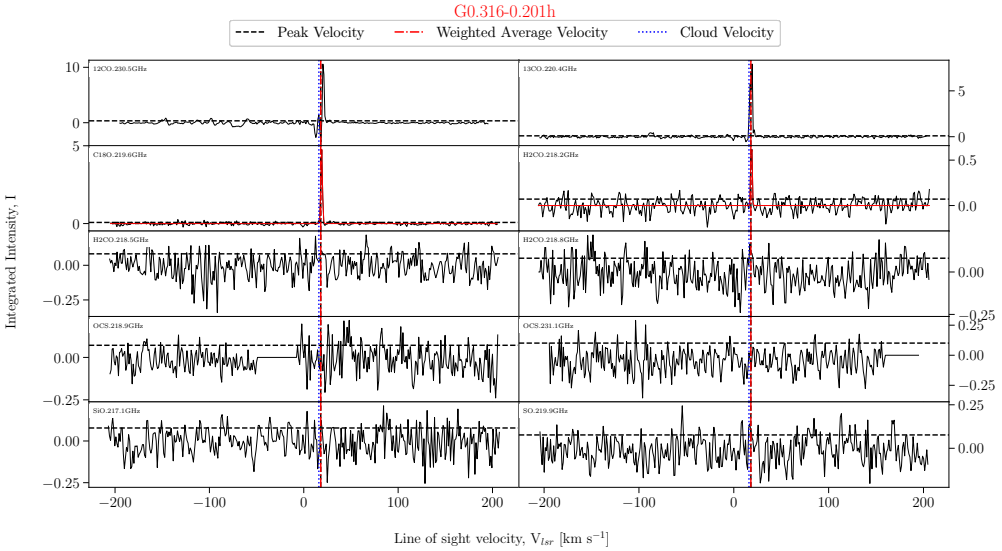

FIGURE A.128: Fitted spectra for dendrogram leaf G0.316-0.201h, with scouse fits overlaid in red.

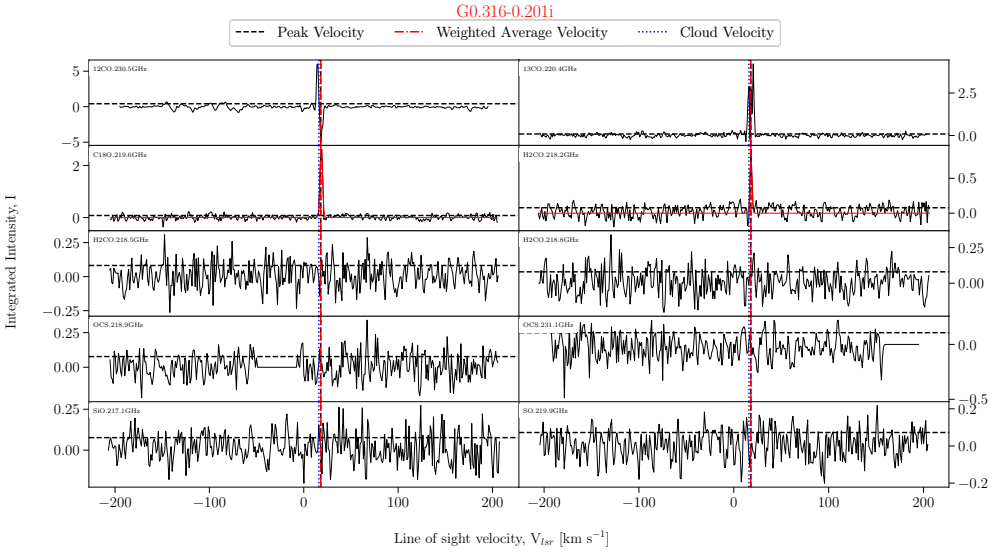

FIGURE A.129: Fitted spectra for dendrogram leaf G0.316-0.201i, with scouse fits overlaid in red.

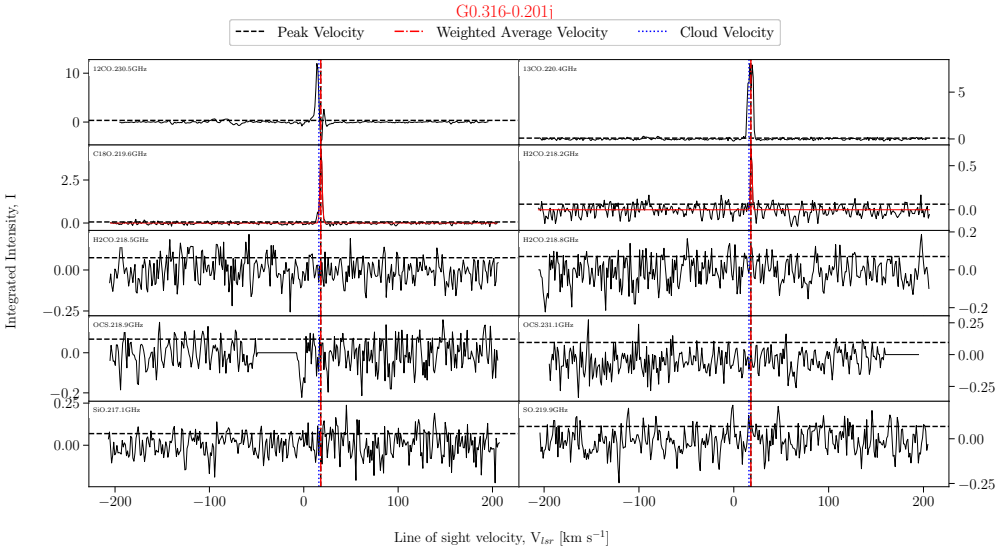

FIGURE A.130: Fitted spectra for dendrogram leaf G0.316-0.201j, with scouse fits overlaid in red.

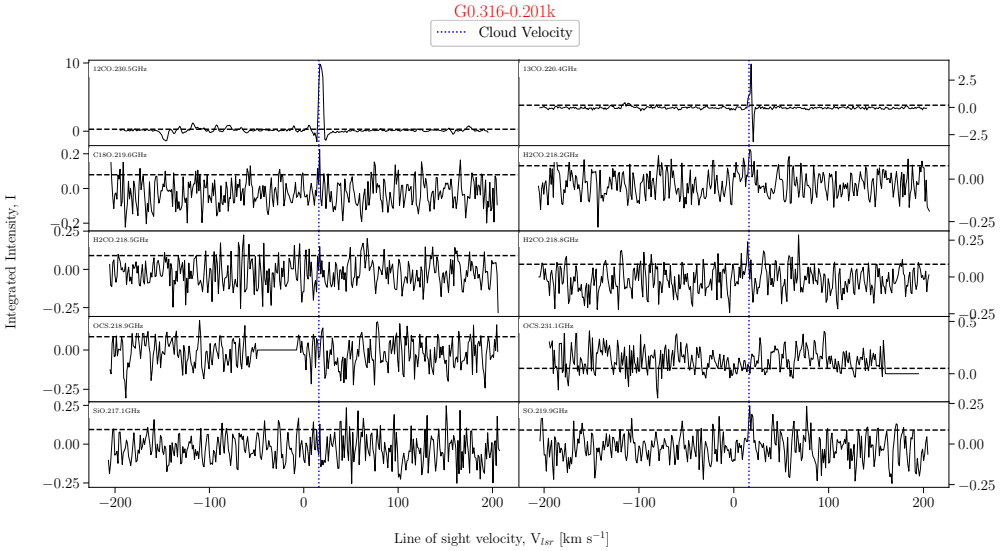

FIGURE A.131: Fitted spectra for dendrogram leaf G0.316-0.201k, with scouse fits overlaid in red.

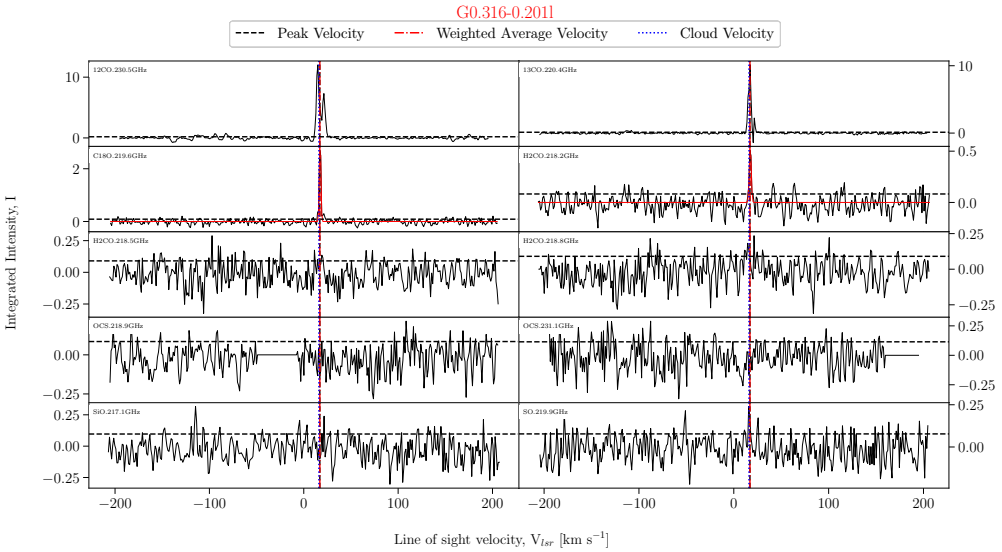

FIGURE A.132: Fitted spectra for dendrogram leaf G0.316-0.201l, with scouse fits overlaid in red.

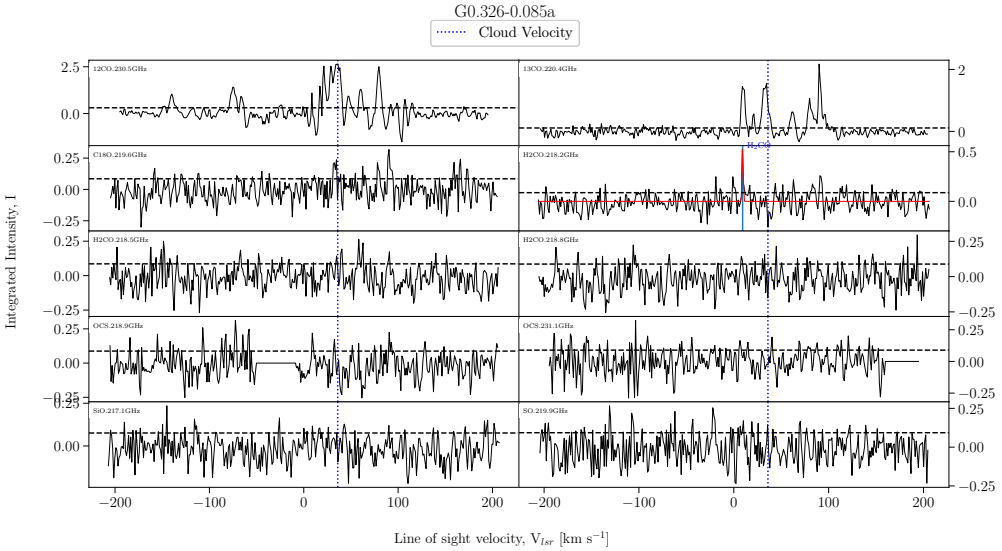

FIGURE A.133: Fitted spectra for dendrogram leaf G0.326-0.085a, with scouse fits overlaid in red.

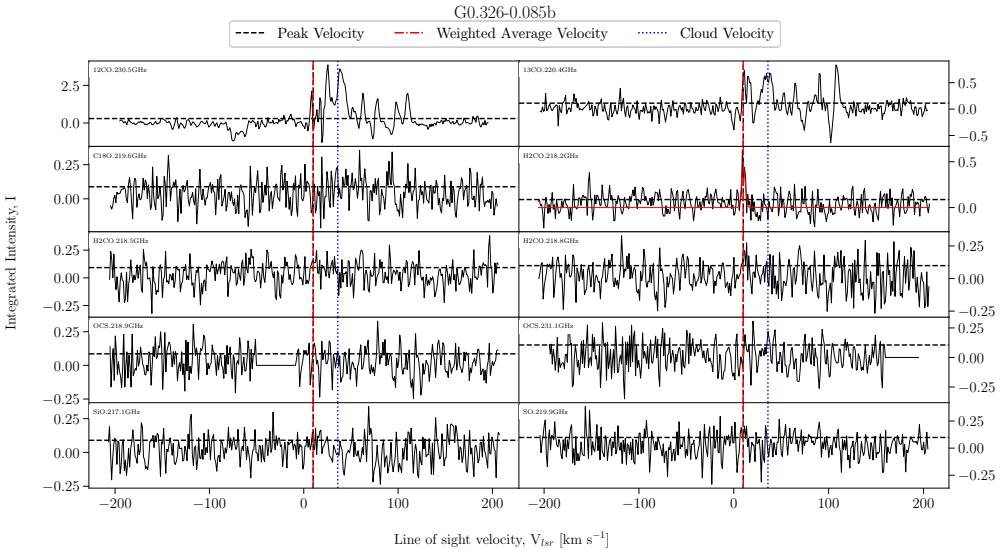

FIGURE A.134: Fitted spectra for dendrogram leaf G0.326-0.085b, with scouse fits overlaid in red.

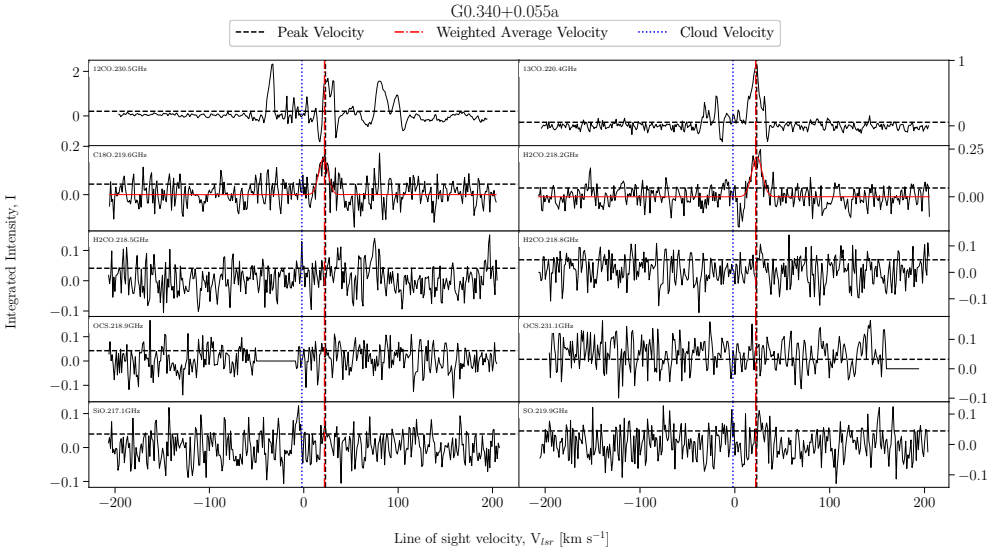

FIGURE A.135: Fitted spectra for dendrogram leaf G0.340-0.055a, with scouse fits overlaid in red.

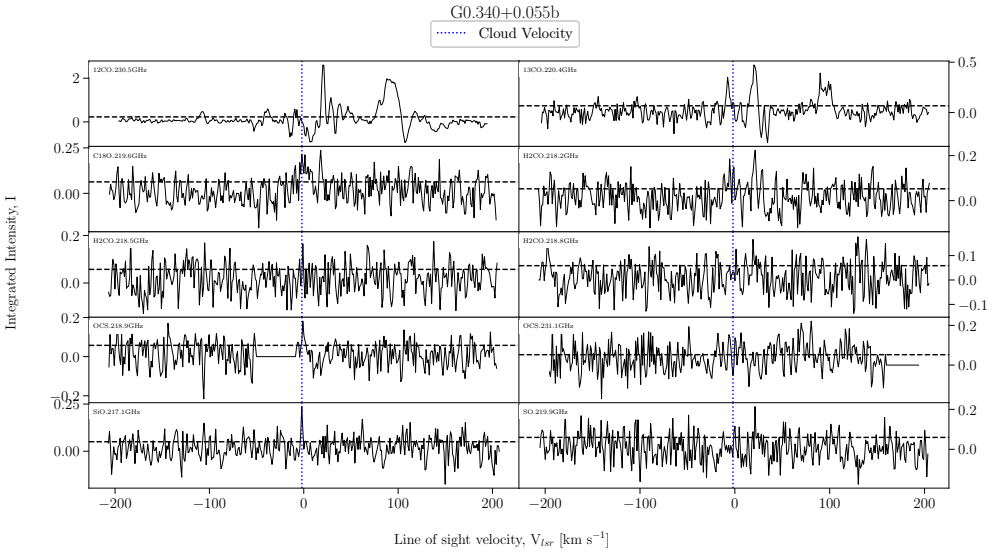

FIGURE A.136: Fitted spectra for dendrogram leaf G0.340-0.055b, with scouse fits overlaid in red.

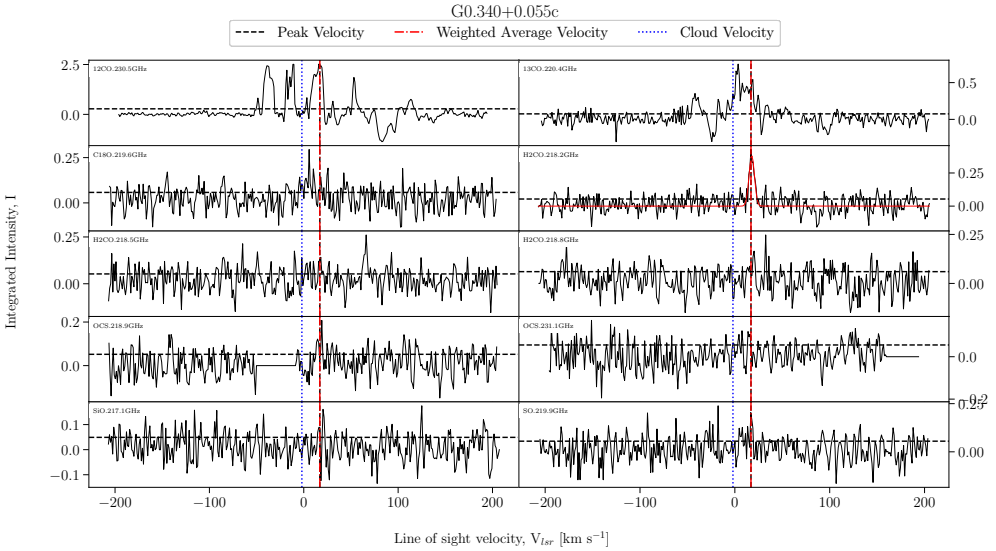

FIGURE A.137: Fitted spectra for dendrogram leaf G0.340-0.055c, with scouse fits overlaid in red.

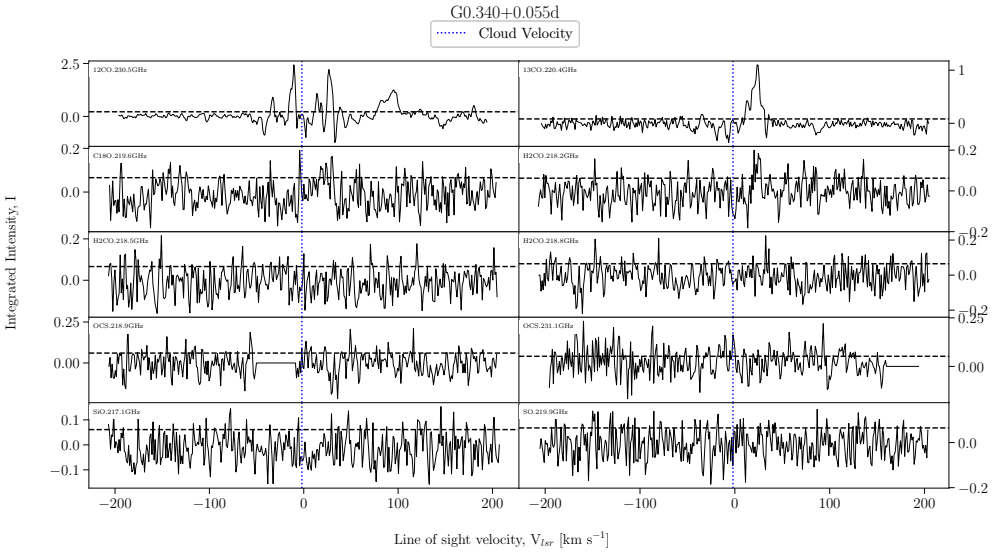

FIGURE A.138: Fitted spectra for dendrogram leaf G0.340-0.055d, with scouse fits overlaid in red.

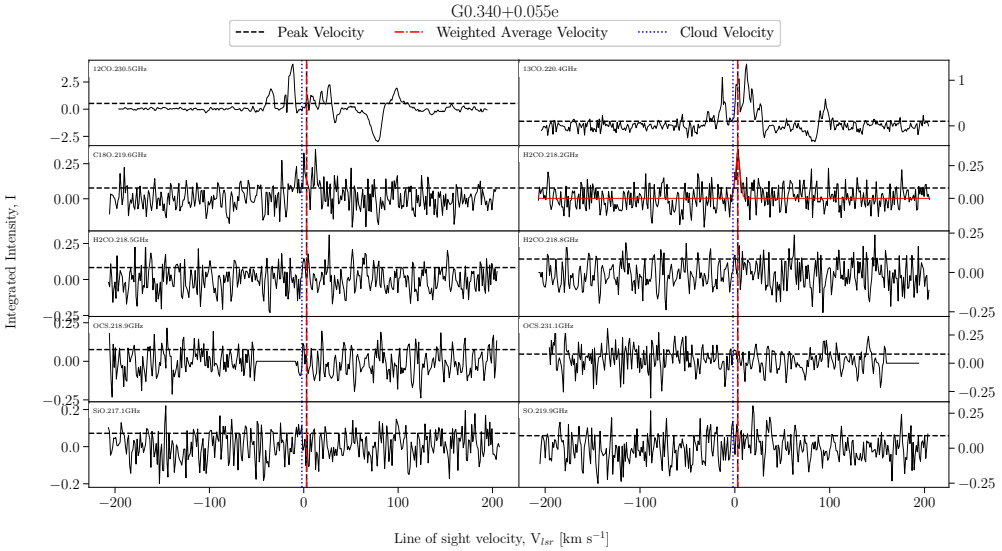

FIGURE A.139: Fitted spectra for dendrogram leaf G0.340-0.055e, with scouse fits overlaid in red.

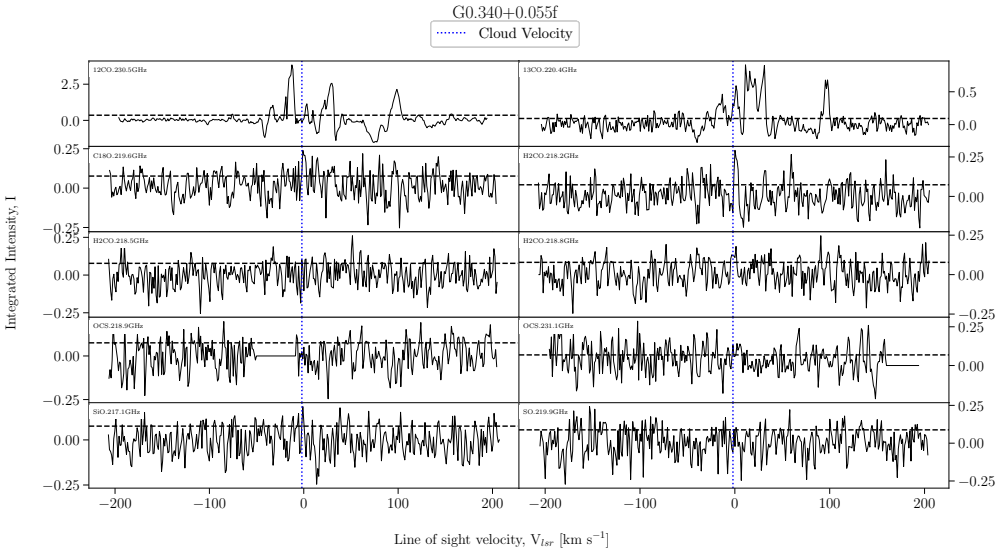

FIGURE A.140: Fitted spectra for dendrogram leaf G0.340-0.055f, with scouse fits overlaid in red.

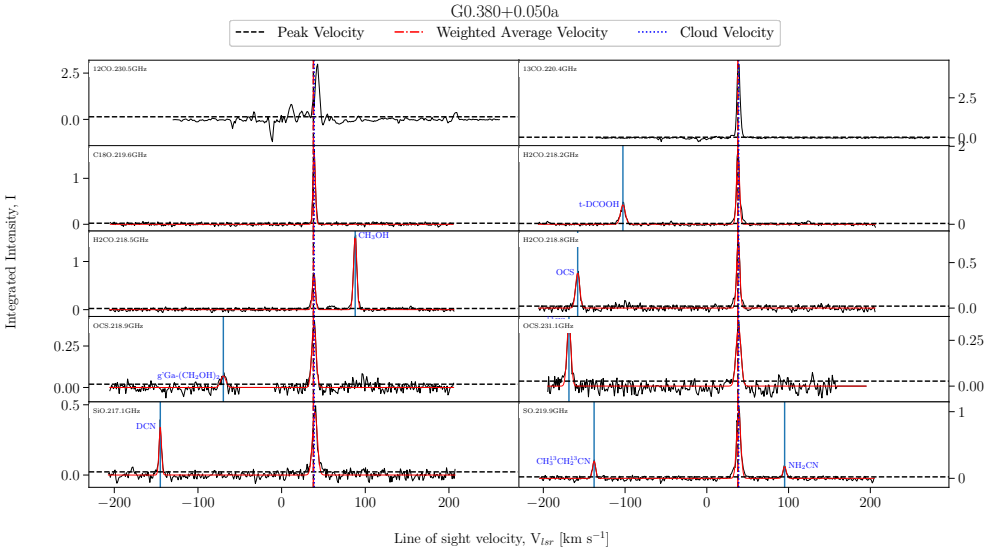

FIGURE A.141: Fitted spectra for dendrogram leaf G0.380-0.050a, with scouse fits overlaid in red.

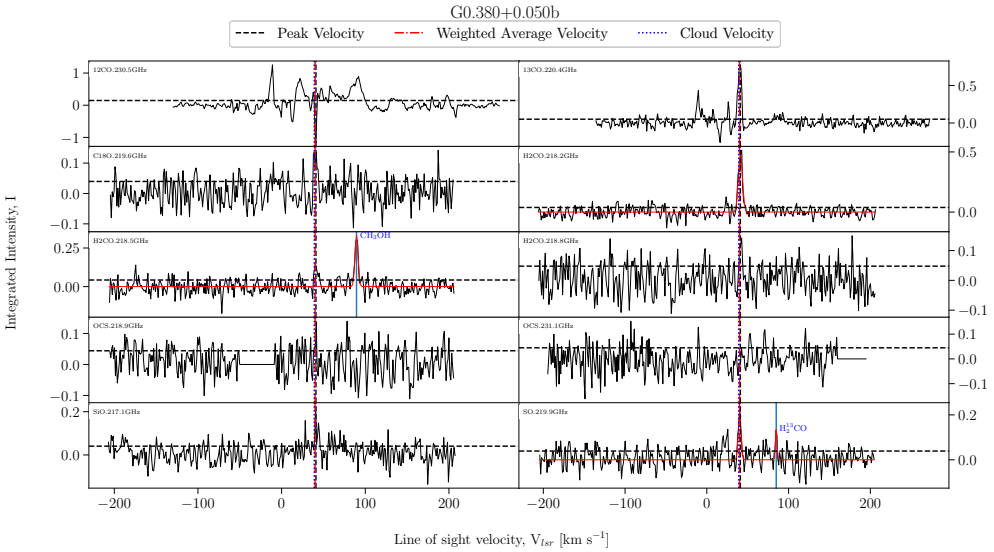

FIGURE A.142: Fitted spectra for dendrogram leaf G0.380-0.050b, with scouse fits overlaid in red.

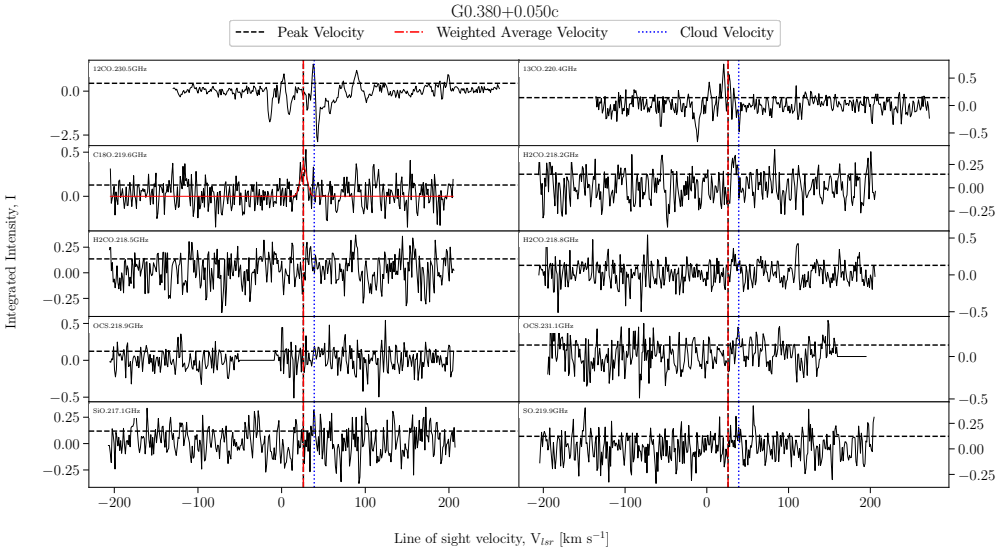

FIGURE A.143: Fitted spectra for dendrogram leaf G0.380-0.050c, with scouse fits overlaid in red.

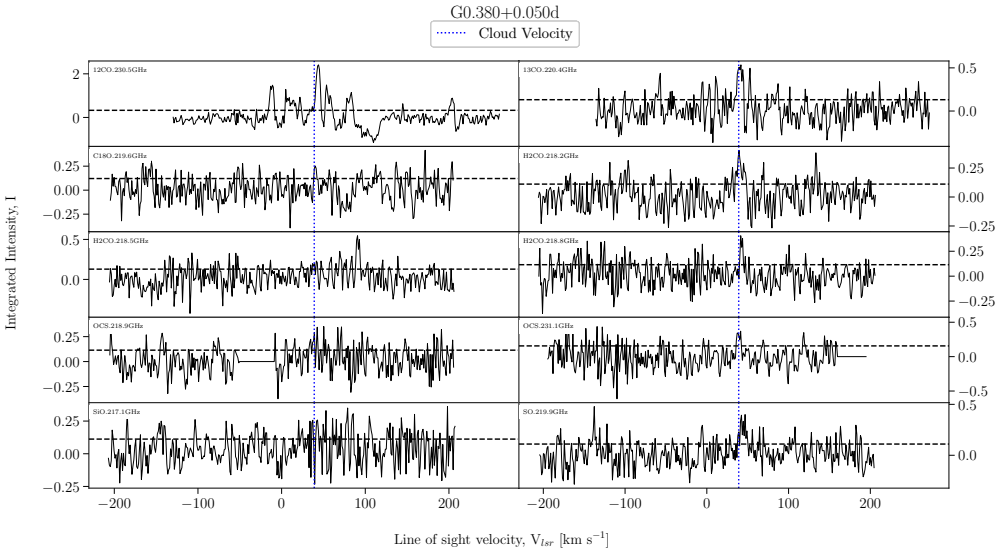

FIGURE A.144: Fitted spectra for dendrogram leaf G0.380-0.050d, with scouse fits overlaid in red.

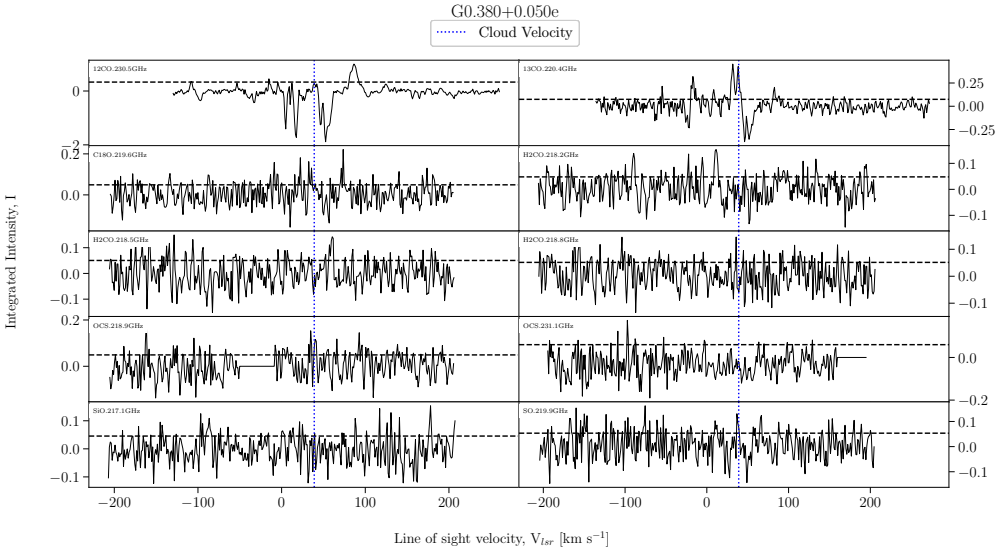

FIGURE A.145: Fitted spectra for dendrogram leaf G0.380-0.050e, with scouse fits overlaid in red.

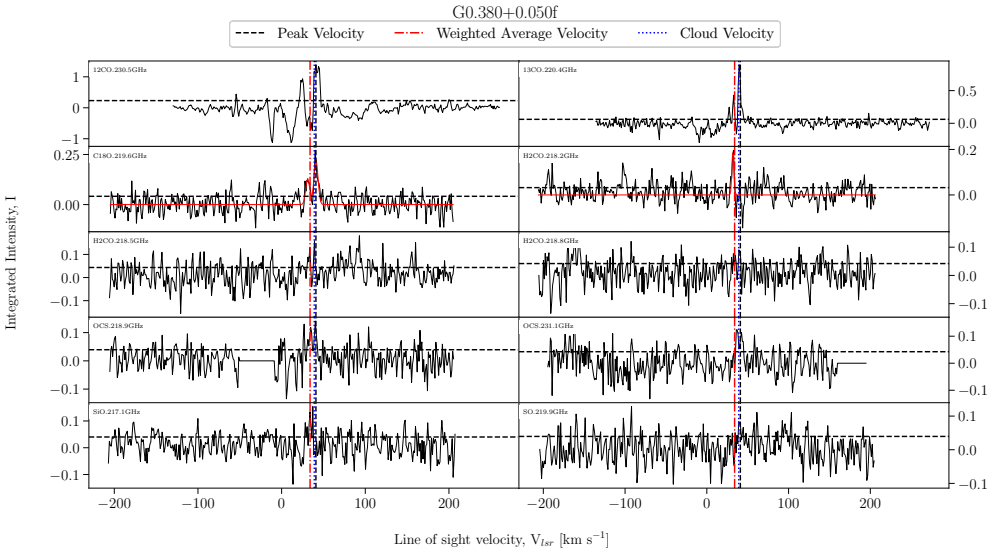

FIGURE A.146: Fitted spectra for dendrogram leaf G0.380-0.050f, with scouse fits overlaid in red.

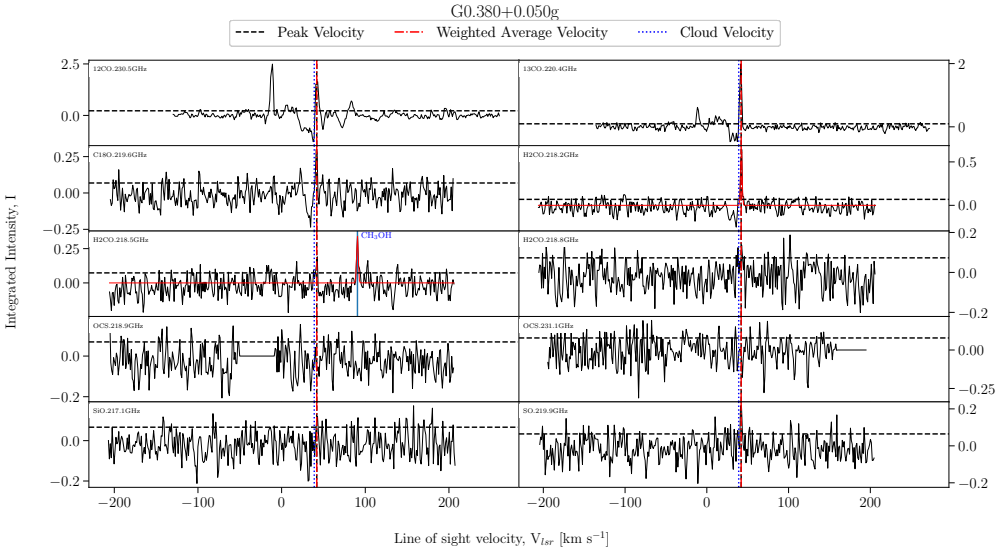

FIGURE A.147: Fitted spectra for dendrogram leaf G0.380-0.050g, with scouse fits overlaid in red.

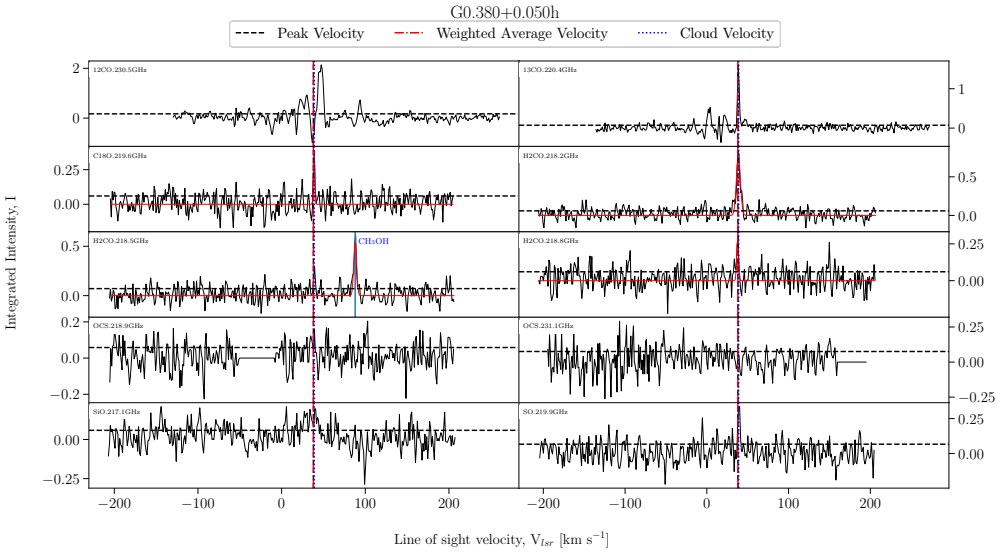

FIGURE A.148: Fitted spectra for dendrogram leaf G0.380-0.050h, with scouse fits overlaid in red.

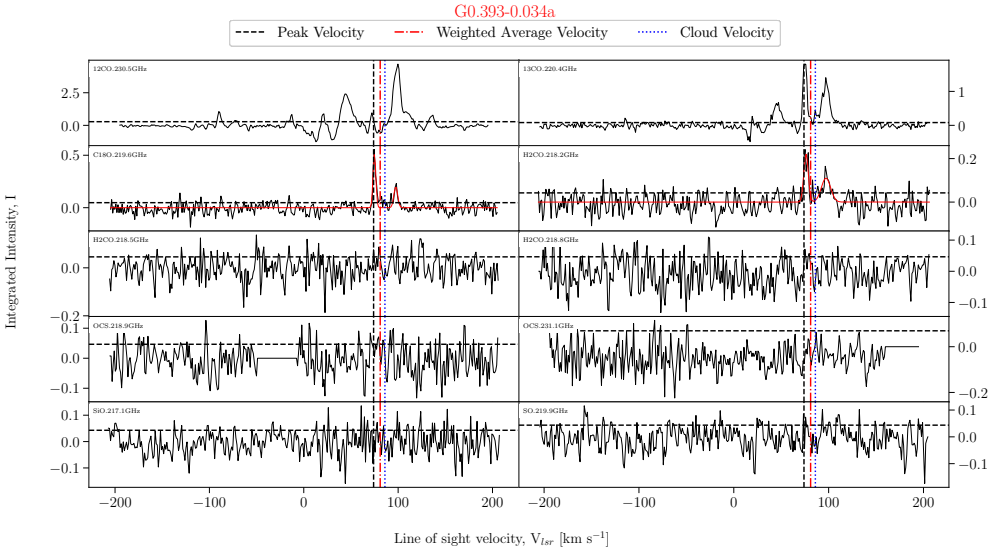

FIGURE A.149: Fitted spectra for dendrogram leaf G0.393-0.034a, with scouse fits overlaid in red.

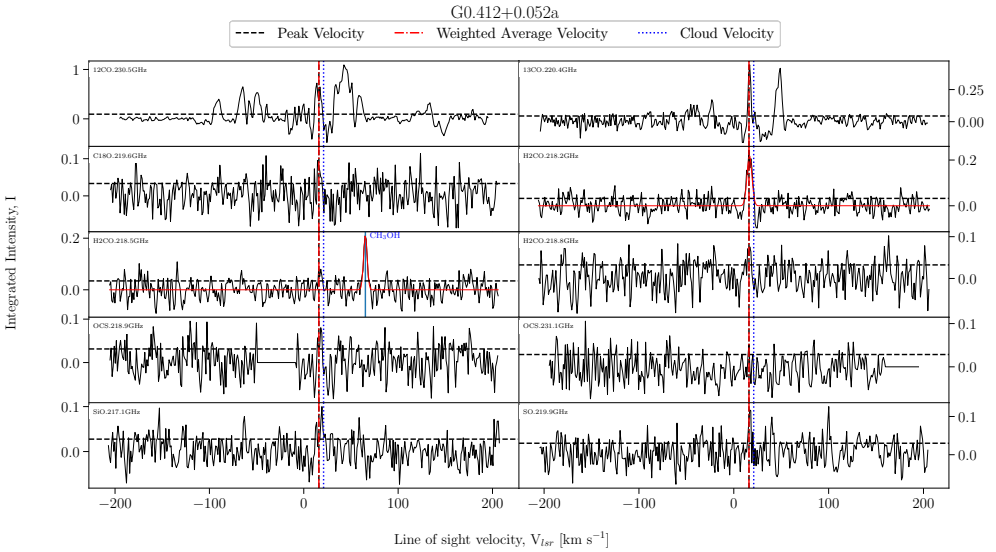

FIGURE A.150: Fitted spectra for dendrogram leaf G0.412+0.052a, with scouse fits overlaid in red.

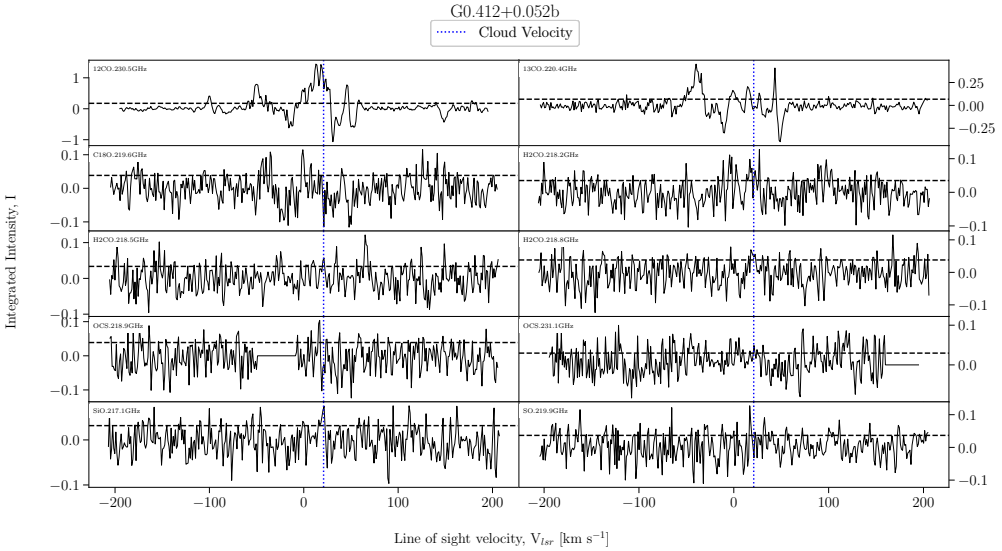

FIGURE A.151: Fitted spectra for dendrogram leaf G0.412+0.052b, with scouse fits overlaid in red.

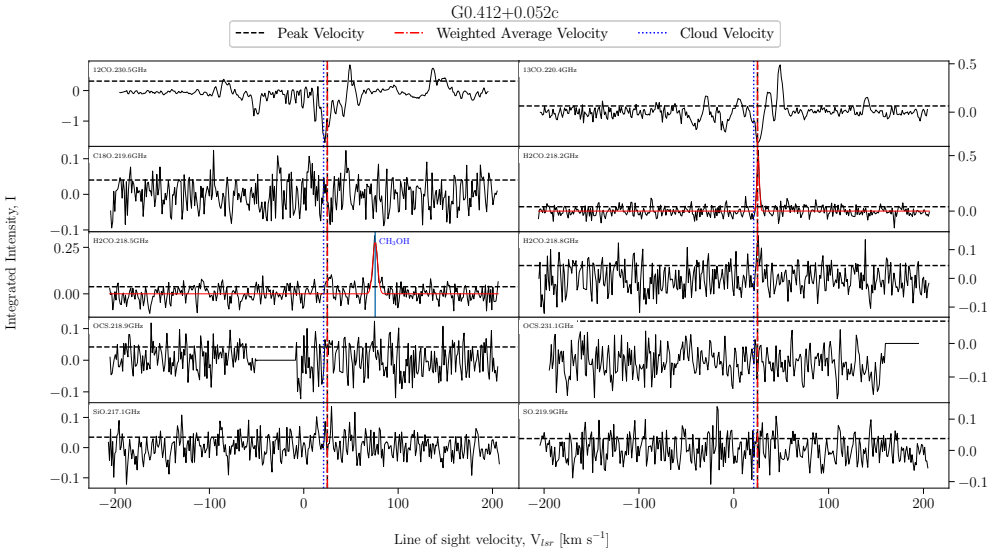

FIGURE A.152: Fitted spectra for dendrogram leaf G0.412+0.052c, with scouse fits overlaid in red.

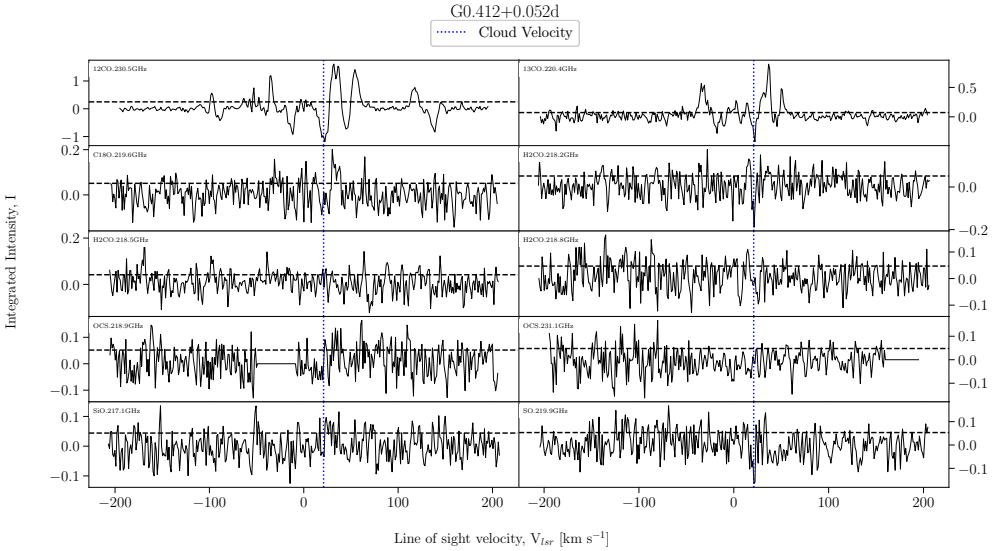

FIGURE A.153: Fitted spectra for dendrogram leaf G0.412+0.052d, with scouse fits overlaid in red.

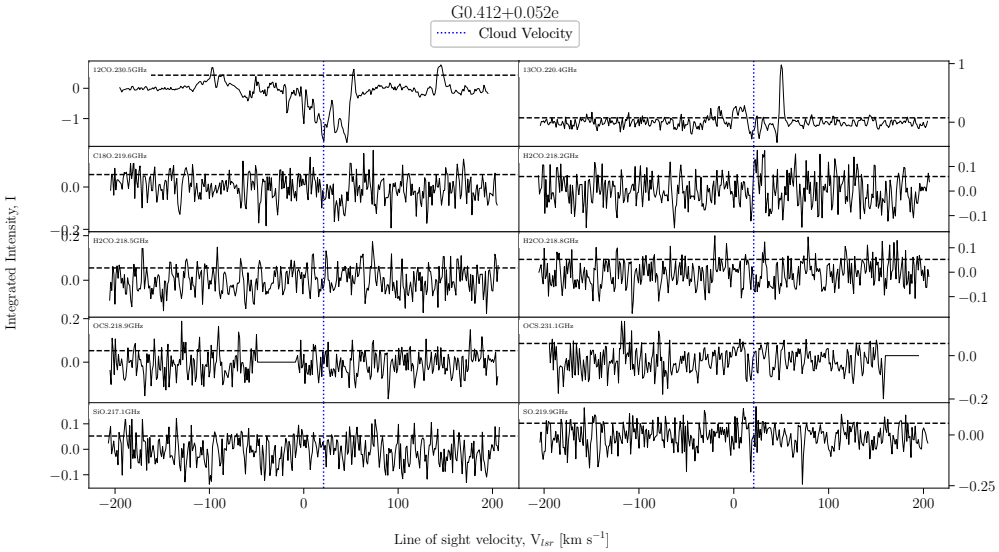

FIGURE A.154: Fitted spectra for dendrogram leaf G0.412+0.052e, with scouse fits overlaid in red.

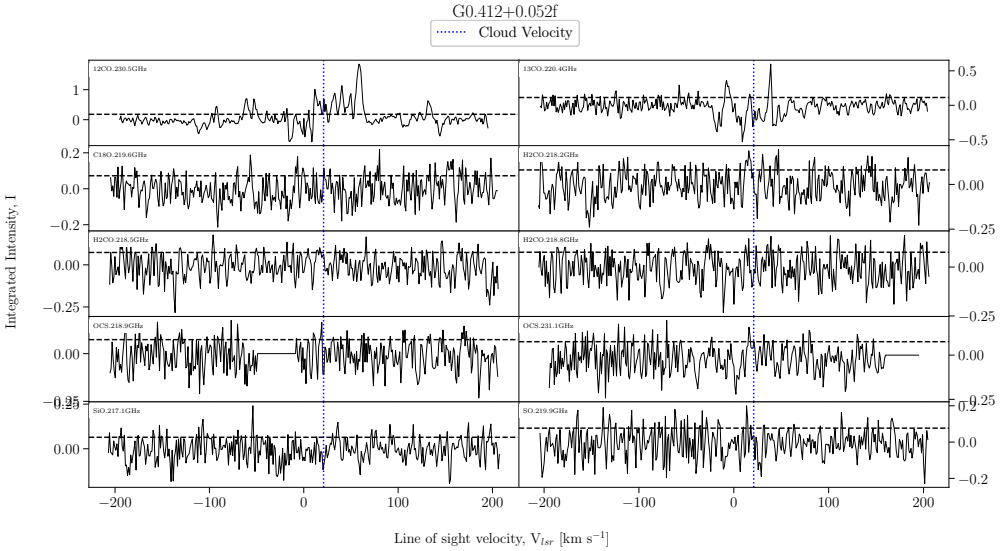

FIGURE A.155: Fitted spectra for dendrogram leaf G0.412+0.052f, with scouse fits overlaid in red.

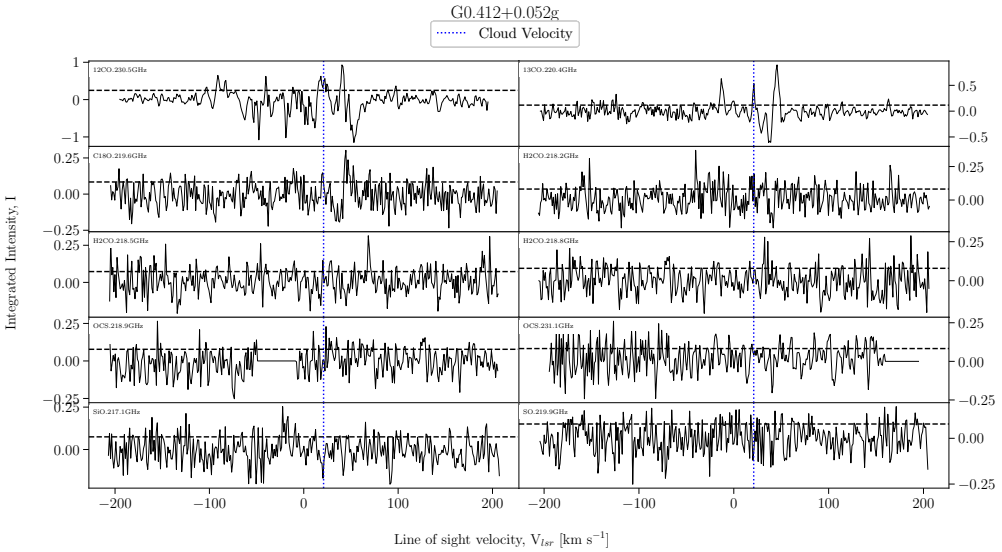

FIGURE A.156: Fitted spectra for dendrogram leaf G0.412+0.052g, with scouse fits overlaid in red.

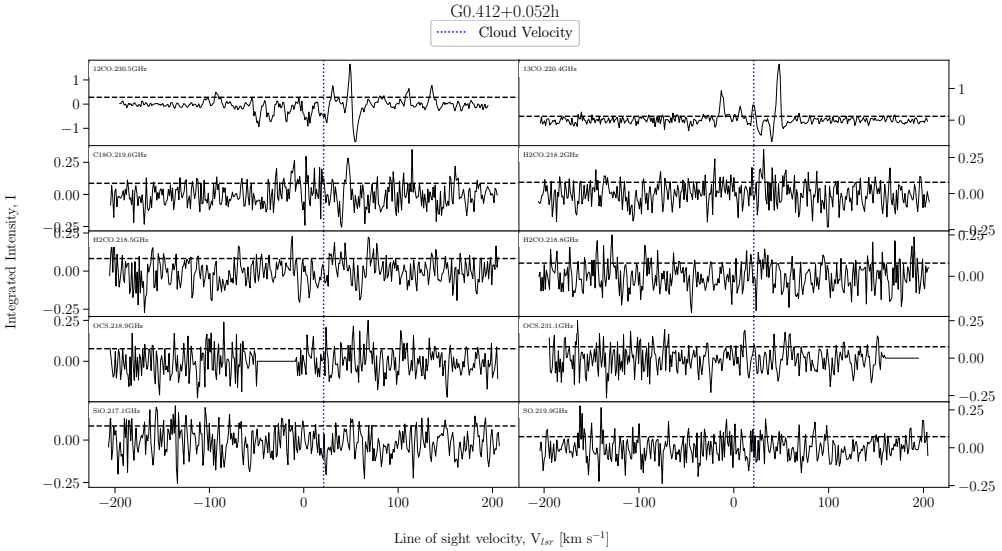

FIGURE A.157: Fitted spectra for dendrogram leaf G0.412+0.052h, with scouse fits overlaid in red.

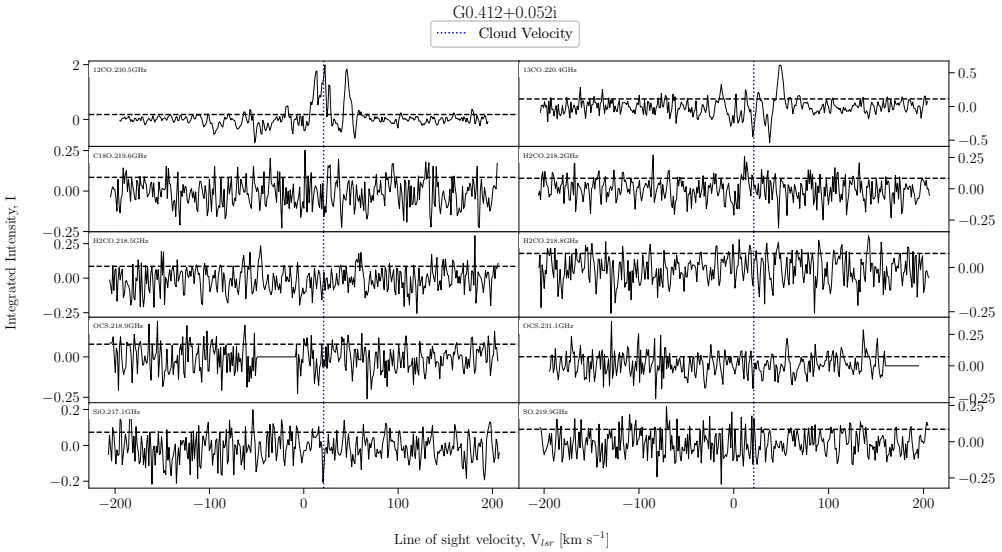

FIGURE A.158: Fitted spectra for dendrogram leaf G0.412+0.052i, with scouse fits overlaid in red.

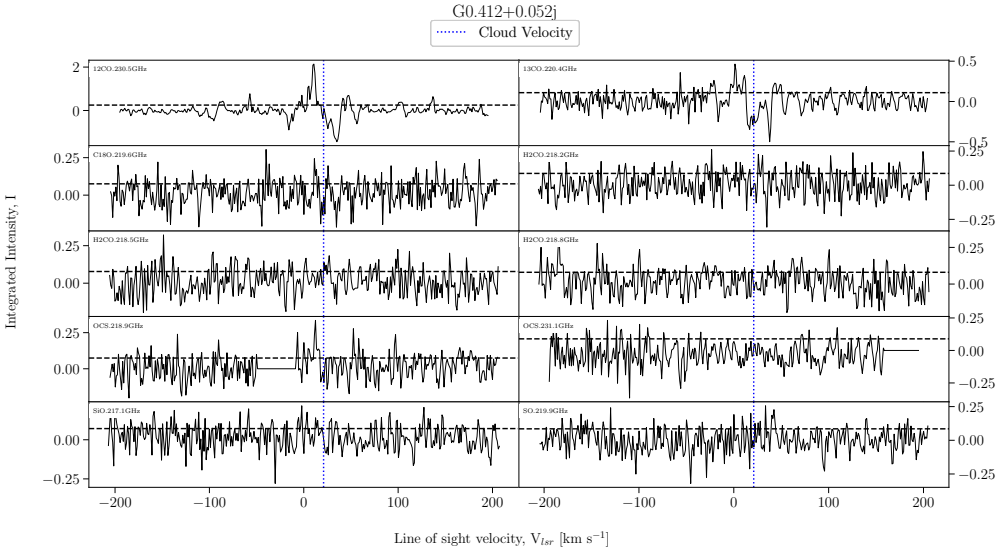

FIGURE A.159: Fitted spectra for dendrogram leaf G0.412+0.052j, with scouse fits overlaid in red.

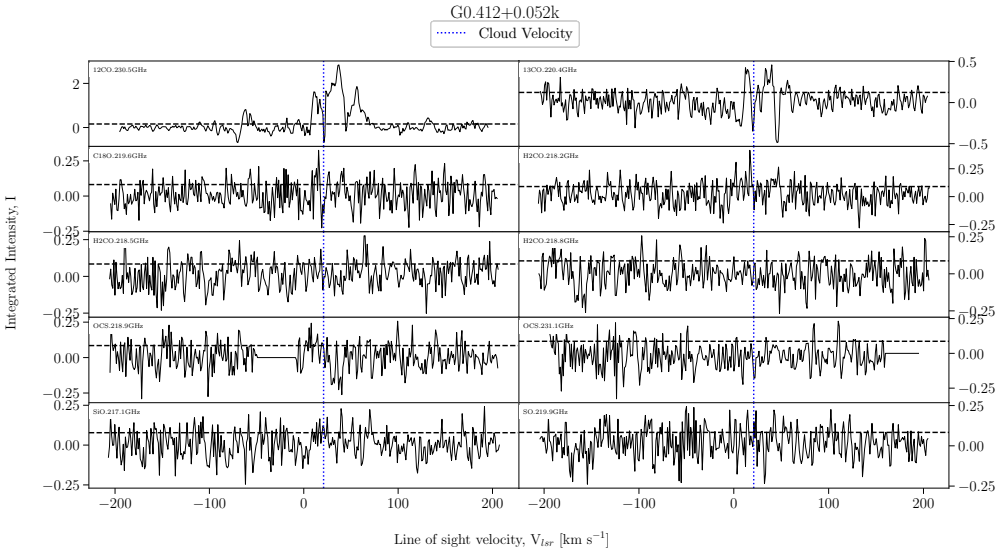

FIGURE A.160: Fitted spectra for dendrogram leaf G0.412+0.052k, with scouse fits overlaid in red.

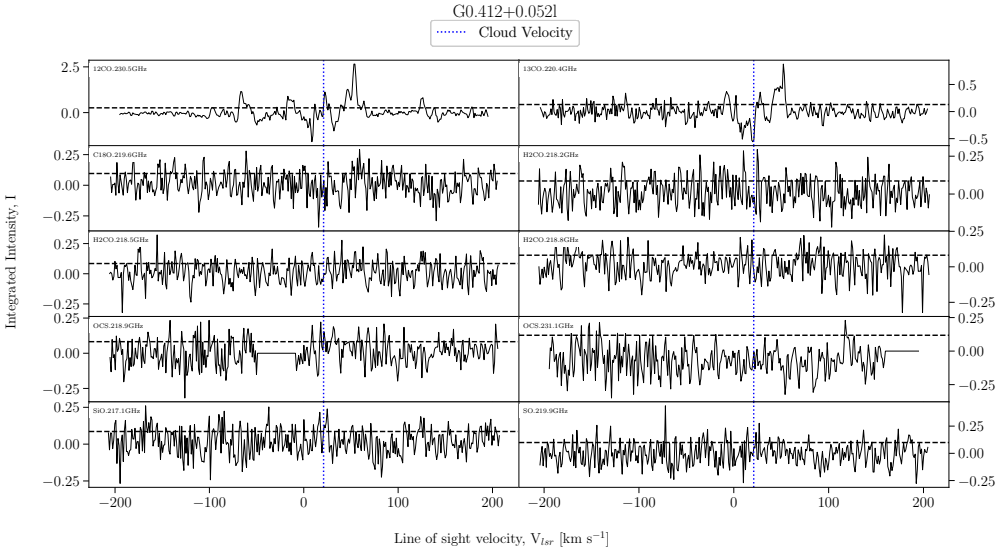

FIGURE A.161: Fitted spectra for dendrogram leaf G0.412+0.052l, with scouse fits overlaid in red.

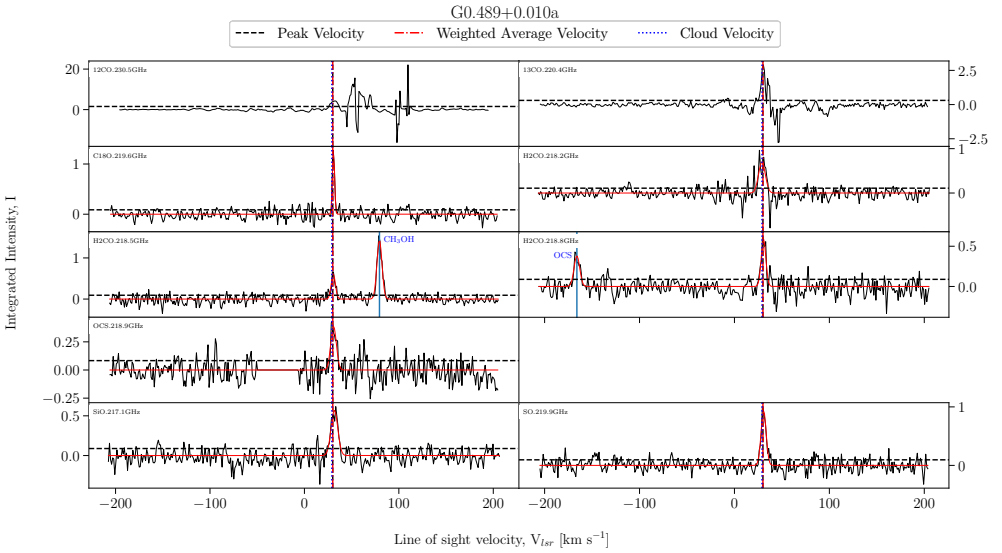

FIGURE A.162: Fitted spectra for dendrogram leaf G0.489+0.010a, with scouse fits overlaid in red.

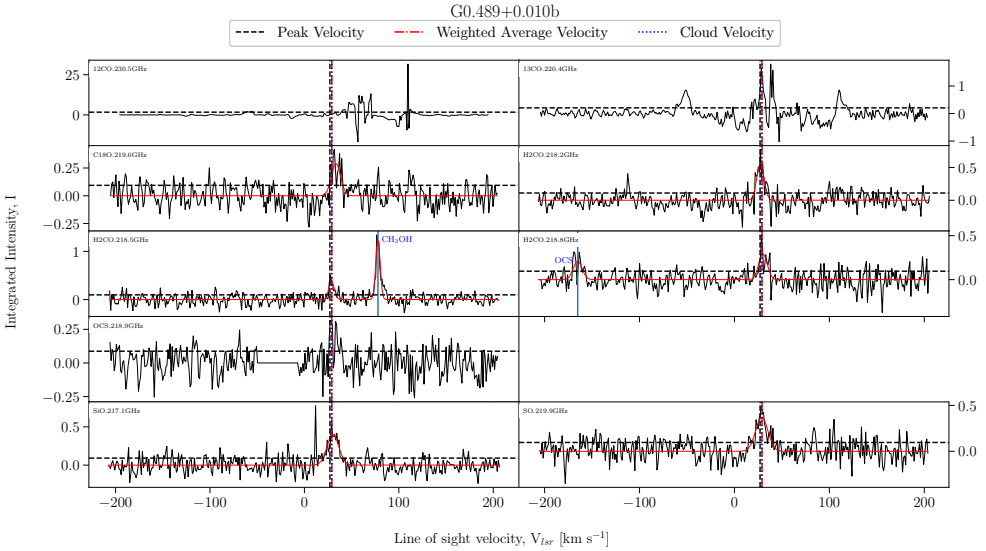

FIGURE A.163: Fitted spectra for dendrogram leaf G0.489+0.010b, with scouse fits overlaid in red.

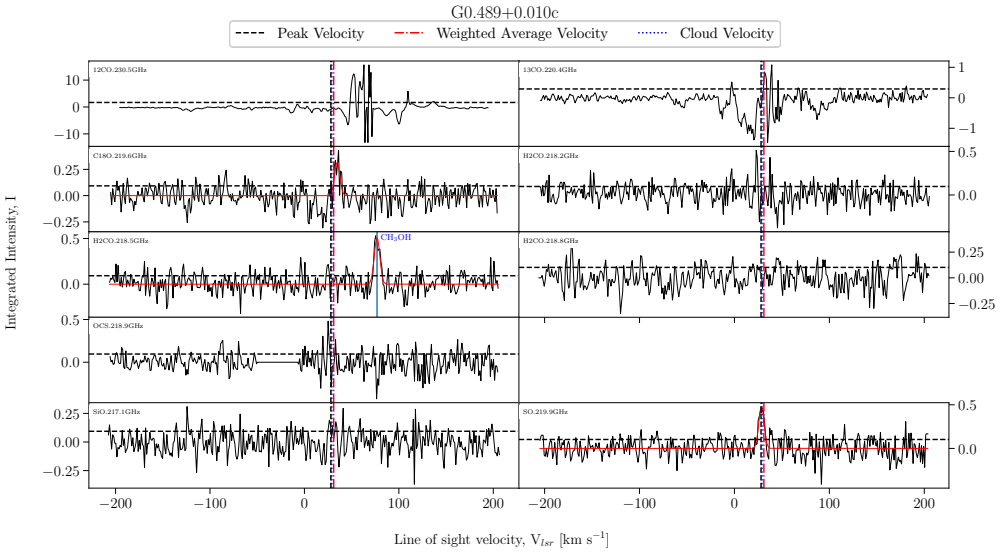

FIGURE A.164: Fitted spectra for dendrogram leaf G0.489+0.010c, with scouse fits overlaid in red.

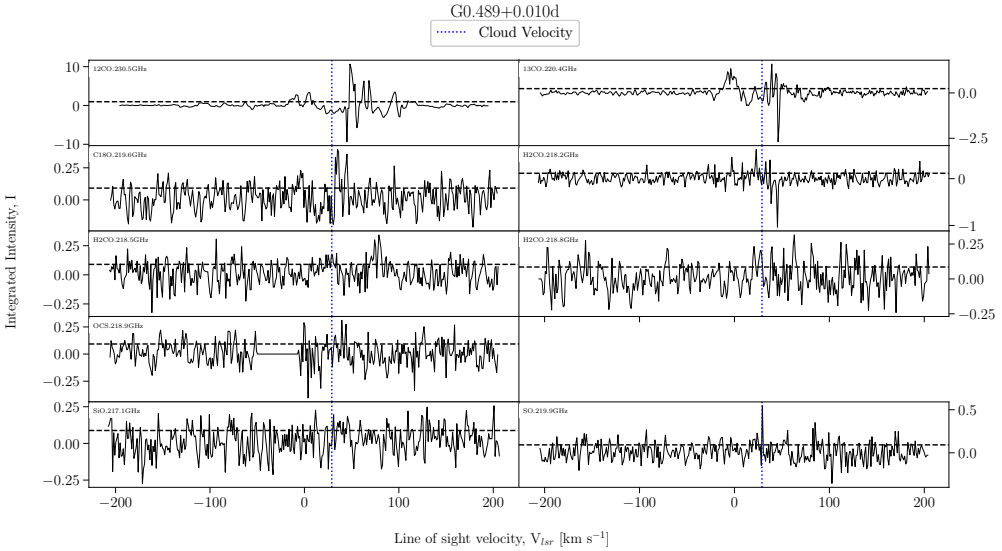

FIGURE A.165: Fitted spectra for dendrogram leaf G0.489+0.010d, with scouse fits overlaid in red.

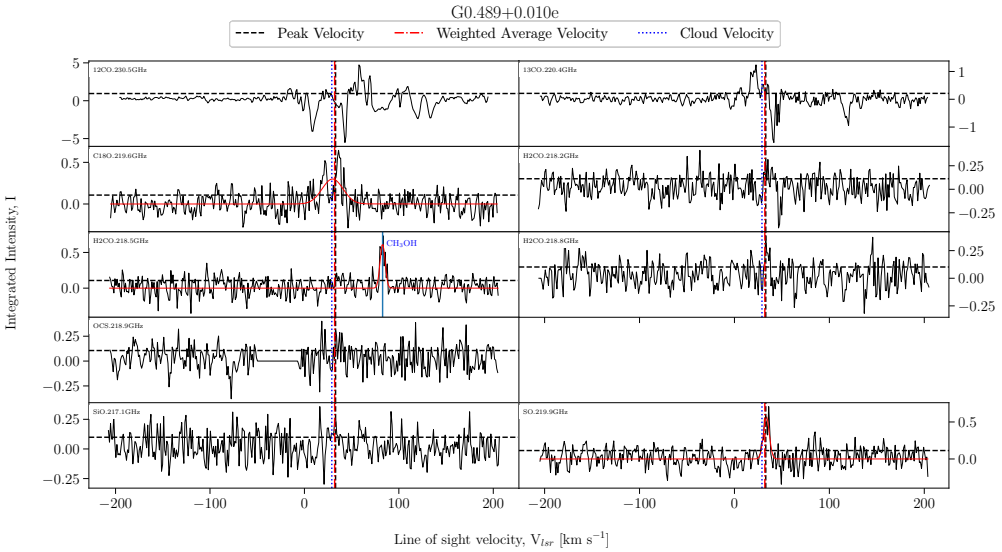

FIGURE A.166: Fitted spectra for dendrogram leaf G0.489+0.010e, with scouse fits overlaid in red.

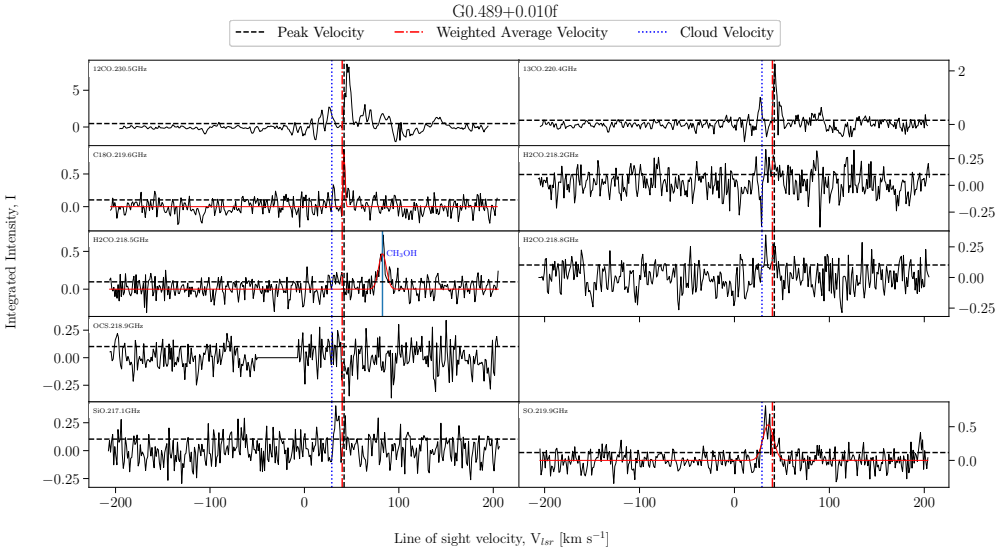

FIGURE A.167: Fitted spectra for dendrogram leaf G0.489+0.010f, with scouse fits overlaid in red.

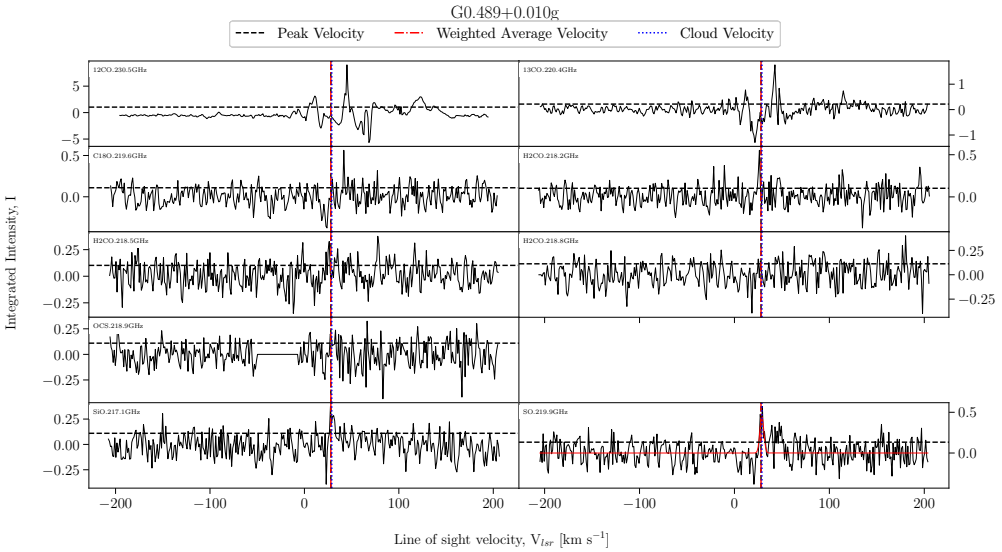

FIGURE A.168: Fitted spectra for dendrogram leaf G0.489+0.010g, with scouse fits overlaid in red.

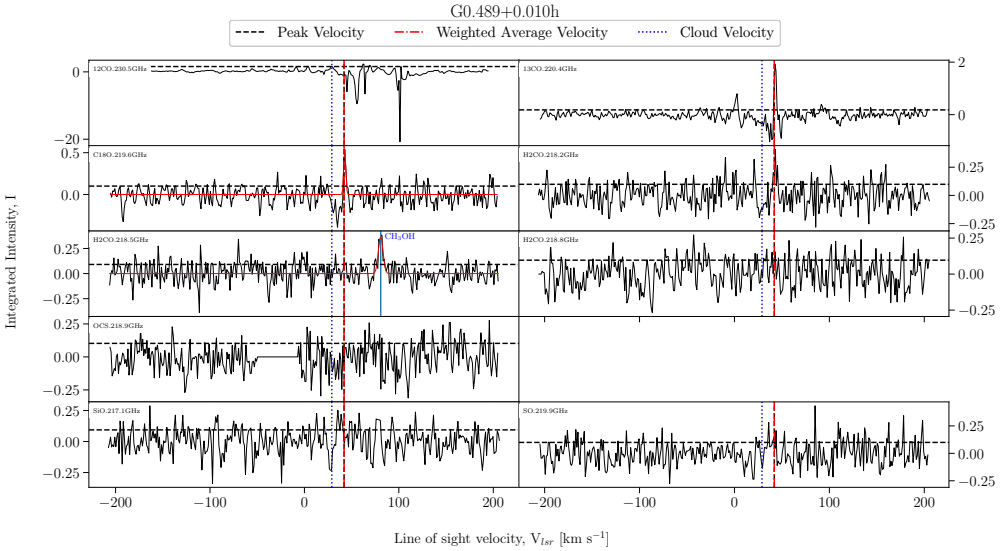

FIGURE A.169: Fitted spectra for dendrogram leaf G0.489+0.010h, with scouse fits overlaid in red.

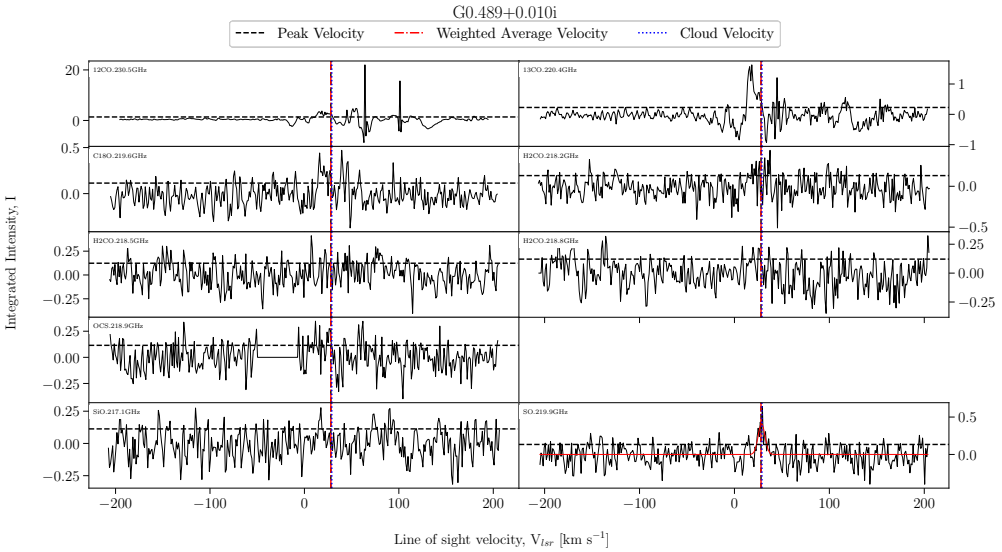

FIGURE A.170: Fitted spectra for dendrogram leaf G0.489+0.010i, with scouse fits overlaid in red.

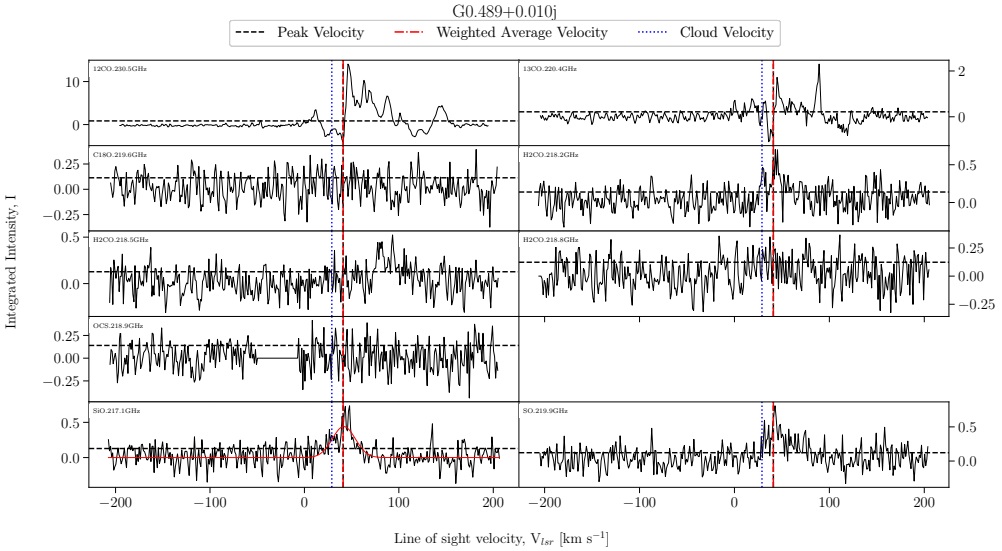

FIGURE A.171: Fitted spectra for dendrogram leaf G0.489+0.010j, with scouse fits overlaid in red.

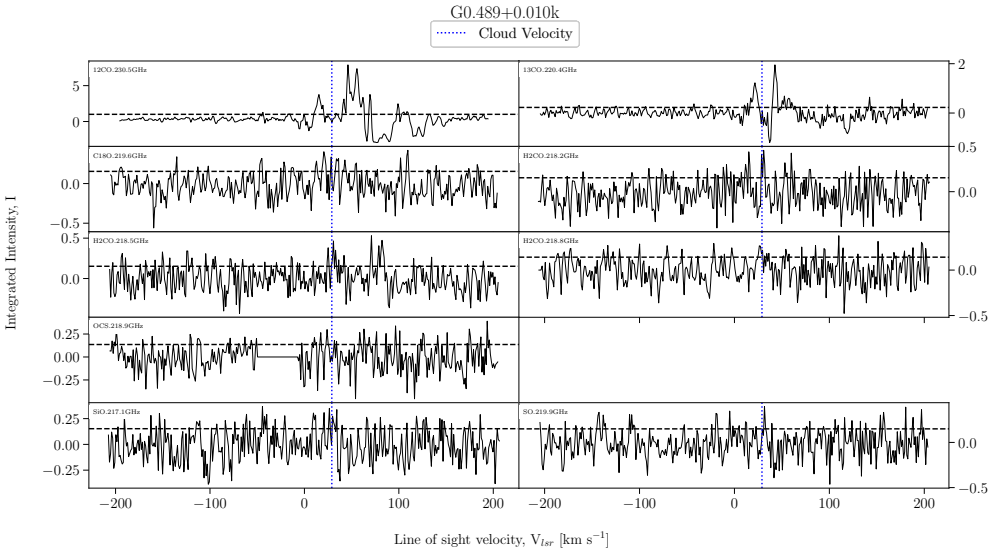

FIGURE A.172: Fitted spectra for dendrogram leaf G0.489+0.010k, with scouse fits overlaid in red.

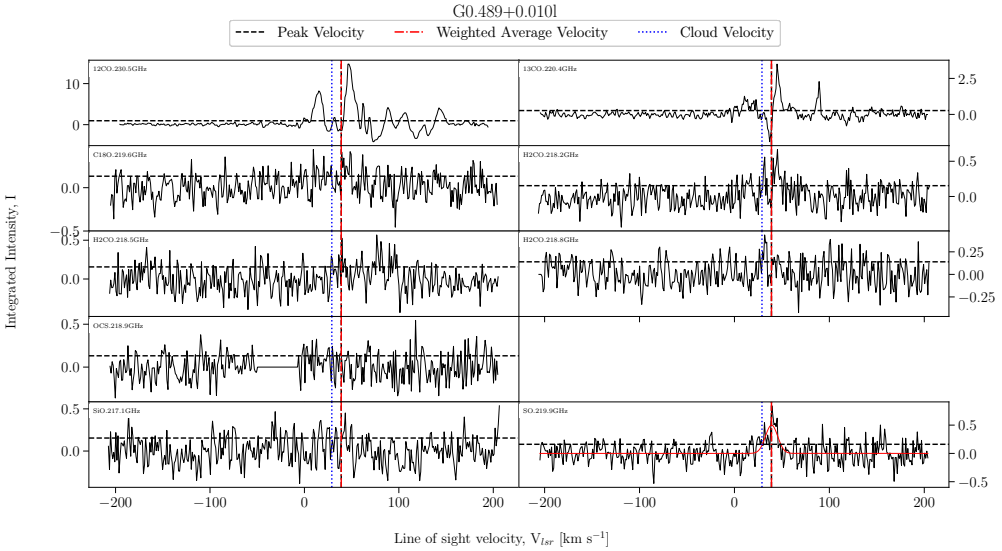

FIGURE A.173: Fitted spectra for dendrogram leaf G0.489+0.010l, with scouse fits overlaid in red.

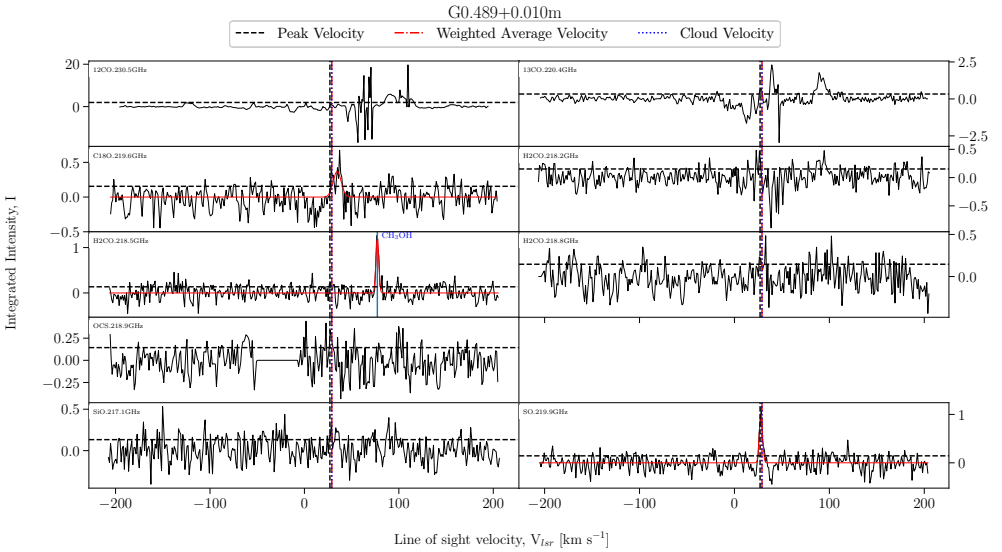

FIGURE A.174: Fitted spectra for dendrogram leaf G0.489+0.010m, with scouse fits overlaid in red.

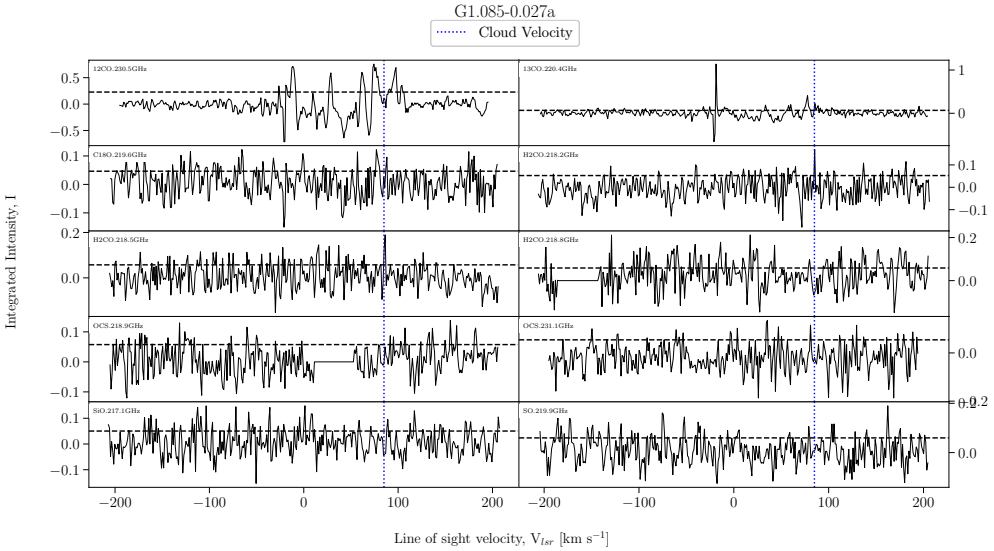

FIGURE A.175: Fitted spectra for dendrogram leaf G1.085-0.027a, with scouse fits overlaid in red.

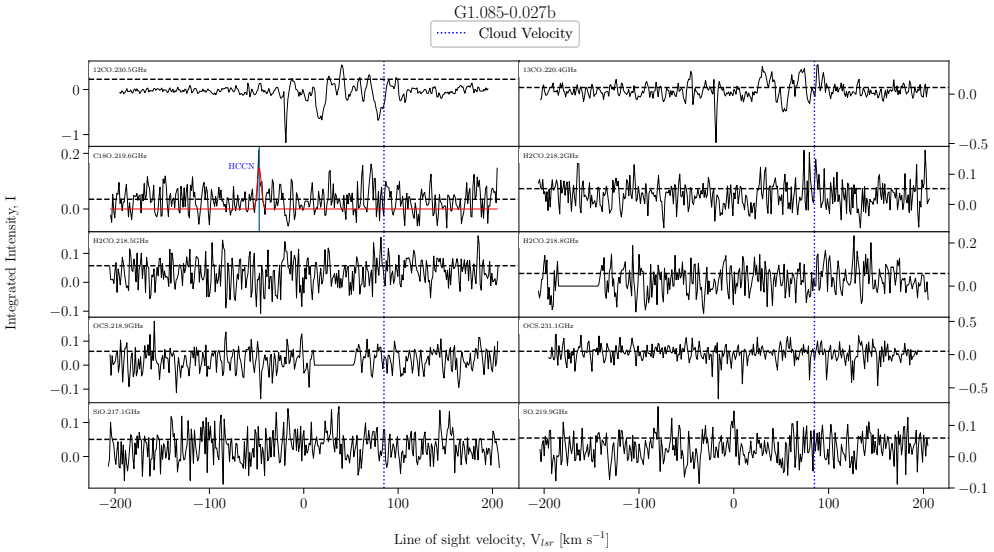

FIGURE A.176: Fitted spectra for dendrogram leaf G1.085-0.027b, with scouse fits overlaid in red.

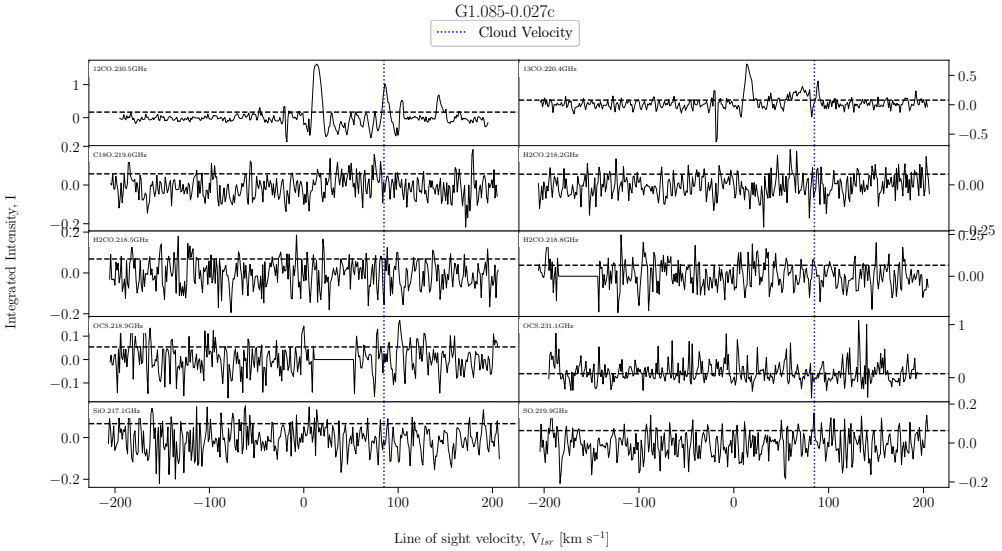

FIGURE A.177: Fitted spectra for dendrogram leaf G1.085-0.027c, with scouse fits overlaid in red.

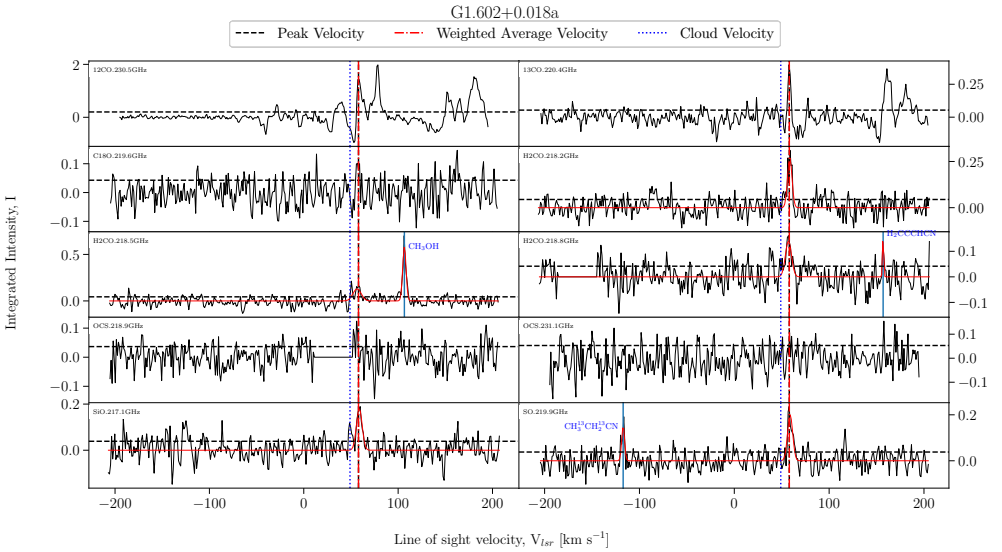

FIGURE A.178: Fitted spectra for dendrogram leaf G1.602+0.018a, with scouse fits overlaid in red.

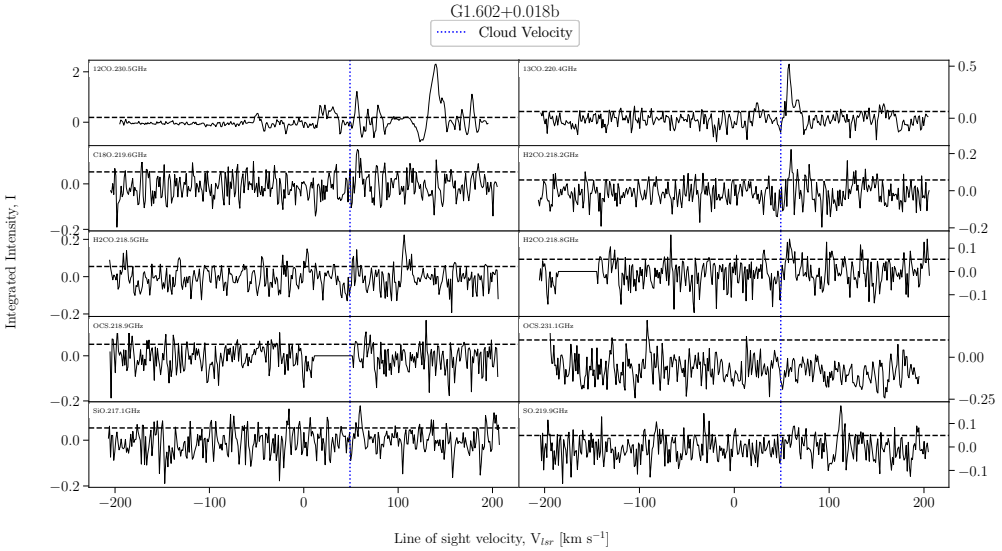

FIGURE A.179: Fitted spectra for dendrogram leaf G1.602+0.018b, with scouse fits overlaid in red.

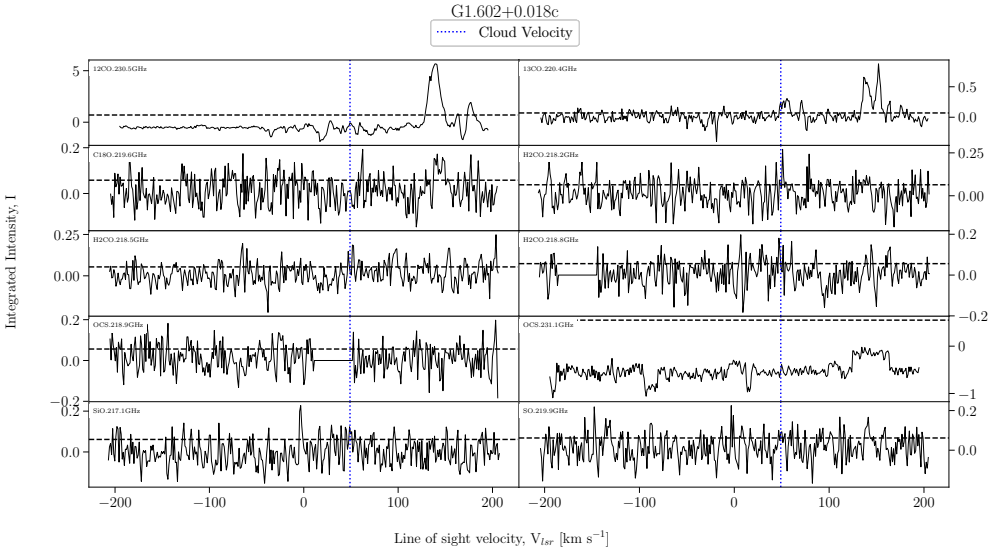

FIGURE A.180: Fitted spectra for dendrogram leaf G1.602+0.018c, with scouse fits overlaid in red.

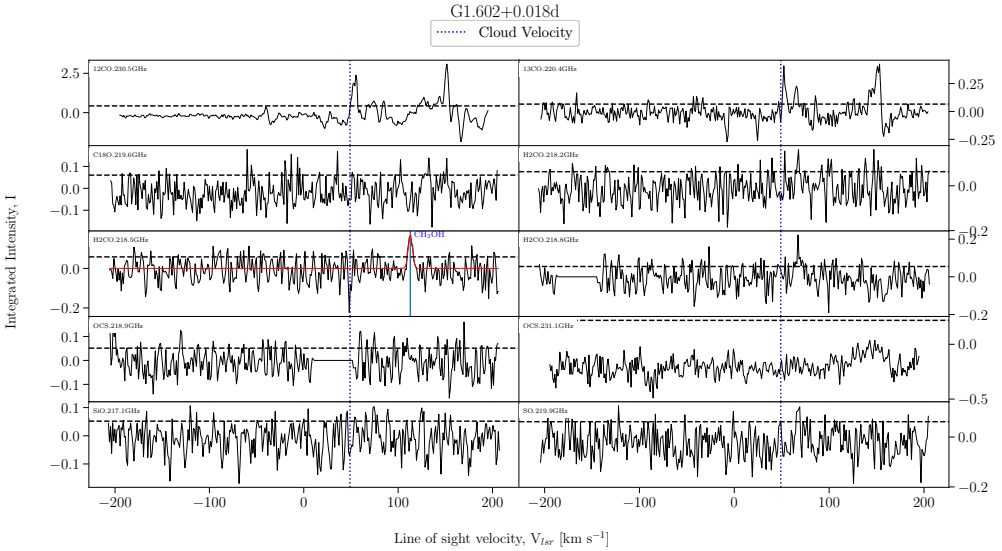

FIGURE A.181: Fitted spectra for dendrogram leaf G1.602+0.018d, with scouse fits overlaid in red.

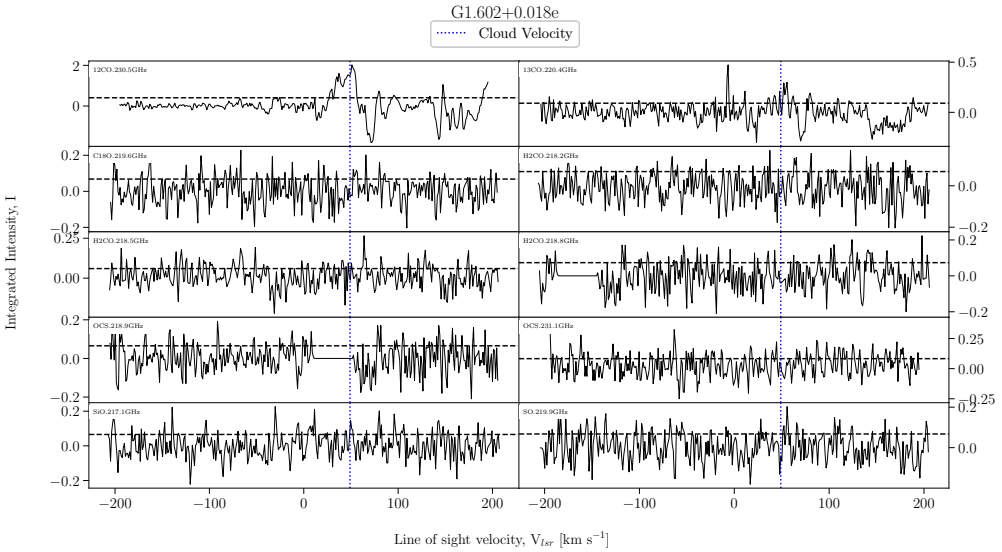

FIGURE A.182: Fitted spectra for dendrogram leaf G1.602+0.018e, with scouse fits overlaid in red.

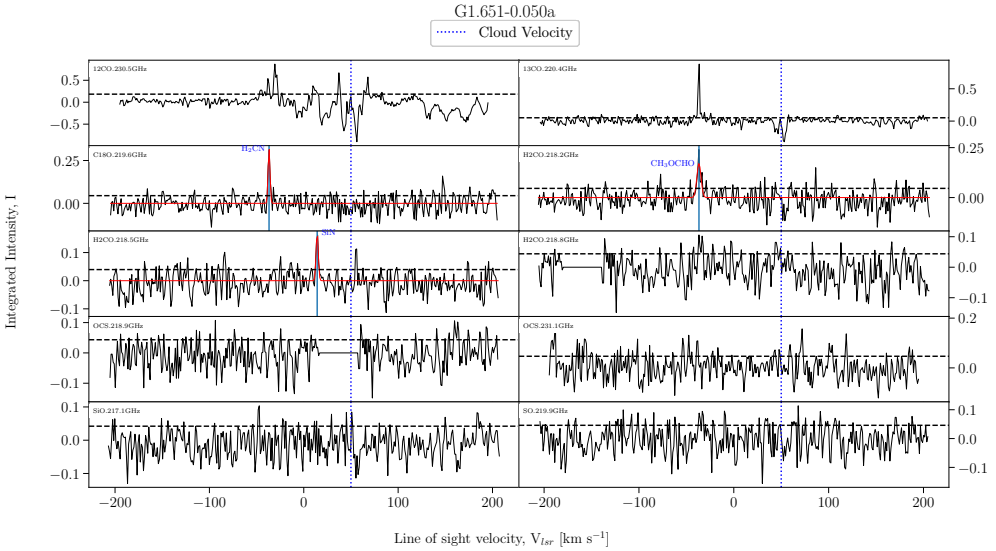

FIGURE A.183: Fitted spectra for dendrogram leaf G1.651-0.050a, with scouse fits overlaid in red.

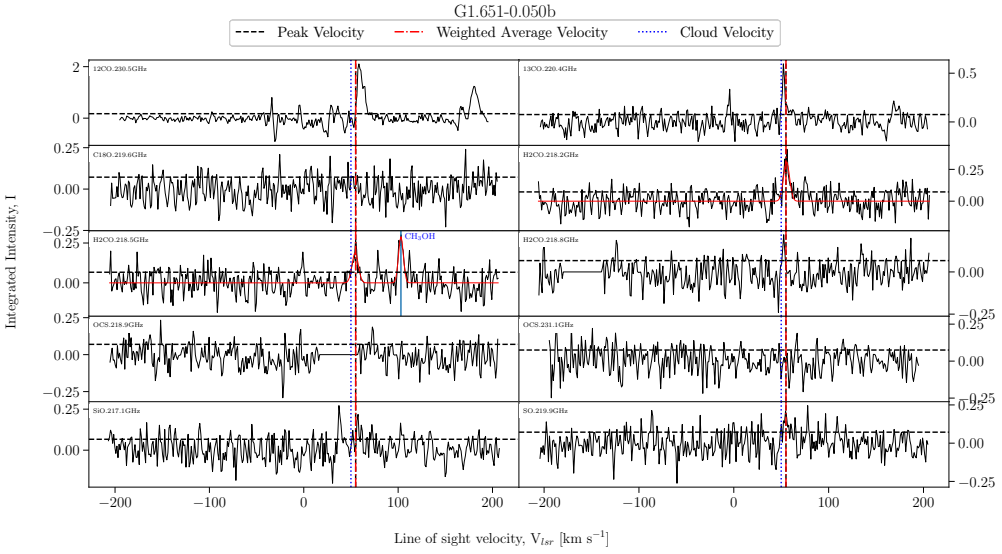

FIGURE A.184: Fitted spectra for dendrogram leaf G1.651-0.050b, with scouse fits overlaid in red.

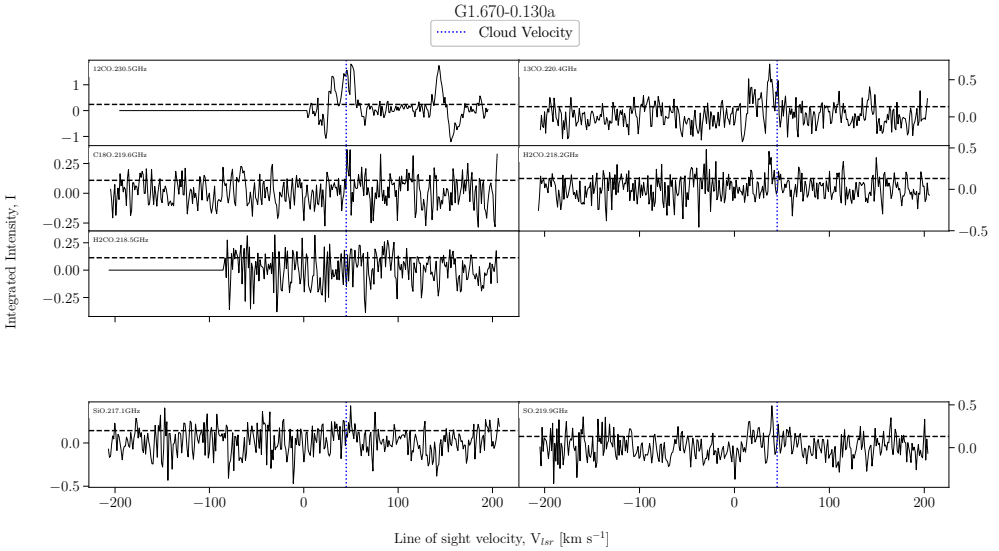

FIGURE A.185: Fitted spectra for dendrogram leaf G1.670-0.130a, with scouse fits overlaid in red.

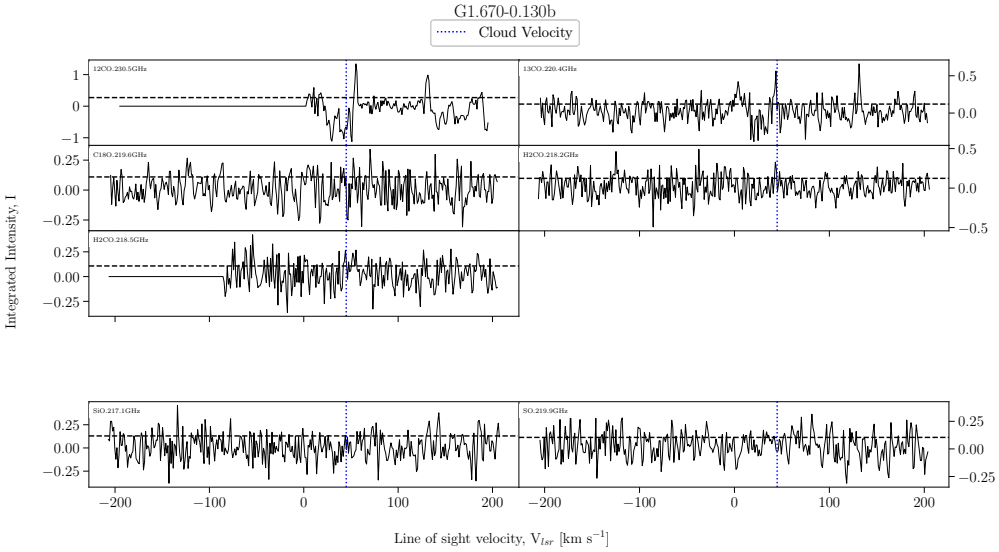

FIGURE A.186: Fitted spectra for dendrogram leaf G1.670-0.130b, with scouse fits overlaid in red.

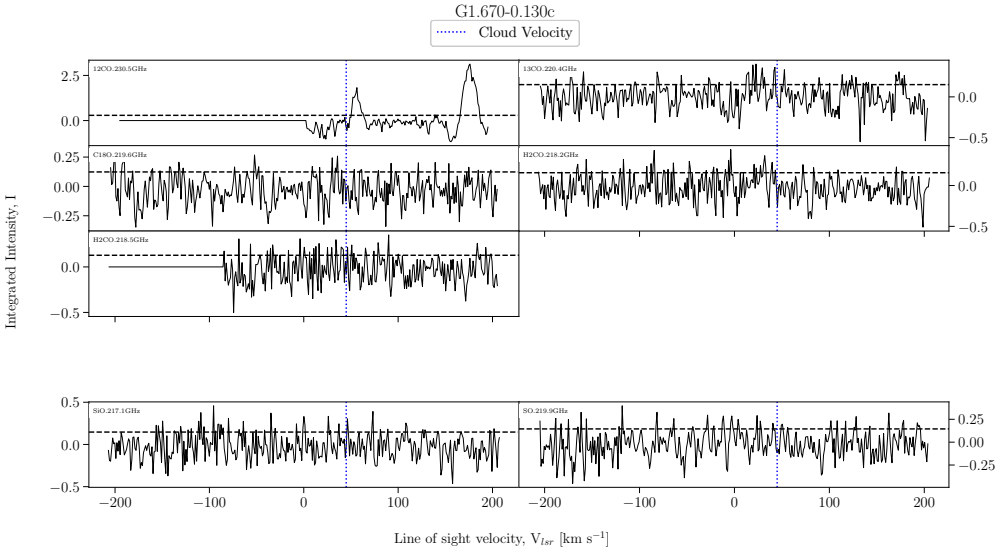

FIGURE A.187: Fitted spectra for dendrogram leaf G1.670-0.130c, with scouse fits overlaid in red.

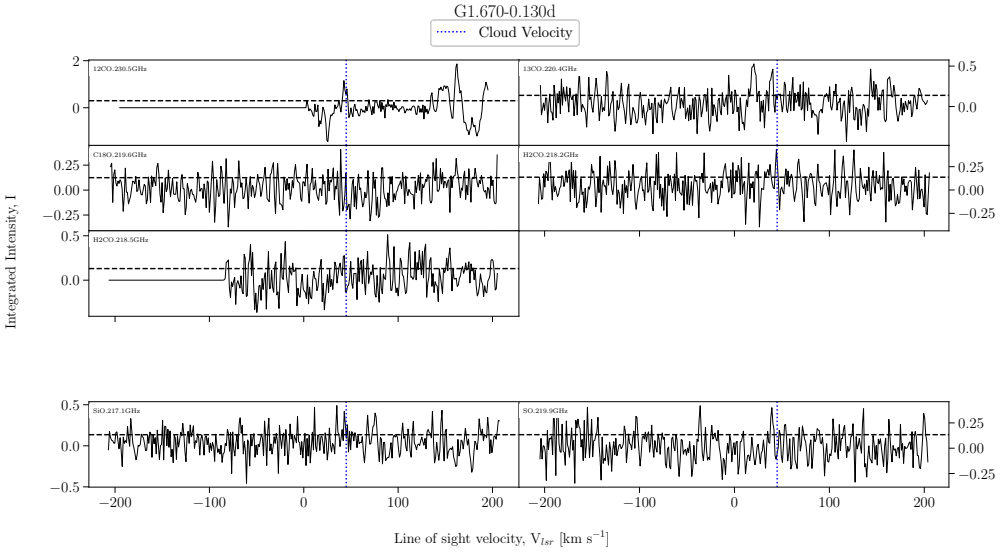

FIGURE A.188: Fitted spectra for dendrogram leaf G1.670-0.130d, with scouse fits overlaid in red.

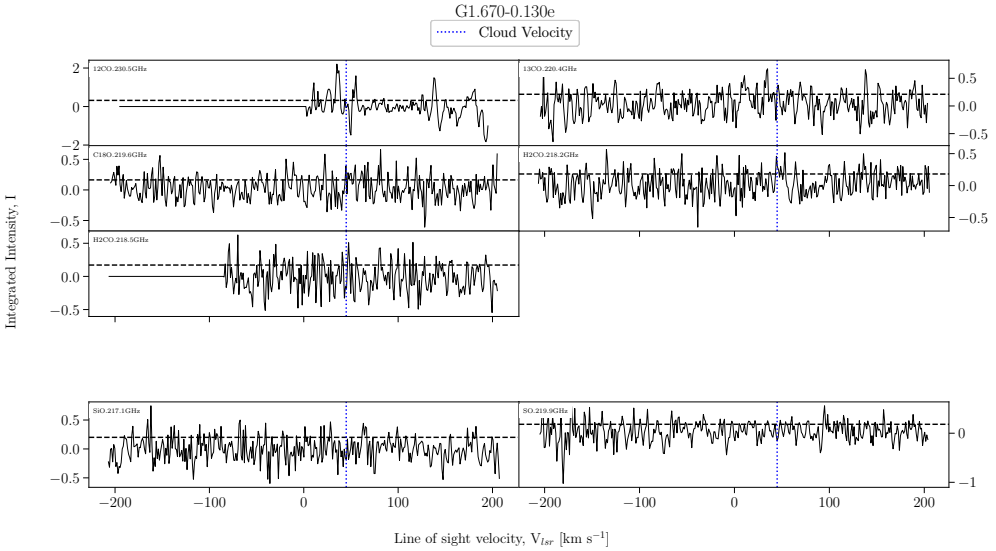

FIGURE A.189: Fitted spectra for dendrogram leaf G1.670-0.130e, with scouse fits overlaid in red.

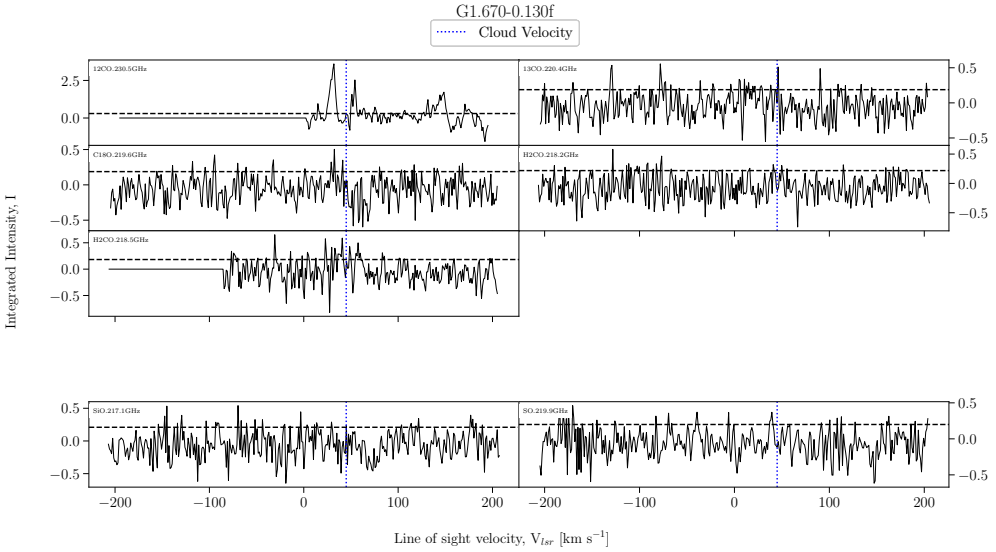

FIGURE A.190: Fitted spectra for dendrogram leaf G1.670-0.130f, with scouse fits overlaid in red.

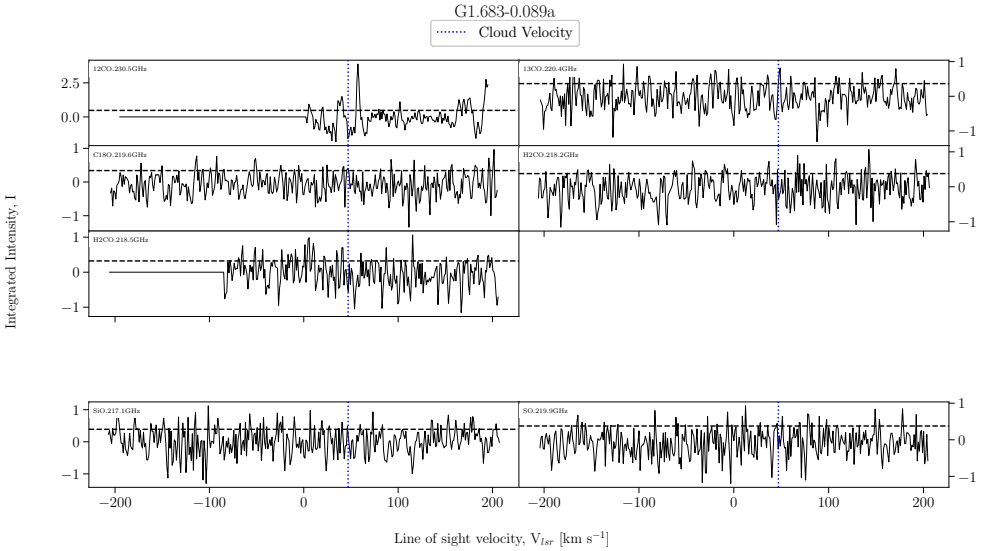

FIGURE A.191: Fitted spectra for dendrogram leaf G1.683-0.089a, with scouse fits overlaid in red.

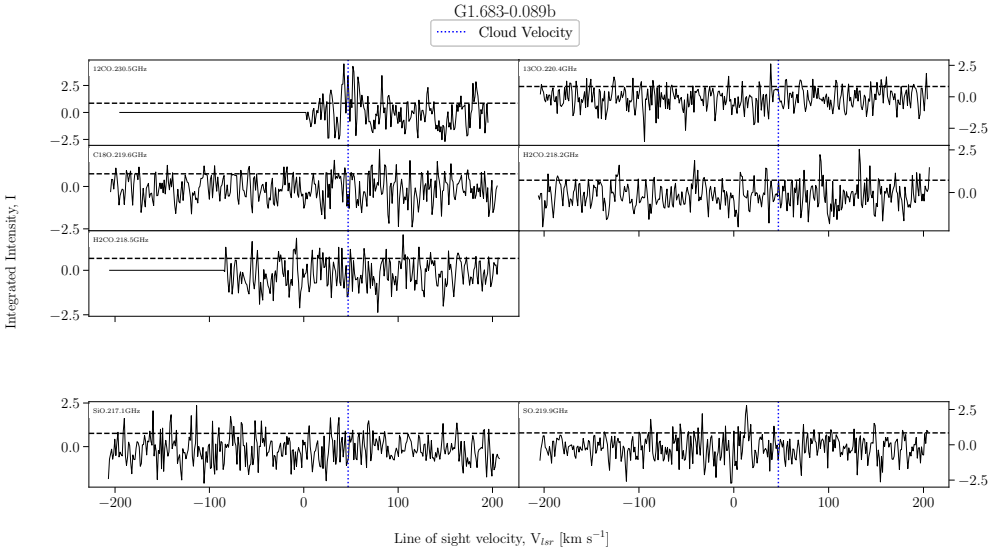

FIGURE A.192: Fitted spectra for dendrogram leaf G1.683-0.089b, with scouse fits overlaid in red.

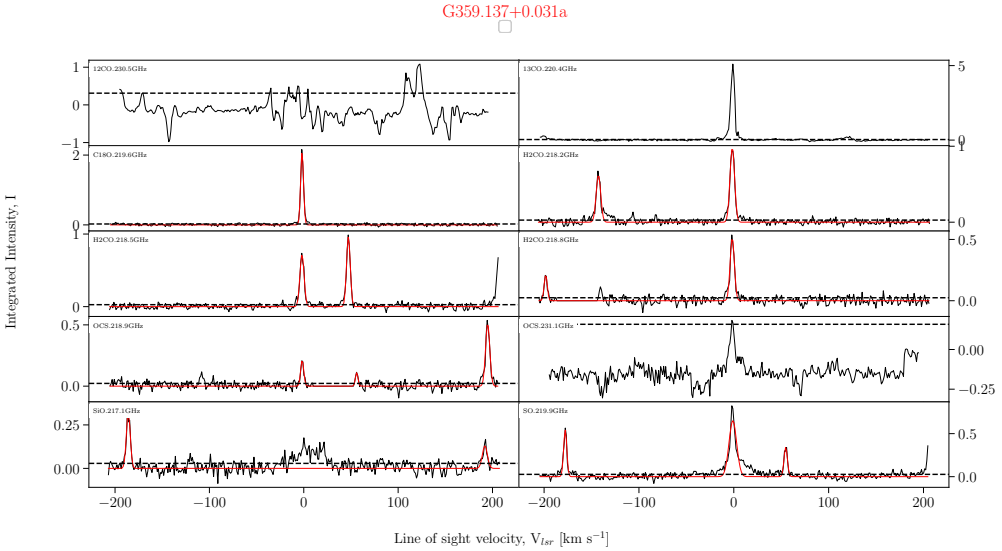

FIGURE A.193: Fitted spectra for dendrogram leaf G359.137+0.031a, with scouse fits overlaid in red.

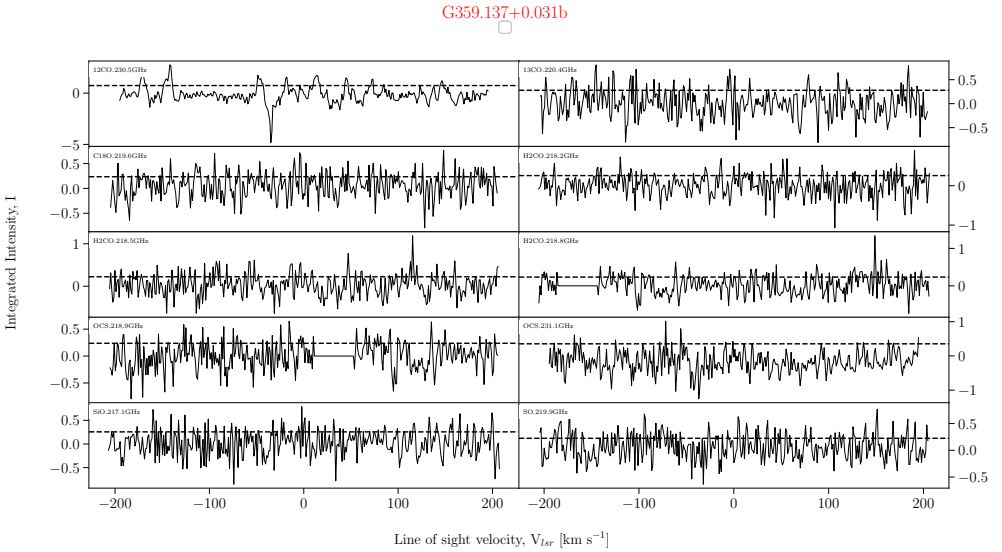

FIGURE A.194: Fitted spectra for dendrogram leaf G359.137+0.031b, with scouse fits overlaid in red.

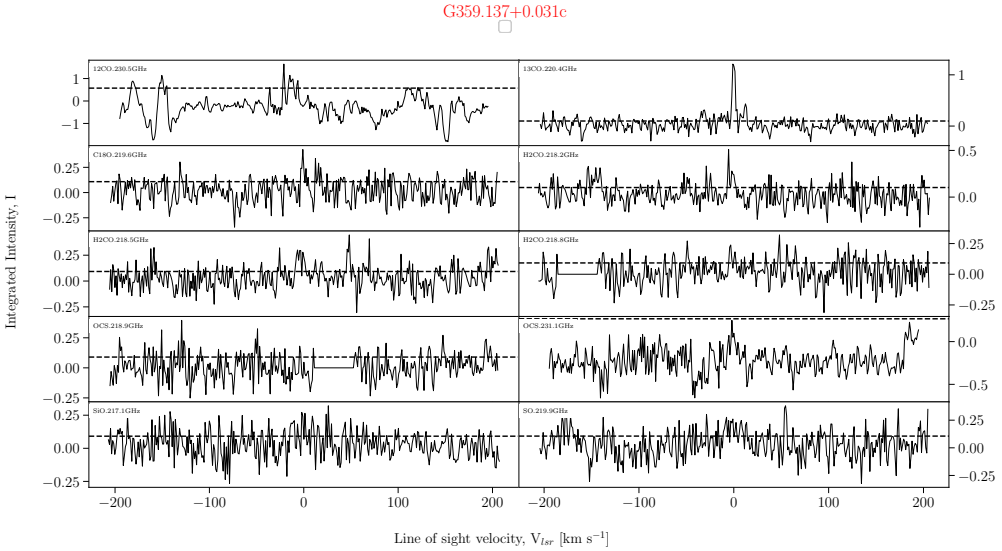

FIGURE A.195: Fitted spectra for dendrogram leaf G359.137+0.031c, with scouse fits overlaid in red.

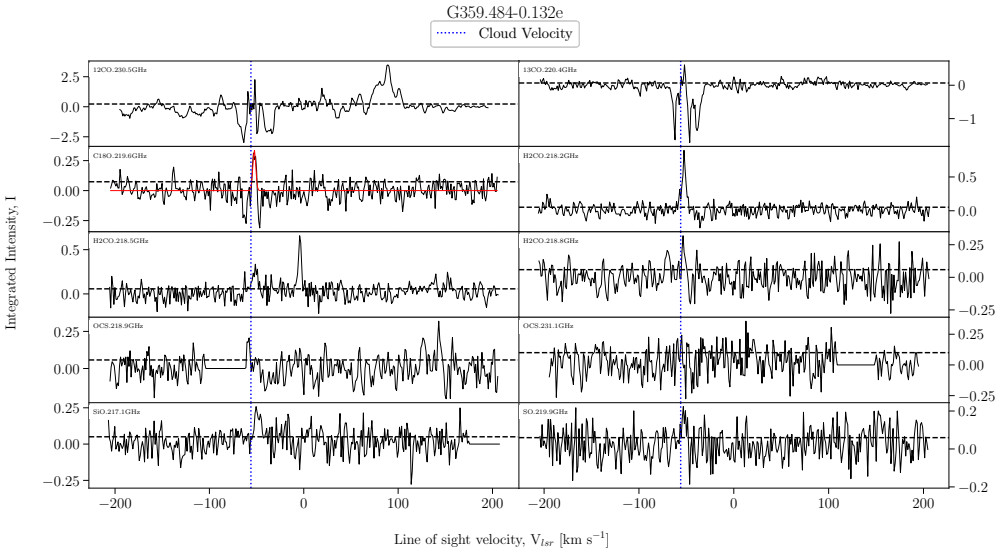

FIGURE A.196: Fitted spectra for dendrogram leaf G359.484-0.132e, with scouse fits overlaid in red.

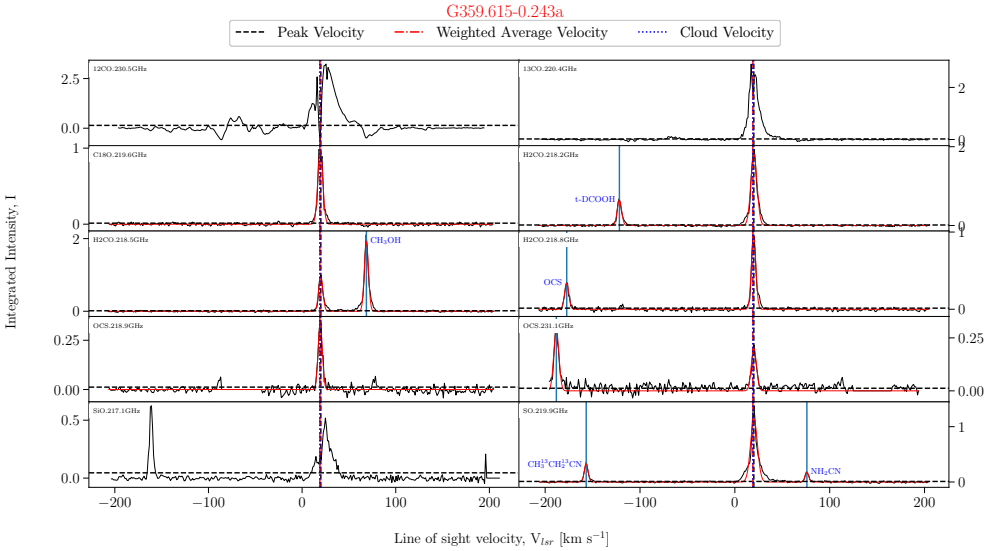

FIGURE A.197: Fitted spectra for dendrogram leaf G359.615-0.243a, with scouse fits overlaid in red.

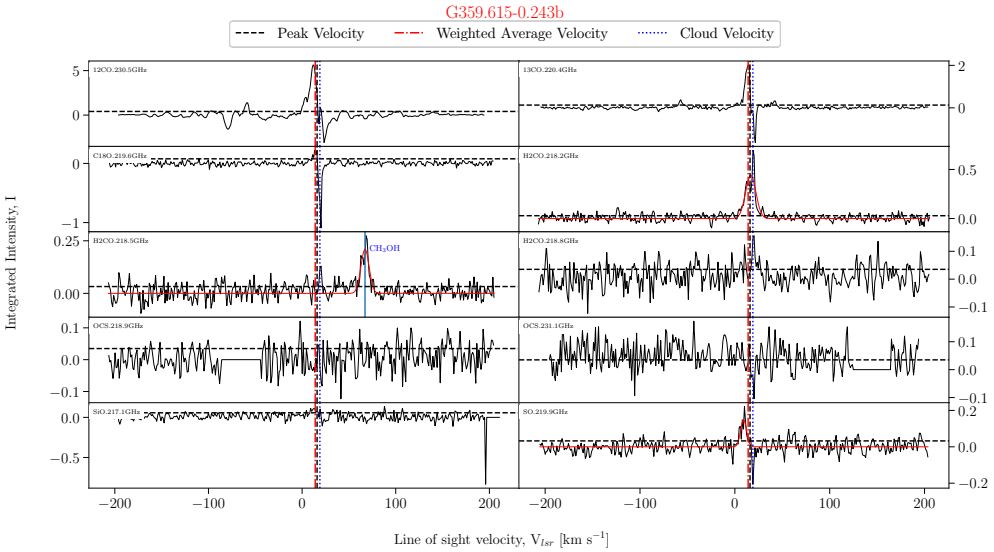

FIGURE A.198: Fitted spectra for dendrogram leaf G359.615-0.243b, with scouse fits overlaid in red.

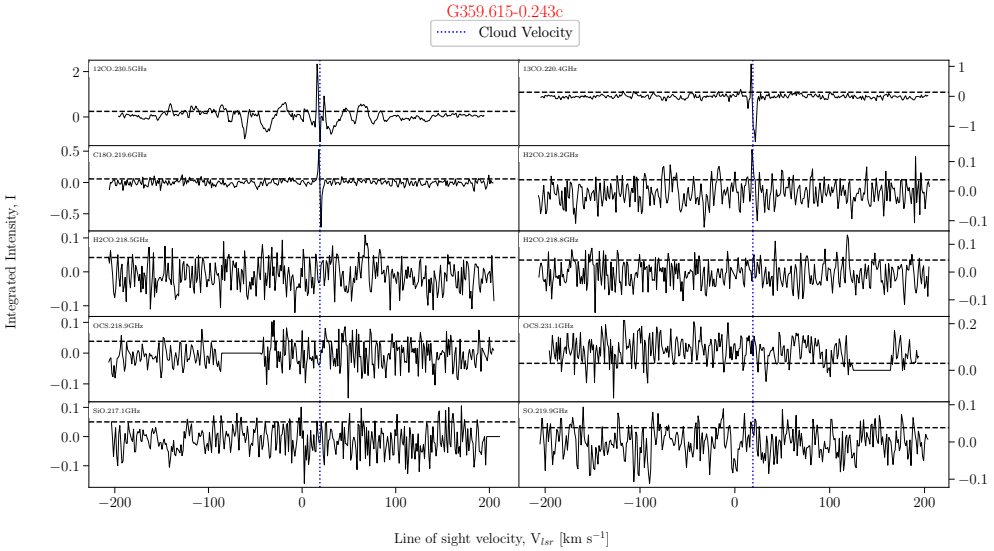

FIGURE A.199: Fitted spectra for dendrogram leaf G359.615-0.243c, with scouse fits overlaid in red.

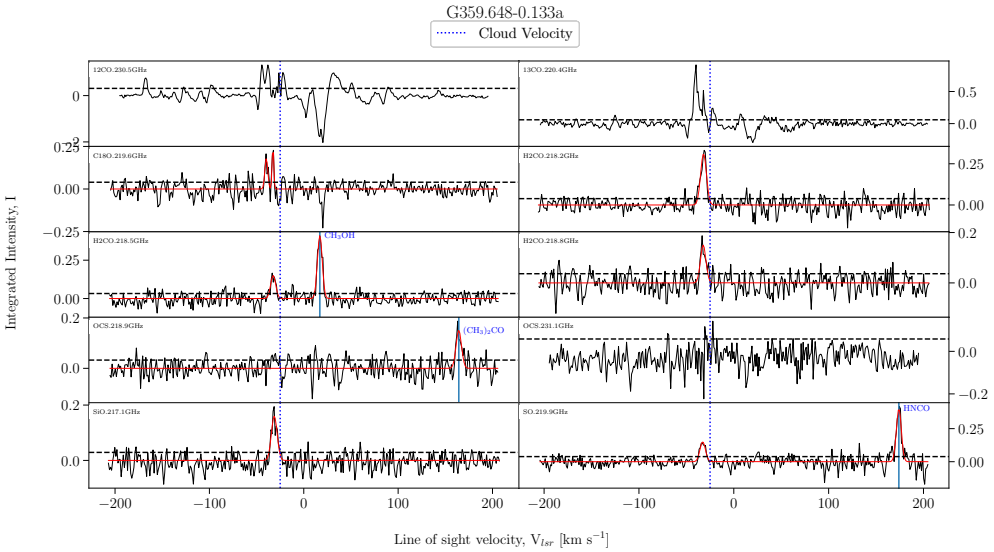

FIGURE A.200: Fitted spectra for dendrogram leaf G359.648-0.133a, with scouse fits overlaid in red.

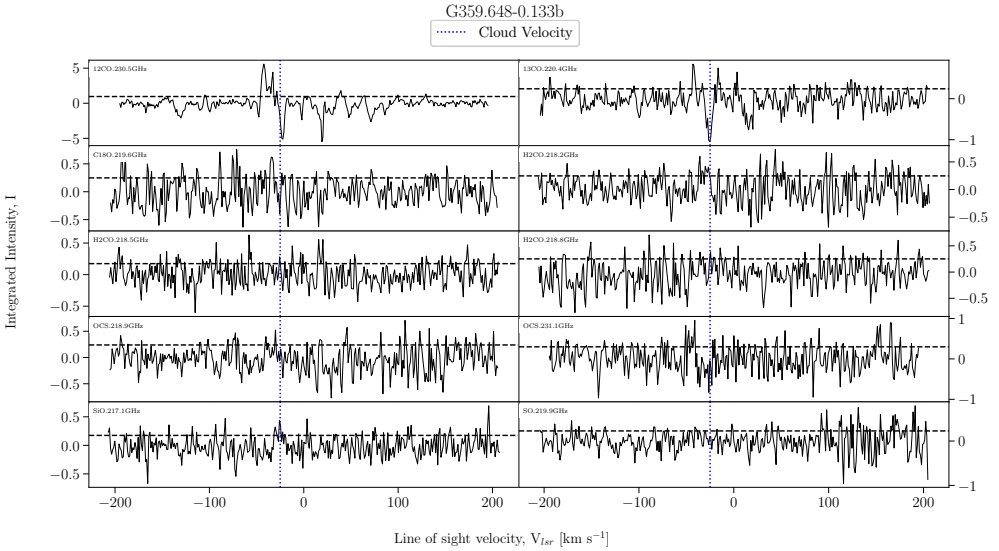

FIGURE A.201: Fitted spectra for dendrogram leaf G359.648-0.133b, with scouse fits overlaid in red.

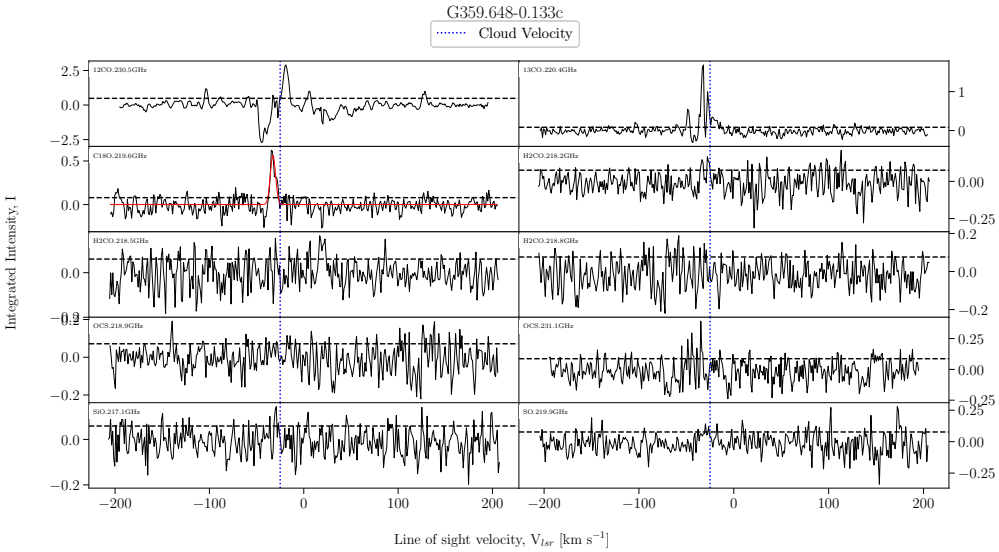

FIGURE A.202: Fitted spectra for dendrogram leaf G359.648-0.133c, with scouse fits overlaid in red.

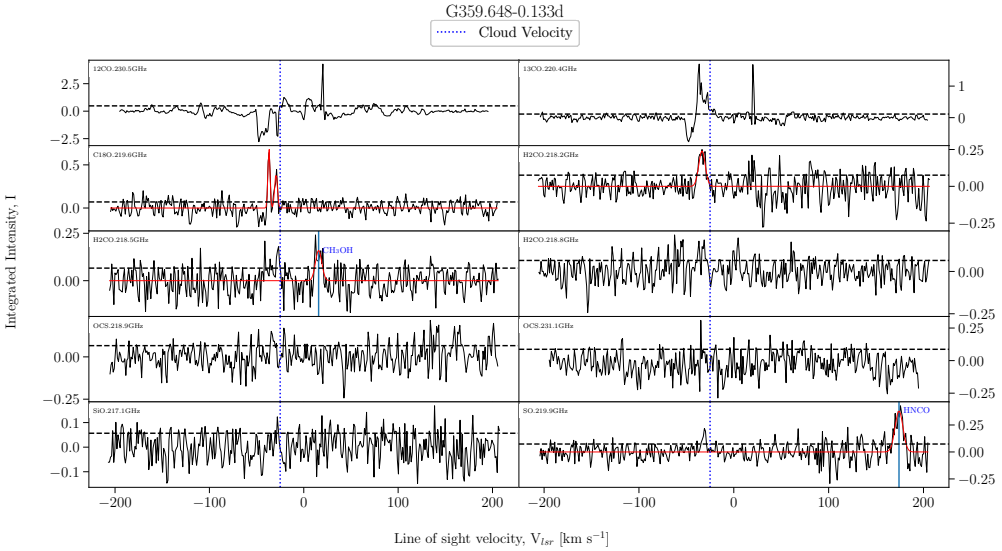

FIGURE A.203: Fitted spectra for dendrogram leaf G359.648-0.133d, with scouse fits overlaid in red.

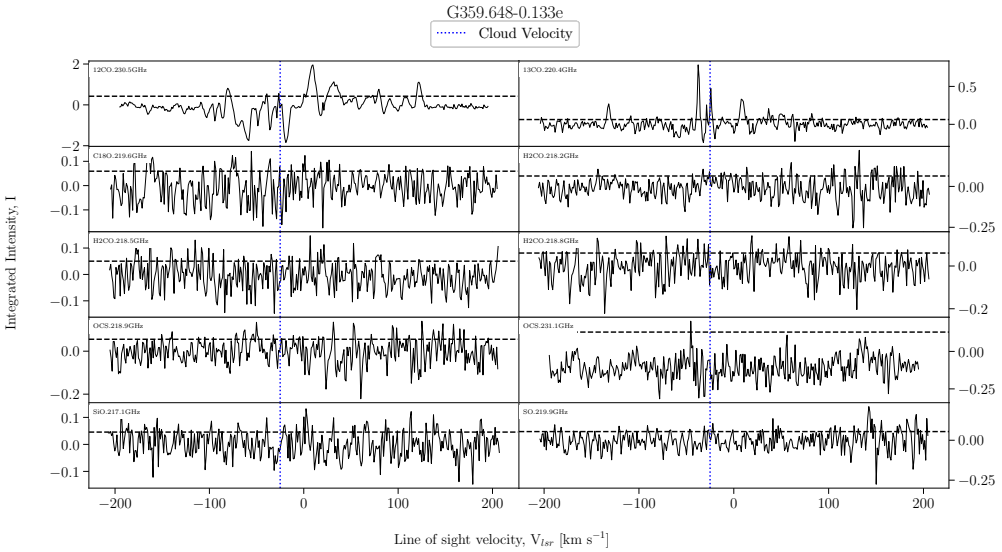

FIGURE A.204: Fitted spectra for dendrogram leaf G359.648-0.133e, with scouse fits overlaid in red.

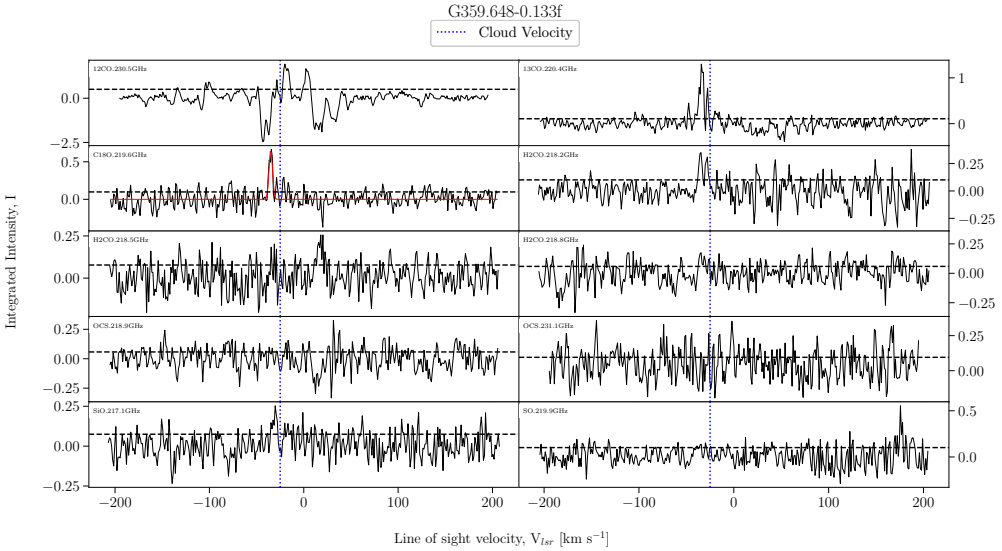

FIGURE A.205: Fitted spectra for dendrogram leaf G359.648-0.133f, with scouse fits overlaid in red.

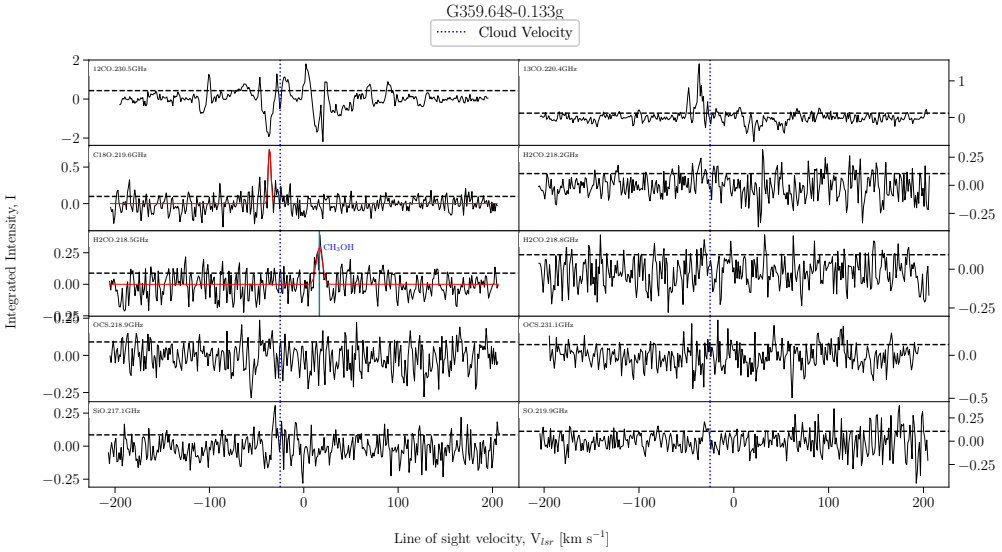

FIGURE A.206: Fitted spectra for dendrogram leaf G359.648-0.133g, with scouse fits overlaid in red.

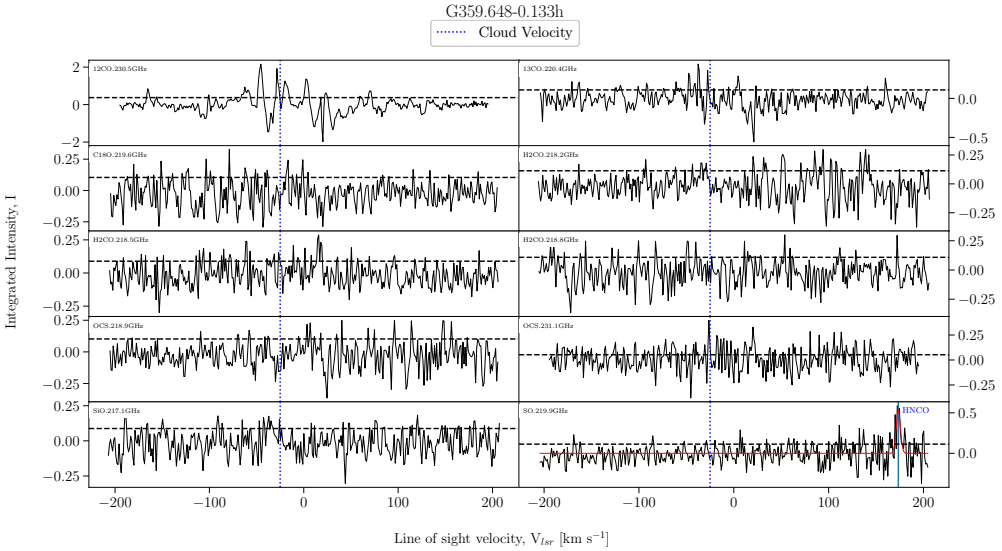

FIGURE A.207: Fitted spectra for dendrogram leaf G359.648-0.133h, with scouse fits overlaid in red.

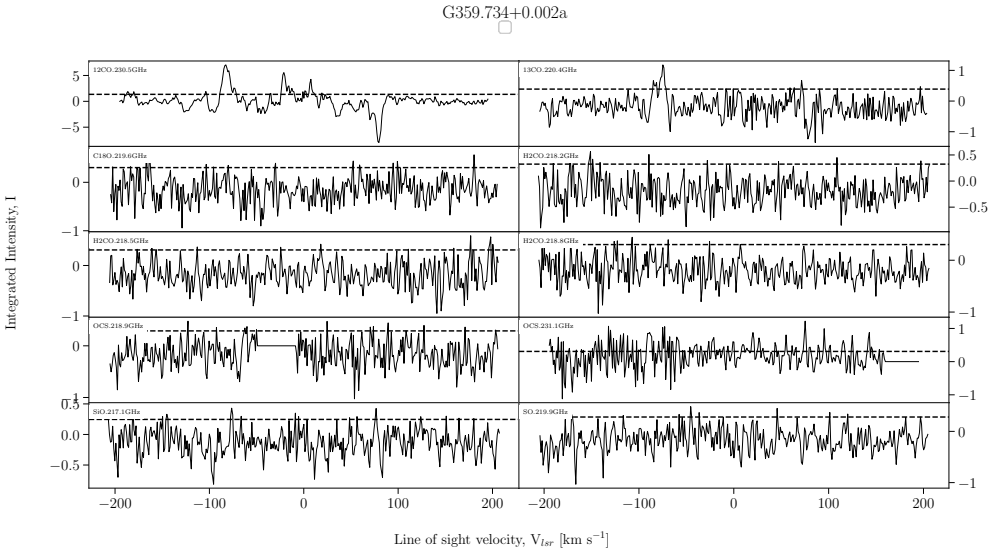

FIGURE A.208: Fitted spectra for dendrogram leaf G359.734+0.002a, with scouse fits overlaid in red.

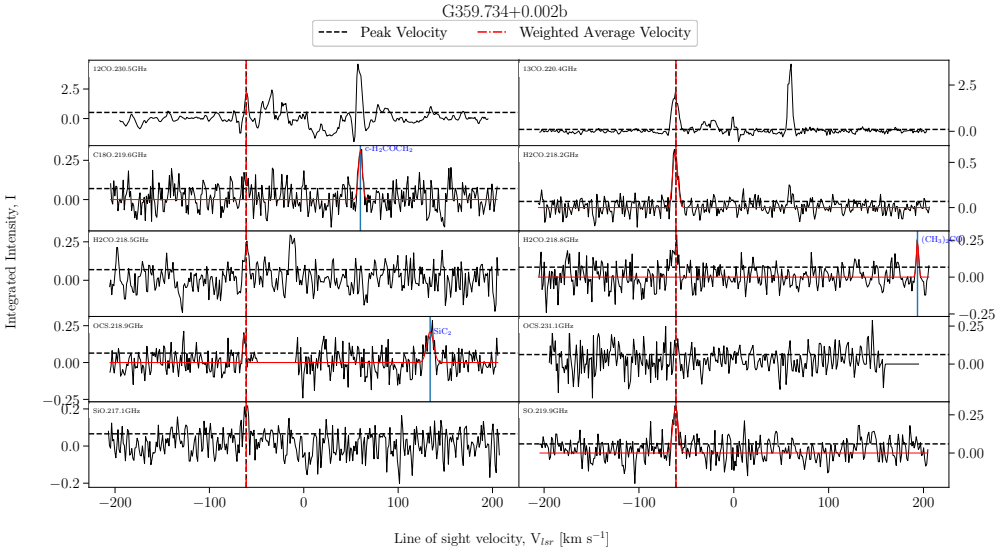

FIGURE A.209: Fitted spectra for dendrogram leaf G359.734+0.002b, with scouse fits overlaid in red.

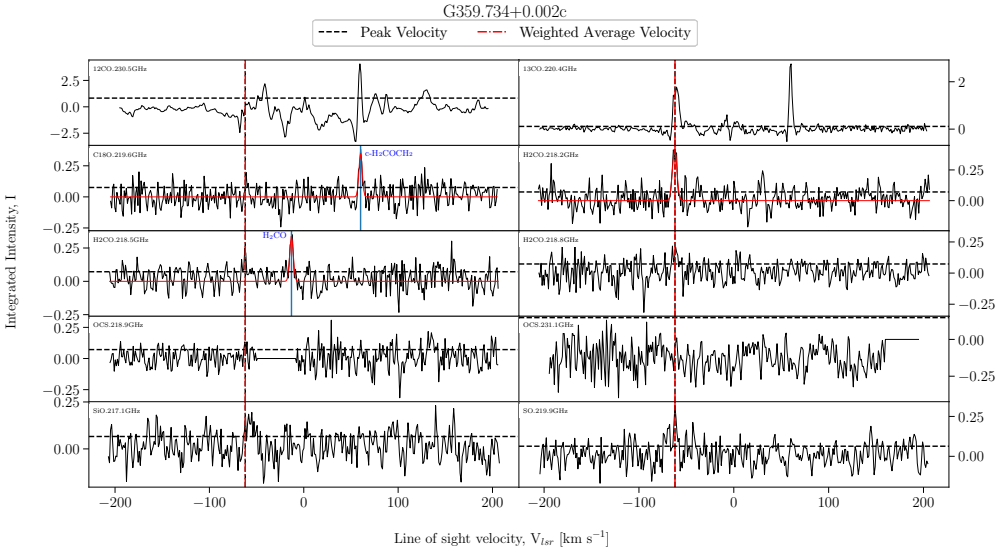

FIGURE A.210: Fitted spectra for dendrogram leaf G359.734+0.002c, with scouse fits overlaid in red.

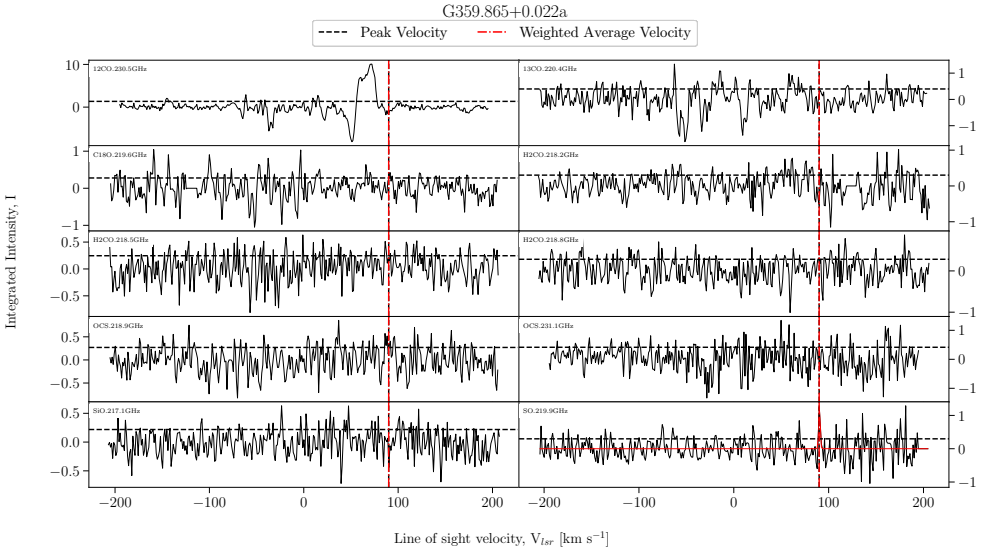

FIGURE A.211: Fitted spectra for dendrogram leaf G359.865+0.022a, with scouse fits overlaid in red.

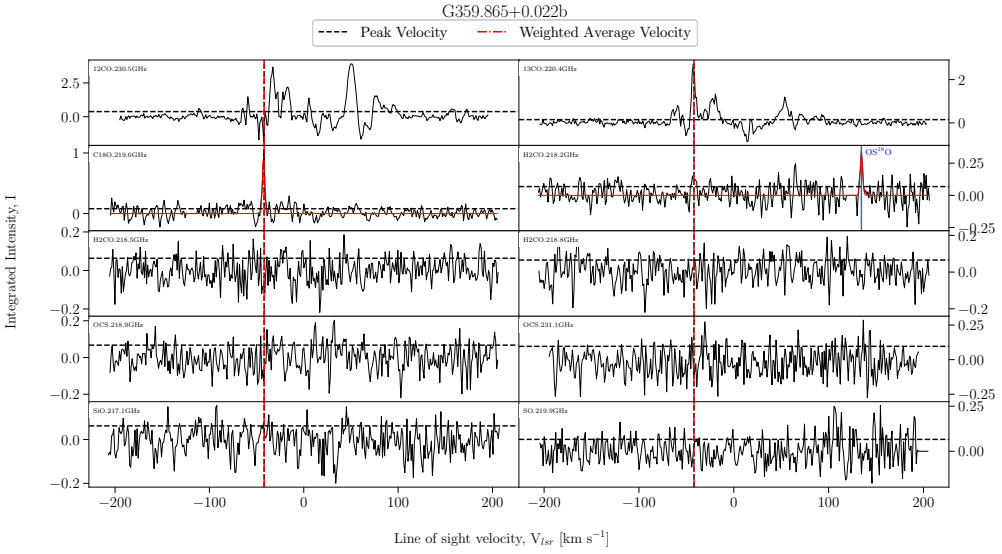

FIGURE A.212: Fitted spectra for dendrogram leaf G359.865+0.022b, with scouse fits overlaid in red.

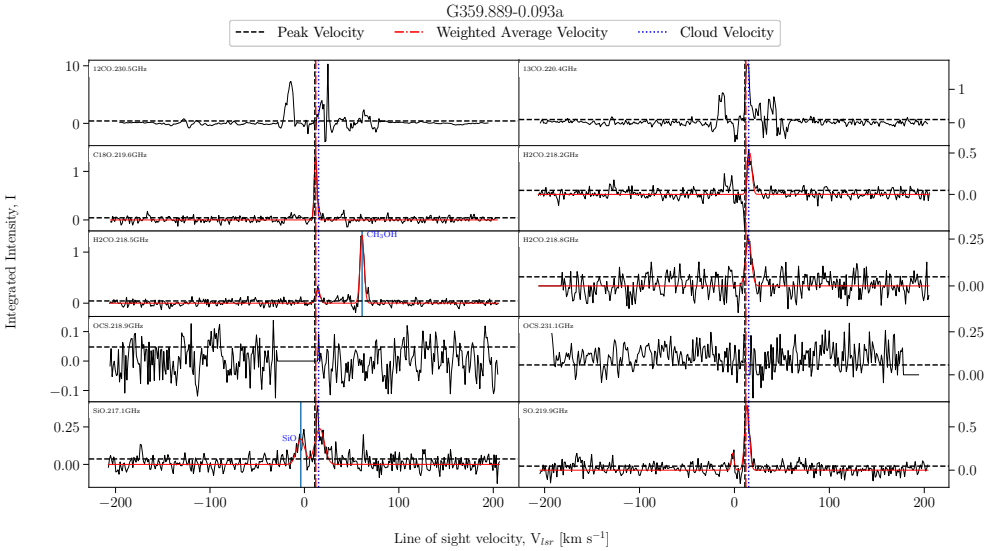

FIGURE A.213: Fitted spectra for dendrogram leaf G359.889-0.093a, with scouse fits overlaid in red.

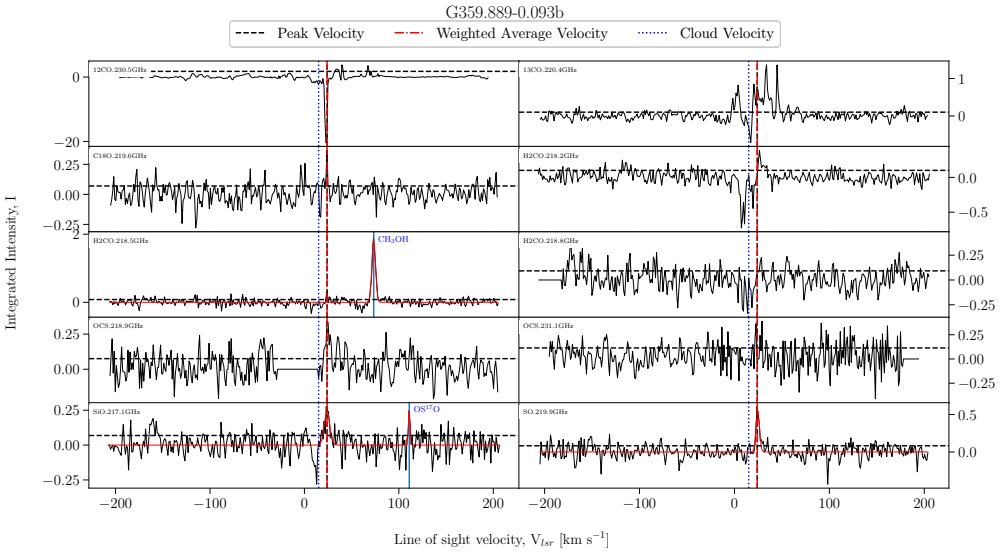

FIGURE A.214: Fitted spectra for dendrogram leaf G359.889-0.093b, with scouse fits overlaid in red.

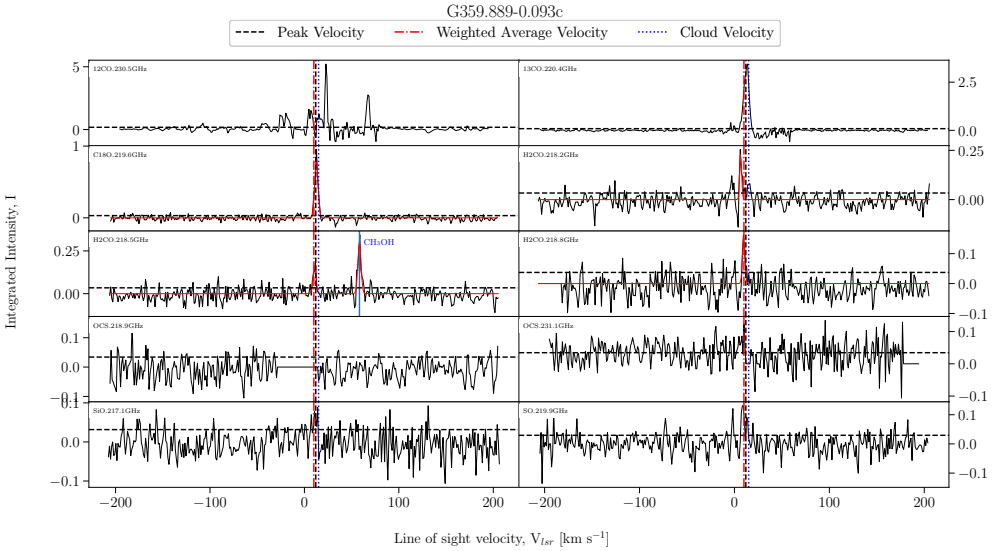

FIGURE A.215: Fitted spectra for dendrogram leaf G359.889-0.093c, with scouse fits overlaid in red.

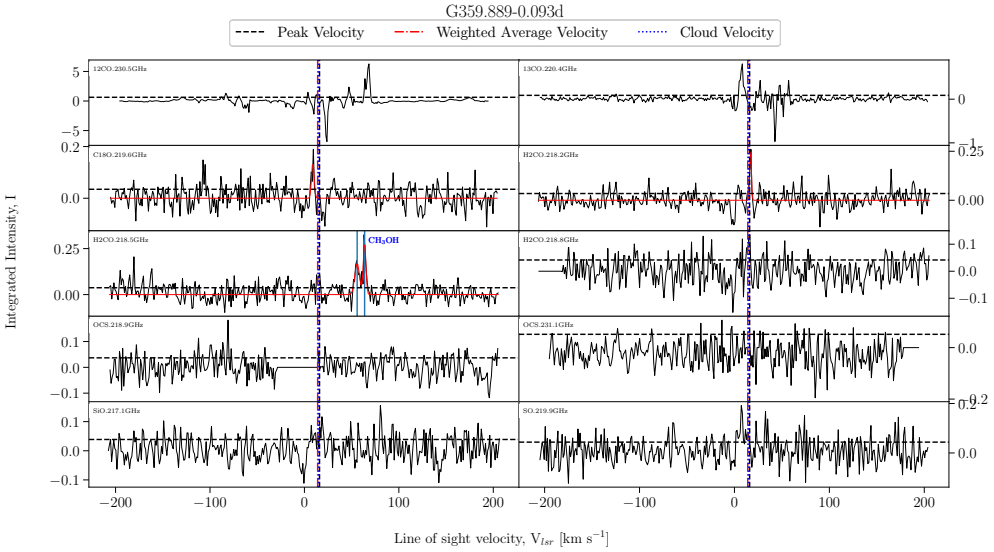

FIGURE A.216: Fitted spectra for dendrogram leaf G359.889-0.093d, with scouse fits overlaid in red.

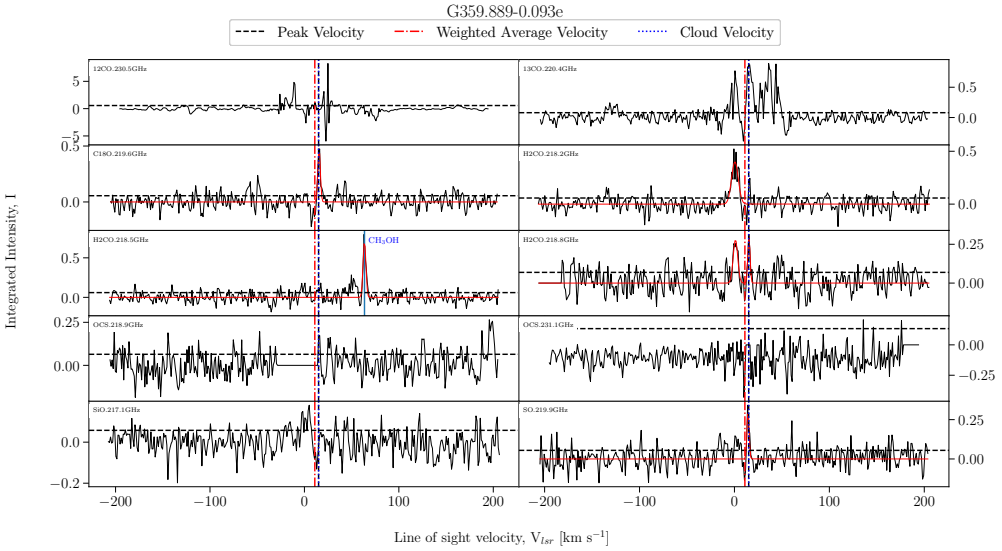

FIGURE A.217: Fitted spectra for dendrogram leaf G359.889-0.093e, with scouse fits overlaid in red.

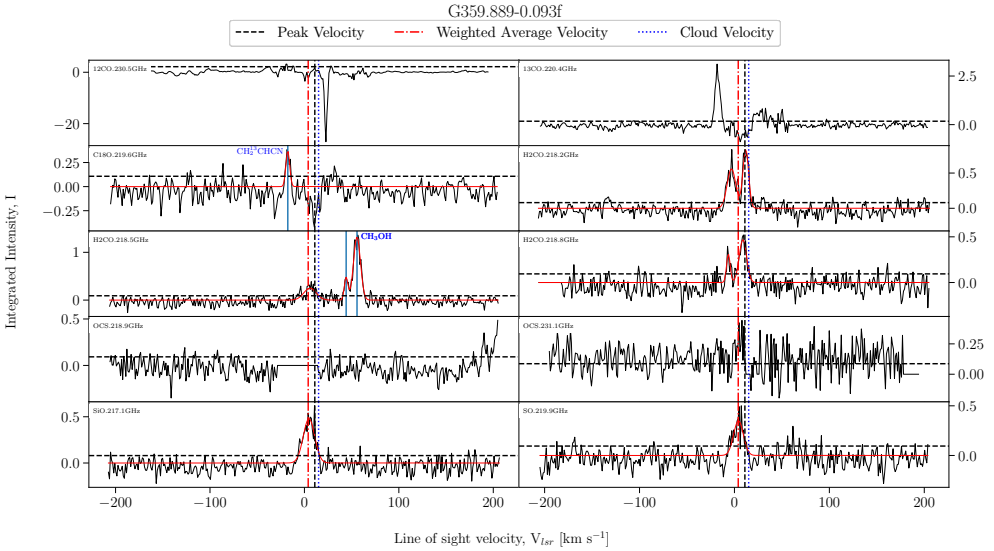

FIGURE A.218: Fitted spectra for dendrogram leaf G359.889-0.093f, with scouse fits overlaid in red.

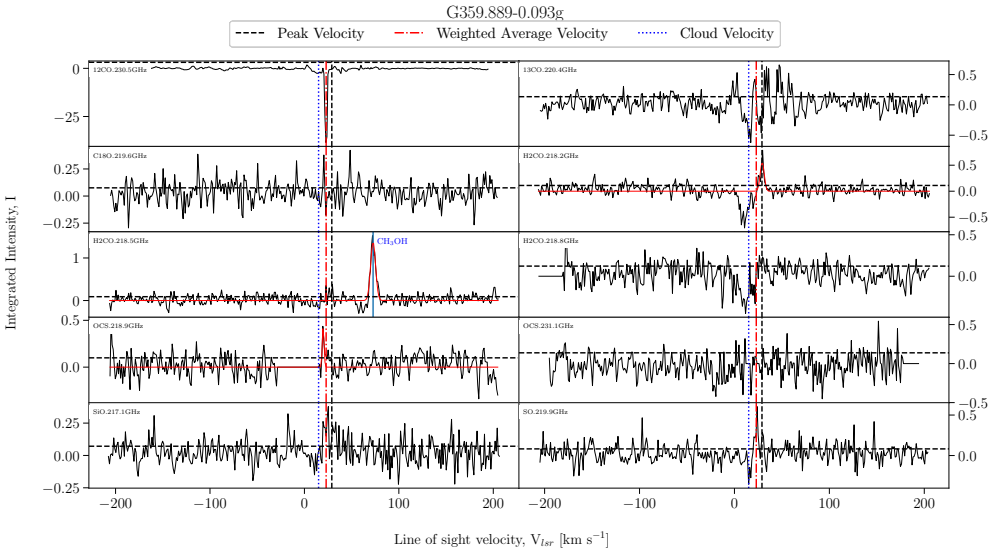

FIGURE A.219: Fitted spectra for dendrogram leaf G359.889-0.093g, with scouse fits overlaid in red.

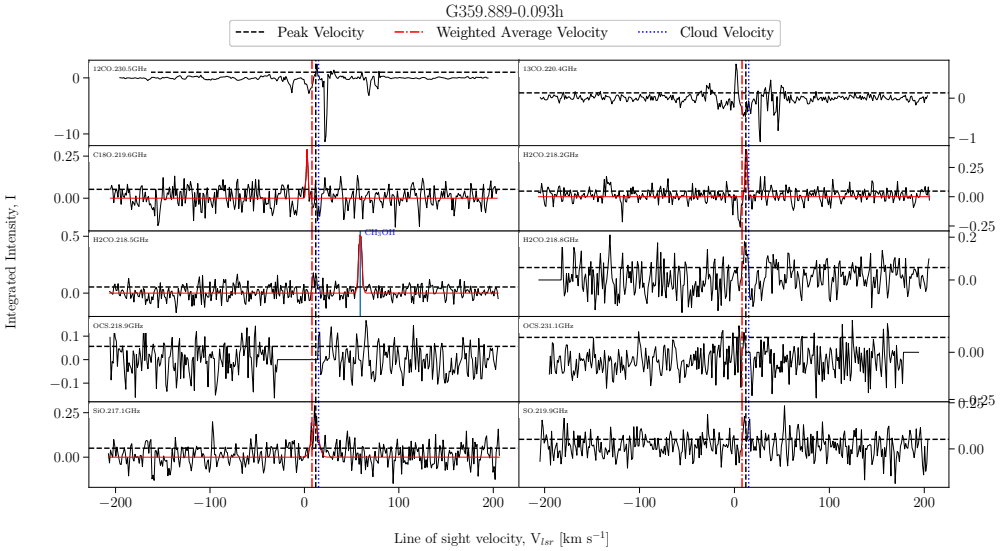

FIGURE A.220: Fitted spectra for dendrogram leaf G359.889-0.093h, with scouse fits overlaid in red.

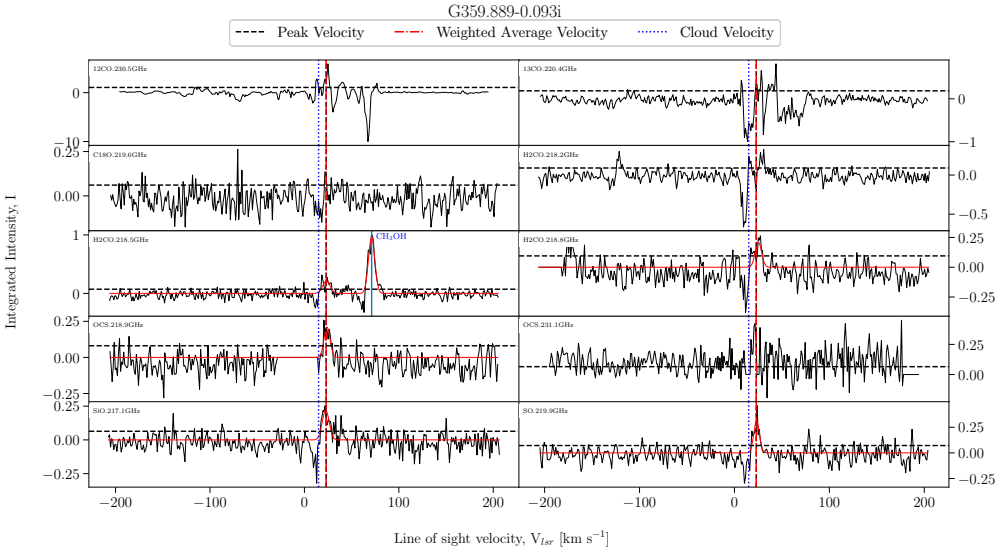

FIGURE A.221: Fitted spectra for dendrogram leaf G359.889-0.093i, with scouse fits overlaid in red.

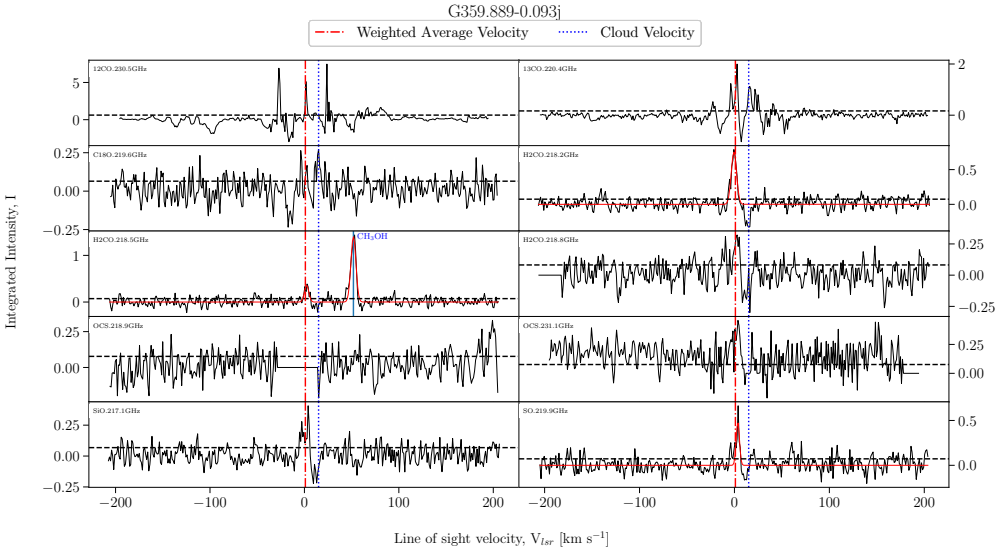

FIGURE A.222: Fitted spectra for dendrogram leaf G359.889-0.093j, with scouse fits overlaid in red.

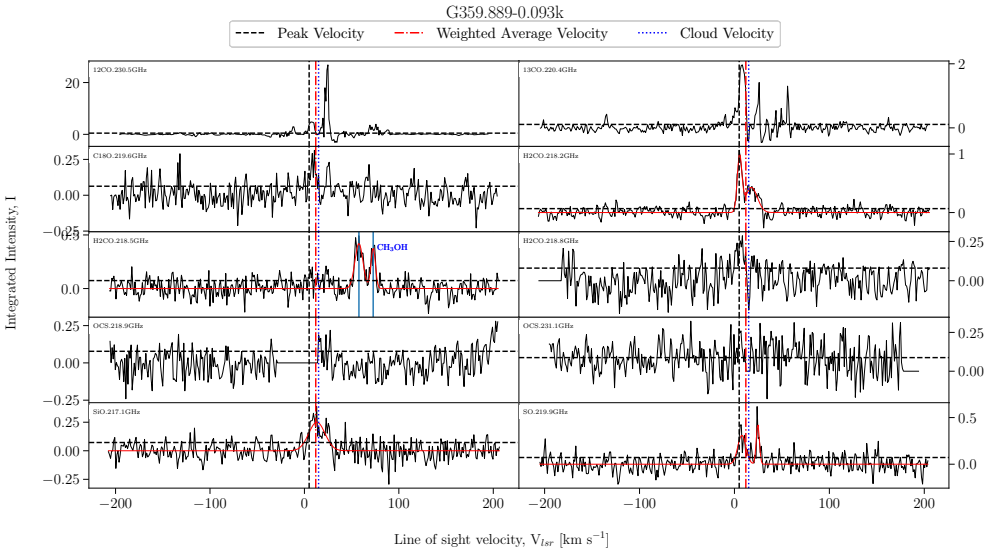

FIGURE A.223: Fitted spectra for dendrogram leaf G359.889-0.093k, with scouse fits overlaid in red.

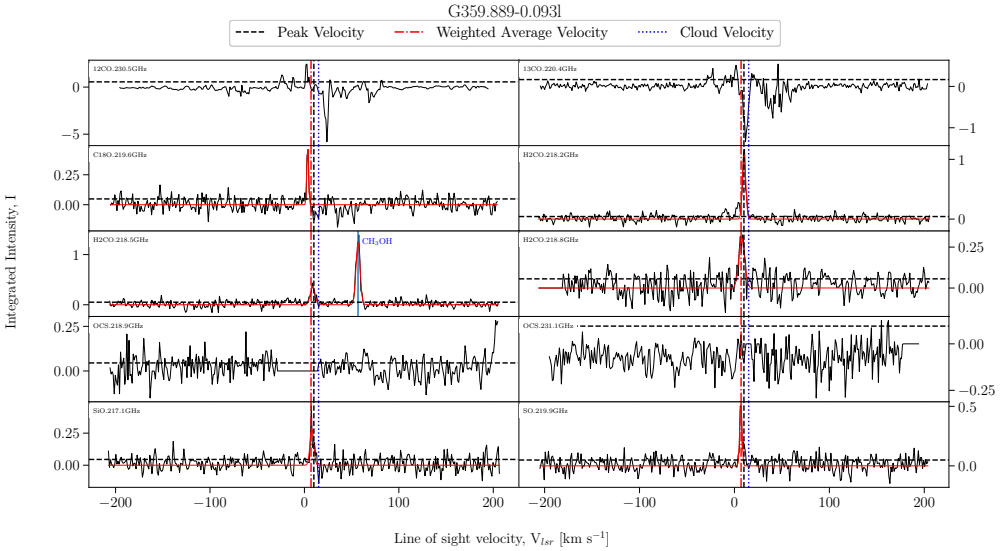

FIGURE A.224: Fitted spectra for dendrogram leaf G359.889-0.093l, with scouse fits overlaid in red.

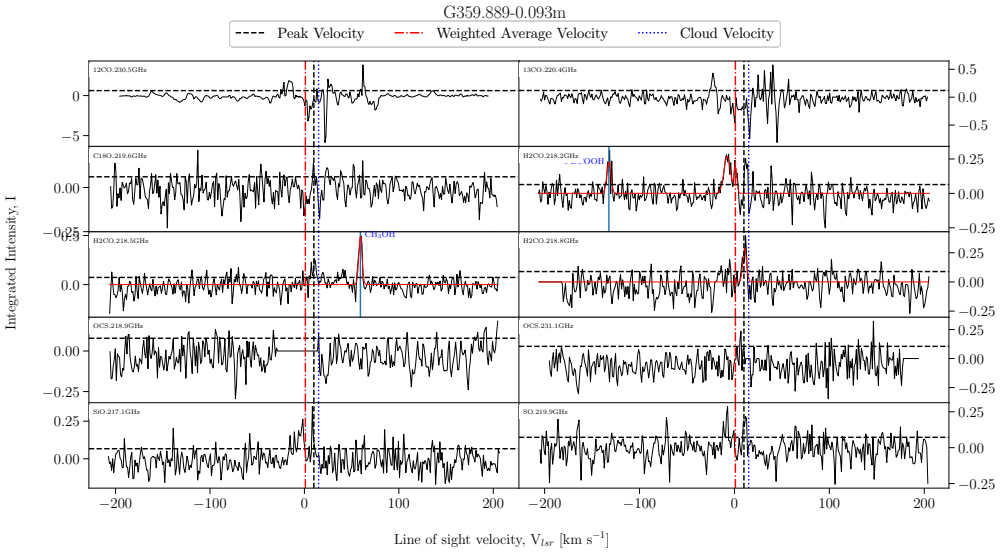

FIGURE A.225: Fitted spectra for dendrogram leaf G359.889-0.093m, with scouse fits overlaid in red.

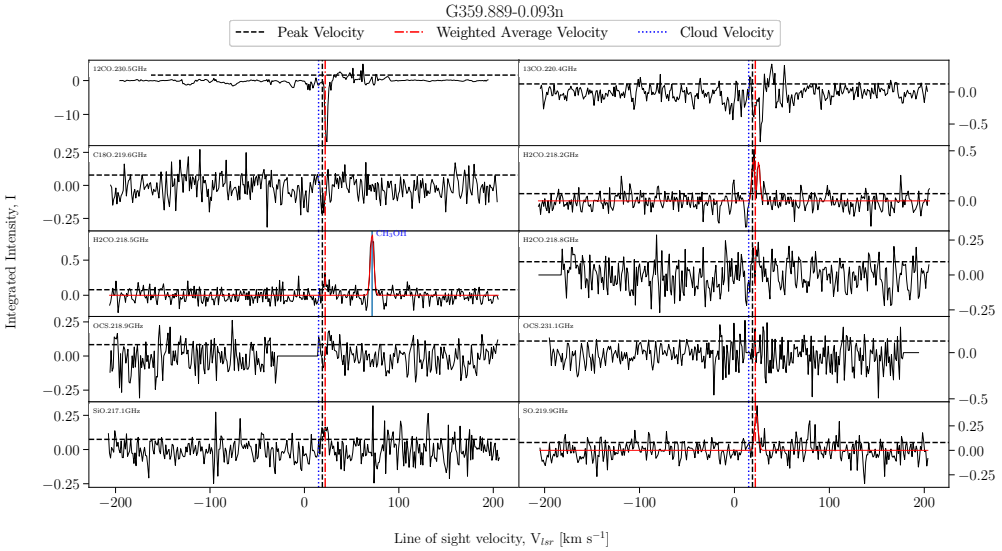

FIGURE A.226: Fitted spectra for dendrogram leaf G359.889-0.093n, with scouse fits overlaid in red.

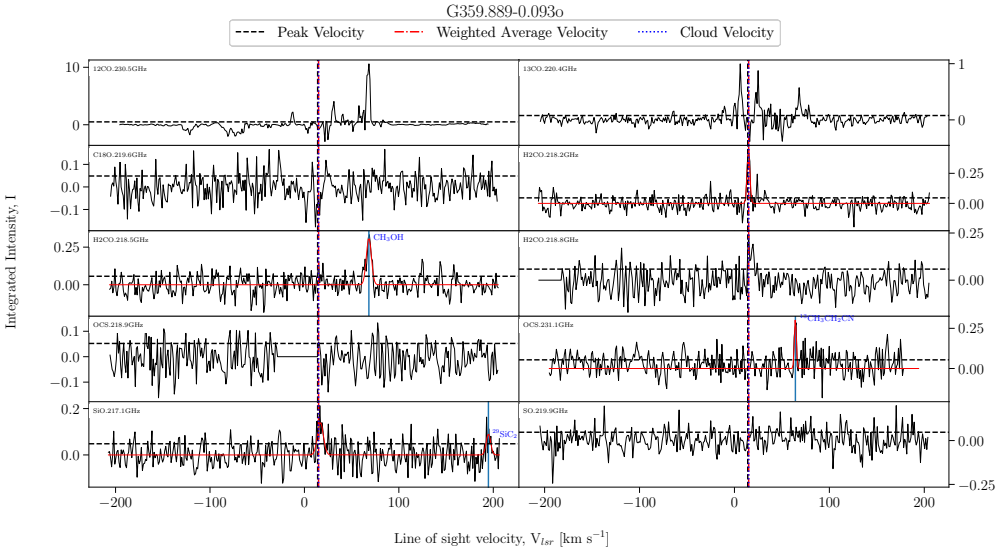

FIGURE A.227: Fitted spectra for dendrogram leaf G359.889-0.093o, with scouse fits overlaid in red.

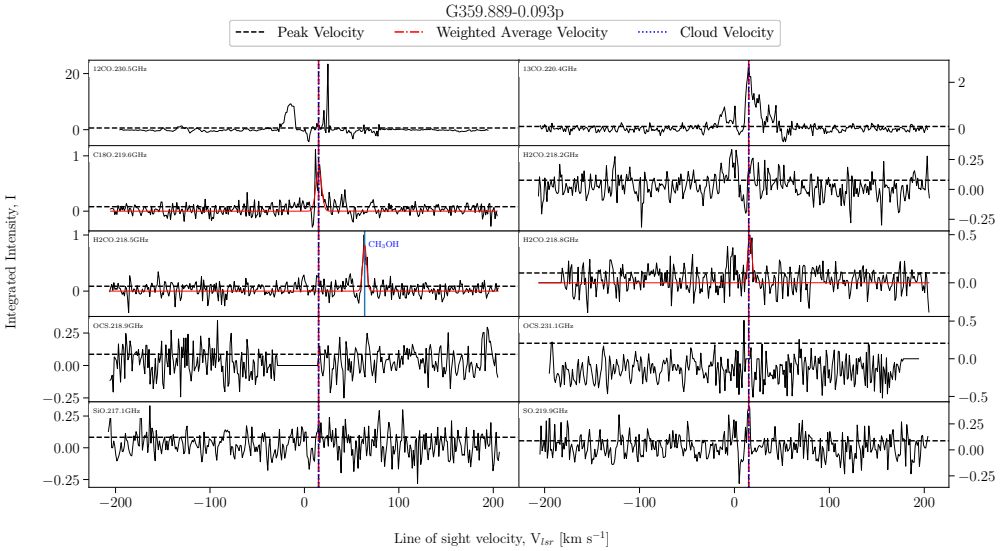

FIGURE A.228: Fitted spectra for dendrogram leaf G359.889-0.093p, with scouse fits overlaid in red.

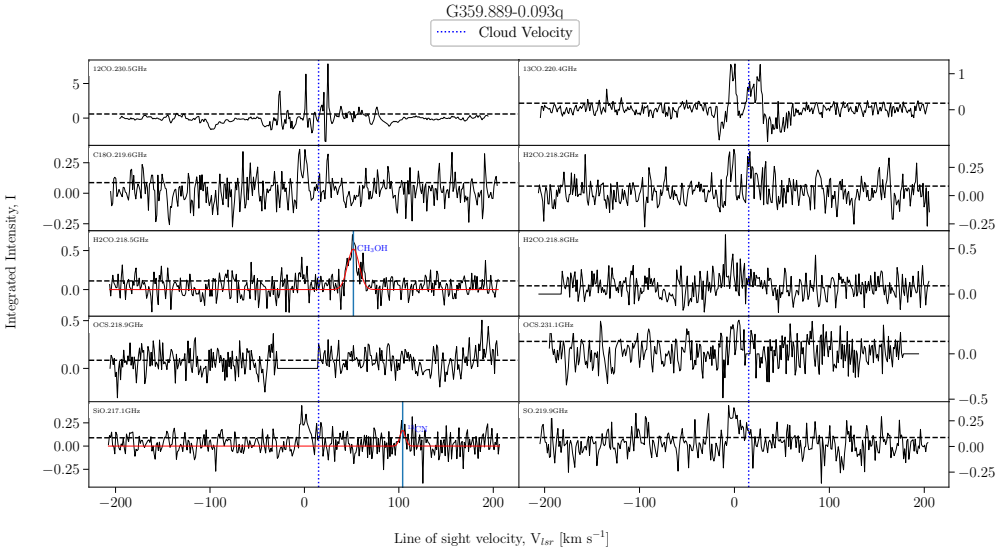

FIGURE A.229: Fitted spectra for dendrogram leaf G359.889-0.093q, with scouse fits overlaid in red.

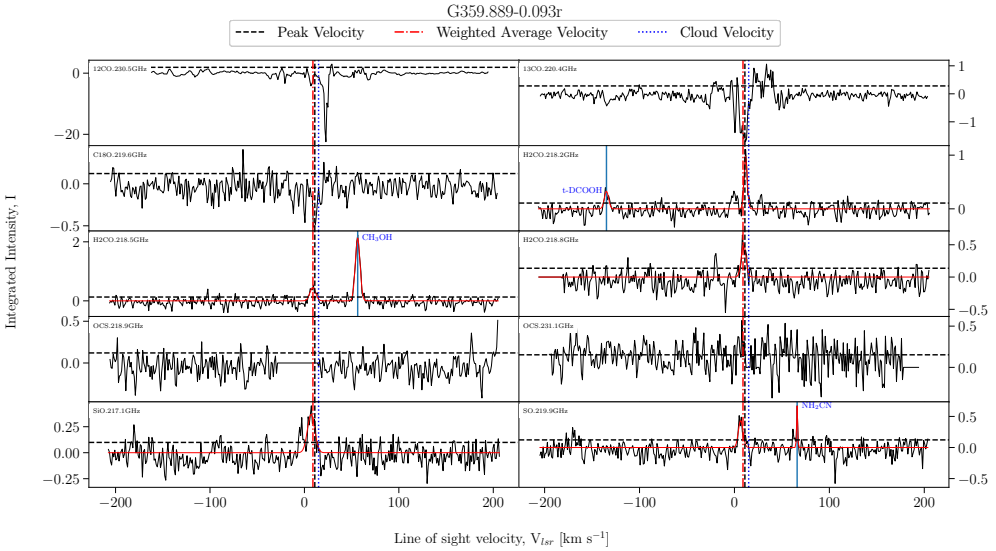

FIGURE A.230: Fitted spectra for dendrogram leaf G359.889-0.093r, with scouse fits overlaid in red.

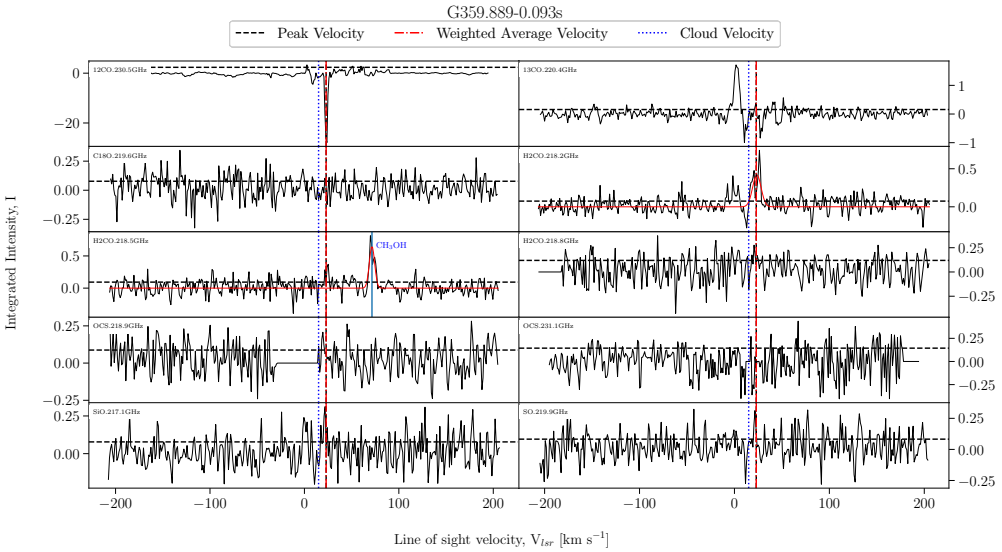

FIGURE A.231: Fitted spectra for dendrogram leaf G359.889-0.093s, with scouse fits overlaid in red.

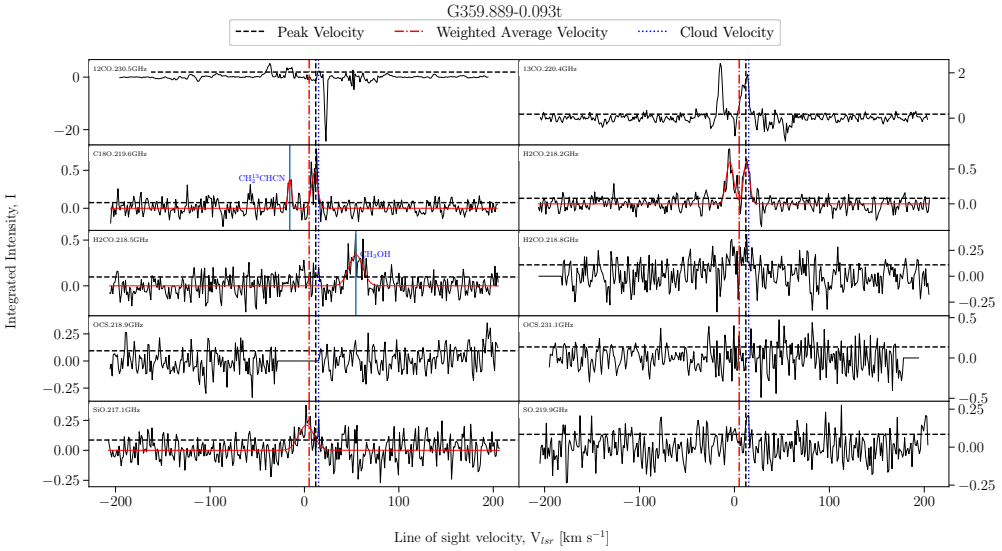

FIGURE A.232: Fitted spectra for dendrogram leaf G359.889-0.093t, with scouse fits overlaid in red.

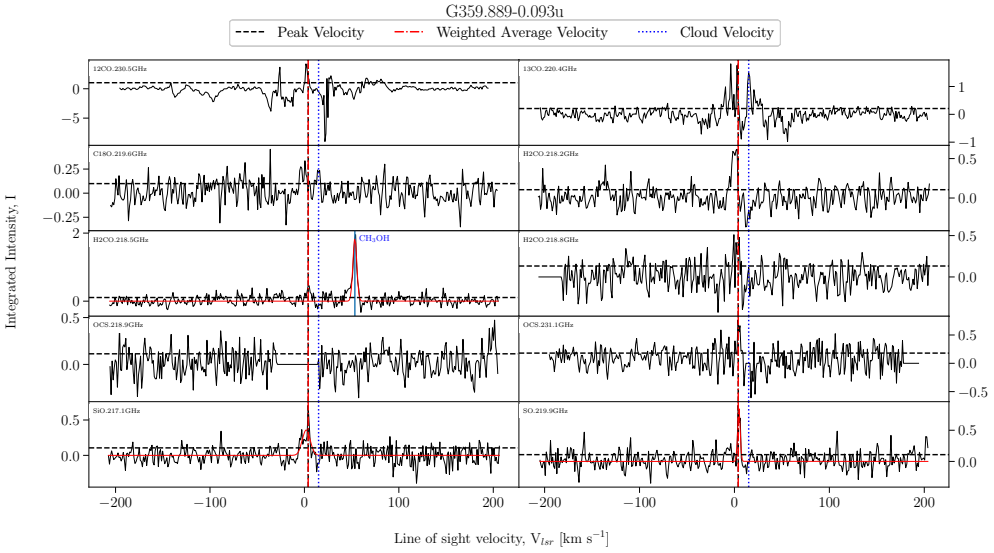

FIGURE A.233: Fitted spectra for dendrogram leaf G359.889-0.093u, with scouse fits overlaid in red.

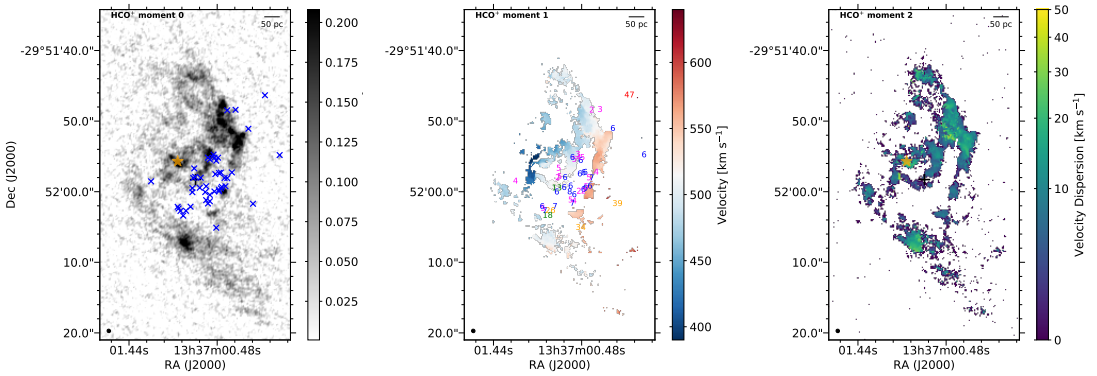

FIGURE A.234: [
Moment maps for HCO$^+$ $(1-0)$][Left] Integrated intensity; [Middle] intensity weighted centroid velocity; [Right] intensity weighted velocity dispersion for HCO$^+$ $(1-0)$. The structures and trends present in these maps are very similar to those in HCN $(1-0)$, as shown in Figure 3.2.

A.4 Appendix 4: Additional M83 Maps

Figure A.234 shows the integrated intensity, intensity weighted centroid velocity and intensity weighted velocity dispersion for HCO$^+$ $(1-0)$. Figures A.235 and A.236 shows the HCN and HCO$^+$ $(1-0)$ channel map respectively. Figure A.237 shows the integrated intensity maps of CCH (N = 1 - 0) and CS (J = 2 - 1).

Figures A.238, A.239 and A.240 show the spectra taken from intensity peaks along the dust lanes, the outer circumnuclear ring and the inner circumnuclear ring, respectively. To increase the signal-to-noise ratio of these spectra they were averaged over an area of $1''$ ($\sim$ 24 pc), the largest size scale at which it is still possible to reliably isolate individual clouds. Table A.2 shows the peak brightness temperature and velocity dispersions of these spectra.

Table A.2: **SCOUSE Fit Data**

Component	Spectrum	T_B (K km s^{-1})	σ (km s^{-1})
Dust Lanes	1	1.20 ± 0.05	14.1 ± 1.2
(Figure A.238)		1.56 ± 0.06	11.4 ± 0.7
	2	0.84 ± 0.04	19.6 ± 1.0
	3	1.62 ± 0.07	11.2 ± 0.7
		2.88 ± 0.05	14.7 ± 0.6
	4	1.31 ± 0.19	14.1 ± 1.5
		0.83 ± 0.09	30.4 ± 3.3
	5	1.98 ± 0.04	25.2 ± 0.6
	6	1.80 ± 0.06	14.1 ± 1.0
		2.10 ± 0.10	11.4 ± 0.6
	7	0.89 ± 0.08	8.9 ± 1.5
		1.20 ± 0.08	8.9 ± 1.1
	8	2.64 ± 0.06	13.6 ± 0.5
		1.30 ± 0.06	14.1 ± 1.2
	9	0.74 ± 0.05	20.8 ± 1.5
	10	1.32 ± 0.05	15.6 ± 0.6
Outer Ring	1	1.54 ± 0.04	16.5 ± 0.5
(Figure A.239)	2	2.74 ± 0.05	13.2 ± 0.3
	3	1.84 ± 0.05	14.3 ± 0.4
	4	-	-
	5	0.50 ± 0.04	18.6 ± 1.5
	6	0.79 ± 0.03	29.2 ± 1.2
Inner Ring	1	0.98 ± 0.03	31.1 ± 1.1
(Figure A.240)	2	1.00 ± 0.04	23.8 ± 1.1
	3	2.60 ± 0.05	18.0 ± 0.4
	4	2.81 ± 0.05	13.0 ± 0.3
	5	2.51 ± 0.06	13.4 ± 0.4
	6	2.10 ± 0.05	13.7 ± 0.4
	7	1.21 ± 0.05	11.5 ± 0.5
	8	1.27 ± 0.04	16.6 ± 0.6
		0.51 ± 0.04	14.1 ± 1.4

Velocity dispersions and brightness temperatures of Gaussian components fit to spectra taken at integrated intensity peaks throughout key regions in the observed gas structure. These values have been extracted in apertures of 1″. Two values are given for a single spectrum in cases where a two-component Gaussian fit was used. No value is reported if the fit was unreliable.

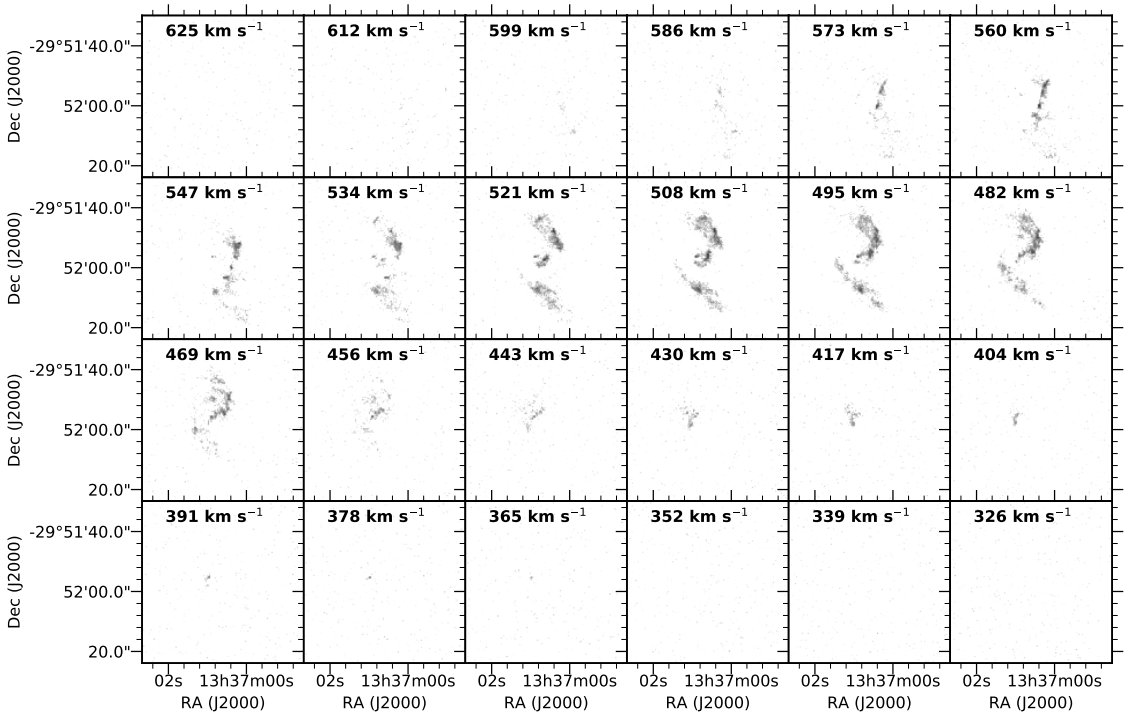

FIGURE A.235: [
Channel map of HCN $(1-0)$]Channel map of HCN $(1-0)$ emission, with every $13\,\mathrm{km\,s^{-1}}$ averaged together between $326\,\mathrm{km\,s^{-1}}$ and $625\,\mathrm{km\,s^{-1}}$. The central velocity of each velocity bin is shown.

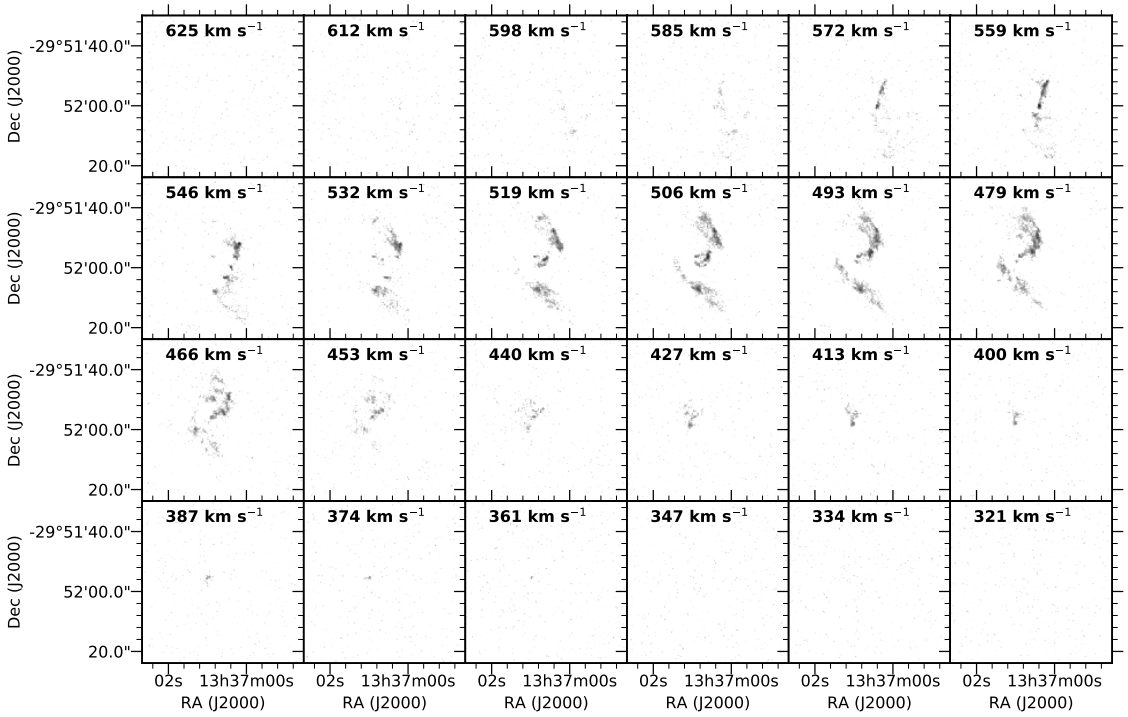

FIGURE A.236: [
Channel map of HCO^+]Channel map of HCO^+ $(1-0)$ emission, with every 13 km^{-1} averaged together between 326 km s^{-1} and 625 km s^{-1}. The central velocity of each velocity bin is shown.

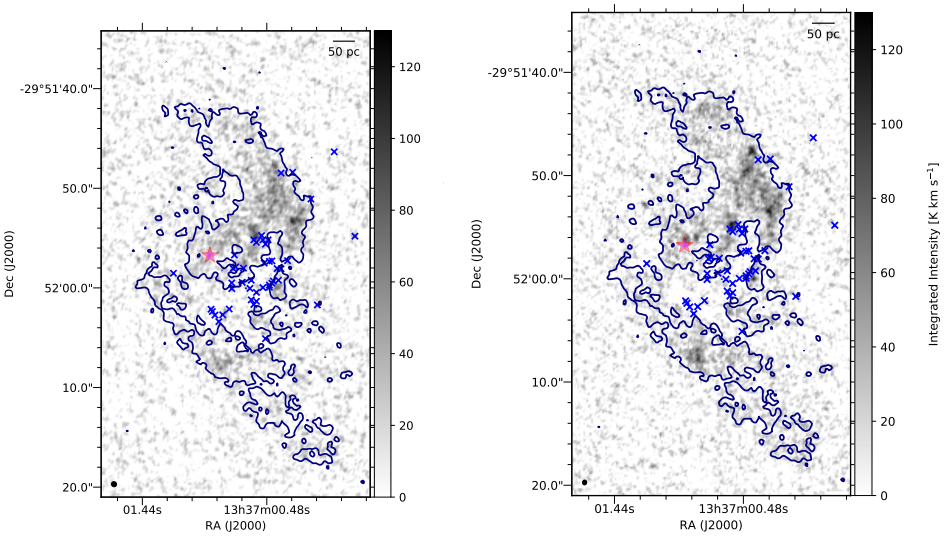

FIGURE A.237: [
Integrated intensity maps of CCh and CS]Integrated intensity maps of the two other detected lines. [Left]: CCH (N = 1 - 0), [Right]: CS (J = 2 - 1). Blue crosses show positions of massive stellar clusters as found by Harris et al. (2001). The orange star indicates the visual centre of M83, the green star indicates the location of the secondary nucleus observed by Thatte et al. (2000). CCH and CS maps also show HCN $(1-0)$ contours overlaid at 30 K km s^{-1} integrated intensity levels. Due to the significantly lower signal to noise ratio of these data, they were not used for analysis.

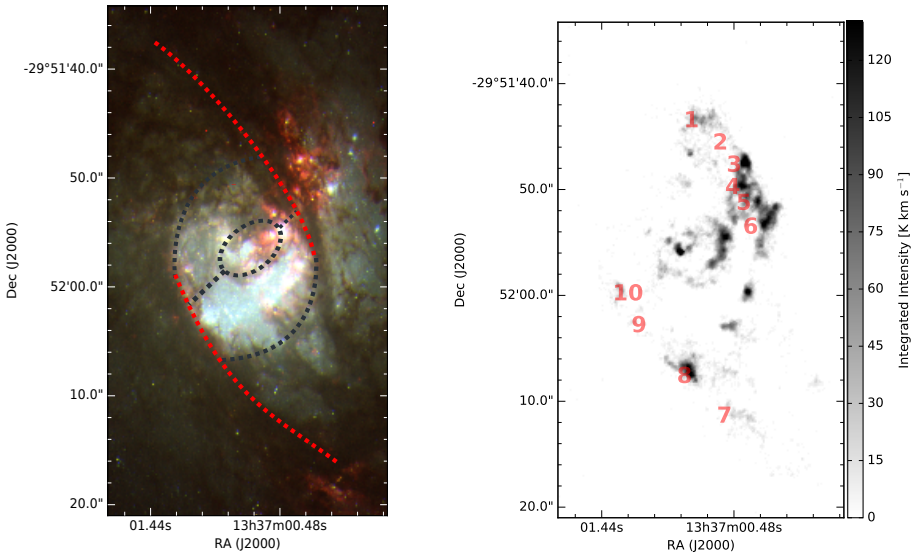

A.5 Appendix 5: Line-fitting of HCN (1-0) and HCO^+ (1-0) with SCOUSE

Due to the possibility of multiple spectral components per sightline, which leads to unreliable results when using moment analysis, the HCN $(1-0)$ and HCO^+ $(1-0)$ data were run through the **S**emi-automated multi-**CO**mponent **U**niversal **S**pectral-line fitting **E**ngine (SCOUSE) as presented in Henshaw et al. (2016a). The method and results of the SCOUSE fitting process are described in Appendix A.5. We use the results of the line fitting analysis to investigate how the kinematics of the gas varies with position in the central few hundred pc of the galaxy.

SCOUSE is a line-fitting algorithm that is capable of fitting Gaussian profiles to large spectral-line datasets efficiently. It does this by breaking the input dataset into smaller equally sized regions, rejecting those regions in which less than 50% of the cells exceed a user-defined noise threshold. For the remaining regions, the signal is averaged over the entire region on per-channel basis to produce a spatially averaged spectrum. Each of these spectra are then manually inspected, and all lines are fit by the user, with the number of guassian components, and their given parameters estimated manually. This fitting process is then used as a template for the spectra of each cell that comprises each spatially averaged area (SAA). These SAAs were selected to be $0.5''$ ($\sim$11 pc) in radius as this is twice the expected cloud size within this environment. We enforced a 5σ cut with an RMS of 0.25 K per 3.2 km s^{-1} channel. This allowed us to get maximum coverage over the important emission whilst minimising the time needed to fit all spectra. Figure A.241 demonstrates how this coverage is defined in SCOUSE. Each red box is a spectral averaging area with a user defined radius of, in this case, $0.5''$.

Moment maps were created using CASA, as well as their corresponding maps using the SCOUSE output. Figure 3.2 shows the continuum and zeroth, first and second order moment maps for HCN $(1-0)$ output from CASA. The velocity maps delineate the structure of the gas within this region; particularly demonstrating the contiguous gas lanes from the north and south that appear to be feeding the circumnuclear ring sitting at a distance of $\sim$150 pc from the centre. A second circumnuclear ring is also observed sitting at $\sim 50-100$ pc from the nucleus.

Figure A.242 shows the integrated intensity maps as produced using the output of SCOUSE for HCN $(1-0)$ and HCO^+ $(1-0)$ data, each of which shows almost identical structure to the gas as seen in the integrated intensity maps output from CASA. Centroid velocity and velocity dispersion maps of HCN $(1-0)$ and HCO^+ $(1-0)$ were also created using the ouput from SCOUSE. Figure A.244 shows maps of the number of fitted Gaussian components per pixel, the centroid velocity, and the minimum and maximum velocity dispersions at each pixel (from left to right, and top to bottom) for HCN $(1-0)$; Figure A.243 show the same maps for HCO^+ $(1-0)$. To ensure the quality of these fits were sufficient, two rounds of visual inspection were performed. The first being a vital step in the SCOUSE process in which the user is shown each spectra output from the fitting process. The second being an inspection of spectra randomly selected from various locations in the map once the entire SCOUSE process was completed. Both rounds of inspection showed the fitting process had done a good job of recovering the gas kinematics. The output of the fits and fit results are available as an online resource here: XXX.

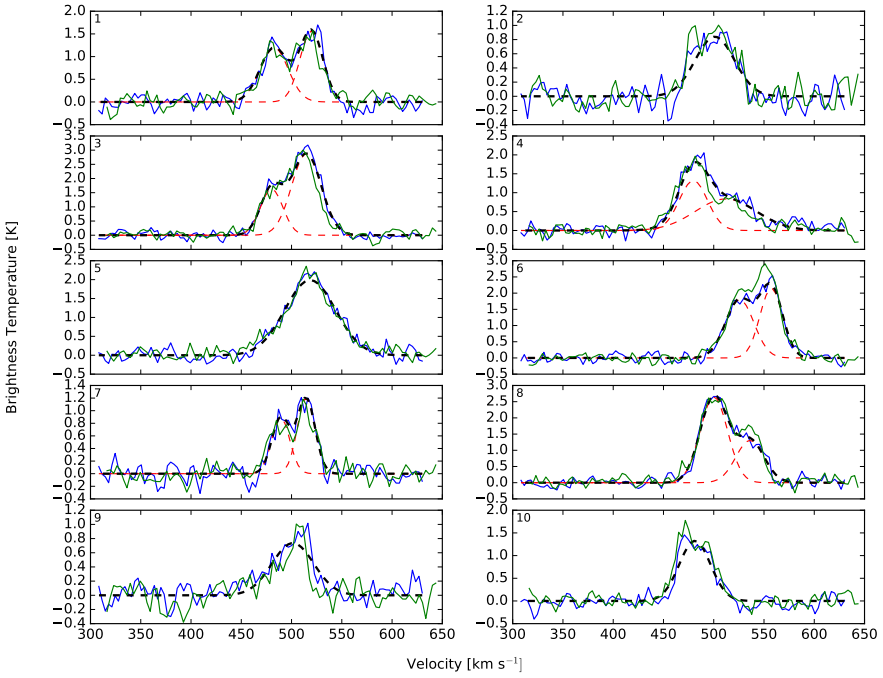

FIGURE A.238: [
Example spectra at intensity peaks within dust lanes]Example spectra of HCN $(1-0)$ [blue] and HCO^+ $(1-0)$ [green] taken at HCN $(1-0)$ integrated intensity peaks throughout key regions of the observed gas structure. [Top Left]: the same colour scale image as Figure 3.1 overlaid with the overall schematic and the relevant region highlighted – in this case, the dust lanes highlighted in red. [Top Right]: the HCN $(1-0)$ integrated intensity image in grey scale overlaid with the locations at which each spectra was taken. The spectra shown start at 1 (upper left) and end at 10 (lower right), and were averaged over a region $1''$ in size. The black dashed line shows the Gaussian component fit to the HCN $(1-0)$ spectra. In cases where a multi-component Gaussian fit was used the red dashed line shows the properties of each Gaussian component individually. As shown in Table A.2, there is no monotonic trend between gas velocity dispersion and galactocentric radius in the dust lanes.

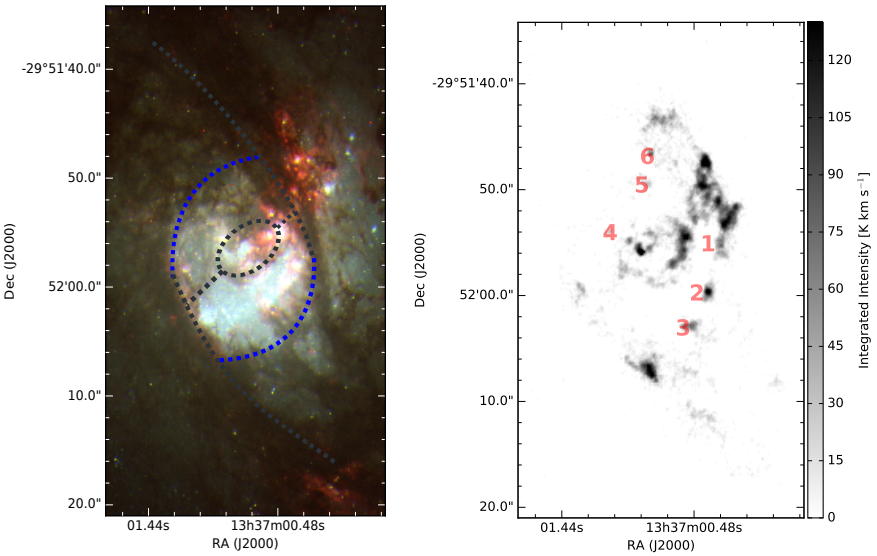

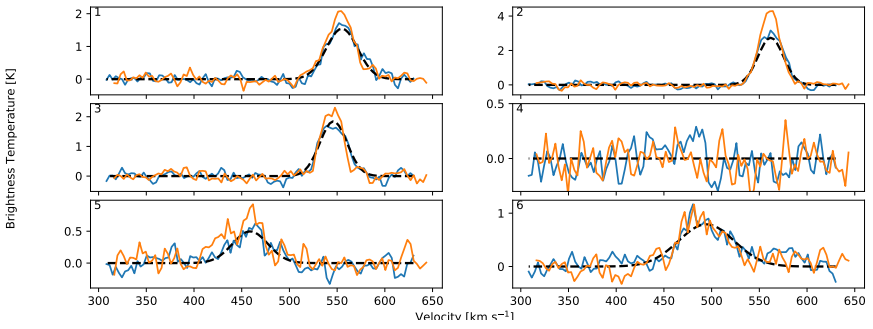

FIGURE A.239: [
Example spectra at intensity peaks within outer circumnuclear ring]HCN $(1-0)$ and HCO^+ $(1-0)$ spectrum as in Figure A.238 but extracted from key locations within the outer circumnuclear ring, as shown in blue in the upper left panel.

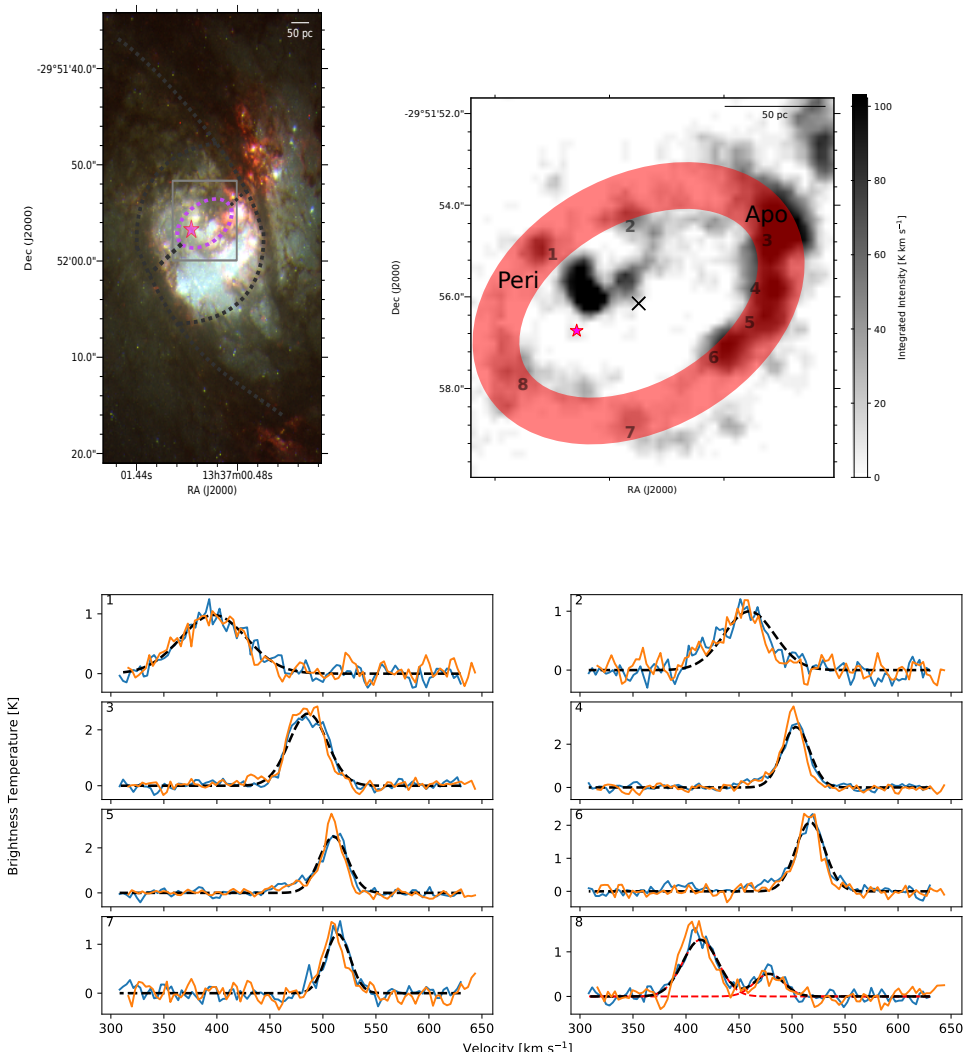

FIGURE A.240: [
Example spectra at intensity peaks within inner circumnuclear ring]HCN $(1-0)$ and HCO^+ $(1-0)$ spectrum as in Figure A.238 but extracted from key locations within the inner circumnuclear ring as shown in purple in the upper left panel. The box on the left-hand panel shows the field of view of the right-hand panel. The cross shows the location of the centre of the manually fitted ellipse (red shaded region) to the circumnuclear ring, and the plus is the location of the visible nucleus of M83, which was used as the zero-point for radius and azimuthal angle calculations. The ellipse has semi-major and semi-minor axes of $a = 45$pc and $b = 27$pc with a position angle of 60°. The locations of peri- and apocentre from the visible nucleus are also labeled.

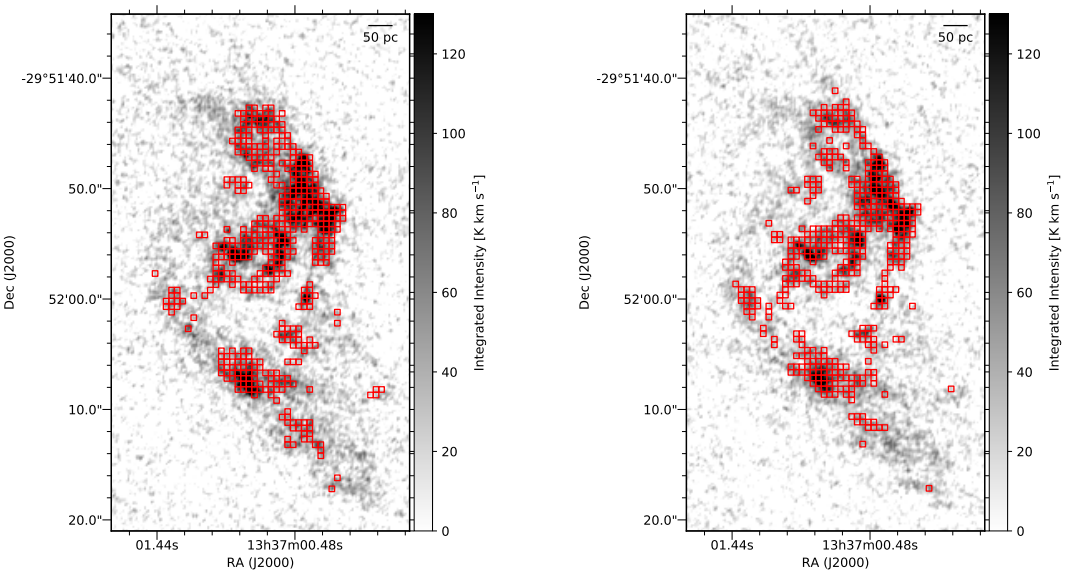

FIGURE A.241: [
SCOUSE coverage]Coverage of SCOUSE. Red boxes denote an individual spectral averaging area, overlaid on top of a HCN $(1-0)$ [Left] and HCO^+ $(1-0)$ [Right] integrated intensity map.

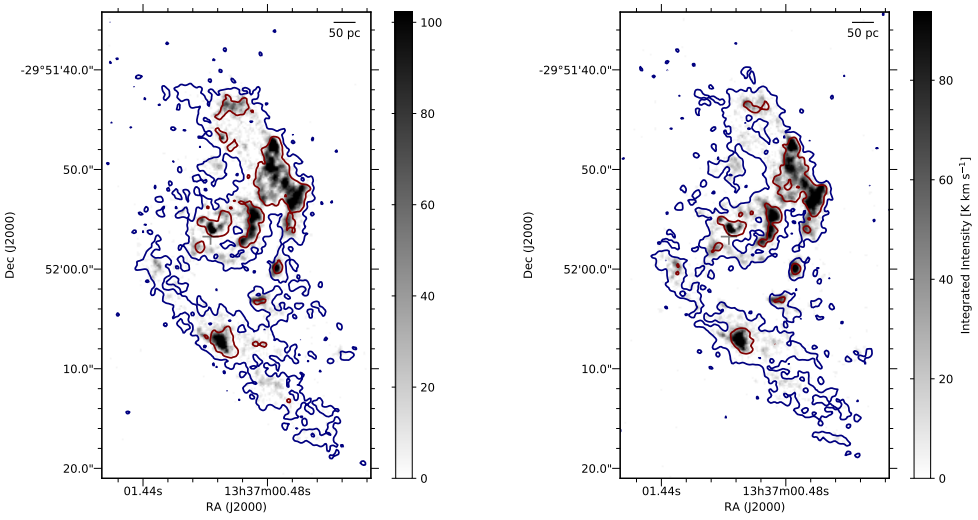

FIGURE A.242: [
Integrated intensity map of HCN and HCO^+ produced by SCOUSE.]Integrated intensity map of HCN $(1-0)$ and HCO^+ $(1-0)$ produced by SCOUSE. Blue contours show the integrated intensity as produced by CASA at the [25, 75] K km s^{-1} level.

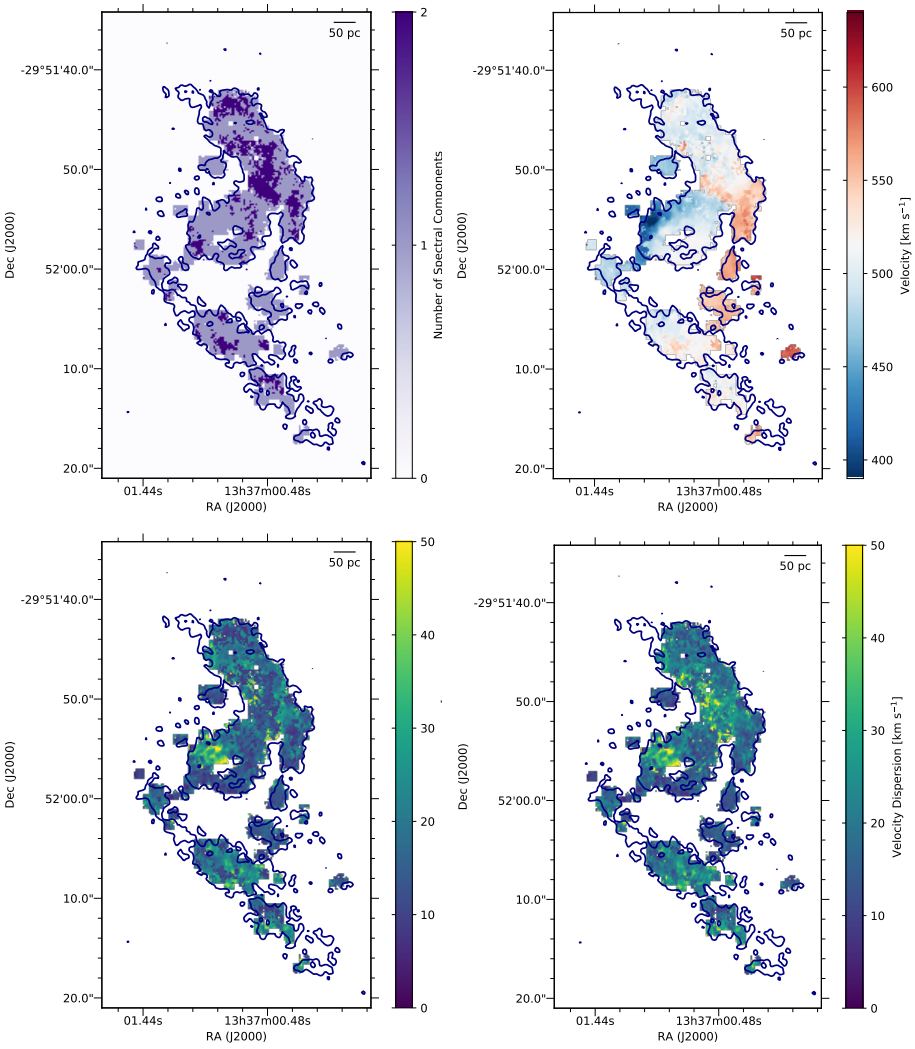

FIGURE A.243: [
Moment maps of HCN produced from SCOUSE]SCOUSE outputs for HCN $(1-0)$. [Top Left]: Number of spectral components per pixel; [Top Right]: centroid velocity; [Bottom Left]: minimum velocity dispersion; [Bottom Right]: maximum velocity dispersion

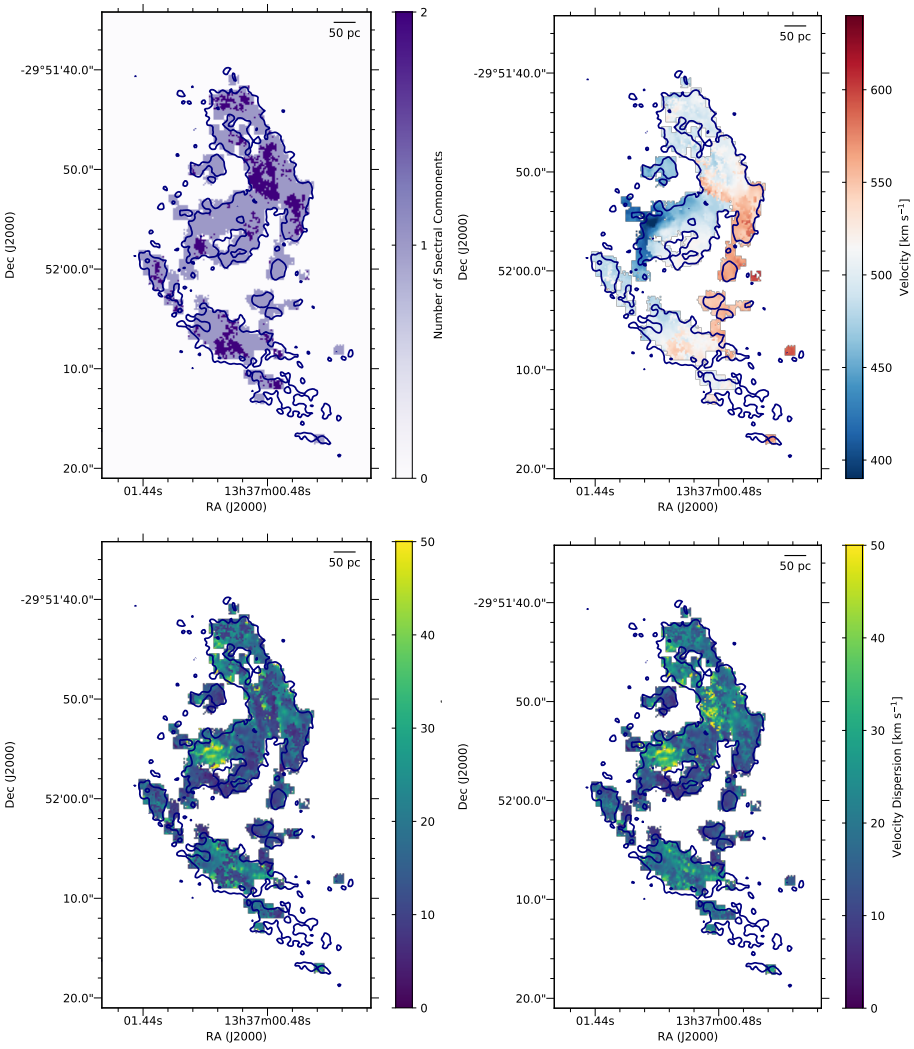

FIGURE A.244: [
Moment maps of HCO^+ produced from SCOUSE]SCOUSE outputs for HCO^+ $(1-0)$. [Top Left]: Number of spectral components per pixel; [Top Right]: centroid velocity; [Bottom Left]: minimum velocity dispersion; [Bottom Right]: maximum velocity dispersion

Bibliography

Aguirre J. E., et al., 2011a, Astrophysical Journal, Supplement, 192, 4

Aguirre J. E., et al., 2011b, Astrophysical Journal, Supplement, 192, 4

Allard E. L., Knapen J. H., Peletier R. F., Sarzi M., 2006a, Monthly Notices of the Royal Astronomical Society, 371, 1087

Allard E. L., Knapen J. H., Peletier R. F., Sarzi M., 2006b, Monthly Notices of the Royal Astronomical Society, 371, 1087

André P., et al., 2010, Astronomy & Astrophysics, 518, L102

André P., Di Francesco J., Ward-Thompson D., Inutsuka S. I., Pudritz R. E., Pineda J. E., 2014, in Beuther H., Klessen R. S., Dullemond C. P., Henning T., eds, Protostars and Planets VI. p. 27 (arXiv:1312.6232), doi:10.2458/azu˙uapress˙9780816531240-ch002

André P., et al., 2016, Astronomy & Astrophysics, 592, A54

Ao Y., et al., 2013, Astronomy & Astrophysics, 550, A135

Armijos-Abendaño J., Martín-Pintado J., Requena-Torres M. A., Martín S., Rodríguez-Franco A., 2015, Monthly Notices of the Royal Astronomical Society, 446, 3842

Armillotta L., Krumholz M. R., Di Teodoro E. M., McClure-Griffiths N. M., 2019a, Monthly Notices of the Royal Astronomical Society, 490, 4401

Armillotta L., Krumholz M. R., Di Teodoro E. M., McClure-Griffiths N. M., 2019b, Monthly Notices of the Royal Astronomical Society, 490, 4401

Athanassoula E., 1992, Monthly Notices of the Royal Astronomical Society, 259, 328

Baade W., 1946, Publications of the ASP, 58, 249

Bally J., Stark A. A., Wilson R. W., Henkel C., 1988a, The Astrophysical Journal, 324, 223

Bally J., Stark A. A., Wilson R. W., Henkel C., 1988b, The Astrophysical Journal, 324, 223

Bally J., et al., 2010, Astronomy & Astrophysics, 518, L90

Barnes A. T., Longmore S. N., Battersby C., Bally J., Kruijssen J. M. D., Henshaw J. D., Walker D. L., 2017, Monthly Notices of the Royal Astronomical Society, 469, 2263

Barnes A. T., et al., 2019, Monthly Notices of the Royal Astronomical Society, 486, 283

Barnes A. T., Longmore S. N., Dale J. E., Krumholz M. R., Kruijssen J. M. D., Bigiel F., 2020, Monthly Notices of the Royal Astronomical Society, 498, 4906

Bastian N., Covey K. R., Meyer M. R., 2010, Annual Review of Astron and Astrophys, 48, 339

Battersby C., et al., 2011, Astronomy & Astrophysics, 535, A128

Battersby C., et al., 2017a, in Crocker R. M., Longmore S. N., Bicknell G. V., eds, IAU Symposium Vol. 322, The Multi-Messenger Astrophysics of the Galactic Centre. pp 90–94 (arXiv:1610.05805), doi:10.1017/S1743921316012266

Battersby C., et al., 2017b, in Crocker R. M., Longmore S. N., Bicknell G. V., eds, Vol. 322, The Multi-Messenger Astrophysics of the Galactic Centre. pp 90–94 (arXiv:1610.05805), doi:10.1017/S1743921316012266

Battersby C., et al., 2020, Astrophysical Journal, Supplement, 249, 35

Beuther H., Schilke P., Stanke T., 2003, Astronomy & Astrophysics, 408, 601

Beuther H., et al., 2018, Astronomy & Astrophysics, 617, A100

Bigiel F., Leroy A., Walter F., Brinks E., de Blok W. J. G., Madore B., Thornley M. D., 2008a, The Astronomical Journal, 136, 2846

Bigiel F., Leroy A., Walter F., Brinks E., de Blok W. J. G., Madore B., Thornley M. D., 2008b, The Astronomical Journal, 136, 2846

Binney J., Gerhard O. E., Stark A. A., Bally J., Uchida K. I., 1991, Monthly Notices of the Royal Astronomical Society, 252, 210

Blaauw A., 1961, Bulletin Astronomical Institute of the Netherlands, 15, 265

Blair W. P., et al., 2014, The Astrophysical Journal, 788, 55

Blitz L., Shu F. H., 1980, The Astrophysical Journal, 238, 148

Boehle A., et al., 2016, The Astrophysical Journal, 830, 17

Bolatto A. D., Wolfire M., Leroy A. K., 2013, Annual Review of Astron and Astrophys, 51, 207

Bondi H., Hoyle F., 1944, Monthly Notices of the Royal Astronomical Society, 104, 273

Bonnell I. A., Bate M. R., Clarke C. J., Pringle J. E., 1997, Monthly Notices of the Royal Astronomical Society, 285, 201

Bressert E., et al., 2012, Astronomy & Astrophysics, 542, A49

Buta R., Combes F., 1996, Fundamental Cosmic Physics, 17, 95

Calzetti D., 2001, Publications of the ASP, 113, 1449

Cappellari M., et al., 2012, Nature, 484, 485

Caselli P., Walmsley C. M., Tafalla M., Dore L., Myers P. C., 1999, Astrophysical Journal, Letters, 523, L165

Caswell J. L., et al., 2010, Monthly Notices of the Royal Astronomical Society, 404, 1029

Chabrier G., 2003, Publications of the ASP, 115, 763

Chandrasekhar S., Fermi E., 1953, The Astrophysical Journal, 118, 116

Chevance M., et al., 2019, Monthly Notices of the Royal Astronomical Society submitted

Chevance M., et al., 2020a, Monthly Notices of the Royal Astronomical Society, 493, 2872

Chevance M., et al., 2020b, Monthly Notices of the Royal Astronomical Society, 493, 2872

Clark P. C., Glover S. C. O., Ragan S. E., Shetty R., Klessen R. S., 2013, Astrophysical Journal, Letters, 768, L34

Codella C., Cabrit S., Gueth F., Cesaroni R., Bacciotti F., Lefloch B., McCaughrean M. J., 2007, Astronomy & Astrophysics, 462, L53

Cole B., et al., 2017, in American Astronomical Society Meeting Abstracts. p. 144.18

Colman T., Teyssier R., 2020, Monthly Notices of the Royal Astronomical Society, 492, 4727

Comte G., 1981, Astronomy and Astrophysics, Supplement, 44, 441

Condon J. J., 1992, Annual Review of Astron and Astrophys, 30, 575

Conroy C., Dutton A. A., Graves G. J., Mendel J. T., van Dokkum P. G., 2013, Astrophysical Journal, Letters, 776, L26

Contreras Y., Rathborne J., Garay G., 2013, Monthly Notices of the Royal Astronomical Society, 433, 251

Corbelli E., et al., 2017, Astronomy & Astrophysics, 601, A146

Cordes J. M., Downs G. S., 1985, Astrophysical Journal, Supplement, 59, 343

Cosentino G., et al., 2018, Monthly Notices of the Royal Astronomical Society, 474, 3760

Crowther P. A., 2013, Monthly Notices of the Royal Astronomical Society, 428, 1927

Crutcher R. M., Roberts D. A., Mehringer D. M., Troland T. H., 1996, Astrophysical Journal, Letters, 462, L79

Cyganowski C. J., et al., 2014, Astrophysical Journal, Letters, 796, L2

Dabringhausen J., Hilker M., Kroupa P., 2008, Monthly Notices of the Royal Astronomical Society, 386, 864

Dahmen G., Huttemeister S., Wilson T. L., Mauersberger R., 1998b, Astronomy & Astrophysics, 331, 959

Dahmen G., Huttemeister S., Wilson T. L., Mauersberger R., 1998a, Astronomy & Astrophysics, 331, 959

Dale J. E., Kruijssen J. M. D., Longmore S. N., 2019a, arXiv e-prints,

Dale J. E., Kruijssen J. M. D., Longmore S. N., 2019b, Monthly Notices of the Royal Astronomical Society, 486, 3307

Dame T. M., Hartmann D., Thaddeus P., 2001, The Astrophysical Journal, 547, 792

Díaz R. J., Dottori H., Aguero M. P., Mediavilla E., Rodrigues I., Mast D., 2006, The Astrophysical Journal, 652, 1122

Dyson J. E., Williams D. A., 1997, The physics of the interstellar medium, doi:10.1201/9780585368115.

Eden D. J., et al., 2020, Monthly Notices of the Royal Astronomical Society, 498, 5936

Ellison S. L., Thorp M. D., Pan H.-A., Lin L., Scudder J. M., Bluck A. F. L., Sánchez S. F., Sargent M., 2020, Monthly Notices of the Royal Astronomical Society, 492, 6027

Elmegreen B. G., 1982, The Astrophysical Journal, 253, 655

Elmegreen B. G., 1989, The Astrophysical Journal, 338, 178

Elmegreen B. G., 2000, The Astrophysical Journal, 530, 277

Elmegreen B. G., 2008, The Astrophysical Journal, 672, 1006

Elmegreen B. G., Falgarone E., 1996, The Astrophysical Journal, 471, 816

Elmegreen D. M., Chromey F. R., Warren A. R., 1998, The Astronomical Journal, 116, 2834

Engelbracht C. W., Gordon K. D., Rieke G. H., Werner M. W., Dale D. A., Latter W. B., 2005, Astrophysical Journal, Letters, 628, L29

Evans Neal J. I., 1999, Annual Review of Astron and Astrophys, 37, 311

Fathi K., et al., 2008, Astrophysical Journal, Letters, 675, L17

Federrath C., et al., 2016, The Astrophysical Journal, 832, 143

Ferrari G. G., Dottori H., Díaz R. J., 2013, Journal of Modern Physics, 4, 55

Ferrière K., Gillard W., Jean P., 2007, Astronomy & Astrophysics, 467, 611

Field G. B., Blackman E. G., Keto E. R., 2011, Monthly Notices of the Royal Astronomical Society, 416, 710

Flower D. R., Pineau des Forets G., Field D., May P. W., 1996, Monthly Notices of the Royal Astronomical Society, 280, 447

Foreman-Mackey D., Hogg D. W., Lang D., Goodman J., 2013, Publications of the ASP, 125, 306

Foyle K., et al., 2012, Monthly Notices of the Royal Astronomical Society, 421, 2917

Freeman P., Rosolowsky E., Kruijssen J. M. D., Bastian N., Adamo A., 2017, Monthly Notices of the Royal Astronomical Society, 468, 1769

Fregeau J. M., Joshi K. J., Portegies Zwart S. F., Rasio F. A., 2002, The Astrophysical Journal, 570, 171

Frerking M. A., Langer W. D., Wilson R. W., 1982, The Astrophysical Journal, 262, 590

Gao Y., Solomon P. M., 2004a, The Astrophysical Journal, 606, 271

Gao Y., Solomon P. M., 2004b, The Astrophysical Journal, 606, 271

Gazak J. Z., et al., 2014, The Astrophysical Journal, 787, 142

Genzel R., Eckart A., 1998, Academie des Sciences Paris Comptes Rendus Serie B Sciences Physiques, 326, 69

Genzel R., Hollenbach D., Townes C. H., 1994, Reports on Progress in Physics, 57, 417

Genzel R., Thatte N., Krabbe A., Kroker H., Tacconi-Garman L. E., 1996, The Astrophysical Journal, 472, 153

Genzel R., Eisenhauer F., Gillessen S., 2010a, Reviews of Modern Physics, 82, 3121

Genzel R., Eisenhauer F., Gillessen S., 2010b, Reviews of Modern Physics, 82, 3121

Ghez A. M., et al., 2008, The Astrophysical Journal, 689, 1044

Gillessen S., Eisenhauer F., Trippe S., Alexand er T., Genzel R., Martins F., Ott T., 2009, The Astrophysical Journal, 692, 1075

Ginsburg A., Kruijssen J. M. D., 2018, Astrophysical Journal, Letters, 864, L17

Ginsburg A., et al., 2013, Astrophysical Journal, Supplement, 208, 14

Ginsburg A., et al., 2016, Astronomy & Astrophysics, 586, A50

Ginsburg A., et al., 2018a, The Astrophysical Journal, 853, 171

Ginsburg A., et al., 2018b, The Astrophysical Journal, 853, 171

Ginsburg A., Mills E. A. C., Battersby C. D., Longmore S. N., Kruijssen J. M. D., 2019, Bulletin of the American Astronomical Society, 51, 220

Goddard Q. E., Bastian N., Kennicutt R. C., 2010, Monthly Notices of the Royal Astronomical Society, 405, 857

Goicoechea J. R., Rodríguez-Fernández N. J., Cernicharo J., 2004, The Astrophysical Journal, 600, 214

Goldreich P., Lynden-Bell D., 1965, Monthly Notices of the Royal Astronomical Society, 130, 97

Goto M., Indriolo N., Geballe T. R., Usuda T., 2013, Journal of Physical Chemistry A, 117, 9919

Gravity Collaboration et al., 2018, Astronomy & Astrophysics, 615, L15

Grudić M. Y., Hopkins P. F., Lee E. J., Murray N., Faucher-Giguère C.-A., Johnson L. C., 2019, Monthly Notices of the Royal Astronomical Society, 488, 1501

Guesten R., Downes D., 1980, in Astron. Soc. Inform..

Guesten R., Henkel C., 1983, Astronomy & Astrophysics, 125, 136

Guesten R., Walmsley C. M., Ungerechts H., Churchwell E., 1985, Astronomy & Astrophysics, 142, 381

Gueth F., Guilloteau S., Bachiller R., 1998, Astronomy & Astrophysics, 333, 287

Güsten R., Downes D., 1980, Astronomy & Astrophysics, 87, 6

Gutermuth R. A., Heyer M., 2015, The Astronomical Journal, 149, 64

Gutermuth R. A., Pipher J. L., Megeath S. T., Myers P. C., Allen L. E., Allen T. S., 2011a, The Astrophysical Journal, 739, 84

Gutermuth R. A., Pipher J. L., Megeath S. T., Myers P. C., Allen L. E., Allen T. S., 2011b, The Astrophysical Journal, 739, 84

H. E. S. S. Collaboration et al., 2018, Astronomy & Astrophysics, 612, A1

Hankins M. J., et al., 2020, The Astrophysical Journal, 894, 55

Harada N., et al., 2015, Astronomy & Astrophysics, 584, A102

Harada R., et al., 2019, Publications of the ASJ, 71, 44

Harris J., Calzetti D., Gallagher III J. S., Conselice C. J., Smith D. A., 2001, The Astronomical Journal, 122, 3046

Harwit M., 1988, Astrophysical Concepts

Hatchfield H. P., et al., 2020, Astrophysical Journal, Supplement, 251, 14

Haydon D. T., Kruijssen J. M. D., Hygate A. e. P. S., Schruba A., Krumholz M. R., Chevance M., Longmore S. N., 2018, arXiv e-prints, p. arXiv:1810.10897

Haydon D. T., Kruijssen J. M. D., Chevance M., Hygate A. P. S., Krumholz M. R., Schruba A., Longmore S. N., 2020, Monthly Notices of the Royal Astronomical Society, 498, 235

Heitsch F., Mac Low M.-M., Klessen R. S., 2001, The Astrophysical Journal, 547, 280

Henshaw J. D., et al., 2016a, SCOUSE: Semi-automated multi-COmponent Universal Spectral-line fitting Engine, Astrophysics Source Code Library (ascl:1601.003)

Henshaw J. D., et al., 2016b, Monthly Notices of the Royal Astronomical Society, 457, 2675

Henshaw J. D., Longmore S. N., Kruijssen J. M. D., 2016c, Monthly Notices of the Royal Astronomical Society, 463, L122

Henshaw J. D., et al., 2019a, Monthly Notices of the Royal Astronomical Society, 485, 2457

Henshaw J. D., et al., 2019b, Monthly Notices of the Royal Astronomical Society, 485, 2457

Henshaw J. D., et al., 2020, Nature Astronomy, 4, 1064

Heyer M. H., Brunt C. M., 2004, Astrophysical Journal, Letters, 615, L45

Heyer M., Krawczyk C., Duval J., Jackson J. M., 2009, The Astrophysical Journal, 699, 1092

Heywood I., et al., 2019, Nature, 573, 235

Hillenbrand L. A., Hartmann L. W., 1998, The Astrophysical Journal, 492, 540

Hong S., et al., 2011, The Astrophysical Journal, 731, 45

Hopkins P. F., 2014, The Astrophysical Journal, 797, 59

Hopkins P. F., Narayanan D., Murray N., 2013, Monthly Notices of the Royal Astronomical Society, 432, 2647

Houghton R. C. W., Thatte N., 2008, Monthly Notices of the Royal Astronomical Society, 385, 1110

Hoyle F., Lyttleton R. A., 1939, Proceedings of the Cambridge Philosophical Society, 35, 405

Hsieh P.-Y., Koch P. M., Ho P. T. P., Kim W.-T., Tang Y.-W., Wang H.-H., Yen H.-W., Hwang C.-Y., 2017, The Astrophysical Journal, 847, 3

Humphreys E., Miura R., Brogan C. L., Hibbard J., Hunter T. R., Indebetouw R., 2016, in Proceedings of the 2016 ALMA Conference. p. 1

Hunter C., 1977, The Astrophysical Journal, 218, 834

Inutsuka S.-I., Miyama S. M., 1992, The Astrophysical Journal, 388, 392

Israel F. P., Baas F., 2001, Astronomy & Astrophysics, 371, 433

Jackson J. M., et al., 2006, Astrophysical Journal, Supplement, 163, 145

Jackson J. M., Finn S. C., Chambers E. T., Rathborne J. M., Simon R., 2010, Astrophysical Journal, Letters, 719, L185

Jackson J. M., et al., 2013, Publications of the Astron. Soc. of Australia, 30, e057

Jeans J. H., 1902, Philosophical Transactions of the Royal Society of London Series A, 199, 1

Jeffreson S. M. R., Kruijssen J. M. D., Krumholz M. R., Longmore S. N., 2018, Monthly Notices of the Royal Astronomical Society, 478, 3380

Jiang F., Jiang S., 2019, Physica D Nonlinear Phenomena, 391, 17

Jimenez-Serra I., et al., 2020, arXiv e-prints, p. arXiv:2004.07834

Jones P. A., et al., 2012, Monthly Notices of the Royal Astronomical Society, 419, 2961

Kahn F. D., 1974, Astronomy & Astrophysics, 37, 149

Kant I., 1755, Allgemeine Naturgeschichte und Theorie des Himmels

Kauffmann J., Pillai T., 2010, Astrophysical Journal, Letters, 723, L7

Kauffmann J., Pillai T., Shetty R., Myers P. C., Goodman A. A., 2010a, The Astrophysical Journal, 712, 1137

Kauffmann J., Pillai T., Shetty R., Myers P. C., Goodman A. A., 2010b, The Astrophysical Journal, 716, 433

Kauffmann J., Pillai T., Goldsmith P. F., 2013, The Astrophysical Journal, 779, 185

Kauffmann J., Pillai T., Zhang Q., Menten K. M., Goldsmith P. F., Lu X., Guzmán A. E., Schmiedeke A., 2016, preprint, (arXiv:1610.03502)

Kauffmann J., Pillai T., Zhang Q., Menten K. M., Goldsmith P. F., Lu X., Guzmán A. E., 2017a, Astronomy & Astrophysics, 603, A89

Kauffmann J., Pillai T., Zhang Q., Menten K. M., Goldsmith P. F., Lu X., Guzmán A. E., 2017b, Astronomy & Astrophysics, 603, A89

Kennicutt Jr. R. C., 1998a, Annual Review of Astron and Astrophys, 36, 189

Kennicutt Jr. R. C., 1998b, Annual Review of Astron and Astrophys, 36, 189

Kennicutt R. C., Evans N. J., 2012, Annual Review of Astron and Astrophys, 50, 531

Kepley A. A., Tsutsumi T., Brogan C. L., Indebetouw R., Yoon I., Mason B., Donovan Meyer J., 2020, Publications of the ASP, 132, 024505

Kim J., Hong S. S., 1998, The Astrophysical Journal, 507, 254

Kim W.-T., Moon S., 2016, The Astrophysical Journal, 829, 45

Kim W.-T., Ostriker E. C., 2001, The Astrophysical Journal, 559, 70

Kim W.-T., Ostriker E. C., 2006, The Astrophysical Journal, 646, 213

Kim W.-T., Ostriker E. C., Stone J. M., 2003, The Astrophysical Journal, 599, 1157

Kim W.-T., Seo W.-Y., Stone J. M., Yoon D., Teuben P. J., 2012, The Astrophysical Journal, 747, 60

Knapen J. H., Sharp R. G., Ryder S. D., Falcón-Barroso J., Fathi K., Gutiérrez L., 2010, Monthly Notices of the Royal Astronomical Society, 408, 797

Koda J., et al., 2009, Astrophysical Journal, Letters, 700, L132

Kolmogorov A. N., 1941, Akademiia Nauk SSSR Doklady, 32, 16

Kong S., Tan J. C., Caselli P., Fontani F., Liu M., Butler M. J., 2017, The Astrophysical Journal, 834, 193

Krieger N., et al., 2017a, The Astrophysical Journal, 850, 77

Krieger N., et al., 2017b, The Astrophysical Journal, 850, 77

Krieger N., et al., 2019, The Astrophysical Journal, 881, 43

Kroupa P., 2001, Monthly Notices of the Royal Astronomical Society, 322, 231

Kroupa P., Weidner C., Pflamm-Altenburg J., Thies I., Dabringhausen J., Marks M., Maschberger T., 2013, The Stellar and Sub-Stellar Initial Mass Function of Simple and Composite Populations. p. 115, doi:10.1007/978-94-007-5612-0˙4

Kruijssen J. M. D., Longmore S. N., 2013a, Monthly Notices of the Royal Astronomical Society, 435, 2598

Kruijssen J. M. D., Longmore S. N., 2013b, Monthly Notices of the Royal Astronomical Society, 435, 2598

Kruijssen J. M. D., Longmore S. N., 2014a, Monthly Notices of the Royal Astronomical Society, 439, 3239

Kruijssen J. M. D., Longmore S. N., 2014b, Monthly Notices of the Royal Astronomical Society, 439, 3239

Kruijssen J. M. D., Pelupessy F. I., Lamers H. J. G. L. M., Portegies Zwart S. F., Icke V., 2011, Monthly Notices of the Royal Astronomical Society, 414, 1339

Kruijssen J. M. D., Longmore S. N., Elmegreen B. G., Murray N., Bally J., Testi L., Kennicutt R. C., 2014a, Monthly Notices of the Royal Astronomical Society, 440, 3370

Kruijssen J. M. D., Longmore S. N., Elmegreen B. G., Murray N., Bally J., Testi L., Kennicutt R. C., 2014b, Monthly Notices of the Royal Astronomical Society, 440, 3370

Kruijssen J. M. D., Dale J. E., Longmore S. N., 2015, Monthly Notices of the Royal Astronomical Society, 447, 1059

Kruijssen J. M. D., Schruba A., Hygate A. e. P. S., Hu C.-Y., Haydon D. T., Longmore S. N., 2018, Monthly Notices of the Royal Astronomical Society, 479, 1866

Kruijssen J. M. D., et al., 2019a, Monthly Notices of the Royal Astronomical Society, 484, 5734

Kruijssen J. M. D., et al., 2019b, Monthly Notices of the Royal Astronomical Society, 484, 5734

Kruijssen J. M. D., et al., 2019c, Nature, 569, 519

Krumholz M. R., Dekel A., 2012a, The Astrophysical Journal, 753, 16

Krumholz M. R., Dekel A., 2012b, The Astrophysical Journal, 753, 16

Krumholz M. R., Kruijssen J. M. D., 2015a, Monthly Notices of the Royal Astronomical Society, 453, 739

Krumholz M. R., Kruijssen J. M. D., 2015b, Monthly Notices of the Royal Astronomical Society, 453, 739

Krumholz M. R., McKee C. F., 2008, Nature, 451, 1082

Krumholz M. R., Klein R. I., McKee C. F., 2007, The Astrophysical Journal, 656, 959

Krumholz M. R., Kruijssen J. M. D., Crocker R. M., 2017, Monthly Notices of the Royal Astronomical Society, 466, 1213

Kudritzki R. P., 2002, The Astrophysical Journal, 577, 389

Kundert K., Rau U., Bergin E., Bhatnagar S., 2017, IEEE Transactions on Antennas and Propagation, 65, 644

Kurtz S., 2005, in Cesaroni R., Felli M., Churchwell E., Walmsley M., eds, IAU Symposium Vol. 227, Massive Star Birth: A Crossroads of Astrophysics. pp 111–119, doi:10.1017/S1743921305004424

Lachowicz P., Zdziarski A. A., Schwarzenberg-Czerny A., Pooley G. G., Kitamoto S., 2006, Monthly Notices of the Royal Astronomical Society, 368, 1025

Lada C. J., Lada E. A., 2003, Annual Review of Astron and Astrophys, 41, 57

Lada C. J., Lombardi M., Alves J. F., 2010, The Astrophysical Journal, 724, 687

Lada C. J., Forbrich J., Lombardi M., Alves J. F., 2012a, The Astrophysical Journal, 745, 190

Lada C. J., Forbrich J., Lombardi M., Alves J. F., 2012b, The Astrophysical Journal, 745, 190

Lamers H. J. G. L. M., Gieles M., Portegies Zwart S. F., 2005, Astronomy & Astrophysics, 429, 173

Langer W. D., Velusamy T., Morris M. R., Goldsmith P. F., Pineda J. L., 2017, Astronomy & Astrophysics, 599, A136

Larson R. B., 1969, Monthly Notices of the Royal Astronomical Society, 145, 271

Larson R. B., 1981, Monthly Notices of the Royal Astronomical Society, 194, 809

Larson R. B., 2003, Reports on Progress in Physics, 66, 1651

Launhardt R., Zylka R., Mezger P. G., 2002, Astronomy & Astrophysics, 384, 112

Le Petit F., Ruaud M., Bron E., Godard B., Roueff E., Languignon D., Le Bourlot J., 2016, Astronomy & Astrophysics, 585, A105

Leitherer C., Ekström S., Meynet G., Schaerer D., Agienko K. B., Levesque E. M., 2014, The Astrophysical Journal Supplement Series, 212, 14

Leroy A. K., Walter F., Brinks E., Bigiel F., de Blok W. J. G., Madore B., Thornley M. D., 2008a, The Astronomical Journal, 136, 2782

Leroy A. K., Walter F., Brinks E., Bigiel F., de Blok W. J. G., Madore B., Thornley M. D., 2008b, The Astronomical Journal, 136, 2782

Leroy A. K., et al., 2018, The Astrophysical Journal, 869, 126

Li A., Draine B. T., 2002, The Astrophysical Journal, 564, 803

Li Y., Mac Low M.-M., Klessen R. S., 2005, The Astrophysical Journal, 626, 823

Lis D. C., Serabyn E., Zylka R., Li Y., 2001, The Astrophysical Journal, 550, 761

Longmore S., Kruijssen J. M. D., 2018, Galaxies, 6, 55

Longmore S. N., Pillai T., Keto E., Zhang Q., Qiu K., 2011, The Astrophysical Journal, 726, 97

Longmore S. N., et al., 2012, The Astrophysical Journal, 746, 117

Longmore S. N., et al., 2013a, Monthly Notices of the Royal Astronomical Society, 429, 987

Longmore S. N., et al., 2013b, Monthly Notices of the Royal Astronomical Society, 429, 987

Longmore S. N., et al., 2013c, Monthly Notices of the Royal Astronomical Society, 429, 987

Longmore S. N., et al., 2013d, Monthly Notices of the Royal Astronomical Society, 433, L15

Longmore S. N., et al., 2014, Protostars and Planets VI, pp 291–314

Longmore S. N., et al., 2017, Monthly Notices of the Royal Astronomical Society, 470, 1462

Lu J. R., Do T., Ghez A. M., Morris M. R., Yelda S., Matthews K., 2013, The Astrophysical Journal, 764, 155

Lu X., Zhang Q., Kauffmann J., Pillai T., Longmore S. N., Kruijssen J. M. D., Battersby C., Gu Q., 2015, Astrophysical Journal, Letters, 814, L18

Lu X., et al., 2019, Astrophysical Journal, Supplement, 244, 35

Lu X., Cheng Y., Ginsburg A., Longmore S. N., Kruijssen J. M. D., Battersby C., Zhang Q., Walker D. L., 2020, Astrophysical Journal, Letters, 894, L14

Lundgren A. A., Wiklind T., Olofsson H., Rydbeck G., 2004a, Astronomy & Astrophysics, 413, 505

Lundgren A. A., Olofsson H., Wiklind T., Rydbeck G., 2004b, Astronomy & Astrophysics, 422, 865

Mac Low M.-M., 1999, The Astrophysical Journal, 524, 169

Maddox L. A., Cowan J. J., Kilgard R. E., Lacey C. K., Prestwich A. H., Stockdale C. J., Wolfing E., 2006, The Astronomical Journal, 132, 310

Malin D., Hadley B., 1997, Publications of the Astron. Soc. of Australia, 14, 52

Manicò G., Ragunì G., Pirronello V., Roser J. E., Vidali G., 2001, Astrophysical Journal, Letters, 548, L253

Mathis J. S., Rumpl W., Nordsieck K. H., 1977, The Astrophysical Journal, 217, 425

Matzner C. D., McKee C. F., 2000, The Astrophysical Journal, 545, 364

McKee C. F., Tan J. C., 2002, Nature, 416, 59

McKee C. F., Tan J. C., 2003, The Astrophysical Journal, 585, 850

McMullin J. P., Waters B., Schiebel D., Young W., Golap K., 2007, in Shaw R. A., Hill F., Bell D. J., eds, Astronomical Society of the Pacific Conference Series Vol. 376, Astronomical Data Analysis Software and Systems XVI. p. 127

Meyer M. J., et al., 2004, Monthly Notices of the Royal Astronomical Society, 350, 1195

Miller G. E., Scalo J. M., 1979, Astrophysical Journal, Supplement, 41, 513

Mills E. A. C., Battersby C., 2017a, The Astrophysical Journal, 835, 76

Mills E. A. C., Battersby C., 2017b, The Astrophysical Journal, 835, 76

Mills E. A. C., Morris M. R., 2013a, The Astrophysical Journal, 772, 105

Mills E. A. C., Morris M. R., 2013b, The Astrophysical Journal, 772, 105

Mills E. A. C., Ginsburg A., Immer K., Barnes J. M., Wiesenfeld L., Faure A., Morris M. R., Requena-Torres M. A., 2018a, The Astrophysical Journal, 868, 7

Mills E. A. C., Ginsburg A., Immer K., Barnes J. M., Wiesenfeld L., Faure A., Morris M. R., Requena-Torres M. A., 2018b, The Astrophysical Journal, 868, 7

Molinari S., et al., 2010, Astronomy & Astrophysics, 518, L100

Molinari S., et al., 2011a, Astrophysical Journal, Letters, 735, L33

Molinari S., et al., 2011b, Astrophysical Journal, Letters, 735, L33

Molinari S., et al., 2014, Protostars and Planets VI, pp 125–148

Molinari S., et al., 2016, Astronomy & Astrophysics, 591, A149

Molster F. J., Waters L. B. F. M., Tielens A. G. G. M., 2002, Astronomy & Astrophysics, 382, 222

Morris M., Serabyn E., 1996a, Annual Review of Astron and Astrophys, 34, 645

Morris M., Serabyn E., 1996b, Annual Review of Astron and Astrophys, 34, 645

Morris M., Serabyn E., 1996c, Annual Review of Astron and Astrophys, 34, 645

Mróz P., et al., 2019, Astrophysical Journal, Letters, 870, L10

Mueller K. E., Shirley Y. L., Evans Neal J. I., Jacobson H. R., 2002, Astrophysical Journal, Supplement, 143, 469

Müller H. S. P., Schlöder F., Stutzki J., Winnewisser G., 2005, Journal of Molecular Structure, 742, 215

Muraoka K., et al., 2007, Publications of the ASJ, 59, 43

Myers P. C., Dame T. M., Thaddeus P., Cohen R. S., Silverberg R. F., Dwek E., Hauser M. G., 1986, The Astrophysical Journal, 301, 398

Nagasawa M., 1987, Progress of Theoretical Physics, 77, 635

Nakamura F., Hanawa T., Nakano T., 1993, Publications of the ASJ, 45, 551

Nony T., et al., 2018, Astronomy & Astrophysics, 618, L5

Oka T., Hasegawa T., Sato F., Tsuboi M., Miyazaki A., 1998, Astrophysical Journal, Supplement, 118, 455

Oka T., Hasegawa T., Sato F., Tsuboi M., Miyazaki A., Sugimoto M., 2001, The Astrophysical Journal, 562, 348

Oka T., Geballe T. R., Goto M., Usuda T., McCall B. J., 2005, The Astrophysical Journal, 632, 882

Oka T., Nagai M., Kamegai K., Tanaka K., Kuboi N., 2007, Publications of the ASJ, 59, 15

Oka T., Onodera Y., Nagai M., Tanaka K., Matsumura S., Kamegai K., 2012, Astrophysical Journal, Supplement, 201, 14

Oka T., Mizuno R., Miura K., Takekawa S., 2016, Astrophysical Journal, Letters, 816, L7

Onus A., Krumholz M. R., Federrath C., 2018, Monthly Notices of the Royal Astronomical Society, 479, 1702

Ossenkopf V., Henning T., 1994, Astronomy & Astrophysics, 291, 943

Padoan P., Cambrésy L., Langer W., 2002, Astrophysical Journal, Letters, 580, L57

Pan H.-A., Kuno N., Hirota A., 2014, Publications of the ASJ, 66, 27

Parker E. N., 1966, The Astrophysical Journal, 145, 811

Parravano A., McKee C. F., Hollenbach D. J., 2011, The Astrophysical Journal, 726, 27

Pawsey J. L., 1955, The Astrophysical Journal, 121, 1

Penston M. V., 1969, Monthly Notices of the Royal Astronomical Society, 144, 425

Pillai T., Kauffmann J., Tan J. C., Goldsmith P. F., Carey S. J., Menten K. M., 2015, The Astrophysical Journal, 799, 74

Pineda J. E., Caselli P., Goodman A. A., 2008, The Astrophysical Journal, 679, 481

Plume R., Jaffe D. T., Evans Neal J. I., Martín-Pintado J., Gómez-González J., 1997, The Astrophysical Journal, 476, 730

Ponti G., et al., 2019, Nature, 567, 347

Portegies Zwart S. F., McMillan S. L. W., Gieles M., 2010, Annual Review of Astron and Astrophys, 48, 431

Pound M. W., Yusef-Zadeh F., 2018, Monthly Notices of the Royal Astronomical Society, 473, 2899

Primiani R. A., et al., 2016, Journal of Astronomical Instrumentation, 5, 1641006

Purcell C. R., et al., 2012, Monthly Notices of the Royal Astronomical Society, 426, 1972

Raboud D., Mermilliod J. C., 1998, Astronomy & Astrophysics, 333, 897

Ragan S. E., Henning T., Tackenberg J., Beuther H., Johnston K. G., Kainulainen J., Linz H., 2014, Astronomy & Astrophysics, 568, A73

Ragan S. E., Moore T. J. T., Eden D. J., Hoare M. G., Elia D., Molinari S., 2016, Monthly Notices of the Royal Astronomical Society, 462, 3123

Rathborne J. M., et al., 2014, Astrophysical Journal, Letters, 795, L25

Rathborne J. M., et al., 2015, The Astrophysical Journal, 802, 125

Reid M. J., et al., 2009, The Astrophysical Journal, 700, 137

Requena-Torres M. A., Martín-Pintado J., Rodríguez-Franco A., Martín S., Rodríguez-Fernández N. J., de Vicente P., 2006, Astronomy & Astrophysics, 455, 971

Requena-Torres M. A., Martín-Pintado J., Martín S., Morris M. R., 2008, The Astrophysical Journal, 672, 352

Ridley M. G. L., Sormani M. C., Treß R. G., Magorrian J., Klessen R. S., 2017, Monthly Notices of the Royal Astronomical Society, 469, 2251

Rodríguez-Fernández N. J., Martín-Pintado J., Fuente A., Wilson T. L., 2004, Astronomy & Astrophysics, 427, 217

Rogers H., Pittard J. M., 2013, Monthly Notices of the Royal Astronomical Society, 431, 1337

Rosolowsky E., 2005, Publications of the ASP, 117, 1403

Rosolowsky E. W., Pineda J. E., Kauffmann J., Goodman A. A., 2008, The Astrophysical Journal, 679, 1338

Sabha N., et al., 2010, Astronomy & Astrophysics, 512, A2

Sakamoto K., Matsushita S., Peck A. B., Wiedner M. C., Iono D., 2004, Astrophysical Journal, Letters, 616, L59

Salpeter E. E., 1955, The Astrophysical Journal, 121, 161

Sandstrom K. M., Peek J. E. G., Bower G. C., Bolatto A. D., Plambeck R. L., 2007, The Astrophysical Journal, 667, 1161

Sarzi M., Allard E. L., Knapen J. H., Mazzuca L. M., 2007, Monthly Notices of the Royal Astronomical Society, 380, 949

Sawada T., Hasegawa T., Handa T., Cohen R. J., 2004, Monthly Notices of the Royal Astronomical Society, 349, 1167

Schinnerer E., et al., 2013, The Astrophysical Journal, 779, 42

Schinnerer E., et al., 2019, The Astrophysical Journal, 887, 49

Schruba A., et al., 2011a, The Astronomical Journal, 142, 37

Schruba A., et al., 2011b, The Astronomical Journal, 142, 37

Schuller F., et al., 2021, Monthly Notices of the Royal Astronomical Society, 500, 3064

Shapley H., 1918, The Astrophysical Journal, 48, 154

Shetty R., Beaumont C. N., Burton M. G., Kelly B. C., Klessen R. S., 2012, Monthly Notices of the Royal Astronomical Society, 425, 720

Shirley Y. L., 2015a, Publications of the ASP, 127, 299

Shirley Y. L., 2015b, Publications of the ASP, 127, 299

Shirley Y. L., Evans Neal J. I., Young K. E., Knez C., Jaffe D. T., 2003, Astrophysical Journal, Supplement, 149, 375

Shu F. H., 1977, The Astrophysical Journal, 214, 488

Shu F. H., Adams F. C., Lizano S., 1987, Annual Review of Astron and Astrophys, 25, 23

Skrutskie M. F., et al., 2006, The Astronomical Journal, 131, 1163

Smartt S. J., 2009, Annual Review of Astron and Astrophys, 47, 63

Sofue Y., Handa T., 1984, Nature, 310, 568 EP

Solomon P. M., Rivolo A. R., Barrett J., Yahil A., 1987, The Astrophysical Journal, 319, 730

Sormani M. C., Barnes A. T., 2019a, Monthly Notices of the Royal Astronomical Society, 484, 1213

Sormani M. C., Barnes A. T., 2019b, Monthly Notices of the Royal Astronomical Society, 484, 1213

Sormani M. C., Li Z., 2020, Monthly Notices of the Royal Astronomical Society, 494, 6030

Sormani M. C., Binney J., Magorrian J., 2015a, Monthly Notices of the Royal Astronomical Society, 449, 2421

Sormani M. C., Binney J., Magorrian J., 2015b, Monthly Notices of the Royal Astronomical Society, 451, 3437

Sormani M. C., Binney J., Magorrian J., 2015c, Monthly Notices of the Royal Astronomical Society, 454, 1818

Sormani M. C., Treß R. G., Ridley M., Glover S. C. O., Klessen R. S., Binney J., Magorrian J., Smith R., 2018, Monthly Notices of the Royal Astronomical Society, 475, 2383

Sormani M. C., Tress R. G., Glover S. C. O., Klessen R. S., Battersby C. D., Clark P. C., Hatchfield H. P., Smith R. J., 2020, Monthly Notices of the Royal Astronomical Society, 497, 5024

Spitzer Lyman J., Fitzpatrick E. L., 1993, The Astrophysical Journal, 409, 299

Stahler S. W., Shu F. H., Taam R. E., 1980, The Astrophysical Journal, 242, 226

Su M., Slatyer T. R., Finkbeiner D. P., 2010, The Astrophysical Journal, 724, 1044

Tabone B., Godard B., Pineau des Forêts G., Cabrit S., van Dishoeck E. F., 2020, arXiv e-prints, p. arXiv:2003.01845

Tafalla M., Bachiller R., Lefloch B., Rodríguez-Fernández N., Codella C., López-Sepulcre A., Podio L., 2015, Astronomy & Astrophysics, 573, L2

Talbot Jr. R. J., Jensen E. B., Dufour R. J., 1979, The Astrophysical Journal, 229, 91

Tan J. C., Kong S., Butler M. J., Caselli P., Fontani F., 2013, The Astrophysical Journal, 779, 96

Tasker E. J., Tan J. C., 2009, The Astrophysical Journal, 700, 358

Terrier R., et al., 2010, The Astrophysical Journal, 719, 143

Terrier R., Clavel M., Soldi S., Goldwurm A., Ponti G., Morris M. R., Chuard D., 2018, Astronomy & Astrophysics, 612, A102

Thatte N., Tecza M., Genzel R., 2000, Astronomy & Astrophysics, 364, L47

Tielens A. G. G. M., Allamandola L. J., 1987, in Morfill G. E., Scholer M., eds, NATO ASIC Proc. 210: Physical Processes in Interstellar Clouds. pp 333–376

Tokuyama S., Oka T., Takekawa S., Iwata Y., Tsujimoto S., Yamada M., Furusawa M., Nomura M., 2019, Publications of the ASJ, 71, S19

Tomisaka K., 1995, The Astrophysical Journal, 438, 226

Tomisaka K., 1996, Publications of the ASJ, 48, 701

Toomre A., 1964, The Astrophysical Journal, 139, 1217

Tremblay C. D., Walsh A. J., Longmore S. N., Urquhart J. S., König C., 2015, Publications of the Astron. Soc. of Australia, 32, e047

Tully R. B., et al., 2013, The Astronomical Journal, 146, 86

Turner J. L., Ho P. T. P., Beck S., 1987, The Astrophysical Journal, 313, 644

Usero A., García-Burillo S., Martín-Pintado J., Fuente A., Neri R., 2008, in Kramer C., Aalto S., Simon R., eds, EAS Publications Series Vol. 31, EAS Publications Series. pp 117–122, doi:10.1051/eas:0831024

Usero A., et al., 2015, The Astronomical Journal, 150, 115

Vogler A., Madden S. C., Beck R., Lundgren A. A., Sauvage M., Vigroux L., Ehle M., 2005, Astronomy & Astrophysics, 441, 491

Wada K., Koda J., 2004, Monthly Notices of the Royal Astronomical Society, 349, 270

Wada K., Baba J., Saitoh T. R., 2011, The Astrophysical Journal, 735, 1

Walker D. L., et al., 2018a, Monthly Notices of the Royal Astronomical Society, 474, 2373

Walker D. L., et al., 2018b, Monthly Notices of the Royal Astronomical Society, 474, 2373

Walker D. L., et al., 2018c, Monthly Notices of the Royal Astronomical Society, 474, 2373

Walmsley C. M., Guesten R., Angerhofer P., Churchwell E., Mundy L., 1986, Astronomy & Astrophysics, 155, 129

Walsh A. J., et al., 2011a, Monthly Notices of the Royal Astronomical Society, 416, 1764

Walsh A. J., et al., 2011b, Monthly Notices of the Royal Astronomical Society, 416, 1764

Walsh A. J., Purcell C. R., Longmore S. N., Breen S. L., Green J. A., Harvey-Smith L., Jordan C. H., Macpherson C., 2014, Monthly Notices of the Royal Astronomical Society, 442, 2240

Whittet D. C. B., Duley W. W., Martin P. G., 1990, Monthly Notices of the Royal Astronomical Society, 244, 427

Williams J. P., McKee C. F., 1997, The Astrophysical Journal, 476, 166

Williams J. P., Blitz L., McKee C. F., 2000, in Mannings V., Boss A. P., Russell S. S., eds, Protostars and Planets IV. p. 97 (arXiv:astro-ph/9902246)

Williams S. J., Bonanos A., Whitmore B., Prieto J. L., Blair W. P., 2015, IAU General Assembly, 22, 2255001

Yukita M., et al., 2016, The Astrophysical Journal, 824, 107

Yusef-Zadeh F., et al., 2008, in American Astronomical Society Meeting Abstracts #212. p. 213

Zeng S., et al., 2018, Monthly Notices of the Royal Astronomical Society, 478, 2962

Zetterlund E., Glenn J., Rosolowsky E., 2019, The Astrophysical Journal, 881, 90

Zhang Q., Wang Y., Pillai T., Rathborne J., 2009, The Astrophysical Journal, 696, 268

Zinnecker H., Yorke H. W., 2007, Annual Review of Astron and Astrophys, 45, 481

Zschaechner L. K., et al., 2018, The Astrophysical Journal, 867, 111

Zucker C., Battersby C., Goodman A., 2018, The Astrophysical Journal, 864, 153

van Dishoeck E. F., 2014a, Faraday Discussions, 168, 9

van Dishoeck E. F., 2014b, Faraday Discuss., 168, 9

van Dokkum P. G., 2008, The Astrophysical Journal, 674, 29

van der Tak F. F. S., van Dishoeck E. F., Caselli P., 2000, Astronomy & Astrophysics, 361, 327

van der Tak F. F. S., Black J. H., Schöier F. L., Jansen D. J., van Dishoeck E. F., 2007, Astronomy & Astrophysics, 468, 627